JOURNAL OF APPLIED PHYSICS

Vol. 31, No. 6 June, 1960

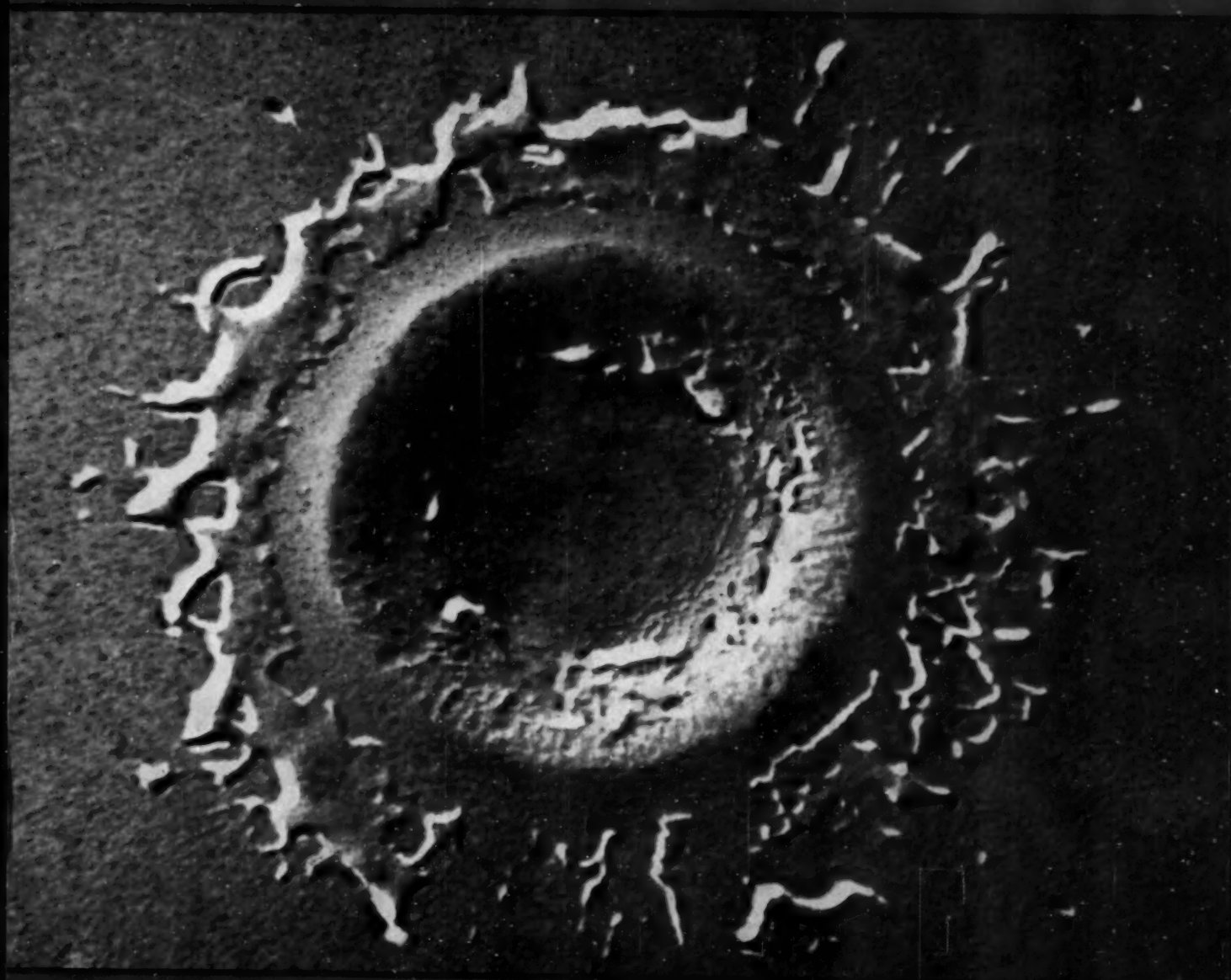

Electron Micrograph of a Crater in a Thin Aluminum Film.
See Page 1121.

NEW FRAMING CAMERA

for the research group that has everything

This is the production model of the new Beckman & Whitley Model 192 Continuous-Writing Framing Camera.

Delivered to Avco Research and Advanced Development Division, outside Boston, the instrument will be used in experimental studies with high-temperature electric arcs or plasma jets, hypervelocity instrumentation, aeroballistics, and aerothermodynamics.

Shown focusing the objective lens of the newly installed camera is Glenn Hanson, head of the physics photography section of the division.

Chiefly, the advantage of the Model 192 is that it is capable of making 80 35-mm photographs of an ultra-high-speed event without the necessity of synchronizing the camera and the event. Its top operating speed is 1,400,000 exposures per second.

May we send you further details or discuss with you the problems you may have which the Model 192 or one of our other cameras might solve?

Beckman & Whitley

SAN CARLOS 8, CALIF. · U.S.A.

JOURNAL OF APPLIED PHYSICS

Vol. 31, No. 6 JUNE, 1960

In This Issue

Dislocation Damping Effects in Rock Salt . . . Charles L. Bauer and Robert B. Gordon 945
Intervalley Noise . . . P. J. Price 949
Minority Carrier Recombination in a Cylindrical Transistor Base Region . . . David P. Kennedy 954
Transport of Noise at Microwave Frequencies through a Space-Charge-Limited Diode . . . W. E. Vivian 957
On the Flow of a Non-Newtonian Liquid on a Rotating Disk . A. Acrivos, M. J. Shah, and E. E. Petersen 963
Photoemission in the Photovoltaic Effect in Cadmium Sulfide Crystals . . . Richard Williams and Richard H. Bube 968
p Layers on Vacuum Heated Silicon . . . F. G. Allen, T. M. Buck, and J. T. Law 979
Paramagnetic Susceptibilities of Fe and Fe-Si Alloys . . . Sigurds Arajs and D. S. Miller 986
Production and Properties of Thin Layers of Indium Antimonide . . . G. Bate and K. N. R. Taylor 991
Vapor-Deposited Single-Crystal Germanium . Ralph P. Ruth, John C. Marinace, and W. C. Dunlap, Jr. 995
Positive Column Formation in Ion Sources Employing Surface Ionization . P. L. Auer and H. Hurwitz, Jr. 1007
Measurement of Elastic Constants of RbBr, RbI, CsBr, and CsI by an Ultrasonic cw Resonance Technique . . . D. I. Bolef and M. Menes 1010
Mechanism of Inert Gas Cleanup in a Gaseous Discharge . . . K. B. Blodgett and T. A. Vanderslice 1017
On the Neutron Bombardment Reduction of Transistor Current Gain . . J. W. Easley and J. A. Dooley 1024
Bias in Ferroelectric Colemanite . . . Ennio Fatuzzo 1029
Beta Particle Transmission Currents in Solid Dielectrics . . . Bernhard Gross, Arthur Bradley, and Arthur P. Pinkerton 1035
Single-Crystal Magnetic Anisotropy and Magnetostriction Studies in Iron-Base Alloys . . . R. C. Hall 1037
Surface Wave Excitation and Propagation . . . Joseph B. Keller and Frank C. Karal, Jr. 1039
Range of Radiation Induced Primary Knock-Ons in the Hard Core Approximation . . . D. K. Holmes and G. Leibfried 1046
Displacement of the Sulfur Atom in CdS by Electron Bombardment . . . B. A. Kulp and R. H. Kelley 1057
Electron Probe Measurements of Evaporated Metal Films . . . W. E. Sweeney, Jr., R. E. Seebold, and L. S. Birks 1061
On the Theory of the Close-Spaced Impregnated Cathode Thermionic Converter . . . E. S. Rittner 1065
Etch Pits at Dislocations in Copper . . . J. D. Livingston 1071
Theory of Dislocation Climb in Metals . . . Jens Lothe 1077
Photoeffects in Nonuniformly Irradiated p-n Junctions . . . Gerald Lucovsky 1088
Tensile Properties of Thin, Evaporated Gold Films . . . C. A. Neugebauer 1096
Simple Radiant Heating Method for Determining the Thermal Diffusivity of Cellulosic Materials . . . Stanley B. Martin 1101
Properties of p-Type GaAs Prepared by Copper Diffusion . F. D. Rosi, D. Meyerhofer, and R. V. Jensen 1105
Excitation Processes in Ceramics and Anomalous Increase in Thermal Conductivity at Elevated Temperatures . . . D. H. Whitmore 1109
Ferromagnetic Resonance in Polycrystalline Ferrites Using Circularly Polarized Radiation . . . R. J. Zeender and E. Schlömann 1112
Preparation of Large Area Single-Crystal Cuprous Oxide . Robert S. Toth, Rein Kilkson, and Dan Trivich 1117

Letters to the Editor:

Tensile Strength of Pyrolytic Graphite up to 2750°C . . . H. E. Martens and L. D. Jaffe 1122
Discussion of Criteria for the *In Situ* Combustion of Crude Oil . . . S. E. Szasz 1122
Remarks on "Some Criteria for the *In Situ* Combustion of Crude Oil" . . . H. R. Bailey and B. K. Larkin 1123
Reply to the Letters of Szasz, and Bailey and Larkin . . . Philip Cooperman 1124
Dielectric Behavior of Single Crystals of Tri-Glycine Sulfate (TGS) from 1 kc to 2500 Mc . A. Lurio and E. Stern 1125
Hooke's Law in Shear and Polymer Melt Fracture . . . E. B. Bagley 1126
Surface Deformation of Aluminum in Fatigue . . . J. C. Grosskreutz and C. M. Gosselin 1127
Comments on a Ruptured Soap Film . . . F. E. C. Culick 1128
More Experiments on Liquid Films . . . R. M. Koros, J. Deckers, and M. Boudart 1129
Antiferromagnetic $FeVO_3$ . . . Chester R. Berry and Charles M. Combs 1130
Comments on "Determination of Atomic Scattering Factors" . . . D. R. Chipman and Arthur Paskin 1130
Reply to Comments on "Determination of Atomic Scattering Factors" . . . R. B. Roof, Jr. 1131
Solubilities and Diffusivities of Nitrogen in Polyethylene . . . J. L. Lundberg, M. B. Wilk, and M. J. Huyett 1131
Distribution of Spray from Impinging Liquid Jets . . . K. Dexter Miller, Jr. 1132
Use of SF_6^- for Calibration of the Electron Energy Scale . . . G. J. Schulz 1134
Diode Capacitors for Parametric Amplification . . . R. C. Knechtli and R. D. Weglein 1134
Comments on "Diode Capacitors for Parametric Amplification" by R. C. Knechtli and R. D. Weglein . . . K. E. Mortenson 1135
Preparation of Tin Single Crystals for Transmission Electron Microscopy . . . J. T. Fourie, F. Weinberg, and F. W. C. Boswell 1136
Continuous Series of Metastable Solid Solutions in Silver-Copper Alloys . . . Pol Duwez, R. H. Willens, and W. Klement, Jr. 1136
Metastable Electron Compound in Ag-Ge Alloys . . . Pol Duwez, R. H. Willens, and W. Klement, Jr. 1137
Erratum: Motion of High-Speed Arc Spots in Magnetic Fields . . . D. Zei and J. G. Winans 1137

Books Reviewed . . . 1137
Books Received . . . 1139
Announcements . . . 1140
Cover Photograph . . . 1121

JOURNAL OF APPLIED PHYSICS

A journal of general physics and its applications to other sciences and to industry

Published by the

American Institute of Physics

THE JOURNAL OF APPLIED PHYSICS is devoted to general physics and its applications to other sciences, to engineering, and to industry. Previous to 1937, this journal was called PHYSICS.

The JOURNAL OF APPLIED PHYSICS welcomes articles of two distinct kinds: (1) Descriptions of new results in experimental or theoretical physics which are of general interest to physicists. The author should explain his contribution in such a way that a physicist or engineer in another field of specialization can appreciate its objectives and essential features. (2) Critical reviews of particular areas of physics or surveys of extensive investigations at a single laboratory. Authors contemplating writing such should correspond with the Editor before they begin writing.

The JOURNAL OF APPLIED PHYSICS welcomes Letters to the Editor which are short [approximately four (4) typewritten pages] communications without abstracts. Timeliness, briefness, and degree of current importance of the subject matter will be of primary concern in the publication of Letters. Letters should not be looked upon as partial publication or announcement of more comprehensive work, but rather self-contained presentations in themselves.

Manuscripts should be submitted to the Editor, James A. Krumhansl, Rockefeller Hall, Cornell University, Ithaca, New York. Authors should read the "Information for Contributors," facing page 1 of the January issue, before writing articles or letters. The *Style Manual* of the American Institute of Physics is also helpful to writers preparing manuscripts for journals published by the American Institute of Physics. It can be obtained for $1.00 from the American Institute of Physics, 335 East 45 Street, New York 17, New York.

Corrected proofs and all correspondence concerning papers in the process of publication should be addressed to the Publication Manager, American Institute of Physics, 335 East 45 Street, New York 17, New York.

Subscriptions, renewals, and orders for back numbers should be addressed to the American Institute of Physics, 335 East 45 Street, New York 17, New York.

Subscription Price	U.S. and Canada	Elsewhere
To members of member organizations of the American Institute of Physics and Affiliated Societies ..	$12.00	$13.00
To all others	14.00	16.00

Back Number Prices

Yearly back number rate when complete year is available: $17.00.
Single copies: $1.75 each (exception: March, 1958—$3.00 each).

Changes of address should be sent to the American Institute of Physics.

Advertising rates supplied on request. Orders, advertising copy, and cuts should be sent to the American Institute of Physics.

The Journal of Applied Physics is published monthly at Prince and Lemon Streets, Lancaster, Pennsylvania.
Second-class postage paid at Lancaster, Pa.

IN TOUCH WITH NEW DIMENSIONS

Another achievement of IBM Applied Scientists: general computer program for job shop simulation

Creating imaginative solutions to problems never solved before is a job of IBM Applied Science Representatives. Through unique applications of data processing, they are exploring new dimensions in engineering, the sciences, and business.

One team of Applied Scientists, for example, worked closely with customers to simulate industrial job shop operations on a computer. A general program for this purpose allows firms to pre-test changes in production scheduling.

Other Applied Science Representatives are working on design analysis, forecasting, problems of mathematical computation, and process control. The range of projects is unlimited.

You may play an important and rewarding part in this stimulating profession. There are openings in many cities for men and women with advanced degrees in engineering, mathematics, or a physical science, or a degree in one of these areas plus a Master's in business administration or experience in programming.

For a confidential interview, please call any IBM Branch Office or one of these Regional Managers of Applied Science:

L. M. Fulton
IBM Corporation
425 Park Avenue
New York 22, N.Y.

R. W. DeSio
IBM Corporation
618 S. Michigan Ave.
Chicago 5, Ill.

L. C. Hubbard
IBM Corporation
3424 Wilshire Blvd.
Los Angeles 5, Calif.

DATA PROCESSING DIVISION **IBM.**

We promise that you will hear from us within one week!

Important openings for senior E.E.'s and Physicists to assume responsibility for development of

new infrared search systems

Progress of the Hughes Infrared and Guidance Department reflects Hughes overall growth. In the past ten years, employment has risen from under 2,000 to over 34,000 in the several semi-autonomous divisions of Systems Development, Research, Commercial Products, Ground Systems, Communications and Manufacturing. The infrared activity includes the typical projects listed at the right.

These activities have created a number of new openings for graduate engineers and physicists with analytical and inventive abilities.

You are invited to investigate these openings if you have several years of applicable experience in infrared, optics or electronics, and can assume responsibility for systems analysis and preliminary design.

The importance of infrared development at Hughes is shown in substantial development contracts and in the fact that Hughes is investing its own funds in further exploration.

1. **Air-To-Air Missiles**
2. **AICBM**
3. **Air-To-Air Detection Search Sets**
4. **Satellite Detection & Identification**
5. **Infrared Range Measurement**
6. **Detection Cryogenics**
7. **Detector Application Physics**
8. **Optical Systems Design**

We invite your earliest inquiry. Wire collect, or airmail resume directly to:

Mr. William Craven, *Manager, Infrared*
Hughes Systems Development Laboratories
Culver City 21, California

HUGHES

Write for reprints of these important technical papers, written by Hughes staff members...
Infrared Search-Systems Range Performance: R. H. Genoud /Missiles Seekers and Homers: W. A. Craven, et al.
Servomechanisms Design Considerations for Infrared Tracking Systems: J. E. Jacobs /Simulation of Infrared Systems: H. P. Meissinger

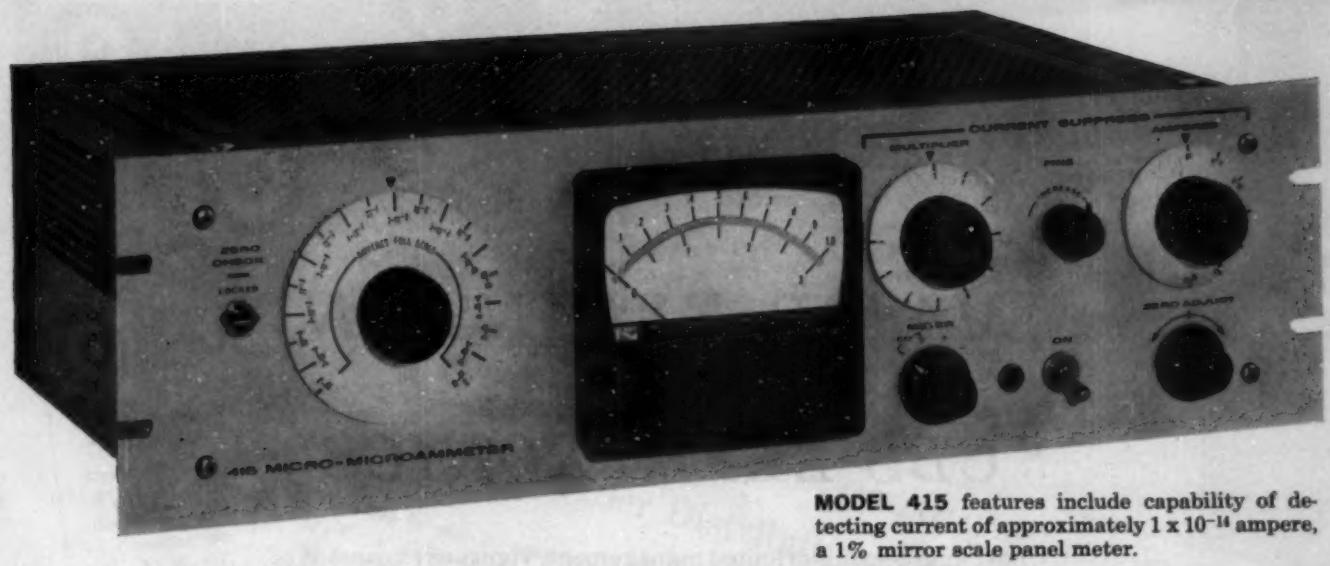

MODEL 415 features include capability of detecting current of approximately 1×10^{-14} ampere, a 1% mirror scale panel meter.

new high-speed research micro-microammeter

Model 415 offers high speed of response, accuracy, and zero suppression.

The new Model 415 incorporates advanced high-speed circuitry developed by Keithley Instruments for rocket and satellite experimentation — where measurements of Lyman-Alpha night glow and upper air density require fast response.

A speed response of less than 600 milliseconds to 90% of final value at 10^{-12} ampere is possible where external circuit capacity is 50 picofarads ($\mu\mu$f). Critical damping of the circuit, with any input capacity, is maintained on all ranges through one infrequent adjustment. There is no possibility of oscillation or poor response, on any range.

Accuracy is ±2% of full scale on 10^{-3} through 10^{-8} ampere ranges, and ±3% of full scale on 3×10^{-9} through 10^{-12} ampere ranges.

The 415 also provides zero suppression up to 100 full scales, permitting full scale display of one per cent variations of a signal. Once suppressed to zero, such variations may be observed on any of the next four more sensitive ranges without re-setting the suppression.

Excelling other Keithley 400 Series Micro-micro-ammeters in speed of response, the 415 is ideal for current measurements in ion chambers, photomultipliers, gas chromatography, mass spectrometry.

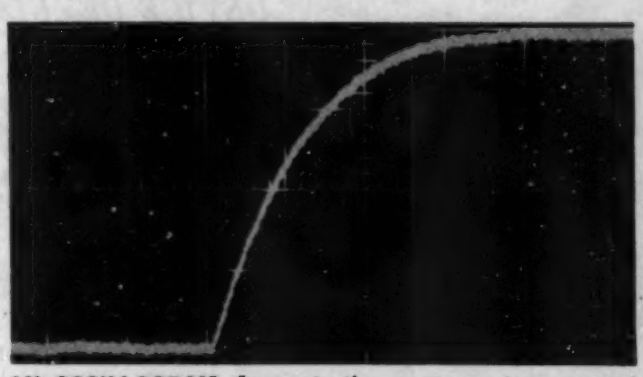

AN OSCILLOGRAM demonstrating response to a current step of 10^{-12} ampere. Input capacity is 35 picofarads ($\mu\mu$f). One major horizontal division equals 200 milliseconds.

BRIEF SPECIFICATIONS

RANGES: 10^{-12}, 3×10^{-12}, 10^{-11}, 3×10^{-11}, etc. to 10^{-3} ampere f.s.

ACCURACY: ±2% f.s. 10^{-3} thru 10^{-8} ampere ranges; ±3% f.s. 3×10^{-9} thru 10^{-12} ampere ranges.

ZERO DRIFT: Less than 2% of f.s. per day after warmup.

INPUT: Grid current less than 5×10^{-14} ampere.

OUTPUT: 1 v f.s. at up to 5 ma. Noise less than 20 mv.

RISE TIME: Typical values given in sec. to 90% of final values.

Range amps f.s.	C_{in} = 50 $\mu\mu$f seconds	C_{in} = 150 $\mu\mu$f seconds	C_{in} = 1500 $\mu\mu$f seconds
10^{-12}	.600	.800	2.5
3×10^{-12}	.200	.300	1.0
10^{-11}	.060	.080	.250
3×10^{-11}	.020	.030	.100
10^{-10}	.006	.010	.030
3×10^{-10}	.002	.003	.010
10^{-9}	.001	.001	.003
3×10^{-9} and above	.001	.001	.001

PRICE: Model 415, $750.00

For complete details, write:

KEITHLEY INSTRUMENTS, INC.
12415 EUCLID AVENUE CLEVELAND 6, OHIO

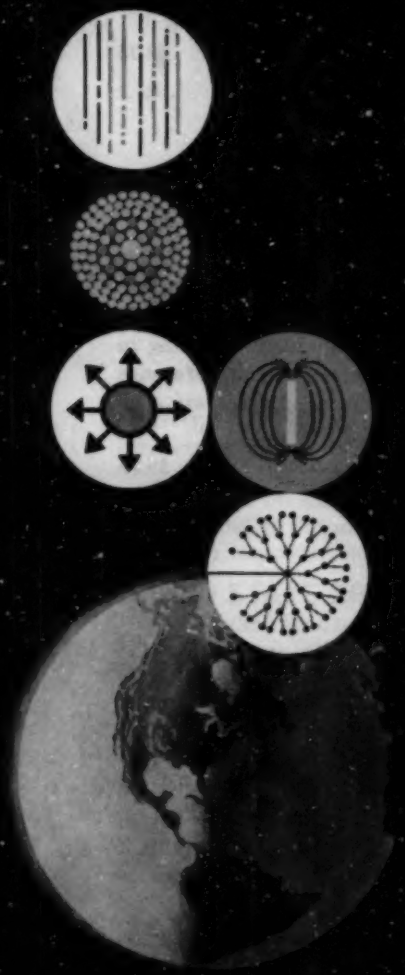

Expanding the Frontiers of Space Technology in

PHYSICS

Lockheed Missiles and Space Division is engaged in a broad, long-range program of basic scientific research at its laboratories adjacent to Stanford University in Palo Alto, California. Equipment is modern and includes extensive facilities for plasma and spectroscopic research; a variety of shock tubes; a 3.5 mev Van De Graaf accelerator; complete laboratory test facilities; and one of the largest and most modern computing centers in the world.

A group of more than fifty physicists is engaged in research and the fundamental investigation of problems in the following areas:

Nuclear Physics: The measurement and theory of nuclear cross sections; beta, gamma and X-ray spectroscopy; theory of nuclear structure; radiation physics.

Theoretical Physics: The phenomenology and effects of atomic explosions and radiative properties in air under conditions of very high temperatures.

Space Physics: Basic research on the physics of the earth's upper atmosphere and beyond, including: measurement of atmospheric composition and density at orbital altitudes; laboratory experiments on upper atmospheric atomic and molecular reactions; hydro magnetic interactions with the earth's magnetic fields; simulation and study of meteor impacts; and particle radiation.

Plasma Physics: Energy transfer between a plasma and external electromagnetic fields; the transport of microwave and optical radiation through plasmas.

Atomic Physics: Mass spectroscopy; theory and measurements of low energy interactions.

Such programs reach far into the future and deal with unknown and challenging environments. If you are experienced in one of the above areas, or in related work such as astrophysics or chemical physics, you are invited to share in the efforts of a company that has an outstanding record of achievement, and make an important individual contribution to your country's scientific progress. Write Research and Development Staff, Dept. F-32, 962 W. El Camino Real, Sunnyvale, California. U.S. citizenship or existing Department of Defense industrial security clearance required.

Lockheed

MISSILES AND SPACE DIVISION

Systems Manager for the Navy POLARIS FBM; the Air Force AGENA Satellite in the DISCOVERER, MIDAS and SAMOS Programs; Air Force X-7; and Army KINGFISHER

SUNNYVALE, PALO ALTO, VAN NUYS, SANTA CRUZ, SANTA MARIA, CALIFORNIA
CAPE CANAVERAL, FLORIDA • ALAMOGORDO, NEW MEXICO • HAWAII

Physicists...

S

I

RESEARCH AND DEVELOPMENT IN SEMICONDUCTORS

Pacific Semiconductors, Inc. recently has made a number of notable accomplishments in the field of semiconductors, including a range of high frequency power transistors, micro miniaturized diodes and transistors. For example, the PSI high frequency transistor line ranges from the largest (100 watts at 5 mc) to the smallest silicon mesa transistors available.

These accomplishments have created important new opportunities at PSI. In addition, PSI is broadening its range of activities to include such new fields as solid state circuits.

The nature of the semiconductor field has created an unusual need and opportunity for physicists at PSI. We are seeking highly competent scientists who have an interest in solid state research and development.

Experience in the field is highly desirable. However, if you lack such experience but believe you have unusual ability and a desire for stimulating and challenging work, we would like to hear from you.

SURFACE RESEARCH Basic research on semiconductor surfaces with the ultimate objective of increasing the state of understanding of semiconductor surface phenomena. Whatever theoretical and experimental approaches are required in order to accomplish this goal will be employed. An important part of this objective will be the correlation of surface film composition and structure with the physical model of the surface. A surface design theory of fundamental value might reasonably be expected to be an important outgrowth of this endeavor.

SOLID STATE DIFFUSION Investigation and improvement of solid state diffusion processes. This includes fundamental work on diffusion mechanisms and the growth and control of oxide layers at the surface. Some or all of the following experience is highly desirable: High furnace temperature operation, gaseous purge systems, light interference measurement techniques.

DEVICE PHYSICS Balanced experimental and theoretical research on new processes and new devices of advanced types. Read and understand semiconductor literature. Work with chemists, metallurgists and electronic engineers. Supervise experiments involving advanced laboratory measurement techniques, including infrared, X-ray and electrical. Diffusion, surfaces, crystal imperfections, device theory, process theory.

SEMICONDUCTOR MATERIALS — INTERMETALLIC COMPOUNDS Physical chemists or physicists to work in preparation and purification of semiconductor elements and intermetallic compounds. The work also may include the study of decomposition reactions of silanes and halides of silicon to form single crystal deposits of pure silicon. Interest in infrared absorption studies desirable.

These are only a few of the many fine opportunities available at PSI. If you have an M.S. or Ph.D. degree in physics or a B.S. degree and equivalent experience in semiconductor physics, write today in confidence to:

DR. J. W. PETERSON, *Director, Research and Development*

or MR. LARRY LONG, *Head, Technical Staff Placement*

PSI® *Pacific Semiconductors, Inc.*

10451 WEST JEFFERSON BOULEVARD • CULVER CITY, CALIFORNIA

RESEARCH AT COLLINS

THE UNUSUAL SHAPE OF PROGRESS

A company sponsored research program to investigate the operation of parametric amplifiers has resulted in improved communication equipment in the uhf frequency range. Collins engineers decided to attack the problem from the standpoint of circuitry rather than device design, and the two-port uhf parametric amplifier shown above emerged from Collins Research Laboratories. Final development resulted in an amplifier with a gain-bandwidth product more than twice that of previous amplifiers.

In the Advanced Circuits Division of Collins Research Laboratories, physicists, mathematicians and engineers are planning basic research programs in solid state physics. Research in the field of thermoelectric phenomena is now in progress. Other studies are being conducted in this division in the general area of modulation and information theories, and traveling wave principles. To further this work, and to advance scientific knowledge with the resultant development of new technologies in other areas, unique professional opportunities are now being offered by Collins Research Division in radio astronomy, advanced circuits, advanced systems, antennas and propagation, mechanical sciences and mathematics. Your inquiry is invited.

COLLINS

COLLINS RADIO COMPANY • CEDAR RAPIDS, IOWA • DALLAS, TEXAS • BURBANK, CALIFORNIA

Journal
of
Applied Physics

Volume 31, Number 6 June, 1960

Dislocation Damping Effects in Rock Salt*

CHARLES L. BAUER† AND ROBERT B. GORDON
Hammond Metallurgical Laboratory, Yale University, New Haven, Connecticut
(Received November 18, 1959; revised manuscript received February 10, 1960)

Internal friction measurements made as a function of strain amplitude on deformed sodium chloride single crystals were followed by elastic modulus measurements made during x irradiation of the same crystals. Etch pit densities were also determined. These data were used to evaluate the constants in a theory, proposed by Granato and Lücke in 1956, which permits the calculation of the average length of the dislocation segments, L, which vibrate under an applied alternating stress. An independent determination of the magnitude of L was made from the elastic modulus data using a method developed by Gordon and Nowick.

It is concluded that the theories tested in this paper give a useful representation of dislocation damping phenomena in sodium chloride and permit use of internal friction measurements for the continuous observation of dislocations.

INTRODUCTION

INTERNAL friction in crystals resulting from the motion of dislocations under a periodic driving stress was first recognized about twenty years ago.[1] The observed energy losses were much smaller than those to be expected from freely moving dislocations and it was concluded that dislocation motion is restricted in some manner.[2] Dislocation network, impurity atom, and vacancy pinning all may possibly contribute to this restriction. The interaction of the stress fields of oscillating dislocations may also be a contributing effect, particularly in heavily deformed material. Although a number of theories of dislocation damping have been developed very few of them have been worked through to the point where they can be critically tested against experiment. The theory of Granato and Lücke,[3] however, has been sufficiently developed to make a number of quantitative predictions. The model used in their theory describes dislocation damping as being composed of two parts: One part is amplitude independent and is due to the damped vibration of dislocation segments lying between point defect pinning points. The other part is amplitude dependent and is caused by the breakaway of the dislocation segments from their pinning points; only the node points where several dislocations intersect then anchor the dislocation line. There is a decrease in elastic modulus relative to that of the perfect crystal associated with each of these damping mechanisms.

It has been found that in ionic crystals the number of pinning points along dislocations can be increased by irradiation with x rays or γ rays. A theory of the elastic modulus change resulting from this radiation induced pinning has been given by Gordon and Nowick.[4] Both this theory and that of Granato and Lücke make use of the dislocation density and the average distance between pinning points so that it should be possible to compare the two quantitatively, provided that all the necessary measurements are made on each crystal used. Once the reliability of the models used to describe these effects is known for a given material, it will be possible to use internal friction and elastic modulus measurements to follow such quantities as dislocation density and dislocation segment length during deformation and recovery. Perhaps then information about the

* Research supported by The National Science Foundation.
† Based on a report prepared in partial fulfillment of the requirements for the degree of Master of Engineering at the School of Engineering, Yale University.
[1] T. A. Read, Trans. AIME 143, 30 (1941).
[2] J. S. Kochler, *Imperfections in Nearly Perfect Crystals* (John Wiley & Sons, Inc., New York, 1952), p. 197.
[3] A. Granato and K. Lücke, J. Appl. Phys. 27, 583, 789 (1956); *Dislocations and Mechanical Properties of Crystals* (John Wiley & Sons, Inc., New York, 1957), p. 425.
[4] R. B. Gordon and A. S. Nowick, Acta Met. 4, 514 (1956).

TABLE I. Experimentally determined quantities needed to evaluate the parameters of the theories.

Spec.	% Comp.	$I\times10^{8}$	$S\times10^{8}$	$\Delta_I\times10^{4}$	$(\Delta E/E)_I\times10^{8}$	$\Lambda\times10^{-6}$ cm^{-2}	J min^{-1}
A	3.3±0.1	18±1.0	3.8±0.3	81±2	40.2±0.5	16±2.0	0.33±0.02
B	2.4	12±0.6	3.9	61	32.8	11±1.5	0.83±0.04
C	1.6	9.8±0.4	4.1	40	23.9	8.1±1.0	1.3 ±0.1
D	1.5	7.2±0.3	4.6	34	19.4	6.4±0.8	1.8 ±0.2
E	0.6	5.8±0.2	5.2±0.5	21	16.6	2.3±0.3	2.9 ±0.3
F	0	2.5±0.5	9±5	0	8.8	0.5±0.3	...

amount and distribution of impurities, the apparent increase of vacancy content during deformation, dislocation vibration amplitudes and the damping constant could be obtaned.

EXPERIMENTAL PROCEDURE AND RESULTS

The experiments were performed with single crystals of sodium chloride obtained from the Harshaw Chemical Company. Crystals were cleaved and ground along [100] planes to the appropriate size and were then deformed in compression so as to introduce fresh dislocations and vary the dislocation density. Measurements were made using a composite piezoelectric resonator operating at 89.7 kc and the ac bridge method developed by Cooke and Brown[5] and Read.[6] This method allows simultaneous determination of the elastic modulus and internal friction as a function of strain amplitude. Measurements could also be made during irradiation with 31 kv x rays from a copper target. The information needed to determine the rate of formation of F centers was obtained from optical absorption measurements made with a Bausch and Lomb spectrophotometer.[7]

A solution of absolute ethyl alcohol to which was added a small amount of ferric nitrate [$Fe(NO_3)_3\cdot9H_2O$] was used to etch the crystals. Etch pit densities were obtained from photographs of a freshly cleaved and etched surface. Only etch pits in the interior of the sub grains were used to calculate the etch pit densities.

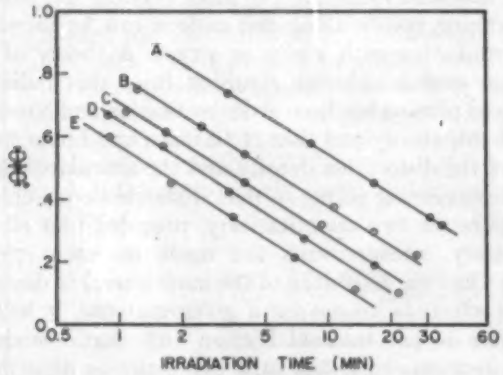

FIG. 1. Φ/Φ_0 as defined by Eq. (5) plotted vs log t for specimens A through E listed in Table I.

The Granato and Lücke theory gives the amplitude independent decrement, Δ_I, and the associated elastic modulus change, $(\Delta E/E)_I$, resulting from dislocation vibration in the kilocycle range of frequencies as

$$\Delta_I = A_1\Lambda L^4 \tag{1}$$

and

$$(\Delta E/E)_I = A_2\Lambda L^2, \tag{2}$$

where Λ is the dislocation density and the average dislocation loop length, L, is defined by the expression

$$1/L = 1/L_c + 1/L_N. \tag{3}$$

L_c is the length of the dislocation segment between defect pinning points and L_N is the distance between intersections of the dislocation network. The constants A_1 and A_2 in these equations are given by

$$A_1 = 120\omega\Omega B/\pi^3 C \quad A_2 = 6\Omega/\pi^2,$$

where Ω is an orientation factor taking into account the fact that the resolved shear stress on the slip plane is less than the applied longitudinal stress. Ω is given a value of 0.1 following Granato and Lücke. C is the tension of the dislocation line, the frequency is $\omega/2\pi$, and B is the damping constant of a moving dislocation. The elastic modulus observed in these experiments is $1/s_{11}$. Δ_I was obtained by subtracting the decrement of the fully irradiated crystal, i.e., the crystal with the dislocations fully pinned, from that measured at low strain amplitude.

At the frequency used (89.7 kc) the strain amplitude dependent part of the decrement, derived for a random distribution of pinning points, is given by Granato and Lücke as

$$\Delta_H = A_3\Lambda L_N^3/\epsilon_m L_c^2 \exp(-A_4/\epsilon_m L_c) \tag{4}$$

where

$$A_3 = \Omega A_4/\pi^2 \quad A_4 = \pi P_m/4aQE.$$

Here ϵ_m is the maximum strain amplitude, P_m is the force exerted by the dislocation line on a pinning point which will just cause break-away, Q is a resolved shear stress factor which is 0.354 for sodium chloride stressed in a [100] direction and a is the lattice constant. In the case of NaCl, where there are electrostatic as well as elastic interactions between point defects

[5] W. T. Cooke and W. F. Brown, Phys. Rev. **50**, 1158 (1936).
[6] T. A. Read, Phys. Rev. **58**, 371 (1940).
[7] R. B. Gordon and A. S. Nowick, Phys. Rev. **101**, 977 (1956).

TABLE II. Calculated values of the parameters of the theory of Granato and Lücke and that of Gordon and Nowick using the data from Table I.

	Granato and Lücke Theory					Gordon and Nowick Theory	
Spec.	$P_m \times 10^5$ dynes	$L \times 10^4$ cm	$L_c \times 10^4$ cm	$L_N \times 10^4$ cm	$B \times 10^4$ gm/sec cm	$\beta \times 10^{-4}$	$L \times 10^4$ cm
A	1.6±0.3	2.1±0.5	3.7±0.5	4.8±0.5	21±3	16±8	0.70±0.03
B	1.8±0.3	2.2	4.1	4.9	13	9±6	0.88
C	1.9±0.3	2.2	4.0	4.9	12	8±5	0.93
D	2.1±0.3	2.2	4.0	5.2	9	8±5	0.96
E	3.8±0.4	3.5	6.9	6.9	0.7±0.3	6±5	1.1
F	13±5	5.4±0.6	13±2	9.0±1.1	...	...	...

and dislocations,[8] it is better to use a constant which represents the total force exerted by a dislocation on a pinning point, i.e., P_m, rather than just a term for the elastic interaction alone as is done in the usual way of writing Eq. (4). Equation (3) may be written in the form $\ln(\Delta_H \epsilon_m) = \ln I - S/\epsilon_m$ where $I = A_2 \Lambda L_N^3 / L_c^2$ and $S = A_4/L_c$. Thus, from a plot of $\ln(\Delta_H \epsilon_m)$ vs $1/\epsilon_m$, S and I can be determined.

Gordon and Nowick have approached the subject of dislocation pinning by studying the effect of x irradiation on the room temperature elastic modulus of rock salt single crystals. Assuming the number of pinning points created by irradiation is proportional to the number of F centers formed, they derive the expression

$$\frac{\Phi}{\Phi_0} = \frac{1}{\alpha d}\left[\frac{1}{1+Jt} - \frac{1}{1+Jte^{-\alpha d}} + \ln\frac{1+Jte^{-\alpha d}}{(1+Jt)e^{-\alpha d}}\right]. \quad (5)$$

The "modulus defect" Φ is defined as $(E^\infty - E)/E^\infty$ where E^∞ is the saturation value of the elastic modulus, E, of the specimen attained after prolonged irradiation. The quantity Φ_0 represents the modulus defect at the start of irradiation. α is the effective adsorption coefficient of x rays in the crystal, d is the crystal thickness, t is the irradiation time, and J is defined as

$$J = LD/\Lambda\beta, \quad (6)$$

where β is the number of F centers formed for each pinning point created by the irradiation. The quantity D, which may be obtained from optical absorption measurements on a crystal irradiated in the same manner as the modulus specimens, is a measure of the rate of formation of F centers with the x ray source used (see Appendix). Φ_0 is shown to be

$$\Phi_0 = \Lambda L^2/\xi, \quad (7)$$

where ξ is a dimensionless constant found by Gordon and Nowick to be about 2.5.

The expression on the right-hand side of Eq. (5) has the property that, in a plot of Φ/Φ_0 vs $\ln t$, the factor α determines the slope of the curve while J only determines its position along the $\ln t$ axis. Figure 1 shows data for five rock salt specimens plotted so that α and J may be found. The best fit of Eq. (5) to the data of Fig. 1 is obtained with $\alpha = 12$ cm^{-1}. The values of J were then obtained from the position of the curves along the $\ln t$ axis and are given in Table I.

In order to obtain a complete set of data the following experimental program was used with each crystal: After deformation the internal friction is measured as a function of strain amplitude. The crystal is then irradiated and the modulus measured as a function of x-ray dose. Finally the etch pit density is measured in order to determine Λ. Then a total of seven equations [(1), (2), (3), (6), (7) and the definitions of S and I] are available for the calculation of six unknown parameters, viz., P_m, L, L_c, L_N, β, and B. There is, thus, an independent check on one of the parameters for each crystal used; an important feature of the present experiments.

Figure 2 shows the experimental data for a series of crystals deformed different amounts plotted in such a manner that the slope S and intercept I may be found [see Eq. (4)]. The experimentally determined values of S and I are listed in Table I. All the necessary data to determine the six unknowns in the two theories are

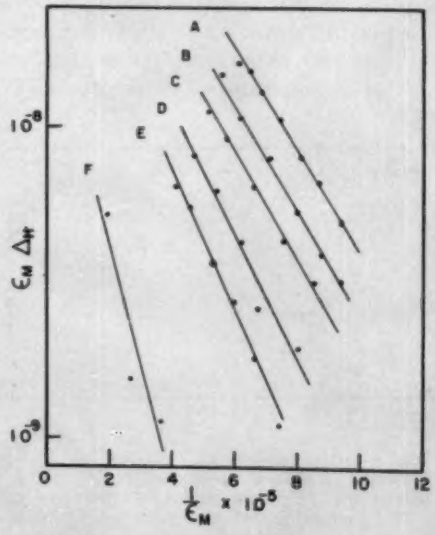

FIG. 2. Logarithm of the product of the amplitude dependent decrement, Δ_H, multiplied by the maximum strain amplitude, ϵ_m, plotted vs the reciprocal maximum strain amplitude for the six sodium chloride specimens listed in Table I.

[8] J. D. Eshelby, C. W. A. Newey, P. L. Pratt, and A. B. Lidiard, Phil. Mag. 3, 75 (1958); F. Bassani and R. Thomson, Phys. Rev. 102, 1264 (1956).

now available. The seven values (one unknown being found in two different ways) obtained for each specimen are shown in Table II. The results for specimens E and F are not as reliable as those for the more heavily deformed specimens because of the lack of data points in the plots of $\ln(\Delta_H \epsilon_m)$ vs $1/\epsilon_m$.

DISCUSSION

The values of L obtained by the two independent methods show sufficient agreement to indicate that the theories used give a useful representation of dislocation vibration phenomena in rock salt. In both cases L decreases with increasing deformation indicating the number of pinning agents per unit length of dislocation segment is increased by deformation. However, this trend may not be particularly significant because of the accompanying change in P_m and β. These quantities would be expected to remain constant, at least to a first approximation. Actually they show a systematic variation with increasing deformation for reasons that are not clear at present. However useful values of Λ and can be calculated from the internal friction and modulus data by using averages of the P_m and β values listed in Table II.

Another test of the Granato-Lücke theory can be made in the following way: Inspecting Eqs. (1) and (2) it is seen that if L is approximately constant the dislocation density should be a linear function of both the elastic modulus change $(\Delta E/E)_I$ and the amplitude independent internal friction Δ_I. As shown in Fig. 3 this holds quite well except for crystal E and F which are lacking in fresh dislocations.

The dislocation density increases rapidly with small amounts of deformation indicating that fresh dislocations are created as plastic deformation proceeds, and that grown-in dislocations probably play a minor part in the plastic flow of rock salt. Other experiments on both metals and ionic crystals also show this rapid increase in dislocation density.[9] Thus for small deformations one might expect that the model assumed in the Granato and Lücke theory does not obtain because of the absence of fresh dislocations.

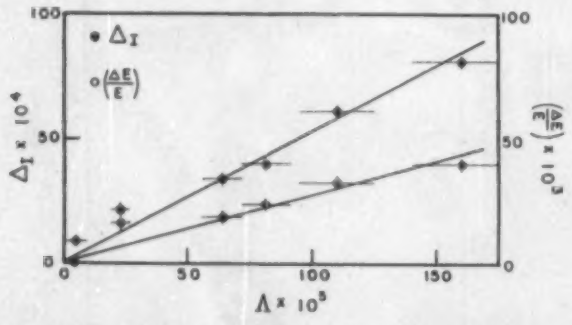

FIG. 3. Strain amplitude independent decrement Δ_I and modulus change $(\Delta E/E)_I$ plotted vs the measured dislocation density Λ. The straight lines were drawn so as to pass through the origin.

While the exact impurity content of the crystals used is unknown, a concentration of about 3×10^{-6} has been suggested for Harshaw rock salt.[10] Using this value and assuming a cubic dispersion of particles, L_c should be about 30 A. However, as dislocation lines provide low energy sites for solute atoms, it is reasonable to assume that, given sufficient time for diffusion, most of the impurities will cluster around dislocations. Therefore it seems probable that dislocations in the sub grain boundaries are fully pinned and do not contribute appreciably to the damping. It would be expected, then, that the dislocations in an annealed crystal would be fully pinned; in fact, measurements on such a crystal showed virtually no dislocation damping or modulus change upon irradiation.

The exact mechanism by which dislocations are pinned during irradiation of rock salt has not yet been resolved. The large value of β found in the present experiments may be explained by assuming that a large number of F centers are formed, during early irradiation, from vacancies already present in the crystal. The value of β was also calculated by comparing the rate of formation of F centers, determined optically, with the rate of formation of pinning points determine from the change of damping with x-ray dose, i.e., $d(\Lambda/L)/dt$. For a typical crystal, β was found in this way to have a value of 4×10^5. This is in general agreement with the results in Table II.

The dislocation network length $L_N \simeq 5\times10^{-4}$ cm found in these experiments appears to be reasonable although it is of nearly the same magnitude as L_c. Methods which allow the direct microscopic observation of dislocation segments by "decoration" have been developed by Amelinckx,[11] who applies this method to the study of dislocation patterns in deformed and annealed sodium chloride single crystals. The network lengths observed are similar to those found here. This implies that L_N does not change very much during the heat treatment of the crystals in the decorating process and that recovery after deformation involves point defect pinning rather than extensive dislocation rearrangement.

For a network length of 5×10^{-4} cm the calculated maximum displacement of the dislocation loop was found to be approximately 36 A for a strain amplitude of 5×10^{-7}. The displacement at the largest strain amplitude used in these experiments is 150 A. These values are consistent with the model used in the Granato-Lücke theory of damping. Some difficulty with the magnitude of the dislocation bowing had been encountered previously which made the breakaway picture questionable.[10]

[9] W. G. Johnston and J. J. Gilman, J. Appl. Phys. **30**, 129 (1959); A. Hikata, R. Truell, A. Granato, B. Chick, and K. Lücke, J. Appl. Phys. **27**, 396 (1956).

[10] A. Granato, A. Hikata, and K. Lücke, Acta Met. **6**, 470 (1958).

[11] S. Amelinckx, Phil. Mag. **1**, 269 (1956).

Another theory of damping, based on the Mott-Nabarro theory of dislocation motion,[12] has been presented by Weertman and Salkovitz,[13] who obtained the expression

$$\Delta_I = (\Delta E/E)_I \simeq \Lambda a^2 \times 10^{-2}/(c\eta)^{\frac{1}{3}}, \quad (8)$$

where c is the concentration of foreign atoms and η is the fractional difference in size between the solute and solvent atoms. Using the value of Λ for specimen C in Table I, for example, Eq. (8) is found to have the approximate value of 6.8×10^{-3}. Comparing this value with the measured values of Δ_I and $(\Delta E/E)_I$ from Table I, it is evident there is a measure of agreement; however, according to Eq. (8), $\Delta_I = (\Delta E/E)_I$ which is not observed; experimental evidence indicates that $\Delta_I < (\Delta E/E)_I$.

Since the internal friction measurements were not made as a function of frequency, the linear dependence of the damping on frequency predicted by Eq. (1) could not be checked. There is some evidence that the damping loss does not vary linearly with frequency in the kilocycle range[14] so that Eq. (1) could not be used to calculate the true damping constant. This does not influence any of the above conclusions because Eq. (1) is used only to calculate B.

CONCLUSION

The two theories tested in this paper give a useful representation of dislocation vibration phenomena in rock salt: The dependence of Δ_I and $(\Delta E/E)_I$ on the dislocation density as predicted by Granato and Lücke is found to be valid. The calculated segment lengths give a reasonable model for the internal dissipation of energy and are consistent with all the present measurements. In addition the number of F centers created per pinning point was obtained.

Finally, it may be pointed out that a method in which one can continuously observe dislocation densities and loop lengths may be of value in studying other mechanism involving the rearrangement, pinning, and creation (or extinction) of dislocations. Therefore, such a technique as outlined here may be a useful research tool for the study of recovery, recrystallization, age-hardening effects, polygonization, creep, and other allied phenomena.

APPENDIX

It is known from optical measurements[7] that it is possible to express the number of F centers per unit volume N as

$$N = De^{-\alpha x}t, \quad (9)$$

where x is the distance below the crystal surface. According to Smakula's equation,[15] N is related to the absorption coefficient, $\alpha_F(\text{cm}^{-1})$, at the peak of the F band in a rock salt crystal by the expression

$$N = 6.7\times10^{15}\alpha_F. \quad (10)$$

For a very thin plate of rock salt, of thickness d_1, the distance below the surface x can be approximated as zero. By combining Eq. (9) and (10) an expression for D is obtained

$$D = 6.7\times10^{15}(\alpha_F d_1)/td_1. \quad (11)$$

As a plot of $\alpha_F d_1$ vs t will yield a slope for the initial stage of coloring and d_1 is known, D may be experimentally determined.

In the present work a thin rock salt plate 0.068 cm thick was used and a slope of 0.10 min^{-1} was measured. Therefore D was found to have a value of 1.0×10^{16} cm^{-3} min^{-1}.

[12] N. F. Mott and F. R. N. Nabarro, *Report of a Conference on Strength of Solids* (Physical Society, London, 1948), p. 1.
[13] J. Weertman and E. J. Salkovitz, Acta Met. 3, 1 (1955).
[14] See discussion in footnote reference 2, p. 212.
[15] A. Smakula, Z. Physik 59, 603 (1930).

JOURNAL OF APPLIED PHYSICS VOLUME 31, NUMBER 6 JUNE, 1960

Intervalley Noise

P. J. Price
IBM Corporation, Watson Laboratory, Columbia University, New York, New York
(Received August 28, 1959)

A theory is developed for the spectrum of electrical noise due to electron transitions between several quasi-isolated groups of states, in the general case where each group may carry part of an electric current. It is applied to the noise due to transitions between valleys of the conduction band of germanium, and the possibility of observing this noise is discussed using the data of Weinreich, Sanders, and White on the frequency of intervalley transitions.

1. INTRODUCTION

THIS paper concerns a possible source of electrical "noise" in semiconductors which belongs in the same class as the statistical noise arising from the capture and release of electrons by traps.[1] This class of noise is that generated when the electron states divide

[1] See, for example, K. M. Van Vliet and J. Blok, Physica 22, 231 (1956); A. L. McWhorter, *Semiconductor Surface Physics* (University of Pennsylvania Press, Philadelphia, 1956), p. 207.

into two or more physically distinct groups such that intergroup transitions (to and from one or more of the groups contributing substantially to the conductivity) are much less frequent than intragroup transitions (for these groups). In the case of conduction band and traps ("generation-recombination noise"), the conduction band is the only group of states contributing to the conductivity. The more general situation with several groups contributing can be foreseen to occur when the groups are distinct quasi-isolated parts of the band structure. In the example to be discussed here they are the "valleys" (the regions of the Brillouin zone neighboring band-edge states) of the conduction bands of germanium and silicon.[2] The condition for the analysis given here to apply to "intervalley noise" is that the frequencies of electron transitions *between valleys* be small compared with the frequencies of intravalley scattering. For germanium this condition is probably fairly well satisfied at room temperature, and is now known to be realizable at low temperatures.[3]

If the average current contributed by any one group is zero for the thermal equilibrium state,[4] the "intergroup noise" appears only when a net electric current is passed through the substance; and the corresponding noise power is proportional to the square of the current, when the latter is small enough for Ohm's law to be satisfied. The spectral density G of the intergroup noise power characteristically is proportional to a factor

$$\tau/(1+\omega^2\tau^2)$$

(or to a sum of such terms), where $\omega/2\pi$ is the frequency and τ represents the mean time for an intergroup transition. When the latter is very large, the intergroup contribution to the low-frequency[5] power density may become an important part of the total—and in fact large compared with the ordinary thermal contribution.[1]

A theory of intergroup noise is presented in Sec. 2. The calculation of the spectral density is reduced essentially to the solution of N simultaneous linear inhomogeneous algebraic equations [Eqs. (11)] where N is the number of groups. In Sec. 3 this general theory is applied to intervalley noise, and the possibility of its observation in n-germanium is discussed.

[2] See, for example: C. Herring, Bell System Techl. J. 34, 237 (1955).

[3] G. Weinreich, T. M. Sanders, and H. G. White, Phys. Rev. 114, 33 (1959).

[4] This is not necessarily so, as an example shows: if at thermal equilibrium an appreciable fraction of the electrons in a semiconductor "valley" have energies greater than those at which the energy is a quadratic function of the wave vector (i.e., at which the mass tensor has its band-edge value), then in general the net average current carried by the valley will *not* vanish. (It does vanish, of course, if the band edge is at the zone center or zone boundary.) In any case, for thermal equilibrium, the Nyquist relation rigorously relates the *total* zero-frequency noise power (as given by Eq. (2) with $\psi=v_z, \omega=0$) to the Ohmic conductivity.

[5] That is, for frequencies not large compared with $1/\tau$.

2. GENERAL THEORY

The general formulation and notation here follows that of a previous publication.[6] We confine ourselves to calculating the spectral density, $G(v'_z,\omega)$, of the mean square fluctuation, $\langle(v'_z)^2\rangle$, of a component of the velocity $\mathbf{v}$ of a single electron in the conductor, and take for granted the connection between the fluctuations of $\mathbf{v}$ and the noise power as it is observed in practice.

Here

$$\mathbf{v}'\equiv\mathbf{v}-\mathbf{u},$$

where

$$\mathbf{u}\equiv\langle\mathbf{v}\rangle$$

is the mean velocity of the electron. The spectral density of the fluctuation of a suitable function $\psi(t)$ of of the electron's state may be defined as

$$G(\psi,\omega)=\lim_{s\to\infty}\left(\frac{2}{s}\left|\int_0^s\psi(t)e^{-i\omega t}dt\right|^2\right). \tag{1}$$

Then, according to the Weiner-Khinchine theorem,

$$G(\psi,\omega)=4\,\mathrm{Re}\int_0^\infty ds\,e^{-i\omega s}\langle[\psi(t)\psi(t+s)]\rangle_{\text{Time Av}}. \tag{2}$$

The second factor in the integrand of Eq. (2) is the autocorrelation for ψ at instants separated by the interval s. $\langle[\ ]\rangle_{\text{Time Av}}$ denotes a time average (over the variable t) which is equivalent (since we are concerned here with a steady state) to the ensemble average $\langle\ \rangle$ at any instant.

Let $\mathbf{w}(q)$ be the ensemble average of $\mathbf{v}$ over the qth group of states alone. We may regard q, and hence $\mathbf{w}(q)$, as functions of the state of an individual electron, and so as varying in time. We wish to separate the fluctuations of $\mathbf{v}$ relative to $\mathbf{w}$ from the fluctuations of $\mathbf{w}$ on account of intergroup transitions. Let

$$\mathbf{w}'(q)\equiv\mathbf{w}-\mathbf{u}, \tag{3}$$

and let

$$\mathbf{v}''\equiv\mathbf{v}-\mathbf{w} \tag{4}$$

—a function of q and of the state of the electron while it is in the qth group. Then

$$\mathbf{v}'=\mathbf{v}''+\mathbf{w}'. \tag{5}$$

We now make our first *assumption:*

Assumption I. There is no correlation between $\mathbf{v}''$ and $\mathbf{w}'$:

$$\langle[\mathbf{v}''(t)\mathbf{w}'(t+s)]\rangle_{\text{Time Av}}=0. \tag{6}$$

This must be true if Eq. (A3) of reference 2, generalized to intergroup transitions, holds. (Intragroup transition rates need only be invariant under simultaneous reversal of initial and final velocities.) It should be true in any case when s is large compared with the "aging

[6] P. J. Price, IBM J. 3, 191 (1959).

time" introduced below; and the results obtained here are anyhow not valid when smaller values of s contribute significantly to (2).

From (2), (5), and (6), we have

$$G(v'_z,\omega)=G(v''_z,\omega)+G(w'_z,\omega). \tag{7}$$

The present work is concerned with the second term on the right of (7), which we shall identify with *intergroup noise*. (Since intergroup transitions are supposed to be much less frequent than intragroup transitions, the former may be expected to have negligible influence on the first term of (7), whose value and frequency dependence should be typical of ordinary thermal noise.)

We have now come to the second assumption to be made here. It concerns the fact that, in general, the distribution of the "arrival" states of electrons immediately after an intergroup transition to any one group is not the same as the distribution of states of electrons *while they are in that group*. Consequently, intergroup transitions are not a Markoffian set of processes: and there is an "aging" after its arrival, during the period an electron survives in one group, before its probabilities, per unit time, of transitions to other groups become constant. This aging process is a kind of thermalization. The lapse of time required for it we call the "aging time."

Assumption II. The aging time, after an electron transition to a new group, is small compared with the mean time of survival in that group (before the next intergroup transition).

This assumption is consistent with the supposition mentioned in Sec. 1, that the intragroup transition frequencies are large compared with the intergroup ones; but the aging time must be expected to depend on the value of the applied electric field. Granted Assumption II, a simple general theory for evaluating $G(w'_z,\omega)$ can be set up.

It is convenient to introduce a variable with the character of a partial "mean free path"[6,7] for $\mathbf{w}'$:

$$\mathbf{h}(\omega,q)\equiv\int_0^\infty e^{-i\omega s}\langle \mathbf{w}';s\rangle ds, \tag{8}$$

where $\langle\psi;s\rangle$ means the expectation of ψ at a time later by an interval s than the time at which the electron was definitely in a specified state. Here, the "specified state" is the group q, and $\langle\mathbf{w}';s\rangle$ depends on q and s. Then by (2)

$$\tfrac{1}{4}G(w'_z,\omega)=\mathrm{Re}\langle w'_z h_z(\omega)\rangle$$
$$=\textstyle\sum_q P_q w'_z(q)\ \mathrm{Re}h_z(\omega,q), \tag{9}$$

where P_q is the average fraction of electrons in the qth group.

Let the frequency of transitions from the pth group to the qth be ν_{pq} (with $\nu_{pp}=0$, of course). The total frequency ν_p of transitions out of the pth group is then

$$\nu_p=\textstyle\sum_q \nu_{pq}. \tag{10}$$

We obtain an equation for $\mathbf{h}$ by separating the right-hand side of (8) into two parts[8]: the contributions from before, and from after, the first intergroup transition for $s>0$. The first of these two contributions is

$$\mathbf{w}_q\int_0^\infty ds[-d(e^{-\nu_q s})/ds]\int_0^s e^{-i\omega s'}ds'=\mathbf{w}_q/(\nu_q+i\omega).$$

(The second integral above gives the contribution from the interval s before an electron is scattered, and the first is taken over the probability density for values of s.) For an electron making a transition to group p after an interval s, the subsequent contribution to (8) will be $\exp(-i\omega s)\mathbf{h}(\omega,p)$. Since the probability that any transition will be to group p is ν_{qp}/ν_q, the second part of (8) is therefore

$$\int_0^\infty ds[-d(e^{-\nu_q s})/ds]e^{-i\omega s}\sum_p\frac{\nu_{qp}}{\nu_q}\mathbf{h}(\omega,p)$$
$$=\textstyle\sum_p \nu_{qp}\mathbf{h}(\omega,p)/(\nu_q+i\omega).$$

Taking the sum of these two terms as equal to (8),[8] we have

$$(\nu_q+i\omega)\mathbf{h}(\omega,q)-\textstyle\sum_p \nu_{qp}\mathbf{h}(\omega,p)=\mathbf{w}'(q). \tag{11}$$

The intergroup noise spectrum is found by substituting the solution of (11) into (9).

Some properties of the set, (11), of inhomogeneous linear equations should be noted here. The occupation probabilities P_q must satisfy the equations

$$\textstyle\sum_p P_p\nu_{pq}=P_q\nu_q. \tag{12}$$

By (11) and (12),

$$i\omega\textstyle\sum_q P_q\mathbf{h}(\omega,q)=\sum_q P_q\mathbf{w}'(q). \tag{13}$$

Thus, mathematically, in virtue of the existence of a solution of (12) and since the $\mathbf{w}'$ are real, $\sum P\,\mathrm{Re}\mathbf{h}$ must vanish. Also for $\omega=0$ a solution of (11) does not exist unless $\sum P\mathbf{w}'=0$. Actually, because of their physical nature, both sides of (13) are necessarily zero. The right-hand side is $\sum P\mathbf{w}-\mathbf{u}=\langle\mathbf{w}\rangle-\mathbf{u}=0$. The left-hand side is

$$i\omega\left\langle\int_0^\infty e^{-i\omega s}ds(\langle\mathbf{w};s\rangle-\mathbf{u})\right\rangle$$
$$=i\omega\int_0^\infty e^{-i\omega s}ds\langle(\langle\mathbf{w};s\rangle-\mathbf{u})\rangle.$$

[7] P. J. Price, *Proceedings of the 1958 International Conference on Semiconductors* J. Chem. Phys. Solids **8**, 136 (1959).

[8] For a similar treatment of the "vector mean free path," see P. J. Price, IBM J. **2**, 200 (1958). Each part of (8) has extension both in the domain of the integral over time (s) and in the domain of the averaging $\langle\,\rangle$ over groups. Therefore, as is noted in the foregoing reference, this analysis is not rigorous.

The last factor in the integral is clearly zero, since $\langle\langle \mathbf{w}; s\rangle\rangle = \langle \mathbf{w}\rangle$ for all values of s.

For *thermal equilibrium*, the detailed balance principle requires that

$$P_p \nu_{pq} = P_q \nu_{qp}. \tag{14}$$

Therefore by a linear transformation on the $\mathbf{h}_q$ we may reduce (11) to a "diagonal" set of equations (with no cross terms like the sums on ν_{qp}) with the consequence[1] that the intergroup noise density is of the form

$$G(w'_x,\omega) = u^2 \textstyle\sum_\alpha A_\alpha \tau_\alpha / [1+(w\tau_\alpha)^2], \tag{15}$$

where the A_α and τ_α are real positive constants. (The dependence on u comes from the fact that, near thermal equilibrium, the w'_x are proportional to u.) This argument is not valid, however, for appreciable departures from thermal equilibrium.

3. APPLICATION

A single example will show how (9) and (11) can be used to calculate intervalley noise. We consider n-germanium with an electric field (and current) in the (1, 1, 0) direction, which is chosen to be the Z direction, and noise measured for the (0, 0, 1) direction, which is chosen to be the X direction. The conduction band of germanium has four equivalent "valleys," each with an axis of cylindrical symmetry. The axes are in the four (1, 1, 1) directions (Fig. 1). There are two valleys for which w_x(equal to w'_x, since $u_x=0$) is zero: we take their electron states together as a single group, labeled "O." The other two have equal and opposite values of w_x: we label them as groups "+" and "−". Then

$$\left.\begin{aligned} w_+ &= -w_- \equiv u_1, \\ h_+ &= -h_- \equiv h_1, \\ \nu_{0+} &= \nu_{0-} \equiv \nu_{01}, \\ \nu_{+0} &= \nu_{-0} \equiv \nu_{10}, \\ \nu_{+} &= \nu_{-} \equiv \nu_{1}. \end{aligned}\right\}$$

(The subscript x, signifying the component of a vector, has been suppressed.) Also

$$\nu_0 = 2\nu_{01}; \quad \nu_1 = \nu_{+-} + \nu_{10}. \tag{16}$$

The first of Eqs. (11) is

$$(\nu_0 + i\omega)h_0 = 0,$$

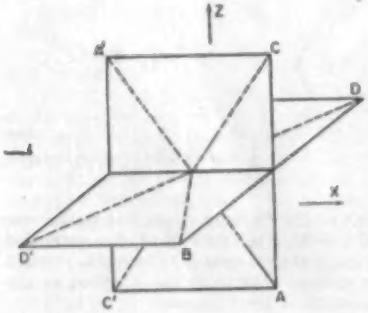

FIG. 1. The dashed lines AA′, etc., full diagonals of the cube ABCDA′B′C′D′, are valley axis directions for n germanium. D′B is the (0, 0, 1) direction (X axis), and AC is the (1, 1, 0) direction (Z axis), in the text.

or

$$h_0 = 0. \tag{17}$$

The other two equations (11), combined with (17), give

$$(\nu_1 + i\omega)h_1 + \nu_{+-}h_1 = u_1,$$

or

$$h_1 = u_1\tau/(1+i\omega\tau) \tag{18}$$

where, by (16),

$$\tau = 1/(\nu_{10} + 2\nu_{+-}). \tag{19}$$

The fraction of the electrons in the "+" and "−" valleys is

$$P_1 \equiv P_+ + P_- = 1 - P_0 = 2\nu_{01}/(2\nu_{01} + \nu_{10}), \tag{20}$$

and, by (9),

$$\tfrac{1}{4}G(w'_x,\omega) = P_1 u_1^2 \tau/(1+\omega^2\tau^2). \tag{21}$$

In this case the relations (14) hold for reasons of symmetry, and irrespective of the nearness of the system to thermal equilibrium. In the ohmic range, we have

$$G = \frac{\tau}{1+\omega^2\tau^2}\left(\frac{K-1}{K+\frac{1}{2}}\right)u^2$$

where K is here the usual anisotropy factor for the mobility tensor of a single valley.

Returning to the general situation: if all the $\frac{1}{2}N(N-1)$ transition frequencies, for transitions between the N valleys, remain equal when the field is applied (each is ν, say) then the solution of (11) is

$$\mathbf{h}_q = \mathbf{w}'_q/(N\nu + i\omega); \tag{22}$$

and by (9), if the P's remain equal also,

$$\tfrac{1}{4}G(w'_x,\omega) = \frac{\tau}{1+\omega^2\tau^2}\frac{1}{N}\sum_1^N (w'_{qx})^2, \tag{23}$$

where

$$\tau = 1/N\nu.$$

The practical prospects for observing intervalley noise evidently turn on (a) the magnitude of the characteristic time τ which represents the frequency dependence, as in the first factor on the right of (23) (we would like this to be large enough so that the intervalley noise power can be measured through the frequency range in which it falls off); (b) the attainable magnitude of the intervalley noise power, at the low-frequency limit where it is "white," relative to the thermal noise power; (c) the possible masking of intervalley noise by that due to trapping and release of electrons,[1] which depends on u in the same way.

Let us take the intervalley noise power as given by

$$G_{1V} \sim u^2\tau_{1V}/(1+\omega^2\tau_{1V}^2).$$

(We are not interested here in numerical factors of order unity.) This compares with thermal noise

$$G_{th} \sim \langle \tau_{th} v^2\rangle \sim \langle \tau_{th}\rangle\langle v^2\rangle$$

for $\omega\langle\tau_{th}\rangle \ll 1$ (where $1/\tau_{th}$ is the ordinary total collision frequency of the electrons). For G_{IV} to be detected and measured, presumably it should be at least comparable with G_{th}. So the current passed will have to be at least that given by

$$u^2 \sim \langle v^2\rangle\langle\tau_{th}\rangle/\tau_{IV}.$$

This expression is small compared with $\langle v^2\rangle$, according to our assumption (Sec. 1) that $\tau_{th} \ll \tau_{IV}$: i.e., $u^2 \ll \langle v^2\rangle$. Therefore we shall probably not need to greatly disturb the electron system from thermal equilibrium. The mobility is given by

$$\mu \sim (e/m)\langle\tau_{th}\rangle;$$

and therefore the power which will be absorbed, *per electron*, from the field is

$$W = eEu = eu^2/\mu \sim \langle mv^2\rangle/\tau_{IV}.$$

Therefore, if in fact the system remains near thermal equilibrium, we shall require

$$W \sim KT/\tau_{IV}. \tag{24}$$

(K is Boltzmann's constant.)

For n germanium the magnitudes of the intervalley transition frequencies below 150°K have been inferred by Weinreich *et al.*[3] from their measurements of the acoustoelectric effect. At the higher temperatures the dominant contribution is due to absorption and emission of phonons with the appropriate wave vector to connect the valleys. At 77°K, this contribution is roughly 5×10^9 sec^{-1}: therefore for high-purity material ($n\sim10^{13}$ cm^{-3}) the intervalley noise should be detectable for $nW\sim100$ w/cm^3, and should fall off at microwave frequencies. Weinreich *et al.* confirmed that at lower temperatures the frequency of transitions by the phonon mechanism is much smaller, and concluded that the remaining measured frequency is the sum of a term proportional to the number of neutral donors and a term proportional to the number of donor ions. At 20°K, for a donor concentration of 10^{13} cm^{-3}, the intervalley transition frequency evidently should be $\sim10^8$ sec^{-1}. Thus the dissipation nW, at current strengths sufficient for the intervalley noise to be detectable, should be a few w/cm^3, and the noise should fall off in the VHF range. However, it might be important not to have the intervalley frequency reduced to the point where it fell within the range of a trapping-noise component.

It is interesting to inquire into the possibility of eliminating the donor-induced intervalley transitions studied by Weinreich *et al.*, by doping the germanium so heavily that there are no bound donor states. The obvious remaining mechanism is direct transitions, between Bloch states in different valleys, due to the Coulomb fields of the donor ions. As indicated by Weinreich *et al.*, one may calculate this according to the Born approximation by expanding $\phi(\mathbf{r})$, the electron's potential energy in an ion's field, in Fourier components

$$\phi_F(\mathbf{k}) \equiv \int \phi(\mathbf{r}) e^{i\mathbf{k}\cdot\mathbf{r}} d^3\mathbf{r}.$$

The matrix element for Bloch wave functions is

$$\phi_F(\mathbf{k}'-\mathbf{k}'')I(\mathbf{k}';\mathbf{k}'')/V$$

where $\mathbf{k}'$ and $\mathbf{k}''$ refer to the two states and $I(\mathbf{k}';\mathbf{k}'')$ is the integral $\int \alpha_{\mathbf{k}'}^* \alpha_{\mathbf{k}''} d^3\mathbf{r}$ (normalized so that $I(\mathbf{k};\mathbf{k}) = 1$), $\alpha_{\mathbf{k}}(\mathbf{r})$ being the periodic part of the Bloch wave function. The matrix element may be taken to be that between the band-edge states, and held constant for all transitions between the same two valleys. On assuming that the band structure may be taken as the same as for undoped material, that the electron distribution is completely degenerate, that the density of electrons n is equal to the density of ions, and that correlations in the relative positions of the ions may be neglected, one finds for the intervalley frequency (between two valleys) by this mechanism:

$$\nu_{IV}(\text{coulomb}) = \left\{ \left(\frac{3}{\pi}\right)^{\frac{1}{3}} \frac{m_s n^{\frac{1}{3}}}{2\hbar^3 N^{\frac{1}{3}}} \right\} |\phi_F|^2 |I|^2, \tag{25}$$

where m_s is the density-of-states mass (reckoned for a single valley and a single spin direction) and N is the number of valleys. For n-germanium, with $n\sim10^{18}$ cm^{-3}, $\{\}\sim10^{77}$ cgs. The length of the wave vector connecting two valleys is $k_{IV} = 1\times10^7$ cm^{-1}. So $1/k_{IV}$ will be small compared to a shielding length, but not large enough for ϕ_F to be set equal to $4\pi e^2/k_{IV}^2\epsilon$ (where ϵ is the dielectric constant), and presumably not small enough for ϕ_F to be set equal to $4\pi e^2/k_{IV}^2 (= 3.3\times10^{-34}$ erg cm^3). Making a guess, $|\phi_F|^2|I|^2 \sim 10^{-68}$ cgs., we obtain from (25):

$$\nu_{IV}(\text{coulomb}) \sim 10^9 \text{ sec}^{-1}.$$

This is no better (i.e., smaller) than the prevailing values, according to Weinreich *et al.*, for high-resistance material; and the dissipation required would be very much greater because of the larger value of n. One may show that (24) applies also for extreme degeneracy. Therefore, at 4°, we would require $nW\sim10^5$ w/cm^3.

ACKNOWLEDGMENTS

I am indebted to J. Berger, R. E. Burgess, R. Landauer, and G. D. Whitfield for criticisms of the first draft of this paper.

Minority Carrier Recombination in a Cylindrical Transistor Base Region

DAVID P. KENNEDY
IBM Corporation, Poughkeepsie, New York

(Received November 13, 1959; revised manuscript received February 5, 1960)

An analysis is given on the influence of bulk recombination within the base region of a mesa-type drift transistor. The minority carrier transport efficiency is established for a solid cylinder base region and also for a simplified one-dimensional structure. A comparison of the two minority carrier transport equations shows the approximate analysis will result in a negligible error when applied to practical semiconductor devices.

INTRODUCTION

FREQUENTLY, a one dimensional structure is assumed when calculating the bulk recombination current within a cylindrical transistor base region, Fig. 1. However, this approximation eliminates the radial component of minority carrier current and, therefore, is equivalent to a reduction of the effective base width. This paper establishes the validity of such an analytical simplification when applied to a wide range of practical devices.

The theoretical magnitude of transistor current gain, assuming only bulk recombination of minority carriers, is established for a one-dimensional base region; this magnitude is shown to be in excellent agreement with the value determined by a rigorous treatment of the problem.

ANALYSIS

The excess minority carrier (hole) distribution in a cylindrical base region of n-type semiconductor material is governed by the differential equation,

$$\frac{\partial^2 P_n}{\partial r^2}+\frac{1}{r}\frac{\partial P_n}{\partial r}+\frac{\partial^2 P_n}{\partial z^2}-\left(\frac{qE_z}{kT}\right)\frac{\partial P_n}{\partial z}-\frac{P_n}{L_p^2}=0. \quad (1)$$

This expression is applicable to a structure of circular symmetry having an axially directed drift field of constant magnitude E_z. Throughout this analysis, a constant-magnitude field is assumed to approximate the influence of base-region conductivity grading introduced by diffusion techniques.

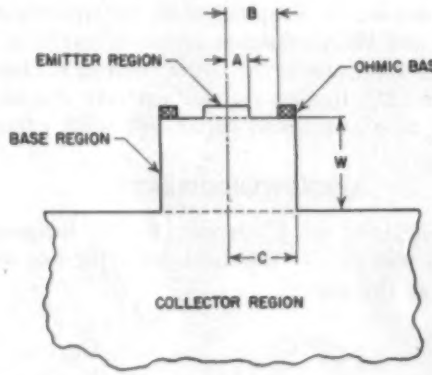

FIG. 1. Analytical model for cylindrical mesa type transistor.

A useful solution of Eq. (1) must satisfy the boundary conditions assumed to approximate a practical transistor. These boundary conditions are given by

$$P_n(r;z)=0 \qquad 0<r<C;\ z=W \quad (2a)$$

$$\partial P_n/\partial r=0 \qquad r=C;\ 0<z<W \quad (2b)$$

$$\frac{\partial P_n}{\partial z}=\begin{cases}(qE_z/kT)P_n-(J_{ps}/qD_p) & 0<r<A;\ z=0\\ (qE_z/kT)P_n & A<r<C;\ z=0.\end{cases} \quad (2c)$$

The collector junction is characterized by Eq. (2a) as a surface of constant (zero) minority carrier concentration, thereby providing a sink for all excess holes within this base region. The only mechanism of minority carrier loss is assumed to be bulk recombination; hence, a surface of zero recombination velocity is established at the outer cylinder wall, Eq. (2b). Further, Eq. (2c) approximates all boundary conditions appearing at the emitter end of this base region when the influence of an ohmic contact is neglected. A constant hole current J_{ps} is assumed to enter this cylindrical structure through the emitter junction face ($z=0$; $0<r<A$) while the exposed surface ($z=0$; $A<r<C$) has a zero recombination velocity.

An adequate solution of Eq. (1) is not obtained when using the Neumann boundary condition specified by Eq. 2(b). Instead, the more general boundary condition of Cauchy is used,

$$\frac{\partial P_n}{\partial r}+hP_n=0 \quad (r=C;\ 0<z<W). \quad (3)$$

Equation (3) is equivalent to the boundary condition specified by Eq. (2b) when $h=0$. The minority carrier distribution equation, $P_n(r;z)$, satisfying Eq. (1), Eq. (2a), Eq. (2c), and Eq. (3) will become zero at $h=0$; yet, it approaches the desired solution when h is sufficiently small. This technique is equivalent to introducing a finite surface recombination velocity S at the outer cylinder wall; the required distribution equation is obtained by reducing S to an insignificant magnitude.

A solution of Eq. (1)—subject to the boundary condi-

tions of Eq. (2)—is given by[1]

$$P_n(r;z)=\frac{2J_{pe}A}{qD_pC}e^{dz/2}\lim_{l\to 0}\left\{\sum_{m=1}^{\infty}\frac{\sinh[\gamma_m(W-z)]}{\alpha_m[(d/2)\sinh(\gamma_m W)+\gamma_m\cosh(\gamma_m W)]}\left[\frac{J_1[\alpha_m(A/C)]J_0[\alpha_m(r/C)]}{J_0^2(\alpha_m)+J_1^2(\alpha_m)}\right]\right\}, \quad (4)$$

where

$$\alpha_m J_1(\alpha_m)-lJ_0(\alpha_m)=0 \quad (5a)$$

$$\gamma_m^2=\left(\frac{d}{2}\right)^2+\left(\frac{\alpha_m}{C}\right)^2+\left(\frac{1}{L_p}\right)^2 \quad (5b)$$

$$\alpha=\left(\frac{qE_z}{kT}\right) \quad (5c)$$

the term α_m within Eq. (4) is obtained from the roots of Eq. (5a), where each selected magnitude of l establishes an infinite set of such roots. The summation of Eq. (4) is conducted over ascending values of α_m.

The axial component of minority carrier current within this base region is expressed by the equation,

$$J_{pz}(r;z)=-qD_p\left\{\frac{\partial P_n}{\partial z}-dP_n\right\}, \quad (6)$$

therefore upon combining Eq. (4) and Eq. (6) we obtain

$$J_{pz}(r;z)=\frac{2J_{pe}A}{C}e^{dz/2}\lim_{l\to 0}\left\{\sum_{m=1}^{\infty}\frac{\gamma_m\cosh[\gamma_m(W-z)]+(d/2)\sinh[\gamma_m(W-z)]}{\alpha_m[\gamma_m\cosh(\gamma_m W)+(d/2)\sinh(\gamma_m W)]}\left[\frac{J_1[\alpha_m(A/C)]J_0[\alpha_m(r/C)]}{J_1^2(\alpha_m)+J_0^2(\alpha_m)}\right]\right\}. \quad (7)$$

The total collector junction hole current, I_{pc}, can be established by a radial integration of Eq. (7) across the collector junction face ($z=W$),

$$I_{pz}=4\pi ACJ_{pc}e^{dW/2}\lim_{l\to 0}\left\{\sum_{m=1}^{\infty}\frac{\gamma_m J_1[\alpha_m(A/C)]J_1(\alpha_m)}{\alpha_m^2[\gamma_m\cosh(\gamma_m W)+(d/2)\sinh(\gamma_m W)][J_1^2(\alpha_m)+J_0^2(\alpha_m)]}\right\}. \quad (8)$$

From Eq. (8) the base region minority carrier transport efficiency is

$$B_{r,l}=\frac{I_{pc}}{I_{pz}}=\frac{4C}{A}e^{dW/2}\lim_{l\to 0}\left\{\sum_{m=1}^{\infty}\frac{\gamma_m J_1[\alpha_m(A/C)]J_1(\alpha_m)}{\alpha_m^2[\gamma_m\cosh(\gamma_m W)+(d/2)\sinh(\gamma_m W)][J_1^2(\alpha_m)+J_0^2(\alpha_m)]}\right\}. \quad (9)$$

Equation (9) characterizes the transport efficiency of a cylindrical base region satisfying all boundary conditions specified in Eq. (2). The notation $B_{r,l}$ is used to indicate the dependence of minority carrier transport efficiency upon both lifetime τ and surface recombination l.

A differential equation governing the minority carrier distribution throughout a one-dimensional base region is obtained by eliminating all radial terms within Eq. (1),

$$\frac{d^2P_n}{dz^2}-\left(\frac{qE_z}{kT}\right)\frac{dP_n}{dz}-\frac{P_n}{L_p^2}=0. \quad (10)$$

In this situation, the base region is assumed to be the solid cylinder of semiconductor material located immediately under the emitter junction. Further, an elimination of all radial terms within Eq. (1) introduces a zero surface recombination velocity upon this new structure.

A satisfactory solution of Eq. (10) must satisfy the boundary conditions specified by Eq. (2a) and Eq. (2c); when $(0<r<A)$. This solution is given by

$$P_n(z)=\frac{J_{pe}}{qD_p}e^{dz/2}\frac{\sinh[\gamma(W-z)]}{\gamma\cosh(\gamma W)+(d/2)\sinh(\gamma W)}, \quad (11)$$

where

$$\gamma^2=\left(\frac{d}{2}\right)^2+\left(\frac{1}{L_p^2}\right). \quad (12)$$

The axial component of minority carrier current within this simplified model is obtained from Eqs. (6) and (11),

$$J_{pz}(z)=J_{pe}e^{dz/2}\times\left\{\frac{\gamma\cosh[\gamma(W-z)]+(d/2)\sinh[\gamma(W-z)]}{\gamma\cosh(\gamma W)+(d/2)\sinh(\gamma W)}\right\}. \quad (13)$$

From Eq. (13) the minority carrier transport efficiency B_r is

$$B_r=\frac{J_{pz}(W)}{J_{pe}}=\frac{\gamma\exp(dW/2)}{\gamma\cosh(\gamma W)+(d/2)\sinh(\gamma W)}. \quad (14)$$

Equation (14) has been numerically evaluated throughout a range of geometrical parameters applicable to practical devices, Fig. 2. This evaluation has been conducted in terms of the common emitter current gain parameter B_r, where

$$\beta_r=B_r/1-B_r. \quad (15)$$

To establish the theoretical current gain of a three-dimensional structure, a test is required for the limit

[1] It has been indicated to the author that a similar analysis was conducted by J. P. McKelvey, IRE Trans. on Electron Devices ED-5, 260(1958).

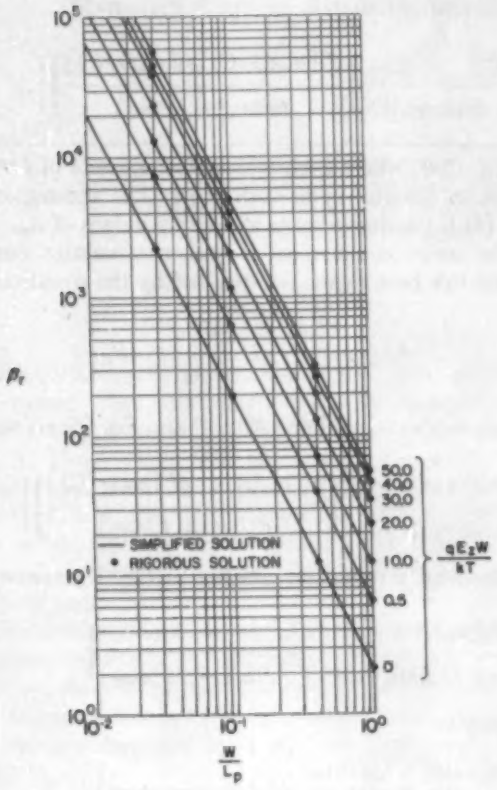

FIG. 2. Comparison of theoretical common-emitter current gains using simplified and rigorous solutions.

specified by Eq. (9). The parameter l, being equivalent to a normalized surface recombination velocity at the outer cylinder wall ($r=C$; $0<z<W$), must be reduced to a magnitude which has little influence upon the transistor current gain. From Eqs. (6) and (15) the common emitter current gain $\beta_{\tau,l}$ is shown to be dependent upon both surface recombination velocity l and minority carrier lifetime τ, within the base region. This expression can be approximated by

$$\frac{1}{\beta_{\tau,l}}=\frac{1}{\beta_l}+\frac{1}{\beta_\tau}. \tag{16}$$

The term β_l, Eq. (16), represents the magnitude of current gain when an infinite minority carrier lifetime τ is assumed. The introduction of the requirement,

$$(\beta_l/\beta_{\tau,l})>10^3$$

assures that the parameter l has little influence upon the calculated current gain; therefore, $\beta_\tau=\beta_{\tau,l}$, approximately.

CONCLUSIONS

Figure 2 illustrates the magnitude of $\beta_{\tau,l}$ throughout a range of parameters applicable to most transistors. Changes in current gain, resulting from changes in emitter junction radius (A/C), are substantially smaller than the error introduced by a non-zero magnitude of l. Minority carrier spreading, therefore, is limited to an insignificant magnitude by the narrow base width used in practical structures; the simplified one dimensional solution appears adequate when computing the transistor current gain resulting from bulk carrier recombination.

ACKNOWLEDGMENT

The author acknowledges the benefit of discussions during the course of this work with his associates at IBM. In particular, he wishes to thank Mr. W. E. Harding for many valuable suggestions on methods for evaluating Eq. (9). Further, a substantial amount of credit is due Mr. R. A. Kuchenbecker, who developed the IBM 704 computer programs used extensively throughout this analysis.

JOURNAL OF APPLIED PHYSICS VOLUME 31, NUMBER 6 JUNE, 1960

Transport of Noise at Microwave Frequencies through a Space-Charge-Limited Diode*

W. E. VIVIAN†
Radiation Laboratory, University of Michigan, Department of Electrical Engineering, Ann Arbor, Michigan
(Received October 14, 1959)

Several analyses of the transport of cathode shot noise through a space-charge-limited diode at microwave frequencies have been published to date. Each of these analyses has been beset by inconsistencies arising from assumptions of monovelocity perturbation flow, direct or reflected. A new method of analysis of diode flow eliminating this problem has been developed. Numerical results based on this method are presented here. Attention is restricted to the now classical problem of one-dimensional longitudinal confined flow.

The magnitude and variation with distance of the so-called beam noise invariants is shown for a range of diode operating conditions. These calculated results, based for economy on an approximate static flow model, essentially substantiate the qualitative expectations suggested by prior analyses, and fit what little experimental data are available.

The method of analysis employed in the calculation of the numerical results comprises a linear multistream formulation, based on representation or approximation of the perturbation particle density for the noise flow as a composite of singular impulse streams, N in number, along characteristic trajectories in the velocity-distance phase space. The set of N coupled first-order linear differential equations resulting is solved by simultaneous numerical extrapolation.

I. INTRODUCTION

THE transport of cathode noise through a space-charge-limited diode was first reported about twenty years ago in publications by several authors of articles on the suppression of noise in an idealized diode.[1,2] The diode model on which the analyses were based was a heterovelocity one-dimensional longitudinal flow model, which has become the classical model for this problem. Because these earliest analyses depended upon an assumption that the transit angles through the diode for essentially all electrons were negligible (that is, that the force fields remained stationary during the passage of an electron), the analyses were suitable only for determination of the transport of the low-frequency component of the cathode noise. The frequency range of applicability of the results obtained later was extended appreciably when it was recognized that the noise flow up to and in the vicinity of the minimum was little influenced by the flow beyond.[2] The flow beyond, a high-velocity flow, was found to be relatively well represented by recourse to a simple (perturbed) monovelocity model. This "pieced together" approach has proved quite productive for the midrange of frequency where, though the angle from minimum to anode may be large, the mean transit angle from cathode to minimum is small. For the higher-frequency range of concern here, where the mean transit angle from cathode to minimum is a significant portion of a cycle, neither the "pieced together" approach nor any monovelocity model has been shown adequate or applicable.

Efforts have been made during the past decade to find a general formulation and solution for the problem.[3–7] These investigations generally have been based on use of the linearized Liouville or Boltzmann transport equation to describe the flow process, with only continuum electric-field forces being retained. In the majority of these efforts, the potential minimum was considered a point current source, driven by the local perturbation voltage at the potential minimum as established by a cathode-emitted space-charge excitation current.[7] The excitation current was assumed to be decelerated by the static field only. Though widely accepted, this approach is not adequate because of the presence of infinite transit time for the potential-minimum-released current.[7]

In addition, a detailed simulation of the motion of discrete electrons in a mathematical diode of convenient parameters has been performed.[8] Unfortunately, such simulation, while providing some numerical results, adds little understanding of the physical process.

The method of analysis of the noise transport presented here permits resolution of the infinite transit time problem; provides a practicable, self-constent procedure for numerical calculations; and sheds light on the role of the linearization postulate and the relation of the postulate to frequency vs time domain resolution

* Based on dissertation, University of Michigan, 1959, same title.

† The Radiation Laboratory of The University of Michigan, Department of Electrical Engineering, Ann Arbor, Michigan. This work was conducted for Project Michigan by the Electron Physics Laboratory, Department of Electrical Engineering of The University of Michigan, under a Department of Army contract administered by the U. S. Army Signal Corps.

[1] D. O. North, RCA Rev. 4, 441–472 (1940); 5, 106–124 (1940).

[2] A. J. Rack, Bell System Tech. J. 17, 592–619 (1938).

[3] J. K. Knipp, *Klystrons and Microwave Triodes* (M.I.T. Radiation Laboratory Series), Vol. 7; (McGraw-Hill Book Company, Inc., New York), Chap. 5.

[4] J. R. Whinnery, IRE Trans. 1, 221–236 (1954). The same material is published in expanded form as TR Series No. 60, No. 132, Electronics Research Laboratory, University of California, University of California, Berkeley, California, February 28, 1955.

[5] D. A. Watkins, J. Appl. Phys. 26, 622–624 (1955).

[6] A. E. Siegman and D. A. Watkins, IRE Trans. on Electron Devices, ED-4, 82–86 (1957).

[7] A. E. Siegman, "Microwave noise fluctuations in the potential-minimum region of an electron beam," Stanford Electronics Laboratories, Tech. Rept. No. 401-1, Stanford University, Stanford, California, April 22, 1957. (see Bibliography also).

[8] P. K. Tien and J. Moshman, J. Appl. Phys. 27, 1067–1078 (1956).

and to infinite transit delays. Numerical results based on this analysis are given here. Implications with regard to low-noise amplification are suggested, and the method of analysis is outlined.

II. STATEMENT OF PROBLEM

A. Field and Transport Equations

A planar diode having no lateral variations is studied. Only the longitudinal motion of the electrons is considered. The effects of lateral motion in creating longitudinal motion are ignored. (These effects are of second order when lateral variations are excluded.) Occurrence of collisions is assumed negligible, and any effects therefrom are ignored. The time-average potential in the diode is assumed to possess a potential minimum. All electrons *incident* on the cathode are assumed absorbed. A phase-space particle density $N_t(x,u,t)$, where $u=dx/dt$ for a particle is assumed to represent the flow of discrete particles comprising the space charge.

The second-order force arising from the nonlongitudinal magnetic field generated by the flow is ignored compared to the first-order force caused by the longitudinal electric field $E_t(x,t)$. The electric field will be assumed representable by an electric potential $\phi_t(x,t)$ (diode length assumed small compared to free-space wavelength). The flow of particles in the phase space is assumed to obey the Liouville condition, and thus satisfy the Boltzmann transport equation. Combining the electric field and transport equations, one arrives at two integro-differential equations coupling the density N_t and the longitudinal electric field E_t,

$$0=\frac{\partial N_t}{\partial t}+u\frac{\partial N_t}{\partial x}+\frac{q}{m}E_t\frac{\partial N_t}{\partial u}, \tag{1}$$

$$0=\int_{-\infty}^{\infty} quN_t\,du+\epsilon\frac{\partial E_t}{\partial t}+Y\int_{x_c}^{x_a}E_t\,dx, \tag{2}$$

where q is the charge of the electron; m its mass; ϵ is the free space dielectric constant; Y is the admittance per unit area of the external circuit connecting the anode and cathode; and x_a, x_c, and x_m are the locations of the anode, cathode, and potential minimum, respectively. Observe that this system is nonlinear.

The noise is represented as a perturbation $N_1(x,u,t)$ to the time-invariant or static solution $N_0(x,u)$ for a diode, which solution is known. Then N_1 and E_1 must satisfy

$$0=\frac{\partial N_1}{\partial t}+u\frac{\partial N_1}{\partial x}+\frac{q}{m}E_0\frac{\partial N_1}{\partial u}+\frac{q}{m}\frac{\partial N_0}{\partial u}E_1+\frac{q}{m}E_1\frac{\partial N_1}{\partial u}, \tag{3}$$

$$0=\int_{-\infty}^{\infty} quN_1\,du+\epsilon\frac{\partial E_1}{\partial t}+Y\int_{x_c}^{x_a}E_1\,dx. \tag{4}$$

It is assumed that the noise perturbations are sufficiently small so that the nonlinear cross term $E_1(\partial N_1/\partial u)$ can be dropped. Implications of this hypothesis will be considered subsequently. Solutions having the spectral form $N_1(x,u,t)=N(x,u)e^{j\omega t}$ will be sought; an appropriately weighted ensemble of solutions of this form will be employed to represent the noise process. The linearized equations then reduce to

$$0=j\omega N+u\frac{\partial N}{\partial x}+\frac{q}{m}E_0\frac{\partial N}{\partial u}+\frac{q}{m}\frac{\partial N_0}{\partial u}E, \tag{5}$$

$$0=\int_{-\infty}^{\infty} quN\,du+j\omega\epsilon E+Y\int_{x_c}^{x_a}E\,dx. \tag{6}$$

B. Transformation to Dimensionless Variables

A transformation to dimensionless variables now will be made to simplify subsequent exposition. The distance and velocity variables (x,u) will be scaled to (ξ,λ), defined as

$$\xi=2L(x-x_m), \tag{7}$$

$$\lambda=2u(\alpha)^{\frac{1}{2}}, \tag{8}$$

where

$$\frac{\alpha(\pi\alpha)^{\frac{1}{2}}}{\epsilon}\frac{q}{m}I_0=L^2, \tag{9}$$

and

$$\alpha=\frac{m}{2kT_c}, \tag{10}$$

Where k is Boltzmann's constant, T_c the cathode temperature, and $I_0=J_0$ is the static current density.

In addition, the potential and density functions (ϕ,N) will be rescaled to (η,P), defined as

$$\eta=\eta(\xi)=-q/kT[\phi_0(x)-\phi_0(x_m)], \tag{11}$$

$$\eta_{c0}=-q/kT[\phi_0(x_c)-\phi_0(x_m)], \tag{12}$$

$$P=P(\xi,\lambda)=2\alpha(I_0/q)^{-1}N(x,u). \tag{13}$$

In addition, the radian frequency ω will be rescaled to μ defined as $\mu=\omega/\omega_{pm}$, where $\omega_{pm}=L/(\alpha)^{\frac{1}{2}}$ is the plasma frequency at the potential minimum. It can be shown that $(1/\omega_{pm})$ is of the order of magnitude of the transit time for motion from the cathode to the minimum plane of a particle moving at the mean forward stream velocity.[7] With the above variables, the transport equation and field Eq. (5) and (6) can be rewritten, after elimination of $E(x)$ as

$$0=j\mu P+\lambda\frac{\partial P}{\partial\xi}+2\frac{d\eta}{d\xi}\frac{\partial P}{\partial\lambda}-\frac{1}{(\pi)^{\frac{1}{2}}j\mu}\frac{\partial P_0}{\partial\lambda}\left[\int_{-\infty}^{\infty}\lambda P\,d\lambda-\frac{2I}{I_0}\right]. \tag{14}$$

C. Physical Static Flow

The static density of particles in a single-cathode physical diode is known to be

$$P_{ob}(\lambda,\xi)=S(\lambda-\lambda_1)\exp[\eta-(\lambda^2/4)]=S(\lambda-\lambda_1)e^{-w}, \quad (15)$$

where

$$\lambda_1=\mp 2\eta^{\frac{1}{2}}=\text{cutoff velocity:} \quad (16)$$

$$w=\frac{\lambda^2}{4}-\eta=\text{the normalized total energy,} \quad (17)$$

$$S(\lambda-\lambda_1)=\begin{cases}0 \text{ for } \lambda<\lambda_1\\ 1 \text{ for } \lambda_1\leq\lambda,\end{cases} \quad (18)$$

where the upper sign pertains to $\xi<0$ and the lower $\xi>0$. All electrons of the static flow having velocities $\lambda>|\lambda_1|$, or $w>0$, have sufficient energy to be transported past the potential minimum on to the anode. This velocity range is designated as the transmitted flow. The range $\lambda_1<\lambda<|\lambda_2|$, or $w<0$, is designated as the reflected flow.

The potential $\eta(\xi)$ is not simply expressible in closed form. It has been calculated and tabulated.[9] At the potential minimum, $\eta=0$. In the region near $\xi=0$, one can approximate as follows:

$$\frac{d\eta}{d\xi}\cong\mp\eta^{\frac{1}{2}}-\frac{2}{3(\pi)^{\frac{1}{2}}}\eta\mp\frac{1}{4}\eta^{3/2}\cdots. \quad (19)$$

In the immediate vicinity of the potential minimum, the potential η has a square-law dependence on the distance, $\eta\cong(\xi/2)^2$.

D. Mathematical Model Static Flow

Solution of the transport equation has been accomplished for a static density not identical to the static density $P_{ob}(\lambda,\xi)$ as described above for a physical diode, but instead for a synthetic mathematical model diode having a static density $P_{os}(\lambda,\xi)$ so defined that it can be made to approximate P_{ob} arbitrarily well. The resulting solution, an exact solution for the mathematical model, then can approximate the solution for the physical diode arbitrarily well. This approach has proved advantageous because it successfully uncovers many of the singular properties the perturbation solutions possess, because it affords a relatively easy procedure for obtaining numerical solutions, because it provides a good qualitative understanding of the frequency character of the noise suppression process, and because it sheds light on the consequences of the linearization postulated earlier.

The solution is generated by superposition of impulse flows along discontinuities in the model static flow, these discontinuities occurring along constant-energy characteristic trajectories of the static flow. The approximating static density $P_{os}(\lambda,\xi)$ used is

$$P_{os}(\lambda,\xi)=\sum_{i=1}^{Nos}\Delta_i S(\lambda-\lambda_i), \quad (20)$$

where

$$\lambda_i^2=4\eta_s+w_i=\lambda_i^2(\xi), \quad (21)$$

$$0=\sum_{i=1}^{Nos}\Delta_i, \quad (22)$$

$N_{os}=N_{os}(\xi)$ such that all $\lambda_i^2<0$ are excluded, and w_i, Δ_i are numerical constants independent of λ, ξ.

A pictorial illustration depicting the character of the physical flow vs the mathematical model is shown in Fig. 1 (see also Fig. 3). Observe that the mathematical model density P_{os} has discontinuous jumps of magnitude Δ_i at a set of corresponding velocities λ_i. These velocities λ_i vary with distance as required by conservation of energy in the static flow.

(Note that N_{os} here is a sum limit, not a density function as were N_t, N_1 and N in II. *A* in the foregoing.)

The foregoing static flow will satisfy the time-invariant transport equation provided the time-invariant potential η is modified to η_s as defined by the differential equation (Poisson's law)

$$\frac{d^2\eta_s}{d\eta^2}=\frac{\int_{-\infty}^{\infty}P_{os}d\lambda}{(\pi)^{\frac{1}{2}}\int_{-\infty}^{\infty}\lambda P_{os}d\lambda}. \quad (23)$$

By selecting the constants Δ_i, w_i appropriately, and letting N_{os} become large, η_s can be made to approach η, and simultaneously $P_{os}(\lambda,\xi)$ to approach $P_0(\lambda,\xi)$, arbitrarily closely.

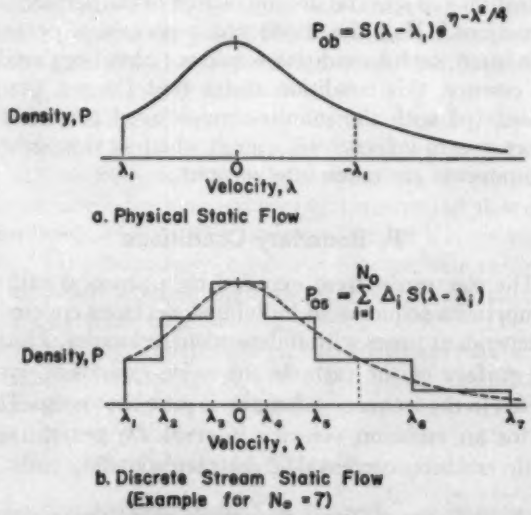

FIG. 1. Static flow velocity dependence (illustrated for an arbitrary point $\xi<0$).

[9] I. Langmuir, Phys. Rev. **21**, 419 (1923).

E. Representation of Perturbation Density

The perturbation solution P_s, which satisfies the transport equation based on P_{os} will be generable as a linear superposition of elements of the type comprising $\partial P_{os}/\partial\lambda$, plus additional purely kinematic flows, so that

$$P_s=-\frac{1}{\lambda}\sum_{i=1}^{N_s} Z_i S'(\lambda-\lambda_i)=\sum_{i=1}^{N_s}\frac{Z_i}{\lambda_i}S'(\lambda-\lambda_i); \qquad (24)$$

that is, the perturbation flow degenerates to a finite set of singular flows, each along a velocity trajectory of the static flow.[10]

On introducing the set of singular flows into the transport equation, and then utilizing the orthogonality properties of impulse functions, one obtains a set of separated, but coupled, ordinary differential equations,

$$0=\frac{j\mu}{\lambda_i}Z_i+\frac{dZ_i}{d\xi}-\Delta_i\frac{1}{j\mu(\pi)^{\frac{1}{2}}}\left(\sum_{\nu}^{N_s} Z_\nu-\frac{2I}{I_0}\right). \qquad (25)$$

This set or matrix of coupled first-order ordinary differential equations having nonconstant coefficients can be solved by straightforward numerical procedures, even for N_{os} large. The solution of the physical continuum problem is thus replaced by solution of an approximating discrete set problem. Though it may appear awkward, computer solution of the problem in this manner proves quite practical.

Examination of the local behavior of the flow near the potential minimum, $\xi=0$, further shows that in order for a unique flow solution to exist, the current Z_1, the cutoff edge current, must vanish at the minimum, and be proportional to distance nearby. The earlier-met problems arising from infinite transit delays are found to be eliminated when this constraint is recognized.

This condition is the only tactic permitting the linearization and spectral decomposition of the perturbation equations.[7] Had the diode not possessed a potential minimum, such a condition would not have been needed. In essence, this condition states that the net current associated with the infinite-time-delayed perturbation flows at zero velocity will vanish when all time-delayed components are taken into account.

F. Boundary Conditions

The electron current expelled by a physical cathode comprises a sequence of individual electrons emitted at independent times with independent velocities. Thus at the surface of the cathode the noise excitation, interpreted in the frequency domain, is pure shot noise. That is, for an emission velocity interval $d\lambda$, generating a static emission current dI_0, the corresponding emission noise-current spectral self-density $dW_{JJ}(\omega/2\pi)$ is

$$dW_{JJ}=2qdI_0=qI_0\lambda P_0 d\lambda, \quad (\lambda>0 \text{ only}). \qquad (26)$$

Because the pure shot noise at the cathode surface is uncorrelated in time and velocity, the postulate of linearity assumed earlier permits the total noise flow to be expressed as the linear superposition of (arbitrary) individual sets of independent flow solutions (satisfying the transport and field equations). The solutions are so weighted that at the cathode the aggregation satisfies the spectral-noise density requirement above. Calculation and superposition of the necessary flow solutions, though tedious, are straightforward.

G. Information Sought

For amplifier design applications, the key parameters presently of interest in design of sensitive amplifiers are the transmitted-flow spectral self- and cross-densities, W_{JJ}, W_{JV}, and W_{VV}[11,12] and certain noise temperatures described below deduced from these parameters, where J indicates convection current and V indicates a potential commonly called the kinetic potential, and defined as[7]

$$V_1=(m/2q)J_1/J_0(\langle u_1^2\rangle-\langle u_0^2\rangle), \qquad (27)$$

where $\langle u_1^2\rangle$ and $\langle u_0^2\rangle$ are convection-current-normalized mean-square velocities defined as

$$\langle u^2\rangle=\int u^2(uNdu)\Big/\int(uNdu). \qquad (28)$$

Each of these spectral densities W are expectations taken over the total, aggregated transmitted flow; each is a function of distance, frequency, and diode operating conditions.

In the limit condition of frequency approaching infinity, that is $\mu\to\infty$, it can be shown that these densities degenerate to constants invariant with distance, attaining the following values: $W_{JJ}=2qI_0$ (full shot noise); $W_{VV}=(2kT_c)^2/2qI_0$ (full velocity noise); and Re $W_{JV}=$ Im $W_{JV}=0$ (zero correlation noise). Conversely, for $\mu\lesssim 1$ it is found that these densities vary radically with distance near the potential minimum.

The theory which has been developed over the past few years for optimization of the sensitivity of a linear stream amplifier (theory based on a simpler monovelocity flow model) states that the minimum achievable amplifier excess noise temperature T_n is[11]

$$\frac{T_n}{T_c}=\left(\frac{T_n}{T_c}\right)_B-\left(\frac{T_n}{T_c}\right)_\pi, \qquad (29)$$

where the total temperature is composed of two

[10] A. E. Siegman, "Signal propagation on a drifting electron beam with a square velocity distribution," unpublished memorandum, 1957.

[11] H. A. Haus, J. Appl. Phys. **26**, 560–571 (1955).

[12] S. Bloom, RCA Rev. **16**, 179–196 (1955).

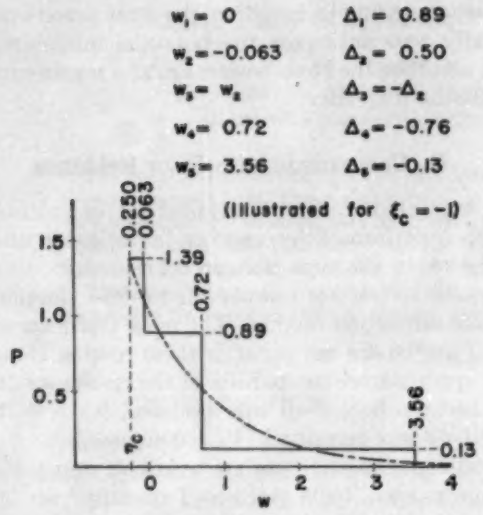

FIG. 2. Static flow approximation (numerical problem).

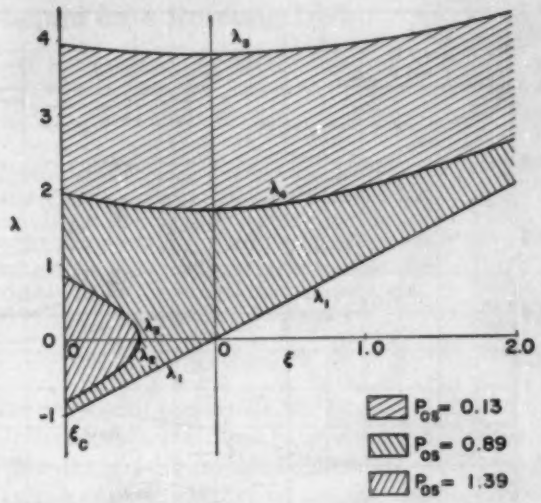

FIG. 3. Static flow approximation (phase plane representation).

components,

$$\left(\frac{T_n}{T_e}\right)_S = \left\{W_{VV}W_{KK} - \mathrm{Im}^2(W_{KV})\right\}^{\frac{1}{2}} \tag{30}$$

$$\left(\frac{T_n}{T_e}\right)_r = \mathrm{Re}(W_{KV}); \tag{31}$$

the foregoing statements are conveniently expressed in terms of the normalized spectral densities,

$$W_{KK} = [2qI_0]^{-1}W_{JJ}$$

$$W_{KV} = [2kT_e]^{-1}W_{JV}$$

$$W_{VV} = \left[\frac{(2kT_e)^2}{2qI_0}\right]^{-1}W_{VV}.$$

Subject to the restrictive assumptions of this earlier monovelocity theory, it can be shown that each of the two temperature components remain invariant along the stream. However, in heterovelocity flow at finite frequency, the two components do vary with distance, particularly near the potential minimum. Yet at moderate distance downstream from the minimum, evaluation of the components using either the hetero- or monovelocity theories must lead quantitatively to essentially the same results, because the velocity dispersion becomes small compared to the mean velocity. Provided that on evaluation for finite frequencies for heterovelocity flow at large distances downstream these components do approach stationary values (as is the case), the calculated temperature T_n will be the minimum achievable amplifier noise temperature. The variation of this temperature and of the spectral densities with frequency and diode operating conditions is graphed below.

III. NUMERICAL SOLUTIONS

Numerical results have been obtained by calculations performed on electronic computing equipment (IBM 704 computer). Corroborative checks were obtained by hand and analogue calculation.

A. Range of Parameters

Because of the limited time and funds available, only simple models could be examined. The numerical calculations covered only the limited range $-2.0 \leq \xi \leq 2.0$; the diode was assumed open-circuited at the frequency of calculation.

The model static flow P_{os} was selected so that the zero, first, third, and fifth velocity moments of $P_{ob}(0,\lambda)$ and $P_{os}(0,\lambda)$ were made identical. The minimal number (three) of transmitted streams permitting this end to be attained was employed. One reflected stream was included to permit a good fit to the static potential close to the cathode. The concomitant static flow is graphed in Fig. 2 and Fig. 3, for $\xi_c = -1$.

Five values of frequency were examined, $\mu = 0.3$, 0.6, 1.0, 2.0, and 3.0. The lowest value for μ corresponds to a "low-frequency" condition (cathode-to-minimum transit angle for average energy transmitted flow electron being $0.1\pi/2$). The largest value for μ corresponds to a "high-frequency" condition (comparable cathode-to-minimum transit angle being $\pi/2$). Three cathode locations were examined: $\xi_c = -1$; -1.5; -2.0; the corresponding emitted-current-to-anode-current static saturation ratios I_{em}/I_0 are 1.3:1, 2.3:1, and 7.0:1, respectively.

B. Calculated Noise Transport

In Fig. 4, the transport of the self- and cross-power spectral densities W_{KK}, W_{VV}, $\mathrm{Im}(W_{KV})$, $\mathrm{Re}(W_{KV})$, also (T_n/T_e), $(T_n/T_e)_S$, and $(T_n/T_e)_r$ is graphed vs

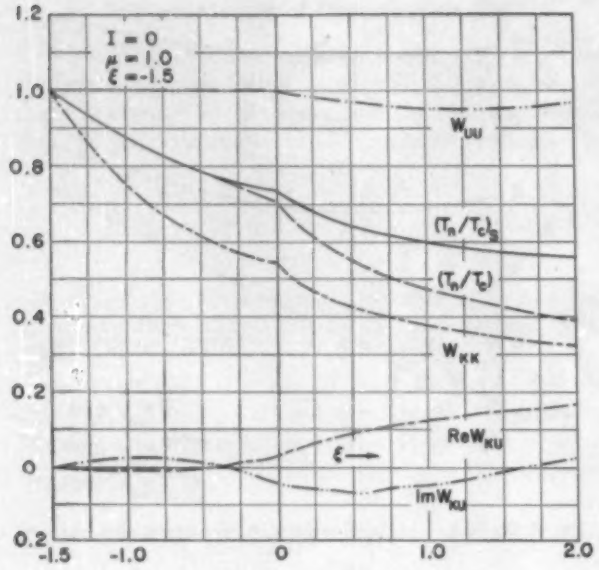

FIG. 4. Transport of noise parameters.

distance for illustration for $\mu=1$, $\xi_c=-1.5$. The transport of these densities at lower and higher frequencies, though not shown here, is similar. Observe that T_n/T_c becomes relatively stationary with distance downstream, as anticipated.

Finally, in Fig. 5, T_n/T_c as evaluated at $\xi=2.0$ (furthest downstream point calculated) is graphed vs frequency. The weakening of the noise suppression process with increasing frequency is clearly evident. The weakening of the noise suppression with decreasing static current saturation is also evident.

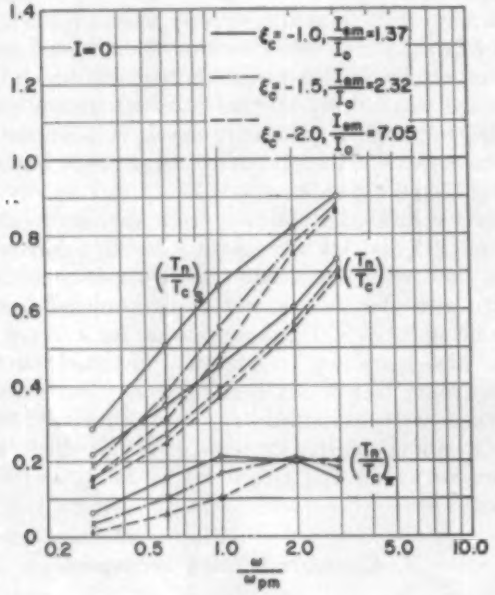

FIG. 5. Noise temperature (frequency dependence).

It is interesting to note that the cross powers remain virtually zero until past the potential minimum. Observe also that the cross-powers are at a maximum near the plasma frequency.

C. Comparison with Prior Evidence

As mentioned earlier, a detailed set of calculations has been performed by another investigator utilizing simulation in the time domain.[8] The results obtained here qualitatively are comparable to those obtained by his time-simulation method. The noise dip observed by him at $\mu=0.6$ did not occur in these results. However, direct quantitative comparison of the results is not possible because here $I=0$ was assumed, whereas in the other $I\neq 0$ was permitted ($V_{cs}=0$ assumed).[7]

Some experimental data are available and pertinent for comparison. Tests performed recently[13] on sample low-noise electron guns adjusted to provide space-charge-limited flow consistently indicated $(T_n/T_c)_T/(T_n/T_c)_S \simeq 0.2$ to 0.3, and $(T_n/T_c)_S \simeq 0.6$ to 0.8. Insufficient experimental data were provided to permit accurate calculation of μ and (I_{em}/I_0) for these tests. However, from examination of the experimental data provided, it seems reasonable to estimate $\mu \cong 2$, and $(I_{em}/I_0) \simeq 2$ or more. On inspection of Fig. 5, it is evident that there is excellent qualitative agreement between the calculated results and the published test data.

D. Remarks

It is important to realize that the noise suppression process examined above occurs very close to the cathode. For example, for a typical diode with $T_c=1000°K$, $I_0=0.5$ amp cm^{-2}, the normalized distance interval treated in Fig. 4 (from $\xi=-1.5$ to $+2.0$) represents a physical distance of 10 μ, or 4×10^{-4} in. This distance is of the magnitude of surface irregularity tolerances commonly permitted in cathode processing. Certainly it is small compared to distances over which control over a given potential profile is readily achieved by introduction of ungridded, nonintercepting electrodes.

ACKNOWLEDGMENTS

The author wishes to acknowledge the contributions of Professor G. Hok and of J. Riordan of The University of Michigan, and of A. E. Siegman of Stanford University with regard to conception of the ideas presented, and of S. Lampert and W. Evans of The University of Michigan with regard to calculation of numerical data. Their assistance was much appreciated.

[13] S. Saito, "New method of measuring the noise parameters of the electron beam especially the correlation between its velocity and current fluctuations," Mass. Inst. Technol., Research Lab. Electronics, Tech. Rept. No. 333, August, 1957.

JOURNAL OF APPLIED PHYSICS VOLUME 31, NUMBER 6 JUNE, 1960

On the Flow of a Non-Newtonian Liquid on a Rotating Disk

A. Acrivos, M. J. Shah, and E. E. Petersen
Department of Chemical Engineering, University of California, Berkeley, California
(Received September 17, 1959; revised manuscript received March 7, 1960)

The equations describing the flow of a power-law non-Newtonian fluid on a rotating disk have been solved in general form. This makes it possible to calculate how the shape of an initial surface contour will vary with time and to investigate the possibility of producing uniform films by applying the materials to a rapidly spinning disk. It is shown that the latter process, which has potential industrial applications, has a much better chance of succeeding if the fluid is Newtonian than if it is not, in the sense that whereas for a Newtonian substance centrifugation will smooth out irregularities in the surface contour, for a non-Newtonian fluid even an initially uniform film thickness will be deformed by rotating the plate.

INTRODUCTION

It has been reported in the literature[1–3] that uniform films of paint, varnish, and asphalt may be produced by applying the material in fluid form to a rapidly spinning disk and then evaporating the volatile constituents from the film after it has been reduced to the desired thickness. It is also known that this same technique has been in actual commercial use for the production of color television screens. These and other intriguing potential applications of this process have therefore brought about of late an interest in the behavior of fluids moving on a rotating plate.

In a recent article on this subject, Emslie *et al.*[1] presented a theoretical analysis of the hydrodynamics of such systems, and arrived at a simple expression for predicting how arbitrary initial surface contours would change with time when placed on a rotating disk. Then, by examining in some detail the deformation of the contour surfaces for a number of typical initial distributions, they were able to show that initial irregularities in these contours tend as a rule towards uniformity upon centrifugation and thus succeeded in demonstrating the general usefulness of such a process for producing uniform films of the desired thickness. However, as Emslie *et al.*[1] have themselves pointed out, their study is not as general as would be desirable. Its main limitation is probably due to the fact that it deals exclusively with Newtonian fluids, whereas at least some of the substances used in the technique under consideration consist of viscous suspensions which exhibit rather pronounced non-Newtonian characteristics, especially at high concentrations. Since it is known then that, when in motion, non-Newtonian fluids often behave quite differently from Newtonians under similar flow conditions, it is of obvious interest to ascertain whether or not this property of the spinning disk in smoothing out the initial surface irregularities is limited only to Newtonian substances, or whether it is a more general characteristic of such a rotating setup.

The purpose of this article will be then to extend the analysis of Emslie *et al.*[1] and to investigate theoretically the flow of a non-Newtonian fluid on a rotating plate in order to establish whether or not the non-Newtonian property of the substance is at all an important factor in determining the general applicability of the process. In particular, since the term "non-Newtonian" is a very broad one which encompasses a large variety of fluids with fundamentally different rheological characteristics, we shall limit ourselves to a special class which obey the so-called "power-law relationship" between shear stress and velocity gradient, since it is well known that a significant number of non-Newtonian fluids with time-independent rheological properties do, in fact, adhere to the power law over a relatively wide range of shear rates.[4,5] Our objective will again be, as in the work of Emslie *et al.*,[1] to derive an expression for predicting how an initial surface contour of such a non-Newtonian liquid film will deform as a function of position and time and especially to find out under what conditions it is possible to obtain a film, which is both uniform and of the desired thickness, by the rotating disk process.

BASIC EQUATIONS

The present analysis parallels that of Emslie *et al.*[1] as far as the basic equations and assumptions are concerned. We shall assume, first of all, that the plate is horizontal and that gravitational effects may be omitted in comparison with the centrifugal forces caused by the rotating disk. In addition, we shall suppose that

(a) the shear resistance is appreciable only in the horizontal planes;

(b) the pressure is everywhere constant;

(c) the inertia terms, except for the centrifugal acceleration, may be neglected in comparison to the viscous terms of the equations of motion; and

(d) the radial velocity is so small that Coriolis forces are not important.

The necessary conditions for the validity of all these

[1] A. G. Emslie, F. T. Bonner, and L. G. Peck, J. Appl. Phys. 29, 858 (1958).
[2] L. R. Kleinschmidt, Am. Soc. Testing Materials Bull. No. 193, 53 (October, 1953).
[3] P. H. Walker and J. G. Thompson, Am. Soc. Testing Materials Proc. 22, Part II, 464 (1922).
[4] A. B. Metzner, in Advances in Chem. Engr. 1, 79–150 (1956).
[5] M. Reiner, *Deformation and Flow* (H. K. Lewis and Company, London, 1949).

simplifying assumptions will be stated at the end of the paper.

In cylindrical polar coordinates, the equation of motion is then

$$\partial\tau/\partial z = -\rho\omega^2 r \tag{1}$$

if radial symmetry is postulated. ω is the angular velocity of the spinning disk, ρ the density of the fluid, and r and z the two polar coordinates in the usual notation. The shear stress τ is related to the velocity gradient $\partial v/\partial z$, where v is the velocity in the radial direction, by an empirical "equation of state" which for non-Newtonian fluids may often be approximated by the power law[4,5]

$$\tau = K(\partial v/\partial z)|\partial v/\partial z|^{n-1}, \tag{2}$$

where K and n are characteristic parameters of the fluid. It should be carefully realized at this point, however, that strictly speaking all non-Newtonian fluids approach Newtonian behavior if the rate of strain $\partial v/\partial z$ is made sufficiently small.[4] Thus, for example, for some substances, the non-Newtonian characteristics do not set in until the shear rate exceeds 100 sec^{-1},[6] whereas for other materials this critical shear rate may be as low as 10^{-2} or even lower.[7] We can see, therefore, the need for keeping firmly in mind that, for the purposes of this analysis, a fluid should be considered non-Newtonian only if the rate of shear at the surface is well within the limits of applicability of the power law with $n \neq 1$.

Since now for this system $\partial v/\partial z \geqq 0$ always, Eq. (1) and (2) may be combined into

$$K = (\partial/\partial z)(\partial v/\partial z)^n = -\rho\omega^2 r \tag{3}$$

with the boundary conditions

$$v = 0 \quad \text{at} \quad z = 0, \text{ the surface of the disk,}$$
$$\partial v/\partial z = 0 \quad \text{at} \quad z = h$$

where h is the thickness of the liquid film. The solution of this system is

$$v = [n/(n+1)](\rho\omega^2 r/K)^{1/n}[h^{1+1/n} - (h-z)^{1+1/n}] \tag{4}$$

from which q, the radial rate of flow per unit length of circumference, may readily be obtained as a function of h and r. Thus

$$q \equiv \int_0^h v\,dz = \frac{n}{2n+1}\left(\frac{\rho\omega^2 r}{K}\right)^{1/n} h^{(2n+1)/n}. \tag{5}$$

It is now possible to make use of the continuity equation and arrive finally at an expression for h as a function of r and the time t. In cylindrical coordinates,

$$r(\partial h/\partial t) + (\partial/\partial r)(rq) = 0, \tag{6}$$

where q is given by Eq. (5). This equation turns out to have a surprisingly simple form. Let

$$T \equiv [nt/(2n+1)](\rho\omega^2/K)^{1/n}$$
$$y \equiv [n/(3n+1)]r^{(3n+1)/(2n+1)} \tag{7}$$
$$x = r^{[(n+1)(n+1)/n(2n+1)]}h^{(n+1)/n}$$

which, when substituted into Eq. (6), transforms it into

$$\partial x/\partial T + x\partial x/\partial y = 0. \tag{8}$$

From the solution of this equation one can therefore readily predict how the surface contour of the film will vary as a function of position and time. We shall also show how, conversely, it is possible to calculate the initial shape of the surface contour which will give a uniform film of the desired thickness, after a time T.

SPECIAL CASES

Before proceeding with the general solution of Eq. (8), it is of interest to discuss here briefly two special cases:

I. Equation (8) has a steady-state solution of the form $x = x_0$, where x_0 is a constant, which may be realized physically only when there is a constant flow of material into the center of the disk. The film thickness under these conditions is given by

$$h = x_0^{n/(1+n)} r^{-[(n+1)/(2n+1)]} \tag{9}$$

and is shown schematically in Fig. 1 for $n = \frac{1}{2}$, $n = 1$ and $n = \frac{3}{2}$. Since the present study is, however, concerned primarily with the transient deformation of a given initial surface contour, the steady-state solution is for our purpose of secondary interest and will not therefore be considered any further.

II. Another class of closed-form solutions of Eq. (8), which will be found especially useful in examining how initially uniform contours are affected by the spinning

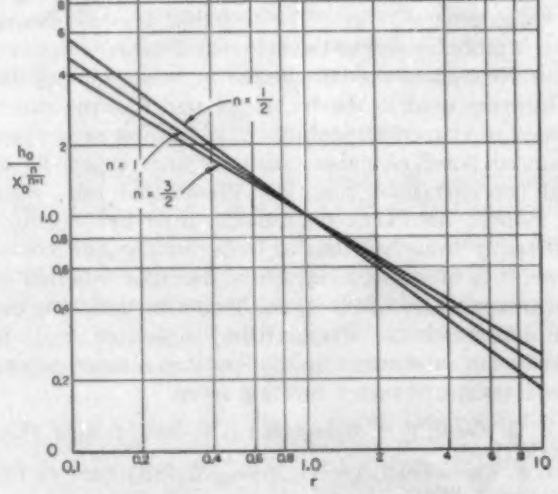

FIG. 1. Schematic diagram of the stable contours for $n = \frac{1}{2}$, 1, and $\frac{3}{2}$.

[6] E. W. Merrill, Ind. Eng. Chem. 51, 868 (1959).
[7] M. Mooney in *Rheology*, edited by Frederick R. Eirich (Academic Press, Inc., New York, 1958), Vol. II, p. 207.

process, may be obtained by a similarity transformation. Let, then,

$$x \equiv f_1(y)\phi(\eta) \quad \text{with} \quad \eta \equiv T/f_2(y), \tag{10}$$

where

$$f_1 = [y+B]^{1-A}$$
$$f_2 = [y+B]^{A} \tag{11}$$

and $\phi(\eta)$ may be shown to satisfy the differential equation

$$\phi'(1-A\eta\phi)+(1-A)\phi^2=0$$
$$\text{with} \quad \phi=\phi_0 \quad \text{at} \quad \eta=0. \tag{12}$$

A and B are arbitrary constants with $B \geqslant 0$.

The solution to Eq. (12) is

$$\phi\eta/[1-\phi\eta]^{1-A}=\phi_0\eta. \tag{13}$$

Thus, if the initial contour is of the form

$$h_0=\phi_0^{n/(1+n)}r^{-[(n+1)/(2n+1)]} \times\{[n/(3n+1)]r^{(3n+1)/(2n+1)}+B\}^{n(1-A)/(1+n)}, \tag{14}$$

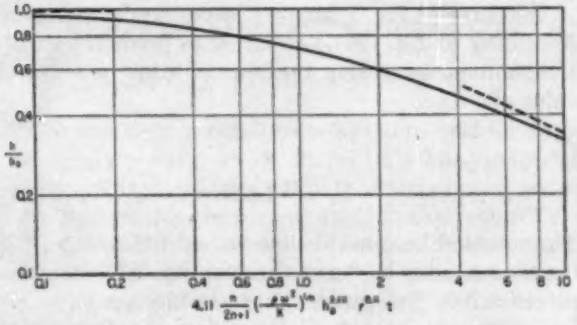

FIG. 2. Distortion of an initially uniform contour for $n=0.9$.

a uniform film thickness cannot be obtained by spinning the disk, unless

$$B=A=0 \quad \text{and} \quad n=1 \text{ (Newtonian fluid).}$$

In that case,

$$h=h_0/(1+4h_0^2T)^{\frac{1}{4}}, \tag{15}$$

which is identical to what Emslie *et al.*[1] have derived, and from which it follows that, for a Newtonian fluid only, an initially uniform fluid layer will remain so with time even though its thickness will decrease due to the presence of the centrifugal force. For a non-Newtonian fluid this is not so strictly speaking, although we would naturally expect that if the non-Newtonian index n were close to unity, the nonuniformity of the liquid film thickness would be rather minor. This is borne out by the following example. If $n=0.9$, then

$$B=0; \quad A=-0.0841; \quad h_0=(0.2432)^{0.5135}\phi_0^{0.4737}$$

Therefore,

$$h/h_0=[\phi/\phi_0]^{0.4737}=[\phi_{0.9}(\eta_{0.9})]^{0.4737},$$

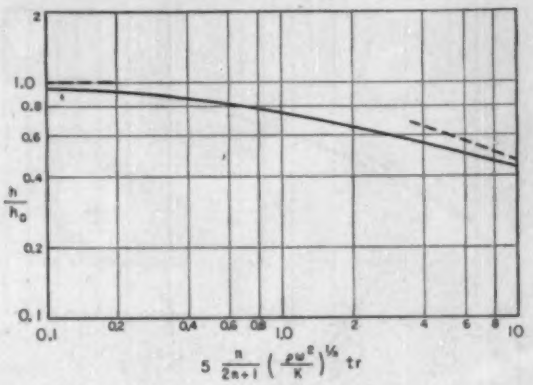

FIG. 3. Distortion of an initially uniform contour for $n=\frac{1}{2}$.

where

$$\phi_{0.9}\eta_{0.9}/[1-\phi_{0.9}\eta_{0.9}]^{1.084}=\eta_{0.9},$$
$$\text{and} \quad \eta_{0.9}=\phi_0\eta=4.111h_0^{2.111}r^{0.11}T,$$

and we can see from Fig. 2 that for such substances the film does indeed retain its original uniform contour for all practical purposes, since the similarity variable η is only slightly affected by changes in the position variable r. On the other hand, if n is considerably different from unity, which would imply a pronounced non-Newtonian behavior on the part of the fluid, then the deformation of the surface contour should be appreciable. This is shown in the following two cases.

(a) $n=\frac{1}{2}$

If h_0 is to be independent of r, then, from Eq. (14)

$$B=0, \quad A=-\tfrac{1}{3}$$

and

$$h_0=(\tfrac{1}{3})^{3/5}\phi_0^{\frac{1}{5}}. \tag{16}$$

Therefore,

$$h/h_0=[\phi_{\frac{1}{2}}(\eta_{\frac{1}{2}})]^{\frac{1}{4}}, \tag{17}$$

where $\phi/\phi_0=\phi_{\frac{1}{2}}$, $\phi_0\eta=\eta_{\frac{1}{2}}$, and $\eta_{\frac{1}{2}} \equiv 5h_0^3Tr$, and $\phi_{\frac{1}{2}}$ is obtained from Eq. (13),

$$\phi_{\frac{1}{2}}\eta_{\frac{1}{2}}/[1-\phi_{\frac{1}{2}}\eta_{\frac{1}{2}}]^{9/5}=\eta_{\frac{1}{2}}. \tag{18}$$

It is immediately seen from Fig. 3 that the ratio h/h_0 quickly decreases for large $\eta_{\frac{1}{2}}$, from which it follows that when $n=\frac{1}{2}$ an initially uniform contour will be rapidly deformed by the spinning process, especially for large values of r.

(b) $n=3/2$

Again, if h_0 is to be independent of r, then

$$B=0, \quad A=8/33$$

and

$$h_0=\phi_0^{3/5}(3/11)^{5/11}.$$

Therefore,

$$h/h_0=[\phi_{\frac{3}{2}}(\eta_{\frac{3}{2}})]^{3/5}, \tag{19}$$

where

$$\eta_{\frac{3}{2}}=(11/3)h_0^{5/3}Tr^{-\frac{1}{3}} \tag{20}$$

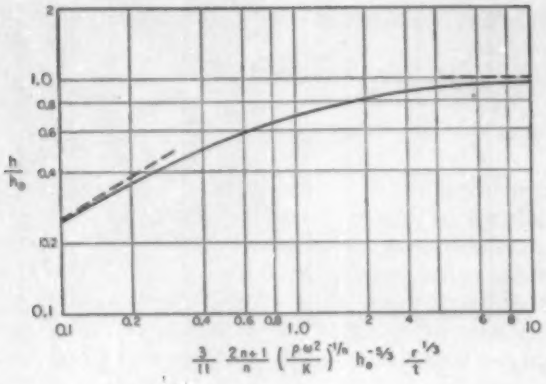

FIG. 4. Distortion of an initially uniform contour for $n=\frac{3}{2}$.

and

$$\phi_1\eta_1/[1-\phi_1\eta_1]^{25/33}=\eta_1. \tag{21}$$

Thus, as seen from Fig. 4, when $n=\frac{3}{2}$ the initially uniform contour is again deformed for large η. However, since according to Eq. (20), $1/\eta_1$ is proportional to $r^{\frac{1}{3}}$, this implies that the deformation takes place primarily near the center of the disk. Therefore, an initially uniform film thickness will

(a) remain fairly uniform near the center but be deformed for large r, if $n<1$;
(b) remain exactly uniform for all r, if $n=1$;
(c) remain fairly uniform for large r but quickly form a dip in the region near the center, if $n>1$.

It follows that if one is interested in obtaining a uniform contour by rotating the disk, one must, in general, be able to begin the spinning process with a nonuniform film thickness which is

(a) monotonically increasing with r when $n<1$;
(b) monotonically decreasing with r when $n>1$.

This will be deomstrated from the properties of the general solution of Eq. (8).

GENERAL SOLUTION

The general solution of Eq. (8) may be obtained numerically without much difficulty by the method of characteristics.[8] Let $x_0(y)$ be the profile at $T=0$. Then

$$x=x_0(y_1) \tag{22}$$

along the characteristic line.

$$T=(y-y_1)/x_0(y_1), \tag{22a}$$

where y_1 is a constant. The film thickness h may then be calculated for all r and T in a straightforward manner, if the initial distribution $x_0(y)$ is given.

It is possible now to find the required initial contour shape $h_0(r)$ which, at a given T, will develop into a film of the desired uniform thickness h_c. Let us suppose that at a given T the thickness is a constant h_c for all r. It immediately follows from Eq. (7) that

$$y=[n/(3n+1)][x_0(y_1)]^{n(3n+1)/(n+1)(n+1)}\times h_c^{-[(3n+1)/(n+1)]} \tag{23}$$

which, when substituted into Eq. (22a), gives

$$y_1=[n/(3n+1)][x_0(y_1)]^{n(3n+1)/(n+1)(n+1)}\times h_c^{-[(3n+1)/(n+1)]}-Tx_0(y_1).$$

Finally, in view of Eq. (7), this can be rearranged into

$$\frac{3n+1}{n}Th_c^{(n+1)/n}r^{(1-n)/n}=\frac{(h_0/h_c)^{(3n+1)/(n+1)}-1}{(h_0/h_c)^{(n+1)/n}} \tag{24}$$

from which (h_0/h_c), the ratio of the initial thickness to the final uniform thickness at the given reduced time T may be calculated. For $n=1$,

$$h_0/h_c=(1-4Th_c^2)^{-1}, \tag{25}$$

while the profiles for $n=\frac{1}{2}$ and $n=\frac{3}{2}$ are shown on Figs. 5 and 6, respectively.

The curve on Fig. 5, for $n=\frac{1}{2}$, needs further comment. According to Eq. (24), (h_0/h_c) is, as predicted earlier, a monotonic increasing function of r up to a critical value of

$$5Th_c^3r=0.290$$

at which point

$$h_0/h_c=1.627.$$

The function becomes double valued for $h_0/h_c>1.627$, for as can readily be shown the quantity $(5Th_c^3r)$ cannot exceed 0.290. This problem has, therefore, a physically realizable solution only if the radius R of the disk is

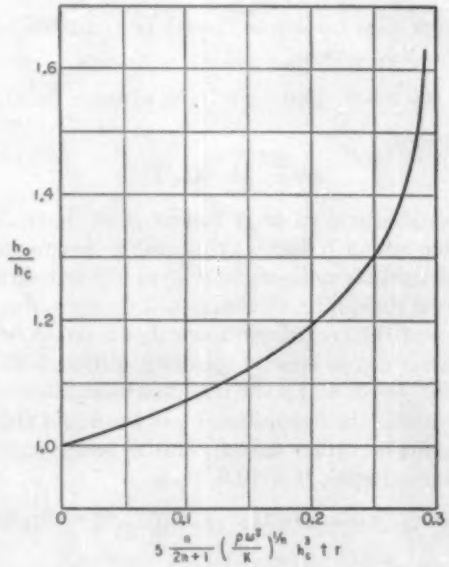

FIG. 5. Required initial contour which will give film of uniform thickness h_c for $n=\frac{1}{2}$.

[8] E. L. Ince, *Ordinary Differential Equations* (Dover Publications Inc., New York, 1956).

such that

$$5Th_c^3R \leqslant 0.290;$$

otherwise, for $n=\frac{1}{2}$, it is not possible to find an initial surface contour which upon rotation will, after a given reduced time T give a film of uniform thickness h_c. A similar restriction in the solution exists for all $n<1$.

CONCLUSIONS

This paper has dealt with the flow of non-Newtonian power-law fluids on a rotating disk. Its purpose has been (1) to extend the analysis of Emslie *et al.*[1] which dealt exclusively with Newtonian fluids; (2) to derive an expression for predicting how the surface contour of a non-Newtonian liquid film would vary as a function of time when placed on a spinning plate; and (3) to determine the shape of the initial contour which when rotated would give a film both uniform and of the desired thickness. It can be shown, by a straightforward analysis of the exact equations of motion, that the mathematical simplifications introduced in our development can be justified rigorously if

(a) $r \gg h$, where h is some characteristic thickness of the film

(b) $h^n(\omega h)^{2-n}\rho/K \ll 1$

which would, in general, be expected to hold for a typical system, with $\rho \sim 70$ lb/ft^3, $K>0.1$ lb-sec^{n-2}/ft, $\omega<10$ rad/sec, and $h<0.005$ ft. Furthermore, as was explained earlier, the present analysis also requires that, for the fluid to be considered as non-Newtonian, the rate of shear at the rotating surface be well within the range of applicability of the power-law with $n \neq 1$. This demands the evaluation of $(\partial v/\partial z)_{z=0}$, which from Eq. (4) is equal to

$$[(\rho\omega^2 r/K)h]^{1/n},$$

and which must then be compared with the available rheological data in order to ascertain whether or not, for the particular system under consideration, the fluid would exhibit a non-Newtonian behavior.

Unlike the conclusions reached by Emslie *et al.*[1] for a Newtonian substance, centrifugation of a non-Newtonian fluid layer that is initially uniform tends to destroy this uniformity. This departure from uniformity is most pronounced for regions away from the axis of rotation when $n<1$ and for regions close to the axis when $n>1$, and becomes particularly noticeable if the fluid has a pronounced non-Newtonian behavior. Thus, in general, irregular fluid distributions which are superimposed on a uniform distribution will not be dampened out by the centrifugation unless the non-Newtonian index n is numerically close to unity.

It is concluded, therefore, that the process of obtaining uniform films by applying the material to a rotating disk has a much better chance of succeeding if the fluid is Newtonian than if it is not, and that, as a consequence, the substance must be in sufficiently low concentrations in order that any departure of its rheological properties from Newtonian behavior be minimized. Thus, it is believed that the reported success of the process even with substances such as paints, which are usually considered as non-Newtonian, may be due in large part to the fact that these materials are for practical purposes Newtonian under sufficiently dilute conditions.

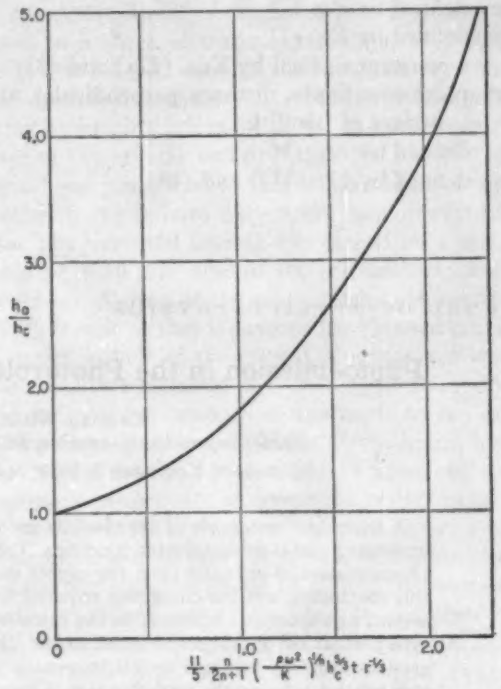

FIG. 6. Required initial contour which will give film of uniform thickness h_c for $n=\frac{1}{3}$.

ACKNOWLEDGMENTS

It is a pleasure to acknowledge the helpful suggestions of the reviewer of this paper. The work was supported in part by a grant from the Petroleum Research Fund administered by the American Chemical Society. Grateful acknowledgment is hereby made to the donors of said Fund.

NOMENCLATURE

A, B—constants defined by Eq. (11)
f_1, f_2—defined by Eq. (11)
h—thickness of the film on the disk
h_0—initial thickness of the film
h_c—the thickness of the desired uniform film
K, n—parameters of the non-Newtonian fluid
q—radial rate of flow of liquid per unit length
r—polar coordinate, the radius of the disk
t—time of spinning
T—defined by Eq. (7)
v—velocity of the fluid in the radial direction

x—defined by Eq. (7)
y—defined by Eq. (7)
y_1—a constant defined by Eqs. (22a) and (23)
z—polar coordinate, distance perpendicular to the surface of the disk
η—defined by Eq. (10)
η_1—defined by Eqs. (17) and (18)
η_2—defined by Eqs. (19) and (20)
ρ—density of the fluid
τ—shear stress
$\phi(\eta)$—defined by Eq. (10)
ϕ_1—defined by Eqs. (17) and (18)
ϕ_2—defined by Eqs. (20) and (21)
ω—the angular velocity of the disk

JOURNAL OF APPLIED PHYSICS VOLUME 31, NUMBER 6 JUNE, 1960

Photoemission in the Photovoltaic Effect in Cadmium Sulfide Crystals

RICHARD WILLIAMS AND RICHARD H. BUBE
Radio Corporation of America, RCA Laboratories Division, Princeton, New Jersey
(Received November 5, 1959; revised manuscript received December 17, 1959)

A study has been made of the photovoltaic effect in Cu-CdS cells and related systems, associated with undiffused metal-semiconductor junctions. The photovoltaic current has been shown to result from the photoemission of electrons from the copper metal into the CdS crystal. Direct evidence is presented for this conclusion, and the conditions required for the photoemission process to occur are demonstrated by several experiments. Important factors contributing to the efficiency of Cu-CdS photovoltaic cells of this type are: (a) the optical properties of copper, (b) the rectifying contact between the metal and CdS, (c) the good conductivity and high optical transparency which can be achieved in CdS crystals, and (d) the favorable relation between the work function of copper and the electron affinity of CdS.

INTRODUCTION

PHOTOVOLTAIC effects have been observed in a variety of systems in which a metal and a semiconductor are in contact. It has been demonstrated that the effect is produced predominantly by the light which is absorbed near this contact.[1] The accepted explanation is that light is absorbed by the semiconductor, producing hole-electron pairs, and that both the holes and the electrons are mobile. These carriers are accelerated by the electric field existing in the barrier layer of the semiconductor where it contacts the metal. Holes and electrons move in opposite directions and give rise to the observed photovoltaic currents. In a number of cases, where the exciting light has energy greater than that of the band gap of the semiconductor, the above explanation fits the experimental facts very well.

In some systems, however, photovoltaic effects are produced with high efficiency by light whose energy is far less than that of the band gap. Two such systems which have been extensively investigated are the Cu-Cu_2O system and the Cu-CdS system.[2] Photovoltaic cells utilizing these junctions may be constructed so that the light must traverse a considerable thickness of the semiconductor before reaching the junctions. This geometry is illustrated in Fig. 1. The dotted line is a schematic indication of the semiconductor barrier layer. Under typical conditions this thickness is 1 μ or less.[3] Only light of those wavelengths, which are not strongly absorbed, may reach the junction where the effect is produced. Light whose energy is as little as half that of the band gap is effective in both the foregoing systems.

These facts raise two major problems in the use of the preceding interpretation of the photovoltaic effect for the description of the results in this part of the spectrum. The first of these may be illustrated by reference to Fig. 1. Only holes and electrons produced in or near the barrier layer are accelerated by the existing internal electric field to produce a net current with high efficiency. Since the thickness of the barrier layer is of the order of a micron, the total thickness of the semiconductor may be more than one thousand times this. For weakly

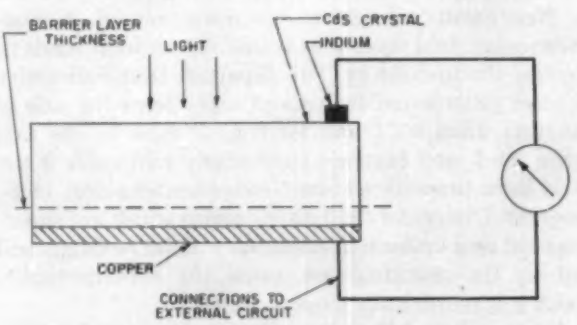

FIG. 1. Schematic construction of a typical Cu-CdS photovoltaic cell.

[1] N. F. Mott and R. W. Gurney, *Electronic Processes in Ionic Crystals* (Oxford University Press, New York, 1948), 2nd ed., p. 192.
[2] D. C. Reynolds, G. Leies, L. L. Antes, and R. E. Marburger, Phys. Rev. 96, 533 (1954); D. C. Reynolds and S. J. Czyzak, Phys. Rev. 96, 1705 (1954). A summary of the results for the Cu-Cu_2O system is given by V. K Zworykin and E. G. Ramberg, in *Photoelectricity* (John Wiley & Sons, Inc., New York, 1949).
[3] See footnote 1, p. 174.

absorbed light the absorption in any given layer is approximately proportional to the thickness of the layer. Thus only one-thousandth of the light would be absorbed in the barrier and this should set an upper limit of 0.001 for the quantum yield of photovoltaic current. The observed quantum yields may be as much as one hundred times larger. In order to account for the experimental facts, it is necessary to assume that the absorption spectrum of the semiconductor in the barrier is several orders of magnitude greater than that in the bulk. Although there may be some basis for such an assumption in the case of a junction formed by diffusing a metal into a semiconductor, it does not appear applicable to the experiments described in this paper with plated nondiffused metal layers.

The second problem arises from the requirement that both the hole and the electron produced by light absorption must be mobile. When the energy of the light is less than that of the semiconductor band gap, then either the electron or the hole produced on absorption must be bound at a level in the forbidden energy gap where its mobility would be very low. This problem can be overcome, at least in principle, by the postulation of the existence of an impurity band in which photo-excited holes could have sufficient mobility to produce the photovoltaic effect.[3] Such a postulation may be relevant when a semiconductor is used with a high concentration of metallic impurity sufficient to cause impurity banding, but in the experiments described in this paper it cannot be applied.

It is the purpose of this paper to show that the resolution of these problems for undiffused plated metallic contacts on transparent semiconducting CdS crystals lies in the interpretation of the effects as resulting from the *photoemission* of electrons from the metal into the CdS crystal. Several properties of the system combine to make it a favorable one for the observation of this phenomenon.

EXPERIMENTAL

Most experiments were done with conducting CdS: I crystals grown by L. A. Barton. These had been grown from the vapor phase in an atmosphere containing a few mm partial pressure of iodine. The crystals are *n*-type semiconductors, with about 3×10^{17} electrons cm^{-3}, and with resistivities of 0.1 to 1 ohm cm. They are in the form of thin flat plates about 0.1 mm thick and 4×5 mm^2 in area. Their optical properties are very similar to those of pure CdS and they are quite transparent to wavelengths longer than 5200 A. Spectrographic analysis of the crystals by H. H. Whitaker showed only the following metallic impurities in parts per million: Cu-3, Si-0.3, and Mg<0.1. Except for about 30 ppm of iodine, therefore, the crystals are relatively free from impurities.

Photovoltaic cells were made with the geometry illustrated in Fig. 1. The metal layer, usually copper, was applied to one of the broad faces of the platelike crystal by electroplating. For this purpose crystals were cemented to a sheet of transparent vinylite $\frac{1}{32}$ thick. Figure 2 shows a side view of the mounted crystal. A 0.050-in. diam indium dot was fused to the crystal before mounting by heating briefly to 180°C. A hole about the diameter of the crystal was drilled in the vinylite and the crystal was positioned so that its broad face covered the hole with the indium dot on the face opposite the vinylite. The mounted crystal was placed on a micromanipulator with the crystal on the bottom of the vinylite sheet. A drop of the plating solution was then placed in the hole so that it covered the exposed portion of the upper surface of the crystal. Contact was made from the negative terminal of a battery to the indium dot and the positive connection was made to the drop of solution through an anode made of the metal being plated. Current densities of the order of 1 ma/cm^2 were used to give a proper rate of deposition of the metal on the crystal. To plate crystals of high resistivity, a wire screen anode was used and the crystal was illuminated from above through the anode to give it the necessary conductivity. Silver paste was used to complete the external contacts to the indium dot and the metal layer. Silver and gold were plated from standard cyanide plating solutions obtained from the plating shop in this laboratory. Other metals were plated from solutions made up according to the recommendations in the Plating and Finishing Guidebook.[4] The area covered by the plated metal was typically 0.1 cm^2.

The nature and appearance of the electroplated copper layer depended on the plating solution used. Layers deposited from copper cyanide solution were smooth and adherent with the bright metallic lustre characteristic of clean copper. Layers plated from acidified copper sulfate solution were darker, less uniform, and less adherent. Since a number of the experiments to be described required uniform, adherent copper layers, most of the layers were plated from cyanide solution. However, somewhat higher photovoltaic yields have been obtained from cells on which the copper was plated from acid solution.

Highly efficient photovoltaic cells, consisting of a junction formed by thermally diffusiug copper into CdS crystals, have been made by Reynolds and co-workers.[2] In contrast to this method of preparation, the cells described in this paper were prepared *without any heat*

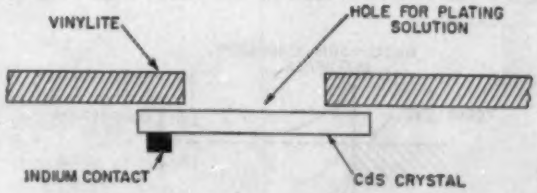

FIG. 2. Schematic drawing of the mounting of crystal for electroplating.

[4] *Plating and Finishing Guidebook* (Metal Industry Publishing Company, New York, 1946), 15th ed.

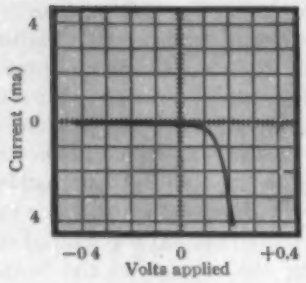

FIG. 3(a). Current-voltage curve showing the rectifying properties of a Cu-CdS junction. The sign of the voltage is referred to the polarity of the metal side of the junction.

treatment, unless otherwise specified. Plated layers of other metals, used in some of the experiments, were applied to crystals in the same way.

To obtain spectral response curves, cells were illuminated with monocrhomatic radiation from a Bausch and Lomb monochromator equipped with a tungsten light source. These were calibrated to give known relative output in photons/sec over the wavelength range used. Photovoltaic currents were measured with a Leeds and Northrup dc micromicroammeter. Absolute quantum yields were obtained using a calibrated tungsten lamp with known color temperature and controlled geometry, together with cells whose spectral response had been measured independently.

RESULTS

General Behavior

The sign of the photo-emf produced by these cells is always such that the metal layer becomes positive. Thus the direction of electron flow within the cell is from the metal to the crystal. According to diode rectifier theory, the contact between an *n* type semiconductor and a metal of high work function should be a rectifying one. The current-voltage characteristic curve for a Cu-CdS photovoltaic cell is shown in Fig. 3(a). Marked rectification is shown and the easy current flow occurs when the metal is positive, which is in agreement with theory. Curvature of the energy bands of the semiconductor near the junction with the metal is responsible for rectification, according to theory. This is illustrated in Fig. 3(b). The electric field resulting from this curvature of the energy bands has the direction necessary to produce the observed sign of the photo-emf. Free electrons would be accelerated away from the metal while free holes would move toward the metal. In either case, the existence of excess free carriers in the barrier region would lead to an emf with the metal becoming positive.

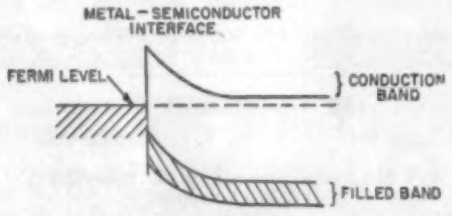

FIG. 3(b). Configuration of energy bands at a metal-semiconductor junction.

As is usual for photovoltaic cells, the open circuit emf increases linearly with light intensity at low intensities and tends toward a fixed value at high intensities. Values of 0.25 to 0.3 v were developed in the light of a focused microscope lamp. The saturation values are probably somewhat higher.

Short circuit currents are proportional to light intensity. Whenever we speak of quantum yield ϕ in the following discussion, we mean the number of electrons measured in the external circuit for each quantum of light incident on the crystal. For typical good cells, ϕ is about 0.1. Figure 4 shows ϕ as a function of the wavelength of the exciting light. The response is highest for light whose energy is smaller than that of the band gap and falls sharply for those wavelengths which are strongly absorbed by the crystal. Absorption spectra of the crystals show that there is not enough absorption of

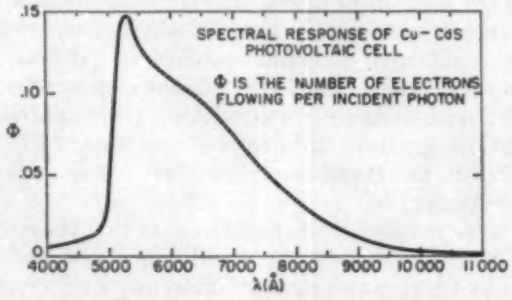

FIG. 4. Quantum yield of photovoltaic short circuit current as a function of the wavelength of the exciting light.

light in the bulk of the crystal to account for the photovoltaic current at long wavelengths. It may be inferred from the spectral response that the light producing the effect is absorbed either by the metal layer or by the semiconductor adjacent to the metal, whose optical properties might differ from those of the bulk material. Since no heat treatment or abrasive action was used in the preparation of the copper layers on the crystals, any diffusion of the metal or extensive surface damage is very unlikely. It is possible that a reaction with the surface layers of the semiconductor might occur during the electroplating process in which a layer of material would be formed between the bulk crystal and the metal layer. If this material had strong optical absorption in the range 5000 to 10 000 A, then it might give rise to the observed photovoltaic effect. Visual inspection of the copper layers plated onto crystals makes this seem rather unlikely since they have an appearance indistinguishable from that of copper metal. Such evidence, however, is suggestive rather than definitive and more direct evidence on this question will be presented.

Results with Layers of Different Metals on CdS

Cells were constructed using CdS crystals with various metals in place of the copper described above. These metals were also applied to the crystals by electroplating. To compare the properties of these the following were observed: the short circuit current per unit area of junction produced by room light; the open circuit voltage developed in the light of a focussed microscope illuminator; the current-voltage characteristic of the junction displayed on an oscilloscope. Results are summarized in Table I. Because of the small currents involved and other experimental difficulties the spectral response was obtained only for Cu and Au layers. These are plotted together for comparison, as a function of photon energy, in Fig. 5. The points of interest here are that the two curves are distinctly different and that the response of the gold layer begins its steep rise at higher photon energies that that of the copper. This is in agreement with the hypothesis that light absorbed by the metal layer produces the photovoltaic current. Strong optical absorption begins at longer wavelengths in copper than in gold (see Figs. 17 and 18). Thus the relationship between the curves shown in Fig. 5 may depend on the optical properties of the metals involved. The alternative hypothesis that the effect originates in an adjacent layer of modified CdS is not excluded by these considerations.

TABLE I. Properties of photovoltaic cells made by plating various metals onto CdS crystals.

Metal	Short circuit current in room light μ amp/cm^2	Maximum open circuit emf, v	Rectifying properties of contact	Electron work function of metal, ev[a]
Cu	20.00	0.3	good rectifier	4.45
Fe	0.08	0.02	good rectifier	4.49
As	0.02	0.5	good rectifier	
Au	0.13	0.3	good rectifier	4.89
Cd	0.06	very small	nonrectifying	4.10
Ag	0.05	0.02	poor rectifier	4.45
Ni	very small	very small	poor rectifier	4.96

[a] Electron work functions are taken from a critical compilation made by G. Herrmann and S. Wagener in *The Oxide Coated Cathode* (Chapman and Hall, Ltd., London, England, 1951), Vol. 2.

Other metals are less effective than copper and gold as seen in Table I. It is evident that the observed differences cannot be explained by differences in the work functions of the metals though one might expect these to be a determining factor. None of the metals tried approaches copper in its usefulness for the construction of photovoltaic cells.

Experiments with Semitransparent Metal Layers

A definite answer to the question of whether the photovoltaic effects in the long wavelength range are produced by light absorbed in the metal or by light absorbed in a layer of the semiconductor adjacent to the metal is provided by experiments with semitransparent metal layers which will now be described.

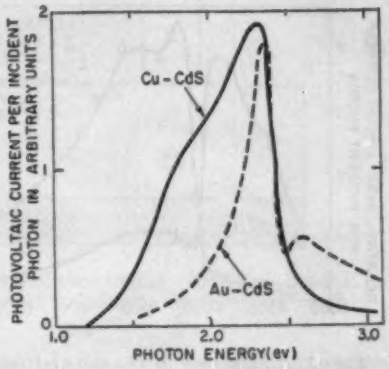

FIG. 5. Photovoltaic current vs photon energy for a Cu-CdS cell and a Au-CdS cell.

In the first of these experiments, a layer of copper was plated onto a CdS crystal and the plating was stopped at a point where the layer was thin enough to be semitransparent. The optical transmission spectrum of this layer is shown in Fig. 6 where the ratio of incident to transmitted light intensity is given as a function of wavelength. It is seen that the intensity of incident light is cut down by a factor ranging from 20 to 70 on passing through the layer of metal. Connections were made using the geometry illustrated in Fig. 1. The spectral response was now determined with light incident on the crystal side of the cell as done in the foregoing. It was then determined again on the same cell, but this time with the light incident on the opposite side of the cell, directly on the metal layer (from the bottom in Fig. 1). These two spectral response curves are compared in Fig. 7. Arbitrary units are employed but the same units are used for each curve and the two curves may be quantitatively compared. When the cell is illuminated from the crystal side the response was similar to that in Fig. 4 as expected. When it was illuminated from the metal side the response was quite different. A new strong current appears from wavelengths shorter than that corresponding to the band gap. This is undoubtedly the result of the formation of hole-electron pairs in the barrier layer of the semiconductor by strongly absorbed light; the process discussed in the introduction. It is the response at longer wavelengths which is of principal interest here. At some particular

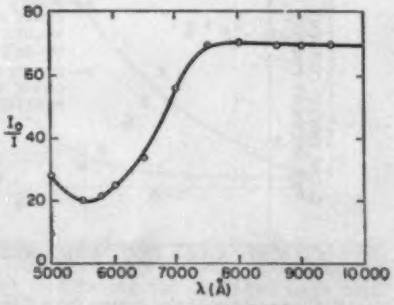

FIG. 6. Ratio of incident light intensity I_0 to transmitted light intensity I for a thin layer of copper on a CdS crystal.

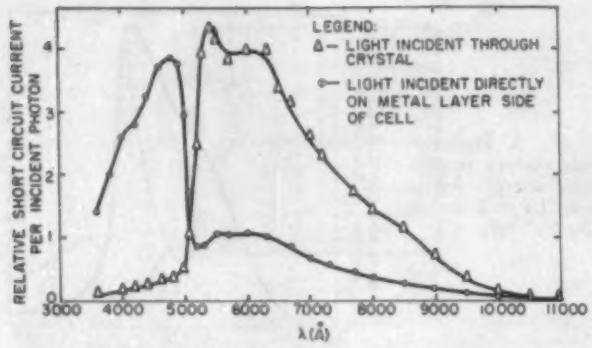

FIG. 7. Comparison of the spectral response curves obtained on illuminating a Cu-CdS cell from two different sides. Equal light intensities were used in each case.

wavelength, say 7000 A, the current produced when the cell is illuminated from the crystal side is 3.8 times as great as when it is illuminated with the same light intensity but from the metal side. From Fig. 6 it can be seen that light of wavelength 7000 A is diminished in intensity by a factor of 55 on passing through the metal layer. If the light producing the photovoltaic current were absorbed in a zone of material lying between the metal layer and the bulk crystal, it would have to pass through the metal layer before producing its effect in the case where the light enters from the metal side of the cell. Light entering from the crystal side of the cell would not have to pass through any regions of strong absorption to reach this hypothetical zone and would arrive with its intensity undiminished. As a result, the photovoltaic currents produced by equal illumination from the crystal side and from the metal side of the cell, respectively, should differ by a factor of about 55. Alternatively, if light absorbed by the metal produces the effect then this difference should be much smaller. For neither direction of illumination would there be a region of strong light absorption between the light source and the origin of the photovoltaic current. The observed difference, a factor of 3.8, strongly supports the contention that light absorbed by the metal layer, itself, produces the effect. Presumably photo-excited electrons are emitted from the metal into the CdS crystal. A second facet of the same experiment is illustrated by Fig. 8. Here the long wavelength parts of the

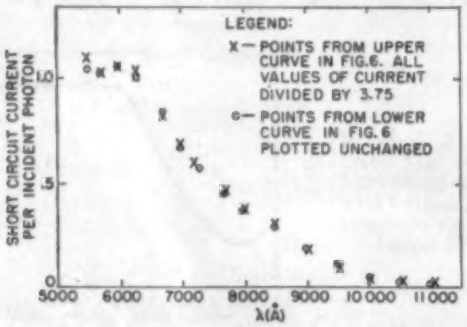

FIG. 8. Comparison of the curves from Fig. 7 after normalization.

curves from Fig. 7 have been replotted after dividing all values of current from the upper curve by 3.75. Both curves now coincide along their entire length and are thus related by a simple factor of proportionality which is independent of wavelength. The physical meaning is that illuminating the cell from the two different directions gives rise to two values of current which differ by a proportionality factor and that this factor is the same for all wavelengths. Referring to Fig. 6, the fraction of light transmitted by the metal layer varies by a factor of 3 between the wavelengths of 6000 and 8000 A. Consider first the case where the light is incident from the metal layer side of the cell. Again, if the light needed to pass through the metal layer to be effective then the photovoltaic current should be diminished 3 times as much at 8000 A as at 6000 A due to the light absorption of the metal layer. This effect would be absent when the cell was illuminated from the crystal side. Hence the spectral response curves obtained with the two different directions of illumination could not be made to coincide along their entire length by a single proportionality factor as is actually done in Fig. 8. This again can best be explained by assuming that light absorbed in the metal layer is producing the photovoltaic current. In this case variations of the optical density of the metal layer with wavelength have the same effect regardless of the direction from which the exciting light is incident.

A second experiment bearing on the same question is the following. A thin layer of copper was plated onto a CdS crystal. The layer was semitransparent, having an optical density of 0.4 at 7000 A. Microscopic examination of the layer showed it to be smooth, continuous, and unbroken. The photovoltaic response was observed with the light coming from the crystal side of the cell. Then the original layer of copper was made thicker by plating more copper on top of it until an optical density of 0.75 was reached. The photovoltaic response was observed again under the same conditions of incident light intensity and geometry. Finally, more copper was plated on top of the layer until it became opaque and the response was observed for the third time. The same alternatives as before are considered. If the response was caused by light absorbed in a zone between the original metal layer and the bulk crystal, then making the metal layer thicker would not affect the photovoltaic response. On the other hand, if the effect originates in the metal layer, making the layer thicker should enhance the response. A separate experiment with a cell having a metal layer as thin as any used here showed the short circuit current to be directly proportional to light intensity up to much higher intensities than were used in the measurements. At these intensities, the cells were carrying much higher currents than were observed in the measurements. Therefore, the resistance of the thin metal layer cannot be limiting the performance of the cell. The results are shown in Figs. 9(a) and 9(b). In 9(a) the three spectral response curves are plotted together. The photovoltaic current is considerably en-

hanced by increasing the thickness of the copper layer, again strongly suggesting that light absorption by the metal produces the effect. There is no quantitative proportionality between the amount of light stopped by the metal and the enhancement of photovoltaic current between curves 1 and 2. This is not an objection to the interpretation of the experiment since the optical density of a thin metal film is a complicated combination of reflection and absorption, and there is no simple relation between the optical density and the amount of true absorption by the metal.

Figure 9(b) compares more carefully the differences in the three spectral response curves from 9(a). The three curves have been normalized by multiplying two two of them by constant factors such that all coincide at their maxima. It is seen that there are small differences which are easily understood from the fact that light of different wavelengths penetrates different depths into the metal. The point of interest here is that making the layer thicker by adding more of the same metal makes only small changes in the spectral response.

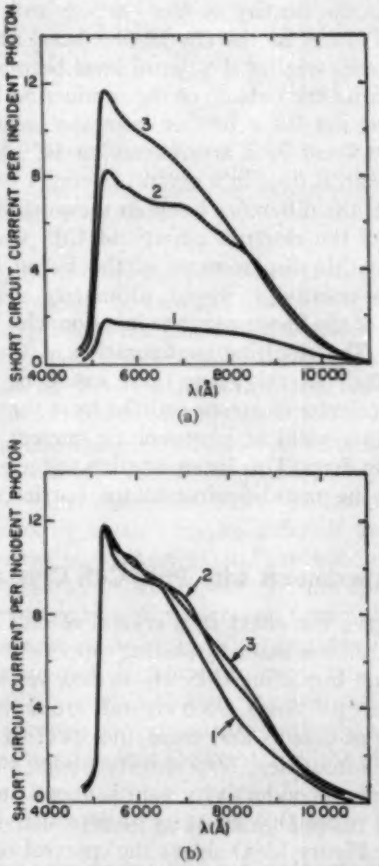

FIG. 9(a). Response of a Cu-CdS photovoltaic cell as the copper layer is made successively thicker. (1) Optical density of copper=0.4. (2) Optical density of copper=0.75. (3) Opaque copper layer. (b) Curves from Fig. 9(a) replotted after normalization to compare their shapes. Curve 3 replotted unchanged. Curves 1 and 2 have been multiplied by constant factors such that all three curves coincide at their maxima.

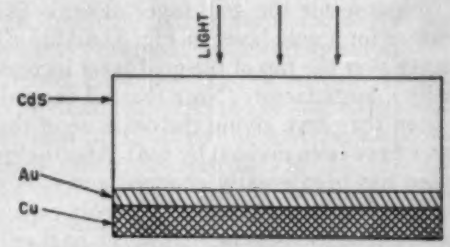

FIG. 10. Construction of photovoltaic cell with successive layers of two different metals.

The final experiment in this vein was the preparation of cells with successive layers of two different metals and observation of the response at each stage, illuminating the cell from the crystal side. Some initial experiments were done by plating semitransparent layers of silver onto CdS, followed by a thicker layer of copper on top of the silver. The short circuit currents produced by exposure to a tungsten lamp of constant intensity were compared for the cell having the silver layer alone and for the finished cell having both layers together. Several such cells were constructed and in each case the response was enhanced by adding the copper layer on top of the silver layer. The factor by which the short circuit current was enhanced ranged from 2 to 4. These cells gave rather small total currents and it was not possible to obtain their spectral response.

A more definitive experiment was done in which a semitransparent gold layer (optical density of 0.8 at 7000 A) was first plated onto CdS. This cell gave enough current to allow the spectral response to be recorded with the light incident from the crystal side. Then a thicker layer of copper was plated over the top of the gold. The final cell is illustrated schematically in Fig. 10. After the copper layer had been added, the spectral response of the cell was again determined. Results are in Fig. 11. Again the parts of the curves lying at wavelengths greater than 5200 A are of primary interest. The

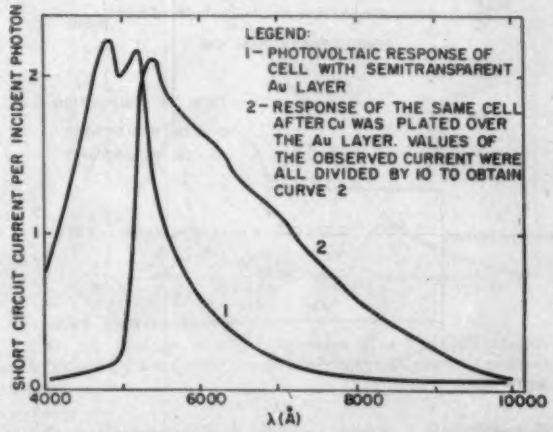

FIG. 11. Spectral response of cell made by plating copper over a thin layer of gold on CdS. The curves compare the cell having only the gold layer with that having the combined layer with copper over gold.

spectral response for the gold layer alone is like that shown earlier for a gold layer in Fig. 5. Addition of the copper layer over the top of the gold layer increases the currents by a large factor. (Note that all the values of current from the curve giving the response of the combined layer have been divided by ten). Also the spectral distribution has been greatly changed and is now that which is characteristic for copper. The only explanation of the experiment seems to be that in the final cell, light passes completely through the gold layer, is absorbed by the copper and produces excited electrons which diffuse back through the gold layer and are emitted into the CdS crystal. Here again the photovoltaic current appears to be caused by photoemission of electrons from the metal into the crystal, but here the electrons are excited in the metal layer furthest from the crystal. The short circuit current per unit light intensity for the cell with combined Cu-Au layer is about $\frac{1}{4}$ that of the cells made with a Cu layer alone.

Experiments with Photoconducting CdS Crystals

Some further experiments will now be described to show how the properties of the CdS crystal can affect the behavior of photovoltaic cells. The effect of variations in the resistivity was investigated by constructing a photovoltaic cell from a crystal of high gain photoconducting CdS. A layer of copper was plated on the crystal, which was illuminated during the plating operation to increase its conductivity. The geometry of the finished cell was that shown in Fig. 1 and its spectral response was the same as that shown in Fig. 4. It was illuminated with the light of a tungsten lamp and various known relative intensities were obtained by interposing calibrated wire screens between the lamp and the cell. The resistance of the cell and the photovoltaic short circuit current were measured for each value of the intensity. It was possible to obtain data over a range of crystal resistivity from 10^5 to 10^8 ohm-cm. In Fig. 12 the relative quantum yield of photovoltaic current is given as a function of the conductivity of the CdS crystal. A sharp drop in the quantum yield occurs when the conductivity drops below 10^{-7} ohm^{-1} cm^{-1}. This may be caused by changes in the metal-semiconductor barrier brought about by changes in the density of free carriers in the semiconductor. In the low resistivity crystals used earlier, the carrier density is high and the energy of the electron Fermi level lies near that of the bottom of the conduction band, as shown in Fig. 3(b). The difference between the electron Fermi energy E_F and the energy E_C of the bottom of the conduction band is given by the equation

$$E_F = E_C - kT \ln(N_C/n),$$

where n is the density of free carriers and N_C is the density of states in the conduction band and $n \ll N_C$. As n becomes smaller the Fermi level becomes further removed from the bottom of the conduction band. The Fermi level lies 0.4 v further from the bottom of the conduction band in a crystal having 10^7 ohm-cm resistivity than it does in a crystal having 1 ohm-cm resistivity. If the difference between the work function of copper and the electron affinity of CdS were around 0.4 v then this displacement of the Fermi level with increasing resistivity would ultimately remove the curvature of the bands near the junction which is shown in Fig. 3. The resulting configuration of the bands is in Fig. 12(a). At this stage there would be no strong field to accelerate electrons emitted from the metal and the quantum yield of photovoltaic current would be expected to drop. This interpretation suggests that the height of the metal-semiconductor barrier is around 0.4 v.

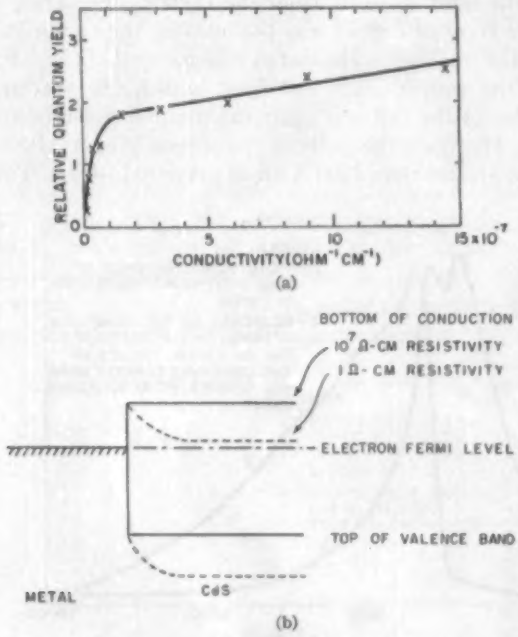

FIG. 12(a). Changes in the quantum yield of photovoltaic current of a Cu-CdS cell as the conductivity of the CdS changes. (b) Theoretically expected changes in a metal-CdS barrier region as CdS resistivity changes.

Experiments with Pure CdS Crystals

To observe the effect in a crystal of still higher resistivity a cell was made by plating copper onto a crystal of very pure insulating CdS whose dark resistance was greater than 10^{11} ohms. Such crystals are normally relatively free of defects and traps (no spectrographically detectable impurities; trap density about 10^{13} cm^{-3}),[5] and their photoconductivity gain is about unity. Thus in light of reasonable intensity their resistivity is still very high. Figure 13(a) shows the spectral response of this cell which was constructed with the geometry shown in Fig. 1. There is no photovoltaic current at longer wavelengths (for the same reasons given in the previous section), but for wavelengths shorter than that corre-

[5] R. H. Bube and L. A. Barton, R. C. A. Rev. **20**, 1959.

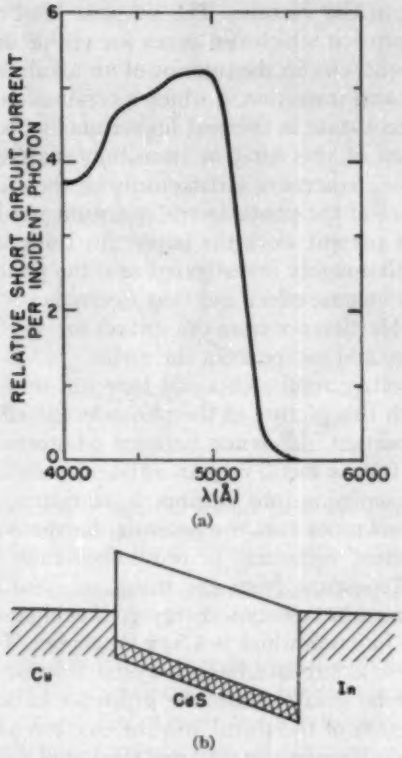

FIG. 13(a). Spectral response of Cu-CdS cell made from insulating CdS crystal. (b) Configuration of the energy bands of an insulating crystal making contact on opposite faces to two metals having different work functions.

sponding to the band gap a response occurs. This is very likely because of the creation of hole-electron pairs by light absorption in the CdS and the subsequent motion of both types of carrier through the crystal. The sign of the photo-emf (0.3 v) is the same as that observed in cells made from low resistance crystals with the copper metal electrode becoming positive under illumination. The assumption of hole motion in pure CdS crystals is supported by experimental evidence,[6] and in an insulating crystal making contact to two different metals a slope of the energy bands may extend throughout the crystal as shown in Fig. 13(b). Apparently, the motion of holes and electrons through the crystal under these circumstances occurs with considerably greater efficiency than photoemission of electrons into the crystal. The results suggest that a smaller accelerating field suffices to move carriers through the crystal efficiently than is necessary to move electrons into the crystal by the photoemission process.

Effect of Heating Layer

One experiment was done in order to determine the effect on a Cu-CdS cell of heating to a temperature where a slight diffusion of copper into the CdS occurs. A copper layer was plated onto one of the conducting CdS crystals described at the beginning of the report. The photovoltaic yield and spectral response of this cell were determined. After this the cell was heated to 380°C for 15 sec, a treatment reported to cause slight diffusion of copper into CdS.[7] Then the spectral response was determined again. As seen in Fig. 14, the diffusion of copper into the CdS greatly lowers the photovoltaic response and changes its spectral distribution. The result indicates that the heat treatment produces a layer of high resistance photoconducting CdS next to the metal and that the photovoltaic effect is then dominated by the properties of this layer. Measurement of the cell resistance showed that there was a large increase in resistance during the heat treatment and the *i-v* characteristic indicated the existence of a photoconducting layer in the CdS.

Experiments Using Other Materials

Photovoltaic cells with CdSe crystals in place of CdS have been made using both copper and gold as the barrier electrode. The CdSe crystals contain incorporated iodine, show *n* type conductivity and have a band gap of 1.74 ev.[8] Thus, only infrared radiation can pass through the crystal without absorption and the photovoltaic response is confined to this region of the spectrum. Spectral response curves are very similar to those obtained with CdS, rising gradually with decreasing wavelength and cutting off sharply when the wavelength corresponding to the band gap is reached. Apparently, the fundamental nature of the effect is exactly the same as in the CdS crystals.

Attempts to make photovoltaic cells by plating metals onto conducting ZnO crystals[9] were not successful. Copper and gold electrodes applied in this way make

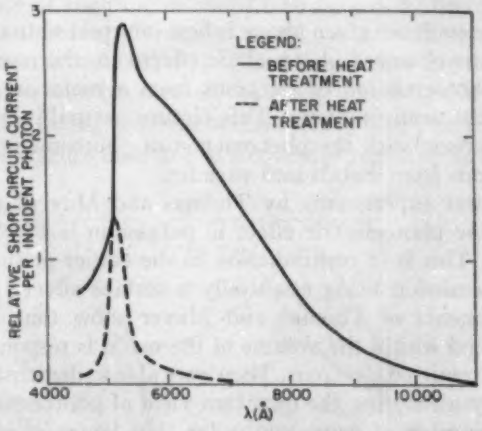

FIG. 14. Change in the properties of a Cu-CdS photovoltaic cell caused by heat treatment. Both curves have the same vertical scale.

[6] H. S. Sommers, R. E. Berry, and I. Sochard, Phys. Rev. **101**, 987 (1956).

[7] D. A. Hammond, F. A. Shirland, and R. J. Baughman, WADC Tech. Rept. 57-770.

[8] R. H. Bube, Proc. I.R.E. **43**, 1836 (1955).

[9] A generous supply of conducting ZnO crystals was provided by the New Jersey Zinc Company.

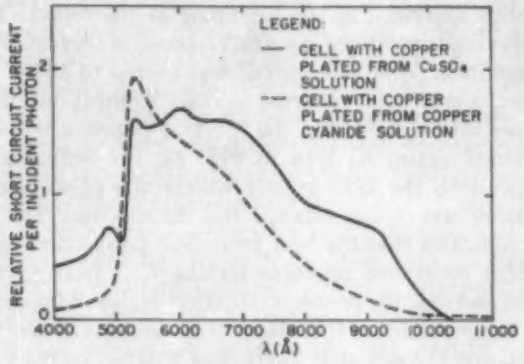

FIG. 15. Spectral response curves for Cu-CdS photovoltaic cells in which the copper was applied by electroplating from different plating solutions.

ohmic contact to the ZnO, and no useful photovoltaic effect can occur at an ohmic contact.

It was mentioned earlier that the character of the copper deposit obtained by electroplating onto CdS crystals depends on the plating solution used. The bright adherent layers plated from copper cyanide solution are most useful for the type of experiments reported here. Layers plated from copper sulfate solution are darker in appearance and less adherent. The spectral response of a CdS cell with such a copper layer is shown in Fig. 15. Though the general features are the same as those shown in Fig. 4, the relative response in the region from 6000 to 9000 A is enhanced. It is possible that this is simply caused by the obvious difference in the optical properties of the copper deposited in this way. The more fundamental question of what makes the optical properties of the copper different is one to which there is no ready answer.

DISCUSSION

The evidence given above is best interpreted to mean that the observed photovoltaic effects are the result of the photoemission of electrons from a metal into an adjacent semiconductor. This picture naturally invites comparison with the phenomenon of photoemission of electrons from metals into vacuum.

Recent experiments by Thomas and Mayer[10] show that the photoelectric effect in potassium is a volume effect. This is in contradiction to the earlier picture of photoemission being essentially a surface effect.[11] The experiments of Thomas and Mayer show that light absorbed within the volume of the metal is responsible for the emitted electrons. They were able to demonstrate this by measuring the quantum yield of photoemission at a number of wavelengths for thin layers of metal having various known thicknesses. It was shown that electrons excited within the metal at distances as great as 1000 A from the surface may reach the surface and emerge into the vacuum. The simplest kind of strong light absorption which can occur for visible and ultraviolet frequencies in the interior of an alkali metal is a band-to-band transition in which a conduction electron is raised to a state in the next higher unfilled band. The assumption of this kind of transition enabled Mayer and Thomas to account satisfactorily for the wavelength dependence of the photoelectric quantum yield.

For the present work the important thing is that in the only thoroughly investigated case the photoelectric effect is a volume effect and that electrons excited at a considerable distance from the surface are able to reach the surface and escape from the metal.

Photovoltaic results obtained here will now be compared with this picture of the photoelectric effect. The most important difference between photoemission of electrons from a metal into an adjacent semiconductor and photoemission into vacuum is, of course, the fact that in the former case the potential barrier which the electron must surmount in order to escape is much smaller. To escape from the metal into vacuum the electron must have excess energy greater than the electron work function which is 4.5 ev for copper. To escape from the metal into an adjacent crystal, its excess energy need only be greater than the *difference* between the work function of the metal and the electron affinity of the crystal. Though the electron affinity of CdS is not accurately known this *difference* is very likely in the range 0.5 to 1.5 ev. Thus photoemission into the crystal might be stimulated by light having quite low energies. A discussion of this point has been given by Mott and Gurney (footnote 1, pp. 73–74) who were apparently the first to suggest that this kind of photoemission might occur. More recent evidence for the existence of the process has been given by Gilleo.[12] Inspection of Fig. 4

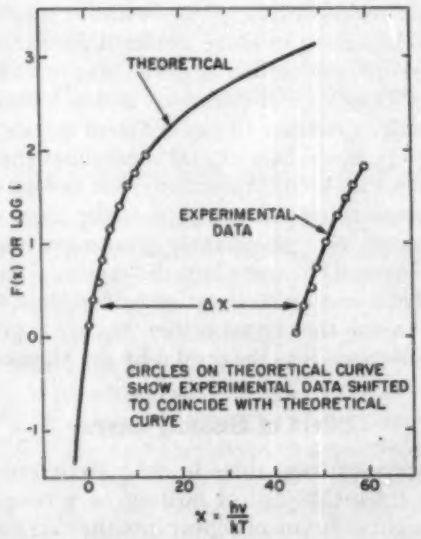

FIG. 16. Fowler plot of the photovoltaic currents near the long wavelength threshold for a Cu-CdS photovoltaic cell.

[10] H. Thomas, Z. Physik **147**, 395 (1957); H. Mayer and H. Thomas, Z. Physik **147**, 419 (1957).

[11] A. L. Hughes and L. A. DuBridge, *Photoelectric Phenonema* (McGraw-Hill Book Company, Inc., New York, 1932).

[12] M. A. Gilleo, Phys. Rev. **91**, 534 (1953).

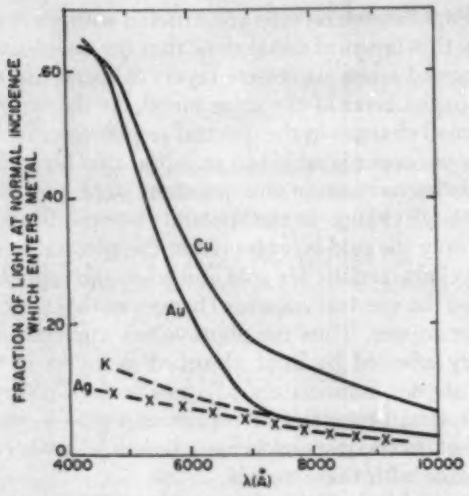

FIG. 17. Fraction of light at normal incidence which enters metals as a function of wavelength. Data for all metals except potassium taken from R. Wood, *Physical Optics*, Macmillan and Company, Ltd., London England, 1934), p. 550; data for potassium from *American Institute of Physics Handbook* (McGraw-Hill Book Company, Inc., New York, 1957), p. 6–106.

shows that the low energy threshold of the photovoltaic effect in the Cu-CdS system occurs for photon energies somewhere around 1 ev. A more quantitative determination of the threshold may be provided by a conventional Fowler plot of the photovoltaic currents near the long wavelength limit.[11] For a photoemission process the shape of the curve of quantum yield vs energy is, in the vicinity of the threshold, determined by the distribution of electrons near the Fermi surface. This allows a plot to be made which gives an objective value for the true threshold energy from data taken near the threshold. Such a plot of the data from Fig. 4 is shown in Fig. 16. The indicated threshold value is 1.1 ev. This value is in disagreement with the value of about 0.4 v obtained from the previous discussion of the results with photoconducting crystals. An accurate knowledge of the electron affinity of CdS would help to answer the question raised by this experiment.

A second consideration is that of the optical properties of the metal involved. Clearly, light which is reflected from the surface can produce no photoeffect. Light which is not reflected enters the metal and is absorbed. The fraction of light at normal incidence which enters the metal is 1 minus the fraction reflected. This is shown as a function of wavelength for four metals in Fig. 17. It is clear that the spectral response curves for photovoltaic cells made with Cu and Au layers are in good agreement with the notion that light must enter into the volume of the metal to produce the effect. The optical absorption coefficient $n\chi$ is also important here. Once light enters the metal, its intensity diminishes with distance d according to the equation

$$I = I_0 e^{\frac{-4\pi n\chi}{\lambda_0} d},$$

$n\chi$ is the absorption coefficient and λ_0 is the vacuum wavelength of the light. A high-absorption coefficient leads to light absorption near the surface and the nearer an excited electron is to the surface the better are its chances of getting out. Hence a high value of $n\chi$ favors a high photoemission efficiency. The absorption constants for Cu, Ag, and Au are shown as a function of wavelength in Fig. 18, taken from the data of Joos and Klopfer.[12] The strong absorption peak lying near 5000 A in the copper spectrum is assigned by these authors as a transition of a $3d$ electron to a $4s$ level,

$$3d^{10}4s \rightarrow 3d^{9}4s^{2}.$$

It may be noted that the high values of the absorption coefficients of copper and gold between 5000 and 6000 A guarantee that there will be appreciable light absorption in the metal within a few hundred angstroms of the surface. Thus both the reflectivity and absorption data are in agreement with the spectral response data for the photovoltaic cells. The low absorption and high reflectivity of silver are also in agreement with its rather poor performance in the photovoltaic cells. In all these metals there is a weaker absorption extending into the near infrared which presumably arises from transitions in which momentum is conserved through the participation of a lattice vibration.

Finally, a comparison must be made between the quantum yields obtained in the photovoltaic cells and those obtained for photoemission of electrons into vacuum. From Fig. 4 it is seen that in the photovoltaic cells there may be quantum yields as high as 0.15 electrons per incident quantum. For photoemission from metals into vacuum the number of electrons per incident light quantum for good metals is likely to be around 0.005. It might appear from this comparison that the efficiency of the process considered here is 30 times as great as that for photoemission into vacuum. However, the comparison based on incident light is not the most instructive one because of the great differences in reflectivity among different metals. (It is given here because literature data are so frequently reported in this

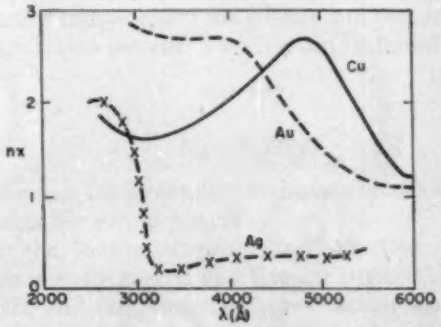

FIG. 18. Optical absorption index for three metals. Data taken from footnote 12.

[12] G. Joos and A. Klopfer, Z. Physik 138, 251 (1954).

way.) A better quantity for comparison is the number of electrons per *absorbed* light quantum. This turns out to be 0.3 electrons/quantum absorbed for the Cu-CdS cells. For photoemission from potassium metal into vacuum the quantum yield reaches 0.08 electrons/quantum absorbed.[10] Thus the quantum yields really differ only by a factor of 3.7 and the high efficiency of the photovoltaic cells is not inconsistent with previous data on the photoelectric effect.

It is worthy of note that the quantum yield of 0.15, although somewhat larger than that expected for photoemission into vacuum, is also significantly smaller than that expected for a photovoltaic effect at a semiconductor-semiconductor junction. Marburger *et al.*,[14] for example, measured a quantum yield of unity on a photovoltaic cell made by diffusing copper into CdS.

SUMMARY

The general features of the behavior of undiffused metal-cadmium sulfide photovoltaic cells are understandable on the basis of a simple model. It has been demonstrated that photovoltaic currents are produced with high-quantum efficiency by the photoemission of electrons from a metal into the CdS crystal. The principal pieces of evidence are the following:

1. Comparison of the spectral response with the cell geometry and the optical properties of the CdS shows that the effect cannot be caused by light absorbed in the bulk CdS.
2. Rectification properties of the Cu-CdS junction show the existence of a typical metal-semiconductor barrier layer.
3. An experiment in which a cell made with a semitransparent layer of copper was illuminated from two different sides shows that the effect is produced by light absorbed in the metal layer.
4. Experiments on cells constructed with several successive thin layers of metal show that the quantum yield is increased when successive layers of metal are added to an initial layer of the same metal. At the same time only small changes in the spectral response occur. When a layer of copper is added to an initial thin layer of gold there is an increase in the quantum yield and there is also a large change in the spectral response of the cell. When only the gold layer is present the spectral response is that characteristic for gold and when the copper layer is added the spectral response changes to that characteristic for copper. Thus the photovoltaic current may be strongly affected by light absorbed in layers of metal which are not immediately adjacent to the CdS crystal.
5. Optical properties of copper and gold agree well with the spectral responses characteristic of photovoltaic cells made with these metals.
6. Comparison with recent work on the photoemission of electrons from metals into vacuum shows that the mean free paths of excited electrons in metals are large enough to explain the results obtained here.

The results suggest that the following features are important in selecting materials for metal-semiconductor photovoltaic cells of this type. The metal should have low reflectivity and a high absorption coefficient over the wavelength range to be covered. For the semiconductor the important requirements are that it should be transparent, have high conductivity, make rectifying contact to the metal used and have an appropriate value of electron affinity. Apparently, the chemical properties of the semiconductor are not the dominating ones.

ACKNOWLEDGMENTS

We wish to thank D. O. North, A. Rose, and W. Spicer for several valuable discussions of this problem, and H. E. MacDonald for assisting in some of the measurements.

[14] R. E. Marburger, D. C. Reynolds, L. L. Antes, and R. S. Hogan, J. Chem. Phys. 23, 2448 (1955).

p Layers on Vacuum Heated Silicon

F. G. Allen, T. M. Buck, and J. T. Law
Bell Telephone Laboratories, Inc., Murray Hill, New Jersey
(Received December 28, 1959)

It has been established that when silicon is heated above 1300°K in a borosilicate glass vacuum system from 10^{11} to 10^{15} acceptors per cm² are normally added to the silicon surface, even though the glass walls remain at room temperature. The acceptor diffuses into the surface upon heating forming a p layer several microns deep.

There is strong evidence that the acceptor is boron from the borosilicate glass envelope. The transfer to the silicon is believed to occur through volatilization of boron oxides by water vapor.

INTRODUCTION

IN the course of recent work[1] involving the preparation of clean silicon surfaces by heating in high vacuum, it was found that these surfaces, although atomically clean in a two-dimensional sense, were characterized by a highly conductive p-type layer extending into the body from the surface. It now appears that such p-type layers form quite generally on silicon, and probably also on germanium, when samples are heated to within a few hundred degrees of the melting point in borosilicate glass vacuum systems. It is to be stressed that this layer forms even though the walls of the system are never heated above room temperature and are never brought into physical contact with the sample. The presence of this layer makes the interpretation of certain electrical surface measurements difficult or impossible. The fact that such layers have undoubtedly been present, though unsuspected, in some semiconductor surface experiments in the past means that a reassessment of the results on such surfaces must be made.

The purpose of the work reported here was to discover the cause of these p-type layers and to prevent their formation.

EXPERIMENTAL METHODS USED TO STUDY p LAYERS

In order to study the nature of the conductive p layers, measurements were made of conductivity and of conductivity type vs depth normal to the surface. Conductivity vs depth was measured in two ways: by the total sample resistance method and by the four point probe method. In the first, leads were alloyed to the ends of a rod having a p layer on its surface and total sample resistance was measured after each of a series of light etches. The depth removed by each etch was determined from the surface area and the measured weight-loss. A cross-calibration on the etching rate was also obtained at large depths by direct micrometer measurements. This method was well adapted to p-type samples with p layers since surface and bulk conductance were in parallel. For this case one can monitor surface conductance changes during heating of a sample in vacuum directly from the change in total sample resistance *provided* that the bulk conductivity of the sample remains constant—a case seldom found in our work. (Bulk conductivity decreased on heating tending to compensate the increase in surface conductance.) When the p layer exists on an n-type sample the conductance of surface and bulk are isolated from each conductance of surface and bulk are isolated from each other by the p-n junction separating them. The impedance of this junction in the reverse direction is so high that current flowing along the axis of the rod cannot cross the junction in order to distribute itself freely between the surface and the bulk. Thus if the total sample resistance method is to be used on n-type samples, good contact must be made to both surface and bulk at the sample ends.

When the total sample resistance method is valid, one can measure the change in conductance caused by the p skin

$$\Delta G = 1/R_1 - 1/R_2, \tag{1}$$

where R_1 is the total sample resistance with the p skin present and R_2 is the same after removal of all or part of the p skin. The surface conductivity of the layer removed is then found from

$$\sigma_s = \Delta G L/P \text{ mhos per square}, \tag{2}$$

where L is the sample length between contacts and P the perimeter of the cross-section. If the average mobility of holes $\bar{\mu}$ is known, the concentration p_s of holes per unit surface area of the p layer and the net acceptor concentration per cm² $N_A - N_D$ can be found from

$$\sigma_s = e\bar{\mu}p_s \tag{3a}$$

$$N_A - N_D \cong p_s. \tag{3b}$$

Corrections for incomplete ionization of acceptors must be made for strong p layers.

In the four-point probe method, four sharpened points equally spaced in a line are pressed against the surface and the potential drop V across the two inner points caused by a current flow I set up by the two outer points is measured by a potentiometer. This method is well suited to p layers on n-type material

[1] F. G. Allen, J. Eisinger, H. D. Hagstrum, and J. T. Law, J. Appl. Phys. **30**, 1563, (1959).

where the surface layer is electrically isolated from the bulk by a p-n junction, but it is also useful for p layers on p type material when the total surface conductance is large compared to the total bulk conductance. Four point measurements were made after each of a series of light etches to deduce the variation of surface conductivity depth. In a few cases surface material was removed by sandblasting instead of etching, and results were qualitatively the same as for etching. Conductivities with the four point probe method are then found from the standard formulas. For a sheet infinite in extent and infinitely thin compared to probe spacing the surface conductivity is given by

$$\sigma_s = [(\ln 2/\pi)]\, I/V \text{ mhos per square.} \qquad (4)$$

When the surface layer is removed the conductivity of the uniform bulk may be found from the formula for the semi-infinite solid

$$\sigma = (1/2\pi S) I/V \text{ mhos-cm}^{-1}, \qquad (5)$$

where S is the probe spacing. For small samples appropriate corrections for (4) and (5) may be found in the literature.[2,3]

The conductivity type of the surface was determined at each depth by the thermal probe method. While there is undoubtedly a limit to the thinness of a p-type layer on a strong n-type bulk that can be detected in this way, no problem arises for strong p films well insulated from the bulk by a junction, as was usually the case in this work.

CONDUCTIVITY vs DEPTH. TYPICAL BEHAVIOR

The data on resistance versus depth removed for a strong p film on an n-type sample are shown in Fig. 1. Measurements were made using the total sample resistance method with end leads in good contact with both surface and bulk. It is seen that sample resistance rises rapidly and the conductivity remains p type as the first 4 μ are removed. The conductivity type indications become mixed n and p as one etches through the junction and finally, below 5 or 6 μ, one finds the uniform n-type bulk conductivity. (The slight upward slope of the resistance vs depth curve beyond 5 μ due to the decrease in sample cross-sectional area is too small to be seen.) From analysis of profiles of this sort one can say that for silicon samples heated at 1300 to 1600°K from 10 minutes to several hours in borosilicate glass vacuum systems the total number of net acceptors added to the surface varies from 10^{12} to 10^{15}/cm^2. The surface conductivity for the strongest p layers reaches 35 000 μmhos per square, while the maximum net acceptor concentration at the surface may be $>10^{19}$/cm^3. Analysis of the profiles reveals that the net acceptor concentration falls off exponentially with depth into the surface, as will be discussed later.

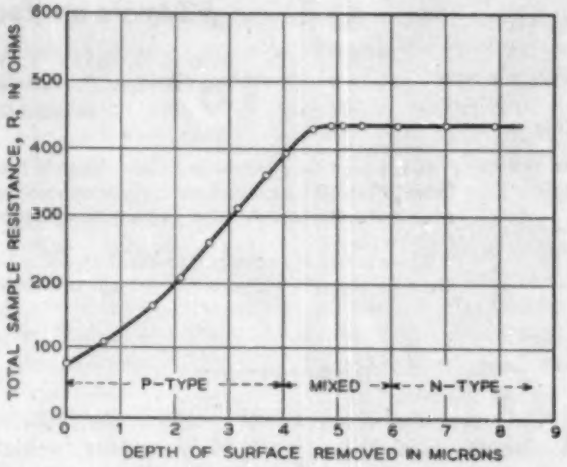

FIG. 1. Variation of sample resistance with depth of surface removed. For an n-type silicon sample of final bulk resistivity of 11 Ω-cm; heated two hours at 1600°K.

P-type layers have been produced on germanium, also, by heating to a few hundred degrees below the melting point. Analysis of resistivity vs depth by etching on a few samples showed that the effect was similar to that for silicon.

POSSIBLE MECHANISMS OF p-LAYER FORMATION

Several mechanisms were considered in explaining the p-layer formation. First, the above results ruled out the possibility that the p layer was merely a space charge layer at the surface induced by p-type surface states in the first atomic layer. The conductivity of such a space charge layer would change abruptly after the very first brief etching and would then remain unchanged on subsequent deeper etches, instead of decreasing gradually over a depth of many microns. Furthermore, the largest changes in surface conductivity that have been produced by changes in the space charge layer caused by various chemical treatments are on the order of 30 to 50 μmhos per sq[4] whereas we are dealing here with surface conductivities as high as 35 000 μmhos per square.

A second mechanism considered was the in-diffusion from the surface of some lattice defect such as a vacancy that migh act as an acceptor. However, it was found that the acceptors introduced at high temperature would not anneal out during long heating at lower temperatures. Furthermore, a means was finally found of heating samples in vacuum without introducing acceptors (see below) so that the effect could not be an intrinsic property of silicon surfaces heated in vacuum.

In-diffusion of oxygen was ruled out as the important factor since there was no evidence of donor formation

[2] F. M. Smits, Bell System Tech. J. 37, 711 (1958).
[3] L. B. Valdes, Proc. I.R.E. 42, 420 (1954).
[4] T. M. Buck and F. S. McKim, J. Electrochem. Soc. 105, 709 (1958).

at the surface when p layers were heated for several hours at ~450°C, as the results of Kaiser, Frisch, and Reiss[5] predict. Furthermore, heating the samples at high temperatures in partial pressures of oxygen never resulted in stronger p layers.

A redistribution of donors and acceptors which might have been already present in the sample was ruled out principally on the ground that strong p layers could be etched off and formed again repeatedly even on high purity zone refined samples. The total reservoir of acceptors in the bulk in these cases was believed too small to form even one p layer.

The simplest explanation that fits all the known behavior of these p layers is that a chemically active acceptor impurity reaches silicon surface and diffuses in during heating. Minute amounts—usually less than one monolayer and sometimes as little as one thousandth of a monolayer—are involved. Such an acceptor must (a) be soluble in silicon to at least $10^{19}/cm^3$ at 1600°K, (b) be an easily ionized acceptor (with an energy level close to the top of the valence band) and (c) have a suitable diffusion coefficient to produce the observed layer depths under the heating conditions involved. Three common acceptors that meet these requirements are boron, aluminum, and gallium.

IDENTITY OF ACCEPTORS IN p LAYERS

Two types of analyses were run on the p layers to detect and identify the acceptor impurity present. In the first a spectrochemical analysis was made of concentrated acid in which a p layer had been dissolved. In the second type A. J. Ahearn analyzed two p-layer samples using the mass spectrometer technique in which a spark discharge to the sample ionizes surface atoms.[6] Suitable controls were used in all tests. Both the spectrochemical and the spark spectrometer analyses, though working near their limits of sensitivity, showed boron to be present in the p layers. The evidence for aluminum was ambiguous.

A radiochemical analysis after activation by thermal neutrons disclosed no radioactive impurity present in the p layer not also present in the bulk; boron and aluminum, with their short half-lives, would not have been detected.

SOURCE OF IMPURITY

The following possible sources of an acceptor impurity such as boron or aluminum were considered:

1. Etching solutions and the de-ionized water used for washing the samples.
2. Filter paper sometimes used for drying samples.
3. Tweezers.
4. Metal clamps used to support samples during heating.
5. The walls of the vacuum system, i.e., borosilicate glass.

It was found by the analytical methods mentioned above that some de-ionized water does contain boron at a concentration of $\sim 1/10^9$, and that filter paper contains both boron and aluminum at about $1/10^6$. However, the successful procedure described below which did not produce p layers involved both these items as well as tweezers so that contamination from these sources was not significant at the purity level of our tests.

Molybdenum has usually been used for sample clamps in our work. A. J. Ahearn[7] has found aluminum and boron at concentrations of $1/10^6$ and $1/10^7$, respectively, in commercial grade molybdenum. In one of our experiments there was unambiguous evidence that molybdenum clamps at about 1000°K had caused a p layer adjacent to their point of contact with the sample, presumably by surface migration. Thus, despite careful preliminary cleaning and outgassing of such clamps, they must be kept cool during sample heating, as, for example, by employing a large thermal mass and low duty cycle.

However, the following experiment showed that there was a major source of contaminant aside from the clamps. A sample of silicon under clean conditions was fractured into small pieces and then heated by rf induction in a completely enclosed clean silicon bucket in a borosilicate vacuum system. Even though most of the surfaces were virgin, they all formed a strong p layer. Thus items 1–4 in the foregoing list were all eliminated and a vapor phase transport of impurity from the vacuum system to the sample was indicated.

Corning Code 7740 borosilicate glass (one of the most common types of pyrex) contains 12.9% B_2O_3 and 2.2% Al_2O_3 along with 3.8% Na_2O, 0.4% K_2O, and 80.5% SiO_2. The walls of the system were, therefore, suspected as a source of boron early in the experiments, particularly during the baking of the system at 400°C and the sealing of the system by torch with the sample in place. However, when both of these were eliminated using ground joints and keeping the system at room temperature—in some cases even keeping the glass walls surrounding the sample at liquid nitrogen temperature—the p layers continued to form on heating of the silicon.

It was found by chance and later confirmed, that the presence of water vapor in the glass system greatly enhanced p-film formation. Evidence was found in the literature (to be discussed below) that water vapor can be expected to release boron from the borosilicate glass walls in volatile form.

M. Nordberg of the Corning Research Laboratory has informed us that a film of sodium and boric oxides is normally left on interior borosilicate glass surfaces

[5] W. Kaiser, H. L. Frisch, and H. Reiss, Phys. Rev. 112, 1546 (1958).

[6] N. B. Hannay, Rev. Sci. Instr. 25, 644 (1954); N. B. Hannay and A. J. Ahearn, Analyt. Chem. 26, 1056 (1954).

[7] A. J. Ahearn, private communication.

after glass blowing operations. It is water-soluble and can be washed off. Also, sodium and boric oxides are the first constituents to leach out of borosilicate glass during prolonged exposure to hot water. It has been confirmed by spectrochemical analyses at our own laboratories that interior surfaces of borosilicate glass containers, after glass blowing, have appreciable amounts of boron on them in a readily water-soluble form. (It is significant that some boron was also found on freshly blown quartz surfaces.) This boron supply is exhausted to a level below our limits of detection by prolonged boiling and rinsing in deionized water.[8] There was evidence in this work that p-layer formation was worst in new systems and gradually abated after many runs provided no freshly torched borosilicate glass was introduced.

QUARTZ TUBE EXPERIMENT

In view of the evidence that borosilicate glass with traces of water vapor was responsible for the p layers, it was decided that vitreous silica (to be referred to hereafter as quartz) known to be very free of boron, should be used instead. Using quartz, a successful procedure was soon evolved.

A. Standard Quartz Tube Procedure (See Fig. 2)

The procedure which seemed to be completely reliable and which gave at least twelve successful results without any inexplicable failures was as follows:

1. The quartz tube was cleaned with toluene, acetone, deionized water, CP-8 (5 parts conc. HNO_3 to 3 parts conc. HF), and ten rinses in deionized water. It was then evacuated with a mechanical pump and heated with a torch. After cooling the tube was let down to air and capped with clean filter paper.

2. The silicon specimen was washed in toluene, acetone and deionized water and then etched 30 sec in CP-8 to remove about 2 mils. It was then rinsed for 30 sec in running deionized water, blotted dry, and wrapped in Whatman #50 filter paper. The silicon was handled with platinum tweezers cleaned in CP-8 and deionized water.

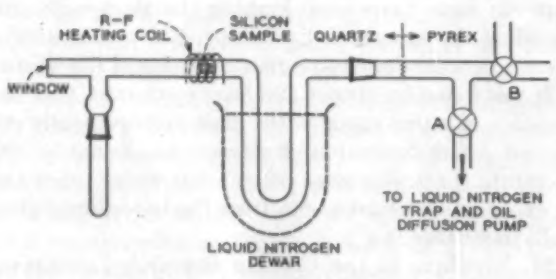

FIG. 2. Schematic of quartz tube experiments.

[8] See section on "Prevention of p layers in borosilicate glass systems."

3. Heating was carried out in the quartz system illustrated in Fig. 2. The U-bend was immersed in liquid nitrogen before the tube was joined to the vacuum system to prevent all volatile compounds from the borosilicate glass from reaching the sample. The quartz tube was pumped down with a separate mechanical pump through valve B, Fig. 2, for one or two minutes and then switched over through valve A to the main system already at about 10^{-5} mm Hg. With the U-tube under liquid N_2, the system was pumped for four to sixteen hours, before the silicon was heated.

4. The specimen was heated for five minutes by rf induction at about 1600°K measured by an optical pyrometer through the quartz window with emissivity correction.[9] Preliminary heating by torch through the quartz wall was necessary to raise the temperature sufficiently for satisfactory coupling.

The results obtained consistently by this method were much better than any ever previously achieved in an all borosilicate glass system. N-type silicon cubes were used and after heating, the thermo-electric probe measurements made over the cube faces gave n-type indications except for a few p spots which were still formed in most experiments. Four-probe resistivity measurements after heating gave the same values before and after etching. (These were often higher than before heating because of the bulk resistivity increases mentioned before.)

From the fact that 80 ohm-cm n-type specimens did not convert at the surface, it can be estimated that no more than $\sim 6\times10^{9}$ acceptors/cm^2 [10] were introduced by the quartz tube procedure whereas 10^{11} to 10^{13}/cm^2 were introduced in the borosilicate glass systems. The few p spots remaining indicated, however, that even in the quartz a slight p-type contamination (or out-diffusion of donors) remained.

B. Effects of Borosilicate Glass in the Quartz System

With a reliable way of preventing p layers at hand, it was possible to go back and investigate the formation of the layers by adding borosilicate glass to the system. P layers were produced when the silicon was heated in the presence of a small piece ($\frac{5}{8}$ in.) of glass tubing placed about 2 in. from the silicon. This glass was at room temperature during heating. Acceptor densities of 2×10^{11} to 9×10^{12}/cm^2 were introduced. Larger, freshly drawn pieces of borosilicate glass tubing caused stronger p layers (5×10^{12} to 8×10^{13} acceptors/cm^2). These experiments contaminated the quartz so that p layers formed even when the glass tubes had been removed. An effective way of removing this contamination was to etch the interior surface of the quartz to a depth of two mils with concentrated hydrofluoric acid.

[9] F. G. Allen, J. Appl. Phys. **28**, 1510 (1957).

[10] We assume the smallest detectable p layer would result from just compensating the donors present to a depth of about one half micron.

C. Effects of Boron Oxide and Aluminum Oxide

Two experiments with B_2O_3 and Al_2O_3 seem to demonstrate conclusively that boron coming from borosilicate glass at room temperature can cause the p layers but that the aluminum in the glass does not contribute significantly to the contamination.

In the first experiment 0.1 g of B_2O_3 powder (Amend C.P. "Boric Anhydride") was left in the bottom of the quartz side-arm throughout the overnight pumping and subsequent heating of the specimen. The B_2O_3 was never above room temperature. A very strong p skin developed, 40 000 μmhos/sq or 5×10^{15} acceptors/cm^2, the strongest ever seen in these experiments.

After the B_2O_3 experiment, the quartz tube was etched heavily (3 to 4 mils) inside with HF, washed further with CP-8 and deionized water and the experiment was repeated using 0.1 g of Al_2O_3 (Johnson and Matthey & Company "Specpure") which contained no detectable boron. This time there was essentially no p skin although there were some weak p spots in the otherwise n-type thermal probe measurements.

REMOVAL OF p LAYERS BY SPUTTERING AND OXIDATION

Several experiments have confirmed that contamination of the sample does not continue during standing under high vacuum conditions. Specimens were heated in a borosilicate glass vacuum system forming p layers. They were then sputtered with 1000 v argon ions long enough to remove the p layer, i.e., 5 to 6 μ of material. Careful precautions to ensure sputtering only the sample and no other portions of the system were found necessary in order to avoid p-layer formation. Subsequent heating of these samples either immediately after sputtering or after standing several days at vacua of $\sim10^{-9}$ mm Hg produced no p layers.[11]

This behavior is consistent with the hypothesis that the boron transfer occurs during initial mounting of the sample and pump-down when appreciable amounts of water vapor are available from the atmosphere to react with the borosilicate glass.

It is important to note that long pumping in a borosilicate system before the first heating of the sample is not sufficient to remove the boron from the surface once it has been deposited.

One might hope to prevent the boron in-diffusion by an initial protective oxide coating. One attempt at this proved unsuccessful, and this appears consistent with the behavior of p layers during controlled oxidation in a borosilicate glass vacuum system. When a p layer is heated many minutes above 1400°K at an O_2 pressure of 10^{-5} mm or more, the surface conductance drops drastically, sometimes approaching the original value before p-layer formation. However, subsequent reheating of this oxidized surface in high vacuum to 1500°K causes much of the surface conductance to return. Apparently only part of the boron is evaporated off with the oxide and the remainder diffuses back from the oxide into the silicon.

When silicon samples are heated at atmospheric pressure of most gases, enough oxygen is probably present so that the surface oxidation usually competes successfully with boron in-diffusion. In this connection, Theurer's technique[12] of removing boron from floating zone silicon by water vapor, even if it could be made to work in a borosilicate glass system, suffers the disadvantage that when the sample is again heated in vacuum the p layer would re-form. P layers are not normally found except on samples heated in vacuum. However, we know of one case[13] in which silicon heated in nitrogen with 1% oxygen in a ceramic oven did form p layers. In the case of vacuum melted samples, the boron that may have arrived at the surface is dissolved uniformly in the cross section and is normally too small in amount to be noted.

PREVENTION OF p LAYERS IN BOROSILICATE GLASS SYSTEMS

Several runs have been made recently using a conventional borosilicate glass system with ground joints. In these runs, however, all interior glass surfaces near the sample up to the first liquid nitrogen trap were boiled in de-ionized water for 48 hours and rinsed thoroughly before the run. The results are very promising—no p layers have formed in the three well-controlled runs made thus far. These results suggest that the important source of boron in glass systems is the relatively soluble layer on the surfaces resulting from glass blowing and that with adequate cleaning borosilicate glass systems may be as good as quartz.

DISCUSSION

Profile of Acceptor Concentration vs Depth

One can derive the actual acceptor concentration as a function of depth from the resistivity vs depth data shown in Fig. 1. This has been done in Fig. 3 by taking the slope dR/dx from Fig. 1 and using the differential form of Eq. (1). Hole mobility values at each resistivity encountered going through the p layers were taken from Morin and Maita[14] with fractional ionization calculated approximately at the highest concentrations. The general correctness of these values has recently been confirmed by Wolfstirn.[15] As seen from Fig. 3 the net acceptor concentration falls off exponentially near the surface

[11] G. E. Moore of these Laboratories, in a mass-spectrometer search, failed to find evidence of any volatile boron compounds present in a borosilicate glass vacuum system even in the presence of water vapor at total pressures of $\sim10^{-5}$ mm Hg. He *has* detected boron species when heating borosilicate glass at 500 to 600°C in vacuum.

[12] H. C. Theurer, *Semiconductors*, edited by N. B. Hannay (Reinhold Publishing Corporation, New York, 1959), p. 121.

[13] H. Lawrence, private communication.

[14] F. J. Morin and J. P. Maita, Phys. Rev. **96**, 28 (1954).

[15] K. B. Wolfstirn, J. Phys. Chem. Solids (to be published).

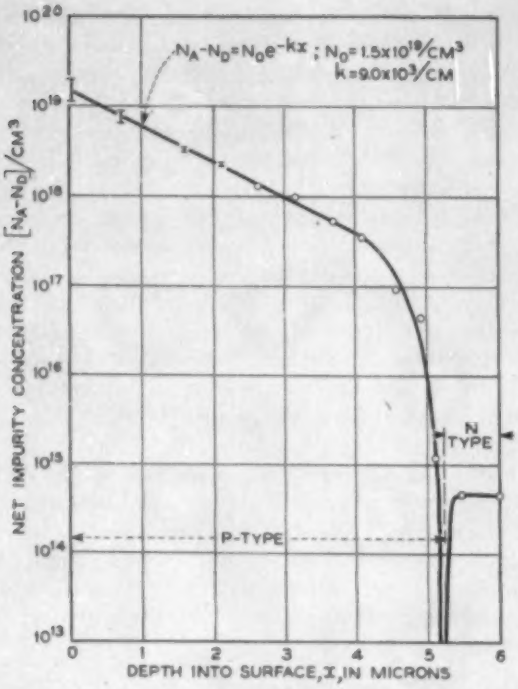

FIG. 3. Net acceptor concentration vs depth for p film on silicon, derived from Fig. 1.

as given by

$$N_A-N_D\cong N_0e^{-Kx}, \tag{6}$$

where N_0 is the surface acceptor concentration. N_D, the donor concentration, may be neglected near the surface. The value of K from Fig. 3 is 9×10^3 cm^{-1} while N_0 is 1.1×10^{19} cm^{-3}. This sample had been heated in a borosilicate glass system near 1600°K for over an hour.

Theory for Steady State In-Diffusion during Evaporation

The theory for in-diffusion of an impurity during evaporation of the surface has been discussed by Batdorf and Smits.[16] When the evaporation rate is finite the diffusion equation has a solution when the time derivative term is zero, showing that a steady state is reached. This steady state solution has the form, at any time,

$$N(x)=N_0e^{-Vx/D}, \tag{7}$$

where D is the diffusion constant, V the evaporation rate of the surface and N_0 is the surface impurity concentration/cm^3. In the work of Batdorf and Smits N_0 is held constant during diffusion by maintaining a constant vapor pressure of the impurity outside the surface. In the present work, once the initial reservoir of impurity on the surface is dissolved into the surface, N_0 falls off as the layer diffuses inward. Its final value in the steady state is determined by the total number of acceptors dissolved in the surface. The evaporation rate of boron dissolved in silicon is assumed negligible in the present work since prolonged high temperature heating did not decrease the conductance of p layers.

Thus, provided the steady state has been reached near the surface, this exponential distribution [Eq. (7)], should fit our measured acceptor profile [Eq. (6)], near the surface, so that we equate K to V/D in the two exponentials. Using the best estimates of V and D at the temperatures involved,[16,17] $V/D\sim4\times10^3$ cm^{-1} for boron in silicon at 1600°K with a probable uncertainty of a factor of 3 in either direction.

The data on five strong p-layer samples are shown in Table I. While some of the these had been heated for only short times so that the acceptor profiles had not yet reached the exponential form of the steady state, a rough fit to an exponential has been made in each case near the surface to give a K value. It is seen that the K values from these profiles are in reasonable agreement with theory for boron in silicon. The surface concentration, N_0; the total number of added acceptors/cm^2, $N_{A\ TOT}$ (obtained from the analysis of the profiles); and the layer depth, are also shown.

Time Dependence of p-Layer Formation

It can be shown from the transient solution that the time required to reach steady state is of the order of

TABLE I. Data on acceptor concentration profiles for five strong p skins on silicon

Silicon sample	Htg time and temp		N_0 cm^{-3}	$N_{A\ TOT}$ cm^{-2}	K cm^{-1}	Depth to steep front or p-n jct in μ
B_2O_3 present in quartz vacuum system (0.7-cm cube)	5 min	1600°K	1.1×10^{20}	5.0×10^{15}	16×10^3	3.7 to junction
0.5-cm×0.5-cm ×2-cm square rod	2 hr	1600°K	1.1×10^{19}	1.4×10^{15}	9.0×10^3	5 to junction
0.5-mm×2-mm ×2-cm bridge	2 hr	1600°K	6.0×10^{17}	6.8×10^{13}	3.3×10^3	Smoothly falling beyond 5
Field emission tip	10 min	1550°K	2.0×10^{17}	2.0×10^{13}	10×10^3	~2 to junction
Sandblasted, sample htd. in Ta bucket	30 min	1600°K	6.0×10^{16}	1.2×10^{13}	2.6×10^3	3 to sharp fall-off

[16] R. L. Batdorf and F. M. Smits, J. Appl. Phys. **30**, 259 (1959).
[17] F. M. Smits, Proc. I.R.E. **46**, 1049 (1958).

D/V^2. For boron in silicon this is ~7 hours at 1500°K and ~1/2 hour at 1600°K. However, a large part of the p-layer conductance will be achieved in a much shorter time, namely, in the time required to dissolve the impurity atoms in a very thin sheet at the surface. This time can be estimated by assuming that initially there is a reservoir of impurity on the surface—probably as an oxide—and that as heating begins at low temperatures, some of the impurity is reduced and dissolves in the surface till the limit of solubility is reached, i.e., $N_0=N_{SAT}$. Without evaporation, the solution to the diffusion equation under this condition is given by Smits[17] as

$$N=N_0 \operatorname{erfc}(x/\sqrt{Dt}), \tag{8}$$

where

$$\operatorname{erfc} y=\frac{2}{\sqrt{\pi}}\int_y^\infty e^{-z^2}dz.$$

(At low temperatures V/D approaches zero fast enough to make the solution valid—particularly since evaporation of silicon must initially be retarded by the presence of an oxide layer.)

In Table II we show the approximate times required to dissolve 10^{12} and 10^{14} boron atoms/cm² in silicon at different temperatures assuming the distribution given by (8). A single value of $N_{SAT}=2\times10^{20}$/cm³ has been assumed for boron at all the temperatues and is probably not wrong by more than a factor of 5. From Table II we see that a typical p layer of 10^{12} acceptors could be dissolved in ~10 secs at as low a temperature as 1000°K for boron in silicon.

At the high concentration $N_{SAT}=2\times10^{20}$/cm³ the acceptors are not fully ionized and their mobility is greatly reduced. As the p layer diffuses inward to reach the steady state (no further impurity atoms are now entering the surface), fractional ionization approaches unity and actual hole mobility increases from less than 100 to over 400 cm²/v sec.

The behavior predicted by this model is in rough agreement with the observed conductance of p layers vs heating time: a sudden rise during the first few moments of heating followed by a gradual increase of about a factor of ten on prolonged heating.

Water Vapor Transfer of Boron

There remains the question of a mechanism that can transfer boron from the borosilicate glass walls to the sample surface at room temperature. Pyrex brand 7740 borosilicate glass contains about 13% B_2O_3, but the vapor pressure of this compound[18] by itself is far too low to account for the transfer. The experiments showed that water vapor is a very important factor in the p-film formation. The reactions between B_2O_3 and water vapor and the volatilization of boric acid solutions have been studied by a number of workers.[19–21] Margrave found that the presence of water vapor greatly enhanced the rate of volatilization of B_2O_3, the most likely reactions being

$$B_2O_3(s)+3H_2O(g)\rightarrow 2H_3BO_3(g)$$
$$B_2O_3(s)+H_2O(s)\rightarrow 2HBO_2(g).$$

He measured the rate of removal of B_2O_3 as a function of the partial pressure of water over the temperature range 280°C to 900°C. Surprisingly, the rate appeared to be almost independent of temperature over this range. The data covers the pressure range 4 to 600 mm Hg and definitely favors the second of the above reactions. While there is no data available that allows one to compute directly the rate at which B_2O_3 can be removed from a borosilicate glass by water vapor at room temperature, an extrapolation of Margrave's data makes it seem reasonable that the effect could be rapid enough to provide the boron contamination of the silicon studied in this work.

TABLE II. Time required for diffusion of boron into silicon surface in first stage of heating. Solubility limit assumed = 2×10^{20}/cm³. N_{TOT} = Total boron atoms dissolved/cm².

T°K	D cm²/sec	10^{12}	10^{14}
1000	2.8×10^{-18}	7 sec	2 hr
1200	3.5×10^{-16}	6×10^{-4} sec	1 min
1400	7.0×10^{-15}	3×10^{-5} sec	0.3 sec
1600	3.5×10^{-11}	6×10^{-7} sec	6×10^{-3} sec

ACKNOWLEDGMENTS

We are indebted to F. M. Smits, R. A. Logan, F. Trumbore, H. D. Hagstrum, and J. J. Lander for helpful discussions, to A. J. Ahearn for the mass spectrometer studies, and to F. S. McKim, G. J. Wolff, and P. S. Meigs for sample preparation and technical assistance.

[18] J. R. Soulen, P. Sthapitonanda, and J. L. Margrave, J. Phys. Chem. 59, 132 (1955).
[19] P. Jaulmas and A. Gontard, Bull. Soc. Chem. (5) 4, 139 (1937).
[20] M. von Stackelberger, F. Quatram, and J. Dressel, Z. Electrochem. 43, 14 (1937).
[21] J. L. Margrave, J. Phys. Chem. 60, 715 (1956).

Paramagnetic Susceptibilities of Fe and Fe-Si Alloys

SIGURDS ARAJS AND D. S. MILLER
Edgar C. Bain Laboratory for Fundamental Research, United States Steel Corporation Research Center, Monroeville, Pennsylvania

(Received January 5, 1960)

Paramagnetic susceptibilities of Fe and Fe-Si alloys (5.75, 6.82, 9.45, 12.65, 14.70, 18.11, 20.85, and 24.38 at. % Si) have been measured up to 1200°C. At high temperatures the paramagnetic susceptibilities of bcc Fe-Si alloys obey the Curie-Weiss law, possibly indicating that the contribution due to *s-d* exchange interactions is small in comparison with the temperature dependent paramagnetism. The effective Bohr-magneton number of Fe from the high-temperature region is independent of Si content up to about 14 at. % Si. At higher Si concentrations, gradual decrease in the effective Bohr-magneton number occurs. According to the paramagnetic susceptibility measurements, the α-γ transition in iron takes place at 910±3°C. Assuming that the critical temperatures for chemical ordering as given by Glaser and Ivanick are correct, our measurements indicate that the paramagnetic susceptibility, within the experimental error, is not influenced by the destruction of the superlattice above 13 at. % of Si.

INTRODUCTION

WE have recently initiated extensive magnetic investigations of various ferromagnetic materials above their Curie temperatures in order to enlarge our knowledge about the origin of paramagnetism in these substances. In this paper we present our magnetic susceptibility measurements in zone-purified Fe and in Fe-Si solid solutions up to 1200°C.

EXPERIMENTAL CONSIDERATIONS

The magnetic susceptibilities of Fe and Fe-Si alloys were determined by a modification of the Faraday method using a magnetic balance as described by Sosman and Austin.[1] Forces acting on samples placed in the inhomogeneous magnetic field produced by two coaxial solenoids were measured with a Mettler type B-5 standard balance capable of detecting, during short time intervals, weight changes of 0.05 mg. The maximum magnetic field obtained at the location of the specimen was about 1200 oe and the value of the magnetic field gradient about 130 oe cm^{-1}. The magnetic field distribution inside the solenoids was calculated with an IBM 650 computer using the characteristic dimensions of the solenoids. The calculated values were found to be in excellent agreement with those obtained experimentally using a sample of $FeSO_4(NH_4)_2SO_4 \cdot 6H_2O$ as a standard. The evacuated silica capsules containing the samples were attached to the pan of the balance with silica rods. The diamagnetic contributions of silica capsules and rods were taken into account for the susceptibility calculations.

The temperatures up to 1200°C were obtained with a bifilar-wound platinum furnace. The silica capsule containing the sample was located in the experimentally determined uniform temperature zone of the furnace. The temperature of the sample was measured with a Pt

TABLE I. Analysis of zone-purified iron.

Impurities	Amount [wt %]
Al	0.0004
As	<0.001 not detected
Be	<0.0005 not detected
C	<0.002
Ca	0.0001
Cd	<0.005 not detected
Cr	0.0001
Co	0.001
Cu	0.0001
Ga	<0.005 not detected
H	0.00003
O	0.0027
Pb	<0.0001
Mg	0.0002
Mn	0.0001
Mo	0.001
Ni	0.0004
N	0.0002
Sb	<0.001 not detected
Si	0.001
Sn	0.0001
V	<0.001 not detected
W	<0.0001 not detected

TABLE II. Analysis of constituents used for preparing iron-silicon alloys.

Impurities	Amount [wt %]
Plastiron 101	
Al	<0.001
B	<0.001
C	0.015
Cr	<0.001
Co	<0.001
P	0.005
S	0.004
Sb	<0.001
Ti	<0.001
Purified Silicon	
Al	0.02–0.03
Ca	<0.01
C	0.02–0.04
Co+Ni	<0.01
Cr	<0.01
Fe	<0.01
H	<0.01
Mn	<0.01
O	0.03–0.08
P	<0.01
Ti+Zr	<0.01

[1] R. B. Sosman and J. B. Austin, J. Wash. Acad. Sci. 25, 15 (1935).

TABLE III. Smoothed values of χ for Fe and Fe-Si alloys.

	$\chi \times 10^4$ [g^{-1} cm^3] Si [at. %]								
T[°C]	0	5.75	6.82	9.45	12.65	14.70	18.11	20.85	24.38
700								3.47	2.17
710							4.97	3.01	1.97
720							4.13	2.67	1.79
730							3.52	2.37	1.66
740						5.95	3.08	2.15	1.53
750						4.85	2.72	1.94	1.43
760						4.08	2.45	1.79	1.33
770					4.52	3.53	2.23	1.66	1.24
780					3.73	3.11	2.05	1.54	1.17
790					3.40	2.77	1.89	1.43	1.09
800					3.03	2.49	1.75	1.33	1.03
810				4.08	2.71	2.25	1.63	1.25	0.977
820	9.52		5.26	3.56	2.46	2.05	1.51	1.18	0.929
830	7.69	4.76	4.35	3.12	2.23	1.89	1.41	1.12	0.884
840	6.21	4.06	3.70	2.79	2.04	1.74	1.32	1.06	0.840
850	5.26	3.53	3.23	2.51	1.88	1.61	1.24	1.00	0.806
860	4.40	3.11	2.86	2.28	1.74	1.50	1.17	0.951	0.770
870	3.77	2.79	2.56	2.08	1.63	1.40	1.10	0.905	0.737
880	3.33	2.51	2.27	1.92	1.51	1.32	1.04	0.862	0.704
890	2.96	2.23	2.11	1.77	1.42	1.24	0.982	0.821	0.677
900	2.63	2.08	1.94	1.64	1.33	1.17	0.936	0.786	0.649
910	α-γ	1.92	1.79	1.54	1.25	1.11	0.891	0.752	0.623
920	0.287	1.78	1.67	1.44	1.18	1.05	0.852	0.722	0.600
930	0.286	1.65	1.56	1.35	1.12	1.00	0.815	0.694	0.578
940	0.286	1.54	1.47	1.27	1.07	0.956	0.780	0.667	0.558
950	0.285	1.45	1.38	1.20	1.02	0.913	0.750	0.643	0.539
960	0.284	1.35	1.30	1.14	0.967	0.873	0.720	0.620	0.521
970	0.284	1.28	1.23	1.09	0.924	0.839	0.693	0.599	0.505
980	0.283	1.21	1.17	1.04	0.885	0.806	0.668	0.579	0.490
990	0.282	1.14	1.11	0.990	0.847	0.776	0.646	0.561	0.475
1000	0.282	1.09	1.05	0.945	0.814	0.748	0.624	0.543	0.461
1010	0.281	1.04	0.997	0.905	0.782	0.722	0.604	0.527	0.448
1020	0.281	0.987	0.953	0.867	0.754	0.697	0.585	0.512	0.436
1030	0.280	0.943	0.912	0.832	0.727	0.673	0.567	0.497	0.424
1040	0.280	0.906	0.873	0.800	0.702	0.652	0.551	0.483	0.414
1050	0.279	0.869	0.839	0.769	0.679	0.631	0.535	0.471	0.404
1060	0.279	0.833	0.806	0.742	0.658	0.612	0.520	0.458	0.393
1070	0.278	0.803	0.776	0.717	0.638	0.594	0.506	0.447	0.384
1080	0.277	0.773	0.749	0.693	0.619	0.577	0.493	0.436	0.375
1090	0.277	0.746	0.722	0.671	0.601	0.560	0.480	0.425	0.366
1100	0.276	0.721	0.698	0.649	0.584	0.545	0.468	0.415	0.358
1110	0.275	0.697	0.676	0.630	0.567	0.531	0.457	0.406	0.350
1120	0.275	0.676	0.654	0.612	0.553	0.517	0.445	0.397	0.343
1130	0.275	0.655	0.635	0.594	0.538	0.504	0.435	0.388	0.335
1140	0.274	0.636	0.616	0.578	0.524	0.491	0.425	0.380	0.328
1150	0.273	0.617	0.599	0.562	0.511	0.482	0.416	0.371	0.322
1160	0.273	0.600	0.582	0.547	0.499	0.468	0.407	0.367	0.315
1170	0.272	0.583	0.567	0.533	0.487	0.457	0.398	0.356	0.309
1180	0.272	0.568	0.551	0.519	0.476	0.447	0.390	0.349	0.303
1190	0.271	0.553	0.538	0.507	0.465	0.438	0.382	0.342	0.297
1200	0.270	0.539	0.524	0.494	0.454	0.427	0.374	0.336	0.292

and Pt-10% Rh thermocouple whose junction was also placed in the uniform temperature zone of the furnace between the silica capsule and the wall of the furnace. This thermocouple was calibrated at the melting point of Sn and of Au. The error in the temperature of the sample was estimated to be ± 3°C.

The zone-purified Fe for which the high-temperature magnetic susceptibilities were determined was obtained from Battelle Memorial Institute. The results of analysis of this material are shown in Table I.

The Fe-Si samples were obtained from melts prepared by melting selected amounts of Fe and Si in stabilized zirconia crucibles under vacuum. Fe (plastiron 101) was supplied by Plastic Metals Division of the National United States Radiator Company. Purified Si came from Union Carbide Corporation. The analyses of Fe and Si as given by the suppliers are given in Table II. Chemical and spectrographic analyses of these melts obtained at this Laboratory were in good agreement with these values.

The error of measured values of magnetic susceptibilities was estimated to be about 3%.

RESULTS AND DISCUSSIONS

The smoothed values of the magnetic susceptibility of zone-purified Fe as a function of temperature are given in Table III. The inverse susceptibility of Fe as a

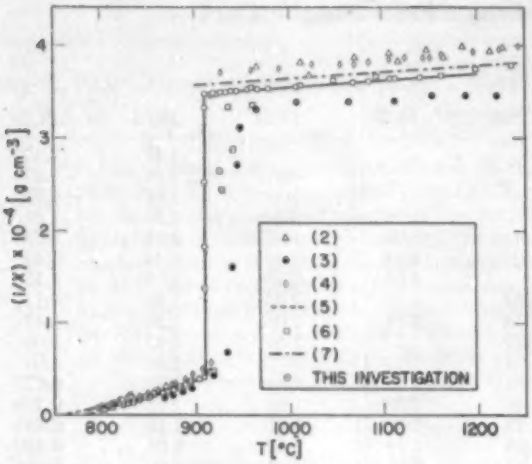

FIG. 1. Inverse paramagnetic susceptibility of Fe as a function of temperature.

function of temperature is shown in Fig. 1 in comparison with measurements by some previous investigators.[2-7] It is apparent that considerable scattering exists among the measured values of the susceptibility obtained by various investigators. Our susceptibility results are in good agreement with those of Sucksmith and Pearce[6] except for the α-γ transition temperature. According to our measurements, the crystal-structure change occurs at 910±3°C.

The smoothed values of magnetic susceptibilities as a function of temperature for various Fe-Si alloys are also given in Table III. The inverse susceptibilities vs temperature are shown in Fig. 2. The high-temperature region is satisfied by the Curie-Weiss law

$$\chi = C/(T-\theta_p), \qquad (1)$$

where χ is the magnetic susceptibility per gram, C the Curie constant, θ_p the paramagnetic Curie temperature, and T the absolute temperature. The paramagnetic Curie temperatures and the Curie constants determined by the method of least squares using the high-temperature magnetic susceptibility data are given in Table IV and shown in Fig. 3. Figure 3 also gives the ferromagnetic Curie temperatures measured by Parsons *et al.*[8] The paramagnetic Curie temperatures and Curie constants of 5.68, 11.97, and 18.59 at. % Si in Fe alloys as obtained by Néel,[9] which is the only known previous work on high-temperature paramagnetic susceptibilities of Fe rich Fe-Si alloys, are also shown in Fig. 3. These quantities and the susceptibility values as a function of temperature are in fair agreement with our measurements.

TABLE IV. Paramagnetic Curie temperatures, Curie constants, and effective Bohr-magneton numbers of iron in iron-silicon alloys.

Si [at %]	θ_p [°C]	$C\times10^3$ [cm³ °C g⁻¹]	μ_{eff} [Bohr magnetons]
0	820[a]	2.20[a]	3.13[a]
5.57	804	2.13	3.13
6.82	801	2.10	3.11
9.45	781	2.07	3.12
12.65	749	2.05	3.13
14.70	732	2.00	3.12
18.11	702	1.86	3.04
20.85	677	1.75	2.98
24.38	653	1.60	2.88

[a] See work cited in footnote 6 for data from δ region.

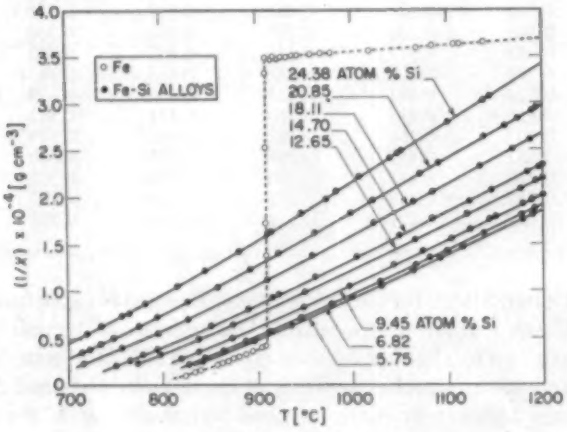

FIG. 2. Inverse paramagnetic susceptibilities of Fe and Fe-Si alloys as a function of temperature.

The effective Bohr-magneton numbers of Fe as a function of Si concentration are shown in Fig. 4. The numbers were calculated from the equation

$$\mu_{eff} = \{3kC[M_{Fe}+xM_{Si}/(100-x)]/N_A\}^{\frac{1}{2}}/\beta, \qquad (2)$$

where C is the Curie constant, x the at. %/Si in Fe, k the Boltzmann constant, N_A the Avogadro number, and β the Bohr magneton. M_{Fe} and M_{Si} are the atomic weights of Fe and Si, respectively.

It is seen from Fig. 4 that the average magnetic moment of the Fe atom is not influenced by Si up to about 14 at. % of Si. At higher Si concentrations, the effective Bohr-magneton number decreases by about 2.4×10^{-2} Bohr magnetons per at. % of Si. A similar picture in the Fe-Si system has been obtained recently from studies of the ferromagnetic state by Parsons *et al.*[8] They found that the mean magnetic moment per Fe atom remains at about 2.2 Bohr magnetons and then begins to fall off at about 10 at. % of Si content.

Special attention was given to the magnetic suscepti-

[2] P. Weiss and G. Foëx, Arch. Sci. Natl. **31**, 89 (1911).
[3] K. Honda and H. Takagi, Sci. Repts. Tôhoku Univ. **1**, 229 (1911).
[4] E. M. Terry, Phys. Rev. **9**, 394 (1917).
[5] H. H. Potter, Proc. Roy. Soc. (London) **A146**, 362 (1934).
[6] W. Sucksmith and R. R. Pearce, Proc. Roy. Soc. (London) **A167**, 189 (1938).
[7] Y. Nakagawa, J. Phys. Soc. Japan **11**, 855 (1956).
[8] D. Parsons, W. Sucksmith, and J. E. Thompson, Phil. Mag. **3**, 1174 (1959).
[9] L. Néel, Ann. phys. **17**, 5 (1932).

bility measurements at high temperatures in order to study possible influence of chemical ordering. The measurements were obtained with slowly increasing and decreasing temperatures. Above the critical temperatures of disorder, the magnetic susceptibility was studied also as a function of time. Within the experimental error of our measurements, the susceptibility data were independent of either time or the method of changing temperatures.

It is known that in Fe-Si alloys ordering begins at at approximately 13 at. % of Si.[10,11] The critical temperatures for disorder as determined by Glaser and Ivanick[12] are within the temperature range of our susceptibility measurements. The inverse magnetic susceptibility vs temperature curves shown in Fig. 2 do not indicate any unusual behavior associated with the critical temperatures of the ordering process. Thus, within the experimental error of our susceptibility measurements, the destruction of superlattice (assuming that the critical temperatures given by Glaser and Ivanick are correct) does not influence the paramagnetic susceptibility.

It is well known that the ferromagnetic elements of the Fe group all exhibit paramagnetic properties which are not easily correlated with their ferromagnetic properties. The inverse paramagnetic susceptibility vs temperature does not give a completely straight line as expected from the Curie or Curie-Weiss law. The true paramagnetic susceptibility of bcc Fe is considerably larger than that due to a collection of particles with total angular momentum quantum number $J=1.11$. That is, above the ferromagnetic Curie point the paramagnetic behavior of Fe cannot be explained by assuming complete disordering of the ferromagnetic lattice into random collection of particles with $J=1.11$. These observations can be interpreted as an indication that above the ferromagnetic Curie point short-range magnetic order exists between the fundamental magnetic moments. The correctness of this interpretation has been supported by neutron scattering studied in Fe at high temperatures.[13,14] According to these experiments the magnetic moments in Fe relatively far below the ferromagnetic Curie point are aligned parallel with only an occasional moment oriented in a different direction. At temperatures just below the Curie point there still remains an effective domain magnetization both in magnitude and direction, but within the domains there exist regions in which time dependent fluctuations occur. The average amplitude of these fluctuations reaches a maximum at the ferromagnetic Curie temperature and results in a maximum intensity of neutron scattering. The relationship between the magnetic-moment fluctuations and

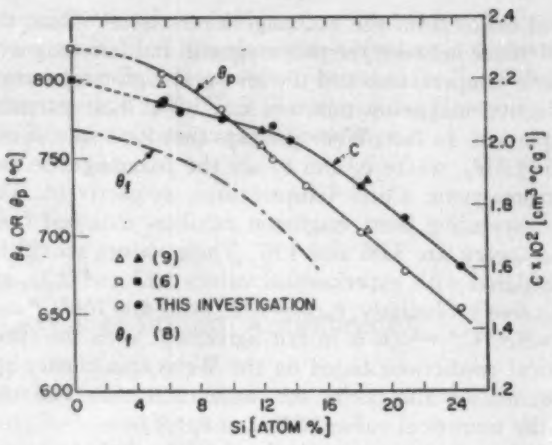

FIG. 3. Ferromagnetic and paramagnetic Curie temperature and Curie constants of Fe-Si alloys.

spin-spin correlations has been discussed theoretically by Gersch *et al.*[15] and Elliott and Marshall.[16] The spin-cluster problem in Fe near the ferromagnetic Curie temperature has also been considered by Averbach.[17] He has interpreted the neutron scattering data in terms of the probability of finding like spins in a given region using an approach similar to that used in the study of atomic short-range order by means of diffuse x-ray scattering. His probability function for like spins as a function of distance at various temperatures appears to be justified by our magnetic susceptibility data.

The effect of the spin-cluster system on magnetic moment has also been investigated by Weiss[18] using the Bethe-Peierls method. According to his model the Curie-Weiss law is not obeyed immediately above the ferromagnetic Curie point because of decreasing ratio of the internal to the external field with increasing temperatures. The internal field in the presence of an external

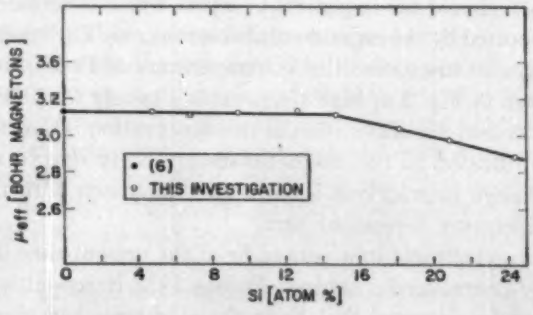

FIG. 4. Average magnetic moment of Fe atom in Fe-Si alloys.

[10] G. Phragmén, J. Iron Steel Inst. (London) **116**, 397 (1926).
[11] L. Zwell (private communication).
[12] F. W. Glaser and W. Ivanick, Trans. Am. Inst. Mining Met. Engrs. **206**, 1290 (1956).
[13] M. K. Wilkinson and C. G. Shull, Phys. Rev. **103**, 516 (1956).
[14] M. Ericson and B. Jacrot, Compt. rend. **246**, 1018 (1958).
[15] H. A. Gersch, C. G. Shull, and M. K. Wilkinson, Phys. Rev. **103**, 525 (1956).
[16] R. J. Elliott and W. Marshall, Revs. Modern Phys. **30**, 75 (1958).
[17] B. L. Averbach, "Spin clusters in iron near the Curie temperature" in *Magnetic Properties of Metals and Alloys*, ASM Seminar, Cleveland, Ohio, October 25–26, 1958 (American Society for Metals, Cleveland, Ohio, 1959), p. 280.
[18] P. R. Weiss, Phys. Rev. **74**, 1493 (1948).

field arises from the exchange interactions. Thus, the difference between the paramagnetic and ferromagnetic Curie temperatures and the low- and high-temperature effective magneton numbers can be at best partially explained. In fact, Weiss predicts that for a spin of one $\theta_p = 1.03\theta_f$, where θ_p and θ_f are the paramagnetic and ferromagnetic Curie temperatures, respectively. The corresponding Bohr magneton numbers obtained from the theory are 3.06 and 1.87. These values should be compared with experimental values 3.13 and 2.22, respectively. Similarly, $\theta_p/\theta_f = 1.08$, using $\theta_f = 760°C$[19] and $\theta_p = 820°C$,[6] which is in fair agreement with the theoretical predictions based on the Weiss spin-cluster approximation and taking into account the uncertainties in the numerical values of θ_f and θ_p.

Although there is no doubt that the *d* electrons are primarily the source for the magnetism in transition metals, the influence of conduction electrons on the magnetic behavior in these materials merits consideration. This problem recently has been discussed by Vlasov and Vonsovskii.[20] They have theoretically examined the high-temperature paramagnetism of ferromagnetic materials on the basis of an *s-d* interaction model. They found that these exchange interactions give a temperature independent term in susceptibility in addition to the usual Curie-Weiss magnetic expression. The theoretical results cannot give quantitative values of this contribution due to the difficulties in evaluating various exchange integrals from fundamental principles (some partially empirical attempts with some success have been made by Gal'perin[21]). However, quanlitatively the ideas of Vlasov and Vonsovskii have been supported by the recent experimental work in Russia on various Ni alloy.[22] It is also of interest that the *s-d* exchange interaction model leads to the conclusion that the effective Bohr-magneton numbers computed from the ferromagnetic data and the paramagnetic susceptibility measurements should not in general be equal, which is definitely supported by the experimental observations. The inverse magnetic susceptibilities vs temperature of Fe-Si alloys shown in Fig. 2 at high temperatures satisfy the Curie-Weiss law. An implication of this observation is that the contribution to the magnetic susceptibility due to *s-d* exchange interactions is small in comparison with the temperature dependent part.

The electronic structure of Fe at the present time is a very controversial subject. Before 1958 it was almost generally accepted that Fe in the solid state had about 7.4 3*d* electrons and 0.6 4*s* electrons. A free Fe atom has 6 3*d* electrons and 2 4*s* electrons. In other words, it was believed that the electronic structure of Fe in the solid state was not very different from the free-atom case. Using this picture, the ferromagnetic properties of Fe resulted from electrons in unfilled *d* subbands.[23] During 1958 a new value for the number of *d* electrons in Fe (2.3 ± 0.3) was suggested by Weiss and DeMarco[24] on the basis of measurements of x-ray scattering factors in single crystals. The conclusions of this investigation have also been recently supported by magnetic scattering studies.[25,26] These investigations stimulated considerable theoretical activity and, as a result of it, new methods for the electronic structure of Fe were formulated.[27–30] It should however, be mentioned that during these developments the work of Weiss and DeMarco has been questioned by DesLattes,[31] Hume-Rothery *et al*,[32] and Komura *et al*.[34] Also, the theoretical models of Mott and Stevens,[27] and Lomer and Marshal[28] were not supported by the hyperfine coupling measurements in Co-Fe and Co-Ni alloys as determined by heat-capacity measurements.[35] The most recent contribution to the problem of the energy bands in Fe is due to Wood,[36] whose theoretical calculations using the augmented plane wave method give results which do not lend support to the hypotheses of Mott and Stevens, Lomer and Pauling[37] but favor the conventional band theory. Obviously, the present status of the electronic structure of Fe is not settled yet. This situation makes a detailed theoretical analysis of the paramagnetic behavior of Fe-Si alloys difficult at the present time.

ACKNOWLEDGMENTS

The authors wish to thank the following members of this Laboratory: A. D. Damick for technical assistance, L. Zwell for supplying Fe-Si samples and for helpful

[19] J. S. Kouvel, "Methods for determining the Curie temperatures of a ferromagnet," General Electric Research Lab. Rept. No. 57-RL-1799, September, 1957.
[20] K. B. Vlasov and S. V. Vonsovskii, Fiz. Metal. i Metalloved. Akad. Nauk S. S. S. R. Ural' Fibial **2**, 403 (1956).
[21] F. M. Gal'perin, Soviet Phys.—JETP **5**, 321 (1957); Bull. Acad. Sci. U. S. S. R. Phys. Ser. (English translation) **21**, 1308 (1957).
[22] D. I. Volkov and V. I. Chechernikov, Bull. Acad. Sci. U. S. S. R. Phys. Ser. (English Translation) **21**, 1099 (1957).
[23] B. R. Coles and W. R. Bitler, Phil. Mag. **1**, 477 (1956).
[24] R. J. Weiss and J. J. DeMarco, Revs. Modern Phus. **39**, 59 (1958); Phys. Rev. Fetters **2**, 148 (1959).
[25] R. Hathans, C. G. Shull, G. Shirane, and A. Anderson, J. Phys. Chem. Solids **19**, 138 (1959).
[26] R. J. Weiss and A. J. Freeman, J. Phys. Chem. Solids **10**, 147 (1959).
[27] N. F. Mott and K. W. H. Stevens, Phil. Mag. **2**, 1364 (1957).
[28] W. M. Lomer and W. Marshall, Phil. Mag. **3**, 185 (1958).
[29] J. B. Goodenough, J. Appl. Phys. **29**, 513 (1958); Quart. Prog. Rept., Solid State Research, Lincoln Lab., MIT. November 1, 1958, p. 91 and April 15, 1959, p. 58.
[30] W. Marshall and R. J. Weiss, J. Appl. Phys. **30**, 2205 (1959).
[31] R. D. DesLattes, Phys. Rev. **110**, 1471 (1958).
[32] W. Hume-Rothery, P. J. Brown, J. B. Forsythe, and W. H. Taylor, Phil. Mag. **3**, 1466 (1958).
[33] B. W. Batterman, Phys. Rev. Letters **2**, 47 (1959); Bull. Am. Phys. Soc. **4**, Ser. II, 175 (1959); Phys. Rev. **115**, 81 (1959).
[34] Y. Komura, Y. Tomiie, and R. Nathans, Phys. Rev. Letters **3**, 268 (1959).
[35] V. Arp, D. Edmonds, and R. Petersen, Phys. Rev. Letters **3**, 212 (1959).
[36] J. H. Wood, Quart. Prog. Rept., Solid State and Molecular Theory Group, MIT, October 15, 1959, p. 4.
[37] L. Pauling, Phys. Rev. **54**, 899 (1938).

discussions, R. W. Whitmore for numberical calculations on the magnetic field distribution inside the solenoids and for computations by the method of least squares, L. S. Darken for valuable suggestions during the course of the work, and R. A. Oriani for helpful comments. We also would like to acknowledge the useful advice of F. F. Cilyo on various electronic problems. Stimulating discussions with A. Arrott of the Ford Motor Company and with C. S. Barrett of the University of Chicago have been greatly appreciated.

JOURNAL OF APPLIED PHYSICS VOLUME 31, NUMBER 6 JUNE, 1960

Production and Properties of Thin Layers of Indium Antimonide*

G. Bate† and K. N. R. Taylor
Department of Physics, University of British Columbia, Vancouver, British Columbia
(Received December 16, 1959; revised manuscript received February 23, 1960)

A new method of producing thin layers of indium antimonide is described. This consists of suddenly squashing a drop of molten indium antimonide between two optical flats and allowing it to cool.

Large area, self-supporting specimens of 10-μ thickness have been prepared in this way and their properties examined. Although these layers are polycrystalline, their electrical and optical properties are in good agreement with the single-crystal materials from which they were obtained.

1. INTRODUCTION

In recent years a great deal of effort has been devoted to the preparation and examination of thin samples of semiconducting materials. Work of this type is essential for obtaining the detailed band structure of the solid by way of optical measurements, and also for the theoretical assessment of Hall effect and infrared sensitive devices.

Indium antimonide is one of the most extensively examined semiconductors because of its striking physical properties: small energy gap, high mobility, and small effective mass of the conduction electrons; and also because it is relatively easy to prepare extremely pure specimens. Unfortunately, the absorption coefficient of this material is very large and optical measurements at wavelengths shorter than that corresponding to the band gap must be made on very thin samples.

Such samples have previously been prepared either by a continuous grinding technique or by the evaporation of the material onto a substrate. The former is essentially a long uncertain process frequently resulting in the appearance of pinholes and cracks in the final layer. The latter method frequently produces a thin film in which the chemical composition changes from one surface to the other.

In order to overcome some of these difficulties, a considerable amount of time has been devoted in this Laboratory to finding a new method for preparing thin specimens. This search resulted in the development of a new technique for the production of thin layers which is described herein. This method simply involves squashing a drop of molten indium antimonide between two optically flat surfaces and allowing it to solidify.

Pieces of self-supporting layer, 10-μ thick of 1 cm^2 area have been obtained in this way and their optical and electrical properties examined. The results of this investigation suggest that optically the films behave in the same way as the bulk material. Unfortunately however, the layers are polycrystalline and the electrical properties are somewhat adversely affected.

The indium antimonide used in these experiments was n-type of three different impurity concentrations, varying from 10^{14}/cc to greater than 10^{16}/cc.

2. PREPARATION

The apparatus for the preparation of the layers consisted essentially of a heated quartz substrate on which rested the piece of indium antimonide. A second (cold) quartz substrate with a weight above it was dropped from a height of about three centimeters onto the molten indium antimonide which then squashed into a thin layer between the two flats. The lower quartz flat was supported on a block of pyrophyllite into which was fitted a heater winding of Nichrome wire and a chromel-alumel thermocouple. A glass cylinder with a brass lid completely surrounded the heater assembly to enable the melting to be done in an inert atmosphere of argon which was allowed to flow through the apparatus for about three hours before the heating was started. A piece of indium antimonide weighing about $\frac{1}{10}$ g was washed in carbon tetrachloride, etched in CP4A diluted with glacial acetic acid, washed in deionized water, and finally dried with an infrared lamp immediately before being placed on the quartz flat. The substrates were also carefully cleaned by scrubbing with detergent and washing for long periods with concentrated nitric acid followed by washing with deionized water and drying under an infrared lamp.

Two different methods of producing the layers were

* The research for this paper was supported by the Defence Research Board of Canada under a grant.

† Now at the IBM Laboratories, Poughkeepsie, New York.

tried. In the first, the indium antimonide was sandwiched between the two flats, the whole heated, and a steady load applied to the top flat. However, the surface-tension forces caused the molten indium antimonide to be squeezed completely from between the flats. The method which gave the best results involved the drop being suddenly squeezed between the hot substrate and a cold one. The cold substrate was attached by means of a small piece of plasticene to a heavy brass rod which could slide in a vertical tube mounted in the lid of the surrounding vessel. The two substrates were arranged to have their surfaces parallel by laying one on the other prior to the indium antimonide being installed. The plasticene was sufficiently flexible to allow any misalignment to be corrected and also damped any vibration set up by the falling weight and the substrate. The heater current was switched off immediately the weight was released, and the whole assembly allowed to cool to room temperature before the apparatus was opened. Invariably, it was found that the thin layer of indium antimonide was completely unattached to the top quartz flat and only loosely attached to the bottom one and could be removed by means of a razor blade.

Because of different thermal expansion coefficients of indium antimonide and the substrate material, the final layer was either cracked in the case of quartz flats or buckled in the case of soda glass flats. In spite of this, pieces as large as 1 cm^2 could be extracted from the final layer. The material whose expansion properties most nearly match those of indium antimonide is molybdenum, and a pair of substrates of this material were prepared. However, the layer adhered firmly to these and could not be removed in pieces sufficiently large for measurement.

Quartz flats of several dimensions were tried and the best results were obtained with those of about the same size as the heater and about three-millimeters thick; the flats were ground and polished on both sides to a tolerance of $\frac{1}{10}$ wavelength.

The effect of varying the height from which the weighted substrate was dropped, the temperature of the lower substrate, and the length of time elapsed after dropping before the heater current was switched off were roughly investigated, and an empirical set of conditions for producing the best layers was obtained. These quantities together with the size of the substrates affected to a greater or less extent the distance over which the molten indium antimonide could flow before its temperature was reduced below the melting point. Laue-back reflection photographs of the layers confirmed their polycrystalline nature.

Indium antimonide is a very friable material, and consequently, layers of 10- to 20-μ thickness were very fragile, and it was found necessary to handle these with a simple vacuum wand constructed of a hypodermic needle ground flat at the point. For the electrical measurements, pieces of the layers of regular size were required, and these were easily obtained by placing the layer on a microscope slide and cutting with a sharp razor blade.

Several methods of thickness measurement were adopted in the initial experiments, but it was found that a dial gauge comparator graduated in steps of 2 μ was the most consistent and convenient and was used in all subsequent measurements. Specimens taken from different parts of the same layer were found to vary only slightly in thickness.

3. ELECTRICAL PROPERTIES

Measurements were made of the Hall coefficient and transverse magnetoresistance in both bulk and layer samples using a conventional six-electrode dc measuring technique. The results of these measurements made at room temperature are shown plotted against field strength in Fig. 1 for one of the layer specimens.

From the layer results of Fig. 1 it was possible to evaluate both electron and hole mobility, and the ratio of electron to hole concentration, using the analysis developed by Barrie and Hilsum.[1] The values obtained in this way are given in Table I and are compared with the accepted values for the single crystal bulk material, whose impurity concentration was 10^{14}/cc, and one other bulk material with an impurity concentration of 2×10^{17}/cc.

4. PHOTOCONDUCTIVITY

Several layer specimens were examined for photoconductive effects at room temperature, using chopped

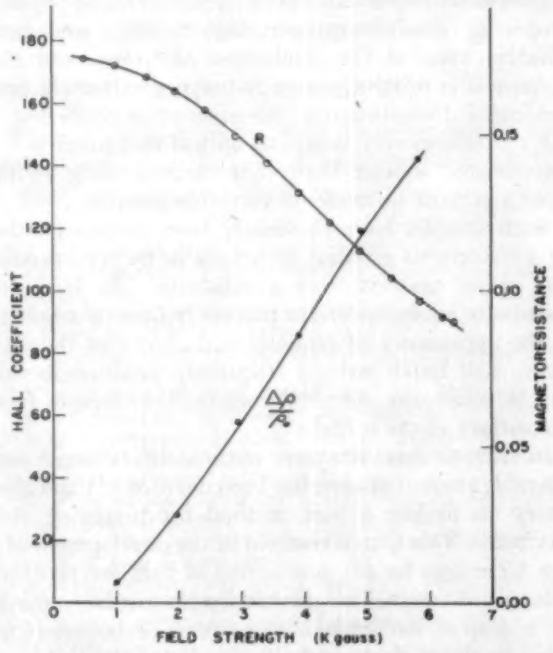

FIG. 1. Hall coefficient and magnetoresistance of the layer specimens.

[1] R. Barrie and C. Hilsum, Proc. Phys. Soc. (London) **71**, 676 (1958).

TABLE I.

	Layer	Bulk	
Impurity concentration[a]	3×10^{16}/cc	10^{14}/cc	2×10^{17}/cc
Electron mobility (cm^2/v-sec)	2.38×10^4	7.6×10^4	2.4×10^4
Hole mobility (cm^2/v-sec)	5.95×10^2	7.5×10^2	5.2×10^2
Electron conc./hole conc.	1.68×10^{-5}	1	8×10^{-3}

[a] Determined at 78°K.

monochromatic infrared radiation. Unfortunately, it was never possible to observe photoconductivity in any of these specimens. The absence of any effect of this type may be accounted for by the small absorption of radiation around 5.5 μ in the thin samples used, or by the very strong surface recombination which must be present in a layer whose thickness is small compared with the diffusion length.

In all these observations however an appreciable photovoltaic effect was observed at the electrodes.

5. OPTICAL PROPERTIES OF ABSORPTION SPECTRA

Measurements of the absorption spectra of the thin layers of indium antimonide were made over the wavelength range from 10.1 μ to 2.2 μ using a Perkin-Elmer type 83 monochromator fitted with a rock-salt prism. A dc carbon arc was used as a source and a vacuum thermocouple as a detector. The specimens were mounted over a small (0.2 cm diam) hole in a brass plate situated directly in front of the entrance slit of the instrument. To avoid any appreciable temperature changes occurring during a series of observations, the specimen was continuously cooled by a stream of cold air blown across its surface. During these measurements it was found that a certain amount of infrared radiation which was passing through the specimen was reaching the detector without passing through the optics of the instrument. This caused an anomalously high transmission at all wavelengths, but was most important below 4 μ where the absorption coefficient of indium antimonide is very large. This scattered radiation was eliminated by the erection of carefully designed screening inside the monochromator, and by the use of various infrared filters to remove that radiation of wavelength greater than that of interest.

The method of attaching the specimen over the hole in the base plate was to paint completely round it with some opaque adhesive. The first adhesive used was an air drying silver paint used in the electrical measurements. This worked satisfactorily on small specimens and provided leak free samples. However, if the specimen size was greater than 5 mm^2, the contraction of the paint on drying was sufficient to fracture the layer. The second method of adhesion was a black cellulose paint employed in the same way, and this allowed specimens up to 1 cm by 0.5 cm to be mounted satisfactorily for periods of up to 48 hours. After a longer period than this however, the sample was visibly buckled and cracks often appeared.

The method of layer preparation described herein is susceptible to the production of pinholes in the material. To ensure that the transmitted radiation is passing through the indium antimonide and not through such pinholes, the samples to be mounted were always painstakingly examined for the presence of these, initially by eye, holding the specimen over an intense light source, and then through a microscope using the dark-adapted eye and strong illumination from below. Finally, after the specimen had been mounted, the holder was situated a short distance from a photomultiplier and the radiation from the carbon arc allowed to fall on it. Only if the specimen gave no signal in this final test was it used in the subsequent observations.

All the absorption measurements were taken by observing the amount of radiation passing through the specimen at any wavelength and comparing it with the radiation passing through at some predetermined wavelength beyond the absorption edge. The absorption coefficient was then found for this standard wavelength and the values at all other wavelengths determined from it. This method has the advantage of eliminating any lens properties which the specimen may have, and avoids repeated alignment of the system.

The variation of the absorption coefficient for one of the layer specimens is shown in Fig. 2 along with similar results for the bulk material.[2]

6. REFLECTION SPECTRA

Measurements were made over the range 0.22–10.1 μ on both bulk and layer samples. From 0.5–10.1 μ the monochromator was used as for the absorption measurements. From 0.23–0.5 μ a fused quartz prism was used with a hydrogen discharge tube as source and a photo-

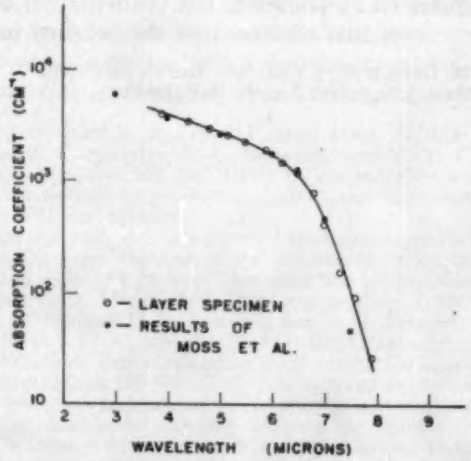

FIG. 2. Absorption coefficient of indium antimonide.

[2] T. S. Moss *et al.*, Proc. Phys. Soc. (London) **B70**, 776 (1957).

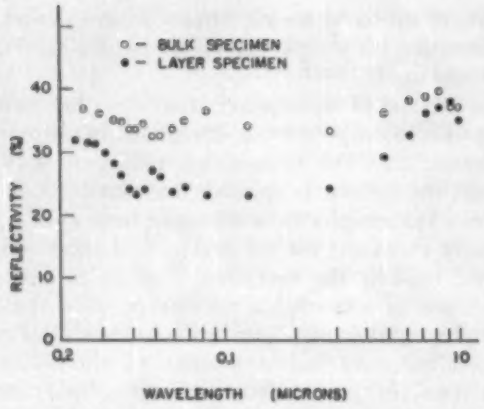

FIG. 3. Reflectivity of bulk and layer indium antimonide.

multiplier as detector. The reflection apparatus was situated immediately before the entrance slit of the monochromator. Parallel light entering the reflection box passed through two limiting apertures before being reflected upwards from an aluminium mirror onto the specimen which was in the horizontal plane, the angle of incidence being 80°. After reflection, the light passed out of the box and into the monochromator by means of a second mirror and two more limiting apertures arranged so that the incident and reflected beams were symmetrically disposed with respect to the normal at the center of the specimen. The two mirrors were attached to either side of a brass triangular prism which could be slid to one side to enable the intensity of the incident beam to be measured. All measurements were made relative to the reflectivity of rapidly deposited aluminium mirrors, the values being taken from the work of Gates *et al.*[3] and Hass.[4]

The bulk specimens of indium antimonide were mounted in bakelite and polished using the standard metallographic procedures. One specimen was etched in CP4A diluted with glacial acetic acid to remove the layer distorted by polishing, but the reflection was no different from that measured on the polished surface. Also, while two of the bulk specimens were single crystals, one was polycrystalline and showed no different spectrum.

The layer specimens were already highly reflecting when formed and required no further treatment before measurement.

In Fig. 3 are given typical reflection spectra for both bulk and layer specimens of the same material. In the infrared beyond the wavelengths corresponding to the energy gap in indium antimonide, the reflectivity of both was about 36%, which was to be expected from a material of refractive index four.[2] As measurements described in the previous section showed, the absorption coefficient in the neighborhood of the band gap varied from 10^2–10^4 cm^{-1}, corresponding to a value of k (the imaginary part of the complex refractive index) of 6×10^{-3} to 2×10^{-1}. These values are far too small to produce any observable change in reflectivity on passing from wavelengths greater than the absorption edge to wavelengths smaller.

The fine structure at short wavelengths deserves a more detailed examination than was possible in the course of this work.

7. CONCLUSIONS

The results described in the foregoing indicate that this method of producing thin layers of indium antimonide results in self-supporting layers of considerable area and whose thickness is appreciably less than other layer specimens of comparable characteristics. In addition, the properties of the thin layers are in reasonable agreement with those of the bulk material.

By a more extensive examination of the various factors affecting the thickness of the final layer, and also the effect of annealing on the specimens, it should be possible to produce even thinner layers, and so allow an examination of the absorption properties to be made to shorter wavelengths.

One of the important possibilities of this method of layer production is in its use for Hall effect and other devices whose sensitivity increases rapidly with decrease in thickness.

[3] D. M. Gates *et al.*, J. Opt. Soc. Am. **48**, 88 (1958).
[4] G. Hass, J. Opt. Soc. Am. **45**, 945 (1955).

Vapor-Deposited Single-Crystal Germanium*

RALPH P. RUTH,† JOHN C. MARINACE,‡ AND W. C. DUNLAP, JR.§
The General Electric Company, Electronics Park, Syracuse, New York

(Received September 8, 1958; revised manuscript received February 23, 1960)

Germanium layers have been formed on single-crystal Ge substrates by the thermal decomposition of GeI_2. The single-crystal nature of the layers has been established by x-ray and electron diffraction examination and by electrical measurements. The deposition process is described briefly. The crystal growth rate varies with crystal direction, and under certain conditions Ge whiskers appear. The layers as deposited are generally n type; ρ ranges from 1 to 5 ohm-cm and μ_H from 1200 to 2700 cm²/v-sec at room temperature. A donor level is found approximately 0.2 ev below the conduction band, with a concentration of active centers of about 10^{16}/cm³. Heat treatment at 550°C gradually converts the layers to p type, for which ρ is 10 to 40 ohm-cm and μ_H 1500 to 2400 cm²/v-sec at room temperature; an acceptor level is found at about 0.05 ev above the valence band, with a density of active centers of 10^{14} to 10^{15}/cm³. The layers can be doped intentionally to produce either conductivity type, permitting fabrication of junction devices. Although iodine and other impurity atoms are considered, it is concluded that interstitial Ge atoms and lattice vacancies, occurring in unequal numbers at the time of deposition, are the most likely source of the donor and acceptor levels, respectively, and of the observed heat treatment properties.

INTRODUCTION

SEVERAL attempts have been made in the past to obtain single-crystal germanium layers by the method of epitaxy, i.e., by promoting oriented growth of germanium crystals upon a variety of single-crystal substrate materials. Most of this work has utilized vacuum evaporation for deposition of the germanium on the substrate.[1,2] In some cases, fairly complete orientation of these layers has been realized when the growth has occurred on substrates at elevated temperatures (400–900°C). In general, the higher degrees of orientation have occurred for the higher substrate temperatures; below a certain temperature (probably 400–500°C for germanium), called the "epitaxial temperature,"[3] polycrystalline or amorphous deposits are generally obtained.

A major difficulty with the vacuum-evaporation technique is the wide departure from equilibrium conditions at the substrate. However, the deposition of material on the substrate by means of chemical decomposition from the vapor phase does not have this disadvantage. Although the general method is not new, it has not been applied extensively to the preparation of high purity single crystals of semiconducting materials.[4,5]

To explore the possibilities of this technique, the germanium diode vapor decomposition process utilized in this work was developed by one of the authors (J.C.M.). With it, single-crystal germanium, of a quality similar in many ways to that of crystals grown from the melt by the Czochralski method, was grown upon single-crystal germanium substrates.

This paper describes some of the results obtained in a study of the structural and electrical properties of these layers.

DEPOSITION PROCESS

A quartz-tube furnace having three independently controlled temperature regions was used; it contained a charge of triply-sublimed iodine[6] at one end (50–75°C), crushed zone-refined intrinsic-conductivity germanium in the center region (450–525°C), and seed wafers of single-crystal germanium in the other end region (325–400°C). A slow flow of dry inert gas, entering the furnace at the iodine end, carried the subliming iodine vapor over the center heated germanium region, where GeI_2 and GeI_4 were both formed. At temperatures above

* This work was first described by the authors at the June 1956 meeting of the American Physical Society at New Haven, Connecticut [Bull. Am. Phys. Soc. Ser. II, 1, 294 (1956)], and later at the Electrochemical Society Semiconductor Symposium at Cleveland, Ohio, October 3, 1956.

† Present address: Bendix Aviation Corporation, Research Laboratories Division, Box 5115, Detroit 35, Michigan.

‡ Present address: International Business Machines Corporation, Research Laboratory, Poughkeepsie, New York.

§ Present address: Raytheon Company, Research Division, Waltham, Massachusetts.

[1] See, e.g., L. E. Collins and O. S. Heavens, Proc. Phys. Soc. (London) **B65**, 825 (1952); H. A. Gebbie, Ph.D. Dissertation, Reading (1952); J. W. Thornhill and K. Lark-Horovitz, Phys. Rev. **82**, 762 (1951); W. H. Brattain and H. B. Briggs, Phys. Rev. **75**, 1705 (1949); G. Hass, Phys. Rev. **72**, 174 (1947).

[2] S. A. Semiletov, Crystallography (U.S.S.R.) **1**, 542 (1956); G. A. Kurov, S. A. Semiletov, and Z. G. Pinsker, Crystallography (U.S.S.R.) **2**, 59 (1957); Doklady Akad. Nauk S.S.S.R. **110**, 970 (1956).

[3] L. Bruck, Ann. Physik **26**, 233 (1936).

[4] M. Davis and R. F. Lever, J. Appl. Phys. **27**, 835 (1956). See also R. C. Sangster, E. F. Maverick, and M. L. Croutch, J. Electrochem. Soc. **104**, 317 (1957), for a description of a vapor deposition method for producing single-crystal Si deposits from gaseous $SiBr_4$ and hydrogen.

[5] Since this work was first reported there have appeared in the Russian literature accounts of the preparation of single-crystal Ge and Si deposits by vapor-phase reduction of the chlorides by hydrogen. See A. I. Mel'nikov, Zhur. Neorg. Khim. **2**, 233 (1957), and N. N. Sheftal', N. P. Kokorish, and A. V. Krasilov, Izvest. Akad. Nauk S.S.S.R., Ser. Fiz. **21**, 147 (1957). Germanium layers up to 200μ thick were obtained on single-crystal Ge substrates at temperatures from 700–900°C. N-type layers of resistivities from 1 to 4 ohm-cm were produced by the process; n-type doped layers were also obtained by exposing the growing deposits to donor elements reduced from the corresponding chlorides. In this way junction elements for transistor fabrication were made.

[6] This iodine, sublimed twice beyond ACS specifications, was obtained from the Gallard-Schlesinger Chemical Company, Long Island City 1, New York.

about 440°C GeI_4 is unstable,[7] and in the presence of a large excess of germanium the GeI_2 predominates. As the GeI_2 vapor was carried into the cooler region where the seed wafers were located, it decomposed to GeI_4 and germanium on, or adjacent to, the surfaces of the wafers. The GeI_4 was carried out the end of the furnace by the carrier gas.

The condensed germanium built up a crystalline germanium layer on the seed wafers in a structure dictated by that of the seed wafer, i.e., single-crystal germanium layers grew on single-crystal seed wafers and multicrystalline layers on multicrystalline seed wafers, duplicating the pattern of grain boundaries of the seed wafers as shown in Fig. 1.

The seed wafers used in these experiments were lapped smooth and etched vigorously, in an etch consisting of four to five parts HNO_3 and one part HF, to produce a bright mirror finish. The impurity concentration and conductivity type of the seed wafers appeared to have no effect on the nature or quality of the deposited layers. Most of the samples were prepared with the seed wafers mounted vertically in the furnace in a slotted quartz holder. Occasionally, seed wafers located at the downstream end of the furnace received contaminating deposits of GeI_4 or undecomposed GeI_2, which tended to clog the exit end of the tube; this disturbed the growth process and resulted in the germanium layer becoming polycrystalline.

From four to 10 seed wafers were coated simultaneously with germanium layers up to 6 mils thick by this process. The average deposition rate for the samples studied was from 0.5 to 0.7 mils/hr of deposition time, except for deposits on {111} crystal planes, where the thickness growth rate was appreciably slower. Slight variations in the rate of deposition could be introduced by means of variations in the flow rate of the carrier gas, changes in the temperature of the iodine, or adjustments in the temperature of the seed region.

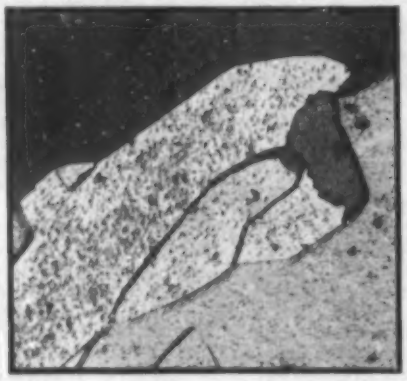

FIG. 1. Multicrystalline vapor-deposited Ge deposited on multicrystalline Ge substrate, showing grain boundaries and different orientations and growth rates.

[7] See *Encyclopedia of Chemical Reactions*, edited by C. A. Jacobson (Reinhold Publishing Corporation, New York, 1949) Vol. III, pp. 512, 532–3.

An obvious extension of the deposition process is to introduce an impurity intentionally into the deposited germanium layer, by adding the desired impurity to either the iodine or the source germanium or, making use of thermal diffusion or a carrier gas, to the main furnace gas stream through sidearm tubes.

Some experimental junction devices (diodes and transistors) were made by these methods, with the doping agent changed abruptly during deposition to produce the desired change in conductivity type; however, description of this work is beyond the scope of this paper.

PHYSICAL CHARACTERISTICS OF THE DEPOSITS

The nature of the germanium deposit was found to depend strongly upon the temperature conditions in the region of the seed wafers. If the temperature in this region approached 440°C (the temperature below which

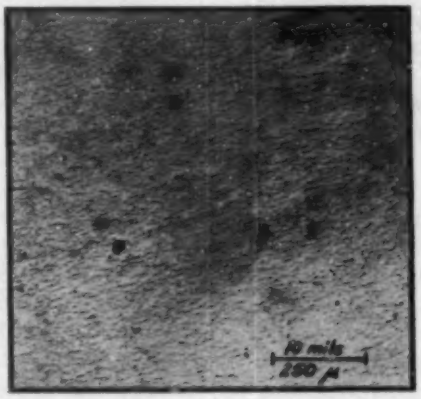

FIG. 2. Photomicrograph of vapor-deposited Ge on (211) surface of single-crystal Ge substrate. Typical platelet structure and surface defects are shown.

GeI_2 decomposes to GeI_4 and germanium) the growth of germanium whiskers was encouraged. The growth habits of these whiskers were not studied in detail. However, they tended to form on surfaces which had been previously nucleated with germanium atoms.

For lower temperatures, where the decomposition of GeI_2 was more abundant, the germanium deposited as a relatively homogeneous layer, indicating that the concentration of germanium vapor in the seed region must be large to encourage layer growth. The temperature difference between the seed wafers and the adjacent vapor mixture and the degree of turbulence of the carrier gas flow in the seed region also probably influence the character of the deposit.

The layers usually had a smooth satiny finish providing specular reflection, indicating at least a very high degree of preferred orientation.

Figure 2 is a photomicrograph of the surface of a germanium layer as deposited upon a (211) surface of a seed wafer. This layer was about 2 mils thick. Numer-

ous pits the order of 10 μ across are visible. The most prominent surface feature, however, is the oriented platelet structure. These platelets are inclined slightly to the original substrate surface. Figure 3 shows the surface of an as-deposited layer formed on a (111) face.

The difference in surface texture in the two figures illustrates the nonuniform growth rate with regard to crystal direction. The growth in area of the {111} planes was more rapid than that of other crystal planes. Thus in the layer of Fig. 2, the rapidly growing (111) platelets were inclined only slightly to the layer-substrate interface and gradually coalesced into a relatively smooth-textured surface. For the case of Fig. 3, the rapidly growing {111} planes were inclined to the interface sufficiently to produce relatively large tetrahedrons in the surface. This resulted in appreciable macroscopic surface roughness for layers deposited on seed faces in or near the {111} planes.

FIG. 3. Photomicrograph of vapor-deposited Ge on (111) face of single-crystal Ge substrate, showing platelet structure and tetrahedral prominences. Magnification same as in Fig. 2.

Because of the long time involved in depositing a layer several mils thick, it might be expected that gradations in conductivity or other properties would exist in the deposits. However, no evidence of a systematic variation in either structural or electrical properties with thickness was observed for as-deposited samples.

The single-crystal nature of the vapor-deposited germanium layers was established by both x-ray and electron diffraction studies, which indicated a high degree of crystal perfection.

X-ray diffraction examination[8] of thin deposits (0.5–0.7 mils thick) still in place on the seed wafers was made by means of back-reflection Laue photographs. Both the substrate and the layer contributed to the x-ray pattern, which was normal and sharp, indicating that the deposited layer retained the crystal orientation and structural perfection of the substrate.

Figure 4 is a back-reflection Laue pattern from a thicker layer (several mils thick) after its removal from the seed wafer. The pattern indicates good single-crystal structure with no appreciable distortion.

FIG. 4. Laue back-reflection x-ray pattern of single-crystal vapor-deposited Ge layer after removal from substrate.

X-ray lattice parameter measurements[9] were also made on some deposited germanium layers and the substrates beneath them. Both as-deposited and heat-treated samples were measured. A rocking-crystal technique was used, with a thin coating of a reference material applied to the crystal surface as a standard. The lattice parameter for one as-deposited layer was found to be 5.6588 A; this exceeded by about 0.01% that of the underlying substrate and by about 0.02% the value 5.6576 A which appears in the literature.[10] The parameter value for the layer on a heat-treated (90 hrs at 550°C) piece of the same sample was found to be 5.6576 A; this exceeded by about 0.01% the value for the substrate beneath the layer. Since the precision of the method used was only about 0.01%, it was concluded that there was no measurable difference in the lattice parameters of layer and substrate in the two cases. The slight difference in the two parameter values for the substrate is not regarded as significant.

Electron diffraction examination[11] of the surfaces of several deposited layers revealed strong patterns typical of single-crystal germanium. Good crystal structure was indicated, except for traces of some randomly oriented surface contamination. This was identified with a layer of GeO_2 on the surface and with some of the random surface roughness mentioned previously. Kikuchi lines, which arise from secondary reflections of diffusely scattered electrons and are generally associated with specimens possessing a high degree of crystal perfection, were observed in the electron diffraction patterns of all of the surfaces examined.

[8] This work was done by F. G. Keihn at this laboratory.

[9] These measurements were made by C. W. Tucker, Jr., at the Knolls Atomic Power Laboratory, Schenectady, New York.

[10] H. E. Swanson and E. Tatge, Natl. Bur. Standards (U.S.) Circ. No. 539, Vol. 1 (1953), pp. 18–19.

[11] This work was done by M. J. Columbe of the General Engineering Laboratory of the General Electric Company, Schenectady, New York.

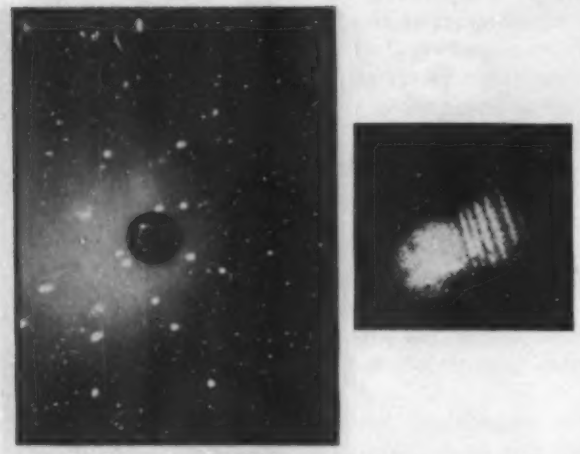

FIG. 5. Laue back-reflection x-ray pattern of single-crystal vapor-deposited Ge on single-crystal Si substrate. Some of the Ge spots are striated, and they are displaced slightly from the corresponding Si spots. At right is an enlargement of a pair of corresponding Si and Ge spots, clearly showing the striations in the displaced Ge spot.

There were occasional evidences of slight deviations in orientation over a limited region of an otherwise good layer. Such a misorientation was observed, for example, in one region of one of the samples examined in the lattice parameter measurements. However, the conclusion that the layers generally had good single-crystal structure receives further support from the large values found for the Hall mobilities of the charge carriers. The other evaluation techniques described in the foregoing are not sensitive to atomic imperfections in the lattice in densities the order of $10^{17}/cm^3$ or less, and yet this type of imperfection is thought to exist in the layers and possibly to provide the electrical properties observed.

An interesting demonstration of the strong tendency of the vapor-deposited germanium to grow in a good crystalline structure was provided on one occasion when a thin single-crystal germanium layer was deposited on a silicon seed wafer. X-ray diffraction examination[8] of this layer verified its single-crystal nature and indicated the orientation of the germanium to be very nearly the same as that of the silicon. Figure 5 is a back-reflection Laue photograph showing both the silicon substrate pattern and the slightly displaced germanium layer pattern superimposed. The spots produced by the germanium lattice exhibit striations which are probably due to periodic abrupt distortion of the lattice due to the difference in normal lattice constants for the two crystals. This suggests that there may be a high concentration of edge dislocations in germanium deposited in this way on a seed wafer having a slightly different lattice spacing.

ELECTRICAL PROPERTIES OF THE LAYERS

Experimental Details

Most of the information about the electrical properties of the layers was obtained from Hall coefficient and resistivity measurements as a function of temperature from 77° to about 475°K. Such measurements were made on all suitable samples; only those having a minimum of surface imperfections were considered as suitable for measurement.

Samples

Early in the investigation, electrical measurements on the layers were made by means of soldered contacts applied directly to the layers still in place on seed wafers of various thicknesses. Later this was modified by depositing the layers on germanium that was doped with gold or manganese,[12] which produce deep acceptor levels resulting in very high resistivities at low temperatures. The results of electrical measurements on such a composite crystal at low temperatures should represent largely the contribution of the layer alone, if the layer has a sufficiently small activation energy.

However, once thicker layers were produced, it was found that the layers could be isolated from their substrates. This was accomplished in two steps: First, all but two or three mils of the substrate material was removed from the layer by lapping with No. 600 Carborundum powder. Second, the remaining substrate and a little of the layer itself were removed by carefully floating the sample, layer side up, on a small puddle of white etch. This entire procedure left the top surface of the layer undisturbed. All of the samples referred to in this work were prepared by this technique and were from one to four mils thick after removal from their substrates.

The foregoing procedure required a knowledge of the layer thickness. For layers deposited on *p*-type substrates, thermoelectric probing indicated the location of the interface, since the layers were *n* type. Other techniques were required when *n*-type substrates were employed. The depth of a masked region provided by a small quartz chip on the wafer, the change in weight of the seed wafer, and identification of the layer-substrate interface as revealed occasionally by etching, were all occasionally used as indications of layer thickness.

All samples were thoroughly cleaned and etched lightly before electrical contacts were applied. For isolated layers six 1.5-mil diam gold wires were fused or pulse-welded to the samples in a hydrogen atmosphere. Gold-gallium alloy wire was used for *p*-type samples and gold-antimony alloy wire for *n*-type layers. The pulsing technique was more satisfactory than thermal fusion. It was found necessary to heat the sample to 200–250°C during the pulsing operation, however, to avoid shattering the sample.

Since breakage during preparation was fairly common, samples frequently measured only a few mils on a side and were irregular in shape. The customary set of six

[12] The Mn-doped Ge was obtained from W. W. Tyler of the General Electric Research Laboratory, Schenectady, New York.

contacts was used in all cases, but all six contacts were applied to a single surface of the sample. Although most of the samples fell short of fulfilling the usual requirement of length being at least four times width, the "one-point" current contacts precluded serious shorting effects on the Hall contacts.

Apparatus and Measuring Techniques

Hall coefficient and resistivity measurements as a function of temperature were made with the sample mounted on a laminated glass-and-plastic tray placed in a slot in a massive copper block, contained in a Dewar flask mounted in the gap of a large electromagnet. The sample and a copper-constantan thermocouple were held on the laminate by paper tape having adhesive on both sides. The sample temperature was lowered by addition of liquid nitrogen to the Dewar flask; elevated temperatures were obtained by means of a heating coil embedded in the copper block.

A vibrating reed electrometer was used to read the dc voltages. Samples with impedance up to 10^9 or 10^{10} ohms could be measured with the apparatus. The Hall voltage was always obtained as the algebraic average of the values for the magnetic field in the forward and the reverse sense, to compensate for asymmetrical placement of the contacts. Reversal of the direction of current flow through the samples revealed only occasionally the presence of internal barriers.

All of the Hall effect measurements were made with approximately the same magnetic field (3110 or 3480 gauss). It was experimentally determined that the difference in Hall coefficients for these field values would be less than 3%. The Hall coefficient in cm³/coul was calculated from the usual expression, with the addition of the factor w/s. On an ordinary rectangular-bar sample the separation of the Hall contacts s and the width of the current carrying region w are identical. On the vapor-deposited samples, however, w and s were seldom equal.

It is estimated that the thickness measurements were accurate to within ±10%. The other dimensions were known to within perhaps three or four per cent, except for the effective width of the current-carrying region, which was less certain for some of the more irregular sample shapes.

Results

All of the as-deposited samples studied were n type at room temperature, with the exception of a few layers prepared early in the investigation which contained p-type impurities presumably from impure starting materials.

One of the most interesting properties of these layers is that heat treating at 550°C gradually converted the n-type as-deposited layers to p type. The time dependence of the conversion process was not accurately determined; some samples were completely converted to

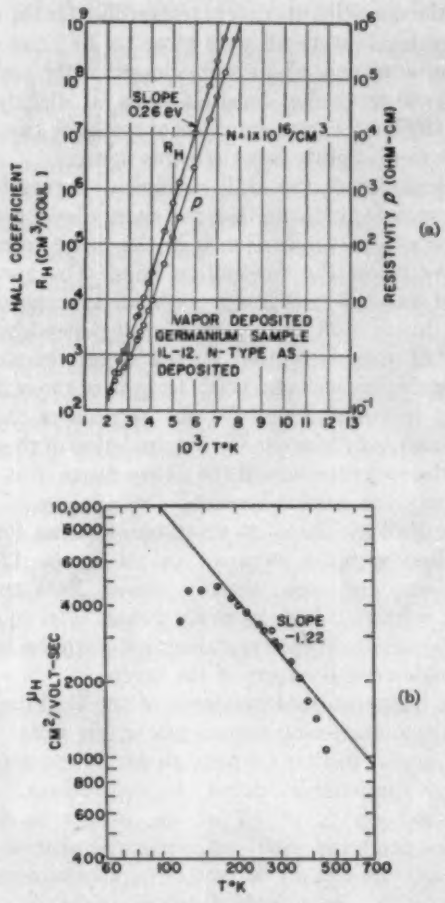

FIG. 6(a), (b). Hall coefficient R_H, resistivity ρ, and Hall mobility μ_H as a function of temperature for a vapor-deposited Ge sample of n-type conductivity.

p type in a matter of a few hours at 550°C,[13] while others remained entirely n type after much longer heat treatment. All of the heat treating was done at 550°C, except for a few rough checks at other temperatures.

As-Deposited n-Type Layers

Figure 6(a) shows the results of Hall coefficient and resistivity measurements upon an n-type as-deposited sample. Figure 6(b) gives the corresponding values of the Hall mobility $\mu_H = R_H/\rho$. The sample was 3×10^{-3} cm thick after removal from its substrate.

Measurements on the other n-type as-deposited samples gave results much like those shown in Fig. 6. Resistivities were in the range from 1 to 5 ohm-cm at room temperature. The layers had high resistivities at low temperatures because of the deep energy level involved. Conduction became intrinsic at temperatures ranging from 110° to 180°C, depending upon the saturation carrier concentration. These concentrations (and

[13] In one case, a layer was converted to p type after only 1 hr at 550°C, but in all other cases appreciably longer times were required.

thus the densities of centers responsible for the observed energy level) were all very close to 10^{16}/cm³ with the exception of two, which were closer to 10^{15}/cm³. Room-temperature carrier densities were all slightly greater than 10^{15}/cm³, except for those of the same two samples, which were slightly less than this figure.

The slopes of the Hall coefficient curves for all of these samples indicate that the energy level responsible for the *n*-type conduction is in the range from 0.18 to 0.26 ev below the conduction band. The average observed value was 0.22 ev, with an average deviation from this of 0.03 ev. No significant dependence of the value of this activation energy upon the saturation carrier density was observed. In spite of the rather large spread in values found for the location of the energy level, and a slight tendency for clustering of these values near the two extremes of the above range, it is believed that only one level is involved.

The Hall mobilities at room temperature for the as-deposited samples were all in the range 1200–2700 cm²/v-sec, and were usually above 2000 cm²/v-sec. These relatively high mobility values tend to corroborate the results of the crystallographic studies regarding the single-crystal nature of the layers.

The temperature dependence of the Hall mobility in the lattice scattering region was in the range $T^{-1.2}$ to $T^{-1.6}$, similar to that for melt-grown *n*-type germanium having comparable donor concentrations.[14] Strong scattering effects in all of the *n*-type as-deposited samples produced mobility maxima similar to that in Fig. 6(b). In several cases this maximum occurred at about 150°K; in no case did it occur below this temperature. The strong effects of these scattering centers first appeared in most of the samples at temperatures between 175° and 200°K, and dominated the scattering processes below about 150°K, producing a sharp decrease in mobility values.

Infrared photoconductivity measurements[15] were made at 80°K on several high-resistivity *n*-type germanium layers after their removal from the substrates. The photoconduction associated with the deep level in one sample was found to extend to photon energies of approximately 0.25 ev; Hall coefficient measurements on another piece of this same layer indicated a thermal activation energy of 0.18 ev. Photoconductivity measurements on other samples indicated responses as far as 0.20 ev. This is in agreement with the energy value assigned to this level on the basis of Hall coefficient data.

n-Type Heat-Treated Layers

Figure 7 shows the electrical properties of a 6×10^{-3} cm thick sample which had been heat treated at 550°C for 22 hrs prior to measurement. The sample remained completely *n* type. The slope of the Hall coefficient

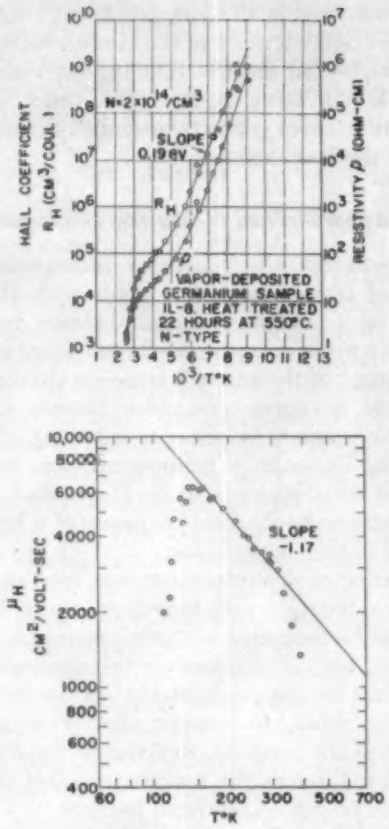

FIG. 7(a), (b). Hall coefficient R_H, resistivity ρ, and Hall mobility μ_H as a function of temperature for a vapor-deposited Ge sample which remained *n* type after 22 hrs heat treatment at 550°C.

curve locates the energy level at 0.19 ev below the conduction band.

The saturation density of carriers is about 2×10^{14}/cm³. This is two orders of magnitude less than the density of centers associated with this energy level in the as-deposited layers.

The resistivity, which becomes very large at low temperatures as with the as-deposited layers, is 14 ohm-cm at room temperature. This is three times as large as the highest value observed for any of the *n*-type as-deposited samples. The conduction becomes intrinsic at approximately 50°C.

The Hall mobility for this heat-treated sample is 3200 cm²/v-sec at room temperature; this is higher than that observed for any of the as-deposited samples. The mobility varies with temperature in the lattice scattering range according to a $T^{-1.2}$ law, as was found for several of the as-deposited samples. The maximum mobility again occurs at approximately 150°K, and the abrupt decrease in mobility values for temperatures below this persists.

Similar information was obtained from heat-treated samples in which the conversion to *p* type was not complete, and for which the conductivity type alternated

[14] E. M. Conwell, Proc. Inst. Radio Engrs. **40**, 1327 (1952); P. P. Debye and E. M. Conwell, Phys. Rev. **93**, 693 (1954).
[15] D. C. Cronemeyer, J. Appl. Phys. **29**, 1730 (1958).

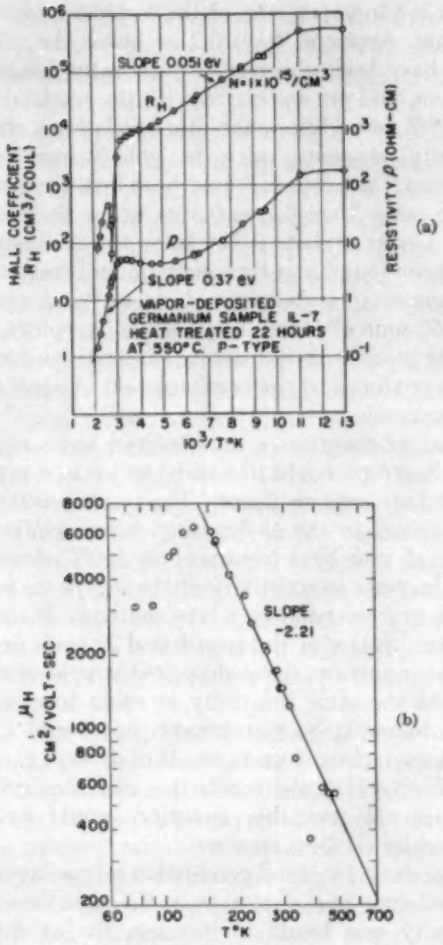

FIG. 8(a), (b). Hall coefficient R_H, resistivity ρ, and Hall mobility μ_H as a function of temperature for a vapor-deposited Ge sample converted to p type by heat treatment for 22 hrs at 550°C.

throughout the temperature range studied. In these cases, which included one sample that had been heat treated at 550°C for 83 hrs and still was of mixed conductivity type, the characteristics in temperature regions providing n-type conductivity indicated room temperature resistivities up to 22 ohm-cm, Hall mobilities in the range from 1700 to 3200 cm²/v-sec, and saturation carrier concentrations of slightly over 10^{14}/cm³.

The removal of many of the active n-type centers from the conduction process by the heat treatment at 550°C resulted in the increased resistivity at a given temperature, since the carrier mobility, if it changed at all, was improved by heat treatment (presumably through ordering of the lattice and reduction in density of scattering centers). That the same set of carriers was still involved was established by the persistence of the 0.2-ev level. However, the scattering centers responsible for the low-temperature mobility behavior shown in Fig. 6(b) were apparently not completely removed by the heat treatment. [See Fig. 7(b).]

p-Type Heat-Treated Layers

When heat-treatment of a sample at 550°C was continued long enough to convert the conductivity completely to p type, electrical properties like those shown in Fig. 8 were observed. This 8×10^{-3} cm thick sample was heat-treated for 22 hrs at 550°C, after which it was found to be p type. Other heat-treated samples, completely or partially converted to p type, supplied similar information regarding the p-type conduction process.

Room temperature resistivities ranged up to 40 ohm-cm, principally because of the smaller carrier concentrations; the resistivities did not become large at low temperatures. Hall coefficient data shows that an energy level located 0.05 ev from the valence band is associated with the p-type conduction, as shown in Fig. 8. The corresponding concentration of active centers ranged from 5×10^{13}/cm³ to slightly greater than 10^{15}/cm³, with an indication of the smaller values occurring for samples having longer heat treatment.

At low temperatures the Hall coefficient and resistivity curves tend to flatten out, possibly because of low-energy acceptor levels of some ordinary p-type impurity in the layer in a concentration the order of 10^{13}/cm³.

The Hall mobility for holes is 1500 cm²/v-sec at room temperature for the sample of Fig. 8, and ranged from this value up to 2400 cm²/v-sec for other samples. This compares favorably with the accepted value for hole mobility in melt-grown, p-type germanium. The mobility curve in Fig. 8(b) exhibits a maximum of 6500 cm²/v-sec at 130°K. This is only a slightly lower temperature than that at which this maximum occurred for the n-type samples. Evidently the principal scattering centers were still present after 22 hrs of heat treatment even though the conductivity type had changed. However, the decrease in mobility at low temperatures for this p-type sample is not as abrupt as it was for the n-type as-deposited samples. The mobility in the lattice scattering region varies approximately as T^{-2}, which is stronger than the theoretical $T^{-1.5}$ behavior, but is in agreement with the experimental results for p-type germanium obtained by others.[16]

Figure 9 shows the results of measurements made on a small piece taken from an as-deposited sample, which had given data like that of Fig. 6 when first measured, after it had been heat-treated at 550°C for 67 hrs. The long heat treatment not only removed the deep level found in the as-deposited sample, but also reduced the density of the 0.05-ev p-type centers to the point where only a slight indication of their presence remains in the Hall coefficient curve between 240°K and the onset of intrinsic conduction. The density of the latter centers is estimated to be 3×10^{14}/cm³. The principal conduction observed is that resulting from a shallow (0.01 ev) acceptor level, probably of one of the ordinary p-type

[16] See, e.g., W. C. Dunlap, Jr., Phys. Rev. **79**, 286 (1950); W. W. Tyler and H. H. Woodbury, Phys. Rev. **96**, 874 (1954).

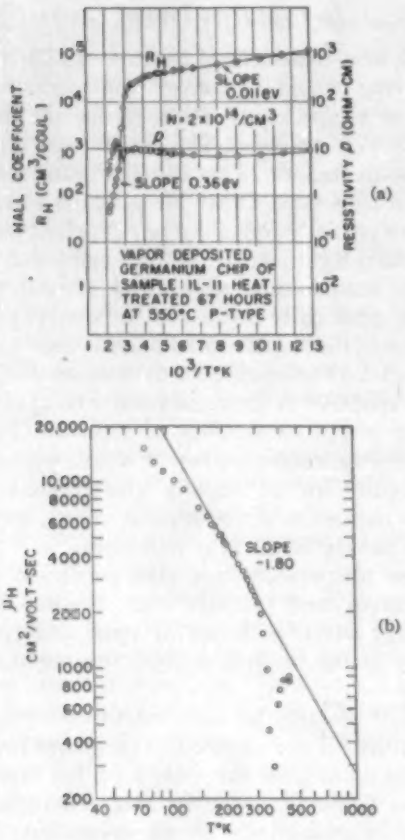

FIG. 9(a), (b). Hall coefficient R_H, resistivity ρ, and Hall mobility μ_H as a function of temperature for a vapor-deposited Ge sample converted to p type by 67 hrs heat treatment at 550°C, showing presence of additional low-lying acceptor level at 0.01 ev above valence band.

impurities, occurring in an apparent concentration of about $2\times10^{14}/cm^3$.

The hole mobility for this sample at room temperature is 2400 cm²/v-sec. The mobility increases steadily with decreasing temperature to a value of 15 000 cm²/v-sec at 77°K. The mobility follows a $T^{-1.8}$ law in the lattice scattering range; only gradual departure from this occurs at low temperatures, beginning at about 160°K. This type of mobility behavior is more nearly characteristic of normal lattice- and impurity-dominated scattering. It indicates a change in the predominant scattering process relative to that found in the p-type sample of Fig. 8, for example. There is a large difference between the electron mobility in this layer as it was deposited [cf., Fig. 6(b)] and the hole mobility in the layer following extended heat treatment [Fig. 9(b)]; the room temperature hole mobility for this heat-treated sample is twice the room temperature electron mobility for the original as-deposited layer.

Discussion

n-Type Layers

The activation energy found for the n-type layers (0.18 to 0.26 ev) is suggestive of other observed deep levels in the upper part of the forbidden band of germanium. Acceptor levels 0.2 ev below the conduction band have been observed in plastically deformed germanium, and are associated with the resulting dislocations.[17,18] In addition, acceptor levels for a number of impurity elements, such as gold,[19] iron,[20] nickel,[20] platinum,[21] and copper,[22] have been found in germanium in the range from 0.2 to 0.3 ev below the conduction band. Levels at about 0.2 ev below the conduction band have been found in n-type germanium bombarded with fast neutrons,[23] high-energy electrons,[24] and γ rays from a Co-60 source[25]; these levels act as acceptors, and are usually associated with ionized interstitial germanium atoms produced by the bombardment in equal numbers with vacancies.

In all of these cases the observed levels apparently provide acceptor (electron trap) action in n-type material and are not true donors. The active n-type conduction centers in the as-deposited layers gradually disappeared with heat treatment at 550°C, leading first to an increase in resistivity of the n-type material and finally to conversion to p-type material. If these were acceptor centers of the type found in gold- or copper-doped germanium, the as-deposited samples would have retained the same resistivity at room temperature or above following heat treatment, but would have lost the characteristic slope in the Hall curve, i.e., only the level from which the conduction electrons originated, and not the available quantity, would have been changed by the heat treatment.

Since the 0.2-ev level persisted in n-type layers which had had some heat treatment, at the same time that the resistivity was found to increase, the acceptor-level mechanism does not fit the observed facts. Thus, the conduction process seems to be fundamentally different from that of the other cases. The active centers responsible for the conduction appear to be true donor centers, occurring in a density of approximately $10^{16}/cm^3$ in the layers as deposited.

---

[17] G. L. Pearson, W. T. Read, and F. J. Morin, Phys. Rev. **93**, 666 (1954).
[18] W. C. Ellis and E. S. Greiner, Phys. Rev. **92**, 1061 (1953).
[19] W. C. Dunlap, Jr., Phys. Rev. **100**, 1629 (1955).
[20] See, e.g., H. H. Woodbury and W. W. Tyler, Phys. Rev. **100**, 659 (1955), for a summary of the known levels of the fourth-row transition elements in germanium.
[21] W. C. Dunlap, Jr., Phys. Rev. **96**, 40 (1954).
[22] H. H. Woodbury and W. W. Tyler, Phys. Rev. **105**, 84 (1957).
[23] J. W. Cleland, J. H. Crawford, Jr., and J. C. Pigg, Phys. Rev. **98**, 1742 (1955).
[24] H. Y. Fan, W. Kaiser, E. E. Klontz, K. Lark-Horovitz, and R. R. Pepper, Phys. Rev. **95**, 1087 (1954), found the level at 0.22–0.24 ev by Hall coefficient and photoconductivity measurements following bombardment with 4.5 Mev electrons at 100°K. F. Stoeckmann, E. E. Klontz, H. Y. Fan, and K. Lark-Horovitz, Phys. Rev. **98**, 1535 (1955), confirmed this result by photoconductivity measurements on n-type Ge after low-temperature bombardment with 6 Mev electrons. See also H. Y. Fan and K. Lark-Horovitz, *Irradiation of Semiconductors*, Special Report, International Conference on Semiconductors and Phosphors, Garmisch-Partenkirchen (1956); also H. Y. Fan and K. Lark-Horovitz, *Report of the Bristol Conference on Defects in Crystalline Solids* (Physical Society, London, 1954).
[25] J. W. Cleland, J. H. Crawford, Jr., and D. K. Holmes, Phys. Rev. **102**, 722 (1956).

This level at 0.2 ev is believed to be the first deep direct donor level found in germanium.[26] The question of its source still remains. Several possibilities exist, and they will be discussed briefly.

Iodine atoms. It is reasonable to expect that iodine atoms may become trapped in the growing germanium layer during the deposition process. Iodine, a Group VII element, could conceivably act as a donor in germanium. The probable position of iodine in the germanium lattice is uncertain; the iodine atom is larger than the germanium atom, so whether it were substitutional or interstitial it would expand the lattice.[27]

In a preliminary investigation of the role played by iodine, radioactive iodine (I-131) was used as a tracer in the high-purity iodine source. Counter measurements of the iodine content of the deposited layers indicated atomic densities ranging from 10^{17} to $10^{20}/cm^3$. The larger concentrations were probably due to iodide inclusions. The smallest apparent iodine concentrations are at least ten times the measured density of donors in the as-deposited layers. Only a fraction of the iodine atoms present may have been electrically active; the others may have been in clusters or attached to imperfections in such a way as to be removed from the conduction process.

On the other hand, heat treatment of some of the layers containing the tracer provided evidence against the possibility of iodine donors. Counter measurements indicated that iodine left the layers upon heat treatment at widely varying rates. This resulted in changes in iodine concentrations which were not consistent with the decrease in carrier concentration which always accompanied heat treatment. In fact, some samples changed conductivity type, and thus exhibited much smaller effective carrier concentrations, without much change in the apparent iodine content. Thus, although iodine was generally driven from the layers by heat treatment, it appears that this probably accompanied other changes occurring within the layers.

Other impurity atoms. No trace impurities were found spectroscopically in the triply-sublimed iodine used. Neither x-ray fluorescence analysis, nor optical spectroscopic examination of the deposited layers revealed any impurities likely to be associated with the donor states. However, such methods cannot reveal concentrations as small as those which may have been involved. It is possible that some impurity entered the furnace in the carrier gas. However, the same energy level was found in all as-deposited layers measured, irrespective of the degree of purification of the iodine or of slight modifications in the deposition procedure; similarly, it was observed for layers formed with either hydrogen or argon as the carrier gas. It thus would seem that the donor level is more to be associated with the manner of formation of the layers than with the presence of a particular impurity in the materials used.

However, copper is always suspect in heat treatment phenomena with germanium. Substitutional copper is a triple acceptor in germanium, and the third or highest acceptor level is 0.26 ev from the conduction band. For this level to exist, the copper atoms must first accept two electrons each, filling the lower two levels. This requires the presence of a compensating donor impurity in a concentration between two and three times that of the copper. This seems rather unlikely, unless iodine atoms supplied the electrons required to fill the lower copper states.

The characteristic slope in the Hall coefficient curve for the 0.26 ev copper level does not appear until temperatures appreciably below room temperature have been reached.[28] Also, solid solubility data for copper in germanium indicate that the equilibrium concentration at the temperatures at which the layers were formed is the order of $10^{11}/cm^3$. Neither of these facts is in agreement with the data for *n*-type vapor-deposited germanium.

Copper might fulfill the proposed donor requirement if it could be involved as an interstitial atom. Copper diffuses rapidly in germanium at elevated temperatures,[28] in a manner very dependent upon the structural perfection of the germanium.[29] The rapid diffusion is associated with positive interstitial copper ions,[21,28] and involves an equilibrium between them and dissociating substitutional copper atoms and lattice vacancies.[30] However, the interstitials are supposedly in much smaller concentration than the substitutional atoms, so it appears even less likely that interstitial copper could be the source of the carriers observed.[31]

Interstitial germanium atoms. Because of the relatively low deposition temperature, probably not all germanium atoms find available lattice sites as they migrate over the newly formed surface during deposition. Similarly, not all lattice sites acquire germanium atoms during the layer growth. This gives rise to interstitial atoms and lattice vacancies, respectively. Once formed, these lattice defects have relatively little chance to anneal out of the structure during the subsequent stages of deposition.

According to the model proposed by James and Lark-Horovitz[32] vacancies act as acceptor centers, probably

[26] Other low donor levels, such as the gold level at 0.05 ev above the valence band in Ge, cannot produce direct donor action, but give their electrons to nearby low-lying acceptor centers of other impurities.

[27] If iodine atoms were in the layers as interstitial atoms in densities greater than about $10^{18}/cm^3$, the lattice parameter measurements would have revealed a difference between the parameters of layer and substrate.

[28] C. S. Fuller, J. D. Struthers, J. A. Ditzenberger, and K. B. Wolfstirn, Phys. Rev. **93**, 1182 (1954).

[29] A. G. Tweet and C. J. Gallagher, Phys. Rev. **103**, 828 (1956).

[30] F. C. Frank and D. Turnbull, Phys. Rev. **104**, 617 (1956).

[31] If more than the equilibrium concentration of interstitial copper should somehow become trapped in the Ge lattice during growth of the layer and be unable to escape at room temperature, either direct donor action or compensation of substitutional copper atoms might then occur, depending upon relative concentrations. However, no energy levels have been reported in the literature for this type of electrical activity for copper in Ge.

[32] H. M. James and K. Lark-Horovitz, Z. physik. chem. **198**, 107 (1951).

with two states of ionization and thus two energy levels in the forbidden band of germanium; interstitial atoms behave as donors, also probably having two states of ionization, and thus two levels. When Frenkel defects are involved there are four levels available for each defect pair. Two electrons, from the interstitial, are distributed among the levels so as to provide the lowest-energy arrangement. This results in two levels (probably those associated with the vacancy) acquiring the electrons from the interstitial atom, leaving two levels (probably those associated with the interstitial) vacant to act as acceptor centers or traps for conduction electrons.

In addition to the vacant levels found at 0.2 ev below the conduction band in irradiated *n*-type germanium,[29–26] the remaining three levels have been observed in the lower half of the forbidden band in studies of fast-neutron damage in *p*-type germanium.[30,31] The one farthest from the valence band (0.2 ev) is an unoccupied acceptor level (electron trap), which is probably associated with the doubly ionized interstitial atom, although this assignment is not definite.[29,35,36]

Since interstitial atoms are regarded as donors, if there were enough more interstitials than vacancies present to permit the excess interstitials to act as direct donors of conduction electrons, then donor action such as that found in vapor-deposited germanium might be observed.[37]

This suggests a mechanism somewhat similar to that advanced for irradiated germanium by Cleland *et al.*[34] The decrease in concentration of active conduction centers in samples heat treated at 550°C but remaining *n* type would correspond to a loss of some of the excess interstitial donors. This could occur by rapid diffusion of the interstitials to the sample surfaces, or to imperfections such as dislocations or vacancies (resulting in recombination), or to other sites where strong bonds would be established, with subsequent inactivation of the interstitials as the final result. As long as an adequate excess of the interstitial donors remained, the sample would remain *n* type. The decreased carrier density, however, would result in the higher resistivity which was observed in such samples.

A requirement of this mechanism is that the interstitial atoms must diffuse more rapidly than the vacancies. That this is the case, even at room temperature, is indicated by room-temperature annealing experiments with neutron-bombarded *n*-type[32] and *p*-type[34] germanium. This is also the view taken by Mayburg,[38] who studied the effects of heat treatment of germanium at high temperatures followed by rapid cooling; it was concluded that at temperatures up to 585°C the interstitial atoms of Frenkel defects produced by the heating and quenching diffuse more rapidly than vacancies, and either cluster at dislocations (below about 520°C) or recombine directly with vacancies (above 520°C).

The mobility data support such a defect mechanism of conduction in vapor-deposited germanium. Although the mobility behavior of the as-deposited samples compares fairly well in the lattice scattering range with that of melt-grown, *n*-type germanium of about the same donor concentration, the mobility below about 150°K is not at all like that of ordinary *n*-type material. Ionized impurity scattering at this concentration would not ordinarily introduce a mobility maximum at such relatively high temperatures, if at all; since a deep donor level is involved, the density of ionized donor scattering centers decreases rapidly with decreasing temperature.

Thus some additional scattering centers must be involved in the vapor-deposited layers.[39] Crystal imperfections and inhomogeneities could produce the unusual scattering effects observed throughout the temperature range. The probable presence of such imperfections was indicated by instabilities in Hall voltage measurements at reduced temperatures.[40]

Very similar scattering effects have been observed in mobility studies on neutron-bombarded *n*-type germanium[23] and were attributed to the induced lattice defects, i.e., vacancy-interstitial pairs. In that work the temperature dependence was stronger than that of ordinary ionized impurity scattering and was quite dependent upon the carrier density of the sample involved. The effects were stronger at low sample temperatures, but extended into the lattice scattering region for samples showing the greatest density of defects. Room-temperature annealing improved the low-temperature mobility behavior considerably, indicating that the vacancy-interstitial pairs, or possibly the interstitials alone, played the major part in determining the mobility behavior at reduced temperatures.

[33] J. W. Cleland, J. H. Crawford, Jr., K. Lark-Horovitz, J. C. Pigg, and F. W. Young, Jr., Phys. Rev. 84, 861 (1951).

[34] J. W. Cleland, J. H. Crawford, Jr., and J. C. Pigg, Phys. Rev. 99, 1170 (1955).

[35] J. W. Cleland *et al.* have reported values from 0.16 ev (footnote 25) for an annealed γ-irradiated Ge specimen and 0.18 ev (footnote 34) for neutron-damaged Ge to 0.26 ev (footnote 25) for γ-irradiated samples before annealing. It has been suggested that the disparity may be caused by nonuniform distribution of defects in neutron-damaged material.

[36] There is some uncertainty about the number of possible states of ionization of interstitials and vacancies, and thus about the number and location of energy levels introduced by these defects into the forbidden band of Ge. For example, three states of ionization for each defect were tentatively proposed to fit data obtained by the Purdue group for Ge bombarded with high-energy electrons. (See H. Y. Fan and K. Lark-Horovitz, *Irradiation of Semiconductors*, footnote 24.) This resulted in the assignment of the vacant interstitial level at 0.2 ev from the conduction band to the *second* state of ionization of the interstitial atom. Clustering of defects probably plays a major role in complicating the energy level distribution in Ge in this way.

[37] It is known from the lattice parameter measurements (footnote 9, 27) that if interstitial Ge atoms were present in the layers they must have occurred in densities less than about 10^{18}/cm^3.

[38] S. Mayburg, Phys. Rev. 95, 38 (1954).

[39] However, some aspects of the mobility behavior of the *n*-type samples, such as the variation of the mobility vs temperature curve with density of active centers from sample to sample, were typical of scattering produced by ionized impurities.

[40] Contacts were undoubtedly responsible for some of the noise and instability encountered, but the effect was sufficiently common to indicate that inhomogeneities did exist in most samples.

p-Type Layers

Identification of the source of the acceptor level at 0.05 ev from the valence band in the *p*-type heat-treated layers is dependent upon the identity of the source of the 0.2 ev level in the *n*-type material.

The Oak Ridge group[34] found occupied energy levels at approximately 0.07 and 0.02 ev (estimated) above the valence band in *p*-type germanium irradiated with fast neutrons. These hole traps (donor levels) have been associated with lattice vacancies.

Electron bombardment experiments with germanium have provided results somewhat different from those of the Oak Ridge group for levels near the valence band.[36] An electron-trapping level at 0.1 ev above the valence band, found by Fan *et al.*[24] in germanium converted to *p* type by exposure to 4.5 Mev electrons at 100°K, was assigned to the interstitials, and an occupied hole trap was found at 0.2 ev from the valence band in initially *p*-type and converted *n*-type germanium after bombardment,[24,41,42] and was identified with vacancies.[42] Two additional occupied levels were postulated very close to the valence band and were associated with vacancies,[43] but their existence was not verified experimentally.

Acceptor levels at from 0.03 to 0.07 ev from the valence band were found by Tweet in grain boundaries in gold-doped germanium,[44] even when the bulk sample was *n* type, and in the range from 0.04–0.12 ev from the valence band in germanium deformed plastically at 550–620°C.[45] The concentrations of active centers in the latter case were about the same as those observed in the *p*-type, vapor-deposited germanium layers. Annealing experiments at temperatures above 750°C indicated that the low-energy acceptors disappeared upon high-temperature heat treatment, and Tweet suggested that the acceptors may have been due to lattice vacancies.

Several impurity acceptor levels in germanium are close to the 0.05 ev level found in the *p*-type layers. Zinc produces acceptor levels at 0.03 ev[21,46] and at 0.09 ev[47] above the valence band, copper[21,22,28,48] and platinum[21] at 0.04 ev, and cadmium[49] at 0.06 ev from the valence band. Impurities could have been acquired by the layers during heat treatment. Copper is the impurity most likely to diffuse into the sample under these conditions, but its equilibrium solid solubility in germanium[22] at 550°C is about $6\times10^{13}/cm^3$; this is less than the observed density of *p*-type centers. Furthermore, the observed tendency for the concentration of active *p*-type centers to be smaller in samples having longer heat treatment does not seem consistent with such a mechanism.

It appears more probable that the source of the *p*-type centers existed in the layers as they were originally deposited. Because of the equilibrium solid solubility at deposition temperatures ($10^{11}/cm^3$), copper is probably not the source of the 0.05 ev level.[50] Iodine atoms were trapped in the germanium layers when they were formed, and in most of the layers examined enough iodine remained following heat treatment to provide the density of *p*-type centers observed electrically. Whether iodine is involved in either the *n*-type or *p*-type conduction process remains to be determined.

However, the lattice defect explanation of the observed *p*-type properties appears quite plausible. The 0.05 ev levels apparently provided direct acceptor action for electrons from the valence band and could represent the unoccupied levels of the vacancies. Tweet apparently observed direct acceptor action[44] for the low-lying vacancy levels,[45] whereas the Oak Ridge group[34] found that the two levels associated with vacancies were occupied hole traps, as would be expected (on the James and Lark-Horovitz model) for the case of equal numbers of interstitials and vacancies. However, the room-temperature annealing experiments of Cleland *et al.*[23,34] showed that the two levels of the vacancy were transformed to vacant acceptors upon the removal by diffusion of enough of the interstitial donors, together with their electrons.

The four-level defect model would thus provide for conversion of the layers from *n*- to *p*-type conductivity during heat treatment when the vacancies become more than half as numerous as the rapidly-diffusing electrically-active interstitials.[51] Further reduction of the concentration of active interstitials would put the vacancies in the majority and empty first the upper and then some of the lower of the two vacancy levels, permitting them to act as direct acceptors of electrons from the valence band.[52]

Continued heat treatment would probably further decrease the density of dominant *p*-type centers, by

[41] E. E. Klontz, R. R. Pepper, and K. Lark-Horovitz, Phys. Rev. **98**, 1535 (1955).
[42] F. Stoeckmann *et al.* (footnote 24).
[43] H. Y. Fan and K. Lark-Horovitz, *Irradiation of Semiconductors* (footnote 24).
[44] A. G. Tweet, Phys. Rev. **99**, 1182 (1955); **96**, 828 (1954).
[45] A. G. Tweet, Phys. Rev. **99**, 1245 (1955); C. J. Gallagher and A. G. Tweet, Phys. Rev. **96**, 834 (1954).
[46] W. C. Dunlap, Jr., Phys. Rev. **85**, 945 (1952).
[47] H. H. Woodbury and W. W. Tyler, Phys. Rev. **100**, 1259 (1955); **102**, 647 (1956).
[48] F. J. Morin and J. P. Maita, Phys. Rev. **90**, 337 (1953).
[49] H. H. Woodbury and W. W. Tyler, Bull. Am. Phys. Soc. Ser. II, **1**, 127 (1956).
[50] The question again arises of the possibility of more than the equilibrium concentration of copper atoms becoming trapped in the Ge lattice in a nonequilibrium condition when the layer is formed, or of an "effective solid solubility" occurring for this type of crystal growth to permit impurity concentrations appreciably larger than those resulting from other growth processes. Such circumstances might alter the conclusions regarding copper as a source of the observed conductivity.
[51] This would first leave some of the lower interstitial levels, at 0.2 ev from the valence band (footnote 34), unoccupied by electrons and free to accept electrons from the valence band.
[52] Such an effect has been observed by J. W. Cleland *et al.* (footnote 34). In *n*-type Ge converted to *p* type by prolonged fast-neutron bombardment and subsequent room-temperature annealing, an acceptor level at 0.08 ev above the valence band was observed shortly after conversion to *p* type. A still lower level, at about 0.03 ev, appeared after further irradiation and room-temperature aging.

recombination or other inactivation process, at a slower rate than that observed for the interstitials. This could explain the observed tendency for the concentration of p-type centers to be smaller in samples having longer heat treatment. Eventually, the concentration might become comparable with that of ordinary acceptor impurities present in the layer, as may have been the case for the sample of Fig. 9.[53]

The mobility data for the p-type layers is consistent with the defect mechanism proposed. The large room-temperature hole mobilities indicate that heat treatment reduced the carrier scattering relative to what it was in the as-deposited layers. Samples converted to p type after relatively brief heat treatment showed some improvement in the mobility at reduced temperatures, but still exhibited the mobility maximum found for electrons in the as-deposited layers. Thus, even though the identity of the effective charge carriers had changed, the same scattering mechanisms remained. Prolonged heat treatment tended to improve the mobility throughout the temperature range and removed this mobility maximum; this is indicative of a major change in the predominant scattering mechanism at low temperatures. All of these changes could have been caused by extensive "healing" of imperfections and inhomogeneities and removal of an appreciable number of interstitial donor centers from the conduction process by the heat treatment.

SUMMARY

Germanium layers were formed on single-crystal germanium substrates by the thermal decomposition of GeI_2. The single-crystal nature of the layers was established by x-ray and electron diffraction examination and verified by electrical measurements. The material was found to exhibit certain unique properties which can be summarized as follows:

(1) The layers as deposited were generally n type, with room-temperature resistivities in the range from 1 to 5 ohm-cm and room-temperature Hall mobilities from 1200 to 2700 cm^2/v-sec.

(2) The n-type layers were characterized by an energy level approximately 0.2 ev below the conduction band, with a concentration of active centers at this level of about $10^{16}/cm^3$.

(3) Heat treatment at 550°C gradually converted the conductivity to p type. Following conversion, the layers were characterized by (a) room temperature resistivities of 10 to 40 ohm-cm, (b) Hall mobilities of 1500 to 2400 cm^2/v-sec, (c) an energy level at about 0.05 ev above the valence band, and (d) a density of active centers of 10^{14} to $10^{15}/cm^3$.

(4) Low-temperature Hall mobilities showed the effects of a large concentration of scattering centers in the as-deposited layers below about 150°K.

(5) Nonuniform growth rates with respect to crystal direction were observed in the layers, and under certain growth conditions germanium whiskers, rather than extended layers, were produced.

(6) The layers could be doped intentionally with selected impurities to control the conductivity type beyond that normally characteristic of the material.

Several possible sources of the observed properties have been considered, including iodine atoms trapped in the layers, other impurity atoms (such as copper) inadvertently present, and lattice defects. It is proposed that interstitials and vacancies occurring in unequal numbers (i.e., not as Frenkel defects) are the most likely cause of the properties observed in n-type as-deposited layers, n-type heat-treated layers, and p-type heat-treated layers. The 0.2-ev level, identified as a donor level, has been associated with an excess of germanium atoms trapped interstitially in the lattice during deposition. The 0.05-ev acceptor level has been attributed to lattice vacancies, which are formed in the deposition process and remain in appreciable density throughout the heat treatment.

It has been suggested that the heat treatment phenomenon is the result of the rapid diffusion and subsequent deactivation (at dislocations and other sites) of the interstitials at elevated temperatures. The removal of these excess donor centers gradually converts the material to p type, in which the uncompensated acceptor levels of the lattice vacancies dominate the conduction.

The over-all model suggested is thus one in which a high degree of crystal perfection exists on a macroscopic scale, as indicated by the various tests for single-crystal structure, but in which a large concentration of imperfections is present on an atomic scale, as indicated by the mobility behavior at low temperatures.[54]

ACKNOWLEDGMENTS

The authors wish to thank their associates in the Advanced Semiconductor Laboratory for the many instances of helpful cooperation encountered in the course of these studies. In particular, the assistance of Philip D. Radin and Walter F. Herzog in preparing the samples and making the measurements is greatly appreciated.

[53] On the other hand, the 0.01 ev level shown in the data of Fig. 9 might represent the lower vacancy level reported by J. W. Cleland *et al.* (footnote 34) at 0.02 ev, left partially unoccupied to provide acceptor action, as in the case mentioned in the preceding footnote.

[54] A generally similar conclusion, differing considerably in detail, however, has been reached by S. A. Semiletov *et al.* (footnote 2) for Ge layers deposited by vacuum evaporation on single-crystal Ge substrates. The layers were always p-type, with low resistivity and very small mobilities, irrespective of the substrate temperature; good single-crystal structure was obtained only when the substrate temperatures were above 750°C. It was proposed that a large concentration of defects, similar to those found in deformed Ge crystals (footnotes 17, 18), may have been formed during deposition, producing acceptor levels. However, no detailed electrical measurements to establish such levels were reported.

Positive Column Formation in Ion Sources Employing Surface Ionization

P. L. Auer and H. Hurwitz, Jr.
General Electric Company Research Laboratory, Schenectady, New York
(Received August 17, 1959; revised manuscript received February 15, 1960)

In order to gain some insight in the problem of space charge neutralization of ion beams we make use of a previous calculation to discuss the unidimensional flow of positive ions in a tube where both ions and electrons issue from an emitter surface but only ion current is collected by means of an accelerating electrode. The resulting ion flow can be neutralized to varying degrees by the electrons present. We find that even in the absence of collisional interactions the potential distribution in the tube may closely resemble the electrode sheath and positive column structure familiar to glow discharges. This is the situation to be expected whenever the ion current has values far in excess of that predicted from a zero degree of neutralization space charge limited theory.

IN a recent article[1] we described the potential distribution in diodes where the electron space charge was neutralized to varying degrees by positive ions. With trivial changes in notation these calculations may be used to discuss the inverse situation where positive ion streams are neutralized to varying degrees by electrons. The latter situation can occur in ion sources consisting of an active hot electrode emitting both positive ions and electrons and an accelerating electrode operated cold without emission. An interesting feature of this situation is that even in the absence of collisional interactions a positive column can develop under the influence of mutual space charge forces and under certain conditions the column can extent almost to the accelerating electrode. In this fashion most of the voltage drop can occur across a relatively thin sheath between the acclerating electrode and positive column.

A quantitative description of the above phenomenon may be developed as follows. We assume for the present that the ions are singly charged. Under suitably idealized conditions we may consider the electrons to be in thermal equilibrium with the emitter electrode and assume the ions issue with a Maxwellian distribution corresponding to the emitter temperature. As mentioned in the foregoing, collisional interactions are neglected and the ions and electrons are allowed to travel in their mutual space charge fields.

The above model is analogous to the one treated previously.[1] In analogy with the notation of the previous reference, an ion density p_0 in the tube is specified in terms of the ionic current density I, as

$$\begin{aligned} I&=ep_0v_0 \\ v_0^2&=2kT/\pi M, \end{aligned} \tag{1}$$

where e is the magnitude of the electronic charge, k is the Boltzmann constant, T is the temperature, and M is the mass of the ion. The reduced potential η and reduced distance ξ are given in terms of the potential maximum V_m and the position of the maximum in the tube x_m measured from the emitter,

$$\begin{aligned} \eta(x)&=-e[V(x)-V_m]/kT \\ \xi(x)&=4(x-x_m)/\lambda\exp(\eta_0/2) \\ \eta_0&=eV_m/kT \\ \lambda^2&=Mv_0^2/e^2p_0, \end{aligned} \tag{2}$$

where η_0 is a measure of the ratio of the ionic current to its saturation limited value I_s,

$$I=\exp(-\eta_0)I_s. \tag{3}$$

The ion density $p(x)$ and electron density $n(x)$ are given by

$$\begin{aligned} p(x)&=p_0e^{\eta}[1+\operatorname{erf}(\sqrt{\eta})]; \quad x<x_m \\ &=p_0e^{\eta}[1-\operatorname{erf}(\sqrt{\eta})]; \quad x>x_m \\ n(x)&=\alpha p_0e^{-\eta} \\ \operatorname{erf}(z)&=\frac{2}{(\pi)^{\frac{1}{2}}}\int_0^z \exp(-t^2)dt, \end{aligned} \tag{4}$$

where α is the ratio of electron density to ion density at the potential maximum. Integration of Poisson's equation leads to the following field distribution:

$$\begin{aligned} \left(\frac{d\eta}{d\xi}\right)^2&=e^{\eta}-1-\alpha(1-e^{-\eta})-e^{\eta}\operatorname{erf}[(\eta)^{\frac{1}{2}}] \\ &\qquad +2(\eta/\pi)^{\frac{1}{2}}+C_1^2; \quad \xi>0 \\ &=e^{\eta}-1-\alpha(1-e^{-\eta})+e^{\eta}\operatorname{erf}[(\eta)^{\frac{1}{2}}] \\ &\qquad -2(\eta/\pi)^{\frac{1}{2}}+C_2^2; \quad \xi<0, \end{aligned} \tag{5}$$

where C_1 and C_2 are constants of integration specifying the field at the potential maximum and are to be taken as zero in the present application.

Integration of Eq. (5) leads to a one parameter family of universal curves for the reduced potential in terms of the reduced distance. The parameter of variation α can be determined for given values of total voltage drop and tube length by the emitter electrode temperature and values of its ionic as well as electronic emissivity. As long as the ionic space charge is but slightly neu-

[1] P. L. Auer and H. Hurwitz, Jr., J. Appl. Phys. 30, 161 (1959).

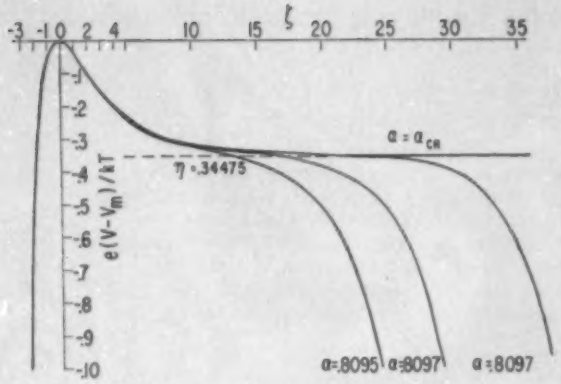

FIG. 1. Universal potential distributions in the region of positive column formation.

tralized, the potential distribution in a plane geometry will resemble the classical Langmuir distribution,[2] with a potential maximum near the emitter and the ion current will be less than the saturation value as given by Eq. (3). However, as the current approaches the saturation limited value interesting changes take place in the potential distribution.

It will be recalled that an infinitely long tube with zero total voltage drop develops the saturation limited value of the current at a degree of neutralization corresponding to α_{CR}.[3] With other variables held constant, the α required for full saturation increases with decreasing length and decreases with increasing voltage drop. As long as the total voltage drop is large with respect to kT, there will be a significant range of tube length and total voltage drop for which the current is nearly equal to the saturation value. Under these conditions the potential distribution in the diode can bear striking similarities to that observed in familiar glow discharge tubes. The potential distribution in the vicinity of the accelerating electrode has the appearance of a cathode sheath and resembles the Langmuir-Child space charge law for large total voltage drops. This region joins smoothly on to a region where the potential changes very slowly with distance and gives the appearance of a positive column, in spite of the fact that the collisional processes which are largely responsible for the existence of a positive column in glow discharges have not been included in the present model.

The region between the emitter and positive column may be termed an anode sheath. The potential in this region will have a maximum and an anode drop as long as the current is less than the saturation limited value. As the current increases to its terminal value the anode drop disappears and becomes replaced by a simple potential rise from the positive column to the emitter electrode. These features are illustrated in Fig. 1 where we present curves indicating the change in potential distribution with increasing degree of neutralization. The potential difference between the maximum value in the anode sheath and the positive column is approximately $kT/3$; consequently, once the saturation limit is approached by the current most of the tube will be very nearly at anode voltage. Figure 2 depicts qualitatively the appearance of a positive column at fixed voltage and electrode separation with increasing degree of space charge neutralization.

In the remainder of this report we shall describe an interpolation scheme for constructing universal η vs ξ curves for the interesting region where pronounced positive column formation exists. This situation is to be expected whenever a tube of given length and total voltage drop operates at ion current values far in excess of that which would exist in the absence of neutralization.

The problem is to find tractable expressions for the curves $\xi(\eta,\alpha)$ in the sensitive region where α is close to but less than α_{CR}. We denote the curve corresponding to α_{CR} as

$$\xi(\eta,\alpha_{CR})=\Xi(\eta). \tag{6}$$

Values of $\Xi(\eta)$ are listed in Table I. It will be seen that $\Xi(\eta)$ is parabolic at the origin, approaches minus infinity on one side as η approaches infinity, and approaches plus infinity asymptotically on the other side of the origin as η approaches $\eta_{CR}=0.34475$. We also list in Table I a function $\Xi^*(\eta)$ which is defined to be zero at $\eta=0.35$ as is obtained by integrating the analytic continuation of $(d\xi/d\eta)$ corresponding to α_{CR} beyond the logarithmic singularity at η_{CR}.

$$\Xi^*(\eta)=\int_{0.35}^{\eta}\frac{d}{d\eta}[\xi(\eta,\alpha_{CR})]d\eta\geq 0. \tag{7}$$

It is now assumed that there exists a significant range of α values lying close to α_{CR} where the universal η vs ξ curves are insensitive to variations in α in the region that encompasses whatever anode sheath structure may exist in the tube. This region extends to all negative ξ values and to positive ξ values corresponding

TABLE I.[a]

η	Ξ	η	Ξ	η	Ξ^*
0.00	0.00	0.00	0.00	0.35	0.00
0.01	0.541	0.04	−0.773	0.49	10.72
0.04	1.082	0.16	−1.335	0.64	12.78
0.09	1.936	0.36	−1.780	1.00	15.33
0.16	3.283	0.64	−2.122	1.50	17.16
0.20	4.209	1.00	−2.416	2.50	19.47
0.25	5.556	2.00	−2.869	4.00	22.14
0.28	6.710	4.00	−3.197	6.00	24.32
0.30	8.346				
0.34	15.35				
0.34475	∞				

[a] The functions $\Xi(\eta)$ and $\Xi^*(\eta)$ for limited values of η.

[2] I. Langmuir, Phys. Rev. **21**, 419 (1923).

[3] In footnote 1 we quote $\alpha_{CR}=0.8097$; this value is not accurate enough and should be replaced by $\alpha_{CR}=0.809764_3$.

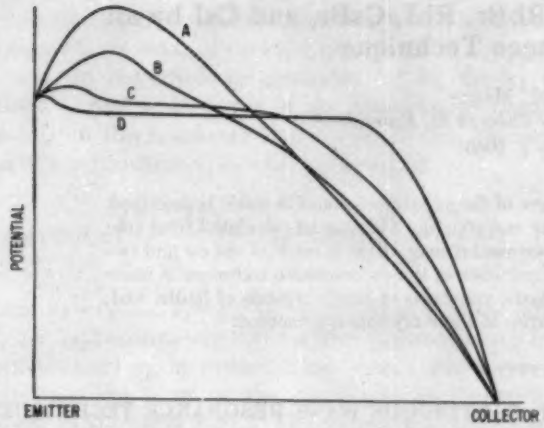

FIG. 2. Schematic evolution of positive column with increasing degree of neutralization. The ion current increases from the Langmuir-Child's space change limited value (curve *A*) to nearly emission limited value (curve *D*).

approximately to $\eta=0.34$. Thus we have

$$\begin{aligned}\xi(\eta,\alpha)&\approx\Xi(\eta);\quad \xi<0\\ &\approx\Xi(\eta);\quad \xi>0\\ &\qquad \eta\lesssim 0.34\\ \alpha&\lesssim\alpha_{CR}.\end{aligned}\tag{8}$$

The region describing the positive column may be arbitrarily ascribed to positive ξ values corresponding to the η range lying between $\eta=0.34$ and 0.35. In this region we may use the interpolation formula

$$\xi(\eta,\alpha)=\Xi(0.34)+(2/b)^{\frac{1}{2}}\times\left\{a(\alpha)+\operatorname{arc\,sinh}\left[1+c\left(\frac{\eta-\eta_{CR}}{\alpha_{CR}-\alpha}\right)\right]\right\};\qquad 0.34\lesssim\eta\lesssim 0.35$$

$$a=\operatorname{arc\,sinh}\left[c\left(\frac{\eta_{CR}-0.34}{\alpha_{CR}-\alpha}\right)-1\right]\tag{9}$$

$$b=\left\{\frac{d^2}{d\eta^2}\left(\frac{d\Xi}{d\eta}\right)^{-2}\right\}_{\eta=\eta_{CR}}$$

$$c=b\exp(\eta_{CR}).$$

Numerically Eq. (9) takes the form

$$\xi(\eta,\alpha)=15.35+3.25\left\{\operatorname{arc\,sinh}\left[1+0.272_8\left(\frac{\eta-\eta_{CR}}{\alpha_{CR}-\alpha}\right)\right]-\operatorname{arc\,sinh}\left[1-\frac{0.0013}{\alpha_{CR}-\alpha}\right]\right\};\tag{10}$$

$$\eta_{CR}=0.34475$$

$$\alpha_{CR}=0.80976_4.$$

The region of the cathode sheath may be described with the aid of the function $\Xi^*(\eta)$. This function is to be joined to the $\xi(\eta,\alpha)$ curve given above at $\eta=0.35$. We thus obtain

$$\xi(\eta,\alpha)=\xi(0.35,\alpha)+\Xi^*(\eta);\quad \eta\gtrsim 0.35\tag{11}$$

where $\xi(0.35,\alpha)$ is given by Eq. (10).

The asymptotic form of $\Xi^*(\eta)$ is

$$\Xi^*(\eta)\approx 14.85+(\pi/4)^{\frac{1}{2}}\eta^{\frac{3}{2}}[\tfrac{4}{3}+(1+\alpha_{CR})(\pi/\eta)^{\frac{1}{2}}]+0(\eta^{-\frac{1}{2}});\tag{12a}$$

or the equivalent form for large η

$$\Xi^*(\eta)\approx 14.85+(\pi/3)[(1+\alpha_{CR})+(4\eta/\pi)^{\frac{1}{2}}]^{\frac{3}{2}}+0(\eta^{-\frac{1}{2}}).\tag{12b}$$

It will be recognized that substitution of Eq. (12b) in Eq. (11) leads to an asymptotic relation for the potential distribution of the cathode sheath which closely resembles the familiar Langmuir-Child formula.[4]

ACKNOWLEDGMENTS

We wish to thank Mr. Russell N. Edwards for stimulating discussions on the present subject. We also wish to acknowledge the help of Miss Ann Warner, who performed all of the numerical calculations in this report.

[4] It may be noted that the expansion given by Eq. (12b) does not lead to a relation of the form $(\eta-\eta^*)/(\xi-\xi^*)^{\frac{3}{2}}=$const. since the error in such an approximation does not go to zero as η and ξ approach infinity. The above statement simply reflects a fundamental difference between the finite and zero temperature space charge situations.

Measurement of Elastic Constants of RbBr, RbI, CsBr, and CsI by an Ultrasonic cw Resonance Technique

D. I. Bolef and M. Menes
Westinghouse Research Laboratories, Pittsburgh 35, Pennsylvania
(Received February 4, 1960)

An ultrasonic cw resonance technique for the measurement of the velocity of sound in solids is described. The end correction due to the presence of the transducer and coupling film can be calculated from consideration of a transmission-line equivalent circuit. An experimental comparison is made of the cw and two pulse techniques over the frequency range 5 to 45 Mc. Application of the cw resonance technique is made to the measurement of the room-temperature adiabatic elastic constants of single crystals of RbBr, RbI, CsBr, and CsI. A tabulation of the important elastic properties of these crystals is presented.

I. INTRODUCTION

IN connection with the study of alkali halide single crystals by the use of nuclear magnetic resonance acoustic absorption techniques,[1] the elastic constants of single crystals of the rubidium and cesium bromides and iodides at room temperature were measured.

The elastic constants were obtained from measurements of the velocity of sound in the single crystals by an ultrasonic cw resonance technique.[2] The technique depends upon setting up standing waves in a composite oscillator consisting of transducer, coupling film, and specimen. The velocity is then obtained in terms of length, density, and frequency. Because the measurements use continuous waves the correction factor for end effects can easily be calculated. The correction factor allows for the effect of the transducer and of the coupling film. It is shown, however, that the correction for the coupling film is small compared to the transducer correction over the range of frequencies used.

The factors in the correction terms involve only the lengths and densities of the specimen, coupling film, and transducer. All of the quantities in the corrected expression for the velocity of sound can be measured to better than one part in 10^3. It is felt, therefore, that the overall accuracy of the cw method is comparable to the best methods now available. In addition, it has the virtue of simplicity in instrumentation.

Section II of this paper presents a description of the theory, experimental arrangement, and procedure for the cw resonance technique. In Sec. III a comparison of this technique with pulse-echo and "long-pulse" ultrasonic techniques is made. In Secs. IV and V, respectively, are given experimental procedures in obtaining the single-crystal elastic constants of alkali halides and a discussion of the results.

[1] D. I. Bolef and M. Menes, Phys. Rev. 114, 1441 (1959); M. Menes and D. I. Bolef; Bull. Amer. Phys. Soc., II, 4, 462 (1959).

[2] A cw resonance technique has been used at low frequencies, of the order of 100 kc, to measure Young's moduli and torsion moduli of cylindrical rods of single crystals. This work is due to S. Quimby and his associates. See, for example, S. Siegel and S. Quimby, Phys. Rev. 49, 663 (36); T. A. Read, *ibid.* 58, 371 (40).

II. CONTINUOUS WAVE RESONANCE TECHNIQUE

Theory

For one-dimensional wave propagation, the mechanical system of transducer, coupling film, and specimen has been shown[3] to be equivalent to a series of simple electrical transmission lines. Since in the present case we are interested only in the mechanical resonance frequencies, we can omit the electromechanical transformer and use the simplified equivalent circuit of Fig. 1. The characteristic impedance is $Z=\rho c$. The density is ρ, the speed of sound is c, and the length is l. The subscripts S, B, or T, indicate specimen, coupling film, or transducer.

If, initially, we neglect the bond, we obtain from transmission line theory

$$Z_S' = \rho_S c_S \tanh j\theta_S \tag{1a}$$

$$Z_T' = \rho_T c_T \frac{Z_S' + \rho_T c_T \tanh j\theta_T}{\rho_T c_T + Z_S' \tanh j\theta_T}, \tag{1b}$$

where Z_S' is the impedance looking from $S-S$ into the short-circuited length of transmission line which represents the specimen, Z_T' is the impedance of the composite oscillator, looking from $T-T$, when the bond is neglected. $\theta_S=\omega l_S/c_S$, and $\theta_T=\omega l_T/c_T$, and $\omega=2\pi\nu$ is the frequency. If each of the elements is assumed to be loss-free, the impedances are purely reactive, and Eq. (1b) may be rewritten as

$$Z_T' = \rho_T c_T \frac{j\rho_S c_S \tan\theta_S + j\rho_T c_T \tan\theta_T}{\rho_T c_T - \rho_S c_S \tan\theta_S \tan\theta_T}. \tag{2}$$

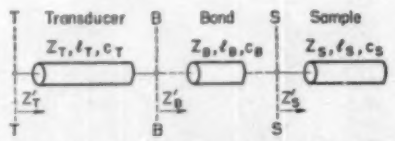

FIG. 1. Transmission-line equivalent circuit of the composite oscillator consisting of transducer, coupling film (bond), and sample. The electromechanical transformer has been omitted. $Z=\rho c$ is the characteristic impedance. Z' is the impedance looking from the planes marked, respectively, T, B, and S.

[3] J. Williams and J. Lamb, J. Acoust. Soc. Am. 30, 308 (1958).

To find the frequencies ν_C at which the composite oscillator is resonant, we set the numerator of Z_T' equal to zero. In the resulting equations for θ_S, θ_T, let us express l_S and l_T in terms of the wavelengths corresponding to the resonance frequencies of the specimen and of the transducer, $l_S=\frac{1}{2}n_S\lambda_S$, $l_T=\frac{1}{2}\lambda_T$:

$$\rho_S c_S \tan n_S\pi\left(\frac{\nu_S-\nu_C}{\nu_S}\right)+\rho_T c_T \tan\pi\left(\frac{\nu_T-\nu_C}{\nu_T}\right)=0, \quad (3)$$

where $\nu_S=c_S/\lambda_S$, $\nu_T=c_T/\lambda_T$. Since n_S is a fairly large integer (approximately 100 for the specimens and frequencies used in the present experiment), the observed frequency spectrum of the composite oscillator will appear as shown in Fig. 2. The narrow line resonances correspond to the running number n_S which characterize the mechanical half-wave resonances of the specimen.

We are interested in obtaining the specimen resonance frequencies ν_S in terms of the observed composite oscillator resonance frequencies ν_C. Equation (3) shows the necessary correction due to the transducer. It will be shown below that the correction is of the order of a few percent under the present experimental conditions. For the values of n_S used, the value of $(\nu_S-\nu_C)/\nu_S$ is of the order of 10^{-3}, making the argument of the tangent in the first term less than 1°. Under the same conditions, the argument of the tangent of the second term is approximately 9°. We may replace the tangent of the first term by its argument to within an accuracy of 0.05%; the tangent of the second term may be replaced by its argument to within an accuracy of 1%, but with an effect on the over-all accuracy of the velocity which is at most 0.05%.

If overtone transducers are used, the analysis above is unchanged except for the introduction of a factor n_T in the argument of the tangent in the second term of Eq. (3). n_T stands for the odd integer denoting the mode of vibration of the transducer. This will affect the error involved in replacing the tangent by its argument.

Setting the tangents equal to their arguments, applying the condition for resonance in the specimen, and rearranging, we obtain

$$\nu_{S,n}=\nu_{C,n}-(\rho_T l_T/\rho_S l_S)(\nu_T-\nu_{C,n}), \quad (4)$$

where $\nu_{S,n}$ and $\nu_{C,n}$ represent, respectively, the specimen and composite oscillator resonance frequencies corresponding to the nth mechanical resonance. Similarly, for the $(n+1)$-th mechanical resonance,

$$\nu_{S,n+1}=\nu_{C,n+1}-(\rho_T l_T/\rho_S l_S)(\nu_T-\nu_{C,n+1}). \quad (5)$$

Method I

By subtracting (4) from (5), we obtain the frequency difference between specimen resonances in terms of the measured frequency difference between composite oscillator resonances:

$$\Delta\nu_S=\nu_{S,n+1}-\nu_{S,n}=\Delta\nu_C[1+(\rho_T l_T/\rho_S l_S)]. \quad (6)$$

$\Delta\nu_S$ can be written

$$\Delta\nu_S=c_S/2l_S. \quad (7)$$

By combining Eqs. (6) and (7), we obtain

$$c_S=2l_S\Delta\nu_C[1+(\rho_T l_T/\rho_S l_S)]. \quad (8)$$

Thus, the velocity of sound in a specimen which is part of a composite oscillator may be obtained by measurement of the lengths and densities of the specimen and transducer and of the frequency separation $\Delta\nu_C$ between mechanical resonances of the composite oscillator. For an alkali halide specimen of length 1 cm and at a frequency of 10 Mc, the correction due to the transducer is approximately 2% of c_S.

Method II

In practice, it has been found that the use of Eq. (8) in obtaining accurate values of the velocity of sound is restricted to relatively high-Q specimens; i.e., specimens in which the damping constant is small. For low-Q specimens, an alternative cw resonance method may be used. In this method it is necessary only to measure two mechanical resonance frequencies, $\nu_{C,n}$ and $\nu_{C,n+1}$, but it is also necessary to measure independently the frequency ν_T of the transducer. This can be done using the pulse-echo display by measuring that frequency at which the amplitude of the first echo is a maximum.

The alternative method utilizes the fact that the velocity of sound in the specimen is given in terms of $\nu_{S,n}$ and $\nu_{S,n+1}$ by the expressions

$$\begin{aligned} c_S&=2l_S(\nu_{S,n}/n)\\ c_S&=2l_S(\nu_{S,n+1}/n+1). \end{aligned} \quad (9)$$

By substituting Eqs. (4) and (5) into (9), we obtain for the integer n,

$$n=\frac{\nu_{C,n}+(\rho_T l_T/\rho_S l_S)(\nu_{C,n}-\nu_T)}{\Delta\nu_C[1+(\rho_T l_T/\rho_S l_S)]}. \quad (10)$$

For typical experimental conditions, $\nu_{C,n}\approx 10^7$ cps, $\nu_{C,n}-\nu_T\approx 10^5$ cps, $\rho_T l_T/\rho_S l_S\approx 10^{-2}$ and $\Delta\nu_C\approx 10^5$ cps. Under these conditions, Eq. (10) reduces to

$$n=(\nu_{C,n}/\Delta\nu_C)[1-(\rho_T l_T/\rho_S l_S)]. \quad (11)$$

The expression for the velocity of sound in the specimen

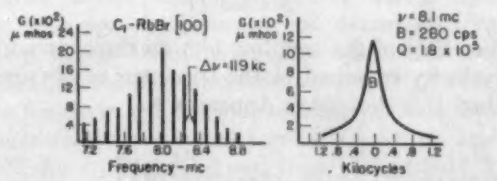

FIG. 2. Observed frequency spectrum of the composite oscillator, using RbBr as the sample. The sound was propagated as a shear wave along the [100] axis of the crystal. At the right is shown in detail one of the lines. The lines are extremely sharp, but may, in certain cases, exhibit structure.

is then

$$c_S=(2l_S/n)[\nu_{C,n}-(\rho_T l_T/\rho_S l_S)(\nu_T-\nu_{C,n})]. \quad (12)$$

Values of c_S in alkali halides obtained by use of Eq. (12) agree to within 0.2% with values obtained using Eq. (8). In all cases, the values obtained using Eq. (12) are felt to be the more accurate.

Effect of Coupling Film

Method I

The effect of the coupling film can be taken into account by an analysis of the complete transmission-line equivalent circuit of Fig. 1. We then obtain for $\Delta\nu_S$, analogous to Eq. (6) (See Appendix A)

$$\Delta\nu_S=\Delta\nu_C\left\{1+\frac{m_T}{m_S}(1\mp 2P\nu_T\delta)-\frac{m_B}{m_S}[1-P\nu_T(\nu_T\pm 4\delta)]\right\}, \quad (13)$$

where

$$m=\rho l, \quad \delta=|\nu_{C,n}-\nu_T|,$$

and

$$P=4\pi^2[m_B m_T/(\rho_B c_B)^2].$$

The top sign is to be used when $\nu_{C,n}-\nu_T$ is positive. By using phenyl salicylate (salol) as the bonding material, a bond thickness of 5×10^{-5} in., a frequency $\nu_T=10$ Mc, and assuming a maximum value of $|\nu_{C,n}-\nu_T|$ of 5×10^5 cps (corresponding, in the experiments to be described below, to $\Delta n_S=5$), we obtain

$$\Delta\nu_S=\Delta\nu_C\left\{1+\frac{m_T}{m_S}(1\mp 0.2)-\frac{m_B}{m_S}[1-10^{-2}(10\pm 2)]\right\}. \quad (14)$$

The ratio m_B/m_T is approximately 5×10^{-3} under the conditions cited in the preceding. Since the correction due to the transducer at this frequency (10 Mc) and for a 1-cm length specimen is approximately 2% of $\Delta\nu_S$ (or c_S), the correction due to the bond can be neglected. The effect of the bond, however, is seen not to be negligible at frequencies of the order of 10^3 Mc or for very thin specimens at lower frequencies.

Method II

The effect of the coupling film on the expression for the velocity of sound in the specimen as obtained by Method II is derived in Appendix B:

$$c_S=\frac{2l_S}{n}\left\{\nu_{C,n}+\left[\frac{m_T}{m_S}(\nu_{C,n}-\nu_T)-\frac{m_B}{m_S}\nu_{C,n}\right]\times[1-P\nu_{C,n}(\nu_{C,n}-\nu_T)]\right\}. \quad (15)$$

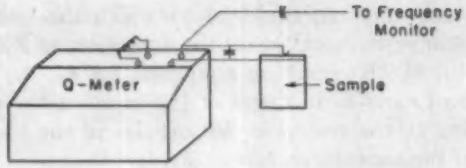

FIG. 3. Continuous-wave resonance method experimental arrangement.

Under experimental conditions as described in the preceding, the term in P is negligible, and we obtain

$$c_S=\frac{2l_S}{n}\left[\nu_{C,n}\left(1-\frac{m_B}{m_S}\right)+\frac{m_T}{m_S}(\nu_{C,n}-\nu_T)\right]. \quad (16)$$

Experimental Arrangement and Procedure

The experimental arrangement is shown schematically in Fig. 3. The composite oscillator, consisting of transducer bonded to the specimen, is connected to the capacitor terminals of a Boonton type 260A Q-meter. A suitable standard inductor is used to tune to resonance in the proper frequency range. A high-frequency electronic counter (Hewlett-Packard type 524B) is coupled to the Q-meter to read the resonance frequency directly. After a warmup period of several hours, the Q-meter frequency drift was less than one part in 10^5 over the period of a run.

A typical cw resonance line spectrum is shown in Fig. 2 for a single crystal of RbBr in which the shear waves are transmitted along a [100] axis. This spectrum is obtained by adjusting the Q-meter frequency for a minimum in Q, corresponding to a maximum in the conductance as shown in Fig. 2. The observed minima sometimes exhibit a complexity in structure which makes more difficult the precise determination of resonance frequencies. The uneven decay pattern and minima structure is often eliminated by rebonding the transducer.

The frequency separation $\Delta\nu_C$ of the mechanical resonance peaks of Fig. 2 is approximately 119 kc. This is the mean value of approximately 10 readings of $\Delta\nu_C$ corresponding to differences in adjacent values of n_S. The detailed shape of an individual mechanical resonance is shown in Fig. 2. The measured bandwidth is 280 cps, corresponding to a Q of 190 000.

III. COMPARISON WITH PULSE TECHNIQUES

A comparison between the velocity of sound measured in a single crystal of CsBr by the pulse-echo technique, by the "long-pulse" technique[4] and by the cw resonance technique was made over the range of frequencies 5 to 45 Mc. The experimental apparatus used in the pulse techniques consisted of an rf oscillator, with frequency variable between 0.5 and 50 Mc, gated by a pulse generator whose pulse width could be varied between

[4] H. J. McSkimin, J. Acoust. Soc. Am. **22**, 413 (1950).

0.5 and 60 μsec. Detection equipment consisted of a broad-band tuned rf receiver. The rectified signals were displayed on a Dumont 246 AR range oscilloscope. Pulse widths of about 2 μsec were used in the pulse-echo technique, 40 to 60 μsec in the long-pulse technique.

In the latter technique the frequencies at which the oscilloscope pattern was "in-phase" were measured with an electronic counter. The "in-phase" pattern was obtained when the applied pulse was widened so that reflections from the specimen overlapped. A pattern which could be reproduced quite precisely, such as that shown in Fig. 4, was found to give the best results.

If we denote the successive frequencies at which the "in-phase" pattern is obtained by the running integer n, then the velocity of sound measured by the long pulse technique is given by[4]

$$c=2l_S\{(\nu_{n+1}-\nu_n)/[1+(\varphi_n-\varphi_{n+1})]\}, \quad (17)$$

where l_S is the specimen length and φ is the phase change on reflection at the specimen surface. If we neglect the phase change, we obtain for the velocity

$$c_S=2l_S\Delta\nu, \quad (18)$$

where $\Delta\nu=\nu_{n+1}-\nu_n$. The correction due to changes in phase upon reflection may be measured by techniques suggested by McSkimin.[4] It will be shown in the following, however, that the correction for the cw resonance technique [see Eq. (8)] holds approximately for the long-pulse technique in the range of frequencies of 5 Mc and up.

Velocities were measured at frequencies of approximately 6 Mc, 8 Mc, 20 Mc, 30 Mc, and 45 Mc using the two pulse techniques and the cw resonance technique. In each case a longitudinal wave was propagated in the [100] direction in a single crystal of CsBr of length 0.4058 in. and cross section $\frac{3}{8}\times\frac{3}{8}$ in. The transducer was bonded under pressure to the specimen by means of salol. The bond thickness varied between 0.05 mil and 0.1 mil among the five sets of measurements. Contact to the top transducer plating was made with a gold wire whisker. A circular set of gold-plated copper fingers was used to make contact with the narrow rings of the "wraparound" bottom plating. All measurements were taken at room temperature. Rectified pulses alone were used in the pulse-echo measurements.

A graph of the results of these measurements is given on a semilog plot in Fig. 5. Each point represents the mean of at least 10 readings. The mean deviation of the velocities obtained by the pulse techniques is 0.4%, of those obtained by the cw technique (Method I) 0.2%. In addition to the three curves of velocity vs frequency, a curve has been drawn through the points [calculated from Eq. (8)] representing the corrected cw values of the velocity. The departure of this straight line from the horizontal may be attributed to the neglect of the bond in Eq. (8). With the possible exception of the frequency range near 5 Mc, the uncorrected values of the velocity as determined by the cw technique most closely approximates the "true" values given by the corrected curve. The long-pulse technique gives uncorrected values closer to the "true" ones than does the pulse-echo technique. If one is satisfied with accuracies of 1% in the measured value of the velocity of sound, uncorrected values determined by either the cw or long-pulse techniques may be used above 15 Mc.

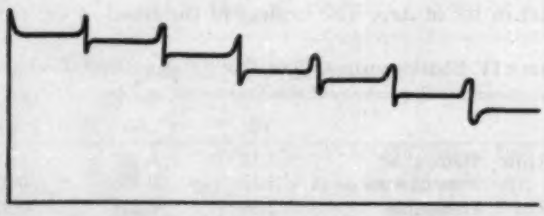

FIG. 4. Typical "in-phase" pattern used in "long-pulse" technique.

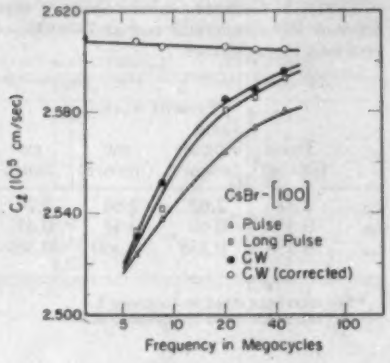

FIG. 5. Comparison of values of velocity of sound obtained by cw resonance technique with those obtained by pulse techniques over frequency range 5 to 45 Mc.

At the low-frequency end, the uncorrected velocity as measured by the cw resonance technique drops precipitously. This behavior agrees with the dependence of c_{uncorr} on frequency obtained from Eq. (8):

$$c_{\text{uncorr}}=c_{\text{corr}}[1+(k/f)]^{-1}, \quad (19)$$

where f is in Mc and $k=0.172$ for the CsBr single crystal used in this experiment. The curve for $c_{\text{uncorr cw}}$ given in Fig. 4 follows Eq. (19) closely.

A comparison of the values of elastic constants of single-crystal KI obtained by the present investigators, by Norwood and Briscoe[5] using the pulse-echo technique, and by Bridgman[6] using a static technique is given in Table I. The data of the present authors was taken at a frequency of 8 Mc, which from Fig. 4, is at the "knee" of the cw curve and where there is expected rather close agreement among the uncorrected values obtained by the three techniques, but where there is also a rather sizeable correction factor. This is verified by the figures in the first four columns of the table. The probable errors in column 4 are 0.4% for c_{11} and c_{44}, and 8% for c_{12}. Norwood and Briscoe list errors of 1% and 9% respectively, for the same constants. Thus, the two sets of values, one obtained by a corrected pulse-

[5] M. H. Norwood and C. V. Briscoe, Phys. Rev. 112, 45 (1958).
[6] P. C. Bridgman, Proc. Am. Acad. Arts Sci. 64, 19 (1929).

TABLE I. Comparison of values of elastic constants of KI in units of 10^{11} dynes/cm^2 and at $T \simeq 300°$ obtained by present and previous investigators.

	Present work				Norwood and	
	Pulse (uncorr)	Long pulse (uncorr)	cw (uncorr)	cw (corr)	Briscoe[a] (pulse)	Bridgman[b] (static)
c_{11}	2.61	2.62	2.64	2.74	2.71	2.66
c_{12}	0.38	0.40	0.41	0.47	0.45	0.425
c_{44}	0.353	0.358	0.360	0.369	0.364	0.412

[a] See reference cited in footnote 5.
[b] See reference cited in footnote 6.

echo technique and one by the corrected cw technique, agree within their estimated probable errors.

IV. ELASTIC CONSTANTS OF RbBr, RbI, CsBr, CsI

Experimental Procedure

The single crystals of RbBr and RbI were obtained from Semi-Elements, Inc., the single crystals of CsBr and CsI from Harshaw Company. In each case the crystal was so oriented that only "pure" longitudinal or transverse modes were propagated. For each crystal five independent measurements of $\rho v^2 c$ were made[7] where ρ is the density and v a longitudinal or transverse velocity of sound. Two sets of crystal faces, perpendicular, respectively, to the (100) and (110) faces, were prepared. For RbBr and RbI the (100) faces were cleavage planes, while the (110) faces were string-saw cut at 45° to the cleavage planes. The CsBr and CsI crystals were oriented by the x-ray Laue back reflection technique.[8] Cuts exposing (100) and (110) faces were made with a string saw. It is estimated that orientations are accurate to ±2°.

The crystal faces were rough ground successively on emery paper, AO 302 and AO 303-½ carborundum, using kerosene. The rubidium salts were etched in a 1:10 solution of distilled water in acetone, followed by rinsing in methyl alcohol. The cesium salts were etched in a 1:25 solution of distilled water in methyl alcohol followed by rinsing in iso-propyl alcohol and in carbon tetrachloride. Final polishing to obtain optical surfaces was accomplished using AO 303-¼ on a cast-iron lap followed by Linde A sapphire dust on cloth, onionskin,

TABLE II. Densities and lengths of specimens.

	RbBr	RbI	CsBr	CsI
Density g/cc	3.349	3.550	4.433	4.509
Length (cm)				
[100]	0.7148	1.249	1.031	1.217
[110]	0.8710	0.9890	1.620	1.882

[7] For propagation in the [100] direction: $\rho v_l^2 = c_{11}$, $\rho v_T^2 = c_{44}$; for propagation in the [110] direction: $2\rho v_l^2 = c_{11} + c_{12} + 2c_{44}$, $\rho v_{T[100]}^2 = c_{44}$, $2\rho v_{T[110]}^2 = c_{11} - c_{12}$.

[8] We are indebted to Dr. A. Taylor and Miss Brenda Kagle of these Laboratories for these x rays.

TABLE III. Elastic constants in units of 10^{11} dynes/cm^2. $T = 300°$K.

	c_{11}	c_{44}	c_{12}
RbBr	3.17±0.02	0.388±0.003	0.42±0.04
RbI	2.56±0.01	0.287±0.003	0.31±0.03
CsBr	3.00±0.01	0.756±0.003	0.78±0.04
CsI	2.46±0.01	0.624±0.003	0.67±0.02

or tissue. N-amyl alcohol was used for the rubidium salts, kerosene for the cesium salts. The finished faces were flat to within a wavelength of light and parallel to within 0.05 mil over the area covered by the transducer. The acoustic path lengths in the specimens are given in Table II. The cross sections, except that of RbBr, were such as to accommodate ½-in. diam transducers. For RbBr $\frac{7}{32}$ in.-diam transducers were used.

The quartz transducers, of frequency 8 or 10 Mc, were of the wraparound type. Contact was made by "pigtails" or by a gold spring wire bearing against the silver-plated electrodes. Bonding was done under pressure, using salol. Measured thickness of the salol film varied between 0.05 and 0.1 mil from specimen to specimen.

Although measurements of the velocity of sound in these crystals were made using the pulse-echo, long-pulse, and cw resonance techniques, the values obtained with the latter technique (Method I) alone were used to obtain the elastic constants. In all cases the measured values of the velocity were corrected by the factor discussed in Sec. II [see Eq. (8)].

V. RESULTS

The elastic constants computed from the measurement of velocity are given in Table III. The densities used in these calculations are given in Table II. The probable errors listed in Table III represent the rms deviations from the mean of 10 or more readings of $\Delta\nu_C$ obtained from the frequencies of the conductance maxima of Fig. 2. An estimate of the accuracy of the values in Table III on the basis of reproducibility is, however, much higher, as can be seen by reference to Fig. 5. The spread in values among five completely different runs, at different frequencies, is there shown to be less than 0.1%, which would introduce a maximum error of 0.2% in the value of the elastic constants c_{11} and c_{44} and of approximately 2% in c_{12}. The lengths of transducers and specimens were measured to within one part in 10^4. Frequencies could be read to within one part in 10^4 of $\Delta\nu_C$. The neglect of the bond in the com-

TABLE IV. Elastic constants in units of 10^{11} dynes/cm^2. $T = 300°$K.

		c_{11}	c_{44}	c_{12}
RbBr	Haussuhle	3.18	0.385	0.48
	Present work	3.17	0.388	0.42
RbI	Haussuhle	2.58	0.281	0.37
	Present work	2.56	0.287	0.31

TABLE V. Elastic properties of the alkali bromides and iodides. Data from present work except where indicated. Room temperature.

	c_{44} (10^{11} dynes/cm^2)	$\frac{1}{2}(c_{11}-c_{12})$ (10^{11} dynes/cm^2)	$K[\equiv\frac{1}{3}(c_{11}+2c_{12})]$ (10^{11} dynes/cm^2)	K(Hydrostatic meas.)[d] (10^{11} dynes/cm^2)	Anisotropy $[\equiv 2c_{44}/(c_{11}-c_{12})]$
NaBr[a]	0.97	1.45	1.94	1.96	0.669
KBr[b]	0.505	1.44	1.54	1.54	0.351
RbBr	0.388	1.38	1.34	1.22	0.290
CsBr	0.756	1.11	1.52	1.42	0.681
NaI[c]	0.737	1.08	1.50	1.4	0.682
KI	0.369	1.14	1.23	1.18	0.324
RbI	0.287	1.13	1.06	1.08	0.254
CsI	0.624	0.90	1.27	1.08	0.693

[a] S. Bhagavantam, Proc. Indian Acad. Sci. **A41**, 72 (1955).
[b] J. K. Galt, Phys. Rev. **73**, 1460 (1948).
[c] S. Eros and J. R. Reitz J. Appl. Phys. **29**, 683 (1958).
[d] See compilation in Landolt-Börnstein (Springer-Verlag, Berlin, 1927).

putation of the correction factor of Eq. (10) was shown in Sec. II to contribute an error of less than one part in 10^4 at the frequencies used in this experiment.

Spangenberg and Haussuhle[9] have measured the elastic constants of RbBr and RbI, using the ultrasonic-elastogram technique. Their values are compared with the present values in Table IV. Since Spangenberg and Haussuhle quote probable errors of the order of a few percent for their values, the two sets of constants agree to well within the stated experimental error.

A tabulation of the important elastic properties of alkali bromides and iodides thus far measured is given in Table V. All values are referred to room temperature. In Table VI are presented the Debye θ's for the alkali bromides and iodides calculated from the room-temperature values of the elastic constants. These are compared with the Debye θ_D obtained from specific-heat data at low temperatures. Values of θ (elastic) in column 1 are obtained by the method of Quimby and Sutton[10]

TABLE VI. Comparison of Debye θ's obtained from elastic and specific-heat data. Elastic Constants taken (at room temperature) from present work except where noted.

	θ (elastic)°K Method I[e]	Method II[f]	Compressibility[g]	θ (specific heat)°K $T=0$°K[h]	$T=\frac{1}{2}\theta_D$[g]
NaBr[a]	200	218	243		
KBr[b]	163	168	185	174	180
RbBr	127	132	133		132
CsBr	134	143	119		
NaI[c]	153	164	201	164	
KI	122	126	155	132	175
KI (0°K)[d]	131	132		132	
RbI	103	105	116		115
CsI	112	121	94		

[a] See reference cited in footnote a, Table V.
[b] See reference cited in footnote b, Table V.
[c] See reference cited in footnote c, Table V.
[d] See reference cited in footnote 5.
[e] See reference cited in footnote 10.
[f] See reference cited in footnote 12
[g] K. Clusius *et al.*, Z. Naturforsch. **4A**, 430 (1949); reference cited in footnote d, Table V.
[h] T. H. K. Barron *et al.*, Proc. Roy. Soc. (London) A242, 478 (1957).

[9] K. Spangenberg and S. Haussuhle, Z. Krist. **110**, 67 (1958).
[10] S. L. Quimby and P. M. Sutton, Phys. Rev. **91**, 1122 (1953).

using curves obtained by Leibfried.[11] Values of θ (elastic) in column 2 are obtained by an approximation method due to Blackman[12] which depends for its accuracy on the smallness of the ratio c_{12}/c_{11}. For completeness, the values of θ (elastic) calculated from measured compressibilities are given in column 3. There is approximate agreement between θ (elastic) and θ for the cases in which both have been accurately measured.

VI. CONCLUSIONS

We have described a cw resonance technique, using a composite oscillator, for the measurement of the velocity of sound in solids. In this technique the end correction due to the presence of coupling film and transducer can be calculated using equations derived from consideration of the composite oscillator equivalent circuit. The technique uses measurements of the quantities length, density, and frequency only. The instrumental setup is simple.

A comparison of the cw resonance technique with two pulse techniques over the frequency range 5 to 45 Mc shows that the uncorrected values of the velocity as measured by the cw technique most closely approximates the "true" corrected value. Over this frequency range the long-pulse technique gives more accurate values than the pulse-echo technique, if end corrections are neglected.

VII. ACKNOWLEDGMENT

We wish to thank R. Farich for his valuable aid in the preparation of the specimens.

APPENDIX A

Correction due to Transducer and Coupling Film—Method I

With reference to the transmission-line equivalent circuit of Fig. 1, the impedance looking from $T-T$ is

[11] G. Leibfried, *Handbuch der Physik* (Springer-Verlag, Berlin, 1955), Vol. VII, p. 1.
[12] M. Blackman, Proc. Roy. Soc. (London) A149, 126 (1935).

given by

$$Z_T'=k_T[(Z_B'+k_T\tanh j\theta_T)/(k_T+Z_B'\tanh j\theta_T), \quad (A.1)$$

where

$$Z_B'=k_B[(Z_S'+k_B\tanh j\theta_B/(k_B+Z_S'\tanh j\theta_B)] \quad (A.2)$$

$$Z_S'=k_S\tanh j\theta_S. \quad (A.3)$$

k_T, k_B, k_S are, respectively, the specific characteristic impedance ρc of transducer, bond, and specimen. $\theta=2\pi\nu l/c$, where ν is the frequency, l the length, and c the velocity of sound. For loss-less lines, the expressions equivalent to (A.1), (A.2), and (A.3) are

$$Z_T'=k_T[(Z_B'+jk_T\tan\theta_T)/(k_T+Z_B'j\tan\theta_T)] \quad (A.4)$$

$$Z_B'=k_B[(Z_S'+jk_B\tan\theta_B)/(k_B+Z_B'j\tan\theta_B)] \quad (A.5)$$

$$Z_S'=jk_S\tan\theta_S. \quad (A.6)$$

By substituting (A.6) and (A.5) into (A.4), simplifying, and setting the numerator of the resulting expression for Z_T' equal to zero, we obtain as the condition for resonance of the composite oscillator

$$k_S\tan\theta_S+k_T\tan\theta_T+k_B\tan\theta_B - \frac{k_Sk_T}{k_B}\tan\theta_S\tan\theta_B\tan\theta_T=0. \quad (A.7)$$

We assume, as in Sec. II, that the tangents can be replaced by their arguments. We further apply the resonance relationships

$$\lambda_S=2l_S/n_S$$
$$\lambda_T=2l_T.$$

θ_B is given by $\theta_B=2\pi\nu_Cl_B/c_B$.

Equation (A.7) becomes

$$m_S(\nu_{S,n}-\nu_{C,n})+m_T(\nu_T-\nu_{C,n})+m_B\nu_{C,n} \times\{1-[4\pi^2m_Sm_T/(\rho_Bc_B)^2](\nu_{S,n}-\nu_{C,n}) \times(\nu_T-\nu_{C,n})\}=0, \quad (A.8)$$

where $m=\rho l$. Solving for $\nu_{S,n}$, we obtain

$$\nu_{S,n}=\nu_{C,n}-\frac{m_T(\nu_T-\nu_{C,n})+m_B\nu_{C,n}}{m_S[1-P\nu_{C,n}(\nu_T-\nu_{C,n})]}, \quad (A.9)$$

where $P=4\pi^2[m_Bm_T/(\rho_Bc_B)^2]$. For the typical experimental conditions cited in Sec. II, P is of the order of 10^{-15} sec. For $\nu_{C,n}=10$ Mc and $\nu_T-\nu_{C,n}=0.5$ Mc, therefore, the term containing P is small compared to unity, and we can rewrite (A.9) as

$$\nu_{S,n}=\nu_{C,n}+\left[\frac{m_T}{m_S}(\nu_{C,n}-\nu_T)-\frac{m_B}{m_S}\nu_{C,n}\right] \times[1-P\nu_{C,n}(\nu_{C,n}-\nu_T)]. \quad (A.10)$$

Similarly, for the $(n+1)$-th half-wave resonance of the specimen and composite oscillator,

$$\nu_{S,n+1}=\nu_{C,n+1}+\left[\frac{m_T}{m_S}(\nu_{C,n+1}-\nu_T)-\frac{m_B}{m_S}\nu_{C,n+1}\right] \times[1-P\nu_{C,n+1}(\nu_{C,n+1}-\nu_T)]. \quad (A.11)$$

By subtracting (A.10) from (A.11), we find for the frequency separation $\Delta\nu_S$ between half-wave resonances of the specimen:

$$\Delta\nu_S=\Delta\nu_C\left[1+\frac{m_T}{m_S}-\frac{m_B}{m_S}\right] -P\left\{\frac{m_T}{m_S}[(\nu_{C,n+1}-\nu_T)^2\nu_{C,n+1}-(\nu_{C,n}-\nu_T)^2\nu_{C,n}] -\frac{m_B}{m_S}[(\nu_{C,n+1}-\nu_T)\nu_{C,n+1}^2 -(\nu_{C,n}-\nu_T)\nu_{C,n}^2]\right\}. \quad (A.12)$$

By using the expansion $\nu_{C,n+1}=\nu_{C,n}+\Delta\nu_C$, and neglecting terms of second order in $\Delta\nu_C/\nu_T$ and higher, we obtain

$$\Delta\nu_S=\Delta\nu_C\left[1+\frac{m_T}{m_S}-\frac{m_B}{m_S}\right] -\Delta\nu_CP\nu_T^2\left[\frac{m_T}{m_S}\left(\frac{3\nu_{C,n}^2}{\nu_T^2}-\frac{4\nu_{C,n}}{\nu_T}+1\right) -\frac{m_B}{m_S}\left(\frac{3\nu_{C,n}^2}{\nu_T^2}-\frac{2\nu_{C,n}}{\nu_T}\right)\right], \quad (A.13)$$

If we expand $\nu_{C,n}=\nu_T\pm\delta$, where $\delta=|\nu_{C,n}-\nu_T|$ and neglect terms of second order in δ/ν_T, we obtain

$$\Delta\nu_S=\Delta\nu_C\left\{1+\frac{m_T}{m_S}-\frac{m_B}{m_S} -P\nu_T^2\left[\frac{m_T}{m_S}\left(\pm\frac{2\delta}{\nu_T}\right)-\frac{m_B}{m_S}\left(1\pm\frac{4\delta}{\nu_T}\right)\right]\right\} \quad (A.14)$$

or, collecting terms,

$$\Delta\nu_S=\Delta\nu_C\left\{1+\frac{m_T}{m_S}(1\mp2P\nu_T\delta) -\frac{m_B}{m_S}[1-P\nu_T(\nu_T\pm4\delta)]\right\}. \quad (A.15)$$

APPENDIX B

Correction due to Transducer and Coupling Film—Method II

The corrected expression for the velocity of sound in the specimen as obtained by Method II may be derived as follows:

From Eqs. (9), (A.10), and (A.15), we obtain

$$n=\frac{\nu_{S,n}}{\Delta\nu_S}=\frac{\nu_{C,n}+\left[\frac{m_T}{m_S}(\nu_{C,n}-\nu_T)-\frac{m_B}{m_S}\nu_{C,n}\right]\left[1-P\nu_{C,n}(\nu_{C,n}-\nu_T)\right]}{\Delta\nu_C\left\{1+\frac{m_T}{m_S}(1\mp 2P\nu_T\delta)-\frac{m_B}{m_S}\left[1-P(\nu_T\pm 4\delta)\right]\right\}}. \quad \text{(B.1)}$$

If we neglect products of small terms, this can be written as

$$n=\frac{\nu_{C,n}}{\Delta\nu_C}\left[1-\frac{m_T}{m_S}(1\mp P\nu_T\delta)\right]\pm\frac{\delta}{\Delta\nu_C}\frac{m_T}{m_S}. \quad \text{(B.2)}$$

Under the conditions cited in Sec. II this can be approximated by Eq. (11):

$$n=(\nu_{C,n}/\Delta\nu_C)[1-(m_T/m_S)]. \quad \text{(B.3)}$$

From Eq. (A.10) and the expression $c_S=2l_S(\nu_{S,n}/n)$, we obtain

$$c_S=\frac{2l_S}{n}\left\{\nu_{C,n}+\left[\frac{m_T}{m_S}(\nu_{C,n}-\nu_T)-\frac{m_B}{m_S}\nu_{C,n}\right]\times[1-P\nu_{C,n}(\nu_{C,n}-\nu_T)]\right\}, \quad \text{(B.4)}$$

where n is given by either Eq. (B.2) or (B.3).

JOURNAL OF APPLIED PHYSICS VOLUME 31, NUMBER 6 JUNE, 1960

Mechanism of Inert Gas Cleanup in a Gaseous Discharge

K. B. Blodgett and T. A. Vanderslice
General Electric Research Laboratory, Schenectady, New York

(Received December 28, 1959; revised manuscript received February 28, 1960)

An investigation has been made of the cleanup of inert gases by a gas discharge. The cleanup of rare gases in a tube in which metal is being sputtered is governed largely by two factors. First, the rate at which the metal is sputtered, and second, the potential of the surface on which the metal lands. At small negative or positive potentials on the surface collecting sputtered metal there is a slow cleanup rate caused by uncharged species being buried by sputtered metal. At more negative potentials burial of ions becomes important, and cleanup is much more rapid. Recovery has been effected by heating to the evaporation temperatures of the metal. As the metal evaporates the buried gas is liberated. Hundreds of equivalent monolayers of argon have been cleaned up with only a total recovery of about one equivalent monolayer by heating at 1500°C. This shows that even with a forced "solubility" of the order of one per cent we find no evidence for significant diffusion of argon in metals. An electrode collecting ions at a uniform current density over the surface will have a net cleanup rate of zero on that surface after the initial cleanup of a small amount of gas. After the initial disappearance of some gas, resputtering will occur liberating the cleaned up gas as fast as it is being cleaned up.

INTRODUCTION

THE gradual decrease in pressure in a tube containing a low-pressure gaseous discharge has been extensively studied.[1–6] Numerous mechanisms have been proposed, none of which is completely satisfactory.

In 1932 Hull and Burger of this laboratory[7] found that the cleanup of argon in a low-pressure gas discharge tube did not saturate. Consecutive charges of argon cleaned up at the same rate. An amount of gas equivalent to 102 monolayers was cleaned up with no significant change in the rate. They also observed that the rate was substantially independent of pressure.

Some years later[8] Gurewitsch and Westendorp designed and built an ion pump with high pumping speed. Recently L. D. Hall[3] has published his work on the construction of a different version of the ion pump.

Siegler and Dieke[9] have made the most complete investigation of the cleanup in electrodeless discharges.

[1] J. Plucker, Pogg. Annal. **103**, 91 (1958).
[2] S. Dushman, *Scientific Foundations of Vacuum Technique* (John Wiley & Sons, Inc., 1949).
[3] L. D. Hall, Rev. Sci. Instr. **29**, 2 (1958).
[4] L. D. Holland, J. Sci. Instr. **36**, 105 (1959).
[5] Von Gerhard Stratzer, Z. angew. Phys. **10**, 5 (1958); *ibid.* **11**, 223 (1959).
[6] K. B. Blodgett and T. A. Vanderslice, Gaseous Electronics Conference, October, 1958.
[7] Unpublished work.
[8] A. Gurewitsch and W. F. Westendorp, Rev. Sci. Instr. **29**, 2 (1958).
[9] E. H. Siegler and G. H. Dieke, "Cleanup of rare gases in electrodeless discharges," Office of Naval Research, Technical Report VIII, November, 1952.

By means of careful vacuum technique they have shown that the inert gases clean up by penetration of the glass walls. They were able to effect complete recovery by heating the glass walls to 300°C for a few minutes. In order to obtain reproducible recovery data, a finely divided uranium "getter" was incorporated into their closed off discharge tubes. Their data strongly suggest that it is argon ions which penetrate the glass walls. The rate of cleanup is proportional to the intensity of the discharge and has a strong pressure dependence.

In the present work, the cleanup of inert gases in the pressure ranges of 10 to 100 μ has been studied. Rare gases have been used in this study because they are normally monatomic and inert chemically. Rare gases should provide the simplest example of cleanup and they offer the best possibility for establishing clearly the basic factors affecting cleanup. The cleanup rate of inert gases in gas discharge tubes containing electrodes of various materials and geometries has been measured.

EXPERIMENTAL

A. General Features

The cleanup of inert gases in a tube in which metal is being sputtered or evaporated in the presence of a discharge cannot be explained solely by simple ion penetration of the cathode. The cleanup of rare gases is governed largely by two factors. First, the rate at which the metal is sputtered, and second, the potential of the surface on which the metal lands. There are two chief mechanisms by which inert gases clean up in a gaseous discharge. At low positive or negative potentials on the surface collecting sputtered metal the cleanup proceeds by burial of excited inert gas atoms, presumably metastables. At more negative potentials the burial of ions becomes increasingly important. The rate of cleanup increases with increasing velocity of the impinging ion until the rate of resputtering becomes important. Then the release of buried inert gas atoms tends to balance the cleanup. A third type of cleanup also can occur at the walls of the glass tube[9] but this rate was comparatively slow in these experiments as will be shown later.

If the cleanup were due to simple ion penetration it would be expected that the cleanup on a surface would saturate. The penetration of ions of velocities less than that corresponding to 1000 ev is not more than a few atomic layers. After the disappearance of a few equivalent monolayers of gas the cleanup rate should approach zero since the gas would be released by sputtering at the same rate as it is being cleaned up. Also with simple ion penetration the rate would be relatively independent of the material of the surface. The behavior found in this study is contrary to the predicted behavior for simple ion penetration.

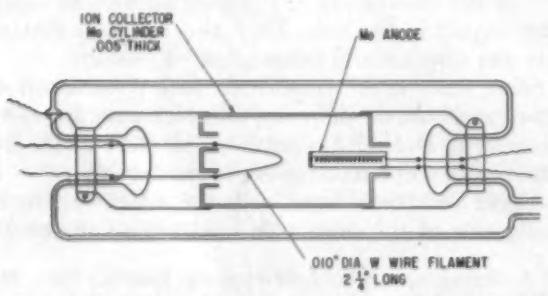

FIG. 1. Tube for measuring gas cleanup operated with discharge between hot filament and anode and negative voltage on ion collector.

In Fig. 1 is shown a tube with a tungsten filament, an anode and a closed metal cylinder which enclosed the region of the discharge between the cathode and the anode. The metal cylinder kept most of the discharge products away from the glass walls of the tube. This tube was evacuated, the metal parts thoroughly outgassed and the residual pressure as measured on a Bayard-Alpert gauge was 10^{-8} mm. The metal electrodes were outgassed at temperatures exceeding 1500°C. The gases used were spectroscopic grade. A McLeod gauge separated from the tube by a liquid nitrogen trap was used to measure the pressure during a run.

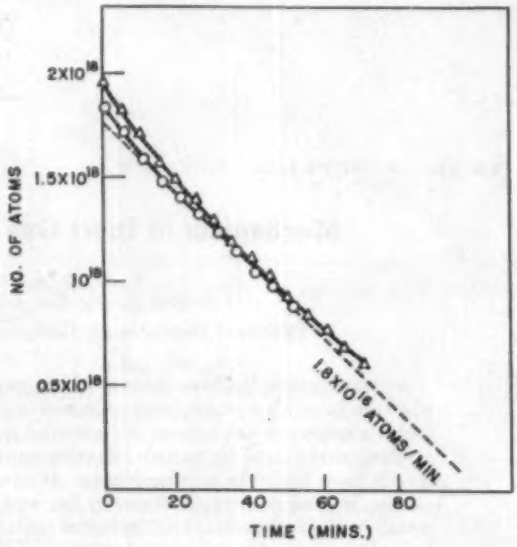

FIG. 2. Cleanup of argon with −350 v on molybdenum cylinder.

A constant anode current was maintained during the course of a run and the potential on the metal cylinder could be varied, independently. Figure 2 shows the pressure vs time data for argon at a constant anode current of 200 ma and a collector potential of −350 v with respect to the anode. The plasma is essentially at anode potential so that the potential of the collector is a measure of the kinetic energy with which the ions strike it. The rate of cleanup is substantially independent of the gas pressure over the pressure range studied. Successive charges of argon clean up at the same rate as shown by the data in Fig. 3 for a different tube. The

total cleanup in any given tube can be calculated to correspond to thousands of equivalent monolayers.

Varying the cylinder material changed the cleanup rate. Data for the number of argon atoms cleaned up per argon ion striking the collecting cylinder, versus voltage, are shown in Fig. 4 for Ta, Mo, and Ti. The rate of cleanup at a given cylinder potential and a given ion current to the cylinder was proportional to the sputtering coefficients of the metal as determined by Wehner[10] for Hg ions.

Upon opening the tubes it was found that metal was sputtered from the central portion of the collector cylinder and deposited near the ends of the cylinder. Microscopic examination showed that the center portion was etched by the bombardment, and the end portions of the cylinders had a mat appearance. X-ray back reflection

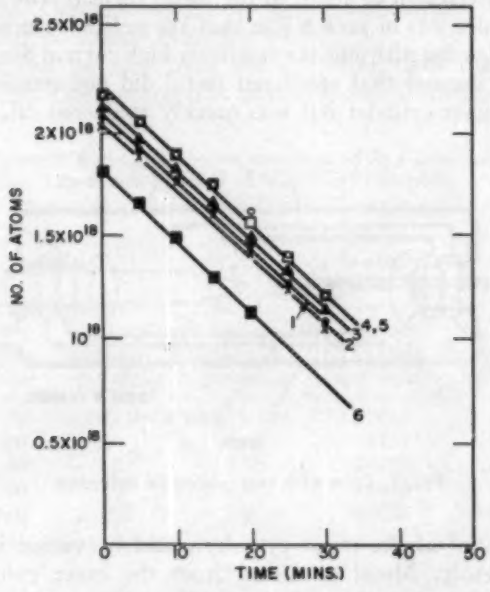

FIG. 3. Cleanup of six successive charges of argon with −600 v on the sputtering electrode.

studies showed that the original metal and the center region of the cylinder which was etched by the bombardment was made up of large crystals. The sputtered metal deposit on the end region of the cylinder was made up of small crystallites. The transition region showed a mixture of large and small crystallites. The fact that small crystallites are found rather than an amorphous deposit is not very surprising when one is aware that Hilsh[11] has shown that an amorphous metal contains large amounts of stored energy. Certainly at room temperatures the natural state of the metal is crystalline.

The cleanup rate was highest for the metal which was most easily sputtered. When the cylinder of tantalum was sectioned into three portions it was found that recovery of argon was effected within one hour only

[10] G. K. Wehner, Phys. Rev. 108, 35 (1957).
[11] W. Buckel and R. Hilsch, Z. Physik 138, 109 (1954).

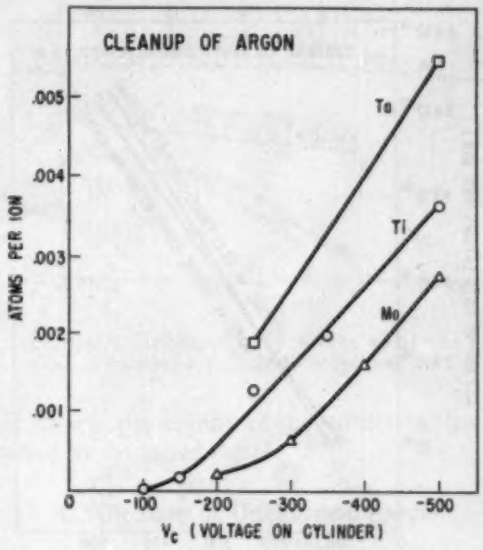

FIG. 4. Number of argon atoms cleaned up per argon ion striking cylinder as a function of voltage.

when the metal was heated to the evaporation point. The evolved gases were analyzed with a mass spectrometer. No argon was recovered from the center portion but the argon was found in the end regions of the cylinder where the sputtered metal had deposited. Less than a monolayer of argon was detected on the anode using the mass spectrometer technique even though the anode was covered with metal sputtered from the collector cylinder. It was evident that the cleaned-up gas was found with the sputtered metal on the collector and little found in the sputtered deposit on the anode.

Precise lattice parameter measurements[12] were made by Dr. C. W. Tucker on a sputtered deposit of nickel containing argon and a slight increase in the lattice parameter was indicated, but the change, if any, was less than 0.01%.

A tube was constructed of identical geometry to the above tube except that the collector cylinder had open ends and the cylinder had a length approximately twice that of the closed-end cylinder. If the cleanup were caused by ion penetration of the collector cylinder alone the cleanup rates should have been identical since the ion current to the cylinder was about the same with both tubes. Also the rate with the open-end cylinder should be higher, not lower if the glass walls of the tube contributed significantly to the cleanup in these experiments. Cleanup does proceed by ion penetration of the glass walls of a tube in an electrodeless discharge[9] but the rates are much smaller and can be neglected in the present work.

From the above experiment it can be seen that nonsaturating cleanup of inert gases in a gas discharge cannot proceed solely by a simple ion penetration mechanism, but on the contrary is intimately connected

[12] C. W. Tucker, Jr., and J. B. Sampson, Acta Met. 2, 433 (1954).

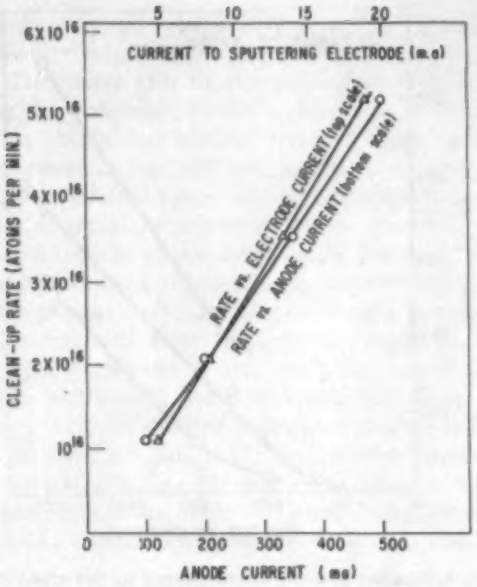

FIG. 5. Cleanup rate of argon proportional to anode current and to current to sputtering electrode.

with sputtering. It has recently been shown[13] mathematically that when there is cathode sputtering the amount of gas accumulated in a very thick plate has a limit that is independent of the rate of diffusion. The present work shows that the gas cleanup on a surface of nonuniform current density does not saturate. If the current density is uniform then the amount of cleanup is very small and there is no net cleanup after a small initial cleanup. The equations of Kuchai and Rodin[12]

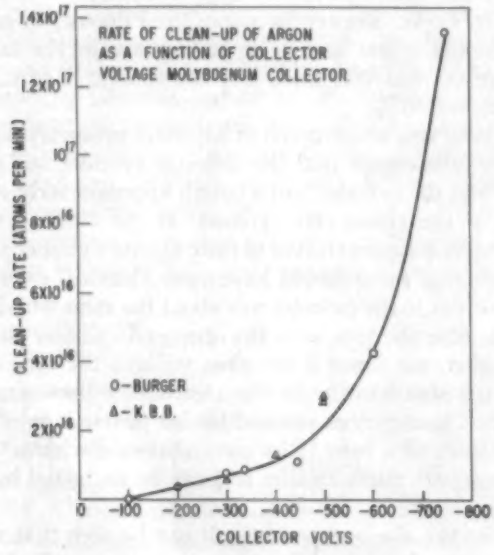

FIG. 6. Rate of cleanup of argon as a function of voltage on molybdenum collector.

[13] S. A. Kuchai and A. M. Rodin, Soviet J. Atomic Energy (English translation) 4, 277–282 (1958).

apply to the situation where the current density, i.e., the removal of metal atoms by sputtering is uniform.

The rate of cleanup with the above experimental tube shown in Fig. 1 is directly proportional to the anode current, i.e., decreasing the current by a factor of two halved the cleanup rate (Fig. 5). The rate is also proportional to the ion current collected by the cylinder. The rate of cleanup increased with increasing negative voltage of the molybdenum cylinder (Fig. 6). No measurable recovery of argon was made even when the metal parts were heated to 1500°C. The cleanup rate decreases with increasing temperature of the cylinder.

B. Cleanup as a Function of Potential on Collector Surface

A tube was built (Fig. 7) to determine the details of the attraction of argon to the metal surface. The inner cylinder was of such a size that the entire surface was bombarded with ions at a relatively high current density. This insured that sputtered metal did not remain on the inner cylinder but was quickly sputtered off. The

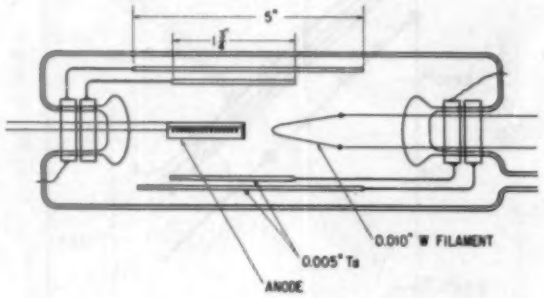

FIG. 7. Tube with two concentric cylinders.

potential of the outer cylinder could be varied independently. Metal sputtered from the inner cylinder landed on the outer cylinder tending to cover up argon. The data with constant anode current of 200 ma are shown in Fig. 8. Curve *A* shows the cleanup obtained with the outer cylinder at −350 v and the inner cylinder connected to the filament. Curve *B* shows the data with −350 v on the inner cylinder and the outer cylinder tied to the filament. Curve *C* was obtained with both cylinders at −350 v. The ion current to each of the two concentric cylinders as measured experimentally was substantially independent of the voltage on the outer cylinder. The cleanup rate with both cylinders negative was more than three times the sum of the other two rates. If the cleanup were only on account of ion penetration no such behavior would be expected and we would expect the rate with both cylinders negative to be the sum of the other two rates.

Figure 9 shows the effect on the rate of cleanup of varying the potential on the outer cylinder while holding the potential on the inner cylinder fixed at −350 v. The cleanup of argon appears to approach a limit at −400 v.

Resputtering from the outer cylinder would be expected to become more and more important as the voltage on the outer cylinder was made more negative. One would expect to liberate buried argon and the cleanup rate would be expected to approach a limit. However, the rate may be limited by the amount of sputtered metal available from the inner cylinder. It was observed that the cleanup rate was lower for a given voltage on the outer cylinder if the voltage on the inner cylinder and consequently the rate of sputtering was decreased. The positive ion current to the outer cylinder is relatively independent of voltage while the cleanup rate increases with voltage. An interesting feature of the data is the apparent threshold at -100 v. The cleanup at less negative voltages and even for slightly positive voltages is independent of the potential with respect to the discharge but is dependent on the amount of sputtered metal. This cleanup is then presumably caused by an uncharged species being buried.

It can be seen from the preceding data that the cleanup rate for argon is relatively independent of the voltage on the collector cylinder until -100 v is reached. The cleanup then increases with increasing velocity of the impinging ion. At the voltages of these experiments the cleanup of gas atoms is relatively inefficient and in Table I are shown the number of metal atoms sputtered for each gas atom cleaned up. Half the sputtered metal is assumed to stick to the collector cylinder. However, the trend to more efficient cleanup per incident ion is apparent from the table.

TABLE I. Ratio of Ta atoms sputtered to Ar atoms cleaned up as a function of voltage of ion collection.

Voltage on ion collector cylinder	No. of Ta atoms sputtered per sec	No. of Ar atoms cleaned up per sec	No. of Ar atoms cleaned up / No. of Ta atoms sputtered	No. of Ar atoms cleaned up / No. of ions striking collector
0	0.93×10^{16}	1.23×10^{15}	0.0133	...
-200	1.0	1.58	0.0159	0.00312
-350	1.0	2.50	0.0250	0.00435
-500	1.0	4.08	0.0416	0.00667
-800	1.23	7.0	0.0556	0.00834

The observed cleanup rates are greater at a given flux of metal vapor for the faster moving ions impinging on the collector surface. That is, the probability of cleanup of a given ion is higher, the higher its kinetic energy. This indicates that the time of deionization is not the critical factor for cleanup but rather a partial penetration effect of the ions. One would expect that a fast moving ion spends less time in the vicinity of the surface than a slow moving ion if it is simply reflected as an atom without penetration. A faster moving ion would penetrate further into the surface and hence spend a longer time in the vicinity of the surface so that it can be buried by sputtered metal.

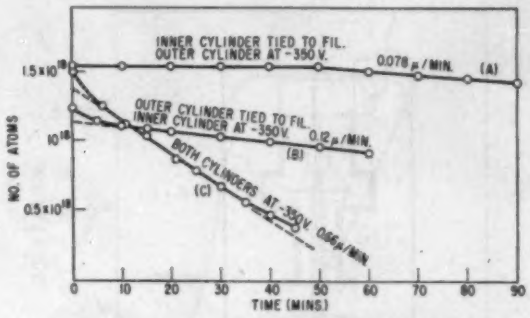

FIG. 8. Cleanup of argon in tube with two concentric cylindrical collectors.

C. Cleanup of Uncharged Species

At low collector voltages there is a small but definite rate of cleanup. This cleanup rate is also proportional to the amount of sputtered metal but is relatively independent of the collector cylinder voltage. The cleanup even occurs on positive surfaces and consequently is caused by an uncharged species.

Another tube was constructed to learn more about the variation of cleanup with voltage on the collector cylinder (Fig. 10). A discharge was maintained between the hot filament and a circular anode. A flat plate of Mo located in the axis of the cylinder was used as the source of sputtered metal. It was hoped that this construction would give a uniform current density over the surface of the sputtering electrode and this would prevent the buildup of any sputtered deposit on the electrode. The outer cylinder could be run at a fixed voltage with respect to the discharge. A magnetic coil surrounding the tube supplied an axial field that held the discharge inside the cylinder. Without the magnetic field the dis-

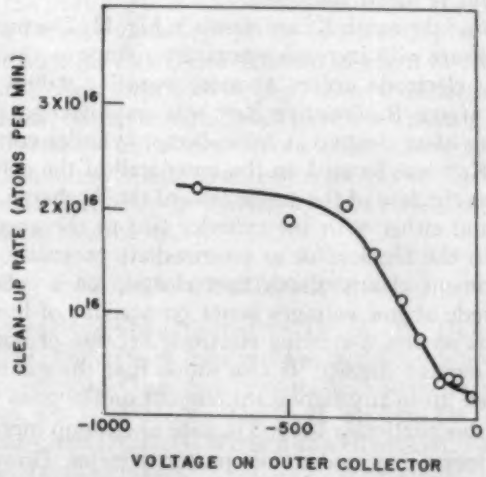

FIG. 9. Cleanup of argon in tube with two concentric cylindrical collectors, -350 v on inner collector.

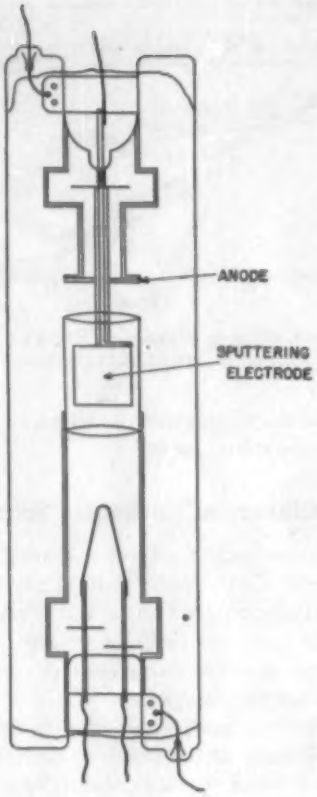

FIG. 10. Tube with axial sputtering electrode.

charge escaped outside the cylinder and the sputtering electrode received little current.

With the sputtering electrode at −500 v and the collector cylinder at filament potential the data of Table II were obtained. The rate of cleanup divided by the ion current to the sputtering electrode is a constant within the experimental error. Therefore, the cleanup at low collector voltages is directly proportional to the amount of metal sputtered.

Data taken with Kr are shown in Fig. 11. The increase in the rate with increasing negative voltage on the sputtering electrode occurs at more negative values than with argon. Radioactive Kr^{85} was employed to locate the gas after cleanup at *low* collector cylinder voltages. The Kr^{85} was located on the inner wall of the cylinder and on the face of the anode toward the discharge. This is found either with the cylinder tied to the anode or tied to the filament or at intermediate potential. This experiment clearly shows that cleanup on a collector electrode at low voltages is not on account of burying of ions on the sputtering electrode because of nonuniform current density. It also shows that the gas is not cleaned up to any significant amount on the glass walls with this particular tube. The rate of cleanup increases with increasing amount of sputtered metal. However, the rate is increased markedly for this tube by having two very negative surfaces, rather than one negative surface and a surface at some small potential. The cleanup can be enhanced at any give flux of metal vapor in a discharge by making the surface on which the sputtered metal lands negative.

The flux of metal vapor to the collector cylinder for the tube shown in Fig. 10 is, at −500 v, 6.8×10^{14} atoms/(cm² sec) while the cleanup rate for argon is 3.0×10^{12} atoms/(cm² sec). It would appear unlikely that the flux of metal vapor is acting like a vapor pump under these conditions.

The question that now arises is "Can van der Waal's binding account for the coverage of inert gas needed to explain the cleanup at low collector voltages?" Redhead[14] and others have demonstrated experimentally that inert gases do not absorb on surfaces at room temperature. Also, it is well known that evaporating a getter in the presence of an inert gas does not clean up inert gases while if this evaporation is done in the presence of a discharge there is cleanup. This again rules out van der Waal's binding.

Another possibility to be considered is that small amounts of gas are carried with the sputtered metal. However, the work of Bradley,[15] for example, using a mass spectrometer to analyze the sputtered metal vapor indicated that the sputtering agent was not carried over with the sputtered metal to any detectable degree.

The larger inert gas atom should have the larger van der Waal's binding energy. In Fig. 12 is shown the cleanup rate as a function of the voltage on the sputtering electrode for the tube shown in Fig. 10. The collector cylinder is at small negative or positive potentials and therefore the cleanup is caused by the uncharged species being buried by sputtered metal. The sputtering rate will increase as the voltage on the sputtering electrode increases. On Wehner's momentum interchange the heavier ion would be expected to sputter more metal. Since the lighter atom, Ne, is cleaned up at lower voltages, and hence lower sputtering rates the coverage for the uncharged Ne species on the collector surface at any given instant must be higher than for the heavier atoms.

TABLE II. Cleanup data with Mo sputtering electrode at −500 v in Ar.

Current to sputtering electrode (ma)	Ions (i_s) striking sputtering electrode (ions/sec)	Cleanup rate R (atoms/sec)	R/i_s (atoms/ion)
8.7	5.5×10^{16}	7.1×10^{13}	0.0013
11.0	6.9	9.1	0.0013
9.4	5.9	8.1	0.0014
6.7	4.2	5.7	0.0013
7.5	4.7	6.1	0.0013

[14] P. A. Redhead, American Vacuum Society Symposium, October, 1959.
[15] Richard C. Bradley, J. Appl. Phys. **30**, 1 (1959).

This coverage may be obtained by an increased impingement rate of uncharged species on the collector surface or a longer time of adsorption, i.e., a larger interaction energy. Lighter inert gases have longer lived metastables and hence larger concentrations in the gas discharge. The attractive interaction energy for metastable Ar, for example, as calculated by Hagstrum[16] is 0.3 ev. However, it is higher for Kr and lower for Ne. At the present time, it can be argued that metastable atoms can account for the slow cleanup rate when the collector cylinder voltage is low if one assumes the higher concentration of metastable atoms for the lower molecular weight gases overshadows the shorter time of adsorption.

Recovery of the cleaned-up inert gas in the sputtered metal deposits was never clearly shown to occur below the evaporation temperature of the metal. Hundreds of equivalent monolayers of argon have been cleaned up with total recoveries in the vicinity of one equivalent monolayer by heating. Recovery of more than an equivalent monolayer was effected in reasonable lengths of time only by heating to the evaporation temperatures of the particular metal. Diffusion of inert gases through metals was not evident since at temperatures where inert gas was released the evaporation of the metal was occurring. The recovery can be more easily explained by this evaporation than by diffusion of a large atom like argon through a metal.

CONCLUSIONS

From studying the effects of various materials and geometries it appears evident that the cleanup of rare gases in a tube containing metal electrodes is largely governed by two factors: first, the rate at which the metal is sputtered, and second, the potential of the surface on which the metal lands. There is evidence of a sharp increase in the cleanup rate at a definite kinetic energy of the impinging ion on the surface even though the amount of sputtered metal arriving from another surface is constant. The cleanup rate also increases with increasing velocity of the impinging ion up to a point where resputtering occurs. Argon ions are driven into the surface where they remain for a sufficient time to be trapped by the impinging metal.

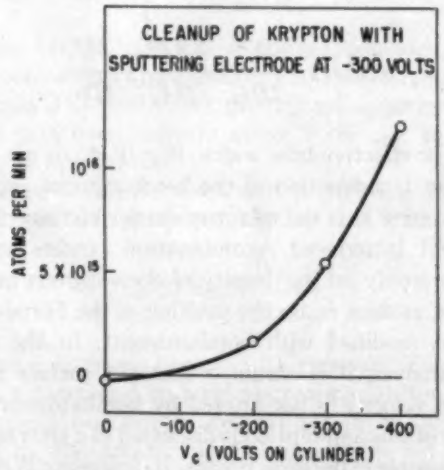

FIG. 11. Cleanup of krypton with sputtering electrode at −300 v as a function of cylinder voltage.

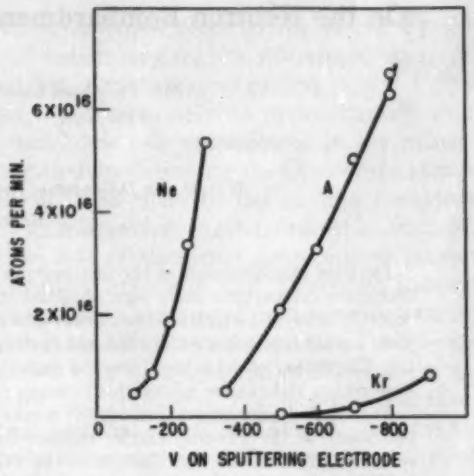

FIG. 12. Cleanup with negligible voltage on the cylinder as a function of voltage on sputtering electrode for Ne, Ar, and Kr.

The rate of cleanup at small positive or negative ion collector voltages is low but not zero. It can be explained by a burying of uncharged excited metastable gas atoms by sputtered metal.

Hundreds of equivalent monolayers of argon have been cleaned up with total recoveries in the vicinity of one equivalent monolayer by heating. Recovery of more than about an equivalent monolayer was effected in reasonable lengths of time only by heating to the evaporation temperatures for the metal. As the metal evaporates the buried gas is liberated. This shows that even with a forced "solubility" of the order of 1% we find no evidence for significant diffusion of argon in metals.

An electrode surface collecting ions at a uniform current density over the surface will have a net cleanup rate of zero after the initial cleanup of a small amount of gas. After the initial disappearance of some gas resputtering will occur liberating the cleaned up gas at the same rate it is being cleaned up.

ACKNOWLEDGMENT

The authors are indebted to Dr. A. W. Hull and Dr. J. M. Lafferty for their interest in this work and for the recommendations they have made, also to Dr. J. D. Cobine, Dr. L. P. Harris, Dr. G. H. Reiling, Dr. F. E. Williams, and Dr. D. G. Worden as well as G. A. Farrall for helpful discussions.

[16] H. Hagstrum, Phys. Rev. **96**, 226 (1954).

On the Neutron Bombardment Reduction of Transistor Current Gain*

J. W. EASLEY
Bell Telephone Laboratories, Inc., Whippany, New Jersey

AND

J. A. DOOLEY
Wright Air Development Center, Wright-Patterson Air Force Base, Ohio

(Received January 5, 1960)

Detailed measurements of the fast-neutron and gamma-ray bombardment behavior of germanium-alloy-transistor current-gain have been obtained concurrent with exposure. These data indicate that previously reported analyses, which lead to a linear dependence of common-base current-gain on fast neutron exposure, yield a good approximation for the *npn* device, but are not of general validity for the *pnp* germanium transistor. The extent of departure from the linear approximation depends on the width and conductivity of the base-region and can be appreciable in many cases of practical interest.

For the *pnp* germanium transistor it is necessary to take additional account of both changes during bombardment of the minority-carrier recombination rate at bombardment introduced and initially present recombination centers and changes in the width of the collector junction depletion layer. Observed bombardment curves are in good agreement with an analysis which includes these effects. From initial slopes of the current-gain bombardment curves, values of the product of fast-neutron-exposure times minority-carrier-lifetime at bombardment introduced recombination centers are 9.7×10^7 for 2.7 ohm-cm *p*-type and 14.2×10^7, 6.0×10^7, and 1.3×10^7, for 3.6 ohm-cm, 1.2 ohm-cm, and 0.2 ohm-cm *n*-type germanium, respectively, in units of sec-neutrons/cm².

INTRODUCTION

IT has been reported[1,2] on the basis of analysis and experiment that the common-base current gain of the transistor decreases linearly with fast neutron exposure. Although this is a good approximation for silicon and *npn* germanium transistors,[3] our experimental data show that it is not of general validity for the *pnp* germanium transistor. The extent of departure from the linear approximation depends on the width and conductivity of the base-region. This departure can be appreciable in many cases of practical interest.

For the *pnp* germanium case it is necessary to consider two effects which result from any appreciable bombardment induced change in the net donor concentration of the *n*-type[4] base region. The first is the decrease in recombination rate at bombardment introduced or initially present recombination centers as the Fermi-level moves toward the lower half of the band-gap; and the second is the change of effective base width, for a given applied collector voltage, as the collector depletion layer widens.

Consideration has been taken of these two effects in an analysis appropriate to the germanium-alloy structure. The alloy-transistor affords a considerable simplification in both analysis and experiment and although the following arguments will be quantitatively most exact for this structure the qualitative results apply to other structures. The application of this analysis provides a good fit to the observed bombardment curves for the current gain of both *pnp* and *npn* devices.

ANALYSIS

The case of a uniform conductivity base-region alloy-transistor will be considered herein for simplicity. The symbols employed are defined in the Appendix.

It can be shown that the injection efficiency and the collector multiplication factor are relatively insensitive to bombardment and the argument is therefore unchanged by considering $\gamma\equiv\alpha^*\equiv1$. Therefore, the current gain[5,6] can be written as:

$$\alpha(\Phi)=1-\frac{W^2}{2D\tau_0}-\frac{SA_eW}{DA_e}-\frac{W^2}{2D\tau_b}, \qquad (1)$$

where the effective base width, $W=W(\Phi)$, is not a constant but is a function of the bombardment exposure. The quantity τ_b is the minority carrier lifetime of bombardment introduced recombination centers and depends not only on the density of these centers but also depends, as does τ_0, on the position of the Fermi-level,[7] which is modified with bombardment. In the subsequent analysis it is assumed that the surface recombination velocity is not altered by bombardment. The validity of this assumption is discussed in a later section. A very simple expression results, if, following Webster,[6] it is assumed that surface recombination occurs predominantly in an annular region about the emitter of

* This work was supported by the Air Research and Development Command, United States Air Force.

[1] J. J. Loferski, J. Appl. Phys. **29**, 35 (1958).
[2] G. C. Messenger and J. P. Spratt, Proc. I.R.E. **46**, 1957 (1958).
[3] J. W. Easley, IRE-WESCON Conv. Rec. **3**, 149 (1958).
[4] J. W. Cleland, J. H. Crawford, and J. C. Pigg, Phys. Rev. **98**, 1742 (1955).
[5] W. Shockley, Bell System Tech. J. **28**, 435 (1949).
[6] W. M. Webster, Proc. I.R.E. **42**, 914 (1954).
[7] W. Shockley and W. T. Read, Phys. Rev. **87**, 835 (1952).

width W. Then the quantity $(1-\alpha)$ can be expressed as

$$(1-\alpha)(\Phi)=\left[(1-\alpha_0)+\frac{W_0^2}{2D\tau_b}\right]\left(\frac{W}{W_0}\right)^2, \quad (2)$$

where the zero subscripts denote initial unirradiated values and W and τ_b are the exposure dependent variables, since $dD/d\Phi \ll d\tau_b/d\Phi$. The value of effective base width is given by

$$W=d-X_m(\Phi), \quad (3)$$

where d is the geometric width of the base-region and $X_m(\Phi)$ is the width of the collector depletion layer. For constant applied voltage, the depletion layer width varies during a bombardment because the net donor acceptor concentration $N_I(\Phi)$ depends on exposure. This variation can be expressed and determined experimentally in terms of the collector capacity since[5]

$$X_m(\Phi)=4.3\times10^3(V/N_I)^{\frac{1}{2}}=1.44[A_c/C_c(\Phi)]\ \text{cm}, \quad (4)$$

where V is the collector voltage in volts, A_c the area of the collector junction in cm^2, $C_c(\Phi)$ the collector capacity in $\mu\mu$f, and the numerical coefficients are appropriate to germanium. In expression (2) the change in recombination rate at initially present centers has been neglected because the relative large values of τ_0 in germanium alloy transistors permit the neglect of these changes in the second term of expression (1). In transistors exhibiting initial low values of τ_0, such that at exposures of interest τ_0 and τ_b are of the same order of magnitude, this approximation may not be valid. Employing a first order approximation for this change in rate of recombination at bombardment introduced recombination centers, the quantity τ_b can be written as

$$\tau_b=(a+b\Phi)/\Phi. \quad (5)$$

Relations (2), (4), and (5), in conjunction with values for the constants a and b and the empirical relationships of Cleland *et al.*[4] for $N_I(\Phi)$, provide a description of the current gain bombardment curve applicable to either the *pnp* or *npn* device.

For cases in which $b\Phi \ll a$ and $W(\Phi)\simeq W_0$, Eqs. (1) and (2) reduce to the previously reported form

$$\alpha(\Phi)=\alpha_0-\frac{W_0^2}{2Da}\Phi \quad (6)$$

by which α decreases linearly with exposure. These conditions are satisfied to good approximation for p-type base-regions but not in general for those of n-type caused by the greater relative change in net carrier concentration for equal exposure and generally larger values of b for the latter material.

EXPERIMENTAL PROCEDURE

Bombardment curves of current gain have been obtained from measurements of $(1-\alpha)$ concurrent with irradiation. A fission plate source at the Brookhaven National Laboratory reactor was employed to provide a mixed flux of neutrons and gamma rays. A Co^{60} source was employed separately to approximately duplicate the gamma dose-rate encountered in the mixed spectrum and thereby determine the effect of the gamma-ray component. The effect of the gamma component on current gain behavior was determined to be negligible.

Various lots of transistor samples were prepared at the Allentown branch of Bell Telephone Laboratories with as uniform characteristics as possible except for a variation in base-width within each lot. For *npn* devices, a single lot with base material of 2.7 ohm-cm average resistivity was employed. For *pnp* devices, three lots with base material of 3.6, 1.2, and 0.2 ohm-cm average resistivity were employed. These values of initial base resistivity were determined from collector and emitter junction capacity and area measurements. Values of initial base widths employed in all calculations were determined indirectly from frequency cutoff measurements for each unit. For these determinations, values of the diffusion constant D as reported by Prince[6] were employed. Direct measurements from subsequent cross sections of approximately 10% of the devices yield values of base width which are on the average 15% less than those obtained indirectly from electrical measurement.

Values of $(1-\alpha)$ were obtained from small signal measurements and recorded on a Leeds and Northrup recorder with a duty cycle of 8% per device, ten of which were employed per bombardment. The calibration of the complete measurement channel was similarly monitored. The resultant bombardment curves and the calibration record, which each comprise more than a hundred data points, are, therefore, essentially continuous. The maximum experimental error in the measured value of $(1-\alpha)$ is estimated as approximately 3% so that the measurement uncertainty in α is of the order of a few tenths of a percent. The emitter bias for all measurements was approximately 0.3 amp/cm^2 so that any correction to the low current level approximation, implicit in Eq. (1), should be small.

The temperature of the transistors was monitored throughout the bombardments by a thermocouple soldered to the case of one of the ten devices measured during a bombardment. The case of these devices was in good thermal contact with the collector. The recorded temperature was constant to within a few tenths of a degree centigrade throughout the bombardments.

The values of fast neutron exposure employed herein were determined from the measured change in conductivity of approximately 2 ohm-cm n-type Ge exposed with the transistors in each bombardment. The observed conductivity change was converted to a value of "fast neutron flux," employing the data of Cleland *et al.*[4] Values of fast neutron flux for neutrons of energy

[6] M. B. Prince, Phys. Rev. 92, 681 (1953).

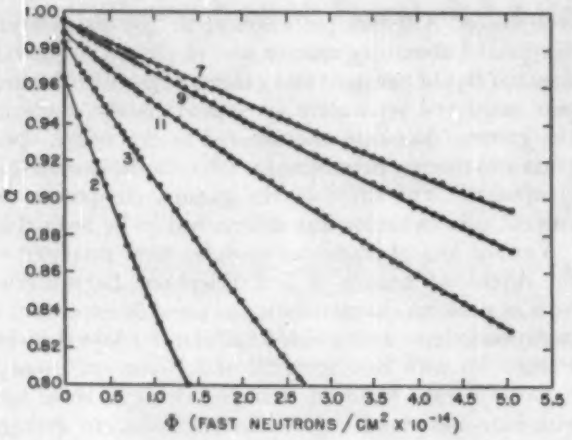

FIG. 1. Representative bombardment curves for five *npn* germanium-alloy-transistors of 2.7 ohm-cm resistivity base-material. The values of frequency cutoff are 7.2, 5.8, 5.0, 2.4, and 1.4 Mc for units 7, 9, 11, 3, and 2, respectively. The solid lines each consist of a smooth curve drawn through the experimental points.

greater than 0.1 Mev obtained by threshold-reaction activation techniques indicate that the fast neutron exposure determined and specified in this manner is approximately 60% of that determined from the conductivity alteration method. The values obtained from conductivity alteration are employed herein as a convenience in correlating data with that of the ORNL group.[4,9]

DATA AND DISCUSSION

Representative bombardment curves of current gain vs fast neutron exposure for the 2.7 ohm-cm *p*-type base transistors are shown in Fig. 1. The curves shown have been selected to include units over the range of base width available in the sample lot. The approximations

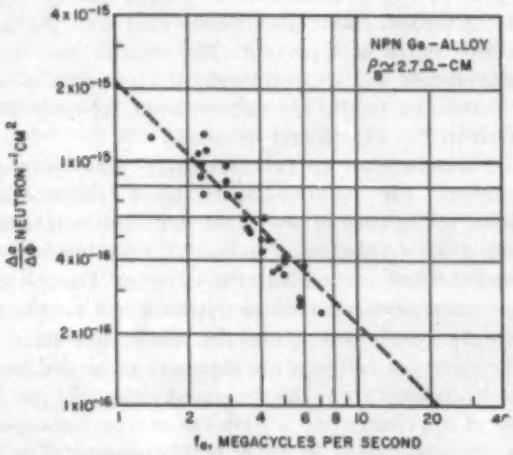

FIG. 2. Values of the initial slope of the bombardment curves versus frequency cutoff for 2.7 ohm-cm base-material *npn* transistors.

[9] O. L. Curtis, Jr., J. W. Cleland, and J. H. Crawford, Jr., J. Appl. Phys. 29, 1722 (1958).

of Eq. (6) are valid and an approximately linear $\alpha-\Phi$ relationship is observed. The small departure from linearity is attributed to annealing of damage during the bombardment. Since the frequency cutoff of the current gain[5] is inversely proportional to W^2, Eq. (6) predicts a slope of the α vs Φ curve inversely proportional to frequency cutoff for any given base material, injection level and junction temperature. Values of the observed initial slope vs frequency cutoff for the 27 samples measured of this lot are shown in Fig. 2. The dotted line is that determined via Eq. (6) employing the average value of the constant $a=\tau_0\Phi$ computed from the measured data. Values of a determined from the initial slopes of the bombardment curves and corresponding to the pre-bombardment base-material resistivity of the four sample lots are tabulated in Table I. The departures of individual points from the average is most likely on account of random errors in the frequency cutoff measurements and departures in device structure from the model on which Eq. (1) is based. Any variations in base resistivity among samples of a lot also result in a displacement of a point perpendicular to the average line and contributes to the spread.

TABLE I. Values of the product $\tau_0\Phi=a$ corresponding to various prebombardment values of germanium base-material resistivity as determined through Eq. (6).

Base	Resistivity ohm-cm	a sec cm^{-2}
p-type	2.7	$9.7\pm1.3\times10^7$
n-type	3.6	$14.2\pm2.1\times10^7$
	1.2	$6.0\pm0.9\times10^7$
	0.2	$1.3\pm0.3\times10^7$

Representative bombardment curves of current gain vs fast neutron exposure for the 1.2 ohm-cm *n*-type base transistors are shown in Fig. 3. As in Fig. 1, the curves have been selected to include units over the range of base width available in the sample lot. A distinct curvature is observed for these *n*-type base region units in contrast to the approximately linear curves for the *p*-type base units. Values of W_0^2/D of Eq. (2) cover a similar range for the two cases. For the exposure durations employed, the α vs Φ curves for the units of smaller W_0 exhibit a minimum, gradual increase and subsequent sudden rapid decrease. The point of initiation of this rapid decrease corresponds to "punch-through" or contact of the collector depletion layer with the emitter. The approximations of Eq. (6), as discussed previously, are not valid for *pnp* units and Eq. (2) must be employed. The initial or approximately zero exposure value of the slope is to good approximation given by

$$\lim_{\Phi\to0}\left(\frac{\Delta\alpha}{\Delta\Phi}\right)\simeq-\frac{W_0^2}{2Da}, \tag{7}$$

and consequently the relationship between initial slope,

frequency cutoff and the constant a is equivalent to that for the *npn* devices discussed previously. Values of the observed initial slope vs frequency cutoff for the 38 samples measured of the 1.2 ohm-cm resistivity *n*-type base material are shown in Fig. 4. The dashed line is determined as in Fig. 2 and the consideration of dispersion of points is equivalent. Bombardment curves obtained from ten samples each for equivalent devices of 3.6 and 0.2 ohm-cm *n*-type base material are qualitatively similar to those shown in Fig. 3 except for those differences expected from the different initial resistivities and the associated differences in recombination rates at bombardment introduced recombination centers. In the devices of 3.6 ohm-cm base material the slopes of the α vs Φ curves are substantially less and punch-through occurs at an earlier point in the exposure history. In the devices of 0.2 ohm-cm base material the

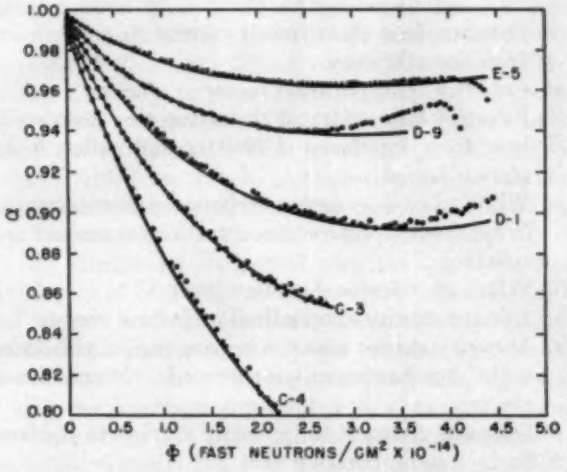

FIG. 3. Representative bombardment curves for five *pnp* germanium-alloy-transistors of 1.2 ohm-cm resistivity base-material. The values of frequency cutoff are 9.8, 6.0, 4.7, 2.7, and 2.3 Mc for units E-5, D-9, D-1, C-3, and C-4, respectively. The solid lines are those calculated from Eqs. (1) and (5) as outlined in the text.

slopes of the bombardment curves are substantially greater. For values of base width available in these samples, α is drastically reduced (i.e., to the order of 0.5) by exposure in which the term $b\Phi$ is small compared with a [see Eq. (5)] and consequently only a small amount of curvature is observed. For this initial resistivity, punch-through is not observed for exposures of the order of magnitude obtained.

From Eqs. (1), (4), and (5), values of the constants a and b of Eq. (5) required to fit each of the 38 measured bombardment curves of the 1.2 ohm-cm base material devices have been determined. The calculations are not sensitive to the relative values of τ_0 and S. An estimated value of τ_0 equal to 10 μsec was employed and the corresponding value of S obtained from the preirradiation values of $(1-\alpha)$. The average value of the constant a employed to fit the curves was $6.0\pm0.9\times10^{7}$ sec-neutrons/cm² and was determined from the initial slope

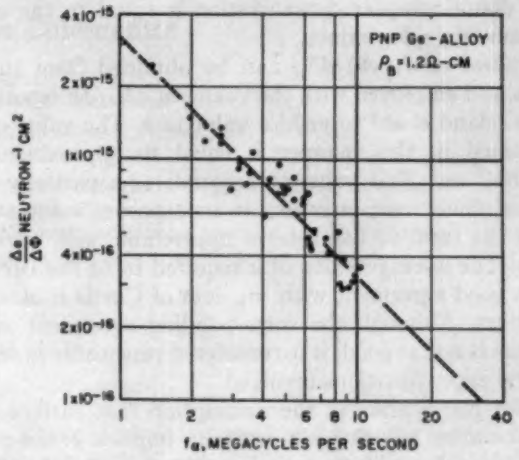

FIG. 4. Values of the initial slope of the bombardment curves versus frequency cutoff for 1.2 ohm-cm base-material *pnp* transistors.

in the vicinity of zero bombardment, as previously mentioned. The average value of b required to fit the curves was $2.5\pm0.4\times10^{-7}$ sec. The fit obtained from these constants begins to depart from the observed curves in the latter portion of the exposure, as shown in Fig. 3. This arises in part from a less rapid decrease in τ_b with Φ than is given by the first-order approximation of Eq. (5). A portion of this departure is also possibly caused by the effect of departures from uniform planarity of the collector and emitter interfaces.

These values of curve fitting parameters can be compared with values obtained independently from other data. Values of $\tau_b\Phi$ products obtained from initial slopes of the bombardment curves for three sample lots and from other sources[9,10] are plotted versus equilibrium electron concentrations in Fig. 5. The value of a for any

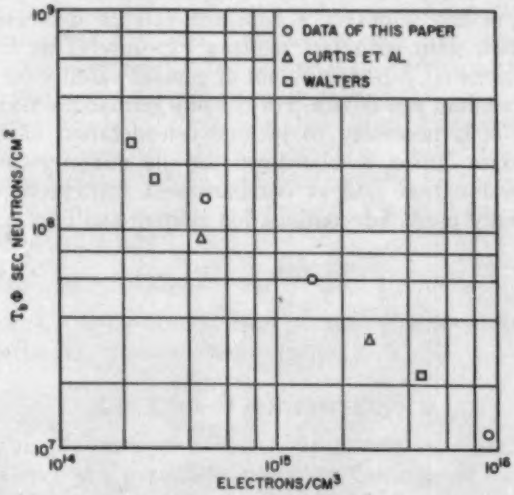

FIG. 5. Values of the product $\tau_b\Phi=a$ versus equilibrium electron concentration for *n*-type germanium from the data of Curtis *et al.*,[9] Walters,[10] and that reported in this paper.

[10] A. E. Walters, private communication.

net donor-acceptor concentration is equal to the corresponding $\tau_0\Phi$ product.

Values of $d(\tau_0\Phi)/dN_I$ can be obtained from these data and employed with the values of $dN_I/d\Phi$ reported by Cleland *et al.*[4] to yield a value of b. The value of b obtained in this manner is equal to approximately 1×10^{-7} sec. This value corresponds to a partially reduced donor concentration at an exposure value such that the term $b\Phi$ has become appreciable with respect to a. The average value of a required to fit the curves is in good agreement with the data of Curtis *et al.* and Walters. Although the corresponding agreement in b values is not as good, it is considered reasonable in view of the approximations involved.

The justification of the assumption that surface recombination velocity is a constant, implicit in the preceding analysis, is based on correlation between the results of analysis and observed behavior, and on the post-irradiation re-etch of devices. The *npn* bombardment curves and relation (1) require that any variation in surface recombination velocity be either small or varying approximately linearly with bombardment. The latter appears unlikely as the bombardment alteration of other surface sensitive parameters which have been measured is generally observed to saturate early in a bombardment. The bombardment behavior of current gain has been observed to not be sensitive to variations in initial surface conditions and ambients. Post-irradiation re-etch and subsequent measurement of current gain indicates that the bombardment alteration of the surface recombination velocity is negligible after any appreciable exposure.

CONCLUSIONS

The bombardment curves of current gain versus integrated fast neutron flux for the *npn* germanium transistor are represented to good approximation by relation (6), which indicates a constant rate of decrease of current gain with fast neutron exposure. This linear relationship, however, is not of general validity for the germanium *pnp* device. For the *pnp* germanium transistor, it is necessary to include consideration of both changes during bombardment of the minority-carrier recombination rate at bombardment introduced and initially present recombination centers and changes in the width of the collector junction depletion layer. A good approximation to the major portion of the observed current gain-exposure curves can be obtained through expressions (1), (4), and (5). The constants required to fit the curves are in reasonable agreement with independently determined macroscopic electrical properties of the semiconductor material.

ACKNOWLEDGMENTS

The authors wish to express their appreciation for the assistance of W. P. Knox and G. Kiriokos in the preparation of experimental apparatus and Mrs. A. K. Knoop for assistance in the considerable amount of data reduction and numerical calculation.

APPENDIX

Symbols Employed in Text

- α Common-base short circuit current gain
- γ Injection efficiency
- α^* Collector multiplication factor
- W Effective base width of transistor, i.e., distance in base from interfaces of emitter and collector depletion layers
- d Width of base as measured between discontinuities in net donor-acceptor concentrations at emitter and collector
- X_m Width of collector depletion layer
- τ_0 Initial minority carrier lifetime in base region
- τ_b Minority carrier lifetime in base region associated with bombardment introduced recombination centers
- D Diffusion constant for minority carriers in the base
- S Surface recombination velocity
- A_s Effective surface recombination area
- A_e Emitter junction area
- A_c Collector junction area
- Φ Fast neutron exposure, i.e., integrated fast neutron flux
- N_I Net donor-acceptor concentration in base
- C_c Collector capacity
- a Constant defined by Eq. (5) and equal to the product $\tau_0\Phi$ for any given resistivity
- b Constant defined by Eq. (5)

JOURNAL OF APPLIED PHYSICS VOLUME 31, NUMBER 6 JUNE, 1960

Bias in Ferroelectric Colemanite

ENNIO FATUZZO
Laboratories RCA Limited, Zurich, Switzerland

(Received January 25, 1960; revised manuscript received February 29, 1960)

The question of the existence of an intrinsic bias in colemanite *above* the Curie point is studied and compared with experimental results. It is concluded that a bias does exist above the Curie point and that it is completely responsible for the pyroeffect experimentally observed there. Some formulas are derived, connecting the pyroeffect and the intrinsic bias, and are compared with data available in the literature.

1. INTRODUCTION

COLEMANITE is a mineral found to be ferroelectric by Goldsmith[1] and previously reported to be pyroelectric by Davisson.[2] The Curie temperature is about -2.5°C at which a second-order transition to a paraelectric state occurs. Like other materials, colemanite often gives a biased hysteresis loop. Wieder[3] studied the dielectric properties of colemanite and investigated their dependence on bias below the Curie point. Contrary to expectations based on the crystal symmetry, colemanite also shows a pyroelectric effect *above* the Curie point. The pyroelectric coefficient decreases with temperature and approaches zero for temperatures much higher than the Curie point as shown by Chynoweth.[4]

Our studies are concerned with the question: Does an electrical bias exist *above* the Curie point T_0 and if so, is there some correlation between this bias and the pyroeffect? In the present paper we first will develop Devonshire's[5] theory for the case where bias is present. Using the information provided by these calculations, we will study the experimental techniques which are suitable to reveal the bias above the Curie point. We then find some theoretical relations between bias and pyroeffect with which we can check our experimental results and other results available in the literature.

2. MATHEMATICAL DEVELOPMENT

2.1. Case of Nonbiased Crystal

Devonshire[5] has formulated a thermodynamical theory of the dielectric behavior of ferroelectrics which applies with success to both first- and second-order transitions.

He develops the free energy F into powers of P:

$$F=F_0+\tfrac{1}{2}[\beta(T-T_0)]P^2+\gamma(\tfrac{1}{4}P^4)+\delta(\tfrac{1}{6}P^6). \quad (1)$$

In a second-order transition the term with P^6 in Eq. (1) is usually negligible so that we can write

$$F=F_0+\tfrac{1}{2}[\beta(T-T_0)]P^2+\gamma(\tfrac{1}{4}P^4) \quad (2)$$

and hence

$$|\partial F/\partial P|_{T=\text{const}}=E=\beta(T-T_0)P+\gamma P^3. \quad (3)$$

Equation (3) does not yield an hysteresis loop directly. However, it is assumed that a negative dP/dE slope must be considered a region of unstable equilibrium with a corresponding jump to a positive slope. With this assumption, Eq. (3) yields a *symmetrical* hysteresis loop.

The equilibrium states are given at $E=0$ so that

$$P_s=0 \quad \text{or} \quad P_s=\pm[\beta(T_0-T)/\gamma]^{\frac{1}{2}}. \quad (4)$$

The solution $P_s=0$, however, corresponds to an unstable state below the Curie point. The pyroelectric coefficient π *below* T_0 is then given by

$$\pi=dP_s/dT=\pm(\beta^{\frac{1}{2}}/2\gamma^{\frac{1}{2}})(T_0-T)^{-\frac{1}{2}}. \quad (5)$$

Above T_0 the solution $P_s=[\beta(T_0-T)/\gamma]^{\frac{1}{2}}$ is imaginary, thus $P_s=0$ is the only real solution for a second-order transition, so that

$$\pi=dP_s/dT=0.$$

From Eq. (3) it follows that

$$|\partial E/\partial P|_{T=\text{const}}\cong 4\pi/\epsilon=\beta(T-T_0)+3\gamma P^2. \quad (6)$$

This expression is valid when the dielectric constant is measured at $T=$const. In practice, however, what is normally measured is the *adiabatic* dielectric constant, and therefore a correction must be made.

The adiabatic correction has been calculated by Baumgartner[6] for KH_2PO_4, by Triebwasser[7] for triglycine sulfate, by Wieder[3] for colemanite, by Drougard *et al.*[8] for $BaTiO_3$, and by Känzig[9] in a general way. For colemanite one finds

$$4\pi/\epsilon=\beta(T-T_0)+[3\gamma+(\beta^2T/C_P')]P^2, \quad (7)$$

where C_P' is the specific heat per unit volume when the polarization is maintained constant.

2.2. Case of a Biased Crystal

The presence of a biased hysteresis loop and the existence of a pyroeffect above the Curie point may be

[1] G. J. Goldsmith, Bull. Am. Phys. Soc. Ser. II, **1**, 322 (1956).
[2] J. W. Davisson, Bull. Am. Phys. Soc. Ser.II, **1**, 177 (1956).
[3] H. H. Wieder, J. Appl. Phys. **30**, 1010 (1959).
[4] A. G. Chynoweth, Acta Cryst. **10**, 511 (1957).
[5] A. F. Devonshire, Phil. Mag. **3**, 85 (1954).
[6] H. Baumgartner, Helv. Phys. Acta **23**, 651 (1950).
[7] S. Triebwasser, IBM J. Research Develop. **2**, 212 (1958).
[8] M. E. Drougard, R. Landauer, and D. R. Young Phys. Rev. **98**, 1010 (1955).
[9] W. Känzig, Solid State Physics **4**, 29 (1957).

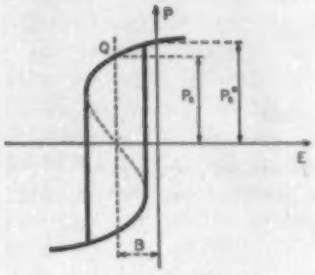

FIG. 1. Biased hysteresis loop, from Devonshire's equations.

accounted for by introducing a constant term B in Eq. (3) which is valid for a second-order transition:

$$E=B+\beta(T-T_0)P+\gamma P^3. \tag{8}$$

The equilibrium states P_s are given by

$$\gamma P_s^3+\beta(T-T_0)P_s+B=0. \tag{9}$$

If the bias is sufficiently strong (see Fig. 1) there is *just one* equilibrium position P_s^*. It can be seen that the necessary and sufficient condition for the presence of a hysteresis loop is the presence of one maximum and of one minimum point in the E vs P curve, i.e., the presence of two points of inflection in the F vs P curve. In other words, the equation

$$3\gamma P^2+\beta(T-T_0)=0, \tag{10}$$

must have two real solutions below the Curie point. Since Eq. (10) has two real solutions when $T<T_0$ and none when $T>T_0$, we conclude that T_0 is still the Curie point for the biased crystal. Therefore, a second-order transition is neither shifted nor blurred by the presence of the bias under consideration at least in first approximation. The fact that P_s^* does not go to zero at T_0 when bias is present, does not mean (Fig. 2) that the material is still in a ferroelectric state above T_0; it simply means that, due to the bias, even without an applied field, the material has a spontaneous polarization (in one direction only).

However, in contrast to the Curie point, what is shifted by an intrinsic bias is the peak in the dielectric constant vs temperature, as was shown by Wieder.[3] He finds that under the influence of a bias the peak in the dielectric constant does not occur at the Curie point any more, but at a higher temperature T_p. This temperature T_p is a function of the bias and has its minimum when the applied field counterbalances the intrinsic bias. Thus, a method to measure the bias (around the Curie point) is by looking for the dc field that minimizes the temperature T_p.

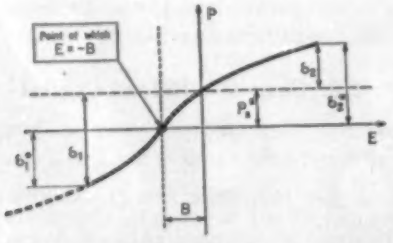

FIG. 2. P vs E just above the Curie point for a biased crystal, from Devonshire's equations.

Unlike the second-order transition which we have discussed so far, in a first-order transition an intrinsic bias does shift the Curie point upwards. This shift is related to the appearance of double loops just above the Curie temperature.[10]

2.3. Measuring Techniques for the Bias

2.3.1. Techniques below the Curie Point

One way to determine the bias below the Curie point T_0 is by measuring the displacement of the hysteresis loop with respect to the origin of the coordinate system. This is the most straightforward and simple way.

There is also a second method. In Fig. 3 we have plotted F, E, and the adiabatic reciprocal dielectric constant $1/\epsilon$ as a function of P for an *unbiased* crystal below the Curie point. The behavior of $1/\epsilon$ vs P can be obtained from Eq. (7). One can see (Fig. 3c) that at the two equilibrium positions, $1/\epsilon$ has a finite value. We first polarize the sample in one direction and then apply a dc field in the same direction, so as to increase P. We can see from Fig. 3(c) that $1/\epsilon$ then increases. Alternatively, we first polarize the sample in the opposite direction and we then apply a field in this new direction, so as to increase again $|P|$. We can see from Fig. 3(c) that $1/\epsilon$ again increases. The curve $1/\epsilon$ vs E *measured this way* is like that shown in Fig. 4(a): the minimum occurs at $E=0$.

Let us now consider the case of a biased crystal. In this case we can use the same technique as described in the foregoing and plot $1/\epsilon$ vs E under the same condi-

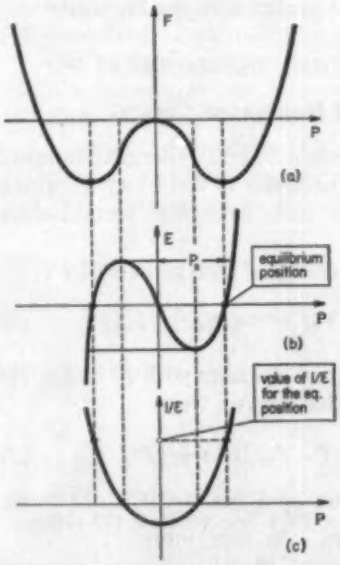

FIG. 3. (a) F vs P, from Devonshire's equations, for a nonbiased crystal. (b) E vs P, from Devonshire's equations, for a nonbiased crystal. (c) Adiabatic $1/\epsilon$ vs P, derived from Devonshire's equations, for a nonbiased crystal.

[10] W. J. Merz, Phys. Rev. 91, 513 (1953).

tions. By differentiating Eq. (8) and taking into account also the adiabatic corrections, it can be seen that the shape of the curve $1/\epsilon$ (adiabatic) vs P is not changed if a bias is present. With a bias $+B$, the minimum in $1/\epsilon$ occurs when the applied field E counterbalances this intrinsic bias (Fig. 4b). Thus, the second way to measure the bias below the Curie point is by looking for the value of an applied dc field that maximizes the dielectric constant under the experimental conditions just described. This value of the applied dc field is then equal to the intrinsic bias.

2.3.2. *Techniques above the Curie Point*

In ferroelectrics, just above the Curie temperature, the P vs E relationship measured with a loop tracer at 50 cps is not linear, because of the presence of the third power term in Eq. (3). Furthermore, the adiabatic corrections[11] add[8,9] odd power terms in P to Eq. (3). When the crystal is not biased, the nonlinearities are symmetrical with respect to $E=0$; when it is biased, the symmetry is destroyed (see Fig. 2). In particular, the quantities δ_1 and δ_2 (Fig. 2) are not equal when bias is present, so that $\delta=\delta_1-\delta_2$ is not zero. We can establish the dependence of the quantity δ on the bias B, from which we can compute the value of B above the Curie point.

Let us assume that the deviations from nonlinearity are very small, so that one can neglect the higher power terms in P and can write

$$E\cong\beta(T-T_0)P+KP^3, \tag{11}$$

where KP^3 represents the deviations from nonlinearity and includes both the term γP^3 of Eq. (3) and the adiabatic corrections.

One can then show that (see Appendix)

$$P=\gamma_1 E-\gamma_3 E^3,$$

where $\gamma_1=1/\beta\Delta T$ and $\gamma_3=K/\beta^4\Delta T^4$, and $\Delta T=T-T_0$.

From this, one can derive (see Appendix)

$$\delta=\delta_1-\delta_2=6\gamma_3 E^2 B=6(K/\beta^4\Delta T^4)E^2 B; \tag{12}$$

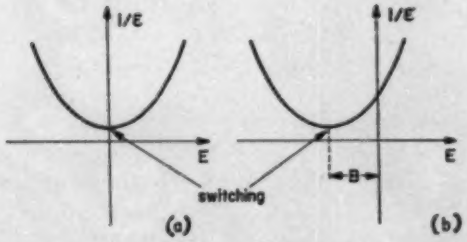

FIG. 4. (a) Theoretical form of $1/\epsilon$ vs E below T_0 for a nonbiased crystal. (b) Theoretical form of $1/\epsilon$ vs E below T_0 for a biased crystal.

[11] Here the field applied to the crystal is not dc but 50 cps, so that one has to take into account also the electrocaloric effect[10] as Drougard *et al.*[8] did for $BaTiO_3$.

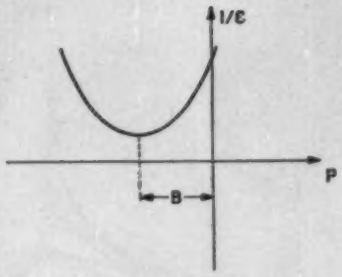

FIG. 5. Theoretical form of $1/\epsilon$ vs E above T_0 for a biased crystal.

hence,

$$B=\delta/6\gamma_3 E^2.$$

If we apply a dc field Δ^*, we observe and additional deviation δ^*, thus,

$$B+\Delta^*=(\delta+\delta^*)/6\gamma_3 E^2$$

and

$$\Delta^*/B=\delta^*/\delta,$$

from which follows that

$$B=\Delta^*\delta/\delta^*.$$

This method of measuring the bias above the Curie point, however, becomes very inaccurate already a few degrees above the Curie temperature, because δ decreases very rapidly with temperature [Eq. (12)].

A second way to measure the bias above T_0 with a higher accuracy than the previous method is the following. As we have shown in Sec. 2.3.1, Eq. (7) is valid also for a biased crystal:

$$4\pi/\epsilon=\beta(T-T_0)+[3\gamma+(\beta^2 T/C_P')]P^2.$$

For $T>T_0$, $1/\epsilon$ is always greater than zero and reaches its minimum at $P=0$. If the sample is biased, $1/\epsilon$ is not at its minimum when $E=0$. The minimum is reached when a field is applied that counterbalances the internal bias so that $P=0$. Here again, if one plots $1/\epsilon$ vs E, one finds a curve like Fig. 5, where the distance of the minimum from the $1/\epsilon$ axis gives the intrinsic bias. This result is similar to that obtained in Sec. 2.3.1 for the case of a sample below the Curie point.

2.4. Correlation between Bias and Pyroeffect

It was observed[4] that in colemanite the pyroeffect occurs both below and above the Curie point T_0. Crystal symmetry, however, does not allow a pyroeffect above T_0. Let us now study whether a bias can be responsible for the pyroeffect above T_0. For a biased crystal, above T_0, P_s is different from zero as we have shown before. Furthermore, since P_s varies with temperature, the pyroelectric coefficient π above T_0 has also to be different from zero.

Differentiating Eq. (9) with respect to temperature, one finds

$$3\gamma P_s^2 dP_s/dT+\beta(T-T_0)dP_s/dT+\beta P_s=0 \tag{13}$$

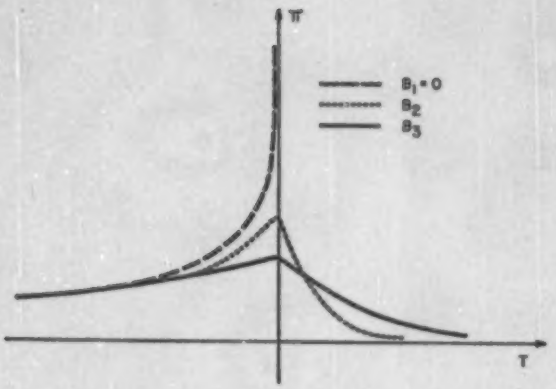

FIG. 6. Theoretical pyroelectric coefficient vs temperature T for different values of the intrinsic bias B: $B_1=0$; $B_3=3.4B_2$.

and hence

$$\pi=dP_s/dT=-\beta P_s/[3\gamma P_s^2+\beta(T-T_0)]. \quad (14)$$

Above the Curie point P_s is usually very small, so that 2°C or 3°C above it we can write

$$\beta(T_0-T)\gg 3\gamma P_s^2$$

which then transforms Eq. (14) into

$$\pi=-P_s/(T-T_0).$$

Neglecting the P^3 term for the same reason, it follows from Eq. (9) that

$$P_s\cong -B/\beta(T-T_0),$$

so that

$$\pi=B/\beta(T-T_0)^2. \quad (15)$$

Thus, above the Curie temperature and so far from it that

$$T_0-T\gg 3\gamma P_s^2\beta^{-1},$$

π decreases like $1/(T-T_0)^2$.

Let us now look at the situation at temperatures below the Curie point and so far from it that the hysteresis loop is rectangular.[12]

There the value P_s^* of the spontaneous polarization with the presence of a bias B is not very different from the value P_s without bias (see Fig. 1). In this case we find, with Eqs. (4) and (5),

$$P_s^*\cong P_s=\pm[\beta(T_0-T)/\gamma]^{\frac{1}{2}}$$

and

$$\pi=(\beta^{\frac{1}{2}}/2\gamma^{\frac{1}{2}})[1/(T_0-T)^{\frac{1}{2}}].$$

Thus, below the Curie temperature and far enough from it, π increases with temperature according to $1/(T_0-T)^{\frac{1}{2}}$. Since with increasing T, π increases below T_0 and decreases above T_0, we expect that somewhere around the Curie point T_0, there is a maximum for π.

Differentiating Eq. (13) once more, one obtains

$$[3\gamma P_s^2+\beta(T-T_0)]d\pi/dT=-2\beta\pi-6\gamma P_s\pi^2,$$

so that

$$d\pi/dT=-2\pi\{(\beta+3\gamma\pi P_s)/[3\gamma P_s^2+\beta(T-T_0)]\}.$$

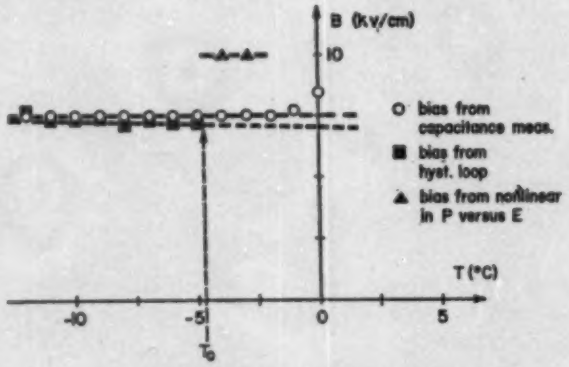

FIG. 8. Experimental intrinsic bias B vs temperature.

Hence, $d\pi/dT$ is zero when $\pi=0$ or when $(\beta+3\gamma\pi P_s)=0$. Since $\pi=0$ only when $T=\pm\infty$, we just consider the second case $d\pi/dT=0$, when

$$\pi=-\beta/3\gamma P_s. \quad (16)$$

Substituting Eq. (14) into Eq. (16) gives $d\pi/dT=0$ when

$$-\beta P_s/[3\gamma P_s^2+\beta(T-T_0)]=-\beta/3\gamma P_s,$$

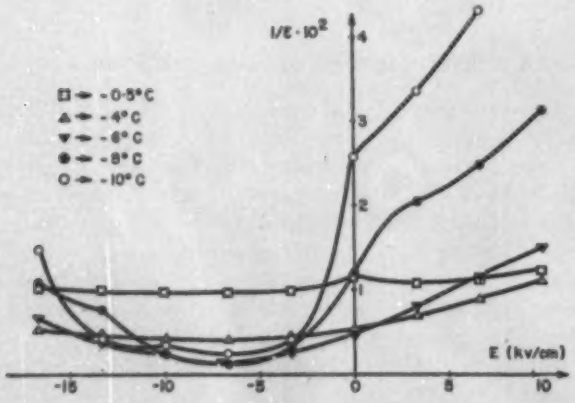

FIG. 7. Experimental $1/\epsilon$ vs E for different values of the temperature T.

[12] This condition means, analytically, that (Fig. 1)

$$P_s^*-P_s\ll P_s.$$

If s is the slope of the hysteresis loop at the point Q (Fig. 1), it follows that

$$P_s^*-P_s\cong sB.$$

From Eqs. (6) and (4) it can easily be seen that

$$s=1/2\beta(T_0-T),$$

so that [see again Eq. (4)] the preceding condition corresponds to

$$B/2\beta(T_0-T)\ll[\beta(T_0-T)/\gamma]^{\frac{1}{2}},$$

and further, that,

$$T_0-T\gg 2^{-\frac{1}{2}}B^{\frac{1}{2}}\beta^{-\frac{1}{2}}\gamma^{\frac{1}{2}}.$$

i.e., $d\pi/dT=0$ when $T=T_0$, which leads to the conclusion that the maximum in π occurs always at the Curie point T_0. At $T=T_0$ we obtain from Eq. (14)

$$\pi=-\beta/3\gamma P_s,$$

and from Eq. (9)

$$P_s=-B^{\frac{1}{2}}\gamma^{-\frac{1}{2}},$$

so that the maximum pyroelectric coefficient π_0 at the Curie point is

$$\pi_0=+\beta/3\gamma^{\frac{1}{2}}B^{\frac{1}{2}}. \qquad (17)$$

The temperature T^* at which the pyroelectric coefficient is reduced to a certain fraction (e.g., $\frac{1}{2}$) of its maximum value, can be calculated from Eqs. (15) and (17). From these equations it follows that $\pi/\pi_0=\frac{1}{2}$ when

$$T^*-T_0=3\gamma^{\frac{1}{2}}B^{\frac{1}{2}}\beta^{-1}. \qquad (18)$$

From Eqs. (17) and (18) it is apparent that with increasing bias B, π_0 decreases and T^* increases, but the

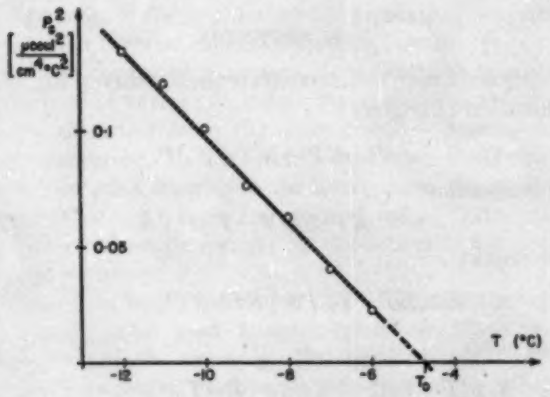

FIG. 9. Experimental P_s^2 vs T.

product $(T^*-T_0)\pi_0^2$ remains constant:

$$(T^*-T_0)\pi_0^2=3\gamma^{\frac{1}{2}}\beta^2/9\beta\gamma^{\frac{1}{2}}=\beta/3\gamma=\text{const.} \qquad (19)$$

In Fig. 6 we have plotted the pyroelectric coefficient as a function of the temperature for different values of the intrinsic bias.

3. EXPERIMENTAL RESULTS

The main purpose of our experiments was to investigate whether the bias normally observed below T_0 does also exist *above* the Curie temperature and hence could explain the pyroeffect observed in colemanite above T_0. The bias was measured with the techniques described in Sec. 2.3.

The dielectric constant ϵ was measured at different temperatures and at different applied dc electric fields as shown in Fig. 7. This enables us to calculate the intrinsic bias B as a function of temperature T. This is shown in Fig. 8 by the dotted line. In the same Fig. 8 are plotted by the solid line the values of the bias B

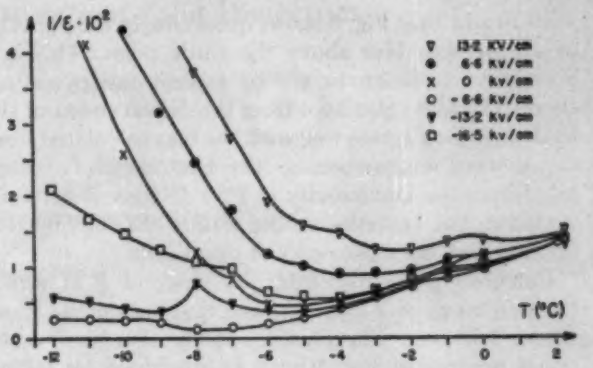

FIG. 10. Experimental $1/\epsilon$ vs T for different values of the applied field E.

determined (below T_0) from the hysteresis loop and (above T_0) from the nonlinearity in P vs E, using Eq. (12). The value of T_0 is also indicated. This value is found by plotting P_s^2 vs T and extrapolating to $P_s^2=0$ (Fig. 9). The values of P_s were measured at the same time as the points of Figs. 7 and 8 so as to avoid any relative error in the position of the Curie point. We found a value of T_0 slightly lower than that found by Goldsmith.[1] In Fig. 10, $1/\epsilon$ is plotted vs temperature for different values of the applied field E; one can see that the minimum of $1/\epsilon$ vs T occurs at a temperature T_p which depends on the applied field E. The value of T_p is plotted vs E in Fig. 11 (solid line). Figure 10 shows that most curves have two smaller minima or inflection points in addition to the main minimum. They are situated at opposite sides of the main minimum and occur at temperatures T' and T''. In Fig. 11 we have also plotted the value of T' vs the applied field E (broken line). Unfortunately, the position of T'' cannot be determined with sufficient accuracy.

4. DISCUSSION

Most of the experimental curves have been explained in Sec. 2; for instance, Figs. 4(b) and 5 are the theoretical anticipation of the results plotted in Fig. 7. We

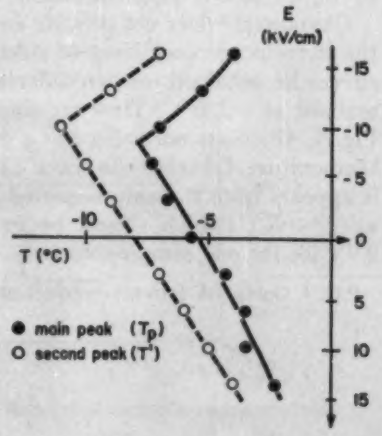

FIG. 11. Experimental T_P and T' vs applied field E.

wish to add that Fig. 8 shows quite clearly the presence of an intrinsic bias above the Curie point. This is a necessary condition to try to explain the pyroeffect there. The bias calculated from the displacement of the hysteresis loop agrees well with the bias calculated from capacitance measurements. The bias above T_0 calculated from the nonlinearity in P vs E curve is not very accurate, but nevertheless the results obtained by this method give the right order of magnitude.

Calculating the bias from the value of E at which the minimum of T_p occurs, one finds again the same value: 7 kv/cm. The presence of the two small additional minima in Fig. 10 can be explained by taking into account higher-order terms in the expansion of Eq. (1). From the $1/\epsilon$ vs T curve in which an external field compensates exactly the intrinsic bias, and from the P_s^2 vs T curve, we can calculate the values of β, γ, and δ in colemanite.[7] We found in one sample: $1/\beta=590°C$; $\gamma=6\times10^{-9}$; $\delta=10^{-19}$ (Gauss system). These values, substituted into Eqs. (17)–(19) give

$$(T^*-T_0)=7.2\times10^{-2}B^{\frac{1}{3}} \tag{20}$$

(T^* and T_0 in °C; B in v/cm) and

$$\pi_0=3.8\times10^{-7}B^{-\frac{1}{3}} \tag{21}$$

(π_0 in coul/cm² °C); from which follows

$$(T^*-T_0)\pi_0^2=10^{-14}. \tag{22}$$

Equations (20)–(22) enables us to calculate any two of the three quantities (T^*-T_0), π_0, and B, once we know the third one.

We have not performed any experiments on the pyroeffect of colemanite, but we can check our formulas with some available results. Goldsmith[18] has measured on one colemanite cyrstal:

$$\pi_0=10^{-7}\text{ coul/cm}^2\text{ °C};\quad (T^*-T_0)=3°C,$$

so that

$$\pi_0^2(T^*-T_0)=3\times10^{-14},$$

in good agreement with Eq. (22). We can calculate from Eq. (20) the values of the bias in this sample to $B=280$ v/cm, which is a quite reasonable value.

Chynoweth[3] does not provide any absolute value for the pyroelectric coefficient of colemanite, but the two curves he obtained on two different samples, are normalized at −100°C. They are similar to the curves of Fig. 6, which are normalized at a very low value of the temperature. One thus can check Eq. (22) again because it appears from the values quoted by Chynoweth that $\pi_0^2(T^*-T_0)$ (which should be constant) is equal to 2.9×10^3 for one sample and to 3.3×10^3 for the other sample (in arbitrary units). The two figures agree rather well with each other. From Eq. (21) one can calculate that the first sample should have an intrinsic bias of 125 v/cm and the second sample an intrinsic bias of 2.5 kv/cm, both being quite reasonable values. With Eq. (20), one can also find the value u of the arbitrary unit used by Chynoweth[3]:

$$u=1.7\times10^{-9}\text{ coul/cm}^2\text{ °C}$$

To summarize, it appears that the presence of a bias above the Curie point does explain why colemanite can show a pyroeffect above T_0. Also, the magnitude of the pyroeffect and its temperature dependence can be explained by the electrical bias assumed in this model.

[18] G. J. Goldsmith (private communication).

5. ACKNOWLEDGMENTS

We would like to thank Dr. W. J. Merz for many helpful discussions, Dr. G. J. Goldsmith for providing the crystals, and Mr. H. Roetschi for his technical assistance and for performing some of the measurements.

6. APPENDIX

We want here to demonstrate the validity of Eq. (12). Equation (11) gives

$$E=KP^3+\beta(T-T_0)P.$$

If we assume

$$KP^3\ll\beta(T-T_0)P, \tag{23}$$

we obtain

$$E\cong\beta(T-T_0)P+[KE^3/\beta^3(T-T_0)^3]$$

and hence

$$P=[E/\beta(T-T_0)]-[KE^3/\beta^4(T-T_0)^4]$$
$$=\gamma_1E-\gamma_3E^3, \tag{24}$$

where $\gamma_1=1/\beta(T-T_0)$ and $\gamma_3=K/\beta^4(T-T_0)^4$.
From Fig. 2 we see that

$$\delta_1=\delta_1^*+\delta_0^*$$
$$\delta_2=\delta_2^*-\delta_0^*$$
$$\delta=\delta_1-\delta_2=\delta_1^*-\delta_2^*+2\delta_0^*. \tag{25}$$

With Fig. 2 and Eq. (24) we obtain

$$\delta_0^*=|\gamma_1B-\gamma_3B^3| \tag{26}$$
$$\delta_1^*=|\gamma_1(-E+B)-\gamma_3(-E+B)^3| \tag{27}$$
$$\delta_2^*=|\gamma_1(E+B)-\gamma_3(E+B)^3|. \tag{28}$$

Equations (25)–(28) lead to

$$\delta=\delta_1^*-\delta_2^*+2\delta_0^*=6\gamma_3E^2B=[6K/\beta^4(T-T_0)^4]E^2B.$$

Beta Particle Transmission Currents in Solid Dielectrics

BERNHARD GROSS
Instituto Nacional de Tecnologia, Rio de Janeiro, Brasil

AND

ARTHUR BRADLEY AND ARTHUR P. PINKERTON
Radiation Research Corporation, New York 21, New York

(Received January 12, 1960; revised manuscript received March 2, 1960)

The current from a beta particle source measured through a thin dielectric cannot be predicted simply from the absorption curve. A model is considered in which the space charge formation in the medium results in a component of current in addition to that of the betas transmitted. Calculations developed from this model give a close approximation to experimental results.

RADIOACTIVE isotopes emitting beta rays have been used for the construction of current and voltage sources.[1] In essence, such a "nuclear battery" consists of two electrodes separated by a dielectric. The radioisotope source is placed at one electrode, which becomes positively charged relative to the other, or collector electrode. The dielectric must be thin enough to pass most of the beta energy yet maintain the voltage separation without excessive leakage current.

In the course of a systematic investigation of the properties of certain dielectric materials,[2] the influence of the thickness D on the short circuit current J has been measured. It has been found that the current decreased with increasing thickness more slowly than the number of particles transmitted, as calculated from the known absorption curve for the beta emission of the isotope employed.

This effect might have been predicted from the work of Spear,[3] who used monoenergetic electrons in a similar electrode assembly. He found that a current could be measured at the collector electrode when the effective range of the electrons was only a little more than half the thickness of the dielectric. A qualitative explanation based on the concept of an internal space charge was presented. The theory developed in this paper permits a quantitative explanation of this type of data.

I. EXPERIMENTAL

The radioactive source was a sealed capsule containing 300 Mc of Kr^{85}. The beta particles passed through a thin window (0.001-in. stainless steel, 0.50-in. diam) positioned close to a metal ring which made contact to the bottom electrode. In these measurements the bottom electrode was grounded. A collector was placed above the sample, protected by a grounded guard ring which made contact with the top electrode. The collector was connected to an electrometric measuring system. The electrodes were thin films of aluminum applied to the samples by evaporation in vacuum. They did not significantly absorb the beta emission of Kr^{85}. A schematic diagram of the experimental arrangement is presented in Fig. 1.

The samples were 2.0-in. diam disks. The electrodes were 0.625-in. diam circles, centered within guard rings of 1.00-in. i.d. and 1.25-in. o.d. The two electrode contact pieces (a $\frac{7}{16}$-in. i.d. ring below and a solid collector-beam stop above) had 0.625-in. o.d. to match the electrodes aluminized on the sample. The irradiated area was approximately 0.15 in², or 1.0 cm², which was about half of the area covered by the electrodes. The window of the Kr^{85} source was located $\frac{9}{16}$ in. below the sample (dimension "L," Fig. 1).

Dielectric samples of varying thicknesses of polystyrene, mica, and fused silica were tested. The thickest (silica) was less than 0.01 in., which was still very small compared to the electrode area. In one experiment the polystyrene sample was divided into two halves separated by a very thin grounded center electrode.

Figure 2 shows the measured current values at different dielectric thicknesses. These currents were not time dependent, being stable over irradiation periods of days. The results for mica and fused silica are in close agreement, but those for polystyrene are slightly higher. The figure shows also the calculated absorption curve for Kr^{85} betas.

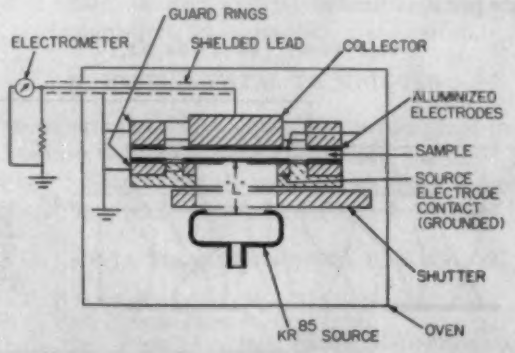

FIG. 1. Schematic diagram of electrode-source assembly.

[1] J. H. Coleman, Nucleonics 11, No. 12, 42 (1953).
[2] A. Bradley, A. P. Pinkerton, and S. Grand, Insulation 5, No. 11, 27 (1959).
[3] W. E. Spear, Proc. Phys. Soc. (London) B68, 991 (1955).

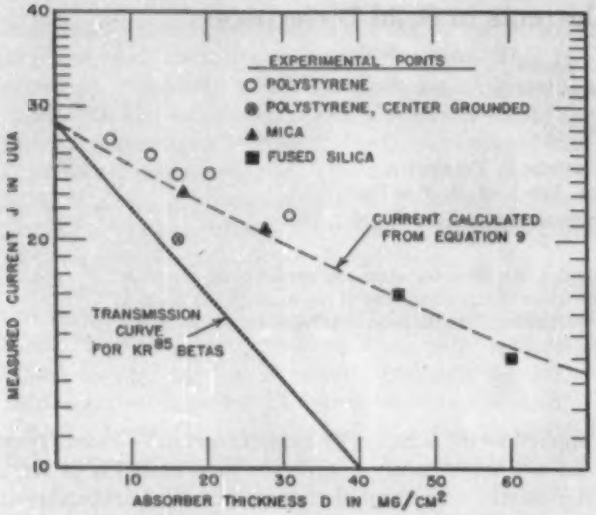

FIG. 2. Comparison of measured current with theory.

II. THEORY

A. General Expressions

We consider a system of two parallel plates separated by a dielectric of thickness D (Fig. 3). One of the plates emits electrons into the dielectric. The electrons might have different ranges and the emission be divergent. The number of electrons coming to rest in a layer of thickness dx at distance x from the emitting plate shall be $n(x)dx$ per unit time. If the emission is uniform in time, a space charge layer $en(x)dxt$ is produced. The charge dq measured in time t in an external integrating circuit connecting the plates depends on the value of x relative to D and is given by the expression

$$dq=e(x/D)n(x)dxt, \tag{1}$$

and the current is given by

$$dJ=dq/t=e(x/D)n(x)dx. \tag{2}$$

The expressions do not account for edge effects. They are correct if the total distance D is small compared to the lateral extension of the plates.

If the source of the particles is a radioactive isotope, the number of particles coming to rest between x and $x+dx$ per unit time is

$$n(x)dx=-[d\psi(x)/dx]dx, \tag{3}$$

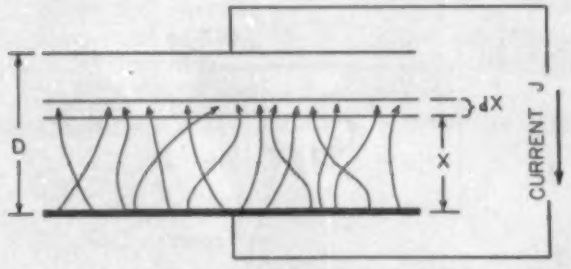

FIG. 3. Electron emission into a dielectric.

where $\psi(x)$ is the absorption curve of the particles expressed as the number of transmitted particles (thru distance x) per unit time.

The total current now contains two components. The first component corresponds to particles with range equal to or greater than D and is given by $e\psi(D)$, and the second is caused by the increase of space charge created by particles stopped inside the dielectric. The second component is obtained from Eq. (2) by substitution of (3) and integration between 0 and D. Thus

$$J(D)=e\psi(D)-e\int_0^D (x/D)[d\psi(x)/dx]dx. \tag{4}$$

The result is

$$J(D)=\frac{e}{D}\int_0^D \psi(x)dx. \tag{5}$$

Some general conclusions can be drawn without indicating any special form for the absorption function $\psi(x)$. Expansion for $D\rightarrow 0$ gives

$$\lim_{D\rightarrow 0} J(D)=e\psi(0)-\frac{D}{2}\psi'(0), \tag{6a}$$

or

$$\frac{dJ(D)}{dD}\Big/_0=-\tfrac{1}{2}D\psi'(0). \tag{6b}$$

The initial slope of the absorption curve is given by

$$\frac{d\psi(D)}{dD}\Big/_0=-D\psi'(0), \tag{6c}$$

and therefore is just twice the slope of the current *vs* thickness curve. For sufficiently large values of D so that $\psi(D)\rightarrow 0$ the integral becomes constant and

$$J(D)=e/D\int_0^\infty \psi(x)dx \quad \text{for} \quad \psi(D)\rightarrow 0. \tag{6d}$$

Equation (5) can be inverted by differentiation and yields

$$e\psi(D)=J(D)+DJ'(D). \tag{7}$$

This expression enables one to determine the absorption curve for particles by actual current measurements at different thicknesses.

B. Exponential Absorption Curve

The typical attenuation curve for continuous beta-ray spectra is an exponential function of the thickness of absorber.[4] Thus

$$\psi(x)=N_0e^{-\mu x}, \tag{8}$$

where the mass absorption coefficient μ is nearly inde-

[4] R. D. Evans, *The Atomic Nucleus* (McGraw-Hill Book Company, Inc., New York, 1955), pp. 625–627.

pendent of the atomic weight of the absorber. The calculated absorption curve for Kr^{85} in Fig. 2 used $\mu = 26$ cm²/g.

Substituting (8) into (5), one obtains a specific expression for the current in this system

$$J(D) = eN_0/\mu D(1-e^{-\mu D}). \quad (9)$$

C. Center Grounded System

If the center of the dielectric sample is grounded, one obtains easily

$$J(D) = \tfrac{1}{2}e\psi(D) + \frac{e}{D}\int_{D/2}^{D}\psi(x)dx, \quad (10)$$

and for an exponential absorption curve (8),

$$J(D) = \tfrac{1}{2}eN_0e^{-\mu D} + \frac{eN_0}{\mu D}(e^{-\mu D/2} - e^{-\mu D}). \quad (11)$$

III. COMPARISON WITH EXPERIMENT

The equations for determining current (using the exponential absorption curve) have been compared with the experimental data. Extrapolation of the measured current values to zero sample thickness gives the value 28.5 $\mu\mu$a ($\equiv eN_0$). The dashed curve in Fig. 2, calculated according to Eq. (9), is in excellent agreement with the experimental results obtained with mica and fused silica.

The discrepancy with polystyrene may be caused by the slightly different absorption characteristics of this material. For a thickness of 16 mg/cm² of dielectric we have also calculated the current to be expected with the center grounded. Both measurement and theory agree at 20 $\mu\mu$a.

We believe that the agreement with the experimental results is good enough to prove the soundness of the theoretical treatment presented. For more precise conclusions the absorption curve would have to be measured with the actual geometry of the current measuring device.

ACKNOWLEDGMENT

One of the authors (B. G.) gratefully acknowledges assistance received from the Brazilian National Research Council.

JOURNAL OF APPLIED PHYSICS VOLUME 31, NUMBER 6 JUNE, 1960

Single-Crystal Magnetic Anisotropy and Magnetostriction Studies in Iron-Base Alloys

R. C. HALL*

Magnetic Materials Development Laboratory, Westinghouse Electric Corporation, East Pittsburgh, Pennsylvania

(Received February 1, 1960; revised manuscript recieved February 24, 1960)

Single crystals of a number of binary iron-base alloys were grown, fabricated, and tested for magnetic anisotropy (K_1) and magnetostriction (λ_{100} and λ_{111}). The additions made to iron included vanadium, molybdenum, germanium, chromium, titanium, and tin. The anisotropy of iron was lowered by the addition elements with the possible exception of tin. On the other hand, λ_{100} of iron was generally raised by these addition elements. Only titanium and tin lowered λ_{100}; however, titanium had limited solublilty in iron and tin caused embrittlement.

I. INTRODUCTION

THE present experiments explored some of the possibilities for the development of a ductile iron-base alloy with zero magnetostriction, zero anisotropy, or both. A number of investigators[1–5] have correlated the exceptionally good magnetic properties of certain polycrystalline materials with zero or small values of magnetostriction and anisotropy. These basic magnetic properties have been reported for only a few magnetic systems including alloys of iron-nickel,[2] silicon-iron,[6,7] cobalt-nickel,[8] aluminum-iron,[8] and cobalt-iron.[8,9] This work extends this knowledge to iron-base alloys of vanadium-iron, molybdenum-iron, germanium-iron, chromium-iron, titanium-iron, and tin-iron.

II. EXPERIMENTAL TECHNIQUES

The experimental techniques will not be given in detail because they have been adequately described previously.[8,10] Single crystals were grown from the melt, fabricated into circular disks, etched, and annealed. The

* Now at the Research and Development Laboratory, Universal-Cyclops Steel Corporation, Bridgeville, Pennsylvania.

[1] R. Becker and W. Döring, *Ferromagnetismus* (Verlag Julius Springer, Berlin, Germany, 1939).

[2] R. M. Bozorth, Revs. Modern Phys. **25**, 42 (1953).

[3] J. L. Snoek, *New Developments in Ferromagnetic Materials* (Elsevier Publishing Company, Inc., New York, 1949).

[4] R. M. Bozorth, *Ferromagnetism* (D. Van Nostrand Company, Inc., Princeton, New Jersey, 1953), p. 101.

[5] D. Pavlovic and K. Foster, J. Appl. Phys. **29**, 368 (1958).

[6] W. J. Carr, Jr., and R. Smoluchowski, Phys. Rev. **83**, 1236 (1951).

[7] L. P. Tarasov, Phys. Rev. **56**, 1231 (1939).

[8] R. C. Hall, J. Appl. Phys. **30**, 816 (1959).

[9] R. C. Hall, Trans. Am. Inst. Mining Met. Engrs. (to be published).

[10] R. C. Hall, J. Appl. Phys. **28**, 707 (1957).

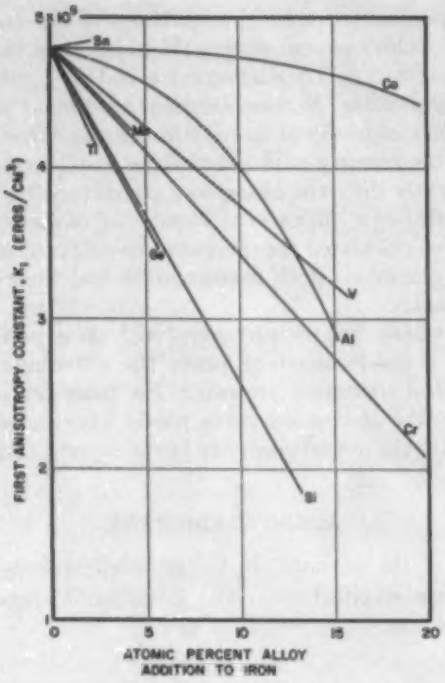

FIG. 1. Anisotropy for several binary iron alloys.

first anisotropy constant (K_1) was derived from torque curves to an accuracy of about $\pm 4\%$. The saturation magnetostriction in the [100] and [111] crystallographic directions (λ_{100} and λ_{111}) was measured by the strain gauge method to an accuracy of about $\pm 6\%$.

Table I lists the crystals and the values of K_1, λ_{100}, and λ_{111}. Figures 1 and 2 illustrate K_1 and λ_{100}, respectively, for these alloys as well as for alloys of silicon-iron, aluminum-iron, and cobalt-iron. The variations of K_1 and λ_{100} with composition are generally represented as straight lines. Such a linear dependence was not necessarily a true one in any particular case but was assumed for lack of more complete data. In most cases such a linear dependence did fit the data quite well.

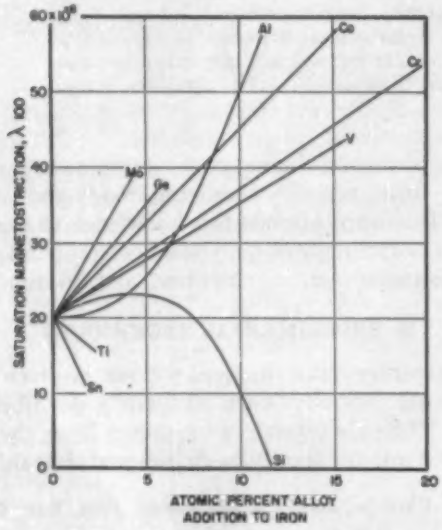

FIG. 2. Saturation magnetostriction in the [100] direction for several binary iron alloys.

III. DISCUSSION

The anisotropy of iron was lowered by the addition elements, as shown in Fig. 1, with the possible exception of tin. Titanium, germanium, and silicon had the largest effect in lowering K_1. Chromium, molybdenum, aluminum, and vanadium had a smaller effect in lowering K_1. Cobalt (in the percentages shown here) and tin had little effect on K_1. On a weight basis, silicon and aluminum are considerably more effective in lowering K_1 than would be indicated in Fig. 1. Titanium, chromium, molybdenum, and vanadium were added to iron to about their maximum solubility limits. Larger percentages of tin and germanium could have been added within their solubility limits, but both of these elements cause grain boundary embrittlement of iron. As a result the development of a ductile, zero-anisotropy material in these alloys appears remote.

TABLE I. Anisotropy and magnetostriction constants.

Wt. % in iron	At. % in iron	Anisotropy const, K_1 (ergs/cm³)	Magnetostriction $\lambda_{100}\times 10^6$	Magnetostriction $\lambda_{111}\times 10^6$
2.79 V	3.05 V	435 000	28.3	−12.4
6.07 V	6.62 V	410 000	28.4	−12.6
11.4 V	12.4 V	355 000	38.7	− 8.4
14.4 V	15.6 V	330 000	42.8	− 9.7
3.69 Mo	2.18 Mo	450 000	31.9	−13.2
5.72 Mo	3.41 Mo	440 000	32.5	−10.3
7.24 Mo	4.35 Mo	420 000	39.3	− 8.3
5.08 Ge	3.95 Ge	400 000	32.2	− 0.8
7.32 Ge	5.73 Ge	330 000	37.1	− 3.5
14.7 Cr	15.6 Cr	265 000	51.3	− 6.3
19.9 Cr	21.1 Cr	200 000	51.7	− 2.7
1.39 Ti	1.61 Ti	395 000	17.7	−15.7
2.09 Ti	2.43 Ti	450 000	14.5	−13.1
2.47 Sn	1.18 Sn	475 000	13.3	−15.3
3.76 Sn	1.80 Sn	495 000	12.1	−13.9

Figure 2 illustrates λ_{100} of the various binary iron-base alloys. Molybdenum, germanium, aluminum, cobalt, chromium, and vanadium all raise λ_{100} of iron to larger positive values. Only tin, titanium, and silicon (and aluminum at higher percentages) lower λ_{100} of iron. Unfortunately, the latter elements all tend to make iron brittle or, in the case of titanium, have limited solubility in iron. Thus, the development of a ductile zero-magnetostriction material in these alloys seems difficult.

The saturation magnetostriction in the [111] direction is given in Table I for the various alloys. All the additions to iron lower λ_{111} toward zero from the value of about -18×10^{-6} for iron.

JOURNAL OF APPLIED PHYSICS VOLUME 31, NUMBER 6 JUNE, 1960

Surface Wave Excitation and Propagation*

JOSEPH B. KELLER AND FRANK C. KARAL, JR.
Institute of Mathematical Sciences, New York University, New York 3, New York
(Received May 26, 1959; revised Manuscript received March 2, 1960)

A geometrical theory is developed for the analysis of surface wave excitation and propagation. The surfaces along which the surface waves propagate may be either curved or flat, and may have either constant or variable properties. The theory is based on the concept of a complex or imaginary ray. The excitation coefficient which enters the theory is determined from the solution of a canonical problem—that of a line source over an impedance plane. Then the theory is applied to the surface wave excited by a line source, on a wedge with variable surface impedance. The result agrees precisely with the asymptotic form of the exact solution. Another application is made to the surface wave excited on a cylinder by a line source. The result also agrees with the exact solution.

1. INTRODUCTION

SURFACE waves are waves which travel along surfaces with their fields confined to the neighborhoods of the surfaces. They occur in electromagnetics, acoustics, elasticity, and other fields in which wave propagation takes place. In electromagnetics they may occur on corrugated metal surfaces, on metal surfaces with other kinds of periodic structure, on dielectric coated metal surfaces, and on other kinds of surfaces. Surfaces supporting such waves can be used to guide the surface-wave energy from place to place and, when properly terminated, can be used as antennas to radiate it. In elasticity a surface wave at the free surface of a homogeneous solid is called a Rayleigh wave. Rayleigh waves predominate in the disturbance produced by an earthquake at a distant point. In hydrodynamics the gravity waves which occur on the free surface of water are surface waves.

A surface wave is characterized by a real or complex propagation constant $k_1=\omega/c_1$, where ω is the angular frequency of the field, and c_1 is the real or complex phase velocity of the wave along the surface. One of the first problems in the theory of such waves is the determination of k_1 or c_1 from the physical properties of the media separated by the surface. We shall not consider this problem, but shall assume that k_1 and c_1 are known. Our problem is to determine the manner in which such waves are excited, how they propagate, and the rate at which their fields diminish with distance from the surface. We shall solve it by constructing a geometrical theory of surface waves, analogous to geometrical optics and to the geometrical theory of diffraction.[1] It is based upon the concept of a complex or imaginary ray. By using this type of ray we shall determine the phase and amplitude of the field. We shall do this for curved as well as for flat surfaces with either variable or constant surface-wave velocity c_1 and for any kind of incident field or source. There seems to be no other method available for treating such general surface-wave problems.

Since our theory is geometrical, it may be expected to be valid when the wavelength of the field is small compared to all other dimensions. We believe that it yields the leading term in the short-wavelength asymptotic expansion of the exact surface-wave field. This belief is confirmed in one case by using our theory to determine the surface wave which a line source of scalar waves excites upon a wedge with a variable surface impedance. The result is found to coincide with the short-wavelength asymptotic form of the exact solution of this problem. It is also confirmed in two other cases by a similar agreement for the surface waves produced on a circular cylinder and on an infinite plane. In the latter case we find that the surface wave occurs only in part of space, which seems to be a new result.

The fact that we permit the propagation constant k_1 to be complex means that we include the possibility of a lossy surface which attenuates the wave. It also enables us to treat loosely bound or "leaky" waves which lose energy by radiation as they propagate. Some authors do not call such waves "true" surface waves, but this distinction is not necessary in our theory.

In Secs. 2–4 we formulate our theory. In Secs. 5 and 6 we determine the excitation and radiation coefficients which enter the theory. For simplicity this is done for scalar fields which satisfy the reduced wave equation and satisfy an impedance boundary condition on the surface. Such a boundary condition is commonly employed in acoustics and electromagnetic theory as an approximate characterization of a surface or medium.[2] For example, in electromagnetics, corrugated and dielectric-coated surfaces and the surfaces of highly conducting media are characterized in this way. The comparison with certain exact solutions, referred to in the foregoing, is made in the final sections.

* This paper is based upon a report of the same title, Research Rept. No. EM-128, Institute of Mathematical Sciences, New York University, February, 1959. This research was sponsored by the Air Force Cambridge Research Center, Air Research and Development Command, under contract, and by a grant from the American Petroleum Institute.

[1] J. B. Keller, in *Calculus of Variations and its Applications, Vol. VIII, Proceedings of Symposia in Applied Mathematics*, "A geometrical theory of diffraction," edited by L. M. Graves (McGraw-Hill Book Company, Inc., New York, 1958), pp. 27–52; NYU, Inst. Math. Sci., Div. EM Research, Research Rept. No. EM-115, July, 1958.

[2] P. M. Morse and H. Feshbach, *Methods of Theoretical Physics* (McGraw-Hill Book Company, Inc., New York, 1953), pp. 1366, 1814, 1817.

2. COMPLEX RAYS

Rays in space can be defined in terms of the propagation velocity $c(\mathbf{x})$ by Fermat's principle or by the differential equations which follow from it. Thus, a ray can be described by a function $\mathbf{x}(s)$ of a parameter s, and this function is a solution of the ray equations. We now consider a complex space in which each of the three coordinates x, y, z of the position vector $\mathbf{x}$ is a complex number. Thus, a point in this three-dimensional complex space can be represented by six real numbers or by a point in a real six-dimensional space. Since Figs. 1, 4, and 5 are two dimensional, they are only suggestive of the actual configuration. A curve is still defined as a complex function $\mathbf{x}(s)$ of a real parameter s. The distance $d(\mathbf{x},\mathbf{x}')$ between two points is defined by $d(\mathbf{x},\mathbf{x}')=[(\mathbf{x}-\mathbf{x}')^2]^{\frac{1}{2}}$, and is, in general, complex. Complex rays can be defined by applying Fermat's principle to complex curves or by considering complex solutions of the ray equations. In either case it is necessary that $c(\mathbf{x})$ be defined for complex values of $\mathbf{x}$, which is the case if $c(\mathbf{x})$ is an analytic function of $\mathbf{x}$. We can also define complex surface rays by applying Fermat's principle to complex curves on the surface S or by considering complex solutions of the equations for surface rays. In this case it is necessary that both the velocity $c_1(\mathbf{x})$ and the surface S be defined for complex $\mathbf{x}$.

Next, by means of Fermat's principle, we may define a ray joining two points Q and P in space and having an arc on S. It follows from Fermat's principle that such a ray consists of a complex space ray from Q to some point Q_1 on S, a complex surface ray from Q_1 to another point P_1 on S, and a complex space ray from P_1 to P. In addition it follows that at both Q_1 and P_1 the unit tangents I and T to the space and surface rays, respectively, must satisfy the condition

$$c^{-1}I+c_1^{-1}T=(c^{-1}I\cdot N+c_1^{-1}T\cdot N)N. \tag{1}$$

Here N denotes the unit normal to S at Q_1 or P_1. The vectors are oriented such that $-I$ and T both point in the direction of increasing arclength along the ray. See Fig. 1. Equation (1) is equivalent to the geometrical conditions that I and T be coplanar with N and lie on opposite sides of N, and that the angle θ between I and N satisfy Snell's law

$$\sin\theta=c/c_1. \tag{2}$$

The preceding considerations enable us to determine all the ray paths which contain arcs on S along which surface wave propagation occurs.

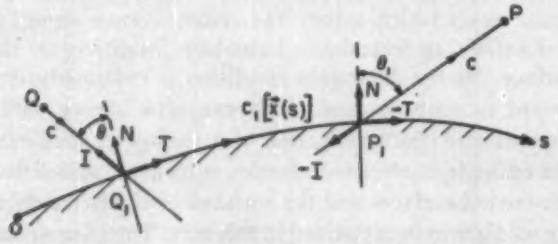

FIG. 1. The complex ray from Q reached the surface at the complex point Q_1 where it produces a complex surface ray. This ray travels along the surface with the velocity c_1 and sheds complex space rays. The ray which leaves the surface at P_1 passes through P. The angles θ and θ_1 are determined by Snell's law (1). (*Note.* Vector designated by superior arrow in figure corresponds to boldfaced letters in text.)

3. AMPLITUDE AND PHASE

The field $u=Ae^{i\phi}$ on any ray is composed of a phase ϕ and an amplitude A. Since both ϕ and A may be complex, the decomposition of u in this form is made unique by the requirement that ϕ be proportional to ω or k. Thus, on a surface ray from Q_1 to P_1 the complex phase change $\phi_1(Q_1,P_1)$ is the following integral with respect to arc length s

$$\phi_1(Q_1,P_1)=\omega\int_{Q_1}^{P_1}\frac{ds}{c_1[\mathbf{x}(s)]}=\int_{Q_1}^{P_1}k_1[\mathbf{x}(s)]ds. \tag{3}$$

On a space ray, with $\kappa=\omega/c[\mathbf{x}(s)]$,

$$\phi(P_1,P)=\omega\int_{P_1}^{P}\frac{ds}{c[\mathbf{x}(s)]}=\int_{P_1}^{P}k[\mathbf{x}(s)]ds. \tag{4}$$

The amplitude variation along any ray depends upon the family of rays in which the ray under consideration is contained. For a complex ray the amplitudes $A_1(Q_1)$ and $A_1(P_1)$, which are vectors for vector fields, are related by

$$A_1(P_1)=A_1(Q_1)[d\sigma(Q_1)c_1(P_1)/d\sigma(P_1)c_1(Q_1)]^{\frac{1}{2}}. \tag{5}$$

In (5) $d\sigma(Q_1)/d\sigma(P_1)$ denotes the ratio of the width at Q_1 to that at P_1 of an infinitesimal band of complex surface rays containing the ray from Q_1 to P_1. The analog of (5) for the space ray from P_1 to P is

$$A(P)=A(P_1)[d\tau(P_1)c(P)/d\tau(P)c(P_1)]^{\frac{1}{2}}. \tag{6}$$

In (6) $d\tau(P_1)/d\tau(P)$ is the ratio of the cross-sectional area at P_1 to that at P of an infinitesimal tube of complex rays containing the ray from P_1 to P. A similar relation holds on any space ray.

The amplitude on the surface ray at Q_1 is proportional to that on the space ray at Q_1, so we have

$$A_1(Q_1)=E(Q_1)A(Q_1). \tag{7}$$

The proportionality factor $E(Q_1)$ in (7) is an excitation coefficient. In the case of vector fields, it is a matrix. Similarly, the amplitude on the space ray at P_1 is proportional to that on the surface ray there, so we have

$$A(P_1)=R(P_1)A_1(P_1). \tag{8}$$

The proportionality factor or matrix, $R(P_1)$ in (8) is a radiation coefficient. Upon combining the foregoing

results, we find that the field $u(P)$ at P is given by

$$u(P)=R(P_1)E(Q_1)A(Q_1)\left[\frac{d\sigma(Q_1)c_1(P_1)d\tau(P_1)c(P)}{d\sigma(P_1)c_1(Q_1)d\tau(P)c(P_1)}\right]^{\frac{1}{2}} \times e^{i[\phi(Q_1)+\phi_1(Q_1,P_1)+\phi(P_1,P)]}. \quad (9)$$

Equation (9) expresses the field at P on a ray which has traveled along an arc of S as a complex surface ray associated with surface-wave propagation. It involves the incident field $A(Q_1)e^{i\phi(Q_1)}$, various geometrical quantities, and the excitation and radiation coefficients.

We shall now restrict our considerations to the two-dimensional case. In addition, we shall assume that c is constant, so that the space rays are straight lines. Due to the two dimensionality, the ratio $d\sigma(Q_1)/d\sigma(P_1)=1$. Because the rays are straight, we have $\phi(P_1,P)=kd(P_1,P)$, where $d(P_1,P)$ is the complex distance from P_1 to P. In addition, we find that

$$d\tau(P_1)/d\tau(P)=\left[1+(\kappa+\dot{\theta})d(P_1,P)\sec\theta\right]_{P_1}^{-1}. \quad (10)$$

In (10) $\kappa(P_1)$ denotes the curvature of S at P_1, $\theta(P_1)$ is the solution of (2) at P_1, and $\dot{\theta}$ is the derivative of θ with respect to arclength along the ray on S, evaluated at P_1. With these simplifications, (9) becomes

$$u(P)=R(P_1)E(Q_1)A(Q_1)\left[\frac{c_1(P_1)}{c_1(Q_1)}\right]^{\frac{1}{2}} \times\left[1+(\kappa+\dot{\theta})d(P_1,P)\sec\theta\right]_{P_1}^{-\frac{1}{2}} \times e^{i[\phi(Q_1)+\phi_1(Q_1,P_1)+kd(P_1,P)]}. \quad (11)$$

4. RECIPROCITY PRINCIPLE

To determine the coefficients $R(P_1)$ and $E(Q_1)$, we will now apply (11) to the case in which the field is produced by an isotropic line source, represented by the point Q in two dimensions. Then the incident field is given by

$$A(Q_1)e^{i\phi(Q_1)}=A_0[d(Q,Q_1)]^{-\frac{1}{2}}e^{ikd(Q,Q_1)}. \quad (12)$$

In (12) A_0 is a constant characteristic of the source, with the dimensions of (length)$^{\frac{1}{2}}$ times those of u. When use is made of (12), (11) becomes

$$u(P)=R(P_1)E(Q_1)A_0[d(Q,Q_1)]^{-\frac{1}{2}} \times\left[1+(\kappa+\dot{\theta})d(P_1,P)\sec\theta\right]_{P_1}^{-\frac{1}{2}} \times\left[\frac{c_1(P_1)}{c_1(Q_1)}\right]^{\frac{1}{2}} e^{i[kd(Q,Q_1)+\phi_1(Q_1,P_1)+kd(P_1,P)]}. \quad (13)$$

We now make use of the reciprocity principle which requires that a source at P must produce at Q the same field as an equal source at Q would produce at P. This implies that the right side of (13) must be unchanged when P is interchanged with Q and P_1 with Q_1. From this constancy, we obtain the condition

$$R(P_1)E(Q_1)[d(Q,Q_1)]^{-\frac{1}{2}} \times\left[1+(\kappa+\dot{\theta})d(P_1,P)\sec\theta\right]_{P_1}^{-\frac{1}{2}}\left[\frac{c_1(P_1)}{c_1(Q_1)}\right]^{\frac{1}{2}} =R(Q_1)E(P_1)[d(P,P_1)]^{-\frac{1}{2}} \times\left[1+(\kappa+\dot{\theta})d(Q_1,Q)\sec\theta\right]_{Q_1}^{-\frac{1}{2}}\left[\frac{c_1(Q_1)}{c_1(P_1)}\right]^{\frac{1}{2}}. \quad (14)$$

Equation (14) enables us to express the excitation coefficient E in terms of the radiation coefficient R by the relation

$$E(Q_1)=a^2R(Q_1)\left[\kappa_i+(\kappa+\dot{\theta})\sec\theta\right]_{Q_1}^{-\frac{1}{2}}c_1(Q_1). \quad (15)$$

Here a^2 is a constant with dimensions (time)$\times$(length)$^{-\frac{1}{2}}$. From (15) we see that $E(Q_1)$ depends upon $\kappa_i=1/d(Q,Q_1)$, the curvature of the incident wavefront at Q_1, in addition to properties of the surface at Q_1. It will be convenient to introduce $R'(Q_1)=a[c_1(Q_1)]^{\frac{1}{2}}R(Q_1)$ in order to avoid carrying along the factor a.

If we now use (15) to eliminate $E(Q_1)$ from (13), we obtain

$$u(P)=R'(P_1)R'(Q_1)A_0\left[1+(\kappa+\dot{\theta})d(Q_1,Q)\sec\theta\right]_{Q_1}^{-\frac{1}{2}} \times\left[1+(\kappa+\dot{\theta})d(P_1,P)\sec\theta\right]_{P_1}^{-\frac{1}{2}} \times e^{i[kd(Q,Q_1)+\phi_1(Q_1,P_1)+kd(P_1,P)]}. \quad (16)$$

This expression for $u(P)$ applies in the two-dimensional case when c is constant and the field is produced by a line source at Q. For a more general incident field we must use (15) in (11).

If the surface S is a plane and if c_1 is constant then κ is zero, $\dot{\theta}$ is zero, $R'(P_1)=R'(Q_1)=R'$, $\phi_1(Q_1,P_1)=k_1d(Q_1,P_1)$, and (16) becomes

$$u(P)=R'^2A_0e^{i[kd(Q,Q_1)+k_1d(Q_1,P_1)+kd(P_1,P)]}. \quad (17)$$

5. DETERMINATION OF THE COEFFICIENTS

To complete the prescription for calculating the field, we must determine the radiation coefficient R'. Since R is dimensionless, R' has the dimensions of (length)$^{-\frac{1}{2}}$. Therefore, it will be more convenient to consider the dimensionless product $k^{-\frac{1}{2}}R'(P_1)$. This product must depend upon the type of field under consideration. We shall assume that it depends upon $\theta(P_1)$ and possibly upon other physical constants of the medium and the surface at P_1, but not upon any geometrical properties of the surface at P_1. Therefore, it can be found by considering the special problem of a line source in the

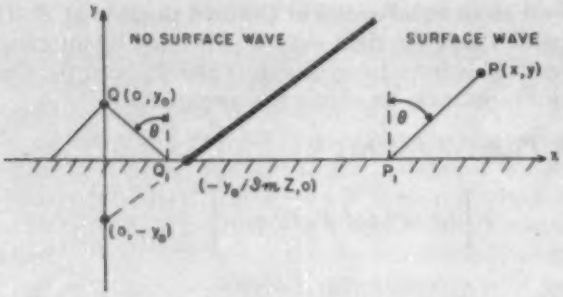

FIG. 2. The surface wave produced by a line source at Q above a plane of surface impedance Z. The figure shows a ray from Q which makes the complex angle θ with the normal to the plane. The angle θ is determined by Eq. (22). This ray gives rise to a complex surface ray which sheds complex space rays. One such ray is shown leaving the surface at P_1 and passing through P. These rays cover the region to the right of the real line $(y+y_0)x^{-1}=-\mathrm{Im}Z$ provided $\mathrm{Re}Z=0$. The figure is symmetric about the y axis.

presence of a uniform plane surface in a homogeneous medium. By comparing the exact solution of such a problem with (17), after expanding the exact solution for large ω (or large k and k_1), R' can be determined. In order to facilitate such a comparison, we will now calculate the distances which appear in (17) in terms of the coordinates of P and Q.

Let us assume that the surface occupies the plane $y=0$, that the source Q is located at $(0,y_0)$, and that the point P is at (x,y) with $x>0$. The ray from Q to Q_1 is a straight line which makes with the y axis the angle θ, determined by (2). Similarly, the ray from P_1 to P is a straight line making the same angle with the y axis. Therefore, the coordinates of Q_1 are $(y_0\tan\theta,0)$ and those of P_1 are $(x-y\tan\theta,0)$. See Fig. 2. Then we find that $d(Q,Q_1)=y_0\sec\theta$, $d(P_1P)=y\sec\theta$ and $d(Q_1,P_1)=x-(y_0+y)\tan\theta$. When these distances are inserted into (17), it becomes

$$u(x,y)=R'^2A_0e^{ik[|x|\sin\theta+(y_0+y)\cos\theta]}. \tag{18}$$

Here x has been replaced by $|x|$ in order that this result remain valid for $x<0$. In obtaining (18) from (17, we used the relation $k/k_1=\sin\theta$, which follows from (2).

In the next section we shall obtain an exact solution of the problem just treated for a scalar field which satisfies the reduced wave equation

$$(\nabla^2+k^2)u=\delta(x)\delta(y-y_0), \quad y>0. \tag{19}$$

On the plane $y=0$, u will satisfy the impedance boundary condition

$$u_y=-ikZu. \tag{20}$$

In (20) the complex constant Z is the surface impedance. In order for the surface to support a surface wave, it is necessary that Z satisfy the conditions

$$\mathrm{Re}Z\geq 0, \quad \mathrm{Im}Z<0. \tag{21}$$

If (18) is inserted into (20), it yields

$$\cos\theta=-Z. \tag{22}$$

From (22) and (2) the propagation velocity c_1 is determined by the surface impedance through the relation

$$c_1=c(1-Z^2)^{-\frac{1}{2}}. \tag{23}$$

When the outgoing solution of (19) and (20) is expanded asymptotically for large values of k, it contains a surface wave of the form (18) with θ given by (22). This surface wave becomes identical with (18) if in (18) we set

$$A_0=(8\pi k)^{-\frac{1}{2}}e^{-i\pi/2} \tag{24}$$

$$R'=(8\pi k)^{\frac{1}{2}}e^{i\pi/4}(\cot\theta)^{\frac{1}{2}}. \tag{25}$$

This equation determines the radiation coefficient.

Let us now insert (24) and (25) into (16). This yields the final result for the surface wave excited on an impedance surface by an isotropic line source of amplitude A_0 in a homogeneous medium. It is

$$u(P)=\left[\tan\theta+(\kappa+\dot\theta)d(Q_1,Q)\sec\theta\tan\theta\right]_{Q_1}^{-\frac{1}{2}} \times\left[\tan\theta+(\kappa+\dot\theta)d(P_1,P)\sec\theta\tan\theta\right]_{P_1}^{-\frac{1}{2}} \times e^{i[kd(Q,Q_1)+\phi_1(Q_1,P_1)+kd(P_1,P)]}. \tag{26}$$

If the line source is not isotropic, we may write its amplitude as $A_0f(\theta)$. Then the right side of (26) must be multiplied by $f(\theta)$. Here $f(\theta)$ represents the radiation pattern of the source. It is proportional to the amplitude on a ray which makes the angle θ with the normal to the surface S. Usually the pattern is expressed as a function $F(\Psi)$ of the angle Ψ which the ray makes with a fixed direction. By determining Ψ as a function of θ from the shape of S and the location of Q, we then have $f(\theta)=F[\Psi(\theta)]$. To maximize the amplitude of the surface wave, it is necessary to maximize the pattern $f(\theta)$ in the complex direction θ of the ray which excites the surface wave. This direction is determined by (2) or (22). If S is a plane and if Ψ is measured from the line through Q normal to S, then $\Psi=\theta$ and therefore $f(\theta)=F(\theta)$.

If the incident field is arbitrary, the surface wave is given by (11), (15), and (25). Upon combining these equations, we obtain

$$u(P)=(8\pi k)^{\frac{1}{2}}u_i(Q_1)\left[\kappa_i\tan\theta+(\kappa+\dot\theta)\sec\theta\tan\theta\right]_{Q_1}^{-\frac{1}{2}} \times\left[\tan\theta+(\kappa+\dot\theta)d(P_1,P)\sec\theta\tan\theta\right]_{P_1}^{-\frac{1}{2}} \times e^{i[\frac{1}{4}\pi+\phi_1(Q_1,P_1)+kd(P_1,P)]}. \tag{27}$$

Here $u_i(Q)=A(Q)e^{i\phi(Q_1)}$ denotes the incident field at Q_1.

6. SURFACE WAVE ON AN IMPEDANCE PLANE

We shall now solve the boundary value problem (19) and (20), also requiring u to satisfy the radiation condi-

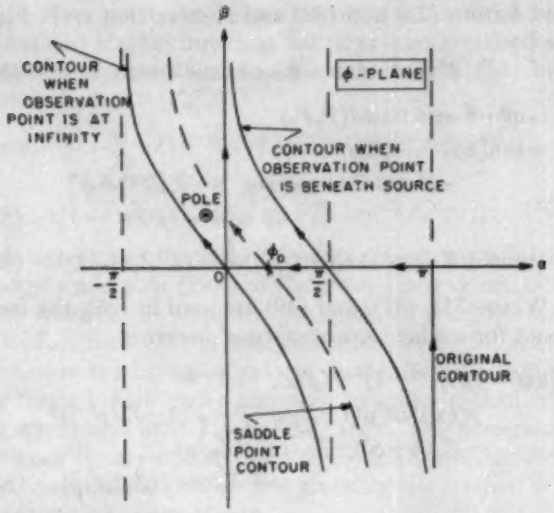

FIG. 3. Saddle-point contour used in the asymptotic evaluation of the reflected field for a line source above a plane with a constant surface impedance.

tion. The solution is

$$u(x,y)=-\frac{i}{4}H_0^{(1)}(kr)+\frac{i}{4\pi}\int_C \frac{\sin\phi-Z}{\sin\phi+Z}e^{ik[x\cos\phi+(y+y_0)\sin\phi]}d\phi. \quad (28)$$

In (28) r denotes the distance from $(0,y_0)$, and C is a contour in the complex plane. It runs from $\pi-i\infty$ to π along the line $\mathrm{Re}\phi=\pi$, then from π to 0 along the line $\mathrm{Im}\phi=0$, and finally from 0 to $i\infty$ along $\mathrm{Re}\phi=0$. See Fig. 3.

To obtain the asymptotic form of u for large k, we can first use the asymptotic form of $H_0^{(1)}(kr)$ for large values of the argument. This yields the asymptotic form of the incident field. The asymptotic form of the reflected field is obtained by performing a saddle-point evaluation of the integral in (28). The saddle point ϕ_0 which lies in the interval $0<\phi_0<\pi$ is given by

$$\phi_0=\tan^{-1}[(y+y_0)/|x|]. \quad (29)$$

The appropriate contour through the saddle point is obtained by setting the imaginary part of the phase $x\cos\phi+(y+y_0)\sin\phi$ equal to its value at $\phi=\phi_0$. If we let $\phi=\alpha+i\beta$, we find in this way two possible contours

$$\alpha=\phi_0\pm\cos^{-1}(\mathrm{sech}\beta). \quad (30)$$

In order that the exponential in the integrand of (28) vanish at infinity on the contour, we must choose

$$\alpha=\phi_0+\cos^{-1}(\mathrm{sech}\beta) \quad \beta<0 \quad (31)$$

$$\alpha=\phi_0-\cos^{-1}(\mathrm{sech}\beta) \quad \beta>0. \quad (32)$$

With this choice of signs, the contour C can be deformed into the saddle contour. See Fig. 3. Then the saddle-point evaluation of the integral yields the asymptotic form of the reflected field.

In the process of deforming C into the saddle contour it may cross the pole of the integrand which is at ϕ_1 given by

$$\sin\phi_1=-Z. \quad (33)$$

If this occurs, the residue of the integral at this pole must be added to the saddle point contribution to u. The residue is just the surface wave. It is easily found to be given by

$$u=[Z/(1-Z^2)^{\frac{1}{2}}]\exp ik[|x|(1-Z^2)^{\frac{1}{2}}-(y+y_0)Z]. \quad (34)$$

We have already stated that this coincides with (18) when A_0 and R' are given by (24) and (25), and θ by (22).

To determine when the surface wave (34) is present, let us consider the saddle contour which passes through the pole. Let ϕ^* denote the value of ϕ_0 for this contour. Because Z satisfies (21), the pole lies in the upper half-plane $\beta>0$. Thus, (32) yields for ϕ^* the result

$$\phi^*=\alpha_1+\cos^{-1}(\mathrm{sech}\beta_1). \quad (35)$$

If $\phi_0<\phi^*$, the pole is crossed and the surface wave occurs, if $\phi_0>\phi^*$, it does not occur. From (29) we thus find that the surface wave occurs if and only if the following condition is satisfied

$$(y+y_0)/|x|<\tan[\alpha_1+\cos^{-1}(\mathrm{sech}\beta_1)]. \quad (36)$$

In (36) α_1 and β_1 are the real and imaginary parts of ϕ_1, the solution of (33). In the special case in which $\mathrm{Re}Z=0$, (33) shows that $\alpha_1=0$. Then $\beta=-\sinh^{-1}(\mathrm{Im}Z)$ and (36) becomes

$$(y+y_0)/|x|<-\mathrm{Im}Z. \quad (37)$$

See Figure 2.

7. SURFACE WAVE ON A WEDGE WITH A NONUNIFORM IMPEDANCE

Let us now apply our method to determine the surface wave which a line source excites on a wedge with a nonuniform surface impedance. If the line source is parallel to the edge of the wedge, this problem is two dimensional. Then the point Q at which the source is located can be described by its polar coordinates (ρ',ϕ') and any other point P by (ρ,ϕ). The origin is at the tip of the wedge, the surfaces of which are at $\phi=0$ and $\phi=\alpha$. See Fig. 4. If the incident wave has the amplitude (24), then the surface wave which it produces on either surface of the wedge is given by (26). To determine this wave excited on $\phi=0$, we assume that Z, the surface impedance of the wedge on $\phi=0$, is proportional to ρ^{-1}. Thus

$$Z=Z_0\rho^{-1}. \quad (38)$$

Here Z_0 is a constant which satisfies (21). Then from (23)

$$c_1=\rho c(\rho^2-Z_0^2)^{-\frac{1}{2}}. \quad (39)$$

To write (26) more explicitly we must evaluate the

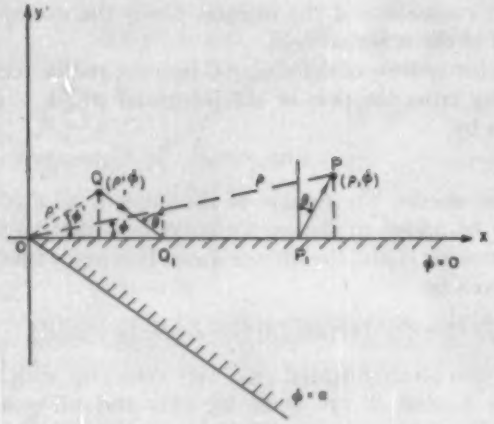

FIG. 4. Excitation of a surface wave on a wedge by a line source at Q. The coordinates of Q are (ρ',ϕ'). A complex ray from Q excites a surface ray at the complex point Q_1. This ray travels along the surface shedding complex space rays. The ray shed at P_1 passes through P which has coordinates (ρ,ϕ). The wedge faces are at $\phi=0$ and $\phi=\alpha$. The complex angles θ and θ_1 are determined by Eq. (22) in which Z is given by Eq. (38).

various geometrical quantities which appear in it. We shall first give them when P is to the right of Q, so that $\rho\cos\phi>\rho'\cos\phi'$. Then

$$d(Q,Q_1)=\rho'\sin\phi'\sec\theta' \tag{40}$$

$$d(P,P_1)=\rho\sin\phi\sec\theta \tag{41}$$

$$\rho(Q_1)=\rho'\cos\phi'+\rho'\sin\phi'\tan\theta' =\rho'\sec\theta'\cos(\phi'-\theta') \tag{42}$$

$$\rho(P_1)=\rho\cos\phi-\rho\sin\phi\tan\theta=\rho\sec\theta\cos(\phi+\theta). \tag{43}$$

From (22) and (38) we have

$$\rho(Q_1)=-Z_0\sec\theta' \tag{44}$$

$$\rho(P_1)=-Z_0\sec\theta. \tag{45}$$

Now from (42) and (44) we determine θ', and from (43) and (45) we find θ:

$$\theta'=\phi'+\cos^{-1}(-Z_0/\rho') \tag{46}$$

$$\theta=-\phi+\cos^{-1}(-Z_0/\rho). \tag{47}$$

From (3) and (39) we obtain

$$\phi_1(Q_1,P_1)=k\int_{\rho(Q_1)}^{\rho(P_1)}\rho^{-1}(\rho^2-Z_0^2)^{\frac{1}{2}}d\rho \tag{48}$$

$$=k[\rho\cos(\phi+\theta)\tan\theta -\rho'\cos(\phi'-\theta')\tan\theta'+Z_0(\theta'-\theta)]. \tag{48}$$

Upon combining (40), (41), and (48) and simplifying, we obtain for the phase in (26)

$$kd(Q,Q_1)+\phi_1(Q_1,P_1)+kd(P_1,P) =k[\rho(1-Z_0^2\rho^{-2})^{\frac{1}{2}}-\rho'(1-Z_0^2\rho'^{-2})^{\frac{1}{2}}-Z_0(\phi+\phi') -Z_0\cos^{-1}(Z_0/\rho)+Z_0\cos^{-1}(Z_0/\rho')]. \tag{49}$$

To calculate the amplitude in (26) we determine θ and θ from (22) and (38) and observe that $\kappa=0$. First we find

$$\theta'\sec\theta'\tan\theta'=\theta\sec\theta\tan\theta=-Z_0^{-1} \tag{50}$$

$$\tan\theta+\theta\sec\theta\tan\theta d(P,P_1) =\tan[\cos^{-1}(-Z_0\rho^{-1})-\phi)] -Z_0^{-1}\rho\sin\phi\sec[\cos^{-1}(-Z_0\rho^{-1})-\phi] =-(\rho^2Z_0^{-2}-1)^{\frac{1}{2}} \tag{51}$$

$$\tan\theta'+\theta'\sec\theta'\tan\theta' d(Q,Q_1)=-(\rho'^2Z_0^{-2}-1)^{\frac{1}{2}}. \tag{52}$$

When (51), (52), and (49) are used in (26), the final result for u when $\rho\cos\phi>\rho'\cos\phi'$ becomes

$$u(\rho,\phi)=(\rho^2Z_0^{-2}-1)^{-1/4}(\rho'^2Z_0^{-2}-1)^{-1/4} \times\exp\{ik[\rho(1-Z_0^2\rho^{-2})^{\frac{1}{2}}-\rho'(1-Z_0^2\rho'^{-2})^{\frac{1}{2}} -Z_0(\phi+\phi')-Z_0\cos^{-1}(Z_0/\rho) +Z_0\cos^{-1}(Z_0/\rho')]\}. \tag{53}$$

If $\rho\cos\phi<\rho'\cos\phi'$, $u(\rho,\phi)$ is obtained by interchanging primed and unprimed quantities in (53). In this case if P is near the tip, then $\rho\ll|Z_0|$ and (53) can be simplified. First we replace $\cos^{-1}(Z_0/\rho)$ by $i\log[\rho^{-1}(Z_0+[Z_0^2-\rho^2]^{\frac{1}{2}})]$. Then, upon omitting some small terms, (53) becomes

$$u(\rho,\phi)=e^{-i\pi/4}(\rho'^2Z_0^{-2}-1)^{-\frac{1}{4}} \times\exp\{ik[-iZ_0+\rho'(1-Z_0^2\rho'^{-2})^{\frac{1}{2}}-Z_0(\phi+\phi') +Z_0\cos^{-1}(Z_0/\rho')+iZ_0\log(2Z_0/\rho)]\}. \tag{54}$$

If Q is also near the tip, (54) can be further simplified.

Let us now compare our results (53) and (54) with the asymptotic form of the exact solution of the corresponding boundary value problem. We seek a solution u of (19) with the source at (ρ',ϕ'). This solution must be defined in the region outside the wedge, i.e., in the region $0\le\phi\le\alpha$. On the surface $\phi=0$, it must satisfy (20) with Z given by (38). On $\phi=\alpha$, we require it to satisfy $u_\phi=0$. The solution must also satisfy the radiation condition.

The solution of this problem has been found by Felsen.[3] It contains a surface wave given by

$$u(\rho,\phi)=-i\pi\frac{\cosh\eta(\alpha-\phi)\cosh\eta(\alpha-\phi')}{\alpha-i(kZ_0)^{-1}\sinh^2\eta\alpha} \times J_{-i\eta}(k\rho_<)H_{-i\eta}^{(1)}(k\rho_>). \tag{55}$$

Here $\rho_<$ and $\rho_>$ denote, respectively, the smaller and larger of the two quantities ρ' and ρ. The constant η is a solution of the equation

$$\coth\eta\alpha=\eta(ikZ_0)^{-1}. \tag{56}$$

For large k the solution of (56) becomes

$$\eta\sim ikZ_0. \tag{57}$$

Thus, (55) becomes

$$u(\rho,\phi)\sim\pi kZ_0e^{ikZ_0(\phi+\phi')}J_{kZ_0}(k\rho_<)H_{kZ_0}^{(1)}(k\rho_>). \tag{58}$$

[3] L. B. Felsen, Polytechnic Inst. of Brooklyn, Microwave Research Inst., Memo. 32, July 19, 1957.

We now insert the Debye asymptotic forms of the Bessel and Hankel functions for large k with order less than the argument in absolute value. Then (58) becomes, if $\rho>\rho'>|Z_0|$,

$$u(\rho,\phi)\sim Z_0(\rho'^2-Z_0^2)^{-\frac{1}{4}}(\rho^2-Z_0^2)^{-\frac{1}{4}}e^{-ik\Xi(\phi'+\phi)}\times\exp\{ik[(\rho'^2-Z_0^2)^{\frac{1}{2}}-(\rho^2-Z_0^2)^{\frac{1}{2}}-Z_0\cos^{-1}(Z_0/\rho')+Z_0\cos^{-1}(Z_0/\rho)]\}. \quad (59)$$

This agrees exactly with (53). If $\rho<\rho'$ we must interchange ρ and ρ' in (59) and the result again agrees with (53) when it is similarly changed. If $\rho\ll|Z_0|$ and $\rho'>|Z_0|$, then (58) becomes identical with (54) when we insert the asymptotic form of the Bessel function for large k with order larger in magnitude than the argument and omit some small terms. The agreement between the asymptotic form of the exact solution (55) and the solution (53) or (54) given by our method is a confirmation of our theory.

8. SURFACE WAVE ON A CYLINDER

Let us finally use our method to find the surface wave excited on a circular cylinder of radius a by a line source parallel to the cylinder axis. If the amplitude of the wave from the source is given by (24), then the surface wave is given by (26). We assume that the cylinder has a constant surface impedance. Then θ in (26) is a constant determined by (22). Let the polar coordinates of Q and P be $(\rho',0)$ and (ρ,ϕ), respectively. There are two rays from Q to P which traverse the cylinder in opposite directions. We first consider the shorter ray. See Fig. 5. The two corresponding pairs of points Q_1, P_1

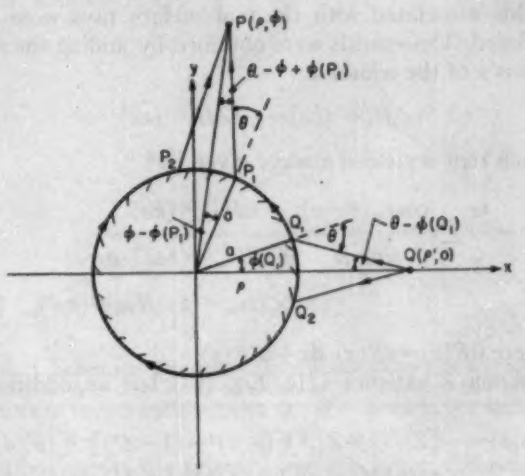

FIG. 5. Excitation of a surface wave on a circular cylinder by a line source at Q. Two complex rays from Q hit the cylinder at the complex points Q_1 and Q_2 where they make the complex angle θ with the normal. This angle is determined by Eq. (22). The two complex surface rays which they excite travel around the cylinder in opposite directions. The complex space rays which they shed at P_1 and P_2 pass through P.

are found to have the coordinates $\rho(Q_1)=\rho(P_1)=a$, and

$$\phi(Q_1)=\cos^{-1}(-Z)-\sin^{-1}[(a/\rho')(1-Z^2)^{\frac{1}{2}}] \quad (60)$$

$$\phi(P_1)=\phi-\cos^{-1}(-Z)+\sin^{-1}[(a/\rho)(1-Z^2)^{\frac{1}{2}}]. \quad (61)$$

Then we find that

$$d(Q,Q_1)=\rho'\{[1-(a/\rho')^2(1-Z^2)]^{\frac{1}{2}}+(a/\rho')Z\} \quad (62)$$

$$d(P,P_1)=\rho\{[1-(a/\rho)^2(1-Z^2)]^{\frac{1}{2}}+(a/\rho)Z\} \quad (63)$$

$$\phi_1(Q_1,P_1)=k_1a[\phi(P_1)-\phi(Q_1)]=ka(1-Z^2)^{\frac{1}{2}}\{\phi-2\cos^{-1}(-Z)+\sin^{-1}[(a/\rho)(1-Z^2)^{\frac{1}{2}}]+\sin^{-1}[(a/\rho')(1-Z^2)^{\frac{1}{2}}]\}. \quad (64)$$

Similar results hold for the longer ray except that ϕ is replaced by $2\pi-\phi$ in (61) and (64). Upon inserting these expressions into (26) and simplifying, we obtain

$$u(\rho,\phi)=[-Z^2/(1-Z^2)^{\frac{1}{2}}][(\rho/a)^2-(1-Z^2)]^{-\frac{1}{4}}[(\rho'/a)^2-(1-Z^2)]^{-\frac{1}{4}}\exp ika((-\rho/a)[1-(a/\rho)^2(1-Z^2)]^{\frac{1}{2}}+(\rho'/a)[1-(a/\rho')^2(1-Z^2)]^{\frac{1}{2}}+(1-Z^2)^{\frac{1}{2}}\{\sin^{-1}[(a/\rho)(1-Z^2)^{\frac{1}{2}}]+\sin^{-1}[(a/\rho')(1-Z^2)^{\frac{1}{2}}]\}+2Z-2(1-Z^2)^{\frac{1}{2}}\cos^{-1}(-Z))[\exp ika(1-Z^2)^{\frac{1}{2}}\phi+\exp ika(1-Z^2)^{\frac{1}{2}}(2\pi-\phi)]. \quad (65)$$

There are also other rays from Q to P each of which encircles the cylinder n times before leaving at P_1. The phase $\phi_1(Q_1,P_1)$ for such rays exceeds that given by (64) by the amount $2\pi nk_1a=2\pi nka(1-Z^2)^{\frac{1}{2}}$. Their fields are computed from (65) by including this additional phase. When the fields on these rays are added together at P, a geometric series results. Its sum is the total surface wave at P which is

$$u(\rho,\phi)=[-Z^2/(1-Z^2)^{\frac{1}{2}}][(\rho/a)^2-(1-Z^2)]^{-\frac{1}{4}}[(\rho'/a)^2-(1-Z^2)]^{-\frac{1}{4}}\times\exp ika((\rho/a)[1-(a/\rho)^2(1-Z^2)]^{\frac{1}{2}}+(\rho'/a)[1-(a/\rho')^2(1-Z^2)]^{\frac{1}{2}}+(1-Z^2)^{\frac{1}{2}}\{\sin^{-1}[(a/\rho)(1-Z^2)^{\frac{1}{2}}]+\sin^{-1}[(a/\rho')(1-Z^2)^{\frac{1}{2}}]\}+2Z-2(1-Z^2)^{\frac{1}{2}}\cos^{-1}(-Z))\times[\exp ika(1-Z^2)^{\frac{1}{2}}\phi+\exp ika(1-Z^2)^{\frac{1}{2}}(2\pi-\phi)][1-\exp[2\pi ika(1-Z^2)^{\frac{1}{2}}]]^{-1}. \quad (66)$$

We shall now compare this result with the solution of the corresponding boundary value problem. That problem was formulated and solved[4] for a cylinder with an impedance Z. However, Z was not assumed to satisfy (21), so that surface waves of the type we are considering were not found. Instead, only the diffracted

[4] B. R. Levy and J. B. Keller, Diffraction by a smooth object; N.Y.U., Inst. Math. Sci., Div. EM Res., Research Report No. EM-109, Dec., 1957; Comm. Pure Appl. Math. 12, 159–209 (1959).

fields associated with the real surface rays were considered. Those fields were obtained by finding the solutions ν of the equation

$$H_\nu^{(1)\prime}(ka) = -iZH_\nu^{(1)}(ka). \tag{67}$$

Each root ν yielded a wave given by[5]

$$u = -\frac{i\pi}{4}\sum_m \frac{\cos\nu_m(\theta-\pi)}{\sin\nu_m\pi}\,\frac{\Omega H_{\nu_m}^{(2)}(ka)}{\partial[\Omega H_{\nu_m}^{(1)}(ka)]/\partial\nu} \times H_{\nu_m}^{(1)}(k\rho)H_{\nu_m}^{(1)}(k\rho'), \tag{68}$$

where $\Omega F(x) = dF(x)/dx + iZF(x)$.

When Z satisfies (21), Eq. (67) has an additional solution which corresponds to the surface wave. It can be found by using in (67) the Debye asymptotic formula for the Hankel function for order and argument both large and $|\nu| > ka$. Then (67) becomes

$$i(2/\pi)^{\frac{1}{2}}[\nu^2-(ka)^2]^{-\frac{1}{4}}(\{[\nu^2-(ka)^2]^{\frac{1}{2}}/ka\}-iZ) \times\exp\{-[\nu^2-(ka)^2]^{\frac{1}{2}}+\nu\cosh^{-1}(\nu/ka)\}=0. \tag{69}$$

The solution of (69) is

$$\nu = ka(1-Z^2)^{-\frac{1}{2}}. \tag{70}$$

When (70) is used in (68) and the asymptotic form of the Hankel function is employed, the surface term in (68) becomes

$$u(\rho,\phi) = -[Z^2/(1-Z^2)^{\frac{1}{2}}][(\rho/a)^2-(1-Z^2)]^{-\frac{1}{4}}[(\rho'/a)^2-(1-Z^2)]^{-\frac{1}{4}} \times\exp ika(\{(\rho/a)[1-(a/\rho)^2(1-Z^2)]^{\frac{1}{2}}+(\rho'/a)[1-(a/\rho')^2(1-Z^2)]^{\frac{1}{2}} +(1-Z^2)^{\frac{1}{2}}\{\sin^{-1}[(a/\rho)(1-Z^2)^{\frac{1}{2}}]+\sin^{-1}[(a/\rho')(1-Z^2)]\}+2Z-2(1-Z^2)^{\frac{1}{2}}\{\tfrac{1}{2}\pi-i\cosh^{-1}(1-Z^2)^{\frac{1}{2}}\}) \times[\exp ika(1-Z^2)^{\frac{1}{2}}\phi+\exp ika(1-Z^2)^{\frac{1}{2}}(2\pi-\phi)]\{1-\exp[2\pi ika(1-Z^2)^{\frac{1}{2}}]\}^{-1}. \tag{71}$$

This is the asymptotic form of the exact surface wave (68). After some algebraic manipulations, it agrees exactly with the result (66) given by our method.

[5] See work cited in footnote 4, p. 43, Eq. (4).

JOURNAL OF APPLIED PHYSICS VOLUME 31, NUMBER 6 JUNE, 1960

Range of Radiation Induced Primary Knock-Ons in the Hard Core Approximation

D. K. Holmes and G. Leibfried
Solid State Division Oak Ridge National Laboratory, Oak Ridge, Tennessee*
(Received April 17, 1959)

The slowing down of a primary displaced atom of high energy in a solid is investigated in detail. Physically interesting quantities, such as the total distance travelled and the vector distance to the end of the path, are discussed in terms of certain averages for hard core potentials with general dependence of the core radius on energy. These averages are explicitly calculated for a screened Coulomb potential for the purpose of comparison with experimental ranges observed in different metals. Theoretical values for the range can be derived. Comparison with the experimental data gives a value for the screening radius of the interaction potential which is about twice the value originally suggested by N. Bohr.

I. INTRODUCTION

FOR the interpretation of radiation effects in solids it is of special interest to obtain information about the collision history of a high energy primary atom which has been displaced from its lattice site by interaction with incoming radiation. The fate of a high energy primary depends very sensitively on the interaction potential between the atoms of the solid. The first theoretical estimates of these potentials have been made by N. Bohr[1] who used a screened Coulomb potential for the interaction. Different investigators in this field have used quite different screening radii for the interaction and since the screening radius "a" is contained exponentially in the potential the numerical results are substantially different.[2] Experiments directly pertinent to a determination of the screening radius were not available until recently when R. A. Schmitt and R. A. Sharp measured the ranges of high energy primaries induced by (γ,n) processes in a number of solids.[3] These experiments can be compared with theoretical estimates using a potential of the Bohr type of arbitrary screening parameter and thus give some information about the most reasonable value of the screening radius. Schmitt and Sharp have compared their experimental

* Oak Ridge National Laboratory is operated by Union Carbide Corporation for the U. S. Atomic Energy Commission.

[1] N. Bohr, Kgl. Danske Videnskab. Selskab. Biol. Medd. 18, No. 8 (1948).

[2] Compare F. Seitz and J. S. Koehler, *Displacement of Atoms during Irradiation*, in Solid State Physics 2, 305 (Academic Press, Inc., New York, 1956).

[3] R. A. Schmitt and R. A. Sharp, Phys. Rev. Letters 1, 445 (1958).

data with theoretical calculations of K. O. Nielsen[4] and have claimed that the original value of "a" given by Bohr fits with the experiment. The calculations of Nielsen are based on a relatively crude approximation which we felt was not good enough for conclusive determination of the parameters involved. Therefore we have used a more exact method to calculate the ranges, with the result that a value of about twice Bohr's original value would fit the experiment best. The methods employed here may also be of interest for radiation damage calculations since the collision history of a fast primary plays an essential role in the production and distribution of the defects in the solid.

In the energy range of interest here one can treat the collision problem by classical collision theory. Furthermore, one can replace the collision potential with sufficient accuracy by a hard core potential with energy-dependent hard core radius. In the following we give first an introduction to the distribution functions involved in a collision series using the hard core approximation. Then it is shown how various averages of interest can be calculated. These results can be applied to any potential where the hard core approximation is justified, for instance in the low energy range where presumably the Bohr potential has to be replaced by a potential of the Born-Mayer type. For a Bohr potential the averages are explicitly calculated. One of these averages is closely related to the measured range, and a lower and upper limit of the ranges may be obtained. The theoretical results are compared with the experimental data to determine an optimal value of the screening radius. Finally, possible application to the problem of radiation damage is discussed.

II. PROBABILITY DISTRIBUTION

We investigate the series of collisions which an energetic primary knock on must undergo in a crystal before coming to rest. The total history of the primary is given by the distances l_ν, the directions $\mathbf{u}^\nu$, and the energy E_ν between the νth and $\nu+1$st collisions (Fig. 1). These quantities are distributed according to statistical laws. The special form of the distribution depends on the scattering law for a single collision and its energy-dependence.

The probability for finding l_0, $\mathbf{u}^0$, and E_0 in respective intervals dl_0, $d\Omega_0$, dE_0 would for instance be given by

$$W_0 dl_0 d\Omega_0 dE_0 = \frac{e^{-(l_0/\lambda_0)}}{\lambda_0} \mathcal{G}(\mathbf{u}^0, E_0) dl_0 d\Omega_0 dE_0. \quad (1)$$

Here $\lambda_0 = \lambda(E_0)$ is the mean free path for energy E_0. The mean free path is defined by $\lambda(E) = 1/n\sigma(E)$ where σ is the total cross section and n is the number of atoms per unit volume. $\mathcal{G}(\mathbf{u}^0, E_0)$ is the angular and energy distribution for the primary and $d\Omega_0$ is the differential solid angle element corresponding to the unit vector $\mathbf{u}^0$. The distribution (1) is to be normalized to unity. Since the factor $1/\lambda_0$ normalizes the l_0-distribution already, $\mathcal{G}$ is to be a normalized function itself. The function $\mathcal{G}$ has to be chosen according to circumstances. If one wants to investigate a given direction $\mathbf{u}$ and a fixed energy E, one has to use $\mathcal{G} = \delta(E-E_0)\delta(\mathbf{u}-\mathbf{u}^0)$ or if the distribution of directions is isotropic $\mathcal{G} = \delta(E-E_0)1/4\pi$. The limits of integration are zero to infinity for distance and energy and the whole range 4π in the solid angle for the angular distribution. The total distribution function W_1 after the first hit is

$$W_1 = \frac{e^{-(l_0/\lambda_0)}}{\lambda_0} \mathcal{G}(\mathbf{u}^0, E_0) \cdot \frac{e^{-(l_1/\lambda_1)}}{\lambda_1} \mathcal{G}(\mathbf{u}^0, E_0; \mathbf{u}^1, E_1). \quad (2)$$

Here λ_1 means $\lambda(E_1)$ and $\mathcal{G}(\mathbf{u}^0, E_0; \mathbf{u}^1, E_1)$ is the distribution function for the angles $\mathbf{u}^1$ and the energy E_1 after one hit with given $\mathbf{u}^0$ and E_0. This function must be normalized with respect to integrations over E_1 and Ω_1.

If one treats a spherically symmetric scattering potential, the distribution of the directions $\mathbf{u}^1$ is azimuthally symmetric about the direction $\mathbf{u}^0$ and the cosine of the included angle, $\mathbf{u}^0 \cdot \mathbf{u}^1$, is a unique function of the energies E_0, E_1. Since in our problem the collision partners have equal masses one has the well known relation

$$\mathbf{u}^0 \cdot \mathbf{u}^1 = \left\{\frac{E_1}{E_0}\right\}^{\frac{1}{2}}. \quad (3)$$

Because of this it is possible to separate $\mathcal{G}$ into a product of two functions

$$\mathcal{G}(\mathbf{u}^0, E_0; \mathbf{u}^1, E_1) = \frac{\delta[\mathbf{u}^0 \cdot \mathbf{u}^1 - (E_1/E_0)^{\frac{1}{2}}]}{2\pi} g(E_0; E_1). \quad (4)$$

The function g describes the distribution of energies E_1 after one collision with initial energy E_0; g is normalized with respect to integration over E_1. The scattering law then comes into the calculation only through the form of $g(E_0; E_1)$. Later on we will deal for the sake of

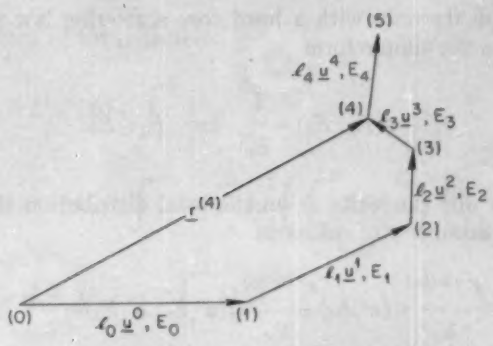

FIG. 1. Schematic diagram of the collision history of a primary starting with energy E_0 in direction $\mathbf{u}^0$. $\mathbf{r}^{(\nu)}$ denotes the vector distance to the νth collision point (ν); $\mathbf{r}^4$ is shown in the figure.

[4] K. O. Nielsen in *Electromagnetically Enriched Isotopes and Mass Spectrometry* (Academic Press, Inc., New York; and Butterworth Corporation, London, 1956).

simplicity only with a hard core scattering law where g has the simple form

$$g(E_0; E_1)=\frac{1}{E_0} \quad \text{for} \quad E_1 \leqslant E_0. \tag{5}$$

Now one can write down the total distribution W_ν for any number ν of collisions

$$W_\nu=\frac{e^{-(l_0/\lambda_0)}}{\lambda_0}\mathcal{G}(\mathbf{u}^0,E_0)\frac{e^{-(l_1/\lambda_1)}}{\lambda_1}\mathcal{G}(\mathbf{u}^0,E_0;\mathbf{u}^1,E_1)\cdots \times\frac{e^{-(l_\nu/\lambda_\nu)}}{\lambda_\nu}\mathcal{G}(\mathbf{u}^{\nu-1},E_{\nu-1};\mathbf{u}^\nu,E_\nu). \tag{6}$$

We will confine our investigations to an infinite number of collisions, that is, we try to get some information about the final state when the primary has come to rest. We call the distribution function for $\tau=\infty$ simply W. The energy decreases continuously hit by hit. In the high energy region one can use an appropriate potential fitted to the experimental data, e.g., a Bohr potential. In the low energy region, where the lattice structure comes into play and where the concept of mean free path becomes meaningless, one may account for the influence of lattice structure by allowing the mean free path λ to become negligibly small at energies in the vicinity of the displacement energy of the crystal in question.

In the following we require some properties of averages taken over the distribution (4). Since the distribution of $\mathbf{u}^1$ has azimuthal symmetry about the direction $\mathbf{u}^0$ the average value of $\mathbf{u}^1$ averaged over the angles Ω_1 in (4) is simply

$$\langle \mathbf{u}^1\rangle_{\mathrm{av}}=\mathbf{u}^0\cdot\left\{\frac{E_1}{E_0}\right\}^{\frac{1}{2}}. \tag{7}$$

Further one gets

$$\langle u_i^1 u_k^1\rangle_{\mathrm{av}}=\frac{1}{2}\left\{u_i^0 u_k^0\left(\frac{3E_1}{E_0}-1\right)+\delta_{ik}\left(1-\frac{E_1}{E_0}\right)\right\} \qquad i,k=1,2,3 \text{ or } x,y,z. \tag{7a}$$

The validity of (7a) may easily be seen by choosing $\mathbf{u}^0$ as lying in the direction of the x axis. Then $\langle(u_x^1)^2\rangle_{\mathrm{av}}$ must be equal to $(\mathbf{u}^1\cdot\mathbf{u}^0)^2=E_1/E_0(u_x^0)^2=E_1/E_0$ whereas $\langle(u_y^1)^2\rangle_{\mathrm{av}}$ and $\langle(u_z^1)^2\rangle_{\mathrm{av}}$ must be equal to $\frac{1}{2}(1-E_1/E_0)$ because $\mathbf{u}^1$ is a unit vector, and the off-diagonal elements of (7a) must vanish.

Further we require the energy distribution $g_\nu(E_0,E_\nu)$ after ν collisions regardless of the angles and distances. This function is given by

$$g_\nu(E_0,E_\nu)=\int g(E_0,E_1)g(E_1,E_2)\cdots \times g(E_{\nu-1},E_\nu)dE_1\cdots dE_{\nu-1}. \tag{8}$$

For the hard core scattering (5) the integration can easily be carried out with the result

$$g_\nu(E_0,E_\nu)=\frac{1}{E_0(\nu-1)!}\ln^{\nu-1}\frac{E_0}{E_\nu} \qquad \text{for} \quad E_\nu\leqslant E_0;\ \nu=1,2,3\cdots. \tag{8a}$$

This function is again normalized with respect to integration over E_ν.

III. CALCULATION OF AVERAGES

Of especial physical interest are the quantities: the total path travelled

$$L=\sum_{\nu=0}^{\infty} l_\nu \tag{9}$$

and the vectorial distance

$$\mathbf{r}=\sum_{\nu=0}^{\infty} l_\nu\mathbf{u}^\nu. \tag{10}$$

One should know the distribution functions $W(L)dL$ and $W(\mathbf{r})d\mathbf{r}$. Because of the difficulties in the calculation of the complete distributions we will be content with the calculation of averages of the quantities above which give an estimate of the magnitude of the effects. Further one can calculate averages over squares of the quantities (9) and (10) to get the variance and an approximate value for the width of the distributions.

The average value of L is given by

$$L=\sum_\nu l_\nu=\sum_{\nu=0}^{\infty}\int l_\nu W d\tau \tag{11}$$

where W is the distribution (6) with infinite number of hits and $d\tau$ refers to all the variables contained in W. Because L does not contain the angles, the integration over the angles may be carried out leaving only energy and mean free path distributions. The integration over the variables l can also be easily done. After the integration over l_ν, one has

$$L=\sum_{\nu=0}^{\infty}\int W\lambda_\nu d\tau=\int g(E_0)\lambda(E_0)dE_0 +\sum_{\nu=1}^{\infty}\int g(E_0)g(E_0;E_1)\cdots \times g(E_{\nu-1};E_\nu)\lambda(E_\nu)dE_0\cdots dE_\nu. \tag{11a}$$

In (11a) the integrations for a given ν over all E_μ with $\mu>\nu$ have been performed; all these integrals contribute a factor 1 because of the normalization of the distributions. $g(E_0)$ is the energy-distribution of the primary.

With the abbreviation (8) one gets, using (8a)

$$L=\int g(E_0)\lambda(E_0)dE_0 + \sum_{\nu=1}^{\infty}\int g(E_0)g_\nu(E_0,E_\nu)\lambda(E_\nu)dE_0dE_\nu$$

$$=\int g(E_0)\lambda(E_0)dE_0 + \sum_{\nu=1}^{\infty}\int g(E_0)dE_0\int_0^{E_0}\frac{1}{E_0(\nu-1)!}\ln^{\nu-1}\frac{E_0}{\epsilon}\lambda(\epsilon)d\epsilon. \quad (11b)$$

The sum over ν may be performed and gives the final result

$$L=\int g(E_0)\lambda(E_0)dE_0+\int g(E_0)dE_0\int_0^{E_0}\lambda(\epsilon)\frac{d\epsilon}{\epsilon}. \quad (11c)$$

For given energy E of the primary one has with $g(E_0)=\delta(E-E_0)$

$$L=\lambda(E)+\int_0^E\lambda(\epsilon)\frac{d\epsilon}{\epsilon}. \quad (11d)$$

In the same way one can proceed to calculate

$$\langle L^2\rangle_{av}=\sum_{\mu,\nu=0}^{\infty}\langle l_\mu l_\nu\rangle_{av}=\sum_\nu\langle l_\nu^2\rangle_{av}+2\sum_{\mu>\nu}\langle l_\mu l_\nu\rangle_{av}. \quad (12)$$

In the first sum the effect of the integration over l is to replace[5] $\langle l_\nu^2\rangle_{av}$ by $2\lambda_\nu^2$ and in the second $\langle l_\mu l_\nu\rangle_{av}$ by $\lambda_\mu\lambda_\nu$. Therefore one has

$$\langle L^2\rangle_{av}=2\{\sum_\nu\langle\lambda_\nu^2\rangle_{av}+\sum_{\mu>\nu}\langle\lambda_\mu\lambda_\nu\rangle_{av}\}. \quad (12a)$$

The first sum can be treated exactly as the one for L with the result

$$\sum_\nu\lambda_\nu^2=\lambda^2(E)+\int_0^E\lambda^2(\epsilon)\frac{d\epsilon}{\epsilon}, \quad (13)$$

for given $E_0=E$. The second sum is for $\nu=0$

$$\lambda(E)\sum_{\mu\geq 1}\langle\lambda_\mu\rangle_{av}=\lambda(E)\int_0^E\lambda(\epsilon)\frac{d\epsilon}{\epsilon}.$$

For $\nu\geq 1$ one has

$$\sum_{\mu>\nu\geq 1}\langle\lambda_\mu\lambda_\nu\rangle_{av}=\int g_\nu(E,E_\nu)g_{\mu-\nu}(E_\nu,E_\mu)\lambda(E_\mu)\lambda(E_\nu)dE_\mu dE_\nu.$$

This can be calculated to be

$$\sum_{\mu>\nu\geq 1}\langle\lambda_\mu\lambda_\nu\rangle_{av}=\int_0^E\lambda(\epsilon)\frac{d\epsilon}{\epsilon}\int_0^\epsilon\lambda(\epsilon')\frac{d\epsilon'}{\epsilon'}=\frac{1}{2}\left\{\int_0^E\lambda(\epsilon)\frac{d\epsilon}{\epsilon}\right\}^2.$$

[5] $\int_0^\infty p\epsilon^{-(l/\lambda)}dl/\lambda=2\lambda^2$.

The final result is then

$$\langle L^2\rangle_{av}=2\left\{\lambda^2(E)+\int_0^E\lambda^2(\epsilon)\frac{d\epsilon}{\epsilon}+\lambda(E)\int_0^E\lambda(\epsilon)\frac{d\epsilon}{\epsilon}+\frac{1}{2}\left(\int_0^E\lambda(\epsilon)\frac{d\epsilon}{\epsilon}\right)^2\right\}$$

$$=L^2+\lambda^2(E)+2\int_0^E\lambda^2(\epsilon)\frac{d\epsilon}{\epsilon}. \quad (12b)$$

This result enables one to calculate the variance $\langle\Delta L^2\rangle_{av}=L^2-\langle L^2\rangle_{av}$ which gives a first approximation to the width of $W(L)$.

In a similar way one can calculate averages over $\mathbf{r}$. This is somewhat more complicated because $\mathbf{r}$ contains the directions $\mathbf{u}^\nu$. The average value of $\mathbf{r}$ itself is given by

$$\langle\mathbf{r}\rangle_{av}=\sum_{\nu=0}^{\infty}\langle l_\nu\mathbf{u}^\nu\rangle_{av}=\sum_{\nu=0}^{\infty}\int W d\tau l_\nu\mathbf{u}^\nu. \quad (14)$$

The integration over the l's can be carried out

$$\langle\mathbf{r}\rangle_{av}=\sum_{\nu=0}^{\infty}\langle\lambda_\nu\mathbf{u}^\nu\rangle_{av}=\int g(\mathbf{u}^0,E_0)\lambda(E_0)\mathbf{u}^0dE_0d\Omega_0 + \sum_{\nu\geq 1}\int g(\mathbf{u}^0,E_0)g(\mathbf{u}^0,E_0;\mathbf{u}^1,E_1)\cdots \times g(\mathbf{u}^{\nu-1},E_{\nu-1};\mathbf{u}^\nu,E_\nu)\lambda(E_\nu)\mathbf{u}^\nu dE_\nu d\Omega_\nu. \quad (14a)$$

In the sum one can integrate over Ω_ν which, using (4) and (7), replaces $\mathbf{u}^\nu$ by $\mathbf{u}^{\nu-1}\{E_\nu/E_{\nu-1}\}^{\frac{1}{2}}$. Further integration over $\Omega_{\nu-1}$ replaces this by

$$\mathbf{u}^{\nu-2}\{E_{\nu-1}/E_{\nu-2}\}^{\frac{1}{2}}\cdot\{E_\nu/E_{\nu-1}\}^{\frac{1}{2}}=\mathbf{u}^{\nu-2}\{E_\nu/E_{\nu-2}\}^{\frac{1}{2}}.$$

Eventually $\mathbf{u}^\nu$ is replaced by $\mathbf{u}^0\{E_\nu/E_0\}^{\frac{1}{2}}$:

$$\langle\mathbf{r}\rangle_{av}=\int g(\mathbf{u}^0,E_0)dE_0d\Omega_0\left\{\lambda(E_0)\mathbf{u}^0 + \int dE_\nu\sum_{\nu\geq 1}g(E_0,E_\nu)\cdot\left\{\frac{E_\nu}{E_0}\right\}^{\frac{1}{2}}\lambda(E_\nu)\mathbf{u}^0\right\}. \quad (14b)$$

The sum over ν is calculated as in (11c)

$$\langle\mathbf{r}\rangle_{av}=\int g(\mathbf{u}^0,E_0)dE_0d\Omega_0\left\{\lambda(E_0)\mathbf{u}^0 + \int_0^{E_0}\lambda(\epsilon)\frac{d\epsilon}{\epsilon}\cdot\left\{\frac{\epsilon}{E_0}\right\}^{\frac{1}{2}}\mathbf{u}^0\right\}. \quad (14c)$$

For an isotropic initial distribution $\langle\mathbf{r}\rangle_{av}$ vanishes. For given energy E and given direction $\mathbf{u}$ one gets with

$$g(\mathbf{u}^0,E_0)=\delta(\mathbf{u}-\mathbf{u}^0)\delta(E-E_0)$$

$$\langle\mathbf{r}\rangle_{av}=\left\{\lambda(E)+\frac{1}{(E)^{\frac{1}{2}}}\int_0^E\lambda(\epsilon)\frac{d\epsilon}{(\epsilon)^{\frac{1}{2}}}\right\}\mathbf{u}. \quad (14d)$$

In a similar way one can treat the averages of r^2.

$$\langle\mathbf{r}^2\rangle_{av}=\sum_{\mu,\nu}\langle l_\mu l_\nu\mathbf{u}^\mu\cdot\mathbf{u}^\nu\rangle_{av}=\sum_\nu\langle l_\nu^2\rangle_{av}+2\sum_{\mu>\nu}\langle l_\mu l_\nu\mathbf{u}^\mu\cdot\mathbf{u}^\nu\rangle_{av}. \quad (15)$$

Using (7) one gets

$$\langle r^2\rangle_{av}=2\{\sum_\nu\langle\lambda_\nu^2\rangle_{av}+\sum_{\mu>\nu}\langle\lambda_\nu\lambda_\mu(E_\mu/E_\nu)^{\frac{1}{2}}\rangle_{av}\}. \quad (15a)$$

The first sum and the $\nu=0$-term of the second sum are easily calculated as above. The expression

$$\sum_{\mu\geq\nu\geq1}\langle\lambda_\nu\lambda_\mu(E_\mu/E_\nu)^{\frac{1}{2}}\rangle_{av}$$

becomes

$$\sum_{\mu>\nu\geq1}\int g(E_0)g_\nu(E_0,\epsilon)g_{\mu-\nu}(\epsilon,\epsilon')\lambda(\epsilon)\lambda(\epsilon')(\epsilon'/\epsilon)^{\frac{1}{2}}d\epsilon'd\epsilon dE_0$$

$$=\int g(E_0)dE_0\int_0^{E_0}\lambda(\epsilon)\frac{d\epsilon}{\epsilon^{\frac{1}{2}}}\int_0^{\epsilon}\lambda(\epsilon')\frac{d\epsilon'}{(\epsilon')^{\frac{1}{2}}}.$$

For given E the final result is

$$\langle r^2\rangle_{av}=2\left\{\lambda^2(E)+\int_0^E\lambda^2(\epsilon)\frac{d\epsilon}{\epsilon}+\frac{\lambda(E)}{(E)^{\frac{1}{2}}}\int_0^E\lambda(\epsilon)\frac{d\epsilon}{(\epsilon)^{\frac{1}{2}}}+\int_0^E\lambda(\epsilon)\frac{d\epsilon}{\epsilon^{\frac{1}{2}}}\int_0^{\epsilon}\lambda(\epsilon')\frac{d\epsilon'}{(\epsilon')^{\frac{1}{2}}}\right\}. \quad (15b)$$

In case $\mathbf{u}^0$ is isotropically distributed the whole $\mathbf{r}$-distribution is isotropic and one has $\langle x^2\rangle_{av}=\langle y^2\rangle_{av}=\langle z^2\rangle_{av}=\langle r^2/3\rangle_{av}$. If one starts with a given $\mathbf{u}^0=\mathbf{u}$, say $\mathbf{u}=(1,0,0)$, in the x direction, then $\langle x^2\rangle_{av}\neq\langle y^2\rangle_{av}=\langle z^2\rangle_{av}$ and (7a) must be used for an exact calculation. One gets

$$\langle x_ix_k\rangle_{av}=2\{\sum_\nu\langle\lambda_\nu^2u_i^\nu u_k^\nu\rangle_{av}+\sum_{\mu>\nu}\lambda_\nu\lambda_\mu u_i^\nu u_k^\nu(E_\mu/E_\nu)^{\frac{1}{2}}\}. \quad (16)$$

Here the exact calculation is more difficult, because the integration over the angles gives terms which contain all energies from E_0 to E_ν. The energy factors do not cancel as in the case of $\langle\mathbf{u}^\nu\rangle_{av}$. For an approximate calculation the energy term in (7a) may be replaced by its average value $E_1/E_0=\frac{1}{2}$

$$u_i^1u_k^1\cong u_i^0u_k^0\cdot\tfrac{1}{4}+\delta_{ik}/4. \quad (7b)$$

With this approximate relation one can calculate (16) relatively easily because

$$\langle u_i^\nu u_k^\nu\rangle_{av}=\tfrac{1}{4}\langle u_i^{\nu-1}u_k^{\nu-1}\rangle_{av}+\tfrac{1}{4}=\frac{1}{4^2}\langle u_i^{\nu-2}u_k^{\nu-2}\rangle_{av}+\frac{1}{4}+\frac{1}{4^2}\cdots$$

and so

$$\langle u_i^\nu u_k^\nu\rangle_{av}=\frac{1}{4^\nu}u_i^0u_k^0+\sum_{\nu'=1}^{\nu}\frac{1}{4^{\nu'}}=\frac{1}{4^\nu}u_i^0u_k^0+\frac{1}{3}\left(1-\frac{1}{4^\nu}\right)\delta_{ik}.$$

If $\mathbf{u}^0$ has only an x component, then

$$\langle y^2\rangle_{av}=\langle z^2\rangle_{av}=\langle r^2\rangle_{av}/3-2\gamma$$
$$\langle x^2\rangle_{av}=\langle r^2\rangle_{av}/3+\tfrac{4}{3}\gamma \quad (16a)$$

with

$$\gamma=\sum_\nu\langle\lambda_\nu^2\rangle_{av}/4^\nu+\sum_{\mu>\nu}\lambda_\nu\lambda_\mu(E_\mu/E_\nu)^{\frac{1}{2}}\frac{1}{4^\nu}.$$

The value of γ can be calculated as before to be

$$\gamma=\lambda^2(E)+\frac{1}{4E^{\frac{1}{2}}}\int_0^E\lambda^2(\epsilon)\frac{d\epsilon}{\epsilon^{\frac{1}{2}}}+\frac{\lambda(E)}{(E)^{\frac{1}{2}}}\int_0^E\lambda(\epsilon)\frac{d\epsilon}{(\epsilon)^{\frac{1}{2}}}+\frac{1}{4E^{\frac{1}{2}}}\int_0^E\lambda(\epsilon)\frac{d\epsilon}{\epsilon^{\frac{1}{2}}}\int_0^{\epsilon}\lambda(\epsilon')\frac{d\epsilon'}{(\epsilon')^{\frac{1}{2}}}. \quad (16b)$$

By calculating these quantities one can get an idea of the shape of a spike originating from a primary E, $\mathbf{u}$ since under the assumption of a hard core scattering law the distribution of all displaced atoms is the same.

IV. APPLICATION TO A BOHR POTENTIAL

To evaluate the expressions for the averages in the foregoing section we choose a screened Coulomb potential following Bohr,[1] as follows

$$\varphi(r)=\frac{Z^2e^2}{r}e^{-(r/a)}. \quad (17)$$

This potential refers to collisions between like nuclei of atomic number Z with charge Ze. The screening radius a has been taken by Bohr as

$$a=a_B/\sqrt{2}Z^{\frac{1}{2}}, \quad (17a)$$

where a_B is the Bohr radius for hydrogen.

It is convenient to use r/a as a variable and to write (17) in the following form:

$$\varphi(r)=\frac{E_Ba}{2}\frac{}{r}e^{-(r/a)}, \quad (17b)$$

with

$$E_B=2Z^2e^2/a. \quad (17c)$$

Since the value of a is rather uncertain[2] one can regard the screening radius as a parameter to be obtained from the experimental data. This is done in Sec. VI.

The scattering effected by a potential of the form (17) can be treated with sufficient accuracy as a hard core scattering provided that the distance of closest approach, $R(E)$, defined by

$$E=E_B\frac{a}{R}e^{-(R/a)}. \quad (18)$$

is larger than the screening radius a. Here E is the energy of the atom which collides with another atom at rest.[6]

The scattering cross section is simply πR^2 and for the mean free path λ one has

$$\lambda(E)=1/n\pi R^2(E) \tag{19}$$

with n being the number of atoms per unit volume.

Mostly we will use $R(E)$ according to (18) rather than E itself to characterize the energy of the collision because the results are more simply expressed in R.

The integrals occurring in $\bar{L}$ and $\langle L^2\rangle_{av}$ can now easily be worked out[7] with the result:

$$\bar{L}=\lambda(E)\left\{\frac{3}{2}+\frac{R}{a}\right\} \tag{20}$$

$$\langle L^2\rangle_{av}=\lambda^2(E)\left\{\frac{3}{2}+\frac{2}{3}\frac{R}{a}\right\}+\bar{L}^2. \tag{20a}$$

The evaluation of the integrals occurring in $\langle \mathbf{r}\rangle_{av}$ and $\langle r^2\rangle_{av}$ is somewhat more difficult but of elementary nature. The final results are

$$\langle \mathbf{r}\rangle_{av}=\{\lambda(E)+I_1(E)\}\mathbf{u} \tag{21}$$

where

$$I_1(E)=\int_0^E \lambda(\epsilon)\frac{d\epsilon}{(E\epsilon)^{\frac{1}{2}}},$$

and

$$\langle r^2\rangle_{av}=2\left\{\lambda^2(E)+\lambda^2(E)\left(\frac{1}{4}+\frac{R}{3a}\right)+\lambda(E)I_1(E)+I_2(E)\right\}, \tag{22}$$

where

$$I_2(E)=\int_0^E \lambda(\epsilon)I_1(\epsilon)d\epsilon/\epsilon.$$

The integral I_1 contains besides powers in R an error function of the argument $\{R/2a\}^{\frac{1}{2}}$. The integration is carried out in Appendix A. The expression I_2 contains besides elementary terms an integral over the error function (Appendix B). This term has been calculated numerically. For small energies or $R\gg a$ one can derive an asymptotic expression for $\langle r^2\rangle_{av}$

$$\langle r^2\rangle_{av}\sim\lambda^2(E)\left\{\frac{7}{2}+\frac{2R}{a}\right\}, \tag{22a}$$

which fits the exact value (22) curiously enough also very well even in the region $R\lesssim a$.

In Fig. 2 the results are plotted versus the energy ratio E/E_B. Here λa is the mean free path for $R=a$: $\lambda a=1/n\pi a^2$.

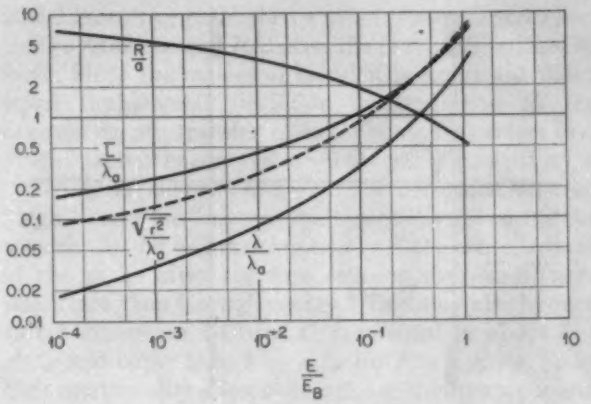

FIG. 2. Dependence of characteristic averages on energy for a Bohr potential.

V. RANGE

If $f(\rho)d\rho$ is the probability that a particle of given initial energy reaches a maximum distance from its starting point between ρ and $\rho+d\rho$ (see Fig. 4) in the solid during the whole slowing down process, then one can define the range $\mathfrak{R}$ by the average of ρ over the f distribution

$$\mathfrak{R}=\bar{\rho}=\int_0^\infty \rho f(\rho)d\rho. \tag{23}$$

This quantity has been measured experimentally. That just $\mathfrak{R}$ occurs in the experimental results may be seen as follows. If one treats the problem of a plate of thickness T large as compared with $\mathfrak{R}$ it is especially easy. If $g(\rho)$ with

$$g(\rho)=\int_\rho^\infty f(\rho')d\rho' \tag{24}$$

is the probability for reaching a distance larger than ρ, then

$$W(x)=\int_0^{\pi/2} g\left(\frac{x}{\cos\theta}\right)\frac{2\pi\sin\theta}{4\pi}d\theta, \tag{25}$$

is the probability that a primary starting at distance x from the surface will leave the plate (Fig. 3). The x direction is normal to the surface and the θ integration

[6] The use of the hard core scattering approximation cannot be justified in detail at present. The arguments given by Nielsen[4] for the $1/r^2$ potential (chosen to match the Bohr potential at $R=a$) are not convincing, since the spectrum for the transferred energy differs greatly from a uniform distribution appropriate to the hard core approximation. An effort to obtain the spectrum for the Bohr potential is now being made by the authors. It is expected, however, that the hard core approximation would apply better to the Bohr potential than to an inverse power potential, particularly for small energy transfers, for which the important part of the Bohr potential falls off more rapidly with distance. Thus the effect of this assumption is smaller for the later collisions in the history of a primary and, since the first collision will contribute only up to 50% of the range even for $R\sim a$, it is thought that the error introduced is not serious.

[7] $\int_0^E \lambda(\epsilon)\frac{d\epsilon}{\epsilon}=\int_{R(E)}^\infty \frac{1}{n\pi R'^2}\left(\frac{1}{R'}+\frac{1}{a}\right)dR'=\lambda(E)\left\{\frac{1}{2}+\frac{R}{a}\right\}$

$\int_0^E \lambda^2(\epsilon)\frac{d\epsilon}{\epsilon}=\int_{R(E)}^\infty \left(\frac{1}{n\pi R'^2}\right)^2\left(\frac{1}{R'}+\frac{1}{a}\right)dR'=\lambda^2(E)\left\{\frac{1}{4}+\frac{1}{3}\frac{R}{a}\right\}.$

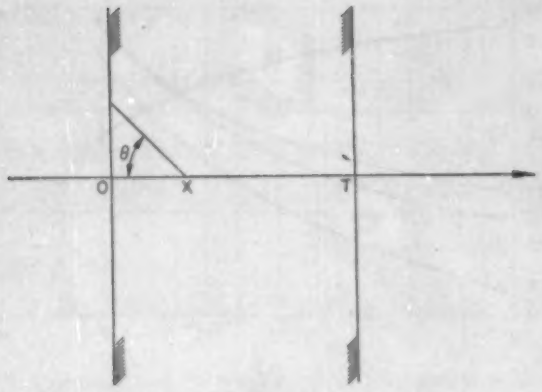

FIG. 3. The geometry for the escape of a primary from a plate.

covers half of the whole solid angle 4π. It is assumed here that the primaries have an isotropic distribution.

If one now produces $n_0(x)$ primaries per unit length in the plate by irradiation and if one assumes that n_0 is independent of x, then $\int_0^\infty n_0(x)W(x)dx = n_0\int_0^\infty W(x)dx$ is the number of primaries leaving the plate to the left. Here we have assumed that the distribution f or g is only different from zero for values small as compared with the thickness of the plate T or roughly $\mathfrak{R} \ll T$. Then one can replace the upper limit T in the integral by ∞. The total number N_{out} leaving the plate on both sides is then twice this value

$$N_{\text{out}} = 2n_0\int_0^\infty W(x)dx = \frac{n_0}{2}\int_0^\infty g(y)dy. \qquad (26)$$

Integration by parts using $\partial g/\partial y = -f(y)$ gives finally

$$N_{\text{out}} = \frac{n_0}{2}\int_0^\infty yf(y)dy = n_0(\mathfrak{R}/2). \qquad (26a)$$

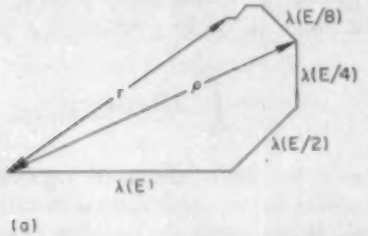

(a)

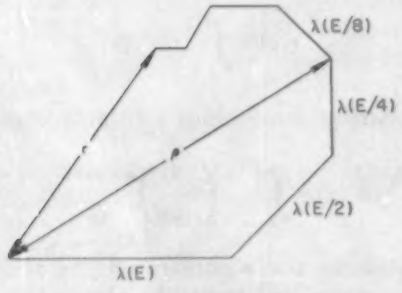

(b)

FIG. 4. Range ρ and distance r for two particular collision sequences. (a) $R(E)/a \cong 0.6$; $E = E_B$; (b) $R(E)/a = 2$; $E \cong 7\times10^{-3}E_B$.

The measurements[3] have been carried out in the following way. A plate was irradiated with γ rays up to about 20 Mev. This irradiation induces (γ,n) processes in the material. The recoil by the evaporating neutrons of the highly excited nucleus gives primaries with a high recoil energy in the order of some ten thousand ev depending on the nuclear masses. The primaries themselves become radioactive and can be observed by their radioactive decay. In this way one can measure the number of radioactive recoil atoms N_{out} which have left the plate as well as the number N_{in} which stayed in the plate. If the production rate n_0 is everywhere constant and if $T \gg \mathfrak{R}$, e.g., if only a small part of recoil atoms leaves the material, then one can replace n_0 by N_{in}/T. Thus one has

$$\mathfrak{R} = 2N_{\text{out}}T/N_{\text{in}}. \qquad (27)$$

In this way one can determine $\mathfrak{R}$ by measuring the ratio $N_{\text{out}}/N_{\text{in}}$ and the thickness T of the plate. Using (27) Schmitt and Sharp[3] have measured the range.

Of course $f(\rho)$ and therefore $\mathfrak{R}$ depend on the recoil energy E. Since the evaporation spectrum of the neutrons is rather broad the spectrum of recoil energies $g(E)$ has to be taken into account. The measured range is then an average over the normalized energy distribution $g(E)$

$$\mathfrak{R} = \int \mathfrak{R}(E)g(E)dE = \frac{2N_{\text{out}}T}{N_{\text{in}}}. \qquad (27a)$$

A discussion and a comparison with the experimental data is given in the next section.

Is seems to be appropriate to remark on the validity of the assumptions leading to Eq. (27). Since the measured ranges are of the order of 100 A, the determination of the range refers to a very thin surface layer of the material and one may worry about the influence of the surface structure of the material, especially oxide layers which usually are at least as thick as the observed ranges. So it seems at first that one determines the range for an oxide layer rather than for the bulk material. That nevertheless (27) is a good approximation for the range in the bulk material even with arbitrarily thick oxide layers may be seen by the following arguments.

The result (26a) for N_{out} is independent of the density of the scattering material even if the density shows variations with the position x. In the case of constant densities this is rather trivial because $\mathfrak{R}$ must vary as the reciprocal of the density. So the number of outgoing recoil atoms is independent of whether one investigates the same material in the normal, a compressed, or a rarefied state, since an increase in the density increases the production rate n_0 and decreases the range $\mathfrak{R}$ by just the same factor. But one can easily convince oneself that this statement holds also for arbitrary density variations. Thus the presence of an oxide layer should not influence the experimental value of $\mathfrak{R}$ for the bulk material very much even if the oxide layer is much thicker than $\mathfrak{R}$. This argument is valid insofar as the oxide layer is regarded as merely a dilute state of the

bulk material, i.e., the oxygen is completely disregarded. The presence of oxygen may be considered as a perturbation for scattering processes in target materials with atomic numbers large as compared with the atomic number 8 of oxygen. First the interaction between target recoil nuclei and oxygen is much smaller than the interaction with other larger nuclei if Z is large as compared with 8. Secondly, the energy loss in a collision with oxygen is smaller because of the mass differences. Thus altogether the scattering by oxygen should not be too important, especially for heavier target material, and thus (27) should give a reliable value for the bulk material irrespective of the presence of oxide layers. The general trend would be that the measured values are somewhat too low as compared with the true values if an oxide layer is present because the additive scattering by oxygen would decrease the result for N_{out}. For the metals which have been investigated we think that the influence of the oxygen is not of importance.

VI. COMPARISON WITH EXPERIMENT

R. A. Schmitt and R. A. Sharp[3] have checked their experimental results with theoretical values of K. O. Nielsen,[4] claiming good agreement by the use of a Bohr potential with the screening radius given by (17a). We felt that this comparison between experiment and theory might be open to some doubt for the following reasons. First the theoretical values are obtained by replacing the screened Coulomb potential by a $1/r^3$ potential chosen so that the potential and its first derivative for $R=a$ agree with the Bohr potential. This potential is everywhere larger than the Bohr potential and it tends to increase the value of R for given E so that the values of λ become respectively smaller. Even if the initial energy corresponds to $R=a$ where Nielsen's approximation should be best, the value of $\bar{L}$ is underestimated by 20%. This gets worse for smaller initial energies leading to deviations of an order of magnitude for $R\cong 3a$. Secondly, the comparison was made using $\bar{L}$ rather than $\mathfrak{R}$. But $\bar{L}$ must always be larger than $\bar{\rho}$ because L is the whole traversed path. Thirdly, the energy used to determine $\mathfrak{R}$ was chosen as the most probable recoil energy, whereas the average energy should have been taken, since $\bar{L}$ in Nielsen's approximation is proportional to E. Since the recoil spectrum is rather broad the average energy is about 1.6 times larger than the most probable value. Altogether we had the impression that the agreement between experimental and theoretical values was to some extent fortuitous and that one had to use better theoretical approximations to get a more reliable value for the screening radius of the Bohr potential.

None of the averages calculated in section V corresponds exactly to the average of ρ which defines the range $\mathfrak{R}$, but they are closely related to $\bar{\rho}$. In Fig. 4 some paths are drawn which show the slowing down history of a recoil atom starting with energy E. For the sake of simplicity it is assumed that the particle travels an initial mean free path, then a mean free path according to its average energy $E/2$ after the first collision, and so forth. Since the masses of collision partners are about equal the angular deviation corresponding to the average energy transfer is 45°. Figure 4(a) refers to a "high" initial energy ($R/a\sim 0.6$) and Fig. 4(b) to a "low" initial energy ($R/a\sim 2$). The difference between "high" and "low" energies is essentially given by the remark that for low starting energy E the contributions of the paths after the first collision are much more important than for high energy.[8] This may also be seen in the expression (20) for $\bar{L}$. $\bar{L}$ is equal to about λ if $R\ll a$ and larger than λ by a factor R/a if $R\gg a$. So at high energies only a few collisions are of importance and at low energies relatively many.

Now the total traversed path L is always larger than ρ. Consequently $\bar{L}$ is an upper limit for $\mathfrak{R}$. Further, the distance $r^{(\nu)}$ to the νth collision point is obviously always smaller than ρ for any ν. Thus $\langle r^{(\nu)}\rangle_{av}$ must be smaller than $\bar{\rho}$. The average distance to the first collision point is just $\lambda(E)$ which gives a lower limit for $\mathfrak{R}$. This lower limit is not very useful, especially for low energies where one has to deal with a large number of subsequent hits.[9]

Presumably $\bar{r}$ would be a rather good approximation for $\mathfrak{R}$. At the same time $\bar{r}$ would establish a lower limit. r is the distance from the starting point to the position where the recoil atom eventually has come to rest. r is always smaller than ρ because during the slowing down process larger values of ρ may have been reached as shown in Fig. 4(a) and (b). But the cases were chosen for these figures to point up the essential differences between r and ρ. In other cases, where the motion tends away from the origin, r and ρ are more nearly equal. Essential differences between r and ρ result from scattering events where the scattering angle is large. Now if the scattering angle is large (it can be at most 90°), the remaining energy is small and the subsequent motion may be partly neglected because small energy means small mean free path. Consequently, large angle scattering events do not contribute much, and therefore $\bar{r}$ should be a quite good approximate value of $\mathfrak{R}$ though it establishes a lower limit.

If the complete distribution function $W(\mathbf{r})$ for an infinite number of hits were known, one could calculate $\bar{r}=\int rW(\mathbf{r})d\mathbf{r}$. But $W(\mathbf{r})$ is not known. However, one can make a guess as to the form of the distribution func-

---

[8] A measure for the importance of subsequent collisions is

$$\lambda(E/2)/\lambda(E)\cong 1-(E/2\lambda)\partial\lambda(E)/\partial E=(R/a)/(1+R/a).$$

This shows that the average mean free path after one collision stays about the same for $R/a\gg 1$.

[9] Even the calculation of the value of $r^{(2)}$ involves complicated, non-elementary integrals. An approximate value may be obtained by calculating the distance for the average positions with average energies as shown in Fig. 4:

$$\langle r^{(2)}\rangle_{av}\cong\{\lambda^2(E)+\lambda^2(E/2)+\sqrt{2}\lambda(E)\lambda(E/2)\}^{\frac{1}{2}}$$

This gives

$\langle r^{(2)}\rangle_{av}\cong 1.4\lambda(E)$ for $R/a=1$ and $\langle r^{(2)}\rangle_{av}\cong 1.85\lambda(E)$ for $R/a\gg 1$.

tion using the calculated value of $\langle r^2\rangle_{\rm av}$. To the extent that Fermi age theory as applied in neutron transport problems is analogous to the case at hand, the distribution is expected to be gaussian[10]: $W(\mathbf{r})=Ce^{-(\frac{3}{2}r^2/\langle r^2\rangle_{\rm av})}$. For such a distribution $\bar{r}$ would be slightly less than $(\langle r^2\rangle_{\rm av})^{\frac{1}{2}}$, namely

$$\bar{r}=\left\{\frac{8}{3\pi}\right\}^{\frac{1}{2}}(\langle r^2\rangle_{\rm av})^{\frac{1}{2}}\cong 0.92(\langle r^2\rangle_{\rm av})^{\frac{1}{2}}.$$

Since $\bar{r}$ is a lower limit it seems quite appropriate to use $(\langle r^2\rangle_{\rm av})^{\frac{1}{2}}$ as a theoretical estimate for $\mathfrak{R}$. $(\langle r^2\rangle_{\rm av})^{\frac{1}{2}}$ is always larger than $\bar{r}$ since the variance $\langle r^2\rangle_{\rm av}-\bar{r}^2$ is always positive. For a gaussian distribution this variance is relatively small so that the difference between $\bar{r}$ and $(\langle r^2\rangle_{\rm av})^{\frac{1}{2}}$ may be neglected in a first approximation. But this result depends of course on the assumed distribution function. One can see this also in Fig. 2. In the high energy region, $R<a$, one has $(\langle r^2\rangle_{\rm av})^{\frac{1}{2}}>\bar{L}$ whereas $\bar{r}$ must be smaller than $\bar{L}$. In the high-energy region where the first collision distance should give most of the contribution to $W(\mathbf{r})$ one should expect a distribution function more like a mean free path distribution $W(r)=Ce^{-(r/\bar{r})}$ or $W(\mathbf{r})=Ce^{-(r/\bar{r})}/r^2$ where $\langle r^2\rangle_{\rm av}=2\bar{r}^2$ and consequently $(\langle r^2\rangle_{\rm av})^{\frac{1}{2}}$ is about 40% larger than $\bar{r}$. But since we are especially interested in values $R/a\gtrsim 1$ these differences should not be too important.[11] Anyhow for $R\ll a$ the hard core approximation breaks down and the results are not conclusive at all. Altogether we think as already pointed out by Nielsen[4] that a reliable estimate is given by

$$\mathfrak{R}_{\rm theo}=(\langle r^2\rangle_{\rm av})^{\frac{1}{2}}. \tag{28}$$

Before a comparison of the theoretical range with experimental data can be given an estimate of the influence of the spectral distribution of recoil energies must be made. For the metals investigated only the neutron evaporation spectrum for Cu is known experimentally. The most probable recoil energy for Cu is about 25 000 ev and the average recoil energy is about 1.6 times larger. Since the neutron evaporation spectra do not seem to be very different for different substances one can assume the same evaporation spectrum for all the materials investigated as a first approximation, keeping in mind that the value for Cu is the most reliable.[12] The recoil spectra are all taken to be similar in shape with a scale factor depending on the atomic mass of the target material.

Now the question remains whether or not one has to integrate $\mathfrak{R}$ according to (27a) using the recoil spectrum or if one can express $\langle\mathfrak{R}\rangle_{\rm av}$ by taking a characteristic energy related to the spectral distribution $g(E)$, e.g., the most probable or the average recoil energy. We will use for the comparison with the experimental data the average recoil energy

$$\langle\mathfrak{R}\rangle_{\rm av}\mathfrak{R}(\bar{E}) \tag{29}$$

with $\bar{E}=\int Eg(E)dE$.

The reason for the validity of (29) can be given as follows. First $\mathfrak{R}(E)$ according to Fig. 2 is a slowly varying function with energy E. Therefore one can try to expand $\mathfrak{R}(E)=\mathfrak{R}(E')+\mathfrak{R}'(E')(E-E')+\frac{1}{2}\cdots$ in (27a) and to determine an appropriate value of E' which gives a good approximation. Thus one has

$$\langle\mathfrak{R}\rangle_{\rm av}\cong\mathfrak{R}(E')+\mathfrak{R}'(E')(\bar{E}-E')+\tfrac{1}{2}\mathfrak{R}''(E')\langle(E-E')^2\rangle_{\rm av} \tag{30}$$

including second order terms. According to (30) it seems most promising to choose $E'=\bar{E}$ because then the second term in (30) vanishes. So one has

$$\langle\mathfrak{R}\rangle_{\rm av}\cong\mathfrak{R}(\bar{E})\left\{1+\frac{\mathfrak{R}''(\bar{E})\langle(E-\bar{E})^2\rangle_{\rm av}}{2\mathfrak{R}(\bar{E})}\right\} \tag{30a}$$

For an estimate of the error introduced by using $\mathfrak{R}(\bar{E})$ instead of $\langle\mathfrak{R}\rangle_{\rm av}$ we use for the sake of simplicity the typical neutron evaporation spectrum

$$g(E)=CEe^{-2E/\bar{E}},\quad \langle(E-\bar{E})^2\rangle_{\rm av}=\bar{E}^2/2.$$

Then one has

$$\frac{\mathfrak{R}''(\bar{E})\langle(E-\bar{E})^2\rangle_{\rm av}}{2\mathfrak{R}(\bar{E})}=\frac{1}{4\mathfrak{R}(\bar{E})}\left\{\frac{\partial^2\mathfrak{R}}{\partial R^2}\frac{1}{(1/R+1/a)^2}+\frac{\partial\mathfrak{R}}{\partial R}\frac{1}{(1/R+1/a)}\left[1+\frac{1}{(1+R/a)^2}\right]\right\}. \tag{31}$$

Here R means $R(\bar{E})$. For a first estimate one may use λ instead of $\mathfrak{R}$ in (31) since the behavior of λ and $\mathfrak{R}$ is not very different at least in the high energy region. Then one gets

$$\frac{\lambda''(\bar{E})\bar{E}^2}{4\lambda(\bar{E})}=\frac{1+R/a-R^2/a^2}{2(1+R/a)^3}. \tag{31a}$$

For $R/a=1$ this is about 0.06, for $R/a=2$ about -0.02, for $R/a=3$ about -0.04, and for $R/a=4$ again about -0.04. Thus the accuracy for $R\gtrsim a$ is better than 10%. If one determines the value (31) by approximating $\mathfrak{R}$ by $(\langle r^2\rangle_{\rm av})^{\frac{1}{2}}$ the behavior is about the same. Thus we take

[10] An estimate of $\langle r^2\rangle_{\rm av}$ may also be obtained from neutron transport theory, using the accurate solution of the slowing-down diffusion theory in hydrogen. The results, as given, for example, by H. Hurwitz and P. F. Zweifel [J. Appl. Phys. 26, 923 (1955)] are, of course, identical with those given here [cf. Eq. (15b)]. The method used here, however, has the advantage that other average quantities of physical interest (besides $\langle r^2\rangle_{\rm av}$) may be computed, such as, for example, the $\langle x^2\rangle_{\rm av}$, $\langle y^2\rangle_{\rm av}$, and $\langle z^2\rangle_{\rm av}$, separately.

[11] One could try to get a better estimate by using a suitable combination of a gaussian and a mean free path distribution. The 3 free parameters in such a combination could be determined by calculating averages as $\langle r^2\rangle_{\rm av}$, $\langle r^4\rangle_{\rm av}$, and $\langle r^6\rangle_{\rm av}$. These averages could be calculated as in Sec. III. But the amount of numerical calculations involved does not seem to be justified since the experimental determination of $\mathfrak{R}$ is surely not better determined than to an accuracy of about 20% taking into regard the uncertainty in the recoil energy spectra.

[12] Cf. the discussion cited in footnote 3.

as a good approximation

$$\mathfrak{R}_{\text{theo}} = (\langle r^2 \rangle_{\text{av}}(\bar{E}))^{\frac{1}{2}}. \tag{32}$$

This value should agree[13] with the true theoretical value within an accuracy of about 20%.

We have compared this theoretical value with the experimental data.[3] The comparison is given in Table I. The first column contains the average recoil energy. As mentioned already one can regard a as a parameter and fit it to the experimental data. To do this we have chosen

$$a = \alpha a_B / \sqrt{2} Z^{\frac{1}{2}}, \tag{33}$$

and given in the table the values for $\alpha = 1, \sqrt{2}, 2$.

The value $\alpha = 1$ corresponds to Bohr's original proposal, $\alpha = \sqrt{2}$ is a value which has been suggested by Seitz and Koehler.[2] An extreme value of about $2\sqrt{2}$ has been used by other investigators.[2]

According to this table the most reliable value for Cu seems to be $\alpha \cong 2$. Because we are here in a region where $(\langle r^2 \rangle_{\text{av}})^{\frac{1}{2}} \cong \bar{L}$ which is an upper limit, one can even take a value somewhat less than 2 in between $\alpha = \sqrt{2}$ and $\alpha = 2$. The theoretical values for $\alpha = 1$ are generally much too large. The overall fit also seems to be best for $\alpha \cong 2$. The extremely large value $\alpha = 2\sqrt{2}$ would give for Cu about $\bar{L} \cong 1$ which is much too small.

The most obvious disagreements for $\alpha \cong 2$ are Fe, Zn, and Au. In the case of Zn, for instance, one must assume that the actual range for Zn is larger than that for Cu because the electronic shell structure is very nearly the same for both elements and the density of Zn is about 50% smaller than that of Cu. The experiment shows just the reverse behavior. An oxide layer on Zn contains about twice as much oxygen as a Cu_2O layer. But it is unlikely that the influence of the oxygen in a possible oxide layer should matter so much. On the other hand, the recoil spectrum for Zn is not known and may easily account for the difference in the observed ranges. The same could apply for Fe where the neutron evaporation temperature may be larger than expected. In the case of Au where $\mathfrak{R}_{\text{theo}}$ is larger than $\mathfrak{R}_{\text{obs}}$ one can also give other arguments. The recoil energy for Au is rather low, in the order of 10 000 ev. This is an energy where the possible influence of the low energy part of the potential must be considered. The screened Coulomb potential is surely invalid for very low energies where one should use rather a pure exponential potential of the Born-Mayer type. Such a potential falls off more slowly than the potential used here. Consequently the mean-free path decreases more rapidly with decreasing energy than for the Bohr potential. This means that by using the Bohr potential the contribution of the paths at low energies is exaggerated. Very roughly one can approximate this behavior without introducing a Born-Mayer potential by cutting off at a certain energy E_d. E_d should be of the order of the displacement energy of the material in question which corresponds roughly to the energy where the mean free path becomes zero due to the lattice structure of the material. The values of E_d are typically of the order of 25 ev. The value of $\mathfrak{R}_{\text{theo}}(E_d)$ for Au and $\alpha = 2$ would be about 0.1×10^{-8} cm and is already 20% of the calculated value. So roughly the calculated value should be about 20% less than that in the table. Using a simple exponential potential in the low energy range would very likely give an even lower value, in better agreement with $\mathfrak{R}_{\text{obs}}$. But again the uncertainty of $\bar{E}$ does not allow one to draw any conclusions. For Cu, for instance, the above mentioned influence would be extremely small, of the order of 2%, because the recoil energy of 40 000 ev is relatively large. Calculations using a combination of an experimentally adapted exponential for low energies and a screened Coulomb potential do not show a marked difference in the theoretical ranges for this energy.

[13] The spectral distribution $g(E)$ has an appreciable value at high energies. For those high energies the hard core approximation would not apply. But, on the other hand, for high energies the ionization loss essentially determines the slowing down process. Thus the high energy part of the spectral distribution should not give an essential deviation.

TABLE I. Comparison of experimental ranges with theory.[a]

Element	$\bar{E}$	E_B	$\bar{E}/E_B$	λa	R/a	$\mathfrak{R}_{\text{theo}}$	$\mathfrak{R}_{\text{obs}}$	$\bar{L}$	α
		10.4	0.51	3.3	0.85	10.4		10.6	1
Ti	5.28	7.38	0.715	1.6	0.70	7.4	3.1	7.3	$\sqrt{2}$
		5.28	1.0	0.81	0.55	5.51		5.5	2
		15.5	0.31	2.35	1.1	4.8		5.2	1
Fe	4.8	10.9	0.44	1.17	0.91	3.3	5.6	3.4	$\sqrt{2}$
		7.74	0.62	0.58	0.75	2.3		2.3	2
		20.0	0.2	2.5	1.3	3.5		4.1	1
Cu	4.0	14.3	0.28	1.25	1.1	2.3	1.6	2.6	$\sqrt{2}$
		10.0	0.4	0.61	0.95	1.6		1.65	2
		21.1	0.19	3.3	1.35	4.5		5.2	1
Zn	4.0	15.4	0.26	1.7	1.15	2.9	1.37	3.35	$\sqrt{2}$
		10.8	0.37	0.83	1.0	2.1		2.1	2
		47.4	0.054	4.3	2.15	2.6		3.4	1
Mo	2.56	33.2	0.077	2.15	1.9	1.6	0.71	2.0	$\sqrt{2}$
		23.3	0.11	1.1	1.7	1.0		1.2	2
		60.5	0.037	5.1	2.45	2.5		3.3	1
Ag	2.24	43.1	0.052	2.5	2.2	1.5	0.71	1.9	$\sqrt{2}$
		30.7	0.073	1.27	1.95	0.9		1.15	2
		205.7	0.007	7.1	3.65	1.8		2.7	1
Au	1.44	144.0	0.01	3.5	3.4	1.0	0.28	1.5	$\sqrt{2}$
		103.0	0.014	1.8	3.1	0.58		0.84	2

[a] The energies are given in units of 10 000 ev and the lengths in units of 10^{-9} cm. The average recoil energies are taken from footnote 3.

VII. CONCLUSIONS

The comparison with the experimental data discussed in the foregoing shows that a screened Coulomb potential of the Bohr type can quite well explain the experimental ranges in metals. But we emphasize that the numerical value for the screening radius should be about twice the value given by Bohr. The only conclusive evidence for this is the comparison with the values for Cu, because for the other target materials the recoil spectrum is not known.

The averages calculated in Sec. IV can also be used to

advantage in radiation damage problems. These averages do not refer to a Bohr potential but can be used for any potential where the hard core approximation is valid. These averages give an idea of the size of the region affected by a primary which has itself produced other interstitials during its slowing down. In the hard core approximation there is no difference at all between the primary and the secondary produced after the first collision of the primary. This means that the primary and the first secondary knock on have the same final distribution $W(\mathbf{r})$. Thus these averages are the same for all secondary, tertiary, etc. displaced atoms. Because one can calculate the number of interstitials eventually produced with sufficient accuracy, the average $\langle \mathbf{r} \rangle_{av}(14d)$ gives the center of a cascade effected by a primary knock on of energy E starting in direction $\mathbf{n}$ and the formulas (16) give the approximate dimensions of the cascade. Consequently one can calculate the average densities in such a cascade if one knows the interaction potential. A detailed discussion would lead beyond the scope of this paper. But it may be mentioned that a reasonable potential for Cu using an appropriate combination of an exponential and a screened Coulomb potential with experimentally fitted constants leads to maximal densities of interstitials of about 5 at. % for primary energies in the order of 1000 ev. The larger contribution to this high density is due to the exponential potential, whereas the Bohr potential alone would give only 1.5 at. % maximum densities. This shows that the low energy part of the potential is essential. This subject will be discussed in a forthcoming paper.

The ranges measured on the basis of the present discussion are not able to account for the observed pinning of dislocations by low temperature neutron bombardment.[14] As has been discussed by one of the authors[15] this can be explained on the basis of the focusing mechanism first postulated by Silsbee.[16] The results of footnote reference 15 may be roughly expressed by saying that the number of pinning points per neutron hit depends on $\nu \bar{L}(E_c)$, where ν is the average number of displaced atoms per neutron hit, and $\bar{L}(E_c)$ is the average range from an initial energy E_c such that a pinning-type interaction with a dislocation line is probable. E_c should be of the order of 100–200 ev; the average range in copper for a 100 ev displaced atom, using $\alpha=2$, is about five atomic distances, whereas for the focusons of footnote reference 15 the corresponding distance is about ten times larger. Since the focusing effect can just account for the experimental observations, it must be concluded that the direct range effect does not contribute significantly to dislocation pinning.

ACKNOWLEDGMENT

The authors wish to thank Dr. J. H. Crawford, Jr., for stimulating the initial interest in this problem.

[14] D. O. Thompson, T. H. Blewitt, and D. K. Holmes, J. Appl. Phys. 28, 742 (1957).
[15] G. Leibfried, J. Appl. Phys. (to be published).
[16] R. H. Silsbee, J. Appl. Phys. 28, 1246 (1957).

APPENDIX A

Evaluation of $I_1(E)$

The expression for I_1

$$I_1(E)=\int_0^E \lambda(\epsilon)\left(\frac{\epsilon}{E}\right)^{\frac{1}{2}}\frac{d\epsilon}{\epsilon}$$

$$=\int_{R(E)}^{\infty}\frac{1}{n\pi\eta^2}\left\{\frac{1}{\eta}+\frac{1}{a}\right\}\left\{\frac{R}{\eta}\right\}^{\frac{1}{2}}e^{R/2a-\eta/2a}d\eta, \quad \text{(A1)}$$

can be transformed by several integrations by parts to

$$I_1(E)=\frac{1}{n\pi R^2}\left\{\frac{2}{5}+\frac{8}{15}\left(\frac{R}{a}-\frac{R^2}{a^2}\right)+\frac{8(\pi)^{\frac{1}{2}}R^2}{15a^2}(R/2a)^{\frac{1}{2}}e^{R/2a}\Gamma(R/2a)^{\frac{1}{2}}\right\} \quad \text{(A2)}$$

where

$$\Gamma(x)=\frac{(\pi)^{\frac{1}{2}}}{2}\int_x^{\infty}e^{-\eta^2}d\eta.$$

With the asymptotic expansion of Γ

$$\Gamma(x)\sim\frac{e^{-x^2}}{(\pi)^{\frac{1}{2}}x}\left\{1-\frac{1}{2x^2}+\frac{3}{4x^4}-\frac{15}{8x^6}+\cdots\right\} \quad \text{(A3)}$$

one gets for I_1

$$I_1(E)\sim\lambda\left\{2-\frac{8a}{R}+\frac{56a^2}{R^2}-\cdots\right\}. \quad \text{(A4)}$$

APPENDIX B

Evaluation of $I_2(E)$

The expression for I_2

$$I_2(E)=\int_0^E \lambda(\epsilon)I_1(\epsilon)\frac{d\epsilon}{\epsilon}=\int_{R(E)}^{\infty}\frac{1}{n\pi R^2}\left(\frac{1}{R}+\frac{1}{a}\right)I_1 dR \quad \text{(B1)}$$

becomes, using (A2),

$$I_2=\frac{1}{n^2\pi^2R^4}\left\{\frac{1}{10}+\frac{14R}{45a}-\frac{8R^2}{15a^2}+\frac{8(\pi)^{\frac{1}{2}}R^4}{15a^4}\int_R^{\infty}\left(\frac{1}{\eta^3}+\frac{1}{\eta^2}\right)\left(\frac{\eta}{2}\right)^{\frac{1}{2}}e^{\eta/2}\Gamma\left(\frac{\eta}{2}\right)^{\frac{1}{2}}d\eta\right\}. \quad \text{(B2)}$$

The last integral has been integrated numerically.

Using the asymptotic expression for I_1 according to (A4) one can easily get the corresponding asymptotic expansion for I_2. Using both asymptotic expansions one finally gets an asymptotic value for $\langle r^2 \rangle_{av}$

$$\langle r^2\rangle_{av}\sim\frac{1}{n^2\pi^2R^4}\left\{\frac{7}{2}+\frac{2R}{a}+\frac{16a}{5R}-\cdots\right\}. \quad \text{(A5)}$$

JOURNAL OF APPLIED PHYSICS VOLUME 31, NUMBER 6 JUNE, 1960

Displacement of the Sulfur Atom in CdS by Electron Bombardment*

B. A. KULP AND R. H. KELLEY
Aeronautical Research Laboratory, Wright Air Development Division, Wright-Patterson Air Force Base, Ohio
(Received December 5, 1959; revised manuscript received February 10, 1960)

The threshold for displacement of the sulfur atom from a lattice point in CdS has been measured to be 8.7 ev. This is accomplished with 115-kev electrons. This is also the threshold for the production of green edge emission centers and of centers for a red fluorescence band with a maximum intensity at about 7200 A. In crystals which show edge emission before bombardment, the edge emission is removed by electron bombardment in the energy range 2.5 to 200 kev. The red luminescence is not removed by electron bombardment but increases in intensity with bombardment above the threshold. The radiation "annealing" of the edge emission is accomplished even in crystals which do not thermally anneal. A model is proposed with the sulfur interstitial atom the center for edge emission, and the sulfur vacancy the center for the red emission band.

INTRODUCTION

CADMIUM sulfide crystals often show a green fluorescence when irradiated with ultraviolet light at liquid nitrogen temperature.[1] The wavelength of this fluorescence radiation (maximum intensity at ~5140 A) is near the fundamental absorption edge of the crystal and the fluorescence is called edge emission. There are other fluorescence bands in the visible region. Of particular interest here is a broad red fluorescence band with a maximum intensity at about 7200 A.[2] Reynolds and Greene[3] have previously reported the production of green edge emission in whisker type single crystals of CdS by proton bombardment at 1 Mev. These whiskers have very high mechanical strength and, according to Brenner and Sears,[4] may have grown about a single screw dislocation through the center of the whisker. Therefore, they should be quite pure and free of mechanical imperfections.

EXPERIMENTAL

The crystals used in these experiments were "pure" crystals. Spectrographic analysis showed maximum impurities of 5 ppm of Si, and 1 ppm Mg in some of the samples. No other impurities were detected. The crystals were: group 1—whiskers, platelets, and large single crystals which did not show edge emission in the as-grown condition; group 2—platelets and large single crystals which showed a low intensity edge emission (usually with the red band centered at 7200 A) in the as-grown condition; and group 3—single crystals which showed bright green edge emission in the as-grown condition. For the bombardment experiments thin chips were cleaved from the larger pieces of CdS.

ELECTRON BOMBARDMENT

The crystals were bombarded in a Cockcroft-Walton electron accelerator at room temperature in vacuum (2×10^{-6} mm Hg). Steady dc electron currents between 2 and 30 μa per cm^2 were used in the experiments. Table I shows a summary of the results with samples which did not show edge emission before bombardment. Green emission has been produced in whiskers by bombardment at 130 kev for 40 μa-hr/cm^2 and persisted to a total of 160 μa-hr/cm^2. However, whiskers bombarded at 120 kev for 240 μa-hr/cm^2 fluoresced red at nitrogen temperature under ultraviolet stimulation. Bombardment of these samples was continued in 240 μa-hr steps with no appearance of the green edge emission. The red fluorescence increased in intensity as the bombardment continued. Bombardment of platelet crystals, which originally showed no fluorescence, at 100 kev for 420 μa-hr/cm^2 followed by 260 μa-hr/cm^2 at 110 kev did not produce fluorescence in the crystals. Subsequent bombardment of these same platelets at 120 kev for 380 μa-hr/cm^2 produced the red fluorescence. Thus, the threshold for the production of the centers for the red fluorescence is about 115 kev.

In another series of experiments, edge emission was produced in a chip (cleaved from a large single crystal) by irradiation at 135 kev for 100 μa-hr. Edge emission was not produced in the same chip by bombardment at 125 kev for 90 μa-hr. The threshold for the green is below 130 kev but the data presented in the next paragraph show that the experiments at 120 and 125 kev do not necessarily show that the threshold is between 125 kev and 130 kev.

The bombardment at 200 kev first produced the green fluorescence, but continued bombardment resulted in destruction of edge emission rather than enhancement as one might expect. In fact, if a crystal which originally showed edge emission is bombarded, the edge emission decreases in intensity with continuing bombardment. If irradiation is continued long enough, the edge emission is completely destroyed. The red fluorescence on the other hand has never been observed to decrease in intensity after it has been produced by electron bombardment.

* Presented in part at the "Second Conference on Nuclear Radiation Effects in Semiconductor devices, Materials and Circuits," see *Proceedings* (Cowan Publishing Company, New York, 1959), p. 31.

[1] F. A. Kroger, Physica 7, 1 (1940).
[2] R. Frericks, Phys. Rev. 76, 1869 (1949).
[3] D. C. Reynolds and L. C. Greene, Bull. Am. Phys. Soc. 3, 108 (1958).
[4] S. S. Brenner and C. W. Sears, Acta Met. 4, 268 (1956).

TABLE I. Summary of bombardment runs.

Sample	Initial condition[a]	Electron energy kev	Current $\mu a/cm^2$	Total bombardment $\mu a\text{-}hr/cm^2$	Final condition[a]
Platelet	No fluorescence	175	10	50	Red
				75	Red
				95	Light green
				135	Green
Whiskers	No fluorescence	130	20	40	Green
				160	Green
Whiskers	Faint red fluorescence	120	30	240	Uniform red fluorescence
				480	Red
				720	Bright red
				960	Bright red
				1200	Bright red
Platelet	No fluorescence	100	5	420	No fluorescence
As above	No fluorescence	110	6	260	No fluorescence
As above	No fluorescence	120	6	380	Red
Chip from a large crystal	Red	200	10	35	Green
				135	Bright red
Chip	Faint red fluorescence	175	9.5	145	Green
Chip above, heat treated at 450°C	No fluorescence	150	10.5	170	Green
Chip above, heat treated at 450°C	Faint red	125	5.8	30	Faint red
				90	Faint red
Chip as above		135	5.6	100	Red with some green

[a] As viewed under a 100-w SP4 mercury light with uv filter at liquid nitrogen temperature.

The "annealing" of the edge emission is observed to take place at electron energies as low as 2.5 kev and as high as 200 kev, the extent of the experiments. All crystals which have been bombarded have eventually lost the edge emission, but the time for complete elimination varied as much as an order of magnitude between crystals procured from different sources or from different crystal growing runs.

If the crystals are very much thicker than the range of the electrons at the bombarding energy, the bottom of the crystal is largely unaffected by the bombardment. For example, crystals 0.6 mm thick when bombarded at 125 kev lose the edge emission when observed under uv light at liquid nitrogen temperature on the bombarded side, but retain the edge emission on the bon-bombarded side. (Note: The uv light is beyond the fundamental absorption edge and the depth of penetration is of the order of 10^{-5} cm).

The radiation annealing of the edge emission makes it difficult to determine the threshold for production of these centers by the electron bombardment.

Thermal Annealing

Previous attempts at thermal annealing of the edge emission in CdS have met with varied results. Lambe[5] has referred to unpublished work of M. E. Bishop who found that firing CdS in a sulfur atmosphere at 800°C removed edge luminescence while similar treatment in cadmium vapor or in vacuum did not produce this effect. Earlier Wendel[6] had reported that slow cooling from 600°C destroyed edge emission in crystals in which the edge emission was originally produced by a water quench from 600°C.

In a series of thermal annealing experiments, platelets and chips from large single crystals were heated in vacuum to various temperatures and the luminescence observed after each cycle. All of the samples from group 2 lost their edge emission after 2 hours at 450°C though some of them still fluoresced an orange color at liquid nitrogen temperature under uv illumination. This orange fluorescence could be removed by heating 18 to 72 hours at 450°C or a shorter period of time at 550°C. The origin of the orange fluorescence is not known at this time. After this heat treatment, most of the crystals have no fluorescence at room temperature or at liquid nitrogen temperature. Some however did have a low intensity deep red fluorescence both at room temperature and nitrogen temperature. Edge emission can be produced again in these crystals by quenching from 650°C and the annealing repeated.

The chips from the crystals of group 3 did not show thermal annealing of the edge emission after heat treatment at 450°C for two hours plus two hours at 550°C.

Resistivity Measurements

Because of the difficulty introduced by the radiation annealing of the edge luminescence, thin platelet type crystals were prepared with sputtered platinum electrodes and the resistivity measured as a function of

[5] J. Lambe, Phys. Rev. 98, 985 (1955).

[6] G. Wendel, Fortschr. Physik 1, 45 (1953).

electron bombardment. The sulfur interstitial atom would probably be a deep electron trap,[7] and the creation of sulfur vacancy-interstitial pairs should result in a difference in the rate of change of resistivity of the crystal as a function of bombardment above and below the threshold for displacement of the sulfur atom. The crystals were bombarded at room temperature with a dc current of 2 μa per cm^2. The electrons struck the crystal only between the electrodes. The resistivity of the crystal was measured as a function of time after the electron beam was shut off after each period of bombardment. After about 20 minutes the resistivity was changing only very slowly. The data for Figs. 1 and 2 were taken as the resistivity 25 minutes after the electron beam was shut off.

Figure 1 shows the resistivity of a platelet crystal as a function of bombardment at 100 kev, 150 kev, 125 kev, and 120 kev in succession. The initial resistivity of the crystal was 2.2×10^9 ohm-cm. The abrupt change in direction of the curve as the electron energy is changed from 100 kev to 150 kev is strong evidence for a threshold between the two energies. When the electron energy was reduced from 150 kev to 125 kev, the resistance first peaked then decreased. Radiation annealing is very evident here, the resistance of the crystal decreases to the value before the 150 kev bombardment. This indicates a difference in dependence on the electron energy of the cross-section for annealing and the cross-section for damage. This observation has been previously noted by MacKay, Klontz, and Gobeli[8] in radiation annealing of germanium at 10°K.

The fact that the slope of the curve for the 125 and 120-kev bombardments is less than the slope of the 100-kev bombardment makes one suspect that the threshold may be below 120 kev. Figure 2 shows the resistivity of a similar platelet which was thermally annealed at 175°C for four days before bombardment. The resistivity at room temperature rose from 8.7×10^2 ohm-cm to 6.3×10^5 ohm-cm during this time. This increase in resistivity with time at a given temperature is typical of the thermal annealing of these crystals.[9] The first part of the bombardment was at 100-kev for 220 μa-hr/cm^2. The resistivity rose to about 1×10^7 ohm-cm during this time but intermediate points were not measured. Next, the electron energy was increased to 120 kev and bombardment continued for 310 μa-hr. The resistivity changes as shown. The initial increase in resistivity of this crystal in contrast to the crystal used for Fig. 1 is probably associated with the thermal annealing before electron bombardment. At 430 μa-hr the electron energy was changed to 110 kev and bombardment continued. After a short time, the slope of the curve increases quite sharply. The electron energy was lowered to 100 kev and then raised to 110 kev again and the downward slope continued. At the end of 950 μa-hr, the crystal was removed from the accelerator and stored at room temperature for six days. The resistivity decreased from 3.1×10^4 to 1.7×10^4 during this time.

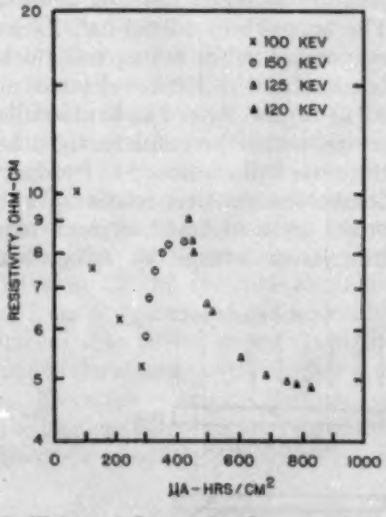

FIG. 1. Resistivity vs bombardment time, platelet crystal 75 μ thick. Initial resistivity 2.2×10^9 ohm-cm.

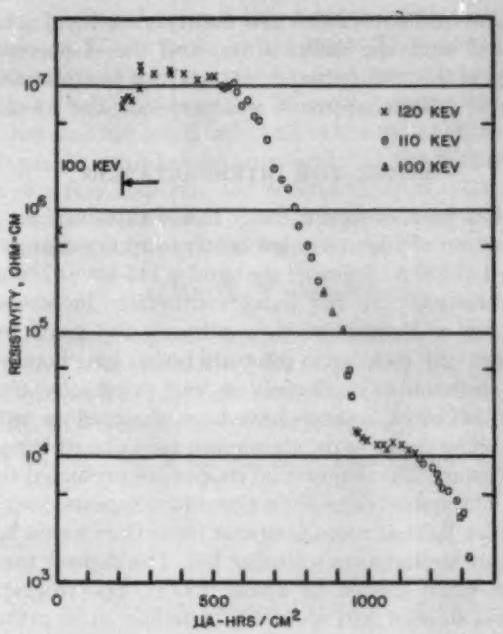

FIG. 2. Resistivity vs bombardment time, annealed platelet crystal. 50 μ thick initial resistivity 6.3×10^5 ohm-cm.

The platelet was returned to the accelerator and bombarded at 120 kev for 190 μa-hr, and then at 110 kev for 175 μa-hr, repeating the previous results. Annealing the crystal for 4 days at 190°C did not appreciably change its resistivity. On the basis of Fig. 2, the threshold is placed at 115±5 kev with the accuracy of the energy measurement ±5%. This represents the transfer of a maximum energy of 8.7 ev to a sulfur atom or 2.5 ev to a cadmium atom. It therefore appears that edge

[7] F. A. Kroger, H. J. Vink, and I. van den Boomgaard, Z. Physik. Chem. **203**, 1 (1954).

[8] J. W. MacKay, E. E. Klontz, and G. W. Gobeli, Phys. Rev. Letters **2**, 146 (1959).

[9] B. A. Kulp (to be published).

emission and the 7200 A red fluorescence band are associated with the sulfur atom, and the displacement energy of the sulfur atom from its lattice position in CdS is 8.7 ev. (Bombardment was perpendicular to the C axis.)

MODEL FOR INTERPRETATION

It has been observed that (1) the threshold for the production of edge emission centers and the centers for the red (7200 A) fluorescence band is 115 kev; (2) above the threshold the red band continually increases in intensity as bombardment continues; the green band may initially increase in intensity but at long bombardment times always diminishes and eventually disappears; (3) black deposits have been observed on copper and yellow deposits on aluminium foils placed beneath the crystals. The deposits on copper are presumed to be CuS. The yellow deposit on aluminum appears deep red under uv light at room temperature as does a thin layer of sulfur melted onto a similar foil. The deposit turned brown when heated to about 150°C. Spectrographic analysis showed 0.01 to 0.03% cadmium to be present, but calculations indicate that stoichiometric CdS should have had 1% Cd in the same size sample; (4) the resistivity of a platelet type crystal decreases much more rapidly with bombardment below the threshold than above the threshold; and (5) the decrease in the resistivity with bombardment is irreversible, that is, the crystal does not thermally anneal to its initial resistivity after bombardment.

Consider that the red band is associated with the sulfur vacancy.[10] Above the threshold for the displacement of sulfur atoms from the lattice, the number of sulfur vacancies increases with increasing bombardment time. The number of red centers therefore increases and the intensity of the fluorescence should increase. This is observed. If the green band is associated with the sulfur interstitial, the number of these centers should also increase with increasing bombardment, except that the interstitial sulfur atoms should be acted upon by the electrons and could conceivably be knocked from one interstitial position to another. If this process should have a preferred direction, it would be in the direction of the electron beam. This could result in a depletion of the density of centers at the bombarded surface, resulting in a decrease in the green fluorescence. In the early stages of bombardment some time would be required to set up such an electron induced "diffusion" so that the density of centers could build up to a detectable number; then after the establishment of the diffusion current, this surface density would decrease to an equilibrium or steady-state value which would depend on the ratio of the cross sections for interstitial collisions and lattice point collisions resulting in displacements. The above model implies that in thin crystals, atoms would be removed from the bottom of the crystal. This accounts for the deposits observed on the foils beneath the crystal, as well as the irreversibility of the damage produced below the threshold.

The very large cross section implied for interstitial collisions indicates that ionization effects may be very important in the above process, but at this time there is no direct way to separate such effects from the effect of direct knock-on collisions between the electrons and the sulfur interstitials.

This model further explains the shape of the resistivity vs bombardment curves. Below the threshold no new vacancy-interstitial pairs are being created, but interstitials are being removed from the bottom of the crystal. The interstitial sulfur atoms would probably be deep electron traps[7] and elimination of these traps would add electrons to the conduction band increasing the conductivity. Above the threshold, new vacancy-interstitial pairs are being created at the top surface and the addition of new deep electron traps partially compensates for the removal of the interstitial from the bottom of the crystals.

It should be noted that the model presented here is different from that of Collins[11] who produced edge emission by electron bombardment at 200 kev and 1.0 Mev. On the basis of a heat treating experiment in a sulfur atmosphere similar to that of Bishop's[8] he proposes that the center for edge emission is the sulfur vacancy. However the results of the experiments on the radiation annealing of edge emission are not explicable on the basis of this model.

Experimental Verification of the Model

As a test of the model, the experiment shown schematically in Fig. 3 was performed. A platelet type crystal 1.5 mm wide×10 mm long×0.25 mm thick which showed no green fluorescence either at room temperature of liquid nitrogen temperature was selected. The crystal was coated half its length with vacuum evaporated sulfur 6.8 $\mu g/cm^2$ thick. This crystal was bombarded with 100-kev electrons at −100°C for about 2.3 μa-hr/cm^2. After 2 μa-hr of irradiation, the half of the crystal under the sulfur turned a brilliant green, while the other half continued to fluoresce red under electron bombardment. After irradiation the crystal fluoresced bright green at liquid nitrogen temperature under uv stimulation where the sulfur had been deposited.

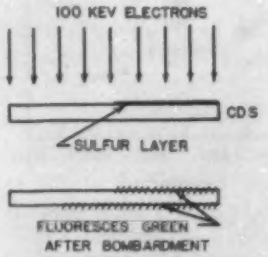

FIG. 3. Electron induced diffusion of sulfur interstitials into CdS.

[10] A. A. Vuylsteke and Y. T. Sihvonen, Phys. Rev. **113**, 40 (1959).

[11] R. J. Collins, J. Appl. Phys. **30**, 1135 (1959).

Furthermore, the underside of the crystal glowed green, but over a larger area of the crystal than the top indicating that electron induced diffusion of interstitials is real. The larger area of fluorescence on the bottom of the crystal is expected since the electrons, as well as the interstitial atoms, will spread out as they pass through the crystal lattice.

A spectrogram of the green fluorescence showed three bands with maximum intensities at about 5140, 5225, and 5310 A, respectively.

CONCLUSIONS

It has been shown that the center for the green edge emission in CdS is the sulfur interstitial atom and that 7200 A red band is a result of sulfur vacancies. The threshold for the production of vacancy-interstitial pairs of sulfur atoms in CdS by electron bombardment is 115±5 kev corresponding to a maximum energy transfer of 8.7 ev to the sulfur atom. The sulfur interstitial exists as a negatively charged ion at room temperature in these crystals. It seems reasonable that another electron could be bound to the sulfur interstitial at liquid nitrogen temperature and that the recombination of a free hole with the second electron trapped at this center would result in edge emission according to the model of Lambe, Klick, and Dexter.[12]

ACKNOWLEDGMENT

The authors wish to thank D. C. Reynolds and L. C. Greene of this laboratory for supplying the crystals used in this investigation, and A/1C James Tiller and Mr. R. G. Peacock for assistance in the experiments.

[12] J. Lambe, C. C. Klick, and D. L. Dexter, Phys. Rev. **103**, 1715 (1956).

JOURNAL OF APPLIED PHYSICS VOLUME 31, NUMBER 6 JUNE, 1960

Electron Probe Measurements of Evaporated Metal Films

W. E. Sweeney, Jr., R. E. Seebold, and L. S. Birks
U. S. Naval Research Laboratory, Washington 25, D. C.

(Received December 16, 1959; revised manuscript received February 11, 1960)

Calibration curves of X-ray intensity vs specimen thickness have been prepared for the electron probe microanalyzer by using evaporated films of Cr, Mn, Zn, and Au in the 0–5000 A range. For each element, the x-ray intensity increased almost linearly with thickness; for a given thickness, the x-ray intensity increased (but not linearly) with atomic number. Using previously published data on electron excitation efficiency to calculate expected x-ray intensities, the measured values from Cr, Mn, and Au were about 0.75 to 0.85 times the calculated value whereas Zn was about 1.25 times the calculated value. The variations are thought to result from some undetermined parameter such as density or internal strain.

INTRODUCTION

In the electron probe microanalyzer, a focused beam of electrons strikes an area 1–2 μ in diameter on a specimen surface and generates characteristic x rays from the elements contained within that area and to a depth of 1–2 μ below the surface.[1] By first measuring the x-ray intensities from a series of known standards, calibration curves of x-ray intensity vs compositon may be prepared for quantitative analysis of precipitates, diffusion zones, etc.[2] However, for the calibration curves to be valid, it is necessary that the region to be analyzed be thick enough to stop all the incident electrons. Otherwise, the x-ray intensity generated will be less by the fraction of electrons that passes through and the calibration curves must take account of the thickness as well as composition. Examples of regions that are too thin to absorb all the incident electrons are evaporated metal films for high-speed computer storage tubes, or corrosion layers.

In this paper, known thicknesses of several evaporated metals are used to prepare calibration curves and the observed intensities are compared with values calculated from published data on electron excitation functions. If the calibration curves for pure metals are plotted in terms of density times thickness (grams/cm^2), they may be used for thin composite or alloy films because, to a first approximation, the number of grams of each element is found independently from the calibration curve for that element.

SPECIMEN PREPARATION

The four elements examined in this experiment were chromium, manganese, zinc, and gold. They are relatively easy to evaporate, give stable films, and their characteristic x rays lie in a narrow range from 1.27 to 2.28 A (K series for Cr, Mn, and Zn; L series for Au). Specimens were prepared by vacuum evaporation onto 4×8 mm sections cut from glass microscope slides. The quantity of starting material and the distance from source to specimen were adjusted to give an expected thickness of about 600 A for each evaporation. The

[1] R. Castaing, thesis, (University of Paris, 1951).
[2] J. Philibert and H. Bizouard, Mem. Sci. Rev. Met. **56**, 187 (1959).

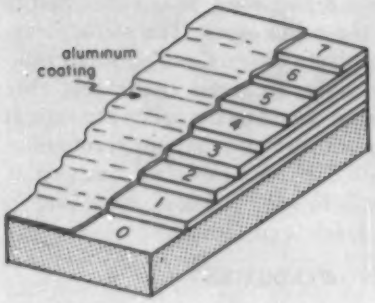

FIG. 1. Step wedge specimen formed by successive evaporations onto glass substrate. One side is coated with a thin reflecting layer of aluminum to aid in interference microscope measurements of layer thickness.

chromium used was Baker's C.P. pellets, the manganese was a special electrolytic grade containing less than 0.1% total impurity, and the gold was spectroscopic grade wire. Zinc cannot be evaporated by itself but was obtained by heating Bureau of Standards 62b brass (37% Zn) in vacuum at about 300 to 350°C to drive out the zinc leaving the copper behind. The known, small concentrations of Sn, Pb, Ni, Fe, Al, Mn, Sb, and As present in 62b brass are, if anything, beneficial because a small amount of impurity seems to be necessary in order for the zinc to stick to the glass substrate.[3]

A step wedge was prepared for each element by a series of evaporations as shown schematically in Fig. 1. The first evaporation was made with a strip 2 mm wide at one end of the glass slide masked off so that it received no evaporated metal. For the next evaporation, the mask was moved in to cover 2 mm of the previous evaporation and so on until 6 to 8 steps of increasing thickness were formed. One part of the specimen as shown in Fig. 1 was further coated with a thin reflecting layer of aluminum to increase the brightness in the interference microscope measurements of layer thickness and to insure against a relative phase shift between the glass substrate and first layer.

EXPERIMENTAL RESULTS

The thickness of each step in the wedge specimens was measured optically in an interference microscope. Figure 2 illustrates the sharpness of the fringe shift going across a step boundary. The fringe shift A divided by the fringe separation B is used in the standard equation[3,4] for determining thickness t in A

$$t=\lambda/2\times A/B, \quad (1)$$

where λ is the wavelength of the light in A and the factor 2 is required because the path difference is doubled for interference by reflection. For these experiments, a Wratten 58B filter was used to pass primarily the 5490 A green line of the mercury arc illuminating lamp.

Measured values for the various elements and layers are listed in Table I. The total thickness column is just the sum of that step plus all the previous layers, and it is the total thickness that determines the x-ray intensity. Lack of sharpness of the fringes and the tendency of some of the evaporated layers to crack made precise measurements of thickness t impracticable and the values in Table I may be in error by about 5%.

After the thickness measurements were completed for an element, the specimen was placed in the electron probe microanalyzer.[5] The characteristic x-ray intensity was measured for each thickness using the curved lithium fluoride crystals and Geiger counter detectors previously described.[6] In addition, for each element, a polished piece of the bulk element was measured along with the step wedge and the intensity from each step was normalized by dividing by the intensity from the bulk material. In this way, the intensity, from each step is expressed as a percentage of the intensity obtained from an effectively infinitely thick specimen. Figure 3 shows these normalized percentages for each of the four elements plotted against the thicknesses from Table I. As may be seen in the figure, the curves for the different elements are similar but the slope increases with atomic number of the element. Each curve must eventually become asymptotic with the 100% value but only the curve for gold shows such a tendency in the thickness range measured.

The calibration curves of Fig. 3 may, of course, be used directly to estimate thickness of other films of these elements. They may also be plotted in terms of ρt (density times thickness) instead of t; then in alloy or composite specimens, the intensity of each element will be a measure (to a 1st approximation) of the

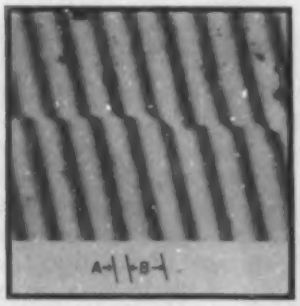

FIG. 2. Interference fringes showing a fringe shift A across the edge of an evaporated layer. The fraction A/B where B is the fringe separation is a measure of the film thickness.

TABLE I. Measured thickness of evaporated layers.

	Cr		Mn		Zn		Au	
step	layer	total	layer	total	layer	total	layer	total
1	430	430	450	450	660	660	580	580
2	690	1120	800	1250	760	1420	720	1300
3	550	1670	850	2100	1250	2670	300	1600
4	530	2200	1100	3200	730	3400	480	2080
5	500	2700	620	3820	1070	4470	520	2600
6	550	3250	860	4680	1030	5500	1050	3650
7	1080	4330			1000	6500	350	4000

[3] L. E. Preuss, Proceedings of the Sixth Annual Vacuum Society, Philadelphia, Pennsylvania, 1959).

[4] S. Tolansky, *Multiple Beam Interferometry of Surfaces and Films* (Oxford Press, London, 1948).

[5] L. S. Birks and E. J. Brooks, Rev. Sci. Instr. 28, 709 (1957).

[6] E. J. Brooks and L. S. Birks, ASTM Bull. No. 245 (1958).

number of grams of that element present for quantitative analysis.

DISCUSSION

Castaing and Descamps[7] have published curves on the relative x-ray intensity $\phi(\rho x)$ generated by an electron beam as a function of ρx (density times distance below the surface) of a specimen. Their data, replotted in terms of x rather than ρx is shown for zinc as the solid curve of Fig. 4. $\phi(x)$ has a value greater than unity at small values of x because they used a substrate of about the same atomic number to support their films. For unsupported films, the curve would be expected to shift to the dotted line in Fig. 4, but such a shift is unimportant when the data is normalized for infinite thickness.

Although their experimental conditions were somewhat different, it is possible to calculate an "expected" x-ray intensity for comparison with the measured values in the previous section. In Fig. 5, the x-ray intensity, dI_1, generated in layer dx at a distance x below the surface, by definition, will be,

$$dI_1=\phi(x)dx. \tag{2}$$

Radiation generated in the layer dx will be diminished before reaching the surface according to the standard x-ray absorption law. Thus

$$dI_2=dI_1\epsilon^{-\mu_c\rho x\csc\psi}, \tag{3}$$

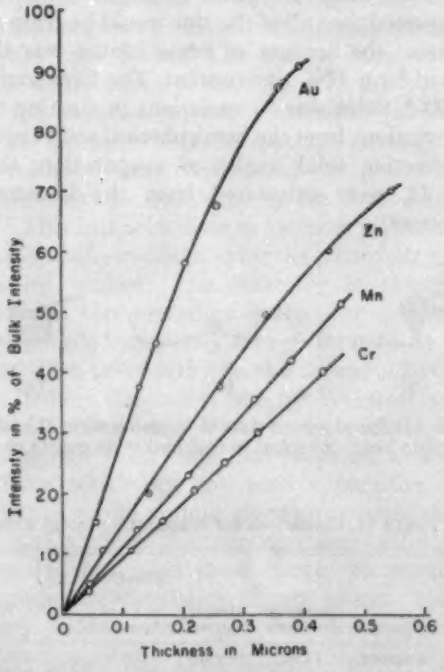

FIG. 3. Normalized x-ray intensity vs thickness for pure-metal evaporated films. Intensity from the evaporated layers of an element was divided by the intensity from a bulk specimen of the same element to obtain the normalized value.

[7] R. Castaing and J. Descamps, J. phys. Radium 16, 304 (1955).

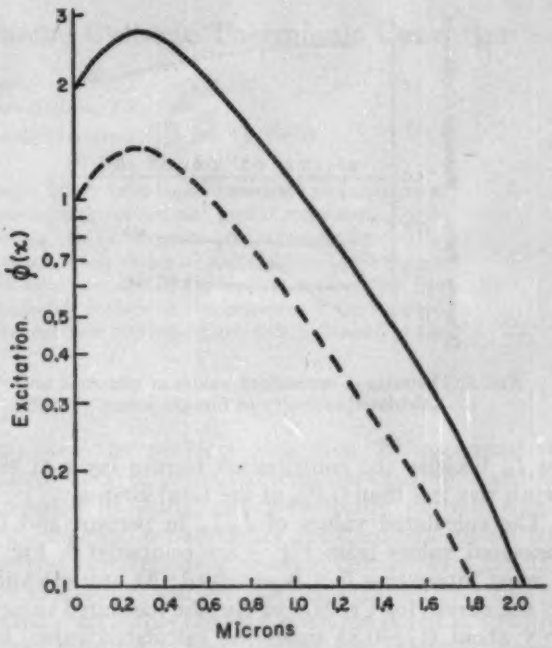

FIG. 4. The relative x-ray intensity generated in a specimen by electron bombardment as a function of distance x below the specimen surface. The solid curve represents the value observed by Castaing and Descamps when the specimen was on a substrate of about the same atomic number. The dotted curve is the limiting value assumed for a specimen on a low atomic number substrate.

where dI_2 is the increment emerging from the surface at the angle ψ in Fig. 5. The term μ_c is the mass absorption coefficient of the element for its own characteristic radiation. Combining Eqs. (2) and (3) and integrating, we obtain the total intensity from a specimen of thickness t

$$I_t=\int_0^t \phi(x)\epsilon^{-\mu_c\rho x\csc\psi}dx. \tag{4}$$

To normalize the calculated intensity in the same way as the measured intensity of Fig. 3, the term I_t must be divided by I_∞, that is, the integral of Eq. (4) must be evaluated over zero to infinity. Although it is possible to express $\phi(x)$ approximately by an analytical function of x and evaluate the integral, it is perhaps simpler to evaluate I_t by direct summation using the curve of Fig. 4 and taking x in 500 or 1000 A steps. It was found in practice to be unnecessary to sum beyond $x=20\,000$ A

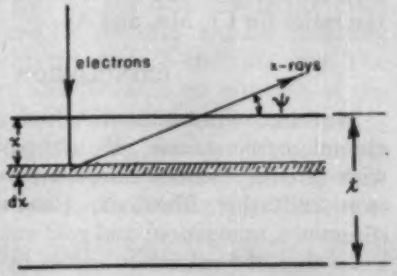

FIG. 5. Electrons normal to the specimen film of thickness t generate characteristic x rays in each incremental layer dx.

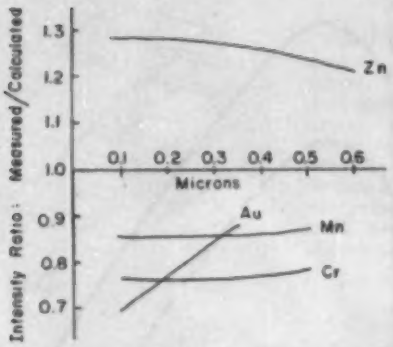

FIG. 6. The ratio of normalized values of measured and calculated intensity vs film thickness.

for I_∞ because the contribution from a layer at that depth was less than 0.3% of the total intensity.

The calculated values of I_t/I_∞ in percent and the measured values from Fig. 3 are compared in Fig. 6. A most interesting fact is observed: At any thickness on the curves for Cr, Mn, or Au, the measured value is only about 0.75–0.85 times the calculated value, but for any thickness on the Zn curve, the measured value is about 1.25 times the calculated value. Even when the excitation function $\phi(x)$ in Fig. 4, is artificially shifted up or down, the same large differences remained between zinc and the other elements. The difference is striking because zinc is closer to chromium and manganese in density than it is to gold and also the K series x-ray lines are measured for Cr, Mn, and Zn but it is the L series x-ray line that is measured for gold. Fluorescent excitation of the zinc by impurities evaporated from the brass or the mere presence of those impurity elements in reducing the relative zinc concentration might be thought responsible for the deviation but such is not the case. The only impurity element likely to excite zinc by fluorescence is lead, and it could not be present to more than 0.6% in the evaporated film. Knowing that electron excitation is some 200–1000 times more efficient than primary x-ray excitation, that much lead could not contribute more than 0.003% to the zinc intensity. If all the impurities present in the brass collected in the evaporated film they would total less than 5% of the zinc. The reduced concentration of zinc would mean that the ratio of measured to calculated intensity should be increased because the measured value would have come from less than 100% zinc. This, of course, would move the ratio for zinc even further away from the ratios for Cr, Mn, and Au.

CONCLUSION

Measured x-ray intensities from evaporated films of chromium, manganese, zinc and gold agree within 20% with intensity values calculated from published electron excitation functions. However, the measured chromium, manganese, and gold values are consistently lower than the calculated values by 20%, and the zinc value is consistently higher by 20%. This indicates that the differences are not random errors but that a real variation in internal strain, density or other unknown parameter exists between the present films and those used by Castaing and Descamps in evaluating the electron excitation originally. It appears that further work is warranted to help explain the peculiarities.

APPENDIX

Preparation of Evaporated Metal Films

Each of the metals—Cr, Mn, Zn, and Au—exhibits different evaporative characteristics; therefore, the form of the thermal source was altered to produce optimum evaporation conditions for each element. Figure 7 and Table II show how these conditions were varied. All of the evaporations were carried out at less than 5×10^{-4} mm Hg in a residual atmosphere of air. The glass substrate was at room temperature or slightly above and at a distance of 5 to 7 cm from the source.

Chromium and gold were evaporated from the spiral cone of tungsten wire shown in Fig. 7(a). Manganese was evaporated from the tantalum boat of Fig. 7(b) and zinc was evaporated by heating brass below its melting point in the quartz cup surrounded by tungsten wire in Fig. 7(c). Using a desired thickness of 600 A for each evaporation, the required milligrams of metal were determined for the known source to specimen distance by assuming a hemispherical distribution of evaporation from the source. In the case of zinc films it was assumed that all of the zinc would be removed from the brass; the amount of brass heated was therefore adjusted for a 37% zinc content. The films varied from the 600-A value due to variations in starting material and deviations from the hemispherical solid angle of 2π. The effective solid angles of evaporation, shown in Table II, were calculated from the measured film thicknesses.

FIG. 7. (a) Spiral wound cone of tungsten wire; (b) tantalum strip boat; (c) spiral wound basket on quartz cup.

TABLE II. Conditions for evaporating metal films.

Element	Heater	Source to specimen	Heater current	Effective solid angle of evaporation	Wire size
Cr	tungsten cone	7 cm	20 amp	2.5π	0.025 in.
Mn	tantalum boat	6	40	0.6	0.005 in. ×0.125 in
Zn	quartz cup	5	16	1.7	0.025 in.
Au	tungsten cone	7.2	20	3.4	0.025 in.

JOURNAL OF APPLIED PHYSICS VOLUME 31, NUMBER 6 JUNE, 1960

On the Theory of the Close-Spaced Impregnated Cathode Thermionic Converter

E. S. RITTNER
Philips Laboratories, Irvington-on-Hudson, New York

(Received December 3, 1959; revised manuscript received February 24, 1960)

The tables associated with the exact Langmuir space charge theory have been represented to a maximum relative error of 0.01% by approximation formulas which are suitable for use with digital computers. Application of the exact theory to a thermionic converter comprising two close-spaced planar impregnated cathodes has permitted a critical evaluation of the approximate space charge theory of Nottingham. The influence of the electrode separation, the emitter and collector work functions and of the emitter temperature has been investigated. Spectral emittance measurements on a cathode surface at two wavelength has resulted in a more firmly based estimate of the radiation heat transfer between two impregnated cathodes and of the maximum efficiency of an ideal design.

I. INTRODUCTION

IT has been known for a long time that a thermionic diode connected across a load resistance represents a thermodynamic system which converts heat to electricity. It is likewise well known that electronic space charge between electrodes severely limits the power output and the efficiency of such a device. A recent quantitative analysis by Moss[1] of a planar diode configuration based upon the Langmuir space charge theory[2] points out that for reasonable performance an interelectrode spacing as small as 0.01 mm or less is needed and that a corresponding degree of permanent flatness and smoothness is required in the electrodes. An interesting device consisting of two close-spaced identical planar impregnated cathodes,[3] which answers this description, has been assembled and studied by Hatsopoulos and Kaye.[4] The theory underlying the operation of this device is the subject of this paper.

Since the emission current is strongly space-charge limited at the interelectrode spacings envisaged, the current-voltage characteristics and the power output of the diode may be computed by the exact Langmuir method.[2] This has been done in footnote reference 4 for the specific configuration and for the particular cathode temperature studied. The difficulty in the general application of this procedure is that the computation technique, while completely straightforward, is highly laborious. Two noteworthy recent attempts have been made to reduce this labor, one by Webster[5] and the other by Nottingham.[6] Webster has employed the exact Langmuir theory and has prepared a family of curves from which one can read a quantity simply related to the output voltage given an assumed emission current and a diode configuration and cathode temperature. He has used these curves to predict the performance characteristics of an energy converter employing oxide-coated cathodes. Nottingham has simplified the problem somewhat by assuming the emitter to be of unlimited emission capability and has succeeded in fitting the numerically derived results with empirical equations for the maximum power output and corresponding emission current as a function of the spacing, the cathode temperature and the potential drop across the load when the potential gradient at the collector is zero. He has also presented several numerical examples for a converter utilizing impregnated cathodes.

Although Nottingham has found excellent agreement between his theory and the measurements of Hatsopoulos and Kaye,[7] we have deemed it of interest to compare the approximate Nottingham theory with the exact Langmuir theory especially because of the large experimental uncertainty in the interelectrode spacing. Our labor saving device has been the use of a digital computer programmed to evaluate the Langmuir equations with interpolation expressions as subroutines to replace all table look-up operations. In this manner it has been possible to examine a wide variety of conditions with high speed and accuracy and we have investigated converter performance as a function of the electrode work functions, the diode spacing and the cathode temperature. Our results differ sufficiently from those obtained using the approximate Nottingham theory as to demonstrate the lack of validity of the unlimited emission capability assumption in the majority of cases studied.

Another outstanding theoretical problem of the impregnated cathode converter is the conversion efficiency. Hatsopoulos and Kaye[4] and Nottingham[6] have computed the efficiency for an ideal design in which heat loss from the emitter via radiation is the main dissipative process and for the case that the radiating area is coincident with the electron emitting area. The former authors have also included an estimate of the heat conduction loss from the emitter. The results vary widely from 13%[4] to only 3%,[6] which differences are attributable partly to differing spacings employed in the two calculations and partly to differing estimates of

[1] H. Moss, J. Electronics **2**, 305 (1957).
[2] I. Langmuir, Phys. Rev. **21**, 419 (1923).
[3] R. Levi, J. Appl. Phys. **24**, 233 (1953); **26**, 639 (1955).
[4] G. N. Hatsopoulos and J. Kaye, J. Appl. Phys. **29**, 1124 (1958); Proc. I.R.E. **46**, 1574 (1958).
[5] H. F. Webster, J. Appl. Phys. **30**, 488 (1959).
[6] W. B. Nottingham, J. Appl. Phys. **30**, 413 (1959).
[7] Nottingham, Hatsopoulos, and Kaye, J. Appl. Phys. **30**, 440 (1959).

the radiant power transported from emitter to collector. Calculation of this power is somewhat involved because of multiple reflections between emitter and collector surfaces and also because neither surface is a gray body. Also, one requires information concerning the spectral emittance of the surfaces, which data have been lacking heretofore for the impregnated cathode. We have carried out measurements of the spectral emittance at 0.65 μ and at 2.5 μ over the usual temperature range of the impregnated cathode and have interpreted the data in terms of a simple model which permits an estimation of the complete spectral emittance distribution. Using these results we have numerically evaluated the Planck radiation integrals which characterize the radiation transport and thus have arrived at a more firmly based estimate of the maximum efficiency of the ideal design.

II. CURRENT-VOLTAGE CHARACTERISTICS AND POWER OUTPUT

A. Langmuir Theory

The Langmuir space charge calculation for a planar diode has been succinctly restated by Kleynen[8] in the course of extending the Langmuir tables. With the use of Kleynen's notation the computation procedure is as follows. The emitter temperature T, the emitter saturation current density I_s, and the interelectrode separation d are assumed to be known. It is further assumed that back emission from the anode is negligible. For any given value of the anode current density I_a the value of η_c is computed from

$$\eta_c=\ln(I_s/I_a) \tag{1}$$

and the corresponding value of ξ_c is obtained from the table. (It will be recalled that η and ξ are dimensionless quantities, which are proportional respectively to potential and to distance in the diode measured from the position of the potential minimum. Subscripts c and a employed with these quantities refer to the cathode and anode spaces respectively.) The quantity ξ_a is then obtained from

$$\xi_a=9.186\times10^5T^{-\frac{1}{2}}I_a^{\frac{1}{2}}d-\xi_c, \tag{2}$$

and the corresponding value of η_a from the table. Finally the potential difference V_a between anode and cathode is computed from

$$V_a=(kT/e)(\eta_a-\eta_c). \tag{3}$$

For sufficiently small currents no potential minimum will exist between electrodes and the I_a-V_a relation will be given by the retarding potential characteristic. In this case the quantity ξ_a will become negative and the value of V_a is to be computed from

$$V_a=-\eta_ckT/e \tag{4}$$

instead of from Eq. (3).

[8] P. A. J. A. Kleynen, Philips Research Repts. 1, 81 (1946).

Of more interest than the interelectrode potential difference V_a is the voltage drop across the load V_L. With the neglect of extraneous series resistances V_L follows readily from V_a via the relation

$$V_L=-V_a+(\phi_c-\phi_a)/e, \tag{5}$$

where ϕ_c is the work function of the cathode (or emitter) and ϕ_a is the work function of the anode (or collector).

The useful specific electrical power output P_L is given by

$$P_L=I_aV_L. \tag{6}$$

From the point of view of programming this problem for a digital computer, the only difficult question is how to handle the table look-up operations. The Kleynen tables, while excellent for desk computer use, are far too voluminous for the size of memory usually encountered in digital computers. The original Langmuir table could be employed together with a multipoint interpolation formula but this would probably prove to be a relatively slow procedure. In certain ranges of η analytical approximation formulas of high accuracy representing the η-ξ relationship are available. Langmuir has presented two sets of series, one for ξ_c for $\eta_c>3.0$ and the other for ξ_a for $\eta_a>8$. Kleynen has derived two sets of series in the neighborhood of the origin by developing and integrating the Langmuir integral. We have made use of these series and have derived additional approximation formulas for intermediate values of the independent variables by applying standard curve fitting techniques to the Langmuir table. It was also necessary to invert the Langmuir series for ξ_a as $f(\eta_a)$ for η_a large in order to obtain a series with ξ_a as the independent variable. The final approximation expressions employed, their validity ranges, and the percentage difference relative to the Langmuir tables are listed in Table I.[9]

The computer was programmed to tabulate I_a, V_a, V_L, and P_L starting with a small value of I_a and employing convenient increments in I_a; computation was discontinued when P_L fell to zero. Then the computation was repeated starting with a value of I_a slightly smaller than that corresponding to the maximum power output and with very much smaller increments in I_a to determine the maximum P_L to high accuracy.

B. Nottingham's Approximate Theory

The formulas derived by Nottingham under the situation that maximum power is being delivered to the

[9] Empirical equations representing the Langmuir tables have been reported previously by W. B. Nottingham in "Thermionic emission," *Handbuch der Physik* (Springer Verlag, Berlin-Gottingen-Heidelberg, 1956), Vol. 21, pp. 39 and 40. [Note that there is a typographical error in his Eq. (37.5). According to W. B. Nottingham (private communication) the plus sign should be changed to minus.] However, because of the larger number of ranges and the higher degree of complexity of the formulas employed by us, the formulas in Table I reproduce the Langmuir tables to a much higher degree of accuracy

TABLE I. Approximation formulas representing Langmuir tables.

Range	Formula	Maximum relative error, %
$0 \leq \eta_c \leq 0.20$	$\xi_c = -2\eta_c^{\frac{1}{2}} + 0.376126\eta_c + 0.0251956\eta_c^{\frac{3}{2}} + 0.00069163\eta_c^2 - 0.00099409\eta_c^{\frac{5}{2}}$	0.01
$0.20 \leq \eta_c \leq 3.0$	$\xi_c = -\dfrac{-6.156143\eta_c - 65.69123\eta_c^2 - 59.48926\eta_c^3 + 4.103353\eta_c^4}{-0.2629089 - 14.62018\eta_c - 49.59515\eta_c^2 - 16.06387\eta_c^3 + \eta_c^4}$	0.01
$3.0 \leq \eta_c$	$\xi_c = -2.55389 + \sqrt{2}e^{-\eta_c/2} - 0.0123e^{-\eta_c} + \dfrac{1}{3\sqrt{2}}[(\eta_c/\pi)^{\frac{1}{2}} + 1]e^{-3\eta_c/2}$	0.002
$0 \leq \eta_a \leq 0.05$	$\eta_a = 0.25\xi_a^2 - 0.047016\xi_a^3 + 0.012627\xi_a^4 - 0.00290\xi_a^5$	0.01
$0.05 \leq \eta_a \leq 11.0$	$\eta_a = 0.0003053192 - 0.001087509\xi_a + 0.2509922\xi_a^2 - 0.04648354\xi_a^3 + 0.01094699\xi_a^4 - 0.002286296\xi_a^5 + 0.0003642352\xi_a^6 - 0.00004062638\xi_a^7 + 0.000002943653\xi_a^8 - 0.000000123597\xi_a^9 + 0.0000000022744\xi_a^{10}$	0.01
$11.0 \leq \eta_a$	$\eta_a = [(\xi_a + 0.5088)/1.2552]^{\frac{1}{4}} - 1.5232(\xi_a + 0.5088)^{\frac{1}{4}} + 1.347 - 0.495(\xi_a + 0.5088)^{-\frac{1}{2}} - 0.140(\xi_a + 0.5088)^{-\frac{3}{4}}$	0.01

load are re-written below in our notation:

$$(I_a)_{P_L=\max} = I_m\left\{1+0.31\left[\frac{(V_L)_{\xi_a=0}}{kT}\right]^{\frac{1}{2}}\right\} \tag{7}$$

where $I_m = 9.664\times10^{-6}(kT)^{\frac{1}{2}}/d^2$ amp/m^2,

$$(P_L)_{\max} = 3.7\times10^{-6}(kT)^{\frac{1}{2}}\left[\frac{(V_L)_{\xi_a=0}}{d}\right]^2 \text{ watts/m}^2 \tag{8}$$

$$(V_L)_{P_L=\max} = 0.383\frac{(V_L)^2_{\xi_a=0}/kT}{1+0.31(V_L)^{\frac{1}{2}}_{\xi_a=0}/kT} \text{ volts.} \tag{9}$$

A program was written to evaluate these equations to permit comparison with the results of the exact theory for a given set of configurations and emitter temperatures. This program made use of that described in Sec. II A in the following way in order to determine $(V_L)_{\xi_a=0}$ (which is V_R in Nottingham's notation). All printed values of V_a corresponding to negative values of ξ_a were tagged. The transition between tagged and untagged values of V_a corresponds to a transition from a retarding to a space charge limited characteristic. This transition region was then recomputed with much finer increments in I_a and the average value of V_a corresponding to the last tagged value and the first untagged value was taken as $(V_a)_{\xi_a=0}$. The maximum error in this quantity was always less than $\pm1\%$. The value of $(V_L)_{\xi_a=0}$ was then obtained via Eq. (5) and the ensuing evaluation of Eqs. (7)–(9) was completely straightforward.

III. CONVERTER EFFICIENCY

A. General Theory

The efficiency of the converter may be expressed in the form:

$$\epsilon = P_L/(P_e+P_r+P_c), \tag{10}$$

where P_L is the useful specific output power, P_e is the specific power absorbed in evaporating electrons from the emitter, P_r is the specific power radiated from the emitter, and P_c is the power conducted away from unit area of the emitter by necessary supports and electrical leads. We shall derive numerical results only for an ideal design with P_c negligible compared to P_r and for an emitting area equal to the radiating area of the emitter.

The expression for P_e employed by us is identical to that used by Nottingham and in our notation is given by

$$P_e = (I_a/e)[\phi_c + (\eta_c+2)kT]. \tag{11}$$

This quantity was readily computed by a minor addendum to the program outlined in Sec. II A.

The specific radiant power transported from emitter to collector is given by:

$$P_r = \epsilon_c^*\sigma T_c^4 - \epsilon_a^*\sigma T_a^4, \tag{12}$$

where σ is the Stefan-Boltzmann constant and ϵ^* represents an effective total emittance which takes into account multiple reflections between electrodes, deviations from gray body distributions, and also the porosity of the tungsten surfaces. The evaluation of ϵ^* proceeds as follows. Consider two infinite non-gray plane parallel plates (a reasonable approximation to the geometry of a close-spaced thermionic converter). For any infinitesmal wavelength interval $d\lambda$ the surfaces may be considered to be gray and, as shown by Hottel,[10] because of multiple reflections each surface will radiate with an effective emittance given by

$$\epsilon_{\text{eff}} = 1/(1/\epsilon_c + 1/\epsilon_a - 1), \tag{13}$$

where ϵ_c and ϵ_a, which represent the emittance of isolated emitter and collector surfaces, respectively, are

[10] H. C. Hottel in *Heat Transmission*, edited by W. H. McAdams (McGraw-Hill Book Company, Inc., New York, 1954), 3rd ed., p. 63.

functions of wavelength and temperature. The quantity ϵ^* is then given by the following ratio of Planck radiation integrals:

$$\epsilon^* = \int_0^\infty \frac{\epsilon_{\lambda t} x^3 dx}{e^x - 1} \Big/ \int_0^\infty \frac{x^3 dx}{e^x - 1} \tag{14}$$

where $x = c_2/\lambda T$, c_2 being the second radiation constant. These integrals must be evaluated twice, first for values consistent with the temperature T_c and then for values consistent with T_a, thus yielding ϵ_c^* and ϵ_a^*, respectively.

B. Experimental Determination of Spectral Emittance

The spectral emittance of the impregnated cathode cannot be expected to be identical to the spectral emissivity of tungsten because of the cathode porosity. We have made some measurements of the former quantity at 0.65 μ with the aid of an optical pyrometer and of the ratio of cathode emittance to tungsten emissivity at 2.5 μ with the use of a germanium filter and a lead sulfide detector.

The impregnated cathode studied was a standard 3 mm diameter type *B* planar cathode mounted in the usual molybdenum supporting cylinder. For comparison purposes a similar structure was assembled with a sheet of polished tungsten replacing the porous tungsten member. Brightness temperature S_λ measurements were taken with a Leeds and Northrup optical pyrometer, with alternate sightings on the Mo body and on the cathode (or polished tungsten) surface in the temperature range 1200–1465°K (true temperature). The emittance was computed by the use of the well-known formula[11]

$$\ln \epsilon_\lambda = \frac{c_2}{\lambda}\left(\frac{1}{T} - \frac{1}{S_\lambda}\right). \tag{15}$$

In the case of the tungsten surface the computed values of ϵ_λ, which displayed a decrease with increasing temperature, agreed within 1–2% with the published values of Forsythe and Adams.[12] The values of ϵ_λ for the cathode surface (and also for an unimpregnated identical tungsten plug) were independent of temperature over the range studied and the mean value of four measurements at each of nine temperatures was 0.50 ± 0.01. (For comparison the average emissivity of tungsten in the same temperature interval is 0.45.)

For the measurements at 2.5 μ the lead sulfide detector viewed the radiation first from a portion of the cathode surface and then from the same area of polished tungsten through a set of blackened apertures, an optically ground and polished window of Corning 7052 glass 3 mm in thickness, and a slab of germanium of optical quality and 1 mm in thickness. The photocell load was constituted by another identical cell to provide temperature compensation and the signal from the load was fed into a type 543 Tektronix scope. The selection of the radiation from the cathode or tungsten surfaces was accomplished by lateral translation of the tube assembly relative to the line of sight of the detector. By alteration of the source-detector distance and verification of the inverse square law it was demonstrated that the overall system was operating in the linearity range. Hence the ratio of output signals on the oscilloscope constituted the desired ratio of cathode emittance to tungsten emissivity. This ratio was determined to be 1.58 ± 0.04, independent of temperature over the range studied, again 1200–1465°K.

C. Interpretation of Data and Calculation of ϵ^*

It might be expected at any wavelength that the fraction f of the cathode surface occupied by pores would emit as a black body whereas the remainder of the surface would emit with the emissivity ϵ_W of polished tungsten, i.e.:

$$\epsilon_c = f + (1-f)\epsilon_W. \tag{16}$$

If this model is reasonably satisfactory, then one would expect the value of f computed from Eq. (16) by insertion of measured values of ϵ_c (or of the ratio ϵ_c/ϵ_W) and of published values[12] of ϵ_W to be independent of wavelength. This indeed proves to be the case. For $T = 1200$°K, we find at $\lambda = 0.65\,\mu$, $f = 0.0842$ and at $\lambda = 2.5\,\mu$, $f = 0.0836$. Moreover, this is a reasonable range for f since the cathode porosity is about 17%. At higher temperatures a similar independence of f and λ is observed, but the value of f drifts slightly upward with T reaching an average value of $f = 0.0956$ at $T = 1465$°K.

With the values of f so computed, the published values of ϵ_W, and Eq. (16) it was possible to obtain the spectral emittance of the cathode as a function of wavelength and temperature for insertion into Eqs. (13) and (14). Equation (14) was then integrated numerically with the use of Simpson's rule, with the employment of linear interpolation between successive entries in the $\epsilon_{\lambda t}$ vs x table, and with the addition of a theoretically based point at $x = 0$ ($\lambda = \infty$) of $\epsilon_{\lambda t} = 0$. The collector temperature T_a was fixed at 900°K in this computation (for reasons to be discussed below) and ϵ_c^* and ϵ_a^* values were obtained for several different values of T_c. The final results for ϵ^* may be well described by the expressions:

$$\begin{aligned} \epsilon_c^* &= -0.0086 + 8.43 \times 10^{-5} T_c \\ \epsilon_a^* &= 0.0558 + 1.55 \times 10^{-5} T_c \end{aligned} \qquad (T_a = 900°\text{K}). \tag{17}$$

With the use of Eqs. (12) and (17) P_r may be computed, thus completing the calculation of the components of the efficiency expression.

[11] A. G. Worthing in *Temperature, Its Measurement and Control in Science and Industry* (Reinhold Publishing Corporation, New York, 1941), Vol. I, p. 1171.

[12] W. E. Forsythe and E. Q. Adams, J. Opt. Soc. 35, 108 (1945).

TABLE II. Configurations studied and results for maximum power output.

	1	2	3	4	5	6	7	8	9	10	11
	T°K	ϕ_c, ev	ϕ_a, ev	d, mm	I_a, a/cm²		V_L, v		P_L, w/cm²		ϵ, %
					exact	approx.	exact	approx.	exact	approx.	
1	1465	2.155	1.855	0.01	1.42	1.81	0.393	0.380	0.558	0.689	8.61
2	1465	2.155	2.155	0.01	0.845	1.11	0.259	0.213	0.219	0.236	4.37
3	1465	2.155	1.655	0.01	1.84	2.34	0.480	0.479	0.884	1.12	11.7
4	1465	2.155	1.855	0.005	3.55	5.79	0.332	0.300	1.18	1.74	10.1
5	1465	2.155	2.155	0.005	1.89	3.25	0.193	0.122	0.365	0.398	4.77
6	1465	2.155	1.655	0.005	4.71	7.77	0.426	0.406	2.00	3.16	13.8
7	1465	2.155	1.855	0.02	0.495	0.558	0.461	0.460	0.228	0.256	5.58
8	1465	2.155	2.155	0.02	0.322	0.367	0.329	0.305	0.106	0.112	2.29
9	1465	2.155	1.655	0.02	0.620	0.698	0.547	0.552	0.339	0.385	7.68
10	1540	2.179	1.855	0.01	1.85	2.19	0.449	0.445	0.831	0.976	9.56
11	1410	2.137	1.855	0.01	1.17	1.55	0.338	0.332	0.396	0.517	7.64
12	1350	2.117	1.855	0.01	0.836	1.29	0.307	0.278	0.256	0.359	6.79
13	1295	2.100	1.855	0.01	0.589	1.08	0.270	0.232	0.159	0.250	5.79
14	1240	2.082	1.855	0.01	0.376	0.887	0.238	0.188	0.0895	0.166	4.73
15	1465	2.355	1.855	0.01	1.09	1.89	0.417	0.395	0.454	0.745	8.06
16	1465	1.855	1.855	0.01	1.62	1.76	0.383	0.370	0.620	0.652	8.88
17	1000	1.600	0.800	0.0254	0.308	0.390	0.534	0.526	0.164	0.205	···

IV. RESULTS AND DISCUSSION

The various converter configurations and cathode temperatures studied are listed in the first four columns of Table II. An emitter temperature of 1465°K has been chosen for most of the cases studied because extensive life tests have been carried out on the impregnated cathode at this temperature and the life is known[3] to be of the order of 10^4 hours. At 1540°K the cathode life is markedly lower, but line 10 has been computed to permit comparison with the experimental results of Hatsopoulos and Kaye. The remaining emitter temperatures were of interest in connection with the Nottingham theory. All values of ϕ_c were computed from the cathode temperature via the relation[13]:

$$\phi_c = 1.68 + 3.24 \times 10^{-4} T_c. \tag{18}$$

The collector temperature was taken to be 900°K in all cases as Welsh[14] has shown that this temperature corresponds to a minimum collector work function of 1.85 ev in the close-spaced diode. This work function is lower than Eq. (18) would predict by about 0.1 ev and may be an indication that evaporation products from the emitter alter the constitution of the collector surface, possibly by the deposition of BaO. A value of $\phi_a = 1.855$ ev was employed in most of the calculations and an arbitrarily higher and lower value were also tried in order to study the importance of this parameter. The interelectrode spacing was taken to be 0.01 mm in most cases and the effect of doubling and halving this value was investigated. Finally, line 17 was computed to permit comparison with the theory of Webster.[15]

Figure 1 displays the power output (solid curve) and the efficiency (dashed curve) as a function of output voltage for the configuration of line 1 of Table II. Note that the efficiency maximum occurs at a higher output voltage than the power output maximum and that the maximum efficiency is about 25% of the Carnot efficiency. It is important to realize that the emission is strongly space charge limited at the maximum power output point. In the case of line 1 the emission density at this point is only one-seventh of the

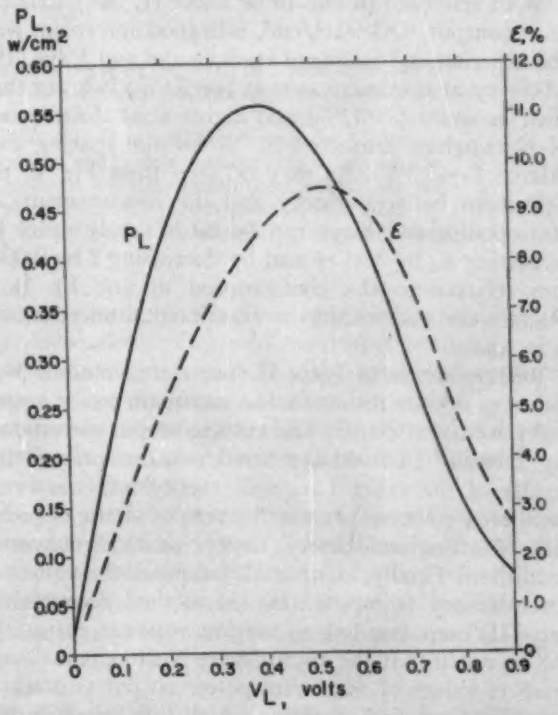

FIG. 1. Power output (solid curve) and efficiency (dashed) as a function of voltage output. $T_c = 1465$°K, $\phi_c = 2.155$ ev, $\phi_a = 1.855$ ev, $d = 0.01$ mm.

[13] E. S. Rittner, R. H. Ahlert, and W. C. Rutledge, J. Appl. Phys. 28, 156 (1957); R. Levi, Philips Tech. Rev. 19, 186 (1958).
[14] J. A. Welsh, private communication.
[15] The conditions corresponding to line 17 do not appear in reference (5), but they were examined in an earlier manuscript by H. F. Webster.

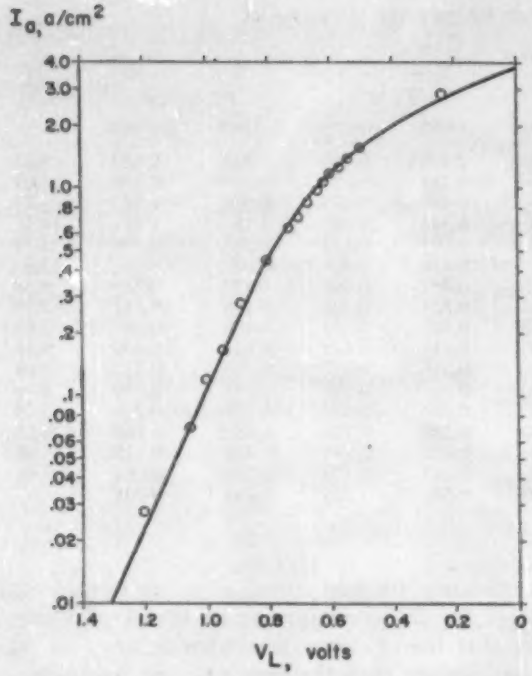

FIG. 2. Comparison of the exact theory (solid line) with the current density-voltage characteristic observed by Hatsopoulos and Kaye (circles). $T_c=1540°K$, $\phi_c=2.179$ ev, $\phi_a=1.885$ ev, $d=0.0098$ mm.

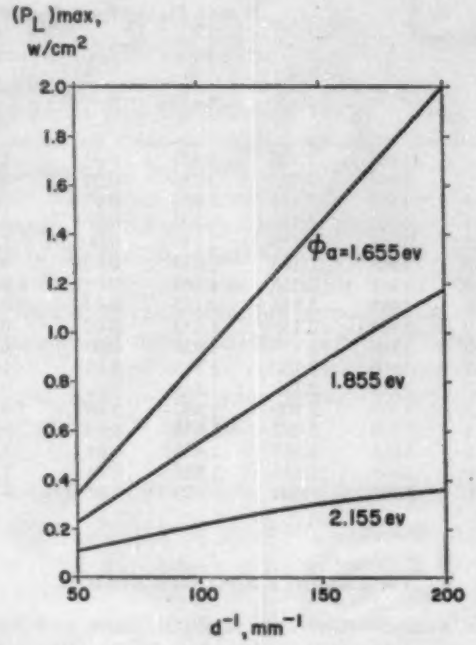

FIG. 3. Maximum power output as a function of anode work function and of reciprocal of interelectrode spacing. $T_c=1465°K$, $\phi_c=2.155$ ev.

saturation emission density; in the case of line 10 this ratio is only one-eleventh.

With reference to line 10 of Table II, the maximum power output, 0.83 watt/cm², is in good agreement with the experimental finding of Hatsopoulos and Kaye. The efficiency at maximum output ($\epsilon=9.6\%$) is lower than their estimate ($\epsilon=12\%$) and higher than the estimate of Nottingham corrected by us for the spacing considered ($\epsilon=5.5\%$). As may be seen from Fig. 2, the agreement between theory and the measurements of Hatsopoulos and Kaye can be made nearly exact by increasing ϕ_a by 0.03 ev and by decreasing d by 0.0002 mm relative to the configuration of line 10. Both changes are well within the experimental uncertainties in ϕ_a and d.

With reference to Table II once more, columns 5–10 inclusive contain results for the maximum power output and the current density and voltage output corresponding thereto. The odd-numbered columns present the results of the exact Langmuir theory and the even-numbered columns present the results of the approximate Nottingham theory under identical converter conditions. Finally, column 11 tabulates the values of the efficiency (computed by the method described in Sec. III) corresponding to maximum power output. It will be noted that the approximate Nottingham theory predicts values of maximum power output and corresponding emission density which are significantly higher than those computed from the exact theory. The percentage difference between the two sets of results tends to increase with decreasing cathode temperature (compare rows 10, 1, 11, 12, 13, 14), thus indicating that the source of the divergence is the infinite emission capability assumption of the Nottingham theory.

Figure 3 displays the maximum power output as a function of the reciprocal of the interelectrode spacing with the anode work function as a parameter. Despite the fact that Eq. (8) seems to imply that the maximum power output is proportional to d^{-2}, it is seen from the figure that the dependence is much closer to d^{-1}. The reason is that $(V_L)_{I_a=0}$ is implicitly a function of d. For the same reason $(V_L)_{P_L=max}$ is not independent of spacing despite the fact that d does not enter into Eq. (9). Figure 3 also stresses the importance of minimizing the anode work function; and Table II, rows 1–9 inclusive point up the importance of a low value of ϕ_a in producing high output current density, voltage and efficiency.

Rows 1, 15, and 16 of Table II show the effect of changing the cathode work function. While such change does not produce as large an effect in the output parameters as corresponding changes in ϕ_a, nevertheless there is a substantial influence.

The results displayed in line 17 of Table II are in excellent agreement with the calculations of Webster ($I_a=0.315$, $V_L=0.525$, $P_L=0.165$).

V. SUMMARY

The theoretical performance characteristics of the close-spaced impregnated cathode thermionic converter are rather impressive. At a spacing of 0.01 mm,

which has already been achieved, and at a cathode temperature of 1465°K, at which temperature the life of the emitter is of the order of a year, the maximum output is 0.56 watt/cm² and occurs at an output voltage of 0.39 v. The corresponding efficiency of an ideal design (emitting area equal to radiating area and negligible conduction losses to the supports) is 8.6% and this could be increased to 9.5% by operation at an output voltage of 0.5 v with a decline in power output to 0.50 watt/cm². The emission is strongly space charge limited, the emission density at maximum output being only one-seventh of the saturation current density at the temperature cited.

The possibility of improving the performance by decreasing the interelectrode separation further does not appear too promising in view of the attendant mechanical difficulties and in view of the fact that the power output is roughly inversely proportional to only the first power of the separation. Replacement of the collector by another material having a lower work function would appear to be a more promising approach, but it must be kept in mind that the lower work function may not necessarily be maintained in the presence of the evaporant stream from the emitter.

The exact Langmuir theory can now be readily applied to any close-spaced thermionic converter by programming Eqs. (1)–(6) inclusive and the formulas of Table I for any digital computer.

ACKNOWLEDGMENTS

The writer is indebted to Professor G. E. Uhlenbeck, Dr. F. K. du Pré, Mr. T. R. Kohler, and to Dr. A. Milch for helpful discussions. He would also like to thank Professor W. B. Nottingham for detailing the nature of the typographical error in Eq. (37.5) of "Thermionic emission" and for pointing out an inconsistency in the units of Eqs. (3) and (4) in an earlier version of the present manuscript. Dr. John A. Welsh has kindly granted permission to quote his unpublished result for the minimum work function of the collector and Dr. H. F. Webster has kindly communicated the results of his computation corresponding to line 17 of Table II.

JOURNAL OF APPLIED PHYSICS VOLUME 31, NUMBER 6 JUNE, 1960

Etch Pits at Dislocations in Copper

J. D. LIVINGSTON
General Electric Research Laboratory, Schenectady, New York
(Received February 8, 1960)

A modification of an etch discovered by Lovell and Wernick has been shown to be a reliable means of revealing dislocations as etch pits on (111) faces of copper crystals. The etch has been employed to study dislocation distributions in as-grown, annealed, and deformed crystals.

A high-temperature anneal is found to lower the dislocation density of melt-grown crystals. A "double-etch" technique is employed to observe the motion of dislocations, and to show that the dislocations initially present in these crystals are mobile at low stresses. Subboundaries are numerous in these crystals and are found capable of hindering dislocation movement. Observations of the dislocation structure of crystals deformed in bending and in tension are reported, including the appearance of "glide polygonization" after room-temperature deformation.

INTRODUCTION

An etch that reliably reveals dislocation sites in crystals by surface pits can be a powerful tool in the study of plastic deformation. Such a technique is particularly useful in studying the early stages of deformation, when the dislocation density is still relatively low. The work of Gilman and Johnston[1] on LiF is a good example of the wealth of detailed information that can be obtained with a reliable etch.

Until recently, the etching techniques for revealing dislocations in ionic and covalent crystals have been better developed and more productive than those for metals. Most of the earlier etches reported for metals require a specific impurity addition to the metal and a heat treatment to allow this impurity to segregate to the dislocations. This heat treatment is usually at a temperature high enough to allow appreciable redistribution of the dislocations that are introduced by room-temperature deformation, and hence these "decoration" techniques are usually not well suited to a study of plastic deformation.

In the past two years, however, several etches have been developed to reveal dislocations in metals and semimetals without apparent need for impurity decoration. Promising etches have been developed for bismuth, antimony, and tellurium,[2] tungsten,[3] and more recently, copper.[4]

[1] J. J. Gilman and W. G. Johnston, *Dislocations and Mechanical Properties of Crystals* (John Wiley & Sons, Inc., New York, 1957), p. 116.

[2] L. C. Lovell, F. L. Vogel, and J. H. Wernick, Metal Progr. 75, 96 (1959).

[3] U. E. Wolff, Acta Met. 6, 559 (1958).

[4] L. C. Lovell and J. H. Wernick, J. Appl. Phys. 30, 590 (1959).

There is a large body of literature on the deformation of fcc metals, particularly aluminum and copper. These metals are also prominent in recent theories of deformation and work-hardening.[5] It therefore seemed to the author that Lovell and Wernick's discovery of a dislocation etch for copper was a particularly significant development. A research program has been undertaken to utilize their etch in a study of the fundamentals of plastic deformation in copper. This report includes evidence of the reliability of an improved etch and initial observations on dislocation structures of as-grown, annealed, and deformed crystals.

EXPERIMENTAL TECHNIQUES

The single crystals studied were of American Smelting and Refining Company copper with an estimated purity of 99.999%. They were prepared by seeded vertical growth from the melt in graphite boats under a rough vacuum of approximately 10 microns. After growth, the ratio of room temperature to 4.2°K resistivities was approximately 1200. The crystals were square in cross section, $\frac{3}{16}\times\frac{3}{16}$ in., and were about 6 in. long as grown. Usually two or more specimens were carefully sawed from each crystal with a jeweler's saw. The orientation of the crystals was such that one pair of the lateral surfaces was within 2° of (111). Several different specimen axis orientations within this (111) plane were used, all located well within the basic stereographic triangle so that only one slip system would be favored in simple bending or tension.

The composition by volumes of the etch used is one part bromine, 30 parts glacial acetic acid, 45 parts hydrochloric acid, and 250 parts water. The bromine is first dissolved in the acetic acid and then added to the diluted hydrochloric acid. This differs from Lovell and Wernick's etch in its proportions, and by the omission of ferric chloride, which was a major component of their etch. This modified etch yields sharper better-defined pits and has less tendency to stain the copper surface.

Crystals were electropolished in a solution of 60% H_3PO_4, 40% H_2O. A water rinse immediately followed the polish, after which the samples were immersed in the etch for times of the order of 30 seconds. Samples were subsequently rinsed in water, then alcohol, and then dried in an air stream.

The tensile deformations were achieved with an Instron testing machine, using split grips with matching grooves designed to hold the specimen ends firmly once the grip halves were tightened together with screws. Strain rates were approximately one percent per minute. Bending experiments were performed with the use of three-point and four-point bending jigs.

FIG. 1. Double-etch result showing dislocation motion in copper. Crystal was etched, stressed, and re-etched. 375×.

[5] A. Seeger, J. Diehl, S. Mader, and H. Rebstock, Phil. Mag. 2, 323 (1957).

OBSERVATIONS

Characteristics and Reliability of the Etch

The etch was found capable of producing satisfactory etch pits only when the crystal surface was less than 2 or 3 deg off the (111) plane. At present, this is the major experimental limitation of this technique. When the surface orientation is satisfactory, the pits are triangular in outline, with the edges parallel to ⟨110⟩ directions in the crystal surface. Since the other (111) planes intersect this surface along ⟨110⟩ directions, slip-plane traces are always parallel to the edges of the triangular pits. If the surface under observation is slightly off the (111) plane, the pits become highly distorted in shape—often elongated in one direction—and become harder to distinguish from other etching features in the background.

Sequential etching studies show that as total etching time is increased, the etch pits remain essentially constant in number but simply get broader and deeper. The pit width is found to increase approximately linearly with total etching time until neighboring pits impinge.

If a crystal is subjected to a light stress between two immersions in the etch, it is found that the second etch reveals three different types of pits. There are large sharp-bottomed pits, large flat-bottomed pits, and small sharp-bottomed pits. All three types can be seen in Fig. 1, which shows the results of such a "double etch" experiment. The large sharp-bottomed pits represent the sites of dislocations unmoved by the stress that was applied between the two etches. The large flat-bottomed pits show the original position of dislocations that were moved by the stress, and the small sharp-bottomed pits show their final position. Apparently, the etch will widen any pre-existing pit, but will only continue to deepen it as long as the dislocation responsible for it remains. Identical observations in etching LiF have been made and discussed by Gilman and Johnston.[1]

The continuous nature of the pitting during repeated etching or alternate etching and polishing shows that the pits follow line defects in the crystal. Double-etch results as those in Fig. 1 show that these defects can move under stress. This seems sufficient proof that the pits reveal dislocations.

Definitive proof of a 1:1 correspondence between pits and dislocations is more difficult to establish. One useful experiment is to bend and anneal some specimens, and

to compare the excess pit densities created with the equilibrium dislocation densities calculable from theory. This method has been used by several previous investigators[6,7] to test the reliability of their etching techniques. Several copper crystals were bent about the [111] axis to radii of curvature of 2 in. and 5 in. and subsequently annealed in nitrogen for three days at 1060°C. The excess etch pits, in some cases now arranged in polygon walls,[8] showed counts within 30% of those calculated from $n=1/rb\cos\chi$.[9] Here n is the equilibrium density of edge dislocations, b the Burgers vector, r the radius of curvature, and χ the angle between the Burgers vector and the specimen axis. The agreement was considered to be within the estimated experimental error.

The dislocations counted in these bent specimens were edge dislocations. For rectangular crystals with (111) lateral surfaces, simple bending or tension experiments will always preferentially activate slip systems with the slip direction lying in this lateral (111) surface, regardless of specimen axis orientation.[10] Thus, the bulk of the dislocations generated by such deformations will emerge from the (111) lateral surface predominantly edge in character. However, small facets parallel to other octahedral planes, for instance $(11\bar{1})$, can be developed on the other lateral surfaces of these specimens by etching heavily in concentrated nitric acid. Immersion in the dislocation etch will then reveal pits on these $(11\bar{1})$ facets as well as on the (111) surface. Such an experiment on a deformed sample suggests that this dislocation etch can also reveal dislocations that are largely screw in character, although a 1:1 correspondence cannot be established as it was for the edge dislocations.

As-Grown and Annealed Structures

Etching an as-grown crystal reveals a structure such as that shown in Fig. 2(a). The total dislocation count averages about 2×10^6 per cm^2. A subsequent anneal in nitrogen at 1050°C for one or two days followed by a slow cooling in the furnace, lowered the total density markedly, as shown by Fig. 2(b). As annealed, the dislocation density within subgrains averages about 3×10^5 per cm^2, and is often considerably lower than this over large areas. A similar effect of annealing has been observed in silicon iron crystals.[11]

A random dislocation count as low as that observed after annealing makes it quantitatively difficult to explain the critical resolved shear stress of these crystals (typically about 100 g/mm^2) on the basis of the random dislocation "forest" or its associated internal stress fields.[5]

(a)

(b)

FIG. 2. (a) Dislocation structure of an as-grown crystal. (b) Different region of same crystal after annealing two days at 1050°C. 187.5×.

[6] W. R. Hibbard, Jr., and C. G. Dunn, Acta Met. 4, 306 (1956).
[7] F. L. Vogel, Jr., Trans. Am. Inst. Mining Met. Engrs. 206, 946 (1956).
[8] Although polygonization in high-purity copper is extremely sluggish [See references cited in footnotes 4 and 14; C. T. Wei, M. N. Parthasarathi, and P. A. Beck, J. Appl. Phys. 28, 874 (1957)]; portions of these specimens did polygonize, some specimens almost entirely. Whether or not this is evidence for residual impurity effects in these samples is not known.
[9] J. F. Nye, Acta Met. 1, 153 (1953).
[10] The single exception is a ⟨110⟩ specimen axis, where four slip systems are equally stressed, two of which have slip directions not lying in the (111) lateral surface.
[11] D. F. Stein and J. R. Low, Jr., J. Appl. Phys. 31, 362 (1960).

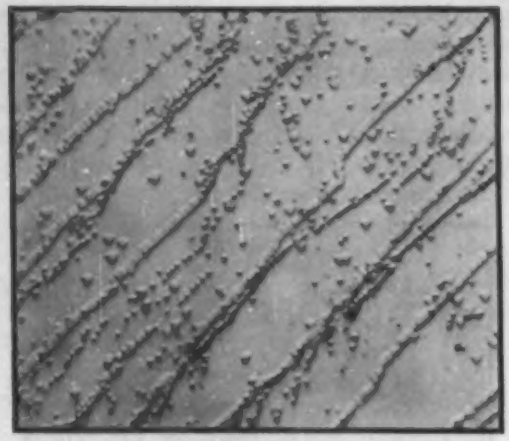

FIG. 3. Motion and dissolution of polygon walls under stress. A polygonized crystal was etched, stressed, and re-etched. 250×.

Dislocation Motion

A question of fundamental interest is whether or not the dislocations present in a copper crystal after an anneal and slow cool can contribute to its subsequent deformation. This question has been answered by double-etch experiments of the kind described earlier. Figure 1 is a case where the maximum *normal* stress applied by bending between the two etches was only about 140 g/mm². Nevertheless a large fraction of the random dislocations were observed to move. Experiments on other crystals have shown that the movement of the annealed-in dislocations in copper at low stresses is a general observation.

In contrast, the dislocations initially present in slow-cooled crystals of LiF and MgO are not observed to move, apparently having been rendered immobile by impurities.[1,12] This greater impurity pinning observed in ionic crystals is most probably not due to a higher impurity content, but rather a stronger dislocation-impurity interaction, probably due to charge effects.

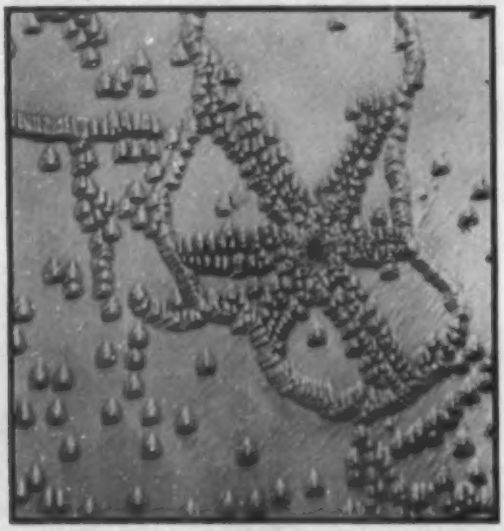

FIG. 4. Dislocation rosette whose outward progress is blocked by subgrain boundaries. 500×.

This observation of dislocation mobility in copper can be extended to simple boundaries consisting of edge dislocations. Polygon walls, consisting of an array of edge dislocations in a plane perpendicular to their slip plane, can be formed in a specimen by a prior deformation and high-temperature anneal. An etch-stress-etch sequence on such a sample led to Fig. 3, which shows the motion and dissolution of polygon walls under a low stress. On the other hand, the subboundaries present in the as-grown crystal do not move, as Fig. 1 shows. The dislocations in these boundaries are most probably not in simple parallel arrays with a single Burgers vector, nor will their Burgers vector in general be that of the most highly stressed slip systems. Hence, the immobility of these boundaries is not surprising. It is possible that individual dislocations leave these boundaries at low stresses, but this would be very difficult to detect by the double-etch method.

Rosettes and Subboundaries

If a steel ball of $\frac{1}{4}$ in. diam is rolled over an electropolished surface of an annealed crystal, subsequent etching reveals that many dislocation "rosettes" have been formed along its path. These rosettes are shallow arrays of dislocations emanating on several slip planes from a central source of concentrated stress, presumably caused by an irregularity on the crystal surface or on the ball. Such arrays have been produced in LiF[1] by this same technique.

Since there were so many subboundaries in these crystals, a large number of the rosettes started very close to the subboundaries. A study of such rosettes showed that the subboundaries were a serious obstacle to dislocation motion. In most cases, the slip band of the rosette was stopped completely by the subboundary. Figure 4 shows a rosette that formed in a subgrain small enough to allow all the arms of the rosette to be blocked by the subgrain boundary. In the cases where some slip did continue beyond subboundaries, the associated pit density was always lower than before reaching the subboundary. Thus a study of these rosettes clearly shows that the subboundaries present in a copper crystal grown from the melt have a hindering effect on the advance of a slip band.

Structures of Deformed Crystals

Glide Polygonization

One of the interesting observations relating to deformed crystals was that of prevalent "glide polygonization" at room temperature. Figure 5 shows the etch-

[12] J. Washburn, A. E. Gorum, and E. R. Parker, Trans. Am. Inst. Mining Met. Engrs. **215**, 230 (1959).

FIG. 5. Glide polygonization structure of a copper crystal bent at room temperature. Slip-plane trace parallel to arrow. Strain approximately 0.1%. 200×.

pit pattern observed on a crystal strained lightly in bending. The edge dislocations seen are found to be aligned along slip planes, although widely spaced. They also show short-range alignments in a direction perpendicular to the slip-plane trace. From their irregularity and the angle they make with the primary slip-plane trace, these short-range alignments are apparently not due to slip on another plane, but are simply a perpendicular alignment of the edge dislocations of the primary slip system geometrically analogous to that occurring in simple polygonization. Whereas the polygonization process normally considered requires dislocation climb, presumably here the alignment was achieved simply by glide motion of the dislocations along their slip planes. Because of the differences and similarities to the classic polygonization process, this may be termed "glide polygonization."

Glide polygonization has also been observed in LiF and silicon iron crystals, although previously unreported. Figure 6 demonstrates the generality of this occurrence. (As seen in Fig. 6(a), the glide polygonization is sometimes so extreme that it completely obscures the alignment of pits along slip lines. This is also seen in copper crystals.) Since in all these cases etching was done after the load was removed from the deformed specimen, it has not been determined whether this alignment occurred under load or after release of the load. Recent observations by transmission electron microscopy on aluminum foils suggest that such alignments may exist during deformation.[13]

The observation of prevalent glide polygonization appears to invalidate an earlier conclusion[14] that dislocations in copper can climb at appreciable rates at 500°C. In this earlier study, Young had bent a copper crystal at room temperature and then given it the 500°C anneal which was a necessary part of his etching technique. His etch revealed a structure much like that in Fig. 5. Although this led to the conclusion that dislocation climb had occurred at 500°C, it now appears that these observations were due to glide polygonization, much of which had already occurred at room temperature. A study of his observations after higher-temperature anneals suggest that appreciable dislocation climb did not occur below 900°C.

It is of interest to estimate the elastic interaction stresses between two edge dislocations on parallel slip planes spaced as far apart as the "polygonized" dislocations in Fig. 5. For a slip-plane spacing of about three

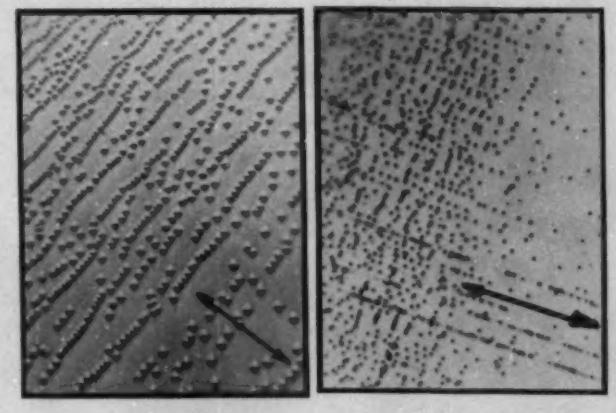

(a) (b)

FIG. 6. Glide polygonization in (a) LiF, 500× (Johnston). (b) Fe-3¼% Si, 1000× (Dunn). In both cases, the deformation was at room temperature, although the silicon iron was subsequently heated near 160°C, allowing decoration of the dislocations. Slip-plane trace parallel to arrow.

[13] A. Berghezan and A. Fourdeaux, J. Appl. Phys. **30**, 1913 (1959).

[14] F. W. Young, Jr., J. Appl. Phys. **29**, 760 (1958).

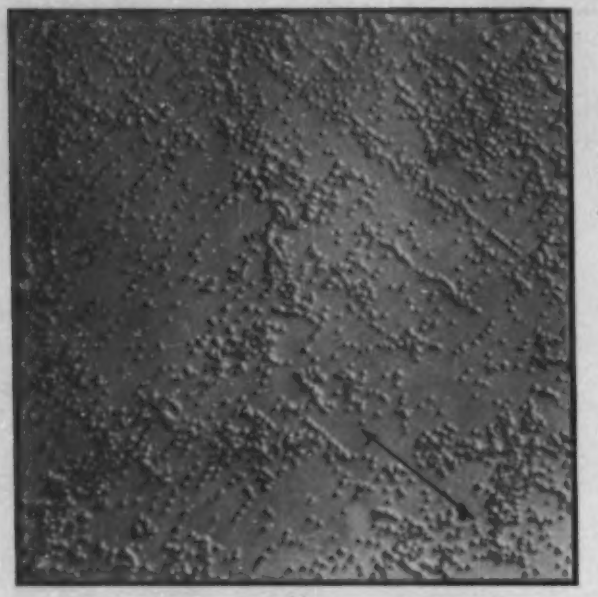

(a)

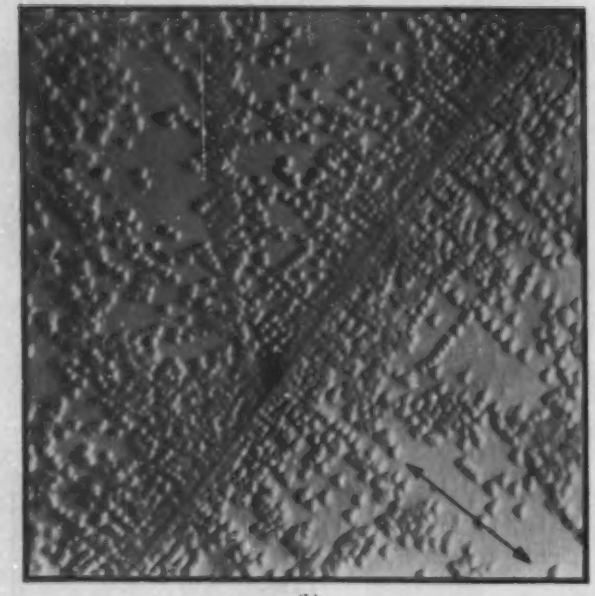

(b)

FIG. 7. Dislocation structures representative of crystals deformed in tension. (a) within the subgrains after 2.5% strain. (b) At a subgrain boundary after 0.5% strain. 1125×. Slip-plane trace parallel to arrow.

microns, the maximum attractive stress is 20 g/mm².[18] Although this is appreciably less than the critical resolved shear stress of these crystals, it is apparently large enough to bring about the process of glide polygonization. A small interaction stress superimposed on a larger applied stress might be expected to have a large effect on dislocations already in motion under the applied stress, since dislocation velocity can be very sensitive to net stress.[11]

[18] A. H. Cottrell, *Dislocations and Plastic Flow in Crystals* (Oxford University Press, New York, 1953), p. 152.

Other Features

Both bending and tension experiments have shown, as expected, a marked increase in dislocation density with strain. The distribution of the dislocations introduced by strain is in some ways different from that observed in LiF and MgO. Figure 7 shows some interesting features representative of the dislocation structure of crystals deformed in tension. Within the subgrains there are some clusters aligned along slip planes, some glide polygonization in the low-density areas, and some irregularly shaped areas of high dislocation density. The subgrain boundaries themselves are nearly always a region of high dislocation density, suggesting that even after considerable strain, the subboundaries are still exerting a hindering influence on the propagation of slip.

CONCLUSIONS

1. Considerable evidence suggests that the etching technique described, a slight modification of that discovered by Lovell and Wernick, is a reliable means of revealing dislocation sites in copper. The etch is applicable only on crystal surfaces within a few degrees of (111), and this is currently its major experimental limitation.

2. The crystals studied had dislocation densities over 10^6 per cm² as grown, but a high-temperature anneal can reduce the density of dislocations within subgrains by an order of magnitude.

3. Double-etch experiments on annealed and slow-cooled crystals show that isolated dislocations and dislocations in simple polygon walls are mobile at low stresses, in contrast to earlier observations on LiF and MgO.

4. The blockage of rosette arms by subboundaries and related observations on deformed crystals suggest that subboundaries may play an important role in the deformation of copper crystals.

5. One of the interesting features of the dislocation structure of deformed crystals is the prevalence of glide polygonization of edge dislocations.

ACKNOWLEDGMENTS

The author is grateful to C. G. Dunn and W. G. Johnston for kind permission to use their previously unpublished photographs. Helpful discussions with W. G. Johnston and other colleagues at the General Electric Research Laboratory are also gratefully acknowledged.

Theory of Dislocation Climb in Metals

JENS LOTHE
Universitetets Fysiske Institutt, Oslo, Norway
(Received February 18, 1960)

An estimate of the climb motion of dislocation jogs is given, which takes into account the fact that dislocations are pipes of easy diffusion. The climb of dislocations under near-equilibrium conditions is then discussed. A new estimate is made of the jog concentration, for which vacancy equilibrium will be established along the entire dislocation. It is argued that the dislocation line tension is an important driving force both in high-temperature creep and in whisker dekinking. Under quench conditions it must be expected that a great number of jogs are nucleated at the nodes of the dislocation network.

INTRODUCTION

THE literature on dislocation climb is quite vague and confusing as regards the theoretical interpretation of experiments. It is usually stated that the creation and annihilation of vacancies takes place at jogs, and that the jog can move with an activation energy E,

$$E \simeq E_{sd},$$

where E_{sd} = energy of self-diffusion in the perfect crystal so that, when the dislocation contains a concentration of jogs near the thermal equilibrium value, it will climb with an activation energy

$$E_{sd}+E_j,$$

where E_j is the energy of one jog.[1]

When the jog concentration is very high, quasi-equilibrium of vacancies will be established along the entire dislocation, and the climb rate is determined by the flow of vacancies to other dislocations or to grain boundaries. The activation energy for climb is then simply E_{sd}. The criterion for this to occur is stated to be that the distance between jogs on the dislocation,

$$l_j = b \cdot \exp(E_j/kT),$$

where b = one lattice distance, is smaller than the distance L to dislocations, climbing in the opposite sense (absorption vs creation of vacancies), or to grain boundaries[2,3]:

$$l_j < L.$$

The purpose of this paper is to give an elementary, but rather careful, analysis of dislocation climb in order to obtain a more precise theory. Many of the ideas to be presented are already latent in the literature, but we do not know that any systematic presentation has previously been given. We shall mainly deal with the theory of climb under near-equilibrium of vacancies, except in the last section, where the annealing-out of quenched-in vacancies is briefly discussed.

CLIMB OF JOGS

We shall consider only dislocations of edge character. For simplicity let b stand for both one lattice distance and the magnitude of the edge component of Burgers vector. If a compressive stress σ acts across the inserted plane (Fig. 1), the dislocation experiences a force

$$F_{el} = \sigma \cdot b \tag{1}$$

per unit length normal to its slip plane. In a crystal with a vacancy concentration c, the dislocation is acted upon by an "osmotic" force

$$F_{osm} = (kT/b^2) \ln(c/c_0) \tag{2}$$

per unit length. c_0 = equilibrium concentration of vacancies.[4] In a crystal containing one-edge dislocation under compressive stress σ, and where the dislocation could be considered to be the only source and sink of vacancies, the concentration of vacancies would be

$$c = c_0 \exp(-\sigma b^3/kT), \tag{3}$$

which follows from $F_{el}+F_{osm}=0$.

Dislocation climb will occur by nucleation and motion of jogs. We shall first study the latter of these processes.

In fcc metals, dislocations are dissociated,[5] and in the low-stacking fault energy metals, the dislocations are wide, of the order $\sim 10\,b$. The geometry and energy of a jog in an extended dislocation is disputed. Seeger[2] maintains that the partials are brought together at the jog and that the jog energy is high, of the order several electron volts in noble metals, while Friedel[3] suggests that it may be energetically favorable for a jog in a near-edge dislocation to dissociate in the way described

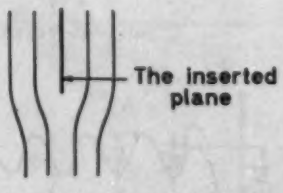

FIG. 1. An edge dislocation schematically.

[1] N. F. Mott, Proc. Phys. Soc. (London) **B64**, 729 (1951).
[2] A. Seeger, *Dislocations and Mechanical Properties of Crystals* edited by J. C. Fisher (John Wiley & Sons, Inc., New York, 1956), p. 243.
[3] J. Friedel, *Les Dislocations* (Gauthier-Villars, Paris, 1956).
[4] J. Bardeen and C. Herring, *Imperfections in Nearly Perfect Crystals*, edited by W. Shockley (John Wiley & Sons, Inc., New York, 1952), p. 261.
[5] R. D. Heidenreich and W. Shockley, *Strength of Solids* (The Physical Society, London, England, 1948), p. 57.

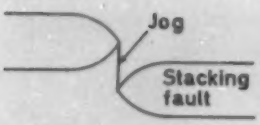

FIG. 2. Jog in an extended dislocation.

by Thompson,[6] and that the jog energy is much lower than suggested by Seeger.

We shall, all through this discussion, assume that the jogs are constricted, so that they will be effective sources and sinks of vacancies (Fig. 2).

The creation of a vacancy at a jog and its motion into the perfect lattice will involve a series of energy jumps, as is schematically pictured on the linear model in Fig. 3.

Here E_f = energy of formation of a vacancy in the perfect lattice, E_m = energy of migration of a vacancy in the perfect lattice, E' = energy barrier to annihilation of a vacancy next to the jog, and E'' = energy barrier to formation of a vacancy next to the jog.

Visualize an assembly of jogs. A fraction

$$\exp\{-(E''-E')/kT\}$$

of these will have vacancies next to them. Imagine temporarily that jumps from 2 to 3, Fig. 3, do not occur. If the relative distribution between jogs in the states 1 and 2 is slightly displaced from equilibrium, it can be shown that the relaxation time to reach equilibrium τ is given by

$$1/\tau=\gamma_0\exp(-E''/kT)+\gamma_0\exp(-E'/kT)\simeq\gamma_0\exp(-E'/kT). \quad (4)$$

γ_0 is a vibrational frequency which is put equal for all processes.

If

$$E'<E_m, \quad (5)$$

the relaxation time τ is shorter than the time for a jump from 2 to 3 to take place, i.e., the vacancy concentration on the sites near to the jog will be nearly in equilibrium *with the jog*, and not with the external surface, say.

We shall throughout this discussion assume that Eq. (5) is satisfied. This is a very reasonable assumption, as the crystal structure is "looser" in the immediate vicinity of the jog than in the perfect crystal.

Consider a jog at the center of a spherical crystal of radius R, with the boundary condition that the vacancy concentration $c=c_0$ on the surface of the sphere, and with the concentration

$$c'=c_0\exp(-\sigma b^3/kT) \quad (6)$$

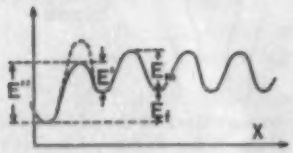

FIG. 3. One-dimensional model of the energy barriers to vacancy creation at a jog.

on a sphere of radius $r\sim b$ around the jog. In the volume between the spheres, the equation

$$D_v\nabla^2 c=0, \quad (7)$$

where

$$D_v\simeq\gamma b^2\exp(-E_m/kT) \quad (8)$$

is fulfilled. The solution satisfying the boundary conditions is only *weakly dependent on* R for reasonable values, so to a good approximation we may put $R=\infty$ and obtain

$$c=(c'-c_0)(b/r)+c_0, \quad (9)$$

so that, by

$$f=\int_{\text{closed surface}} D_v\cdot\nabla c\cdot d\mathbf{s}, \quad (10)$$

the flux f of vacancies to the jog is

$$f=4\pi b\cdot D_v(c'-c_0). \quad (11)$$

When $\sigma b^3/kT\ll 1$, the velocity of the jog then is, by Eq. (6),

$$v=4\pi b^2 D_v c_0\cdot(\sigma b^3/kT)=4\pi\gamma b\exp\{-(E_f+E_m)/kT\}(\sigma b^3/kT) \quad (12)$$

as

$$c_0=b^{-3}\exp(-E_f/kT). \quad (13)$$

By the Einstein relation, the diffusion coefficient D_j for the jog is found from Eq. (12) to be

$$D_j=4\pi\gamma b^2\exp\{-(E_f+E_m)/kT\}=4\pi\gamma b^2\exp\{-E_{sd}/kT\}. \quad (14)$$

Equation (12) agrees with the Mott formula.

It has been assumed that the jog motion is so slow that we may consider the jog as fixed at one point in the diffusion problem. Comments on this and other approximations tacitly made during the discussion, will be found in the Appendices I and II.

Quite certainly, the foregoing calculation underestimates the motion of a jog as a dislocation line constitutes a tube of easy diffusion.[7]

Let us consider the dislocation line as a tube of radius $\sim b$, where the equilibrium concentration of vacancies, when no stress is present, is

$$c_{\text{disl}}=c_0\exp(\Delta E_f/kT) \quad (15)$$

and the diffusion coefficient of vacancies is

$$D_{v,\text{disl}}=D_v\exp(\Delta E_m/kT). \quad (16)$$

In order of magnitude we would expect[8]

$$\Delta E_f\simeq\Delta E_m\simeq\tfrac{1}{2}E_f\simeq\tfrac{1}{2}E_m. \quad (17)$$

Some comments on dislocation pipe diffusion are found in Appendix III.

[6] N. Thompson, *Report on a Conference on Defects in Crystalline Solids* (The Physical Society, London, England, 1955), p. 153.

[7] D. Turnbull, *Report on a Conference on Defects in Crystalline Solids* (The Physical Society, London, England, 1955), p. 203.

We will assume that the creation of a vacancy at a jog and its motion along the dislocation line takes place by a sequence of energy jumps of the same general shape as the fully drawn line, Fig. 3. The vacancy concentration along the dislocation line will then be in near-equilibrium with the jog over some length $\sim l$ along the dislocation, and the rate of absorption of vacancies at the jog will be of the order

$$f \simeq \pi b^2 D_{v,\mathrm{dis}} (c_{\mathrm{dis}}/l) \cdot (\sigma b^3/kT). \quad (18)$$

The current, Eq. (18), must be balanced with the supply of vacancies from the surrounding medium. Equation (7) must then be solved with the boundary condition that $c = c_0 \exp(-\sigma b^3/kT)$ on the surface of a cylinder of radius $\sim b$ and length $\sim l$, and $c = c_0$ at infinity. Approximating the cylinder to an ellipsoid, we find, by simple analogy with the theory of electrical potentials, that

$$f \simeq [4\pi D_v l c_0/2 \ln(l/b)](\sigma b^3/kT). \quad (19)$$

Which value we put for l in the logarithmic term does not matter much; let us put $l \simeq 10^2 b$. Then it follows from the balance of Eqs. (18) and (19) that

$$l \simeq b \exp\{(\Delta E_f + \Delta E_m)/2kT\} \simeq b \exp(\Delta E_{sd}/2kT), \quad (20)$$

so that the jog velocity becomes

$$v \simeq \pi \gamma b \exp\{-(E_{sd} - \tfrac{1}{2}\Delta E_{sd})/kT\} \times (\sigma b^3/kT), \quad (21)$$

corresponding to a jog diffusion coefficient

$$D_j \simeq \pi \gamma b^2 \exp\{-(E_{sd} - \tfrac{1}{2}\Delta E_{sd})/kT\}. \quad (22)$$

The lowering in activation energy from Eqs. (12) and (14) to Eqs. (21) and (22) may be quite significant, as is seen from Eq. (17), while the preexponentials can be considered to be roughly the same.

If the creation of vacancies at jogs requires energy jumps such as the dotted line, Fig. 3, our methods break down. Such a situation might arise from the adsorption of impurities at jogs. Also, impurities might reduce the efficiency of the dislocation as a channel of easy diffusion.

NUCLEATION OF JOGS, DISLOCATION CLIMB

Consider a straight dislocation with no stress acting on it. At a temperature T, the dislocation will, in equilibrium, have acquired a concentration of jogs

$$c_j = b^{-1} \cdot \exp(-E_j/kT), \quad (23)$$

where E_j = jog energy[8] (Fig. 4).

The formation of a double jog, such as CD, Fig. 4, will take place by condensation of vacancies, while to form a double jog such as AB, atoms must be transported to the dislocation, and the nucleus of such a double jog

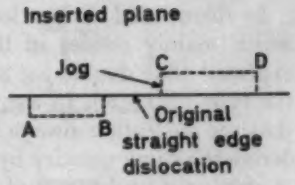

FIG. 4. Creation of jogs in an edge dislocation by addition (AB) or removal (CD) of atoms.

must be, say, one or two "interstitial" atoms on the dislocation. On the dislocation line there will be detailed balance between "interstitials" and vacancies, and any greater difficulty in nucleating a double jog of the AB type compared with the CD type, will be balanced with greater stability against "evaporization," so that the *net* nucleation rate of the two types of double jogs becomes the same.

It can be taken for granted, then, that an edge dislocation, with no stress acting on it, will contain the equilibrium number of jogs and show no tendency to climb when in contact with the equilibrium concentration of vacancies.

When the external stress is *very* small, the jog concentration will not be much different from the equilibrium value. The climb velocity is then simply found from the product of Eqs. (21) and (22):

$$V = \pi \gamma b \exp\{-(E_{sd} + E_j - \tfrac{1}{2}\Delta E_{sd})/kT\} \times (\sigma b^3/kT). \quad (24)$$

For *higher* stresses on the dislocation, in the range

$$\sigma b^3/kT c_j \gg 1 \quad \text{and} \quad \sigma b^3/kT \ll 1,$$

the dislocation velocity will depend on the dislocation arrangement and to some extent on the general shape of the energy curve for double-jog nucleation. Two types may be envisaged, as illustrated in the smoothed-out curves in Fig. 5.

It cannot be excluded that in the nucleation of double jogs of the type AB, Fig. 4, a situation such as depicted in Fig. 5(A) may arise in high-stacking fault energy metals, with small jog energies and a high energy for an interstitial along the dislocation. The nucleation of double jogs of the type CD, Fig. 4, will probably always be in accordance with Fig. 5(B). Thus, the climb mobility of a dislocation may be asymmetrical with respect to its direction of climb.

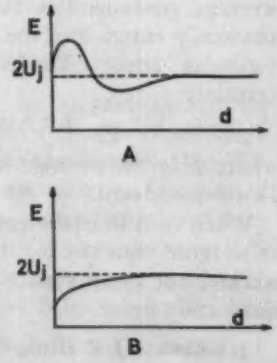

FIG. 5. Double-jog energy E as function of double-jog length d in two typical cases A and B. Only in case B would the energy of double-jog activation be $2U_f$.

[8] Strictly, jogs in fcc metals will have slightly different energies according to whether they form acute or obtuse angles with the dislocation, and the *mean* jog energy should be used in Eq. (23). See A. Seeger, *Report on a Conference on Defects in Crystalline Solids* (The Physical Society, London, England, 1955), p. 391.

In dissociated dislocations with a high jog energy which mainly resides in the constriction, it must be expected that double-jog nucleation always will be of the type Fig. 5(B). In the subsequent we shall assume that the nucleation always is of this type. We may then derive the climb velocity by precisely the same methods as employed by Lothe and Hirth[9] in their treatment of creep over the Peierls barrier, and only a brief outline of the results will be given here.

If the length L of the climbing dislocation segment is longer than the distance l_j between thermal jogs,

$$L>b\exp(E_j/kT),$$

jogs will be removed by double jog-double jog collisions, and the climb velocity is again given by Eq. (24).

If $\quad L<b\exp(E_j/kT), \quad$ and $\quad \sigma b^2 L>kT,$

two different cases (a) and (b) must be considered:

(a): Jogs are not nucleated at the ends of the segment. The activation energy for climb is then

$$E=E_{sd}+2E_j-\tfrac{1}{2}\Delta E_{sd}. \tag{25}$$

(b): The jog concentration is maintained near the thermal equilibrium value at the ends of the segment. The climb velocity V is then again given by Eq. (24). This case may be realized for a climbing straight segment between constricted triple points in near thermal equilibrium, so that line tension complications need not be considered.

The case $\sigma b^2/kT>1$ is rarely encountered, except in strong pileups. However, at isolated points on a dislocation, extremely strong forces may exist because of line-tension misbalance, and large supersaturations of jogs may be nucleated at such points. We think that this possibility has received far too little attention and must be considered to explain several cases of creep and annealing behavior.

So far it has been assumed that the jog concentration is so low that different jogs emit or absorb vacancies independently. However, when the jog concentration is sufficiently high, the climbing dislocation segment will effectively be a source and sink of vacancies along its entire length, and the energy of climb will simply be that of selfdiffusion.

If each of the *independently* climbing segments on an average contains less than one jog, the jog energy obviously enters into the climb rate, and the foregoing formulas apply. Thus, for "saturation" to begin, certainly

$$L>b\exp(E_j/kT), \tag{26}$$

where L is the average length of an independent dislocation segment.

When each independent segment on an average contains more than one jog, the saturation problem can be worked out approximately from the study of infinite dislocation lines:

[9] J. Lothe and J. P. Hirth, Phys. Rev. 115, 543 (1959).

If $l_j<l$, where l is given by Eq. (20), i.e.,

$$E_j<\tfrac{1}{2}\Delta E_{sd}, \tag{27}$$

then saturation would occur for all temperatures.

The inequality (27) is certainly never fulfilled in low-stacking fault energy metals. In metals of high-stacking fault energy, such as aluminium, it may be close to being fulfilled.

When condition (27) is not fulfilled, consider an infinite climbing dislocation along the axis of a square column of side length L' (Fig. 6).

With the boundary condition that $c=c_0$ on the surface of the bar, this model corresponds to a network of dislocations of both signs. It will be realized that this boundary condition and Laplace's Equation (7) are satisfied if we make the column part of an infinite lattice with unit cells $l_jL'^2$, the center of each cell being the origin of a contribution $c\sim\pm 1/r$ to the vacancy concentration, the $\pm$sign changing from one column to the nearest neighboring one.

Comparing Eq. (21) with Eqs. (12) and (9), it is seen, that for r not too small, and when no overlap occurs,

$$c-c_0\sim[c_0b\exp(\tfrac{1}{2}\Delta E_{sd}/kT)/r]\times(\sigma b^3/kT) =\beta(b/r)c_0\times(\sigma b^3/kT). \tag{28}$$

The β is introduced for abbreviation. When the interaction between the different sources and sinks is taken into account, the strength of all sources must be reduced with a factor α. The contribution to $c-c_0$ at one source from all other sources is approximately

$$(2\alpha\beta c_0/l_j)\cdot\ln(L'/l_j)\times(\sigma b^3/kT), \tag{29}$$

so the condition on α must be

$$\alpha\{1+(2\beta/l_j)\ln(L'/l_j)\}=1. \tag{30}$$

Thus, the division line between saturation and non-saturation is given by

$$l_{j,crit}\sim 2\beta\ln(L'/l_j) \tag{31}$$

or, putting $l_j\sim 10b$ on the right-hand side,

$$l_{j,crit}\sim 2b\ln(L'/10b)\cdot\exp(\Delta E_{sd}/2kT), \tag{32}$$

which is quite different from the commonly used criterion referred to in the Introduction. It is noted that the dependence on L' is only weak. Except for metals with very small jog energies, the exponential in Eq. (32) must be expected to be of the order unity before saturation is reached by thermally activated jogs, so in that case, with $L'\sim 10^4 b$,

$$l_{j,crit}\sim 10b$$

and

$$T_{crit}\sim E_j/k\ln 10.$$

In the noble metals T_{crit} is quite certainly well beyond the melting point.

It is important to note that because of the exponential in Eq. (32) only a small concentration of jogs supplied

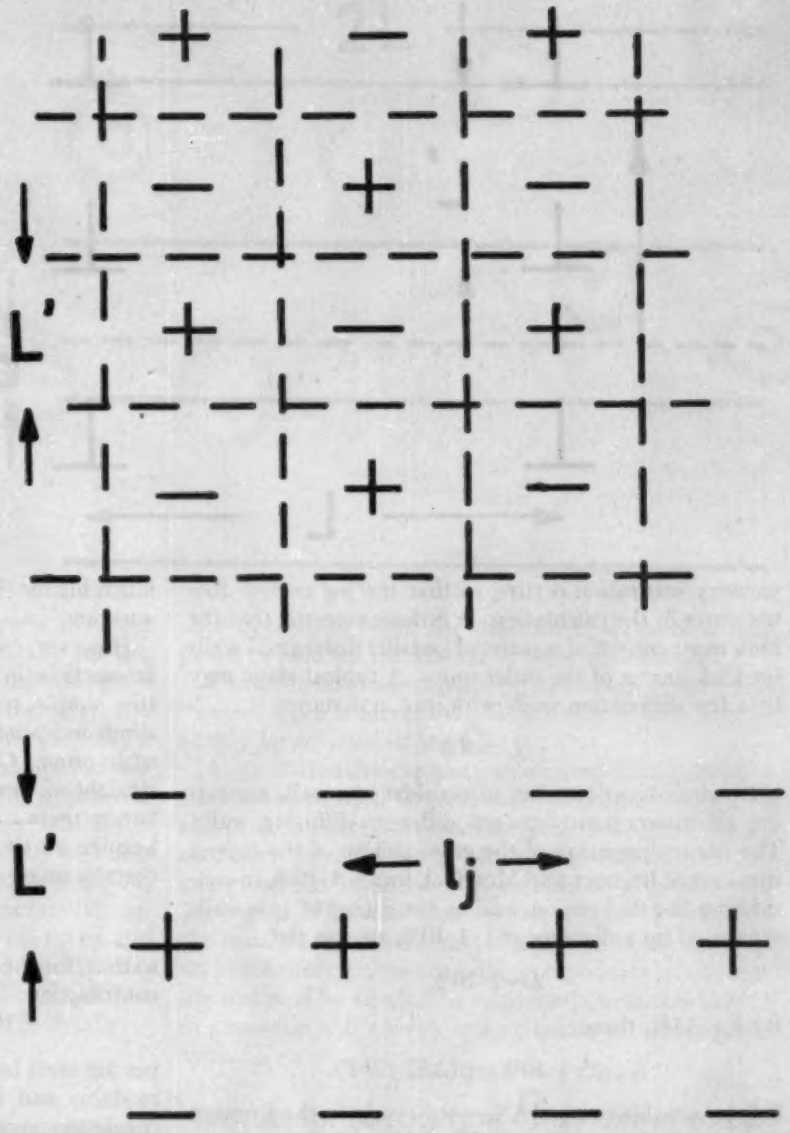

FIG. 6. Two sections of a crystal containing parallel dislocations with a separation L'. Jogs or dislocations emitting vacancies are denoted by +, those absorbing vacancies by −.

by dislocation intersections will bring about saturation at lower temperatures.

The critical jog separation $l_{j,\text{crit}}$ depends on the geometry of the dislocation arrangement. For the climb of dislocation walls $l_{j,\text{crit}}$ has a value quite different from Eq. (32). Consider two dislocation walls, with a separation L' between dislocations in the walls and a separation L between the walls. The two walls are made to climb in opposite directions (Fig. 7).

In this case we derive

$$l_{j,\text{crit}} \simeq 2\pi b(L/L') \exp(\Delta E_{sd}/2kT). \qquad (33)$$

DISCUSSION OF EXPERIMENTS. IMPORTANCE OF LINE TENSION

As the foregoing theory on several points deviates quite strongly from current theories, in terms of which experimental results have been interpreted so far, a rediscussion of relevant experimental results is called for. We shall not take up that task in this paper, but rather briefly discuss some experimental results which we believe *cannot* be adequately explained by the foregoing theory alone, and which bring in the question of the importance of the dislocation line energy.

A. Whisker Dekinking

Nabarro[10] has worked out an elegant theory for whisker dekinking, which agrees well with experiments by Brenner and Morelock.[11] Nabarro shows that dislocation climb is the most reasonable explanation of whisker dekinking. In order to obtain dekinking rates in agreement with experiment, he must assume that

[10] F. R. N. Nabarro, *Dislocations and Mechanical Properties of Crystals*, edited by J. C. Fisher (John Wiley & Sons, Inc., New York, 1956), p. 521.

[11] S. S. Brenner and C. R. Morelock, Acta Met. 4, 89 (1956).

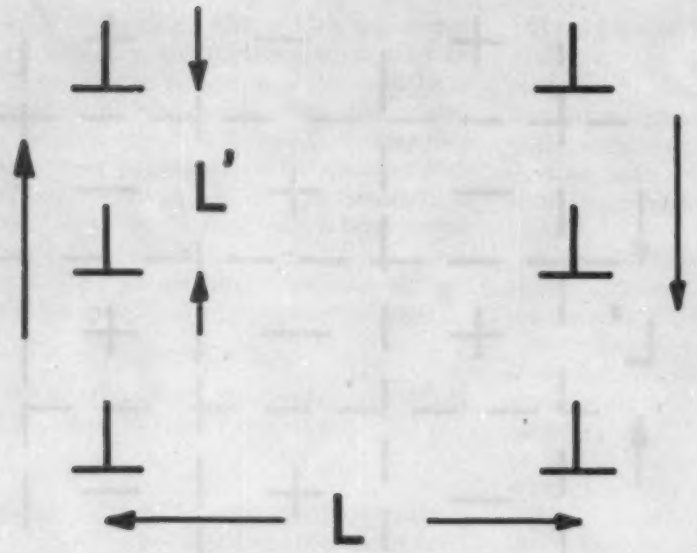

FIG. 7. Two parallel dislocation walls climbing in opposite directions.

vacancy saturation occurs, so that the jog energy does not enter in the calculation. It is demonstrated that the kink must consist of a series of parallel dislocation walls for kink angles of the order unity. A typical stage may be a few dislocation walls with, say, a distance

$$L' \simeq 30b$$

between dislocations. Let us consider one wall, neglecting all interactions between different diffusing walls. The linear dimension of the cross section of the copper whiskers of Brenner and Morelock was $\sim 4 \cdot 10^4 b$, so considering the dislocation wall as consisting of two walls separated by a distance $\sim \frac{1}{2} \cdot 4 \cdot 10^4 b$, we can put

$$L \sim 2 \cdot 10^4 b.$$

By Eq. (33), then,

$$l_{j,\mathrm{crit}} \simeq 4 \cdot 10^3 b \exp(\Delta E_{\mathrm{sd}}/2kT).$$

It is reasonable to put $\frac{1}{2}\Delta E_{\mathrm{sd}} \sim 0.4$ ev. As in the Brenner and Morelock experiments $kT = 0.11$ ev, it follows[12]

$$l_{j,\mathrm{crit}} \simeq 10^5 b. \tag{34}$$

Thus, there must be about one jog on every fifth dislocation in the kink. The jog energy corresponding to Eq. (34) for

$$kT \simeq 0.11 \text{ ev}$$

is

$$U_f \simeq 1.3 \text{ ev}. \tag{35}$$

According to Seeger,[3] the jog energy should be in the range (2–4) ev in copper. The lowest value suggested is of the order ~ 1 ev.[8] A concentration of thermal jogs much higher than that given by Eq. (34) is then out of question.

However, consideration of the dislocation-dislocation interactions in the dislocation walls severely complicates this simple picture. In fact, the dislocations cannot climb *independently*, but must move in sympathy with each other. Consider a dislocation wall of perfectly straight dislocations of length $2L$, with a distance L' between them. Move one dislocation up a distance b, keeping all the others in position (Fig. 8). The energy thereby increases with

$$\delta E \sim 2\mu L b^4/\pi(1-\gamma)L'^2, \tag{36}$$

so that, for the jog concentrations in question, an energy contribution

$$\sim \mu L b^4/\pi(1-\gamma)L'^2$$

per jog must be added to the jog energy, where μ = shear modulus and γ = poissons ratio. For copper, with the previously given values for L and L', this amounts to

$$\sim 10\mu b^3 \sim 50 \text{ ev}$$

which is prohibitively large. Increasing L' to $\sim 100b$, which is about the highest possible value during the beginning of dekinking, we obtain ~ 5 ev, per jog, which also would reduce the dekinking rate most severely.

If the dislocations in a dislocation wall were not completely evenly spaced to start with, we should expect the first thing to happen on heating was climb towards even spacing, after which climb would be very difficult. However, the dislocations cannot be completely evenly spaced except for certain kink angles, and the possible consequences of this fact should be investigated.

If the jogs arranged themselves in such a way that dislocation interactions were relieved, most of the entropy would be lost.

On the whole it appears that additional factors should be sought to explain the observed dekinking rate. We

[12] Nabarro[10] states that every second site along the dislocations must be jogged for saturation to occur. If he correctly had omitted the factor $4b/w$ in the application of the Mott formula, he would deduce that every $\simeq 10^4$-th site must be jogged. It must be understood that in the approximation in which we work, the interaction with stress is only considered during the vacancy creation or annihilation processes.

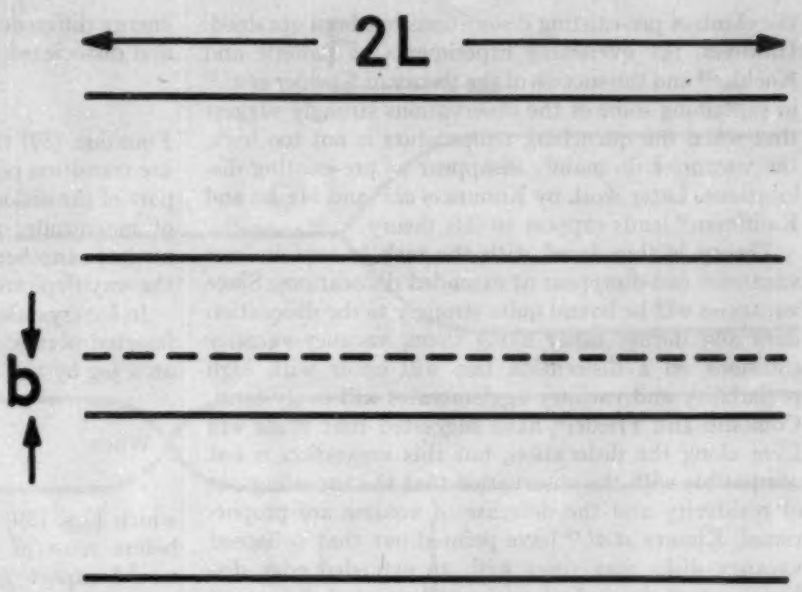

FIG. 8. Wall of evenly spaced dislocations, where one dislocation is then moved up one lattice distance.

think, as has been suggested by Shockley[13]; that the striving of the dislocations to enter normally on the surface, is the wanted factor. When the angle between the dislocation and the surface is ~45° or greater, the reduction in line energy on forming a jog may be greater than the jog energy. Thus, considerable rapid climb towards the surface of the dislocations in the upper and lower regions of the whisker would be expected. If the jog energy is as high as suggested by Seeger, it is still difficult to see how the dislocations in the middle region, where the dislocations enter the surface normally, can follow on. The importance of the stresses set up by the first rapid climb and the repulsion between the dislocations left behind in the central regions of the different dislocation walls, should be considered in detail.

B. Creep

In metals of both high- and low-energy stacking fault, creep of an activation energy near that of self-diffusion is observed, and which is thought to be due to dislocation climb.[2]

As the observed activation energy is about that of self-diffusion, enough jogs to produce saturation of vacancies along the climbing dislocations must be present. In the noble metals the concentration of thermal jogs would be far too low. Seeger suggests that enough jogs are created by dislocation-dislocation intersections during plastic flow. This idea needs to be made more precise.

As a dislocation segment can only climb a distance b when it aquires a jog, the jogs cannot be supplied while it is doing the *rate-controlling* climb past some obstacle, as that would require that it is frequently intersected by other dislocations, a somewhat unreasonable hypothesis when the dislocation segment is supposed to hold up the motion of other dislocations.

Thus, the dislocation must be sufficiently jogged and "wavy" when it meets the obstacle that it may pass by simply by removal of jogs.

As an alternative explanation we would like to suggest that the nucleation of great supersaturations of jogs at sharp, constricted, dislocation bends may provide the necessary jogs. At sharp bends, the reduction in line energy on the formation of a jog may be so great that a jog begins to form as soon as, say, a vacancy jumps on the bend. In fcc metals cross-slip past barriers cannot go on indefinitely unless the edge components left behind are removed by climb. The edge components left behind in cross-slip will always end at bends of the required type.

QUENCHING. DISLOCATION CLIMB UNDER GREAT SUPERSATURATIONS OF VACANCIES

In treating the annealing-out of quenched-in vacancies, the foregoing quasi-equilibrium theory cannot be used. Great supersaturations of vacancies give rise to extremely strong climb forces on dislocations, and great supersaturations of jogs may be nucleated.

Recently, a wealth of new information on the mechanisms of annealing-out of vacancies has been obtained by electron microscopy.[14] In the annealing-out of high supersaturations of vacancies in the pure metals of Al, Cu, Ag, and Au, the predominant mode of vacancy disappearance appears to be the formation of prismatic disks by the collapse of sheets of vacancies, as predicted by Kuhlmann-Wilsdorf,[15] while little direct evidence for

[13] Discussion to F. R. N. Nabarro, p. 243 of reference cited in footnote 10.

[14] P. B. Hirsch and J. Silcox, *Growth and Perfection of Crystals*, edited by R. H. Doremus, B. W. Roberts, and D. Turnbull (John Wiley & Sons, Inc., New York, 1958), p. 262.

[15] D. Kuhlmann-Wilsdorf, Phil. Mag. 3, 125 (1958).

the climb of pre-existing dislocations has been obtained. However, the quenching experiments of Bauerle and Koehler[16] and the success of the theory of Koehler *et al.*[17] in explaining some of the observations strongly suggest that when the quenching temperature is not too high, the vacancies do mainly disappear at pre-existing dislocations. Later work by Kimura *et al.*[18] and Meshii and Kauffman[19] lends support to this theory.

Theory is thus faced with the task to explain how vacancies can disappear at extended dislocations. Since vacancies will be bound quite strongly to the dislocation lines and diffuse easily along them, vacancy-vacancy collisions on a dislocation line will occur with high probability and vacancy agglomerates will easily form. Coulomb and Friedel[20] have suggested that voids will form along the dislocation, but this suggestion is not compatible with the observation that the annealing-out of resistivity and the decrease of volume are proportional. Kimura *et al.*[18] have pointed out that collapsed vacancy disks may react with an extended edge dislocation to make it climb without increase of the area of stacking fault. Other possible vacancy-agglomerate-dislocation reactions giving the same result have been described by Thomson.[21]

It appears that the possibility that vacancies may nucleate new jogs at constrictions in extended dislocations and disappear, *one by one*, has not yet been discussed in any detail in the literature. Thomson[21] has shown that a jog may multiply by passing a nodal point and split up into one jog on each of the branching dislocations. The energy considerations to follow should cover also this case. Complications due to line-tension misbalance at nodal points are neglected, so our simple considerationas apply only before the dislocation network has been severely distorted by climb.

When a crystal is quenched from a temperature T_1 to a temperature T_2, the free energy per vacancy is, by Eq. (2),

$$H_f=[(T_1-T_2)/T_1]E_f. \tag{37}$$

With, typically,

$$E_f\simeq\tfrac{1}{3}\mu b^3$$

and

$$T_2\simeq\tfrac{1}{2}T_1,$$

Eq. (37) becomes

$$H_f\simeq\tfrac{1}{10}\mu b^3. \tag{38}$$

With typical values inserted in the formula for the energy reduction on dissociation,[3] it is found that the energy difference per unit length between a constricted and dissociated edge dislocation in fcc crystals is

$$F\simeq(1/15)\mu b^2. \tag{39}$$

Equation (39) then gives the "force" required to move the transition point between a constricted and extended part of the dislocation (Fig. 9), and it will also, in order of magnitude, give the maximum force required to nucleate another constriction from a pre-existing one in the way depicted in Fig. 10.

In fcc crystals, the edge dislocation is made up of two inserted planes, so, from Eq. (38), the "force" exerted on a jog by the vacancies is

$$F_v\simeq\tfrac{1}{3}\mu b^2. \tag{40}$$

When

$$F_v>F, \tag{41}$$

which Eqs. (39) and (40) show is likely to be the case before most of the vacancies have annealed-out, we would expect great supersaturations of jogs to be created from constricted dislocation nodes. Probably a vacancy pair is needed for the initial step in the nucleation to supply the necessary energy for the increase in dislocation length on the production of a jog. Depending on the nature of the node, the increase in dislocation length will usually be between $\sim b$ and $3b$. As the additional length of dislocation has no long-range strain field, we need only calculate with the core energy, which is of the order

$$\sim\tfrac{1}{10}\mu b^2 \tag{42}$$

per unit length.[3] Thus, at least an energy

$$\sim\tfrac{1}{10}ub^3 \tag{43}$$

must be supplied in the initial nucleation, and, from Eq. (38), we see that a couple of vacancies should have enough energy to give up. Once the initial nucleation has taken place, the jog can develop fully by absorbing vacancies one by one.

The energy of a vacancy on the dislocation is lower than that of a vacancy in the perfect lattice, but we think that this cannot alter previous conclusions. Vacancies will diffuse to the dislocation line and build up a concentration of vacancies along the dislocation line, which is so great that the free energy per vacancy is about the same as the energy of formation along the dislocation, which is also approximately given by Eq. (38).

SUMMARY AND CONCLUSION

It has been assumed that a near-equilibrium concentration of vacancies is always maintained near jogs. On this assumption, the climb of typical dislocation configurations has been estimated. The fact that dislocations are pipes of easy diffusion has been taken into account. The value derived for the critical concentration of jogs to produce saturation of vacancies along the dislocations is not in agreement with previous theories.

[16] J. E. Bauerle and J. S. Koehler, Phys. Rev. **107**, 1493 (1957).
[17] J. S. Koehler, F. Seitz, and J. E. Bauerle, Phys. Rev. **107**, 1499 (1957).
[18] H. Kimura, R. Maddin, and D. Kuhlmann-Wilsdorf, Acta Met. **7**, 145, 154 (1959).
[19] M. Meshii and J. W. Kauffman, Acta Met. **7**, 180 (1959).
[20] P. Coulomb and J. Friedel, *Dislocations and Mechanical Properties of Crystals*, edited by J. C. Fisher (John Wiley & Sons, Inc., New York, 1956), p. 555.
[21] R. Thomson, "Theory of Dislocation Climb," I and II, ASTIA AFOSR, TN 59-59, AD 209 430.

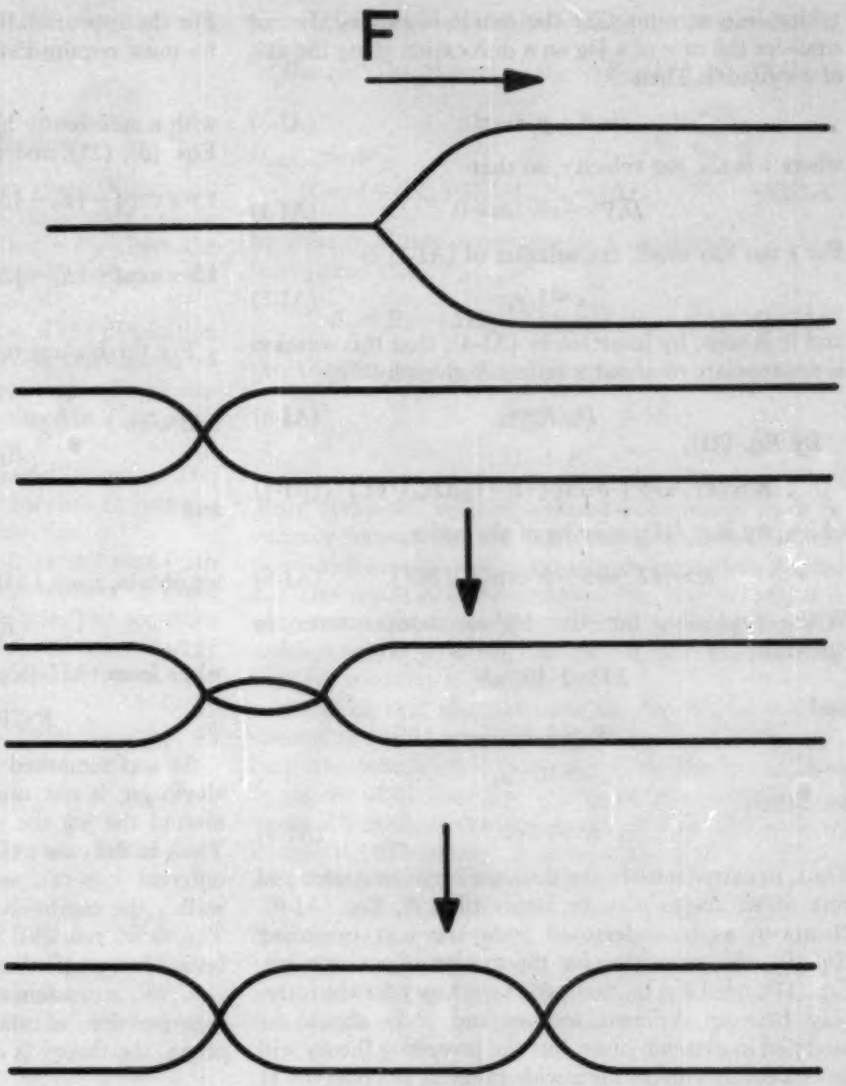

FIG. 9. A "force" F is needed to make a constricted part of a dislocation grow at the expense of an extended part.

FIG. 10. Sequence showing the nucleation of a new constriction from a pre-existing one.

It is estimated that in a random network containing only thermal jogs, about every 10th lattice site must be jogged for saturation to occur. For the climb of dislocation walls, a much lower concentration of jogs will lead to saturation.

At lower temperatures very low concentrations of jogs will suffice to maintain vacancy equilibrium along the dislocations because of the rapid diffusion along dislocations. It is stressed that in this region climb will be greatly facilitated by jogs created to reduce line-tension misbalances. The dislocation line tension is probably an important driving force both in high-temperature creep and whisker dekinking.

In the last section it is shown that during quenching new jogs may easily be created at constricted nodal points of the dislocation network.

The mathematical treatment involves several approximations, and we are aware that for certain dislocation configurations and in certain regions of temperature and stress, the somewhat rough and expedient methods employed in this paper may break down. For the sake of brevity we have not presented any detailed discussion of the range of validity of the theory. In Appendices I and II, a few simple considerations regarding the mathematical approximations are given, and it should be clear that the theory must be expected to cover a wide range of common experimental situations.

APPENDIX I

Approximation of Immobile Sources and Sinks of Vacancies

It has been assumed throughout that the motion of jogs could be found from an appropriate solution of

$$\nabla^2 c = 0. \tag{AI-1}$$

Strictly, we should have solved the equation

$$D_v \nabla^2 c = \partial c / \partial t, \tag{AI-2}$$

taking into account that the source is moving. Let us consider the case of a jog on a dislocation along the axis of a cylinder. Then

$$c=c(x, y, z-vt), \tag{AI-3}$$

where v is the jog velocity, so that

$$D_v\nabla^2 c+v\partial c/\partial z=0. \tag{AI-4}$$

For r not too small, the solution of (AI-1) is

$$c\sim 1/r, \tag{AI-5}$$

and it is seen, by insertion in (AI-4), that this solution is appropriate to about a radius R given by

$$D_v/R\simeq v. \tag{AI-6}$$

By Eq. (21),

$$R\simeq(kT/\pi\sigma b^3)\cdot b\cdot\exp\{(E_f-\tfrac{1}{2}\Delta E_{sd})/kT\} \tag{AI-7}$$

which, by Eq. (17), may be of the order

$$R\simeq(kT/\pi\sigma b^3)\cdot b\cdot\exp(E_f/2kT). \tag{AI-8}$$

With, typically, for the highest temperatures in question,

$$kT\simeq 2\cdot 10^{-2}\mu b^3$$

and

$$E_f\simeq\tfrac{1}{5}\mu b^3$$
$$\sigma\simeq 10^{-4}\mu,$$

we obtain

$$R\simeq 10^3 b. \tag{AI-9}$$

Thus, in extreme cases the distance between source and sink of vacancies may be larger than R, Eq. (AI-9). However, as is understood from the text preceding Eq. (9), the expression for the motion of a single jog, Eq. (17), need not be modified. The theory for the interplay between different sources and sinks should be modified in extreme cases, but the preceding theory will be essentially correct for a wide range of parameters. It is sufficient for our theory to hold that the "rigid" solution (AI-5) extends well into the smoothed-out region of overlap between solutions centered on different jogs.

APPENDIX II

Transients in the Diffusion

It has been assumed in the foregoing paragraphs that dislocation climb could be described as a *stationary* diffusion process. The transients occurring upon the production or annihilation of jogs have been neglected.

When a jog is created, the time needed for a region within a radius R to attain the stationary vacancy concentration in "equilibrium" with the jog is

$$t_1=R^2/D_v. \tag{AII-1}$$

The lifetime of a jog is

$$t_2=l_j/v, \quad \text{when} \quad l_j<L \tag{AII-2a}$$

$$t_2=L/v, \quad \text{when} \quad l_j>L. \tag{AII-2b}$$

For the approximation of stationary diffusion to apply, we must require that

$$t_2>t_1, \tag{AII-3}$$

with a sufficiently high value for R in Eq. (AII-1). By Eqs. (8), (21), and (23), Eq. (AII-3) becomes

$$1>\pi\exp\{-(E_f-\tfrac{1}{2}\Delta E_{sd})/kT\}\times(R/b)\cdot(R/L)\cdot(\sigma b^3/kT) \quad \text{when} \quad L<l_j, \tag{AII-4a}$$

$$1>\pi\exp\{-(E_f-\tfrac{1}{2}\Delta E_{sd})/kT\}\times(R/b)\cdot(R/l_j)\cdot(\sigma b^3/kT) \quad \text{when} \quad L>l_j. \tag{AII-4b}$$

For the highest temperatures in question,

$$kT\simeq 2\cdot 10^{-2}\mu b^3,$$

and with

$$E_f-\tfrac{1}{2}\Delta E_{sd}\simeq\tfrac{1}{10}\mu b^3,$$
$$\sigma\simeq 10^{-4}\mu,$$

and

$$L\simeq 10^4 b,$$

we obtain, from (AII-4a),

$$R<10^4 b, \quad L<l_j, \tag{AII-5a}$$

while from (AII-4b), we obtain

$$R<10^2(l_j/b)^{\frac{1}{2}}\cdot b, \quad L>l_j. \tag{AII-5b}$$

As was remarked in Appendix I, the motion of the single jog is not much dependent on to what radius around the jog the stationary solution is appropriate. Thus, in the case (AII-5a), where the interplay between different jogs can be neglected (except for dislocation walls), the conditions for our theory are well fulfilled. The same remarks then apply to the case (AII-5b) before "saturation" occurs.

As the saturation effects have been estimated by the superposition of stationary solutions with different origin, the theory is only valid in this region if

$$R>l_j. \tag{AII-6}$$

At distances from the dislocations much greater than l_j, the vacancy concentration is smoothed out and is insensitive to the transient accompanying jog creation and annihilation.

Consider the two cases Eqs. (32) and (33).

In the first case we have $l_{j,\text{crit}}\sim 10b$, so that, from Eq. (AII-5b), $R<300b$, and condition (AII-6) is well fulfilled.

In the second case, put $L'\simeq 100b$ and otherwise use the parameters employed in the first case. The condition corresponding to (AII-6) is

$$R>(L'l_j)^{\frac{1}{2}}. \tag{AII-7}$$

From Eq. (33), with $\frac{1}{2}\Delta E_{sd}\simeq\frac{1}{10}\mu b^3$,

$$l_{j,\text{crit}}\simeq 10^5 b,$$

so that, from (AII-7),

$$R>3\cdot 10^2 b,$$

and it is seen from Eq. (AII-5a) that this condition also will be close to fulfilled in this example.

APPENDIX III

Dislocation Core Diffusion

The Turnbull[7] work on diffusion along dislocation walls indicates that in fcc metals a dislocation can be regarded as a channel of cross section $\sim b^2$, where the activation energy of diffusion is about half that of the perfect crystal [see Eq. (17)].

The details of the atomic structure of the dislocation core are not known, and the precise mechanism of diffusion along the dislocation is correspondingly uncertain. Several possibilities are discussed in Thomson's paper.[21]

Let us assume that the vacancy model is appropriate, and that the line of easy diffusion consists of just *one* string of atomic sites along the dislocation.

In this model, a vacancy on the string will pass forth and back a given atomic site a large number of times before it escapes from the dislocation line. This sequence of *correlated* jumps will influence the activation energy severely. We proceed to make a rough estimate. The notation of Eqs. (15) to (22) is used.

Consider an atom on the string. From Eq. (20), all vacancies within a distance

$$l \simeq b \exp\{(\Delta E_f + \Delta E_m)/2kT\} \qquad \text{(AIII-1)}$$

will pass one or several times past the atom, before they, after a time

$$\tau = 1/\Omega = l^2/D_v \exp(\Delta E_m/kT) \qquad \text{(AIII-2)}$$

have left the dislocation. Regardless of how many times a given vacancy passes a given atom on the string, the net random displacement of the atom is only b. Thus, the coefficient of self-diffusion along the string must be

$$D_{sd,disl} \simeq \Omega(l/b) \exp\{-(E_f - \Delta E_f)/kT\} \cdot b^2 \qquad \text{(AIII-3)}$$

or

$$D_{sd,disl} \simeq \gamma b^2 \times \exp\{-(E_m + E_f - \tfrac{1}{2}\Delta E_m - \tfrac{1}{2}\Delta E_f)/kT\}. \qquad \text{(AIII-4)}$$

In order to obtain agreement with experiment, it must be required that

$$E_m + E_f - \tfrac{1}{2}\Delta E_m - \tfrac{1}{2}\Delta E_f \simeq \tfrac{1}{2}(E_m + E_f), \qquad \text{(AIII-5)}$$

i.e., allowing only positive energies,

$$\begin{aligned} \Delta E_m &\simeq E_m \\ \Delta E_f &\simeq E_f. \end{aligned} \qquad \text{(AIII-6)}$$

Thus, compared with experiments, the model leads to vacancy formation—and jump energies on the dislocation which are an order of magnitude lower than E_m and E_f. This result is quite unreasonable, and in fact, if it were true, the vacancy concentration along the dislocation would be so high in the diffusion experiments, that our estimate is invalid.

We think that the unreasonable consequences of the one-string model strongly suggest that the dislocation core structure is such that the dislocation can be said to consist of at least two strings of easy diffusion, between which vacancies may easily jump so that no large correlation effects arise. Equation (17) is then a reasonable interpretation of experiment.

The possibility that thermal activation may displace the dislocation, with the vacancies attached to it, randomly between parallel positions, should also be considered; but we think that this is a less likely solution, particularly for dislocations in a dislocation wall.

Photoeffects in Nonuniformly Irradiated p-n Junctions*

GERALD LUCOVSKY
Philco Corporation, Research Division, Philadelphia, Pennsylvania

(Received January 18, 1960; revised manuscript received March 8, 1960)

A theoretical basis is provided for the interpretation of photoeffects observed in nonuniformly irradiated p-n junctions. Differential equations describing the junction photovoltage are developed through an application of the continuity and diffusion equations. Solutions of the small-signal steady-state photoeffect equation indicate that the effects of nonuniform irradiation become increasingly important as the ratio of the lateral to the transverse resistance increases. α, a parameter introduced in this paper and designated as the lateral-fall off parameter, is a measure of this resistance ratio. The lateral photovoltage resulting from nonuniform irradiation can be eliminated by reverse biasing the junction into saturation. Experimental curves in agreement with the predictions of the analysis are presented.

INTRODUCTION

IT is well known that sufficiently energetic radiation normally incident on a p-n junction produces a photovoltage across the junction. If the junction is nonuniformly irradiated, the photovoltage will, in general, vary with position, producing an additional photovoltage parallel to the plane of the junction. Wallmark first recognized this effect and demonstrated how it could be utilized to produce a position sensitive photocell.[1] In this paper the restricted analysis of Wallmark is expanded and a theoretical basis is provided for the interpretation of the photoeffects observed in nonuniformly irradiated p-n junctions.

In a uniformly irradiated junction, the absorption of radiation results in the creation of hole-electron pairs in the neighborhood of the surface upon which the radiation is incident. If the radiation is incident on the surface of the p region and if the thickness of this region is approximately equal to or less than a minority carrier diffusion length, then an appreciable number of optically generated hole-electron pairs diffuse to the junction where they are separated by the electrostatic forces of the transition region. The electron is swept into the n region and the hole remains in the p region. The separation process therefore cancels a portion of the barrier space charge which in turn causes a reduction of the internal barrier potential. In an attempt to reestablish the equilibrium barrier configuration a net current of negative charge now flows from the n to the p region. This current consists of electrons being reinjected from the n to the p region and holes being injected from the p to the n region. As long as a generating source of pairs is present, the barrier does not return to its equilibrium configuration. A steady-state condition results when the rate of hole-electron pair separation by the barrier is equal to the reinjected current.

In the steady-state condition a photovoltage φ, representing a reduction in the barrier potential, is generated across the junction. φ is related to f, the number of hole-electron pairs separated/sec/cm^2 by the junction by the relationship[2]

$$\varphi=(kT/q)\ln[(qf/J_s)+1], \tag{1}$$

where q is the magnitude of the electronic charge, k is Boltzmann's constant, T is the absolute temperature, and J_s is the saturation current density of the junction. Neglecting reflection losses, f_λ is related to the monochromatic incident flux density I_λ by

$$f_\lambda=\eta_\lambda\epsilon_\lambda I_\lambda, \tag{2}$$

where η_λ is the fraction of the optically generated hole-electron pairs that reaches the junction and is separated, and ϵ_λ is the quantum efficiency of the excitation process. If the incident radiation is not monochromatic and I_λ is the incident flux density in the interval λ to $\lambda+d\lambda$, then

$$f=\int_0^{\lambda_0}\eta_\lambda\epsilon_\lambda I_\lambda d\lambda, \tag{3}$$

where λ_0 is the long-wavelength limit of the junction determined by the width of the forbidden gap of the semiconductor.

Analytical expressions for J_s and η_λ can be obtained by a solution of the one-dimensional diffusion equations which govern minority carrier current flow in a p-n junction.[3,4] Implicit in the derivation of these expressions is the assumption of a uniform radiant flux over the entire junction. This assumption validates the use of a one-dimensional analysis. In any practical junction configuration, there is usually some constraint that destroys the uniformity which justifies a one-dimensional analysis. The nonuniformity may result from the presence of opaque electrical contacts made to the irradiated surface or it may result from incomplete irradiation of the junction. In the analysis

* Based upon a thesis submitted to the Temple University Graduate Council in partial fulfillment of the requirements for the degree of Doctor of Philosophy.

[1] T. Wallmark, Proc. I.R.E. 45, 474 (1957).

[2] E. S. Rittner, *Photoconductivity Conference, November 4, 1954* (John Wiley & Sons, Inc., New York, 1956).

[3] W. Schockley, *Electrons and Holes in Semiconductors* (D. Van Nostrand Company, Inc., Princeton, New Jersey, 1950).

[4] E. Wolfendale, *The Junction Transistor* (The Macmillan Company, New York, 1958).

that follows a method for treating these types of problems will be developed.

NONUNIFORMLY IRRADIATED JUNCTIONS

The condition of uniform irradiation will be relaxed and the general problem of photoeffects in nonuniformly irradiated junctions will be investigated. A rather specific problem, namely, the interaction between a point source of radiation and an infinite p-n junction, will first be analyzed in order to illustrate the physical processes that occur in a nonuniformly irradiated junction. This approach will also serve to indicate the method of analysis that will be used to develop the general photoeffect equations.

Point Source of Radiation Incident on an Infinite Junction

We will first consider a circle of radius a of uniformly dense radiant energy normally incident on the p side of an infinite p-n junction. It will be assumed that the incident radiation is monochromatic and sufficiently energetic to create hole-electron pairs in the semiconducting crystal. If the thickness of the p region is less than a minority carrier diffusion length, then an appreciable number of the optically generated hole-electron pairs will diffuse to the junction where they will be separated. If the radius of the irradiated region is large compared to a minority carrier diffusion length, the separation process will then occur in a region whose radius is essentially equal to that of the irradiated region. This diffusion process can therefore be analyzed in terms of the one-dimensional minority carrier diffusion equations.

The separation process cancels a portion of the barrier space charge in a restricted region whose area is approximately equal to that of the irradiated region thereby producing an electric field in a direction which is parallel to the plane of the internal barrier. If the junction were uniformly irradiated the separation process would then produce a uniform cancelation of space charge over the entire barrier and hence no lateral electric field would result. (The direction parallel to the junction will henceforth be designated as the lateral direction; the direction perpendicular to the plane of the junction will be designated as the transverse direction.)

In a nonuniformly irradiated junction, the lateral electric field is so directed as to induce a flow of both separated majority carriers laterally away from the irradiated region; i.e., electrons flow out radially in the n region and holes in the p region. The lateral majority carrier current cancels a portion of the barrier space charge outside of the irradiated region causing a reduction in the barrier potential. The reduction in barrier potential makes possible a net flow of negative charge from the n to the p region. In the steady state this net flow of reinjected charge integrated over the entire area of the junction must equal the total of number of hole-electron pairs separated per second by the junction in the irradiated region. In a uniformly irradiated junction this charge conservation condition served to determine the junction photovoltage. In a nonuniformly irradiated structure it is necessary to consider the lateral flow of the separated carriers in order to determine the steady-state barrier configuration. The semiconducting material on either side of the junction is ohmic and may therefore be described by a resistivity which depends on the number and mobility of the majority charge carriers. As a result of this nonvanishing lateral resistance, the lateral flow of majority carriers is accompanied by a lateral potential drop which gives rise to the lateral photovoltage discussed by Wallmark. In order to obtain an expression for the junction photovoltage as a function of the radial distance from the center of the irradiated region, it is necessary to apply the continuity equation to the lateral flow of majority carriers.

If an ohmic contact is made to the entire surface of the n region making this region an equipotential, it then follows that the lateral flow of current is limited by the lateral resistance of the p region. The lateral current density $J_L(r)$ of holes in the p region is related to the transverse photovoltage $\varphi(r)$ by

$$d\varphi(r)/dr=-\rho_p J_L(r), \tag{4}$$

where ρ_p is the resistivity of the p region. Steady-state continuity of current requires that in any given region the net change in lateral current must equal the transverse current. Therefore, one constructs an annulus of height W_p, the thickness of the p region, and radii r and $r+\Delta r$, and integrates the transverse and lateral current densities over the faces of the annulus. Assume first that $r>a$, the radius of the irradiated region. In this region the transverse current I_T is given by

$$I_T=2\pi r\Delta r J_T(r), \tag{5}$$

where

$$J_T(r)=J_s(e^{q\varphi(r)/kT}-1). \tag{6}$$

The total change in the lateral current ΔI_L is found by integrating the lateral current density J_L over the walls of the annulus. Therefore,

$$\Delta I_L=2\pi W_p[(rJ_L(r)-(r+\Delta r)J_L(r+\Delta r)]. \tag{7}$$

By combining (5) and (7) and passing to the limit, it follows that

$$dJ_L/dr=-(J_L/r)-(J_T/W_p). \tag{8}$$

By combining (4) and (8), the differential equation which describes the variation of the transverse photovoltage outside of the irradiated region is given by

$$(d^2/dr^2)\varphi+(1/r)(d/dr)\varphi -(\rho_p J_s/W_p)(e^{q\varphi/kT}-1)=0. \tag{9}$$

If r lies inside the irradiated region and f is the number

of hole-electron pairs separated/sec/cm², then the transverse current is given by

$$I_T = 2\pi r \Delta r [J_T(r) - qf]. \tag{10}$$

By combining (4), (7), and (10) and passing to the limit, the differential equation governing the variation of the transverse photovoltage inside of the irradiated region is then given by

$$\frac{d^2}{dr^2}\varphi + \frac{1}{r}\frac{d}{dr}\varphi - \frac{\rho_p J_s}{W_p}(e^{q\varphi/kT} - 1) = -\frac{\rho_p q f}{W_p}. \tag{11}$$

If $qf/J_s < 1$, then Eqs. (9) and (11) can be linearized for this small signal to yield the following equations:

$$\frac{d^2}{dr^2}\varphi + \frac{1}{r}\frac{d}{dr}\varphi - \frac{\rho_p q J_s}{W_p kT}\varphi = \begin{cases} q\rho_p f/W_p & r < a \\ 0 & r > a \end{cases} \tag{12}$$

The solution of Eq. (12) appears in the Appendix.

Generalized Steady-State Photoeffect Equation

The generalization of Eq. (12) to an arbitrary geometric configuration is straightforward. The total current density that exists in the p region is made up of two components, $\mathbf{J}_L$, the lateral current density and $\mathbf{J}_T$, the transverse current density. In the steady state,

$$\operatorname{div}(\mathbf{J}_L + \mathbf{J}_T) = 0. \tag{13}$$

If $f(\mathbf{r})$ represents the number of hole-electron pairs separated/sec/cm² by the junction at the point $\mathbf{r}$,[5] then

$$\operatorname{div}\mathbf{J}_L = -(J_T(\mathbf{r})/W_p) + (qf(\mathbf{r})/W_p), \tag{14}$$

where $J_T(\mathbf{r})$ is given by

$$J_T(\mathbf{r}) = J_s(e^{q\varphi(\mathbf{r})/kT} - 1). \tag{15}$$

The ohmic character of the p region is described by the relationship

$$\operatorname{grad}\varphi(\mathbf{r}) = -\rho_p J_L(\mathbf{r}). \tag{16}$$

By combining (14)–(16), the generalized steady-state photoeffect equation is given by

$$\nabla^2\varphi(\mathbf{r}) - (\rho_p J_s/W_p)(e^{q\varphi(\mathbf{r})/kT} - 1) = -(\rho_p q/W_p) f(\mathbf{r}). \tag{17}$$

The solution of Eq. (17) subject to appropriate boundary conditions gives the transverse photovoltage $\varphi(\mathbf{r})$ as a function of the two-dimensional coordinate system that is defined in the plane of the junction. If

$$qf_{\max}(\mathbf{r})/J_s < 1, \tag{18}$$

then Eq. (17) can be linearized for the small-signal case to give

$$\nabla^2\varphi(\mathbf{r}) - (\rho_p q J_s/W_p kT)\varphi(\mathbf{r}) = -(\rho_p q/W_p) f(\mathbf{r}). \tag{19}$$

For several of the experiments described in this paper, Eq. (19) is applicable and therefore will be discussed in detail. It will be convenient to introduce a new parameter α, defined by the relationship

$$\alpha \equiv (\rho_p q J_s/W_p kT)^{\frac{1}{2}}. \tag{20}$$

This parameter will be designated as the lateral falloff parameter; the provocation for this designation will be made apparent.

In general, Eq. (19) is subject to boundary conditions of the form

$$\partial\varphi/\partial n + h\varphi = K, \tag{21}$$

where $\partial\varphi/\partial n$ is the normal derivative of φ at the boundary of the junction and where h and K are constants defined for these boundary points. The formal solution of (19) is then given by

$$\varphi(\mathbf{r}) = \iint_{S_0} g(\mathbf{r}/\mathbf{r}_0)\frac{\rho_p q f(\mathbf{r})}{W_p} dS_0 + \oint_{l_0} \frac{K}{h} g(\mathbf{r}/\mathbf{r}_0) dl_0, \tag{22}$$

where $g(\mathbf{r}/\mathbf{r}_0)$ is the Green's function defined by

$$\nabla^2 g(\mathbf{r}/\mathbf{r}_0) - \alpha^2 g(\mathbf{r}/\mathbf{r}_0) = \delta(\mathbf{r} - \mathbf{r}_0). \tag{23}$$

dS_0 is the two-dimensional element of area in the plane of the junction, and dl_0 is the element of length along the boundary of the junction.

Expression (22) indicates that nontrivial solutions of Eq. (19) can be generated by either inhomogeneous terms in the photoeffect equation, by inhomogeneous boundary conditions ($K \neq 0$), or by both. The solution generated by inhomogeneous boundary conditions gives the current-voltage characteristics of p-n junctions in which an electrical contact covers a restricted portion of the p region. If a bias voltage is applied to an opaque contact that covers a portion of an irradiated junction, then it is necessary to deal with an inhomogeneous equation subject to inhomogeneous boundary conditions. This particular situation is of interest when considering photoeffects in a junction which has been biased into the saturation region of its current voltage characteristic.

Time-Dependent Photoeffect Equation

The physical processes that occur in an irradiated junction have been analyzed as taking place in two discrete steps. The first step was taken to be the diffusion of the optically generated hole-electron pairs to the barrier and their subsequent separation by the barrier. The second step was a rearrangement of the separated charge, consistent with current continuity requirements and the conditions imposed by the presence of the internal barrier.

[5] If $I_\lambda(\mathbf{r})$ is the incident photon flux at the point $\mathbf{r}$, then $f_\lambda(\mathbf{r}) = \eta_\lambda \alpha_\lambda I_\lambda(\mathbf{r})$, whenever the distances over which $I_\lambda(\mathbf{r})$ changes are large compared to a minority carrier diffusion length or whenever the radiation is confined to a restricted portion of the junction whose dimensions are large with respect to a minority carrier diffusion length. The latter condition is the one that was encountered in the experiments described in this paper.

The time required for the diffusion of pairs to the barrier and the separation of pairs by the barrier is in the order of, or less than, a minority carrier lifetime.[6] The characteristic time required for the redistribution of the separated charge is, in general, determined by the junction impedance and the junction capacity. If the minority carrier lifetime is small and if the analysis is restricted to the small-signal case, then redistribution process is the rate limiting process. The capacity that is then considered is the barrier capacity which may be treated as a constant for the small-signal case.[7]

In the analysis that follows it will be assumed that the $f(\mathbf{r},t)$, the function that represents the number of hole-electron pairs separated by the junction/sec/cm², has the same time dependence as the incident radiant flux. This in turn restricts the analysis to modulation frequencies which are smaller than the reciprocal of the time required for the separation process.

The generalization of Eq. (19) to the time-dependent case is again straightforward. The steady-state continuity condition is replaced by the general continuity condition, namely,

$$\operatorname{div}(\mathbf{J}_L+\mathbf{J}_T)=-\partial\rho(\mathbf{r},t)/\partial t, \tag{24}$$

where $\rho(\mathbf{r},t)$ is the charge density in the p region at the point $\mathbf{r}$ at the time t. By restricting the analysis to the small-signal case, it follows that

$$\rho(\mathbf{r},t)=C\varphi(\mathbf{r},t)/W_p, \tag{25}$$

when C is the barrier capacity. If $f(\mathbf{r},t)$ is the hole-electron pair separation function, it then follows that

$$\operatorname{div}\mathbf{J}_L=-\frac{J(\mathbf{r},t)}{W_p}\frac{C}{W_p}\frac{\partial}{\partial t}\varphi(\mathbf{r},t)+\frac{qf(\mathbf{r},t)}{W_p}. \tag{26}$$

For the small-signal case,

$$J(\mathbf{r},t)=(qJ_s/kT)\varphi(\mathbf{r},t). \tag{27}$$

Since

$$\operatorname{grad}\varphi(\mathbf{r},t)=-\rho_p J_L(\mathbf{r},t), \tag{28}$$

it follows at once that the time-dependent photoeffect equation for the small-signal case is given by

$$\nabla^2\varphi-(\rho_p C/W_p)(\partial\varphi/\partial t)-\alpha^2\varphi=-(\rho_p q/W_p)f(\mathbf{r},t). \tag{29}$$

The formal solution of (29) is given by

$$\varphi(\mathbf{r},t)=\int_0^t d\tau\iint_{S_0} g(\mathbf{r}/\mathbf{r}_0;t-\tau)\left[\frac{q}{C}f(\mathbf{r}_0,\tau)+\Phi(\mathbf{r}_0)\right]dS_0$$

$$+\frac{1}{h}\int_0^t d\tau\oint g(\mathbf{r}/\mathbf{r}_0;t-\tau)X(\mathbf{r}_0,\tau)dl_0, \tag{30}$$

where the boundary conditions are given by

$$\partial\varphi/\partial n=(\mathbf{r},t)\quad\text{for } t>0 \tag{31}$$

and where

$$\varphi(\mathbf{r},t)=\Phi(\mathbf{r})\quad\text{for}\quad t=0. \tag{32}$$

$g(r/r_0,t-\tau)$ is the Laplace transform of the Green's function defined by the equation

$$\nabla^2 g_s-[\alpha^2+(C\rho_p/W_p)S]g_s=-(C\rho_p/W_p)\delta(\mathbf{r}-\mathbf{r}_0), \tag{33}$$

subject to the boundary condition

$$\partial g_s/\partial n+hg_s=0. \tag{34}$$

EXPERIMENTAL DATA

Sample Preparation

The photosensitive junctions that were studied were formed by diffusing Zn and Cd into heavily doped n-type InAs. The n-type InAs, grown in this Laboratory, was doped with Te; Hall measurements indicated a net donor density of 7.5×10^{17}/cm³ at 300°K and 7.0×10^{17}/cm³ at 77°K.

Samples Nos. 85 and 107 were prepared from Cd-diffused junctions; samples Nos. 18 and 53 were prepared from Zn-diffused junctions. In the course of the experiments it was found that the observed physical phenomena were identical for the Cd- and Zn-doped samples as would be expected.

Experimental Results

Figure 1 is a plot of the transverse junction photovoltage $\varphi(x)$ outside of an irradiated line as a function

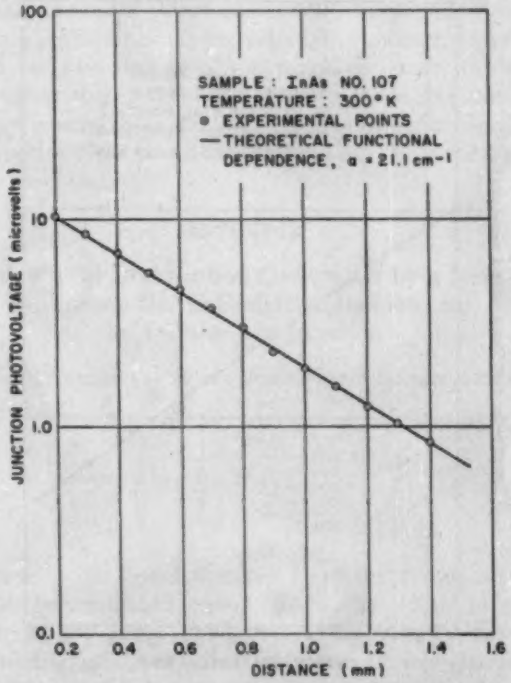

FIG. 1. Junction photovoltage outside of an irradiated line as a function of the distance from the center of the line.

[6] D. E. Sawyer and R. H. Rediker, Proc. I. R. E. 46, 1122 (1958).

[7] A. Van der Ziel, *Solid State Physical Electronics* (Prentice Hall, Inc., Englewood Cliffs, New Jersey, 1957).

of x, the distance from the center of the irradiated line. The radiation source for this measurement is a Sylvania concentrated arc lamp. The radiation is focused onto the sample through microscope optics. A slit placed at the objective of the microscope is used to give a 0.3-mm line of radiation on the sample. The experimental points fall on a curve given by

$$\varphi(X)=K_1e^{-\alpha x}, \tag{35}$$

where K_1 is a constant. This is the functional dependence predicted by expression (3-A) of the Appendix.

Figure 2 is a plot of the transverse junction photovoltage $\varphi(r)$, outside of an irradiated circle, as a function of r, the radial distance from the center of the irradiated region. The experimental points fit a curve given by

$$\varphi(r)=K_2\exp(-\alpha' r), \tag{36}$$

where K_2 is a constant. This is the functional dependence predicted by expression (7-A) of the Appendix. The experimentally determined ratio of α'/α is found to be 1.16. This is in excellent agreement with the predicted value of 1.17.

Figure 3 is a plot of the junction photovoltage $\varphi(r)$ as a function r, the distance from the center of a uniformly irradiated circle for points both inside and outside of the irradiated region. The experimental points show the functional dependence predicted by expression (5-A) of the Appendix.

Figure 4 contains plots of $\varphi(r)$, the junction photovoltage outside of an irradiated circle, as a function of r at various temperatures. It is found that α, the lateral falloff parameter decreases with decreasing temperature. A measurement of the slope of the current-voltage characteristic at the same temperatures for small applied biases, coupled with measurements of α, indicates that the decrease in α is due to a decrease in J_s. There is no evidence to indicate that ρ_p/W_p varies appreciably with temperature in the temperature range from 77° to 300°K. Dixon also finds that ρ_p does not vary in this temperature range.[8]

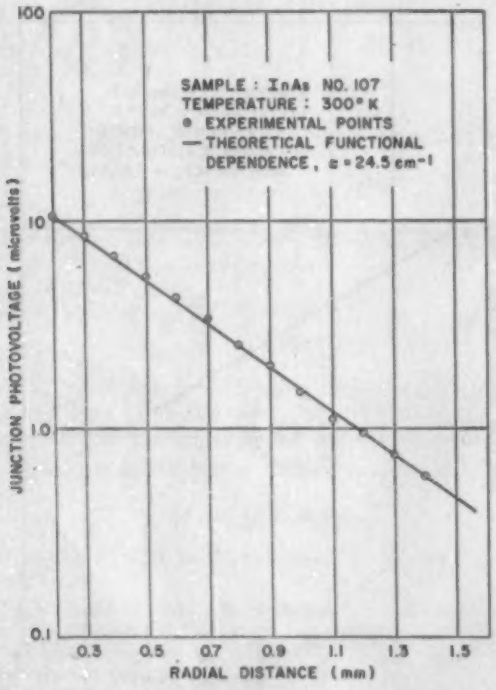

FIG. 2. Junction photovoltage outside of an irradiated circle as a function of the radial distance from the center of the circle.

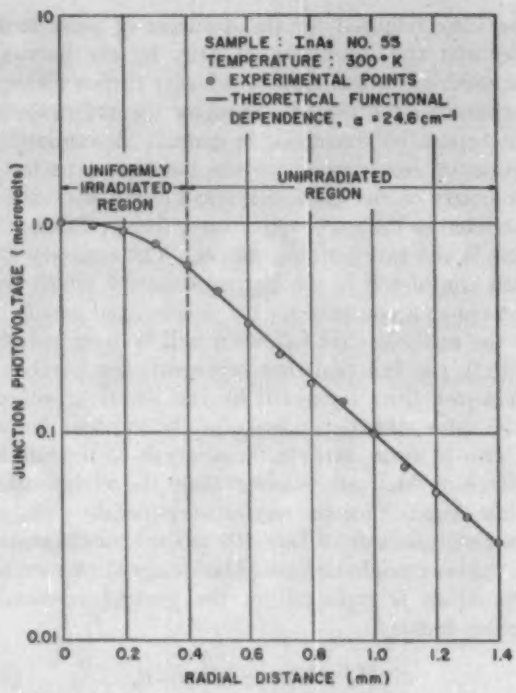

FIG. 3. Junction photovoltage as a function of the radial distance from the center of a uniformly irradiated circle.

Figure 5 contains plots of $\varphi(r)$, the junction photovoltage outside of the irradiated region, as a function of r for a junction to which different values of reverse electrical bias have been applied. The slope of the curve of junction photovoltage vs radial distance decreases as the bias voltage increases. This slope goes to zero when the junction is biased into saturation as is predicted by the analysis given in the Appendix.

The foregoing measurements of junction photovoltage were made using sinusoidally modulated radiation. The modulation frequency was 750 cps. The barrier capacity for the InAs junctions is sufficiently small to insure that capacitive effects can be neglected at this modulation frequency.

SUMMARY AND CONCLUSIONS

In this paper an attempt has been made to provide a theoretical basis for the interpretation of the photoeffects observed in nonuniformly irradiated p-n junc-

[8] J. R. Dixon, J. Appl. Phys. 30, 1412 (1959).

tions. Steady-state and time-dependent phenomena have been analyzed, and differential equations describing the junction photovoltage have been developed. These equations have been solved for the small-signal case; formal solutions are presented in the main body of the paper and particular solutions of experimental interest are developed in the Appendix.

An examination of the particular solutions for the small-signal case allows one to draw several general conclusions. If the incident radiation is confined to a restricted region of the junction, e.g., a circular spot or line, and if $\alpha \neq 0$, then the photovoltage outside of this irradiated region decreases exponentially or faster as the distance from the irradiated region increases. The effects of nonuniform irradiation becomes increasingly important as α, the lateral falloff parameter increases. In the limit as α goes to zero, the lateral photovoltage disappears and an arbitrary irradiation pattern produces a uniform photovoltage over the entire barrier.

If a reverse bias is applied to a photosensitive junction, so that the junction is biased into the saturation, then the photovoltage generated across an external load is independent of the particular details of the irradiation pattern and depends only on the total number of hole-electron pairs separated by the junction. This effect can be utilized to fabricate a single-element multiprobe position sensitive photocell which is capable of operation as the sensing element in a system which can both acquire and track a source of radiant energy. In the acquisition mode, a four-probe position sensitive detector could be biased into saturation, so that the signal produced by a point source of radiation would then be independent of the position of the source and not suffer any degradation due to lateral effects. When a sufficiently strong signal is obtained, the cell could be switched into the tracking mode by the removal of the external bias. In this mode, the photovoltage generated at the four contacts would again give information from which the position of the source point could be obtained.[1,9]

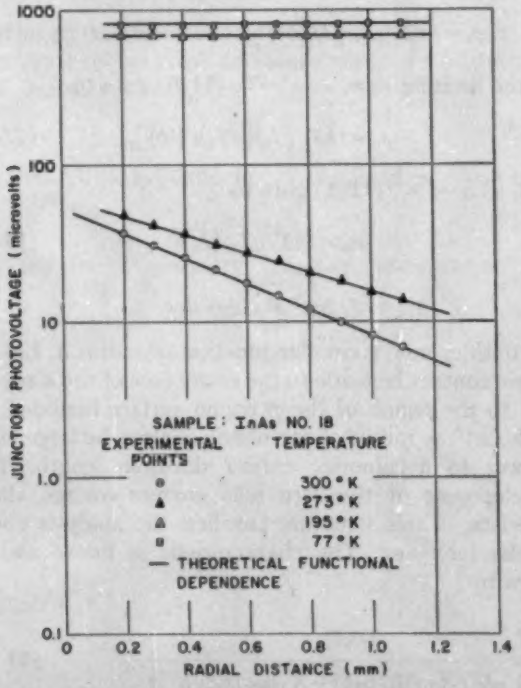

FIG. 4. Junction photovoltage as a function of radial distance at various temperatures.

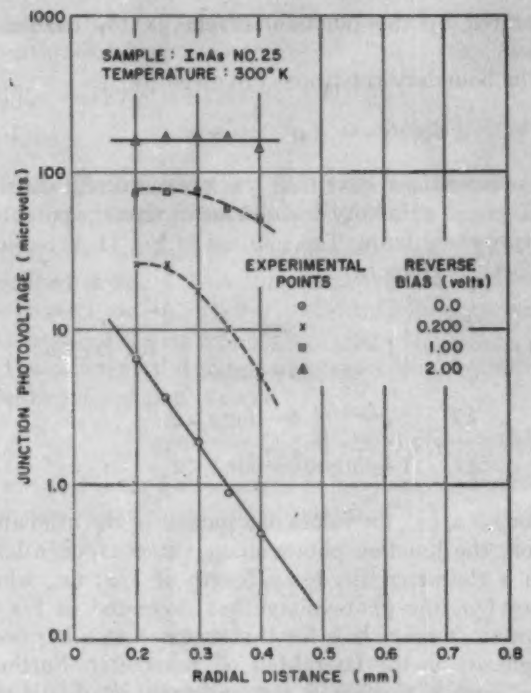

FIG. 5. Junction photovoltage as a function of radial distance for various applied reverse biases. The solid lines shown for curves 1 and 4 indicate the predicted theoretical fractional dependence. The dashed empirical curves indicate the presence of a nonvanishing lateral photoeffect due to incomplete saturation.

APPENDIX

A. Potential Distribution Generated by a Line of Uniformly Dense Radiation Incident on an Infinite *p-n* Junction

The differential equation describing this configuration is given by

$$\frac{d^2}{dx^2}\varphi - \alpha^2\varphi = \begin{cases} \dfrac{-\rho_p q f_0}{W_p} & \text{for } |x| < a \\ 0 & \text{for } |x| > a \end{cases}, \qquad (1\text{-A})$$

where x is the linear distance from the center of the uniformly irradiated region, $2a$ is the width of this region and is large compared to a minority carrier diffusion length, and f_0 is the number of hole-electrons

[9] G. Lucovsky, Proc. Infrared Information Symposium 4, 221 (1959).

separated by the junction/sec/cm² in the irradiated region.

The boundary conditions are given by

$$d\varphi/dx=0 \quad \text{for} \quad x=\pm\infty. \tag{2-A}$$

These conditions state that the lateral current density must vanish at infinity and also insure that the potential is everywhere finite. The solution of Eq. (1-A) subject to (2-A), is given by

$$\varphi(x)=\frac{kT}{qJ_s}qf_0\left\{1-\frac{\cosh\alpha x}{\cosh\alpha a+\sinh\alpha a}\right\} \quad \text{for } |x|<a,$$
$$\varphi(x)=\frac{kT}{qJ_s}qf_0\frac{e^{\alpha(a\mp x)}}{1+\coth\alpha a}\begin{cases}-\text{ for } x>a\\ +\text{ for } x<a\end{cases} \tag{3-A}$$

For $x>a$, i.e., for values of x outside of the irradiated region, the junction photovoltage varies exponentially with a characteristic decay length of $1/\alpha$; i.e., when $x-a=1/\alpha$, the photovoltage has decreased to $1/e$ of its value at $x=a$. It is for this reason that α has been designated as the lateral-fall off parameter. Furthermore, even if the line is not uniformly irradiated, an examination of Eq. (1-A) for $|x|>a$ indicates that the solution will still show an exponential functional dependence outside of the irradiated region.

B. Potential Distribution Generated by a Circle of Uniformly Dense Radiation Incident on an Infinite *p-n* Junction

The differential equation describing this configuration has been developed in the main body of the paper. The boundary condition to which Eq. (12) is subject is given by

$$d\varphi/dr=0 \quad \text{for} \quad r=\infty. \tag{4-A}$$

The solution of Eq. (12) subject to (4-A) is given by

$$\varphi(r)=(kT/qJ_s)qf_0\{1-\alpha aK_1(\alpha a)I_0(\alpha r)\} \quad \text{for } 0<r<a,$$
$$\varphi(r)=(kT/qJ_s)qf\alpha aI_1(\alpha a)K_0(\alpha r) \quad \text{for } a<r<\infty. \tag{5-A}$$

$I_i(Z)$ and $K_i(Z)$ are modified Bessel functions of the first and second kind.[10] For $\alpha r>1$,

$$K_0(\alpha r)\approx(\pi/2\alpha r)^{\frac{1}{2}}e^{-\alpha r}. \tag{6-A}$$

For $5>\alpha r>1$,

$$K_0(\alpha r)\approx\exp(-\alpha' r), \tag{7-A}$$

where $\alpha'=1.17\alpha$.

C. Calculation of the Slope of the Zero Bias Current-Voltage Characteristic

1. Linear Symmetry

Consider a *p-n* junction structure which is infinite in the y direction and of length $a+b$ in the x direction. Let an ohmic contact be made to the entire face of the n region and to the region of the p surface bounded by $x=0$ and $x=-b$. Furthermore, let b be large with respect to a minority carrier diffusion length. Let a voltage φ_a be applied to the contact to the p surface such that $|\varphi_a|<kT/q$. The differential equation describing the barrier potential as a function of the distance from the contact is given by

$$d^2\varphi/dx^2-\alpha^2\varphi=0. \tag{8-A}$$

The boundary condition at $x=a$ is given by

$$d\varphi/dx=0. \tag{9-A}$$

This corresponds to the condition that the lateral current density vanish at the boundary of the junction. If I is the current/unit length (in the y direction) that is required to maintain a potential of φ_a in the region $-b>x>0$, then the boundary condition at $x=0$ is given by

$$d\varphi/dx=-(\rho_p/W_p)[I-J_s b(q\rho_a/kT)]. \tag{10-A}$$

The solution of (8-A) subject to the boundary conditions (9-A) and (10-A) yields a linear current-voltage characteristic that is given by

$$\varphi_a=(kT/qJ_s)[I/(b+\sinh\alpha a/\alpha\cosh\alpha a)]. \tag{11-A}$$

In the limiting case, as $\alpha\to 0$, (11-A) goes to

$$\varphi_a=(kT/qJ_s)[I/(a+b)], \tag{12-A}$$

and, as $\alpha\to\infty$, (11-A) goes to

$$\varphi_a=(kT/qJ_s)(I/b). \tag{13-A}$$

2. Radial Geometry

Consider now a circular junction of radius a. Let an ohmic contact be made to the entire face of the n region and to the region of the p region surface bounded by $r=b$. Let the radius of the ohmic contact be large with respect to a minority carrier diffusion length. The development of the zero bias current-voltage characteristic of this structure parallels the analysis given in the foregoing. The characteristic is linear and is given by

$$\varphi_a=\frac{kT}{qJ_s\pi b^2}\frac{I}{\{1+2[I_1(\alpha a)K_1(\alpha b)-K_1(\alpha a)I(\alpha b)]/\alpha b[I_1(\alpha a)K_0(\alpha b)+K_1(\alpha a)I_0(\alpha b)]\}}. \tag{14-A}$$

[10] P. M. Morse and H. Feshbach, *Methods of Theoretical Physics, Part II* (McGraw-Hill Book Company, Inc., New York, 1953).

For $\alpha \to 0$,

$$\varphi_a = (kT/qJ_s)(I/\pi a^2). \tag{15-A}$$

For $\alpha \to \infty$,

$$\varphi_a = (kT/qJ_s)(I/\pi b^2). \tag{16-A}$$

D. Determination of the Condition for Saturation of the Current-Voltage Characteristic

Consider now the p-n junction structure discussed in Sec. C.1, and let the bias applied to the p-region contact be negative and large with respect to kT/q. Due to the nonvanishing lateral resistance, this condition is not sufficient to insure that the entire junction is biased into saturation. In this section the negative bias required to insure saturation will be calculated as a function of the lateral falloff parameter and the junction geometry.

The differential equation that is applicable for a completely saturated junction is given by

$$d^2\varphi/dx^2 = -(\rho_p/W_p)J_s. \tag{17-A}$$

The boundary conditions are given by

$$\varphi = -\varphi_a \quad \text{for} \quad x=0$$

$$\frac{d}{dx}\varphi = \begin{cases} (\rho_p/W_p)(I - J_s b) & \text{for } x=0 \\ 0 & \text{for } x=a \end{cases}. \tag{18-A}$$

In order for Eq. (17-A) to be valid for all x, it is necessary that $\varphi(a) = -4kT/q$. The minimum value of φ_a that satisfies this condition is given by

$$[\varphi_a]_{\min} = (kT/q)(4 + \tfrac{1}{2}\alpha^2 a^2). \tag{19-A}$$

The larger the lateral falloff parameter the larger the negative bias required to insure complete saturation. If φ_a satisfies (19-A), then

$$I = J_s(a+b). \tag{20-A}$$

Eq. (20-A) is also valid for all values of φ_a, such that

$$\varphi_a > [\varphi_a]_{\min}. \tag{21-A}$$

For the radial geometry junction configuration described in Sec. C.2, the minimum value of φ_a required for saturation is given by

$$[\varphi_a]_{\min} = (kT/q)[4 + \tfrac{1}{2}\alpha^2 a^2[\ln(a/b) - \tfrac{1}{2}] + \tfrac{1}{4}\alpha^2 b^2]. \tag{22-A}$$

E. Photoeffects in a Junction Which has been Biased into Saturation

Consider a junction configuration of the type described in Sec. C.1. Assume that the bias applied to the contact at $-b > x > 0$ is sufficiently large to insure saturation of the current-voltage characteristic.

The differential equation that describes photoeffects in a biased junction is given by

$$d^2\varphi/dx^2 = -(\rho_p q/W_p) f(x), \tag{23-A}$$

where $f(x)$ is the hole-electron pair separation function. The boundary conditions to which (23-A) is subject are given by

$$\frac{d}{dx}\varphi = \begin{cases} (\rho_p/W_p)\Delta I_L & \text{for } x=0 \\ 0 & \text{for } x=a \end{cases}, \tag{24-A}$$

where ΔI_L is the additional current induced by the incident radiant flux.

The solution of (24-A) subject to (25-A) is given by

$$\Delta I_L = q\int_0^a f(x)dx. \tag{25-A}$$

Therefore, the change in current is equal to the number of hole-electron pairs separated by the junction and is not a function of the position at which the pairs are separated.

ACKNOWLEDGMENTS

The author is pleased to acknowledge many helpful and enlightening discussions with M. E. Lasser, R. F. Schwarz, P. Cholet, and E. L. Offenbacher. The assistance of J. E. Slawek, Jr., and H. Altemose in the preparation of experimental samples is also gratefully acknowledged.

Tensile Properties of Thin, Evaporated Gold Films

C. A. NEUGEBAUER
General Electric Research Laboratory, Schenectady, New York
(Received February 16, 1960)

Evaporated gold films in the 500–15 000 A thickness range were prepared on rocksalt substrates. Depending on the temperature of the substrate during deposition, the films were completely, partially, or randomly oriented with respect to the (100) plane of the rocksalt, as determined by x-ray diffraction. The stress-strain curve of the free films was investigated and was found to be quite steep up to very high stresses, but plastic deformation and creep were observed even at relatively low stresses. The ultimate tensile strength of the films is from 2 to 4 times that of the annealed bulk material and is not a function of film thickness. The Young's moduli are found to be normal. Comparing the stress-strain behavior of evaporated films with that of whiskers suggests that the former owe their high strength to a high concentration of defects which were uniformly quenched in during the evaporation process, and which greatly impede dislocation motion and multiplication, and not to an abnormally high stress required to nucleate dislocations which is commonly observed in whiskers.

INTRODUCTION

IN the past decade a great many workers[1] have demonstrated the unusually high tensile strength of small metal whisker crystals. For example, iron whiskers have sustained a tensile stress of up to 1340 kg/mm², compared to a "normal" tensile strength in bulk iron specimens of only 35–70 kg/mm². Similar high strength has been found in whiskers of a great variety of materials, including halides,[1–3] oxides,[1,4] sulfides,[5] and even organic substances.[6] The yield point in whiskers is usually reached only at stresses much higher than those required in bulk materials, and elastic strains of the order of 1% are not uncommon. Below the yield point the stress-strain curve is entirely elastic in nature, although small amounts of pre-yield creep have been reported by one group of investigators[7] in zinc and copper whiskers.

The tensile deformation of thin, evaporated films has been studied principally by two groups. Beams and coworkers[8] prepared gold and silver films by evaporation on to plastic or rocksalt substrates, and tested their tensile strength using the "bulge" method, in which the stress in a film of certain thickness was inferred from the air pressure required to bulge it. From the dimensions of the bulge the corresponding strain in the film was calculated. Films which were prepared on rocksalt had a definite epitaxial relationship to the substrate, namely (100) of gold ‖ (100) of rocksalt, [100] of gold ‖ [100] of rocksalt. The results obtained by Beams *et al.* on the tensile properties of thin, evaporated gold and silver films can be summarized as follows:

(A) The tensile strength of thin gold and silver films, determined by dividing the maximum load sustained by the original cross section of the film, can be as high as 60 kg/mm².

(B) When the films are thinner than 2000 A, there is a dependence of tensile strength on film thickness: the thinner the films, the higher the strength. Films thicker than 2000 A behave like bulk material and have a tensile strength of only about 12 kg/mm².

(C) Plastic deformation was observed in all films after a relatively short elastic region.

(D) The crystalline orientation of the film had apparently no effect on the tensile properties.

(E) The total elongation in the film, both elastic and plastic, was usually of the order of 1%–2% at fracture.

Menter, Pashley,[9–11] Gordon,[12] and Marsh[13] at the Tube Investment Laboratories in England have recently published their work on the tensile properties of thin films. Gold films were prepared by first evaporating silver on mica, and then evaporating the gold on top of it. It was then possible to strip the gold film from the substrate by dissolving the silver in nitric acid. The films were either polycrystalline or had a single crystal orientation, with the 111 plane of gold parallel to the cleavage plane of mica, depending on the temperature of the substrate during the deposition. The stress-strain curves were obtained by using a tensile machine in which the film was mounted between two grips. The stress was applied by means of a torsion wire, and the elongation of the specimen was measured with a mirror-telescope arrangement. In addition, the elastic portion of the strain in some single crystal films was measured

[1] For a comprehensive review, see S. S. Brenner in *Growth and Perfection of Crystals* (John Wiley & Sons, Inc., New York, 1958), p. 157.
[2] Z. Gyulai, Z. Physik **138**, 317 (1954).
[3] C. C. Evans, D. M. Marsh, and J. E. Gordon, Nature **182**, 296 (1958).
[4] G. L. Pearson, W. T. Read, and W. L. Feldman, Acta Met. **5**, 181 (1957).
[5] W. W. Piper and W. L. Roth, Phys. Rev. **92**, 503 (1953).
[6] J. E. Gordon, Nature **179**, 1270 (1957).
[7] N. Cabrera and P. B. Price in *Growth and Perfection of Crystals* (John Wiley & Sons, Inc., New York, 1958), p. 204.
[8] J. W. Beams in *Structure and Properties of Thin Films* (John Wiley & Sons, Inc., New York, 1959), p. 183; see also J. W. Beams, W. E. Walker, and M. S. Marton, Jr., Phys. Rev. **87**, 524 (1952); J. W. Beams, J. B. Breaseale, and W. L. Bart, Phys. Rev. **100**, 1657 (1955).
[9] J. W. Menter and D. W. Pashley in *Structure and Properties of Thin Films* (John Wiley & Sons, Inc., New York, 1959), p. 111.
[10] D. W. Pashley, Nature **182**, 296 (1958).
[11] D. W. Pashley, Phil. Mag. **4**, 316, 324 (1959).
[12] J. E. Gordon in *Growth and Perfection of Crystals* (John Wiley & Sons, Inc., New York, 1958), p. 219.
[13] D. M. Marsh, J. Sci. Instr. **36**, 165 (1959).

directly by straining them in the electronmicroscope and observing the increase in lattice parameter by transmission electron diffraction.

The results of these investigations can be summarized as follows:

(A) The tensile strength of evaporated gold films can be quite high, the maximum strength measured being 80 kg/mm², although most films exhibited tensile strengths between 25 and 50 kg/mm².

(B) Films were prepared and tested in a thickness range between 500 A and 12.5 μ, but there was no dependence of the tensile strength on film thickness, for evaporated films.

(C) The crystalline orientation did not seem to influence the tensile properties appreciably.

(D) The total elongation of the film at fracture was only of the order of 1 to 2%.

(E) A so-called "nonelastic" effect is observed in all films on top of the otherwise elastic stress-strain behavior. The initial load line is irreversible and has a noticeably smaller slope than that of the unloading line.

This initial nonelastic behavior reported by Menter and Pashley[9] was thought to arise from the difficulty of ensuring completely uniform gripping of the films in the tensile apparatus, although it has not been observed when whiskers were tested. This nonelastic effect was therefore disregarded and the stress-strain curve was assumed to be entirely elastic up to almost the maximum stress which the film was able to support. This behavior would then be quite analogous to that of whiskers, where exclusively elastic elongations of the order of 1% or higher are frequently observed. It is clearly important to establish whether the high strength observed in films arises from an abnormally long elastic stress-strain region, as in the case in whiskers, or whether it arises from plastic effects, as in bulk materials, where considerable workhardening is observed before the ultimate tensile strength is reached.

Work which has been done in this laboratory on the tensile properties of evaporated thin gold films has some bearing on this question and is reported in the following section.

Preparation of Films

Gold films were prepared by evaporating a previously weighed quantity of gold on to rocksalt cleaved to expose 100 planes and kept at 300°C or lower temperatures during the evaporation, depending on the degree of orientation required. The demountable vacuum system was capable of a pressure in the 10^{-6} mm range. The 100 planes of the rocksalt crystals were previously polished in ethyl alcohol/water solution to produce a very smooth surface. The evaporation rate was high enough to result in a film growth of several 100 A per minute. Film thickness was estimated from the geometrical relationship between source and substrate, and is therefore accurate only to within about 20%. Films were prepared in the 500–15 000 A range.

The crystalline orientation with respect to the substrate was determined for several of the films by transmission x-ray diffraction after film stripping. Some of the films were single crystals (but containing many sub-boundaries), with the orientation of the gold completely parallel to that of the rocksalt, i.e., (100) gold ‖ (100) rocksalt and [100] gold ‖ [100] rocksalt. In another group of films, while the (100) plane of all the grains was still parallel to the (100) plane of the substrate, only some of them exhibited a particular preferred direction with respect to the rocksalt. The directions of the rest of the grains were randomly distributed. Finally, some films had a completely random orientation. Representative diffraction patterns for these three orientations are shown in Fig. 1(a–c), respectively. The orientation approaches that of a single crystal at the higher temperature (~300°C), while completely random orientation is obtained at temperatures lower than 150°C.

Tensile Test

The tensile apparatus used in this investigation was constructed by S. S. Brenner of this Laboratory and has been more fully described elsewhere.[14] The film was mounted on two grips, one of them stationary and the other attached to a suspended rod on which was also attached a magnet. The magnet in turn was surrounded by a solenoid which, when activated, pulled the magnet toward its center and thereby exerted a stress on the specimen proportional to the current through the solenoid. The current was calibrated against a set of known weights. The elongation in the film was measured by means of a differential transformer. When a soft iron armature attached to the other end of the suspended rod moved away from the center of the transformer, a proportional voltage output signal was recorded. This voltage was calibrated in units of distance by measuring displacements by means of a calibrated reticle eye piece at 26× magnification. With this apparatus it was possible to measure stress and strain to an accuracy of about 10%.

In order to mount a test specimen, the rocksalt crystal bearing the gold film was cleaved with a razor blade to give a piece approximately 1 cm long and 1–2 mm wide. This crystal was then glued with the gold film face down on to the grips of the tensile apparatus using either sealing wax or diphenyl carbazide. The rocksalt backing was then dissolved in water leaving the free film. The length and width of the film under test were measured *in situ* with the microscope. It should be noted that any stress to which the film may have been subjected while on the substrate is relieved by this method of mounting.

In order to ascertain that there was no slipping of

[14] S. S. Brenner, J. Appl. Phys. 28, 1023 (1957).

FIG. 1. X-ray transmission diffraction patterns of (a) a single crystal gold film, (b) a partially oriented gold film, (c) a randomly oriented gold film.

the tensile specimen because of imperfect gripping or plastic flow in the glue, and also to establish any background elongation which might be inherent in the apparatus itself, under stress, a thick steel specimen of dimensions otherwise similar to the gold films was mounted in the apparatus using the same glue. No slipping was observed, and the entirely elastic background elongation intrinsic in the apparatus was recorded as a function of load. This correction, caused by flexing of the glass rods, was then applied in each tensile experiment, and was of the order of 30% of the total elongation in a typical test.

Nature of Stress-Strain Curve

A typical stress-strain curve for a 5000 A film is shown in Fig. 2. The loading curve obtained when increasing the stress for the first time is initially linear with a slope close to or only slightly smaller than Young's modulus. At higher stresses the loading curve becomes less and less steep. When the stress is decreased at any one point on the initial loading line, an unloading curve is established the slope of which is always greater than the initial load line and is, in fact, in the vicinity of the Young's modulus number. This new stress-strain curve which resulted from pre-stressing the film is now reproducible with either increasing or decreasing stress, providing it is less than the maximum stress so far reached on the initial loading curve. If this maximum stress is exceeded, the loading curve will continue on the same nonlinear and irreversible path as before. A new, linear and reversible stress-strain curve is established each time the specimen is unloaded after a new maximum stress has been reached. If a constant stress is applied for several minutes, creep can be observed, and the stress strain curves taken afterwards will be displaced toward larger elongations. Eventually fracture occurs, the total elongation just prior to fracture being of the order of 1%, of which $\frac{3}{4}$ may be elastic and reversible, and the rest irreversible. The stress supported just prior to fracture divided by the original cross-section of the film is taken as the tensile strength of the specimen. The stress-strain curve after the maximum stress has been exceeded was not investigated.

Creep Tests

As indicated above, it was observed that if the film had to support a reasonably large constant load, it had a tendency to creep. This is illustrated in Fig. 3. Here

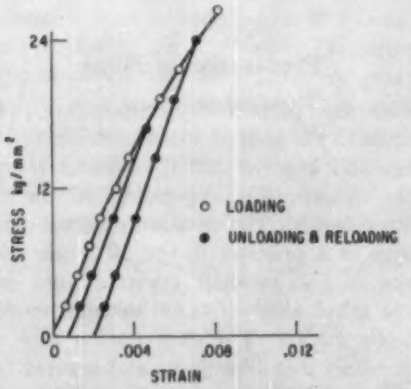

FIG. 2. Stress-strain curve obtained for a typical evaporated gold film, indicating that some plastic deformation is taking place.

the film was allowed to creep at 9 and 18 kg/mm² load. The creep was measured in several specimens, and was between 10^{-7}/min to 10^{-4}/min, depending on the load, the specimen dimensions, and the amount of prestressing. It had been previously ascertained that this creep was not an artifact arising from a relaxation in the glue used to mount the specimens, or a creep inherent in the apparatus itself under stress. Creep in gold films has also been observed by Beams.[8]

Tensile Strength of Gold Films

About 50 different films were tested in the tensile apparatus. The ultimate tensile strength was usually of the order of 20 to 40 kg/mm², with a maximum value of 48 kg/mm². Young's modulus was determined from the slope of the unloading stress-strain curve. In simple crystals of gold the moduli are $E_{100}=4200$ kg/mm², $E_{110}=8500$ kg/mm², and $E_{111}=11\,400$ kg/mm². The moduli obtained in the thin film experiments are between 3000 and 10 500 kg/mm², most of the values being between 4000 and 8000 kg/mm². It should be noted here that although the absolute value of the slope of the stress-strain curve can only be calculated with limited accuracy, the relative differences between the slopes can be ascertained much more accurately in any one film. The slope of the unloading curve (Young's modulus) was always steeper than the initial loading curve. No abnormal moduli were observed within the limits of the accuracy of the experiments.

A representative sample of the values obtained for the tensile strength and Young's modulus of evaporated gold films is given in Table I. For the completely oriented films Young's modulus is expected to be close to 4200 kg/mm², since the load was applied in the [100] direction. No unequivocal dependence of tensile strength on either film thickness or orientation is apparent, although the data are admittedly insufficient.

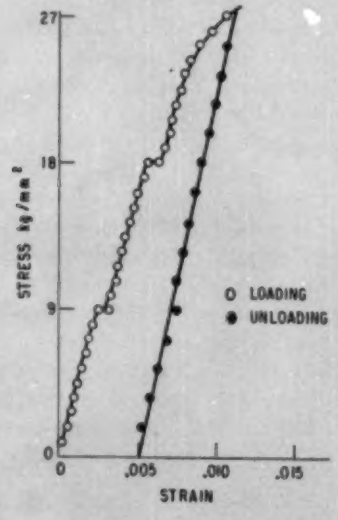

FIG. 3. Stress-strain curve for an evaporated gold film which was allowed to creep at 9 and 18kg/mm², respectively.

TABLE I. Tensile strength and Young's modulus of some evaporated gold films.

Thickness, A	σ_{max} kg/mm²	E, kg/mm²
	Complete orientation	
2650	27.6	4800
2650	30.7	4800
2900	20.4	4850
2900	25.0	4850
2900	15.4	4850
3000	18.5	5160
3000	19.4	4300
3000	6.6	4700
	Partial orientation	
1480	22.4	4000
1480	25.0	5800
1500	22.6	4380
1500	38.4	4800
1900	24.0	3400
1900	16.2	3400
2900	26.5	4430
	Random orientation	
620	39.5	3080
620	20.0	4850
1260	33.2	9500
4175	45.0	7120
5000	26.0	5400
15 500	20.0	6700
15 500	48.0	7150

Comparison with Bulk Material

It has been suggested by J. Fisher[15] that bulk gold could be workhardened to such an extent that the tensile strength could be of the same order of magnitude as that observed for thin, evaporated gold films. The true fracture stress, which is the load sustained by the specimen just prior to fracture divided by the cross-sectional area of the specimen at the point of fracture would give some indication of how much the strength of a material can be increased by workhardening. The values listed in the literature for the strength of gold usually refer to the tensile strength as defined previously. For annealed gold specimens this value is between 10 and 15 kg/mm², while values ranging between 20 and 30 kg/mm² can be found for hard drawn wire.[16–22] H. Rogers[23] of this laboratory has measured the true fracture stress of a tensile bar of gold, and obtained 118 kg/mm², while the tensile strength was only 13.5 kg/mm², comparable to the values given by previous investigators above. Thus, bulk material can be work-

[15] J. C. Fisher in discussion to paper footnote (9).
[16] L. Guillet and M. Balloy, Rev. mét. **20**, 398 (1923).
[17] W. Geibel, Z. anorg. Chem. **70**, 240 (1911).
[18] *International Critical Tables* (McGraw-Hill Book Company, Inc., New York, 1929), 1st ed., Vol. 2, p. 586.
[19] D. F. Miner and J. B. Seastone, *Handbook of Engineering Materials* (John Wiley & Sons, Inc., New York, 1955), 1st ed., p. 2–409.
[20] *Gmelin's Handbuch der anorganischen Chemie* (Verlag Chemie, Berlin, Germany, 1954), 8th ed., Vol. 62, p. 462.
[21] A. E. Van Arkel, *Reine Metalle* (Verlag Julius Springer, Berlin, 1939), p. 423.
[22] E. Raub, *Edelmetalle und ihre Legierungen* (Verlag Julius Springer, Berlin, 1940), p. 57.
[23] H. C. Rogers, Jr., private communication.

hardened to give a strength similar to that found in even the strongest films, but a large amount of deformation and severe necking are usually observed before this high stress is reached.

Comparison with Metal Whiskers

Because of the very steep stress-strain curve observed in evaporated gold films, their relatively high tensile strength, and because dislocation movement was not observed in films under stress, J. Menter and D. Pashley[9] suggested that the tensile properties of thin films are analogous to those found in whiskers, namely, an elastic limit (or yield point) much larger than is normally found in bulk materials. In both cases, it is argued, effective locking of grown in dislocations, probably by the action of point defects quenched into the film or whisker during growth, and the inability to nucleate dislocation sources, which could be associated with the high degree of surface perfection observed in both films and whiskers, leads to a high elastic limit and tensile strength in both. It might therefore be instructive to compare the tensile behavior of evaporated thin gold films and typical whiskers.

First, the stress-strain curves for thin films obtained in this laboratory and also those reported in the literature clearly show some plastic effects as indicated by the nonreproducibility of the initial condition (zero elongation) even at relatively low stresses. Strong whiskers, on the other hand, invariably display an entirely elastic stress-strain behavior, up to very high stresses, the yield stress being usually equal to the ultimate tensile strength.

Secondly, creep was easily observable in the films tested, even at relatively low stresses. Creep in whiskers is often observed *after* yielding, the creep stresses being much smaller than the yield point. Small pre-yield creep has been reported,[7] but it was not confirmed,[1] and in general investigations have failed to uncover creep even at relatively high stresses.

With the exception of the results reported by Beams,[8] the tensile strength of evaporated gold films does not decrease with increasing film thickness, between 600 A and 12.5 μ, but is still of the order of 40–70 kg/mm^2 even for films of thickness of the order of 10 μ. In whiskers, on the other hand, a high tensile strength can as a rule not be expected for the thicker specimen. In iron, for instance, the tensile strength of 16-μ diam whisker will, on the average, be only about $\frac{1}{3}$ as high as that found for an average 2-μ diam whisker.[24] This comparison may not be entirely fair because of the difference in materials involved and the limited thickness range investigated.

Fourth, plastic deformation in films is observable even at stresses considerably below the tensile strength and no sharp yield point is observed. Extremely sharp yield points are commonly observed in most whiskers.

Lastly, the dislocation density in evaporated gold films has been found by Menter and Pashley[9] to be of the order of 10^{10} to 10^{11} per cm^2 by electron diffraction microscopy. On the other hand, while metal whiskers are not necessarily dislocation free, the dislocation density is certainly much lower. Thus it has been found by P. Gorsuch[25] by means of x-ray rocking curves that more perfect iron whiskers have dislocation densities below 10^6/cm^2 at least. Also, the tensile strength of whiskers which do not appear to be perfect crystals usually is quite low. On the other hand, the tensile strength of randomly oriented films, containing many quenched in imperfections, is at least as high, or possibly higher, than that of the more "perfect" single crystal films, where an elevated substrate temperature caused some annealing during and after film growth.

Origin of High Strength in Films

What *is* unique in evaporated gold films when compared to bulk specimen is the very high slope of the stress-strain curve which is usually only a little smaller than Young's modulus at low stresses and decreases slowly at higher stresses. This means that only very few dislocations move or are generated, even at the highest stresses observed. This seems to suggest that the process of film formation by evaporation is equivalent to severely cold working the film by quenching in a high concentration of dislocations and other defects, impeding the motion of dislocations although not altogether preventing it, particularly at higher stresses. The impediments to dislocation motion must be distributed uniformly throughout the film because no necking was observed by Pashley in film specimens examined in the electron microscope even at very high stresses. That cold working can lead to a similar high strength is demonstrated by the true fracture stress of gold quoted above. The fact that films prepared by thinning down from bulk material do not show a high tensile strength[9] is consistent with the idea that, since here the effective coldworking inherent in the evaporation process is absent, localized necking and fracture occurs at small loads. In addition, one would not expect the high strength to be a function of the film thickness of evaporated films, and this is borne out by experiment (see, however, Beams, reference 8). This is not necessarily true for films prepared by other methods, such as electroplating, where a thickness dependence of the strength was observed.[9] Electronmicroscopic observation of only slight dislocation movement is difficult and may have escaped detection.[9–11]

The principal difference between the origin of the high strength of whiskers and evaporated films is therefore that in whiskers the stress required to generate dislocations is equal to the ultimate tensile strength, while in films dislocation movement occurs even at low stresses but is greatly impeded by the large concentra-

[24] S. S. Brenner, J. Appl. Phys. 27, 1484 (1956).

[25] P. D. Gorsuch, J. Appl. Phys. 30, 837 (1959).

tion of defects uniformly quenched into the film by the evaporation process.

CONCLUSIONS

A. The ultimate tensile strength of thin, evaporated gold films as determined by previous investigators and in this laboratory, is between 20 and 80 kg/mm². This compares with a tensile strength of annealed bulk gold of about 12 kg/mm² and a true fracture stress of severely cold-worked bulk gold of over 100 kg/mm².

B. From direct stress-strain measurements it was shown that the deformation of thin, evaporated gold films is not entirely elastic or equivalent to that found in whiskers. In thin, evaporated films one observes: (1) plastic deformation, (2) creep, (3) no sharp yield point, (4) no thickness-strength relationship, and (5) a dislocation density much higher than it is found in whiskers.

C. It is suggested that the quenching in of a high density of defects inherent in a random evaporation process results in what is equivalent to a uniformly and severely cold-worked film, thus leading to only slightly dislocation motion and necking and fracture only at relatively high stresses.

D. There should be no upper limit to the thickness of specimens produced by evaporation above which they no longer exhibit a high ultimate tensile strength.

ACKNOWLEDGMENTS

The author is greatly indebted to S. S. Brenner for the loan of the tensile apparatus and many valuable discussions. Many stimulating suggestions by Gert Ehrlich are gratefully acknowledged. H. C. Rogers kindly permitted his value of the true fracture strength of gold to be quoted. C. W. Tucker was of great help in determining the epitaxial relationship of the films.

JOURNAL OF APPLIED PHYSICS VOLUME 31, NUMBER 6 JUNE, 1960

Simple Radiant Heating Method for Determining the Thermal Diffusivity of Cellulosic Materials

STANLEY B. MARTIN
U. S. Naval Radiological Defense Laboratory, San Francisco, California
(Received January 20, 1960)

A simple radiometric method for the determination of the thermal diffusivity of poorly conducting sheet-form materials such as cellulosic kindling fuels is described. The method is a dynamic one based on the "long time" solution of the heat-conduction equation for the infinite slab with constant heat-input rate, and utilizes fine-wire thermocouples laminated between sheets of the material (whose diffusivity is required) to measure rates of temperature rise at various depths. The geometry of the system is designed to satisfy as many as possible of the boundary conditions imposed on the mathematical model. The magnitude of errors introduced by violating the other boundary conditions is discussed in connection with the results of measurements on α-cellulose.

The value of the thermal diffusivity of α-cellulose containing two percent carbon black and whose density is 0.68 g/cm³ was found to be $1.06\pm0.06\times10^{-3}$ cm²/sec.

INTRODUCTION

IN the analysis of nonsteady-state conduction of heat through material systems, an indispensible property is the thermal diffusivity α, defined as the ratio of the thermal conductivity K to the volumetric heat capacity ρc (where ρ is density and c is specific heat). Examples of its use include the determination of temperature profiles attained during transient heating and the correlation of data on the behavior of rapidly heated or cooled substances. Classically, the value is determined by separate determinations of the conductivity, the density, and the specific heat of the substance. Frequently, one or more of the component values is known for one temperature only, and rather serious errors occur in the values of the diffusivity calculated for other temperatures.

Sinusoidal Methods

A more elegant approach involves measuring the thermal diffusivity directly by nonsteady-state methods. One such dynamic method is the sinusoidal heat-wave method of King.[1] Heat is applied to one surface of a very thick specimen of the material, whose diffusivity is required, in such a way that the temperature at the surface varies sinusoidally. By measuring the velocity of the heat waves produced as they travel through the material, information necessary to the determination of the diffusivity is obtained.

A modification of this method, reported by Starr,[2] measures the amplitude decrement of the heat wave. Both of these methods require the measurement of tem-

[1] R. W. King, Phys. Rev. 6, 437 (1915).
[2] C. Starr, Rev. Sci. Inst. 8, 61 (1937).

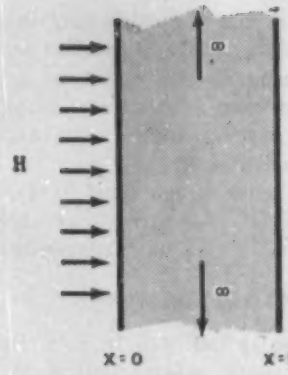

FIG. 1.

perature with time at no less than two separate points in the material for two sinusoidal inputs of differing periods and the solution of the resulting simultaneous equations to eliminate the heat loss term.

More recently, Sidles and Danielson[3] combined the two methods and were able to eliminate one of the inputs and to simplify the whole procedure, thereby improving the reliability.

Constant Input Method

A somewhat different approach to the dynamic measurement is based on the application of a constant input to a relatively thin specimen whose geometry is designed to represent the opaque infinite slab of finite thickness. This heat-flow model is described by Fig. 1 and the following equations and boundary conditions:

$$\partial T/\partial t=\alpha(\partial^2 T/\partial x^2) \tag{1}$$

$$\text{at } t=0 \text{ and } 0<x<L; \qquad T=T_0 \tag{2}$$

$$\text{at } t>0 \text{ and } x=0; \qquad -K(\partial T/\partial x)=\partial q/\partial t=H \tag{3}$$

$$\text{at } t>0 \text{ and } x=L; \qquad \partial T/\partial x=0 \tag{4}$$

(H is a constant net flow of heat across the surface). α is the thermal diffusivity, K is the thermal conductivity, T is temperature, t is time, and q is sensible heat per unit area. The solution of this heat-conduction boundary value problem is given by Carslaw and Jaeger[4] and may be written

$$T(x,t)=T_0+\frac{HL}{K}\left[F_0+\tfrac{1}{2}(1-x/L)^2-\tfrac{1}{6}-\frac{2}{\pi^2}\sum_{n=1}^{\infty}\frac{1}{n^2}\exp(-n^2\pi^2F_0)\cos\frac{n\pi x}{L}\right], \tag{5}$$

where $F_0=\alpha t/L^2$. The series summation rapidly approaches zero as F_0 (the Fourier modulus) increases, i.e., for long times, and we may write the approximation

$$T(x,t)=T_0+\Delta T$$
$$=T_0+(HL/K)[F_0+\tfrac{1}{2}(1-x/L)^2-\tfrac{1}{6}] \tag{6}$$

as the "long time solution." In terms of temperature rise ΔT, at points x_1 and x_2,

$$\Delta T_1=(HL/K)[(\alpha t/L^2)-\tfrac{1}{6}+\tfrac{1}{2}(1-x_1/L)^2]$$

and

$$\Delta T_2=(HL/K)[(\alpha t/L^2)-\tfrac{1}{6}+\tfrac{1}{2}(1-x_2/L)^2].$$

When $\Delta T_1=\Delta T_2$ (i.e., at times t_1 and t_2),

$$(\alpha/L^2)(t_2-t_1)=\tfrac{1}{2}(1-x_1/L)^2-\tfrac{1}{2}(1-x_2/L)^2$$
$$\alpha(t_2-t_1)=\tfrac{1}{2}(L-x_1)^2-\tfrac{1}{2}(L-x_2)^2$$
$$\alpha=[(L-x_1)^2-(L-x_2)^2]/2(t_2-t_1). \tag{7}$$

Butler and Inn[5] made use of this solution to provide values of the thermal diffusivity of metals at temperatures up to about 1000°C. To minimize losses, they made their measurements *in vacuo* and resorted to a relatively complex guard-ring arrangement. It appears that they were largely successful except for the radiative losses from the exposed surface and they devised a graphical cooling-curve method of correcting for those.

In some respects this method is better suited to poorly conducting materials and particularly to sheet-form materials. In poorly conducting materials the temperature profile resulting from relatively low input rates are steep enough that readily measurable differences in temperature result between points separated by small distances. Moreover, the problems of electrically insulating imbedded thermocouples attendant on measurements in metals and similar conductors do not exist. These factors permit the direct incorporation of fine-wire thermocouples directly into the material by laminating them between thin sheets. The problem of losses from the edges may be neglected and the conduction treated as one dimensional when such materials are heated uniformly over an area whose dimensions are large compared to the thickness.

We have recently applied this technique to the measurement of the thermal diffusivity of alpha-cellulose paper. Besides the immediate need for a realistic value of the diffusivity of cellulose, there is a continuing need for a simple direct means of determining the value of this very important thermal property in organic solids and other poorly conducting materials, and so the general utility of the method was kept in mind during this investigation.

EXPERIMENTAL

Attempts were made initially to measure temperatures at two or more points in cellulose exposed on one surface to the refocused radiation from a carbon arc and

[3] P. H. Sidles and G. C. Danielson, J. Appl. Phys. 25, 58 (1954).
[4] H. S. Carslaw, and J. C. Jaeger, *Conduction of Heat in Solids* (Oxford University Press, New York, 1947), p. 104.
[5] C. P. Butler, and E. C. Y. Inn, "Thermal Diffusivity of Metals at Elevated Temperatures" in *Thermodynamics and Transport Properties of Gases, Liquids and Solids*, (McGraw-Hill Book Company, Inc.), pp. 377–390 (1959).

to a bank of photoflood bulbs. Failure to obtain consistent and meaningful data in these attempts was laid to the violation of boundary conditions, principally (4). It was concluded that if the boundary conditions of (4) were rigorously met, the failure to meet the boundary conditions of (3) would not be serious, since it could be kept small (by not allowing the surface temperature to rise excessively and by considering only short intervals at a time) and corrected for by the cooling-curve technique. Experimentally, the desired condition of zero back-surface losses can be realized by arranging two specimens back to back and irradiating their front surfaces identically.

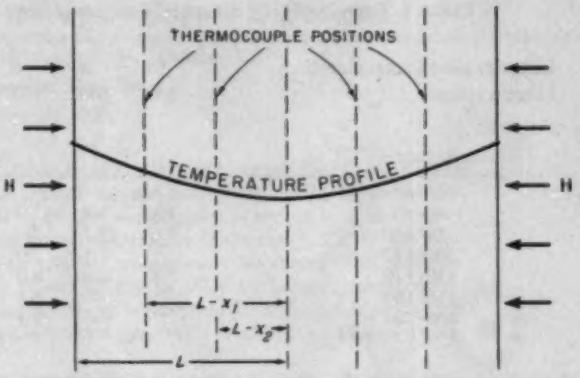

FIG. 2. Schematic diagram of experimental system.

Sample Preparation

Chromel-alumel thermocouple wire, 0.003 in. in diam, was stripped of insulation for about two inches from the end and their ends spot welded together.[6] The couple was then inserted between two tool-steel flats and compressed in an arbor press until most of the exposed wire, including the junction, was reduced in thickness to a 0.0010 to 0.0012-in. foil-junction.

A 0.031-in. thick sheet of alpha-cellulose (containing about two percent carbon black to make it nearly opaque and black) was cut into 3×3½-in. rectangular pieces which were laminated together with the foil-junction of the thermocouple carefully arranged at each interface to measure the temperature near the center of the rectangular area.

The laminating was accomplished by applying a small quantity of aqueous methyl cellulose (clear solution of Dow Methocel 400-cps viscosity) to the surfaces to be joined, spreading uniformly and removing the excess. The methyl cellulose solution is largely water and on drying leaves a very thin clear film of methyl cellulose. Its main action seems to be one of swelling and raising the fibers on the surface of the cellulose, so that when these surfaces are pressed together the fibers of one surface mat together with the fibers of the other. It is felt that, when properly done, this interface presents little or no resistance to the flow of heat, and the conduction of heat through such a laminate will be a very good approximation of the conduction through a single sheet. Finally, the entire surface of the sample was blackened lightly over burning camphor.

Method of Measurement

The exposure arrangement was very simple. The sample was mounted in an upright position on the center of an optical bench. The thermocouple leads were brought out to a junction board immersed in ice and distilled water contained in a Dewar flask from which the various recorder leads ran. Two lightly frosted photoflood bulbs (Westinghouse RFL-2, 115–120 v) were mounted facing the sample with supports which could be moved along the tracks of the optical bench and the bulbs were connected in parallel to the output of a variac.

An important consideration associated with this geometry concerns the need for equal heating of the two surfaces. Equation (7), which is the one utilized here, contains the quantities $(L-x_1)$ and $(L-x_2)$ which are to be interpreted in our experiment as the distances between each thermocouple junction and the lowest point in the temperature profile (see Fig. 2). This point corresponds to the midpoint only if the system is completely symmetric. Symmetry can be achieved by careful control of the output of the two radiation sources.

Equal spacing of the thermocouples provided a direct and simple check on the symmetry of the temperature distribution. Once the photoflood bulbs had been located to provide nearly equal illumination of the two surfaces, the difference in temperature between the two shallow thermocouples and the difference between the two deep thermocouples was measured by opposing their outputs and recording the difference-signal during irradiation. The relative positions of the sources were adjusted and the difference again measured. This was repeated until a minimum difference (generally less than 1½°C) was achieved during a rise to about 200°C. A further check of the symmetry was afforded by the actual temperature time readings which constituted the experimental determination of the thermal diffusivity.

RESULTS

Figure 3 illustrates the recorded traces of the signals generated by one set of thermocouples during exposure. The dotted lines superimposed on the rise curves represent segments of the cooling curve. These represent the temperature-decrement rate at that particular temperature due to losses (primarily unilaterally through the exposed surface) and are used to adjust the measured interval (t_2-t_1).

This cooling-curve correction assumes that the losses are equal during heating and during cooling. This assumption is reasonable as long as the irradiance level is low, so that the surface temperature is not greatly

[6] Raytheon Model 60A "Weldpower."

TABLE I. Experimentally determined values of the thermal diffusivity of α-cellulose for various temperatures.

Lamp to sample distance (in.)	10	8	6	6	4	4	3		
Lamp voltage	100	100	100	60	80	30	80		
Temp. range (°C)	t_2-t_1 (sec)							Mean t_2-t_1 (sec)	α ($\times 10^{-3}$ cm²/sec)
40–60	8.3			8.0		7.4		7.9	1.08
60–80	7.8	7.8		8.0		7.0		7.6	1.12
80–100	7.6	7.7		7.5	7.6			7.6	1.12
100–120		7.8	7.9	7.4	8.0	7.8	7.9	7.8	1.09
120–140	7.8	8.0	8.0	7.6	8.3		8.0	8.0	1.06
140–160			8.8		8.4			8.6	0.99
160–250			9.1		9.3		8.3	8.9	0.95
								Mean	1.06±0.06[a]

[a] Compare this to value calculated from conductivity, density, and specific heat—0.95 $\times 10^{-3}$ cm²/sec [see F. M. Sauer, "Ignition of black alpha-cellulose papers by thermal radiation," U. S. For. Serv., Div. of Fire Res., ITR 869 (September, 1956)].

different from the indicated temperatures and so that quasi-steady state convection is established early.

Table I lists some of the more pertinent data obtained along with the best estimates of the thermal diffusivity for several temperature ranges.

DISCUSSION AND CONCLUSIONS

The method described provides a number. We must evaluate it before assigning it as the value of the diffusivity. It should be pointed out that a considerable range of irradiance levels were used in the various determinations. Having adjustability in both the distance from the source to specimen surface and the voltage applied permitted changing the heat input and the color temperature independently of each other. This in turn allows one to evaluate the effect of violating the conditions imposed on the mathematical model.

The condition of unilateral conduction is adequately met so long as there is uniform heating of an area having dimensions which are large compared to the thickness L. Although the lamps used appear to provide uniform heating, some of the focusing action of the reflector on the light may survive the scattering action of the frosted envelope. Any resulting nonuniformity would be enhanced at certain lamp to sample distances. Furthermore, at the close extreme, the relatively high thermal input steepens the temperature gradient and causes the losses from the exposed surface to exceed that which is estimated from the cooling curve, emphasizing that error. For these reasons, the comparison of measurements made at different lamp positions (at constant lamp voltage) should reveal the magnitude of errors caused by nonuniform heating and uncompensated surface losses. No significant trend of differences resulted in the values measured over the range of lamp positions employed (lamp to sample distances from 3 to 10 in.) and it must be concluded that such effects are small.

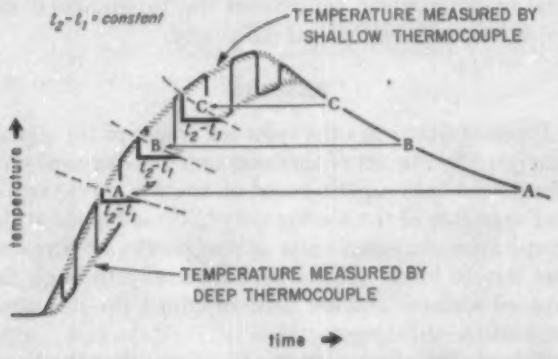

FIG. 3. Application of cooling-curve segment to heating curve in order to obtain t_2-t_1 directly from recording.

Changing the color temperature of the lamps while also changing their positions so as to maintain a constant heat input might be expected to provide a measure of the effect of the diathermancy of the material since it is normally a function of wavelength. No evidence of any effect of changing color temperature resulted in this experiment, an observation which is really not too surprising in view of the fact that α-cellulose containing two percent carbon is quite opaque even in 0.004-in. thicknesses (extinction coefficient estimated to be 10^3 cm^{-1}). Natural cellulosic materials and wood pulp products, on the other hand, though they all have large values of the extinction coefficient at wavelengths of 3μ and longer, are generally quite diathermanous in the red and near infrared. Unfortunately, the glass envelope of the photoflood bulb does not allow the emitted spectrum to be shifted very far into the infrared. To make the method generally applicable, it would probably be better to use banks of glow bars in place of the photofloods, so that the longer wavelengths could be employed.

Finally, it will be noted that there is an apparent maximum value of the diffusivity measured in the 60°–100°C temperature range which seems to be due to the desorption of moisture. The effect of moisture upon the diffusivity of α-cellulose is uncertain and warrants further investigation.

Properties of p-Type GaAs Prepared by Copper Diffusion

F. D. Rosi, D. Meyerhofer, and R. V. Jensen
RCA Laboratories, Princeton, New Jersey
(Received December 10, 1959)

Purification of arsenic by hydrogen sublimation and gallium by vacuum annealing resulted in the preparation of high resistivity ($\sim 10^6$ ohm-cm), n-type GaAs crystals by the horizontal Bridgman technique. Conversion of this material to p-type was accomplished by the inward diffusion of copper from the crystal surface. Measurements of Hall mobility as a function of hole concentration in the range, 2×10^{16} cm^{-3} to 3×10^{17} cm^{-3}, at room temperature showed a dependence which is consistent with theory. The analysis suggests a lattice mobility for holes of 450 cm^2 V^{-1} sec^{-1} at 300°K. The mobility varied approximately as $T^{-2.3}$ in the range 76°–300°K. At the low temperatures the number of ionized impurities ranged from 2×10^{15} cm^{-3}. The energy levels associated with copper in GaAs are 0.023 ev and 0.15 ev above the valence band.

I. INTRODUCTION

VERY little data exist in the literature on the mobility of carriers in p-type GaAs, and much of that available is concerned with the highest value of mobility for a given carrier concentration. In measurements of mobility at room temperature and above, Folberth and Weiss[1] obtained an optimum value of 200 cm$^2V^{-1}$ sec^{-1} at room temperature. More recently, mobilities as high as 400 cm$^2V^{-1}$ sec^{-1} at 300°K were reported by both Whelan and Wheatley[2] and Jenny[3] for crystals with carrier concentrations in the range, 10^{16}–10^{17} cm^{-3}. However, in both cases the small temperature dependence of mobility below 300°K strongly suggested compensation of ionized impurities.

The most detailed measurements of mobility in p-type GaAs were first reported by Edmond, Broom, and Cunnell,[4] who measured Hall coefficient and conductivity from 140°K to 800°K. In their best material which was doped with zinc to a carrier concentration of $\sim 2.4\times10^{16}$ cm^{-3}, the hole mobility was 340 cm$^2V^{-1}$ sec^{-1} at room temperature and varied approximately as T^{-2} in the range 300°K to 500°K. A maximum value of 1000 cm$^2V^{-1}$ sec^{-1} was obtained at 140°K. The T^{-2} dependence was also observed by Whelan and Wheatley[2] above 300°K in a Cu-doped crystal with a room temperature hole concentration of 3×10^{16} cm^{-3}; a maximum value of 850 cm$^2V^{-1}$ sec^{-1} was obtained at $\sim$160°K.

In the course of purification experiments in the preparation of GaAs crystals for device applications, n-type crystals of high resistivity ($\sim 10^6$ ohm-cm) were obtained. The quality of this material could not be properly evaluated, since it was not possible to make reliable measurements of the Hall coefficient at such high resistivities. This difficulty was overcome by converting the high-resistivity, n-type material to low-resistivity, p-type material by the inward diffusion of copper from the crystal surface. By this technique it was possible through suitable heat treatments to obtain a wide range of carrier concentrations in samples taken from the same crystal. The present paper is concerned with measurements on the variation of hole mobility with both carrier concentration and temperature below 300°K in these Cu-diffused, p-type crystals of GaAs.

II. MATERIAL PREPARATION

A. Arsenic and Gallium Purification

High purity arsenic and gallium were used in the preparation of the compound GaAs. The arsenic was obtained from the American Smelting & Refining Company, and purified by first vacuum heating at 300–350°C to remove the arsenic trioxide surface film and then by sublimation through hydrogen at temperatures in the range of 500°–1000°C to remove sulfur in the form of gaseous H_2S. The resulting arsenic had less than 1 ppm of spectrographically detectable impurities.

The gallium was obtained from the Aluminum Company of America, and was further purified by high vacuum heat treatment. The procedure was to heat the gallium in a quartz boat to 650°C, and then anneal for a period of a week or more in a vacuum of better than 1×10^{-7} mm Hg. A water-cooled, quartz "finger" was placed approximately 2 cm above the gallium melt to serve as a trap for the volatile impurities. In a number of these vacuum treatments, spectrographic analysis of the condensate of the cold finger indicated effective removal of Zn, Cu, Mg, Ca, Pb, Ag, Fe, and Si from the Ga, as may be seen from the data in Table I. Moreover, residual resistivity measurements at 4°K on the gallium before and after treatment showed an improvement of more than a factor of 2 in the total impurity content.

B. Preparation of p-Type GaAs Crystals

The GaAs crystals were prepared by direct combination of the component elements in stoichiometric proportions by the horizontal Bridgman technique of gradual solidification from the melt. The furnace design used to produce the crystals is illustrated schematically

[1] O. G. Folberth and H. Weiss, Z. Naturforsch. **10a**, 615 (1955).
[2] J. M. Whelan and G. H. Wheatley, J. Phys. Chem. Solids 6, 169 (1958).
[3] D. A. Jenny, Proc. I.R.E. 46, 959 (1958).
[4] J. T. Edmond, R. F. Broom, and F. A. Cunnel, *Report of the Meeting on Semiconductors* (Physical Society, London, 1957), p. 109.

TABLE I. Removal of impurities from gallium by vacuum annealing at 650°C for seventeen days with cold finger.

Initial gallium (20 g)		Gallium collected on cold finger (0.10 g)	
Si	1 ppm	Si	100 ppm
Mg	10	Mg	100
Cu	1	Cu	200
Al	4	Al	30
	—	Pb	100
	16 ppm	Fe	100
		Sn	100
		Ni	30
		Mn	30
		Ca	30
		Ag	30
		Bi, Sb, B	1–10
			850 ppm

in Fig. 1. It consists of two wire-wound, tubular heaters placed along the reaction tube. The heater at the right is maintained about 20°C above the melting point of the compound (1240°C), and the other at the reservoir temperature of 600°C to maintain an arsenic pressure of 0.9 atmospheres.[5] This gives a temperature profile along the furnace as shown in the lower diagram of Fig. 1. The crystal is then grown by moving the entire furnace over the stationary quartz tube in the direction indicated by the arrow. To permit completely independent treatments of both the gallium and arsenic with no possible subsequent exposure to the air, the quartz reaction tube in Fig. 1 was separated into two sections by a thin quartz window. This window is broken only after the quartz tube is sealed off to permit reaction of the component elements to form the compound.

In growing the GaAs crystals by the Bridgman technique, the procedure was to bring the entire system up to the arsenic reservoir temperature of 600°C, and then to gradually raise the temperature of the reaction zone

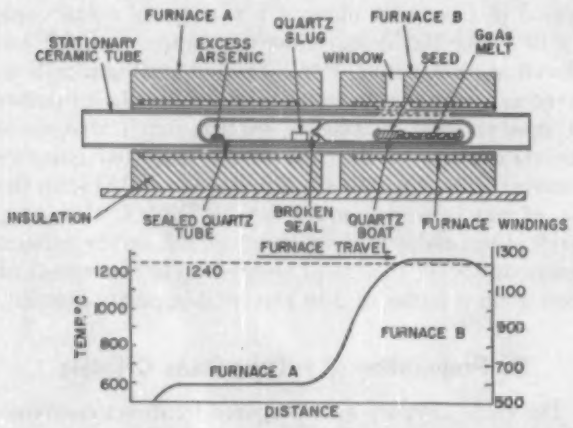

FIG. 1. Horizontal bridgman apparatus for growth of GaAs crystals, and temperature profile of furnace.

[5] J. V. D. Boomgaard and K. Schol, Philips Research Repts. 12, 127 (1957).

containing the molten gallium to 20°C above the melting point of the compound. The growth velocity was 0.5 cm hr^{-1}, and the temperature gradient in the vicinity of the solid-liquid interface was approximately 50°C cm^{-1}.

The major spectrographically detectable impurities in the GaAs crystals prepared, as described in the preceding, were Si and Mg in total amounts of 1 ppm, or less. Moreover, these crystals were always *n*-type and usually had a high electrical resistivity ($\sim 10^6$ ohm-cm). The high resistivity, which is caused by impurity compensation, was also associated with a low Si content estimated to be less than 0.5 ppm. Recent photoelectronic analyses by Bube[6] showed trap densities as low as 1×10^{16} cm^{-3} in these high-resistivity crystals.

To obtain *p*-type crystals, the high-resistivity, *n*-type material was converted to low-resistivity *p*-type crystals by the inward diffusion of copper from the crystal surface. In this procedure the sample, 1 mm×2 mm×10 mm, was first given a flash plating with copper by electrochemical means. It was then heated to temperatures between 600° to 1100°C for periods ranging from ½ to 16 hr, after which the specimen was quenched to room temperature. With this technique, *p*-type crystals were prepared with Hall concentrations varying between 10^{16} to 10^{17} cm^{-3}. The estimated solid solubility of copper in GaAs in the temperature range of these heat treatments was in close agreement with the recent work of Fuller and Whelan,[7] particularly at the lower temperatures. It is also noteworthy that Hall measurements indicated that the diffused copper was distributed quite uniformly throughout the specimens.

III. ELECTRICAL MEASUREMENTS

Measurements of Hall constant, R_H, and electrical resistivity, ρ, were made on a number of Cu-diffused, *p*-type single crystal samples of varying carrier concentration and over a wide temperature range. The number of holes per cm^3, p, was calculated from the Hall measurements using the standard equation,[8]

$$p=\mu_H/\mu_d\ 1/R_H e,$$

where the ratio of the Hall to drift mobility μ_H/μ_d for holes was assumed to be unity. Ohmic contacts to the samples were obtained by pressing indium dots on the crystal surface followed by a vacuum heat treatment between 300°–350°C for a short period of time.

A. Dependence of Mobility on Carrier Concentration

Figure 2 shows the variation of Hall mobility in GaAs with hole concentration in the range, 2×10^{16} cm^{-3} to

[6] R. H. Bube, J. Appl. Phys. 31, 315 (1960).
[7] C. S. Fuller and J. M. Whelan, J. Phys. Chem. Solids 6, 173 (1958).
[8] W. Shockley, *Electrons and Holes in Semiconductors* (D. Van Nostrand Company, Inc., Princeton, New Jersey, 1950).

3×10^{17} cm^{-3}, at room temperature. It may be seen that a strong dependence is obtained, and that the optimum mobility for these Cu-doped crystals is 370 cm$^2V^{-1}$ sec^{-1} corresponding to a hole concentration of 2.1×10^{16} cm^{-3}. Moreover, by assuming an effective mass ratio for holes $m_h^*/m_0=0.5$[4] and using the Brooks-Herring[9] expression for ionized impurity scattering, the data shown in Fig. 2 are in good agreement with theory if one assumes a lattice mobility for holes of 450 cm$^2V^{-1}$ sec^{-1}. The computed, theoretical curve is shown by the dashed line in Fig. 2. This general agreement of experimental data with theory and the strong temperature dependence of the mobility in these crystals, which will be discussed in the section to follow, strongly suggest that the hole concentration truly represents the total number of ionized impurities.

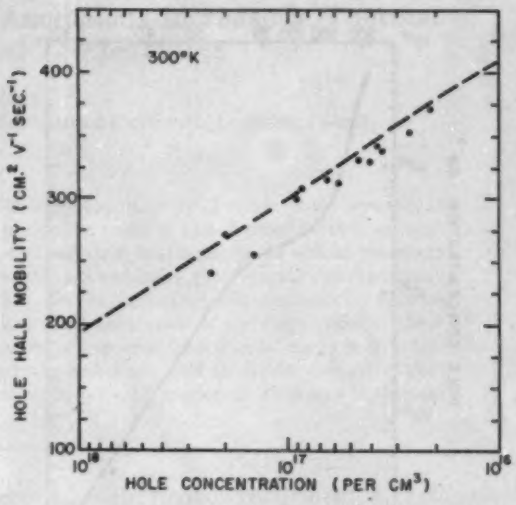

FIG. 2. Variation of Hall mobility with hole concentration in GaAs at 300°K. Dashed line indicates theoretical variation.

B. Dependence of Mobility on Temperature

Data on the mobility and carrier concentration at 300°K and 78°K in some Cu-diffused, p-type GaAs crystals are shown in Table II. It is apparent that in all crystals a marked increase in hole mobility is obtained at the lower temperature. The detailed variation of this temperature dependence in two samples of similar hole concentration at 300°K ($\sim4\times10^{16}$ cm^{-3}) is given in Fig. 3. The mobility of sample no. 16-3 has a stronger temperature dependence and is considerably larger at low temperatures than that of no. 11-2. This means that, at least at lower temperatures, crystal no. 16-3 has fewer ionized impurity scattering centers. In the very low temperature regions, where μ vs T has a positive slope, a rough calculation can be made to determine the number of ionized impurities. If ionized impurity scattering is assumed to be the only active scattering mechanism, then an upper limit for the number of scattering centers can be calculated. For $m_h^*/m_0=0.5$ the number of centers in sample no. 11-2 is calculated to be less than 4×10^{15} cm^{-3}.

TABLE II. Data on mobility and carrier concentration at 300°K and 78°K in p type GaAs.

Sample No.	300°K p, cc^{-1}	300°K μ_h, cm$^2V^{-1}$ sec^{-1}	78°K p, cc^{-1}	78°K μ_h, cm$^2V^{-1}$ sec^{-1}
GAJ 11-3	2.6×10^{16}	350	7.8×10^{15}	2460
GAJ 11-1	3.9×10^{16}	340	6.4×10^{14}	3050
GAJ 16-3	4.0×10^{16}	370	5.4×10^{14}	4290
GAJ 11-2	4.1×10^{16}	330	2.4×10^{15}	2900
GAJ 11-C-1	4.5×10^{16}	331	1.8×10^{15}	2390
GAJ 11-C-3	6.2×10^{16}	314	2.4×10^{15}	2180
GAJ 11-C-7	1.0×10^{17}	267	2.6×10^{15}	1820

It is necessary to know the hole concentrations p for a more detailed analysis of the impurity behavior. A curve of p against the reciprocal of absolute temperature, T, for sample no. 11-2 is shown in Fig. 4. The sample de-ionized very rapidly below 100°K, so that below this temperature p can be neglected compared to the impurity concentrations. Thus, the number of ionized impurities $N_I=2N_D$, where N_D is the number of donors; and $N_D<2\times10^{15}$ cm^{-3}. This substantiates the observation that the material acts as if it were uncompensated, since the number of acceptors must be larger than 4×10^{15} cm^{-3}.

It is now possible to analyze the mobility versus temperature curves using the measured values of hole concentration and $N_D=2\times10^{15}$ cm^{-3}. A good fit is obtained assuming only lattice and impurity scattering of the Brooks-Herring type.[9] The resulting values for lattice scattering and effective mass are

$$\mu_L=435(T/295°)^{-2.3}\ \text{cm}^2V^{-1}\ \text{sec}^{-1}$$

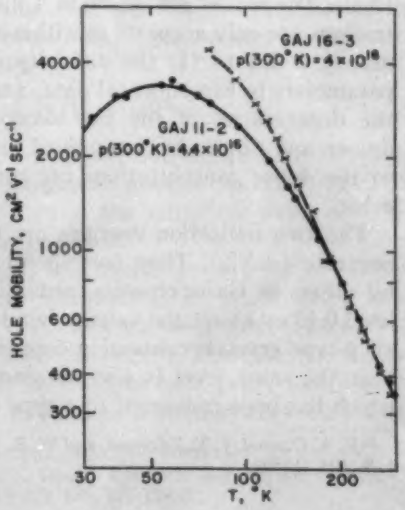

FIG. 3. Mobility vs temperature for two copper diffused, p-type GaAs crystals.

[9] H. Brooks and C. Herring, quoted by P. P. Debye and E. M. Conwell, Phys. Rev. 93, 693 (1954).

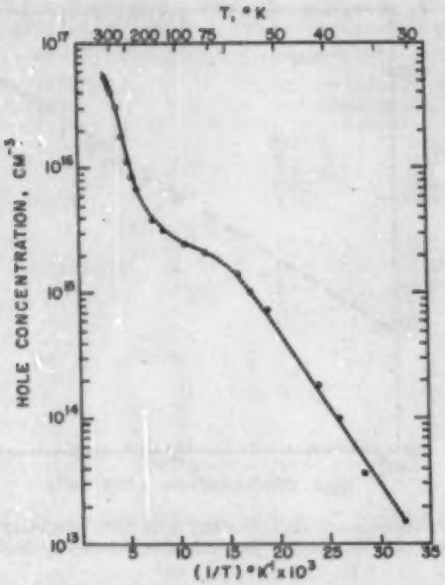

FIG. 4. Hole concentration vs reciprocal temperature of sample GAJ 11-2.

and

$$m^*/m_0=0.5.$$

The value of μ_L corresponds closely to that estimated from the data on carrier concentration (Fig.2). Using these values the number of donors in sample no. 16-3 is calculated to be less than 1×10^{15} cm^{-3}. Other p-type crystals were analyzed assuming the above values of μ_L and m^*/m_0 and gave consistent results.

C. Impurity Concentrations and Energy Levels

The concentrations of the electrically active impurity centers can be determined from the curves of p vs $1/T$ (Fig. 4). This will afford a check with the donor concentrations calculated from the mobility data. The curve of sample no. 11-2 in Fig. 4 can be fitted with Fermi statistics under the assumption of two active acceptor levels. The results are shown in Table III. The concentrations are only accurate to within a factor of approximately 5 due to (1) the difficulty of fitting so many parameters to experimental data, and (2) the fact that the degeneracies of the two acceptor levels are not known and cannot be determined unambigously. Even so the donor concentrations are consistent with each other.

The two ionization energies are considerably more accurate (±5%). They correspond to levels reported by others in GaAs crystals containing copper.[7,10] The level 0.15 ev above the valence band is found in almost all p-type crystals containing copper. It is noteworthy that the same level is also obtained in n-type GaAs which has been converted to p-type by heat-treatment

[10] F. A. Cunnel, J. T. Edmond, and W. R. Harding, SERL Tech. J. 9, 104 (1959).

TABLE III. Energy levels and impurity concentrations of crystal 11-2 calculated from hole concentration and mobility measurements.

Type of impurity	Concentration, cm^{-3}	Ionization energy, ev
Shallow acceptor	7×10^{15}	0.023
Deep acceptor	8×10^{15}	0.15
Donors	3×10^{15}	
Donors calculated from mobility	2×10^{15}	

above 600°C. This is in agreement with the recent work by Cunnell *et al.*[10] and strongly suggests that copper may be responsible for thermal conversion in GaAs.

The number of donors calculated in Table III includes shallow donors (which predominate in conventional, degenerate n-type GaAs) and any deep lying donors (more than 0.15 ev above the valence band). The presence of deep lying energy levels is very likely in view of the high resistivity of the starting material. The measurements by Bube[6] provided direct evidence for such levels. In crystal no.11 Bube obtained a concentration of 1×10^{16} cm^{-3} at a level 0.54 ev from one of the band edges, in addition to other levels at 0.2 ev or less. Since in the Cu-diffused materials there are less than 3×10^{15} cm^{-3} donors, one must conclude that either the 0.54-ev level has disappeared, or that it must be an acceptor level which is not active in p-type material. The former would, for example, be the case if some of the copper atoms were to form complexes with the existing impurity atoms and thereby neutralize them. In this connection, two recent observations are pertinent: (1) It has been shown that copper does have a strong association with the main donor in GaAs, since it has been possible to controllably compensate low-resistivity n-type GaAs to high-resistivity n- or p-type material (10^6 ohm-cm) by copper diffusion. In one crystal, compensated in this manner, a definite indication was obtained by photoconductivity measurements[11] of a marked decrease in trap density. (2) p-type GaAs crystals prepared by doping with zinc and cadmium did not yield as large values of carrier mobility for a given concentration, nor the $T^{-2.3}$ dependence below 300°K as did the Cu-diffused, p-type crystals.

IV. ACKNOWLEDGMENT

The authors would like to express their appreciation to Dr. L. R. Weisberg for his assistance in the design of the crystal growth apparatus and the residual resistivity measurements on gallium, and to Mr. H. H. Whitaker for the spectrographic analyses.

The research reported in this paper has been sponsored by the Electronics Research Directorate of the Air Force Cambridge Research Center, Air Research and Development Command, under a contract.

[11] R. H. Bube, private communication (September, 1959).

JOURNAL OF APPLIED PHYSICS VOLUME 31, NUMBER 6 JUNE, 1960

Excitation Processes in Ceramics and Anomalous Increase in Thermal Conductivity at Elevated Temperatures

D. H. WHITMORE
Department of Metallurgy and Materials Science, Northwestern University, Evanston, Illinois
(Received February 25, 1960)

The problem of the anomalous increase in the observed thermal conductivity of single-phase ceramics at high temperatures has been considered. At temperatures above the onset of this anomalous rise, account has been taken of the possibility that phonon, electronic, and radiative heat transfer, as well as transport of thermal energy by electron-hole pairs, excitons, and dissociated gas molecules, may operate simultaneously and individually contribute significantly to the total heat flow. On the basis of reliable conductivity data on nonporous monocrystals of single-phase ceramics, estimations have been made of the magnitudes of these high-temperature components which reveal that excited states of low excitation energy may occur in certain ceramics. In these instances, such excited energy-carrying states are able to diffuse down the temperature gradient in the specimen thereby producing a non-negligible contribution to its observed thermal conductivity.

I. INTRODUCTION

FOR a number of years a controversy has been waging among solid state physicists regarding the increase in thermal conductivity observed in a number of semiconductors at high temperatures. Since this increase is obviously not attributable to phonon transport which obeys a $1/T$ law, attempts have been made to account for it on the basis of ambipolar transport of gap energy by electron-hole pairs,[1,2] internal radiation,[3] and various other excitation mechanisms.[4]

The existence of a similar, anomalous rise in the high-temperature, thermal conductivity of some single-phase ceramics has been clearly demonstrated by the careful measurements of Charvat and Kingery.[5] The present paper attempts to rationalize this behavior in ceramics by considering the observed conductivity as some linear combination of phonon and electronic components, a radiative heat transfer component, and components resulting from certain excitation processes. In particular, the contribution to the observed conductivity from radiative transfer is considered to be too small to fit the observed deviations from a $1/T$ law in the case of single crystalline TiO_2, CaF_2, and Al_2O_3. Thus, in such cases, consideration must be given to components of the observed thermal conductivity arising from simple excitation processes occurring in the crystal at elevated temperatures.

II. THE MODEL

At temperatures above the onset of its anomalous rise, it is assumed that the observed thermal conductivity, k_{obs}, of the ceramic may in general be written

$$k_{obs}=k_{ph}+k_{el}+k_r+k_{ex}, \tag{1}$$

where k_{ph} is the phonon component, k_{el} is the electronic component, k_r is the component caused by radiative heat transport, and k_{ex} is the sum of components resulting from certain excitation processes.

It is further assumed that the phonon component obeys the usual $1/T$ law for an ideal dielectric predicted by Peierls,[6] and that, below the onset of the anomalous increase in observed conductivity, this is the predominate mechanism. Thus, the phonon component at high temperatures may be evaluated by extrapolation of the low-temperature k_{obs} data according to a $1/T$ law.

The electronic contribution, k_{el}, to the observed thermal conductivity is given by the well-known Wiedemann-Franz law. Thus,

$$k_{el}=S(k/e)^2T\sigma, \tag{2}$$

where k is the Boltzmann constant, e is the electronic charge, T is the absolute temperature, σ is the electrical conductivity, and S is a factor which depends on the degree of degeneracy and the type of scattering of the carriers. For a Boltzmann distribution and thermal scattering $S=2$, and for degeneracy $S=\pi^2/3$.

Assuming that the crystal is optically isotropic and that the absorption coefficient is independent of the wavelength, the radiation component may be computed from the expression[7,8]

$$k_r=(16/3)(bT^3n^2/\alpha), \tag{3}$$

where α is the optical absorption constant for the wavelength corresponding to the peak of blackbody radiation at temperature T, n is the refractive index and b is Stefan's radiation constant.

The component, k_{ex}, results from a major class of heat transporting mechanisms in which there is an excitation energy, E, between the ground state and the first excited states of the system. These include thermal energy transport by electron-hole pairs, excitons and dissociated gas molecules. Assuming that all energy-

[1] H. Frohlich and C. Kittel, Physica **20**, 1086 (1954).
[2] P. J. Price, Phil. Mag. **46**, 1252 (1955); Phys. Rev. **95**, 596A (1954).
[3] E. D. Devyatkova, B. Ya. Moizhes, and I. A. Smirnov, Soviet Phys.—Solid State **1**, 555 (1955).
[4] A. F. Joffe, Can. J. Phys. **34**, 1342 (1956); J. Phys. Chem. Solids **8**, 6 (1959).
[5] F. R. Charvat and W. D. Kingery, J. Am. Ceram. Soc. **40**, 306 (1957).
[6] R. Peierls, Ann. Physik **3**, 1055 (1929).
[7] M. Czerny and L. Gerzel, Glastech. Ber. **25**, 387 (1952).
[8] L. Genzel, Z. Physik **135**, 177 (1953).

carrying states, g in number, are at energy level E above the ground state and that $E/kT \gg 1$, then according to Krumhansl[9] k_{ex} is given by

$$k_{ex} = k\ell v(E/kT)^2 g^2 \exp(-E/kT), \qquad (4)$$

where ℓ is a characteristic length for damping out temperature differences, v is the velocity of transport of these excited energy states, and k is the Boltzmann constant. A similar result has been rigorously derived by Pikus[10] for the case of an exciton mechanism and by Price[2] for an ambipolar mechanism. Depending upon the particular circumstance, the excitation energy, E, may be the gap, exciton, dissociation or ionization energy; the values of ℓ and v must be appropriately chosen for the particular case considered.

It should be remarked that the present model of elevated-temperature, heat transfer mechanisms in ceramics bears a resemblance to an earlier one proposed by Jamieson and Lawson[11] to explain the deviations of the observed conductivity data for porous ceramics from a $1/T$ law. However, their arguments are completely unconvincing for the case of porous ceramics because, if the sum $(k_{ph}+k_r)$ is deducted from $k_{obs}/(1-P)$ the result will be $k_{ex}+P\bar{k}/(1-P)$[12] and not, as claimed, just k_{ex}. In point of fact, if thermal conductivity data for nonporous, monocrystalline Al_2O_3[5] is treated by the method discussed in the present paper, k_{ex} values are larger by a factor of about ten than corresponding ones calculated by Jamieson and Lawson; moreover, the activation energy for the excitation contribution to the total heat flux in Al_2O_3 predicted by the present analysis (0.25 ev) is very much smaller than theirs (1.42 ev).

TABLE I. Calculated values of the radiation and excitation components of the total thermal conductivity of TiO_2, CaF_2, and Al_2O_3.

Temperature (°K)	$\Delta k \times 10^3$ (cal sec^{-1} deg^{-1} cm^{-1})	$k_r \times 10^3$ (cal sec^{-1} deg^{-1} cm^{-1}) $\alpha=10$ cm^{-1}	$\alpha=100$ cm^{-1}	$k_{ex} \times 10^3$ (cal sec^{-1} deg^{-1} cm^{-1}) $\alpha=10$ cm^{-1}	$\alpha=100$ cm^{-1}
		TiO_2			
573	1.14	0.79	0.08	0.35	1.06
673	2.00	1.29	0.13	0.71	1.87
773	3.14	1.94	0.19	1.20	2.95
873	4.38	2.80	0.28	1.58	4.10
973	5.65	3.88	0.39	1.77	5.26
1073	7.15	5.67	0.57	1.95	6.95
		CaF_2			
573	0.11	0.28	0.03		0.08
673	0.40	0.46	0.05		0.35
773	0.68	0.69	0.07		0.61
873	1.02	0.99	0.10		0.92
973	1.65	1.38	0.14		1.51
		Al_2O_3			
773	1.10	1.04	0.10		1.00
873	1.73	1.47	0.15		1.58
973	2.31	2.04	0.20		2.21
1073	2.60	2.72	0.27		2.33
1173	3.18	3.56	0.36		2.82
1273	4.05	4.55	0.46		3.59
1373	5.32	5.70	0.57		4.75
1473	7.11	7.05	0.71		6.40

[9] J. A. Krumhansl, J. Phys. Chem. Solids **8**, 343 (1959).
[10] G. E. Pikus, Zhur. Tekh. Fiz. **26**, 36 (1959); Soviet Phys.—Tech. Phys. **1**, 32 (1957).
[11] J. C. Jamieson and A. W. Lawson, J. Appl. Phys. **29**, 1313 (1958).
[12] Here $\bar{k}$ is an effective thermal conductivity for a heterogeneous region containing both solid and pores. The magnitude of this conductivity term at high temperatures is such that it can seldom be neglected. See A. L. Loeb, J. Am. Ceram. Soc. **37**, 96 (1954) and J. Francl and W. D. Kingery, J. Am. Ceram. Soc. **37**, 99 (1954).

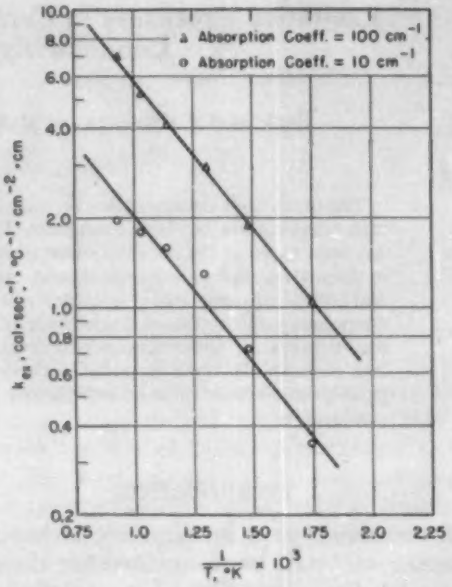

FIG. 1. Variation of the excitation component of the total heat flux in TiO_2 with temperature. (Experimental data from Charvat and Kingery.[5])

As Herring[13] has suggested, unless exciton transport in a crystal has a very much lower activation energy than an ambipolar mechanism, it could not make a contribution of comparable magnitude to the ambipolar mechanism because of its less favorable statistical factor arising from the much smaller number of momentum states accessible to the exciton. Indeed, if the rather large activation energies predicted by Jamieson and Lawson[11] for Al_2O_3 (1.42 ev) and MgO (1.35 ev) were correct, exciton transport would appear to be a remote possibility in these cases.

III. COMPARISON WITH EXPERIMENT

The procedure employed in evaluating the Δk data listed in Table I for single crystalline TiO_2, CaF_2, and Al_2O_3 is to extrapolate the low-temperature conductivity data of Charvat and Kingery[5] to temperatures above the onset of the anomalous rise by means of a $1/T$ law and to take the difference between the observed conductivity and this extrapolated conductivity which represents the phonon component. Thus, according to Eq. (1), Δk represents the sum of k_{el}, k_r, and k_{ex}.

Values of the radiative heat transfer component given in Table I are computed with the aid of Eq. (3), using as a value of the absorption constant either 100 cm^{-1} (Al_2O_3 and CaF_2) or both 10 and 100 cm^{-1} (TiO_2). There

[13] C. Herring, J. Phys. Chem. Solids **8**, 543 (1959).

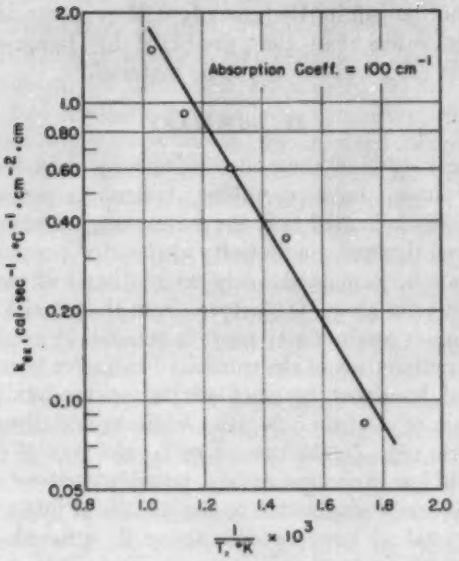

FIG. 2. Temperature dependence of the excitation component of the total heat flux in CaF_2. (Data taken from Charvat and Kingery.[5])

is obviously some arbitrariness in the choice of these values, but it is believed that they bracket the range[14] for this parameter over the temperature range involved.[15]

The k_{el} values for TiO_2 may be evaluated by means of Eq. (2), the electrical conductivity data of Cronemeyer[16] for intrinsic rutile and assuming thermal scattering and non-degeneracy so that the parameter S in Eq. (2) takes on the value two. As expected, the magnitude of this component is so small for stoichiometric TiO_2 ($k_{el}=3.6\times10^{-8}$ cal sec^{-1} °C^{-1} cm^{-1} at 1000°K) that it contributes negligibly to the observed thermal conductivity at all temperatures of interest. However, even though k_{el} is negligibly small for intrinsic TiO_2, this will certainly not always be true; as a matter of fact, it is reasonable to expect that the electronic component might be significant in reduced rutile which is a degenerate semiconductor.

It is apparent from the foregoing discussion that deducting the radiative component from each Δk value listed in Table I results in k_{ex}. According to Eq. (4), the slope of a plot of $\ln k_{ex}$ vs $1/T$ should be $-E/k$ where E is the activation energy of the excitation transport process operating. Figure 1 represents such a plot for TiO_2 with the activation energy computed from the slopes being 0.20 ev for both $\alpha=10$ and 100 cm^{-1}.

It is easy to demonstrate that the diffusion of electron-hole pairs in intrinsic TiO_2 will result in contributions to k_{obs} of such small magnitude that this mechanism can be ruled out as being important in this case. This ambipolar contribution may be evaluated by an expression due to Price[2]

$$k_{amb}=\left(\frac{k}{e}\right)^2 T\frac{\sigma_n\sigma_p}{\sigma}\left[\frac{E_G}{kT}+4\right]^2, \qquad (5)$$

where E_G is the gap energy and σ_n, σ_p are the electrical conductivities of electrons and holes, respectively. A detailed knowledge of the position of the Fermi level and the density of states is needed in order to calculate the dependence of k_{amb} on σ. Fortunately, however, in the present case where TiO_2 is assumed to be intrinsic, Eq. (5) can be simplified to

$$k_{amb}=(k/e)^2T\sigma\left[2+c+\frac{1}{c}\right]^{-1}\left[\frac{E_G}{kT}+4\right]^2, \qquad (6)$$

where c is the ratio of the mobility of electrons to that of holes and σ is the electrical conductivity. A value of 4.7×10^{-6} cal sec^{-1} deg^{-1} cm^{-1} was computed for k_{amb} at 1000°K by assuming $c=2$ and utilizing Cronemeyer's data for E_G and σ. Thus, it is clear, not only from the small magnitude of k_{amb} but also from the excitation energy of about 3 ev required for this ambipolar mechanism, that this process is unimportant in the present instance where an energy of about 0.2 ev has been predicted for the excitation process from thermal conductivity data.

It is probably fortuitous that a 0.2-ev activation energy for the ionization of singly ionized oxygen ion vacancies was likewise observed by Breckenridge and Hosler[17] on reduced rutile. It is unlikely that this mechanism would be significant in intrinsic TiO_2, but it might become important in reduced material. Since it must be assumed, from the manner in which they conducted their experiments, that Charvat and Kingery[5]

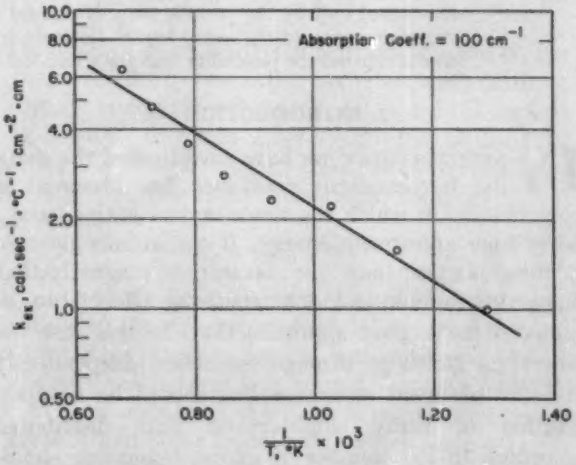

FIG. 3. Variation of the excitation component of the total heat flux in Al_2O_3 with temperature. (Data from Charvat and Kingery.[5])

[14] S. P. Clark, Trans. Am. Geophys. Union 38, 931 (1957).

[15] For instance, if one chooses $\alpha=1$ cm^{-1} as the lower limit for the range of the absorption coefficient in TiO_2, as has been suggested for well-annealed single crystals, the radiation component assumes values much larger than the corresponding Δk values.

[16] D. C. Cronemeyer, Phys. Rev. 87, 876 (1952).

[17] R. C. Breckenridge and W. R. Hosler, Phys. Rev. 91, 793 (1953).

measured the thermal conductivity of intrinsic TiO_2, the enhanced conductivity, k_{ex}, cannot be ascribed to such an ionization process. Moreover, it is not possible, on the basis of our present understanding of excitation processes in rutile, to designate unambiguously the predominate operating excitation mechanism; although, on the basis of the predicted low activation energy, it is attractive to postulate that exciton diffusion may occur. It is noteworthy that the enhanced conductivity of PbTe at elevated temperatures has been attributed by Joffe[4] to the diffusion of unidentified, energy-carrying states of comparably low excitation energy.

Thermal conductivity data[5] on CaF_2 and Al_2O_3 have also been analyzed on the same basis as the TiO_2 data and the results are shown in Figs. 2 and 3. The calculated activation energy for the excitation mechanism operating in the case of CaF_2 is only 0.34 ev by comparison with a gap energy of about 1 ev.[18] As mentioned earlier, the activation energy calculated for the excitation mechanism in Al_2O_3 is only 0.25 ev, a considerably smaller value than that predicted by Jamieson and Lawson (1.42 ev) for the same material.[11]

[18] R. W. Ure, J. Chem. Phys. **26**, 1363 (1957).

IV. SUMMARY

A reanalysis of thermal conductivity data for some single-phase, monocrystalline ceramics, particularly rutile, has indicated that the anomalous increase in the observed thermal conductivity at elevated temperatures may not be explained solely on the basis of radiative heat transfer alone. Departures from the usual $1/T$ law for phonon conductivity may, in general, be ascribed to some combination of electronic and radiative heat transfer and transport by such excitation mechanisms as diffusion of electron-hole pairs, excitons and dissociated gas molecules. In the case of rutile, the flow of excited states of low excitation energy, possibly excitons, makes a significant contribution to the total heat flux through the crystal at temperatures above its anomalous rise in thermal conductivity.

JOURNAL OF APPLIED PHYSICS VOLUME 31, NUMBER 6 JUNE, 1960

Ferromagnetic Resonance in Polycrystalline Ferrites Using Circularly Polarized Radiation

R. J. Zeender and E. Schlömann
Research Division, Raytheon Company, Waltham, Massachusetts

(Received January 15, 1960)

If the saturation magnetization is much smaller than the anisotropy field, the resonance curves observed in polycrystalline ferrites have a well-defined structure with several peaks or shoulders. (See works cited in footnotes 1 and 2.) The use of circularly polarized radiation facilitates a clear identification of the peaks. In cubic materials the central peak (arising from grains which have a [110] direction aligned with the dc field) is partially excited by both senses of circular polarization, whereas the two outer peaks or shoulders are excited only by the positive sense of circular polarization. Experimental results obtained in the compensation region of the nickel ferrite-aluminate system agree well with the theoretical predictions. These results rule out the possibility that the additional absorption peaks are due to an exchange resonance.

1. INTRODUCTION

In a previous paper[1] we have investigated the shape of the ferromagnetic resonance line observed in polycrystals, in which the single-crystal grains have a fairly high anisotropy energy. If the anisotropy field is much larger than the saturation magnetization, dipole interaction and demagnetizing effects can be neglected to a good approximation. In this case the individual grains go through resonance independently and the observed resonance line should be a superposition of many single-crystal lines distributed according to the number of grains resonating simultaneously for a given range of applied field. The theory shows that under these conditions the resonance line should exhibit a well-defined structure with several peaks.[2] These peaks are associated with grains which have an easy, an intermediate, or a hard axis aligned with the magnetic field. The theoretical predictions have been confirmed experimentally by our previous work on nickel ferrite-aluminates and the work of Schlömann and Jones[3] on various ferrites with hexagonal crystal structure.

Measurements carried out by other investigators on polycrystalline lithium ferrite-chromite and various garnets have also shown additional absorption peaks[4–8]

[1] E. Schlömann and J. R. Zeender, J. Appl. Phys. **29**, 341 (1958).

[2] E. Schlömann, J. Phys. Chem. Solids **6**, 257 (1958); J. phys. radium **20**, 327 (1959).
[3] E. Schlömann and R. V. Jones, J. Appl. Phys. **30**, 177S (1959).
[4] T. R. McGuire, Phys. Rev. **97**, 831 (1955).
[5] J. Paulevé and B. Dreyfus, Compt. rend. **242**, 1273 (1956).
[6] J. Paulevé, Compt. rend. **244**, 1908 (1957); **245**, 1604 (1957); J. Appl. Phys. **29**, 259 (1958).
[7] J. Paulevé, Arch. Sci. (Geneva) **9**, 109 (1956).
[8] J. Paulevé, B. Dreyfus, and M. Soutif, J. phys. radium **20**, 335 (1959).

similar to those observed in our experiments on nickel ferrite-aluminates. In these cases the presence of an additional absorption peak has been attributed to the excitation of the exchange resonance. It has been shown by Wangsness[9] that the frequency of this resonance will usually lie in the infrared range, but that it should come down into the microwave range in the vicinity of a magnetic compensation point.[10–12]

If the experiment is performed with linearly polarized radiation, it is quite difficult to determine conclusively whether the additional absorption peak is due to the excitation of the exchange resonance or to the presence of a large anisotropy field. In the vicinity of a magnetic compensation point, both mechanisms can be important. The influence of crystalline anisotropy on the resonance will generally become more pronounced in the vicinity of a magnetic compensation point because the effective anisotropy field becomes very large under those conditions. The use of circularly polarized radiation makes it possible to determine which of the two mechanisms that can give rise to an additional absorption peak is responsible in any given case. It has been shown by Dreyfus[10] that the exchange resonance is excited by the "negative" sense of circular polarization, i.e., the sense opposite to that which excites the usual ferromagnetic resonance. Measurements by Paulevé[5–8] have shown that this is, in fact, the case in $Li_{0.5}FeCr_{1.5}O_4$.

On the other hand, if the additional absorption peak is caused by a large anisotropy field in conjunction with the polycrystalline character of the sample, the following predictions can be made:

1. All the peaks should be excited by the positive sense of circular polarization.
2. With the negative sense one should observe an absorption only for the peak associated with crystallites magnetized along the [110] axis. The reason is that in this case the precessing magnetization vector follows an elliptical rather than a circular cone.

Our experimental results obtained with circularly polarized radiation on polycrystalline nickel ferrite-aluminate confirm these predictions.

In Sec. 2 a theoretical estimate of the ratio of the two circular susceptibilities will be given. The calculation assumes that the sample is a polycrystal with a comparatively large anisotropy field and cubic lattice structure. In Sec. 3 we shall describe the preparation of the samples and the method of measurement. In Sec. 4 the experimental results are compared with the theoretical predictions.

[9] R. K. Wangsness, Phys. Rev. **97**, 831 (1955); Am. J. Phys. **24**, 60 (1956).
[10] B. Dreyfus, Compt. rend. **241**, 552, 1270 (1955).
[11] S. Geschwind and L. R. Walker, J. Appl. Phys. **30**, 163S (1959).
[12] E. Schlömann, *Symposium on Solid State Physics in Electronics and Telecommunications Brussels, 1958* (to be published).

2. THEORY

The experiments described in the following were performed using ferrimagnetic materials with saturation magnetizations ($4\pi M$) of approximately 300 gauss or lower. Under these conditions it is reasonable to neglect by way of approximation the dipolar interaction and also the macroscopic demagnetizing effects. The single-crystal grains of the sample go through resonance essentially independently and the resonance curve of a polycrystalline sample is a superposition of many single-crystal resonance curves each corresponding to a different grain.

Consider now a representative grain and the motion of its magnetization vector. Let $\boldsymbol{\alpha}$ be a unit vector pointing in the direction of the magnetization vector. Similarly let $E(\boldsymbol{\alpha})$ be the energy per unit volume associated with a given direction of the magnetization vector. In our case $E(\boldsymbol{\alpha})$ comprises the Zeeman energy and the crystalline anisotropy energy. For convenience, the coordinate system is fixed in such a way that the α_z axis corresponds to the minimum energy. For small deviations from the equilibrium direction, $E(\boldsymbol{\alpha})$ will then be a second-order form of α_x and α_y. The equations of motion for the magnetization vector are (again for small α_x, α_y)

$$\dot{\alpha}_x = -(\gamma/M)(\partial E/\partial \alpha_y) \tag{1a}$$

$$\dot{\alpha}_y = (\gamma/M)(\partial E/\partial \alpha_x), \tag{1b}$$

where γ is the gyromagnetic ratio (here assumed positive for electrons). Without loss of generality we may choose the directions of the x and y axes in such a way that the bilinear term in $E(\boldsymbol{\alpha})$ (proportional to $\alpha_x\alpha_y$) vanishes. The equations of motion in the presence of a driving field $\mathbf{h}(t)$ are then

$$\begin{aligned} \dot{\alpha}_x &= -\gamma(A\alpha_y - h_y) \\ \dot{\alpha}_y &= \gamma(B\alpha_x - h_x). \end{aligned} \tag{2}$$

In the absence of crystalline anisotropy $A=B=H$, the dc magnetic field. For cubic materials with a finite anisotropy energy, $A=B$ only if the dc field is applied along a [100] direction ($A=B=H-H_a$) or a [111] direction ($A=B=H+\frac{4}{3}H_a$). Here we have assumed that only the first-order anisotropy constant K_1 is nonzero and

$$H_a = -2K_1/M \tag{3}$$

is the anisotropy field. The use of a minus sign in the definition of the anisotropy field is suggested by the fact that K_1 is negative for the materials investigated in this paper as it is, in fact, in most cases of interest. For the later discussion, it will be of particular interest to know A and B for those grains which have a [110] axis aligned with the dc field. A simple calculation shows that, in this case,

$$\begin{aligned} A &= H + H_a \\ B &= H - \tfrac{1}{2}H_a. \end{aligned} \tag{4}$$

(The roles of A and B are interchanged if the coordinate system is rotated by 90 deg around the z axis.)

It can be seen from Eq. (1) that the energy E is constant during the motion of the magnetization vector provided that E is not explicitly time dependent (no rf magnetic field applied). This implies that the precessing magnetization vector follows an ellipsoidal cone if A is not equal to B. It is, therefore, very plausible that the resonance is partially excited by both senses of circular polarizations.

For convenience, Eq. (2) may be expressed in terms of the complex variables

$$\begin{aligned} \alpha &= \alpha_x + i\alpha_y \\ h &= h_x + ih_y. \end{aligned} \tag{5}$$

A simple calculation shows that the equation of motion is now

$$\dot{\alpha} = i\gamma[\tfrac{1}{2}(A+B)\alpha - \tfrac{1}{2}(A-B)\alpha^* - h], \tag{6}$$

where the asterisk denotes the complex conjugate. The real and imaginary parts of Eq. (6) are identical with Eqs. (2). Assume now that the rf magnetic field is circularly polarized, i.e., $h=|h|e^{i\omega t}$. The stationary solution of Eq. (6) is then of the form

$$\alpha = ae^{i\omega t} + be^{-i\omega t}, \tag{7}$$

where a and b are constants. Physically, Eq. (7) means that the precessional motion may be split into one component rotating in the same sense as the rf magnetic field and a counter-rotating component. The precessing magnetization vector thus follows an ellipsoidal cone.

By inserting Eq. (7) into Eq. (6) and separating terms with equal time dependence, one obtains

$$\begin{aligned} [\tfrac{1}{2}(A+B) - \omega/\gamma]a - \tfrac{1}{2}(A-B)b^* &= |h| \\ \tfrac{1}{2}(A-B)a - [\tfrac{1}{2}(A+B) + \omega/\gamma]b^* &= 0, \end{aligned} \tag{8}$$

and eliminating the counter-rotating component b^*,

$$\{[AB - (\omega/\gamma)^2]/[\tfrac{1}{2}(A+B) + \omega/\gamma]\}a = |h|. \tag{9}$$

The circular susceptibility (for the positive sense of polarization) is the ratio of the rf magnetic moment rotating in the same sense as the driving field to the rf magnetic field:

$$\chi_+ = Ma/|h|. \tag{10}$$

Its dependence on the frequency is easily obtained from Eqs. (10) and (9). It should be remembered that a circularly polarized rf magnetic field induces also a counter-rotating component of the rf magnetization in each grain. In the average magnetization of a sample containing many single-crystal grains, however, the counter-rotating components of differently oriented grains cancel each other.

The circular susceptibility for the negative sense of polarization can be obtained from the previous results by reversing the sign of the frequency:

$$\chi_-(\omega) = \chi_+^*(-\omega). \tag{11}$$

In the preceding calculation of $\chi_+(\omega)$ we have not explicitly considered losses. The susceptibility is, therefore, real in the present approximation and the asterisk in Eq. (11) could be omitted without changing the equation. In general, however, for a lossy material the asterisk is necessary.

The ratio of the two circular susceptibilities is, according to Eqs. (9)–(11),

$$\chi_-/\chi_+ = [\tfrac{1}{2}(A+B) - \omega/\gamma]/[\tfrac{1}{2}(A+B) + \omega/\gamma]. \tag{12}$$

This equation was derived on the basis of the lossless equations of motion. It may be expected that, if losses are included, a similar relation is valid for the imaginary part of the susceptibility at resonance. We will now sketch a straightforward calculation which shows that this is indeed the case.

Losses are taken into account by adding a phenomenological damping term to the equations of motion (1). We thus add $-(\lambda/M)(\partial E/\partial\alpha_x)$ to the right-hand side of Eq. (1a) and $-(\lambda/M)(\partial E/\partial\alpha_y)$ to the right-hand side of Eq. (1b). Here λ is a phenomenological loss parameter related to the linewidth of the individual grains. The previously described calculation can easily be repeated starting from the more general equations of motion. The ratio of the imaginary parts of the two circular susceptibilities at resonance $[\omega^2 = (\gamma^2+\lambda^2)AB]$ is found to be

$$\left.\frac{\chi_-''}{\chi_+''}\right|_{\text{res}} = \frac{\tfrac{1}{2}(A+B) - \gamma\omega/(\gamma^2+\lambda^2)}{\tfrac{1}{2}(A+B) + \gamma\omega/(\gamma^2+\lambda^2)}. \tag{13}$$

We now make use of the fact that at resonance

$$\begin{aligned} A+B &= [(A-B)^2 + 4AB]^{\frac{1}{2}} \\ &= 2\omega(\gamma^2+\lambda^2)^{-\frac{1}{2}}[1 + (A-B)^2/4AB]^{\frac{1}{2}}. \end{aligned} \tag{14}$$

Thus, from Eqs. (13) and (14),

$$\left.\frac{\chi_-''}{\chi_+''}\right|_{\text{res}} = \frac{\{[1+(\lambda/\gamma)^2][1+(A-B)^2/4AB]\}^{\frac{1}{2}} - 1}{\{[1+(\lambda/\gamma)^2][1+(A-B)^2/4AB]\}^{\frac{1}{2}} + 1}. \tag{15}$$

This equation shows that the relative magnitude of the absorption in a negatively polarized field increases with increasing damping and increasing ellipticity of the precessional motion. The ratio of the two correction terms $(\lambda/\gamma)^2$ and $(A-B)^2/4AB$ is essentially equal to the square of the ratio of the single-crystal linewidth and the anisotropy field. This ratio is probably very small under the conditions of the present experiment and the contribution of the damping forces to χ_-''/χ_+'' is therefore neglected by way of approximation. We then obtain for grains which have a [110] direction

aligned with the dc field according to Eqs. (4) and (15),

$$\left.\frac{\chi_-''}{\chi_+''}\right|_{\substack{\text{res}\\[110]}} = \frac{(1+\frac{9}{16}k^2)^{\frac{1}{2}}-1}{(1+\frac{9}{16}k^2)^{\frac{1}{2}}+1}, \tag{16}$$

where

$$k=\gamma H_a/\omega \tag{17}$$

is a dimensionless parameter which characterizes the strength of the anisotropy.

Equation (16) is strictly applicable for a polycrystalline material in which all grains are oriented in such a way that their [110] axes are aligned with the dc magnetic field. In practice, the grains usually do not have a preferred orientation. The width of the resonance curve of a polycrystal is then, under the present conditions, proportional to the anisotropy field. Grains with different orientations contribute preferentially to different parts of the resonance curve. It was shown previously[1,2] that the central peak of the resonance curve is due to grains which have their [110] axes aligned with the dc field. We thus expect that this peak is partially excited by the negative sense of circular polarization. The ratio of the two circular susceptibilities should be given by Eq. (16) if the individual resonances were very sharp. The fact that the individual grains have a finite linewidth will reduce χ'' more strongly for the negative than for the positive sense of circular polarization. For this reason Eq. (16) should be regarded as a theoretical limit. The experimental values of χ_-''/χ_+'' may be expected to be smaller than those predicted by this equation.

3. PREPARATION OF THE SAMPLES AND METHOD OF MEASUREMENT

Nine compositions of general formula $NiAl_tFe_{2-t}O_4$, with t ranging between 0.6 and 1.0, were prepared from oxides following standard ceramic techniques. They were fired at 1400°C for 20 hours and then slowly cooled at the rate of 8.33°C/hr (200°C/day). At every 200°C step some samples were quenched to room temperature and this process was continued down to 25°C. Small samples of spherical shape were placed in a cylindrical, degenerate TE_{111} reaction cavity. A circularly polarized mode was excited by a technique similar to that described by Paulevé.[7] The cavity resonance was at 10 000 Mc. For the evaluation of the results it was important to have the complete absorption curves. For this purpose a technique was designed allowing continuous measurements. The microwave source was a frequency-modulated klystron, and the klystron mode was eliminated with a bridge arrangement. Figure 1 shows a schematic diagram of the experimental apparatus.

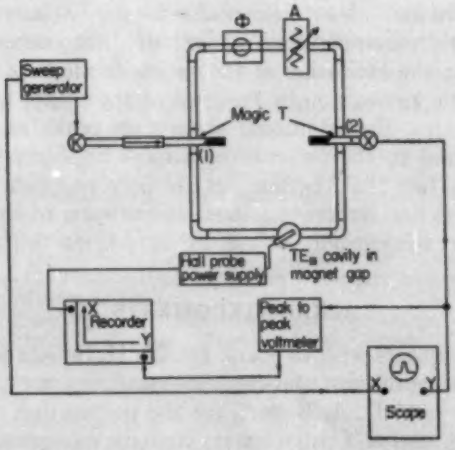

FIG. 1. Schematic diagram of the experimental apparatus. The bridge is adjusted off resonance with attenuator A and phaseshifter Φ for zero output at the difference arm of the magic T(2).

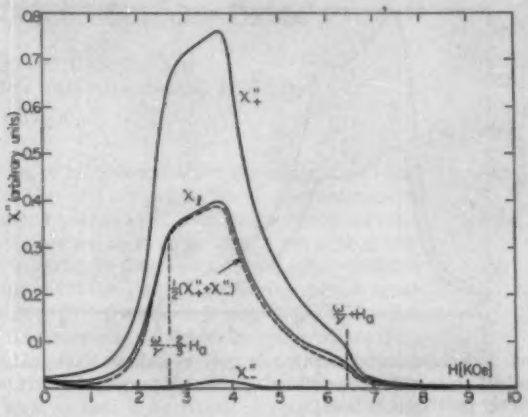

Fig. 2. Resonance absorption in polycrystalline $NiFe_{1.3}Al_{0.7}O_4$ quenched from 1025°C measured at 10 kMc using linearly and circularly polarized radiation.

4. EXPERIMENTAL RESULTS

It has been known since the work of Maxwell and Pickart[13] and Gorter[14] that the substitution of iron by aluminum in nickel ferrite reduces the magnetic moment. In annealed samples of approximately 30 percent substitution, the magnetic moment of the two sublattices cancel each other. If the samples are quenched from approximately 1200°C the magnetic moment is also reduced with increasing aluminum content, but complete compensation is not achieved. In the present experiments annealed samples on both sides of the compensation point as well as quenched samples have been tested.

Figure 2 shows a typical set of resonance curves obtained using circularly and linearly polarized radiation. The structure of the curve obtained with linear polarization has previously been explained[1,2] as arising from the presence of a large anisotropy field. The vertical

[13] L. R. Maxwell and S. J. Pickart, Phys. Rev. **92**, 1120 (1953).
[14] E. W. Gorter, Philips Research Repts. **9**, 295–365, 403–443 (1954).

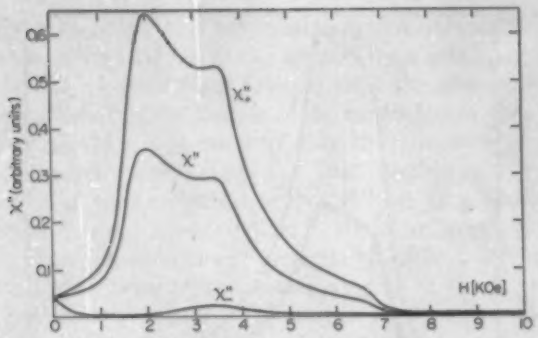

FIG. 3. Resonance absorption in polycrystalline $NiFe_{1.4}Al_{0.6}O_4$ quenched from 600°C measured at 10 kMc using linearly and circularly polarized radiation.

broken lines indicate the dc field strengths at which grains with their [111] or [100] directions parallel to the dc field go through resonance. The resonance curve obtained with positive circular polarization shows essentially the same structure as the one obtained with linear polarization. The resonance curve obtained with negative circular polarization has a single peak which coincides with the central peak of the other two resonance curves. This agrees qualitatively with our theoretical expectations. The dashed curve in Fig. 2 is the average of the two circular susceptibilities. This curve should ideally coincide with the measured linear susceptibility. The deviations between the two curves probably originate in nonlinearities of the recording equipment and indicate the degree of accuracy of the present measurements. Figures 3 and 4 show similar sets of resonance curves obtained on materials with slightly different composition and heat treatment. In these cases the anisotropy field is larger as indicated by the larger width of the lines, the relative strength of the low field peak and the relative magnitude of the two circular susceptibilities at the central peak.

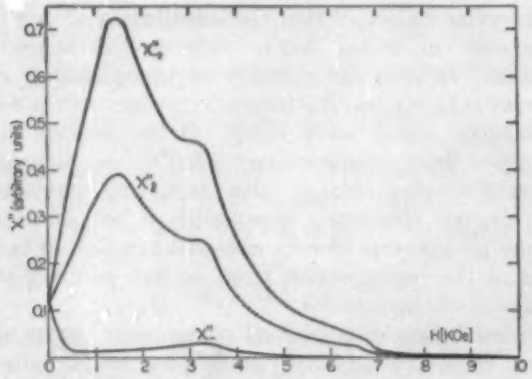

FIG. 4. Resonance absorption in polycrystalline $NiFe_{1.4}Al_{0.6}O_4$ quenched from 200°C measured at 10 kMc using linearly and circularly polarized radiation.

Figure 5 shows a quantitative comparison between the experimental results and the theoretical predictions. Here we have plotted the ratio of the two circular susceptibilities at the central peak vs the square of the dimensionless anisotropy parameter k given by Eq. (17). Observation of the two shoulders of the absorption line (as indicated in Fig. 2) enables us to determine ω/γ as well as H_a, and hence also k. The line in Fig. 5 represents the theoretical limit given by Eq. (16). All experimental points fall below this line in agreement with the theoretical expectation.

It should be noticed that the measured points correspond to significantly different compositions and heat treatments. The fact that they fall on a relatively smooth curve indicates that the ratio of the two circular susceptibilities is almost exclusively determined by the dimensionless anisotropy parameter k of Eq. (17).

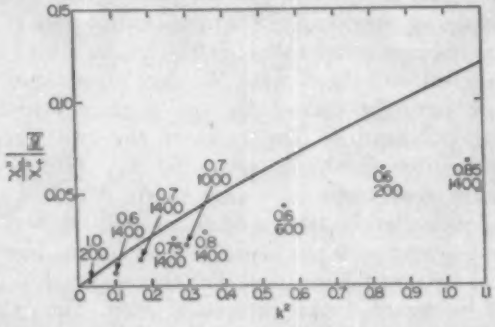

FIG. 5. Ratio of χ_-'' and χ_+'' taken at the fieldstrength corresponding to resonance in the [110] direction for $NiFe_{2-t}Al_tO_4$ as a function of the anisotropy parameter $k=\gamma H_a/\omega$. The two numbers at each point refer to the composition t and the quench temperature (in °C).

5. CONCLUSIONS

The experiments reported in this paper have confirmed our original suggestion[1,2] that the observation of additional absorption peaks in the vicinity of a magnetic compensation point do not necessarily indicate the excitation of the exchange mode of ferromagnetic resonance. In the case of the nickel ferrite-aluminates, the additional absorption peaks must be attributed to the presence of a large anisotropy field and the fact that the samples are polycrystalline. The observed line structure as well as the ratio of the two circular susceptibilities are in agreement with this picture.

ACKNOWLEDGMENTS

The authors wish to thank Dr. M. H. Sirvetz for his stimulating interest and constant encouragement, J. E. Zneimer and D. A. Belforti for the preparation of the samples, and R. Costen for preliminary measurements.

Preparation of Large Area Single-Crystal Cuprous Oxide*†

ROBERT S. TOTH,‡ REIN KILKSON,§ AND DAN TRIVICH
Departments of Chemistry and Physics, Wayne State University, Detroit, Michigan

(Received February 15, 1960)

Large area single crystals of Cu_2O were grown by the process of high temperature annealing. Cu_2O was prepared in finely polycrystalline form by the complete oxidation of Cu plate in air at temperatures of 1020°C to 1050°C. Subsequent annealing of the polycrystalline plates at higher temperatures allowed secondary recrystallization to occur. Single-crystal grains having surface areas larger than 1 in.^{2} were grown consistently on Cu_2O plates having thicknesses of 0.010 in. to 0.060 in. In some cases, entire polycrystalline plates were transformed into single crystals, and as a result, individual single crystals having surface areas of 3 in.^{2} and larger were obtained. The annealing temperature and the annealing time were found to depend markedly on the plate thickness. Thick plates required lower temperatures and longer annealing times than the thinner plates. X-ray analysis of the large grains verified that they were single crystals without excess strain, and indicated preferred orientation, with the (211) and (311) planes predominating. Resistance profile measurements at room temperature on quenched samples showed that a variation in resistance exists through the thickness of the plate.

I. INTRODUCTION

CUPROUS oxide as a semiconductor has been the object of many investigations caused by its interesting electrical properties which have been of theoretical and technical importance. The work has almost invariably been done on ill-defined polycrystalline samples of Cu_2O[1] with only a few exceptions of studies on single crystals.[2,3] This situation has existed because a satisfactory method for consistently obtaining large single crystals of Cu_2O has not been developed. Blankenburg and Kassel[4] studied the growth of Cu_2O by complete oxidation of Cu plate and they found that a post-oxidation anneal can produce samples having an average grain size of 2 mm^2, and in rare instances grains having a surface area of 1 cm^2. Recently Gritsenko[5] described a method for producing coarse-grained Cu_2O plates from which single crystals having surface areas of 30 mm^2 on the average and 120 mm^2 in individual cases can be extracted. The above methods are either not consistently successful or produce only small grains, and as a result the recent studies of the properties of Cu_2O have still been done on polycrystalline samples.[6,7]

The purpose of this article is to describe a method for consistently obtaining Cu_2O single crystals having surface areas of 1 in^2 or larger and thicknesses ranging from 0.010 in. to 0.060 in. Data concerning the uniformity in resistance of the single crystals are also presented.

II. FURNACE DESIGN AND TEMPERATURE CONTROL

The large area single crystals have been prepared in both horizontal and vertical furnaces. The construction of both types of furnaces is identical, with the main heating unit consisting of an 18 in. long alundum furnace core wound with heating wire Alloy No. 815 obtained from Hoskins Manufacturing Company. The alundum core has a diameter of $1\frac{5}{8}$-in. which readily allows the insertion of a 38-mm Vycor tube in which the samples are placed. The temperature in the furnace is regulated by a Micromax Temperature Controller and the temperature at the sample is measured with a Pt-13%Pt-Rh thermocouple read on a Leeds and Northrup 8662 Potentiometer. The temperature can be held constant to ±3°C by this method. Filtered gas, usually air, is allowed to pass through the Vycor tube.

III. OXIDATION AND CRYSTAL GROWTH

A. General Method

The method for the production of the large single crystals is to oxidize copper plate completely and then to anneal the resulting polycrystalline cuprous oxide sheet at a preselected higher temperature.

High purity Cu, 99.999%, was obtained from the Johnson-Matthey Company in the form of sheet. Plates having dimensions of approximately $\frac{7}{8}$ in.×6 in. are cut from the sheet and etched in dilute HNO_3. The Cu plate is supported on platinum since the resultant Cu_2O was found to react with most other construction materials at high temperatures. For use in the vertical furnace the Cu plate is supported from a Pt hook placed in a small hole drilled at one end of the sample and the Pt wire in turn is suspended from a steel rod which allows positioning of the sample in the middle of the furnace.

For the horizontal furnace arrangement, the Cu plate

* This research was supported by the United States Air Force through the Air Force Office of Scientific Research of the Air Research and Development Command, under a contract.

† Based upon a portion of a thesis submitted to the Graduate School of Wayne State University by R. S. Toth, in partial fulfillment of the requirements for the degree of Doctor of Philosophy.

‡ Now at the Physics Department, Ford Scientific Laboratory, Dearborn, Michigan.

§ Now at the Biophysics Department, Yale University.

[1] H. K. Henisch, *Rectifying Semi-Conductor Contacts* (Oxford University Press, London, 1957), pp. 88–94.

[2] O. V. Snitko and Y. I. Gritsenko, Ukrain. Fiz. Zhur. (Suppl). 2, 70 (1957).

[3] A. I. Andrievskii, N. N. Karelin, and A. V. Sandulova, Doklady L'vov Politekh Inst. 1, 23 (1955).

[4] G. Blankenburg and K. Kassel, Ann. Physik 10, 201 (1952).

[5] Y. I. Gritsenko, Izvest. Akad. Nauk. Ser. Fiz. 21, 153 (1957).

[6] K. Stecker, Ann. Physik 3, 55 (1959).

[7] R. Frerichs and R. Handy, Phys. Rev. 113, 1191 (1959).

is bent at the four corners to form small "feet". The plate which is usually shorter in length than that used in the vertical furnace, is placed on a Pt sheet which in turn rests on an alundum block. This assembly is pushed into the center of the furnace. Since there exists only a small contact area between the Pt and resultant Cu_2O, very little reaction occurs. The thermocouple is placed inside the Vycor tube near the sample, and can be moved to read the temperature along the length of the sample.

The Cu plate is then allowed to oxidize in air at a temperature from 1020° to 1040°C. From the stability diagram for the $Cu/Cu_2O/CuO$ system,[6] and from data of Blankenburg and Kassel,[4] and Zuev,[8] it has been found that Cu_2O is stable in air only at temperatures above 1020°C. Since the eutectic point for Cu/Cu_2O is at 1065°C, it is necessary to oxidize at a temperature intermediate between these two points.

After the oxidation is complete, the temperature is raised to a value between 1085°C and 1130°C, depending upon the thickness of the plate. The samples are then allowed to anneal at these temperatures for times ranging from 5 hr to 150 hr.

After the annealing is over, the samples are quenched by quick withdrawal from the furnace, a process which requires less than 10 sec. During this operation, cupric oxide is formed on the surface since the material has been taken from the Cu_2O stability region into the CuO region. However, the cooling is rapid so that only a thin layer of CuO is formed on the surface. This is removed by etching in dilute HNO_3 or by use of abrasives. The Cu_2O is then revealed showing clearly the grain boundaries in the plate, and when the plate is viewed with transmitted light, one can see the characteristic ruby red color of cuprous oxide.

The final grain size obtained has been found to depend upon the thickness of the Cu_2O plate (or equivalently upon the thickness of the original Cu plate), the annealing temperature, and the time of annealing. The effect of each of these variables will be discussed below.

B. Effect of Temperature on Grain Size

The effect of the annealing temperature on the final grain size is closely related to the thickness of the Cu_2O plate. The oxidation temperature has no noticeable effect on the final grain size. For thick Cu plates, e.g., those having thicknesses greater than 0.020 in., the annealing temperatures must be lower than that used for the thinner samples. Thus, an average annealing temperature for a Cu_2O plate obtained by oxidizing a 0.030-in. thick Cu plate is about 1085°C, while that used for 0.015-in. Cu is 1115°C. In general, large grains are not formed in any sample if the temperature is lower than 1070°C. Figures 1 and 2 show two samples having identical dimensions, oxidized at the same temperature for the same length of time, but annealed at different temperatures for the same time. In the sample annealed at the higher temperature, one grain has grown to a large area at the expense of the matrix, while no appreciable growth has occurred on the sample annealed at the lower temperature.

To judge whether a temperature gradient is necessary for the growth of the large grains, a comparison can be made between samples grown in the horizontal furnace, in which the temperature variation is ±5°C within a 4-in. region in the center, and those grown in the vertical furnace in which the temperature decreases 25°C over a 2 in region from the hottest point in the tube. The

FIG. 1. An example of a large single crystal in a Cu_2O plate obtained by oxidizing a 1 in.×¾-in.×0.010-in. Cu plate for 1 hr. at 1050°C and annealing for 5 hr at 1100°C.

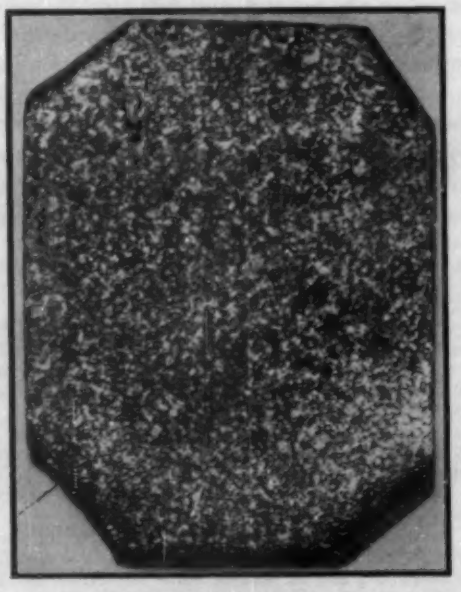

FIG. 2. An example of a Cu_2O plate consisting of only small crystals as a result of oxidizing a 1-in.×¾-in.×0.010-in. Cu plate for one hour at 1050°C and annealing for 5 hr at 1067°C.

[8] K. P. Zuev, Soviet Phys. Solid State 1, 111 (1959).

thermocouple is always positioned at that point near the sample where the highest temperature exists. It is found that large grains of equivalent size are produced in both furnaces, and it is concluded that the growth of the grains does not depend on whether a temperature gradient exists, but is affected only by the magnitude of the temperature.

In both thick and thin samples, it has been observed that grain coarsening does not develop if the temperature is too high. Although the melting point of stoichiometric Cu_2O is 1235°C, no success in grain coarsening was obtained with samples annealed at temperatures higher than 1130°C.

C. Effect of Annealing Time on Grain Size

The annealing time necessary for the production of large grains depends upon the thickness of the oxide plate presumably because the annealing temperature depends upon thickness. Large grains, at least 0.25 in.^{2}, are obtained from 0.008-in. and 0.010-in. thick Cu sheet by oxidizing for 1 hr at 1035°C and annealing for only 5 hr at 1120°C. On the other hand, for Cu sheet thicknesses of 0.030-in. annealing times in the range of 100 hours are employed to obtain grains having surface areas larger than 1 in.^{2}.

Once the growth process has stopped, further annealing has no noticeable effect on the grain size. Causes for the stoppage of the growth in Cu_2O have not yet been established, although it is possible to obtain Cu_2O plates which have been transformed into only one crystal. Such a plate is shown in Fig. 3. In Fig. 4 is shown a sample which apart from a few small grains, is a bicrystal.

D. Effect of Thickness on Grain Size

Cu_2O grains having surface areas larger than 0.25 in.^{2} are grown on oxidized Cu sheets having thicknesses ranging from 0.008 in. to 0.035 in. Attempts to grow grains of areas larger than 0.25 in.^{2} on thicker samples have failed. Figures 5 and 6 show typical results on samples of various thicknesses which were annealed under the most favorable conditions

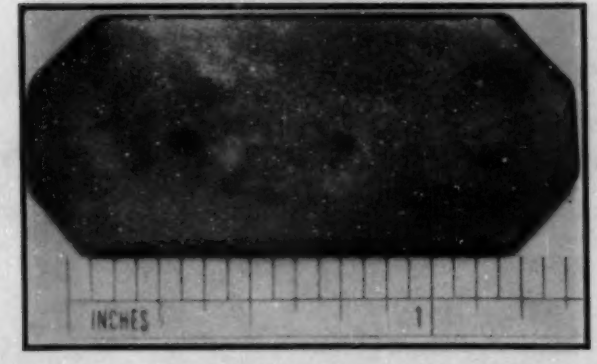

FIG. 3. Single crystal plate of Cu_2O obtained by oxidizing 0.019-in. Cu plate for 2 hr at 1030°C and annealing for 92 hr at 1125°C.

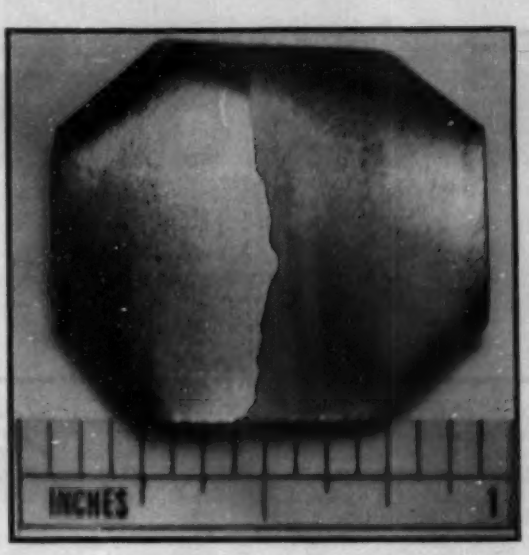

FIG. 4. Bicrystal of Cu_2O obtained by oxidizing 0.008-in. Cu plate for 1 hr at 1040°C and annealing for 6 hr at 1115°C.

E. Effect of History of Initial Copper on Grain Size

The initial Cu used is in the form of polycrystalline plates. Some work was done using single-crystal Cu plate as the starting material. As found also by Gritsenko,[5] larger grains of Cu_2O were obtained on the average, but the orientation of the single crystal of Cu_2O was not the same as the orientation of the Cu plate. Indeed, the complete oxidation of a single crystal Cu plate leads to a polycrystalline Cu_2O plate. The fact that a polycrystalline Cu sheet can be transformed entirely into one single crystal of Cu_2O by the oxidation

FIG. 5. Large grain size in a Cu_2O plate obtained by oxidizing 0.015-in. Cu plate for 2 hr at 1030°C and annealing at 1120°C for 21 hr.

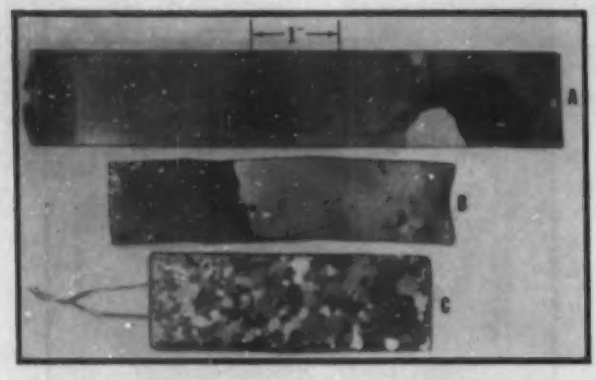

FIG. 6. Variation in grain size in Cu_2O plates of various thicknesses (A) 0.020-in. thick Cu plate oxidized for 3 hr at 1030°C and annealed for 160 hr at 1110°C. (B) 0.028 in. thick Cu plate oxidized for 40 hr at 1036°C and annealed for 144 hr at 1090°C. (C) 0.040-in. thick Cu plate oxidized for 42 hr at 1048°C and annealed for 124 hr at 1095°C.

and annealing process described above dispels the need for single crystal Cu.

Commercial grade Cu was also used as a starting material and found not to differ in final grain size from that of the high purity Cu. This was also observed by Gritsenko.

It should be possible to obtain much larger single crystals of Cu_2O by simply starting with larger sheets of Cu.

IV. X-RAY ANALYSES OF THE LARGE GRAINS

Back reflection Laue pictures were taken of the large single crystals to investigate their quality. A typical picture showing the (100) orientation is given in Fig. 7. In the figure, it can be seen that the spots are sharp and round, indicating that there exist no gross defects in the crystals.

By determining the angle between a [111] or [100] direction and the normal to the plate, and comparing with standard table of angles between crystallographic directions in crystals of the cubic system, it was found that the majority of the large single crystals have a normal direction near the [211] and [311].

V. UNIFORMITY OF SINGLE CRYSTALS

The single crystals of Cu_2O obtained by the oxidation of Cu sheet or rod on all its free surfaces are found to contain a myriad of small pin holes in the center of the material. It is thought that these holes are a memory of the last remaining Cu, since it has been shown that Cu is oxidized by the diffusion of Cu to the $Cu\text{-}O_2$ surface.[9] When a Cu plate is oxidized, the Cu_2O consists of many fine grains on each side of this interface layer. The grains in general do not match across the interface layer as a result of the independent oxidation and grain formation on each side of the center of the plate. The interface layer is thereby a result of the oxidation process and not of the annealing process. Upon annealing, the grains become coarse and grow not only laterally across the face of the plate but also through the thickness of the plate. In this way, the large single crystals formed extend through the entire thickness of the plate but nevertheless still contain the interface layer of pin holes.

Resistance profile measurements across the thickness of single-crystal plates were performed to determine the effect of the hole region on the resistance of the material. To do this, a diagonal slice across a single crystal plate was made by polishing a test sample. These diagonal slices were made by mounting the sample on a stainless steel piston which had one surface ground six degrees from the horizontal. The piston was then placed in a stainless steel collar, and the sample was polished to form a wedge, with the hypotenuse of the wedge being along the diagonal of the plate. The sample was then mounted with this surface face down on a horizontal block, and the remaining Cu_2O was polished away to form a slice having a thickness of about 0.004 in. Two current contacts were made by evaporating Au on the ends of the sample, and phosphor bronze wires with Au plated tips were used as voltage probes. The voltage probes were mounted on 3-dimensional micromanipulators. Resistance measurements were obtained for 0.050-in. intervals along the slice using a Leeds and Northrup K-2 Potentiometer. Such a profile measurement is shown in Fig. 8. It is seen that the plate is not uniform in resistance through its thickness, and that the interface layer is a region of high resistance.

Resistance profiles were also measured on samples from which the interface region was first removed. The

FIG. 7. Back reflection Laue picture showing the (100) orientation in a large Cu_2O grain taken at 23°40′ from the normal to the plate.

[9] J. Bardeen, W. H. Brattain, and W. Shockley, J. Chem. Phys. 14, 714 (1946).

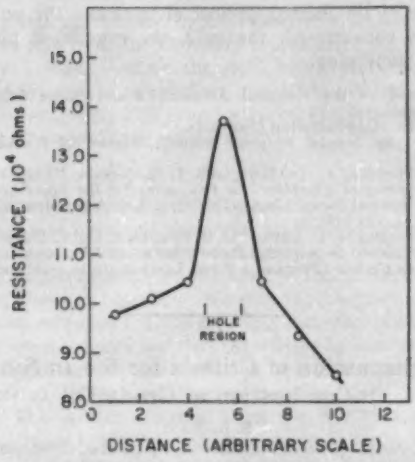

FIG. 8. Resistance profile measurement on a diagonal slice (6°) through the thickness of a Cu_2O plate.

samples were mounted on a horizontal block and polished to eliminate the interface layer. They were then re-annealed in the furnace at 1030°C and quenched to room temperature by being quickly withdrawn from the furnace. Diagonal slices of these were prepared in the previous manner. The results on these samples are similar to those reported by Fritzsche[10] and show that the resistance of the material decreases from the outer surface to the center of the plate.

The reasons for the variation in resistance across the thickness of the plate are not well known. In samples which contain the interface region, the increase in resistance at the center of the plate can be ascribed to the presence of the holes in the plate at that region. However, for plates free of this interface region, the explanation is more complicated. It has been found by Fritzsche that the variation in resistance across the plate depends upon the cooling rate. This indicates that a variation in stoichiometry exists across the plate due to the cooling history, and possibly also due to chemisorption of oxygen during the cooling period. To explain the conductivity at low temperatures, Bloem[11] has suggested that association of cation and anion defects occurs during the cooling process.

[10] C. Fritzsche, Ann. Physik 14, 135 (1954).

VI. CONCLUSION

The empirical results obtained by observing the growth of the grains on a large number of samples, and comparing with results known for metals,[12] indicate that the growth process consists of secondary recrystallization. The effectiveness of this process depends strongly upon optimizing the parameters, thickness and temperature of anneal. Previous workers were unfortunate in selecting much thicker plates of Cu_2O to anneal, resulting in much smaller grains. Since the previous workers annealed their samples at the oxidation temperature, or only slightly higher, they were not able to obtain the maximum benefit from the process.

The method that has been described above is capable of producing single crystals well suited as test samples for the measurement of the semiconducting properties of Cu_2O. A paper concerning the measurements of the high-temperature conductivity made on these single crystals is being prepared for publication.

[11] J. Bloem, Philips Research Repts. **13**, 167 (1958).
[12] J. E. Burke and D. Turnbull, Progr. in Metal Phys. **3**, 220 (1952).

Cover Photograph

The cover picture shows an electron micrograph of a nitrocellulose replica of a crater in a thin aluminum film on glass. The damage was caused by a 0.6-μ diam spherical pellet having an incident velocity of 1.8 km/sec. This micrograph was taken by H. Shelton, C. D. Hendricks, Jr., and R. F. Wuerker, whose article "Electrostatic Acceleration of Microparticles to Hypervelocities" will appear in the July issue of the Journal of Applied Physics.

Letters to the Editor

Tensile Strength of Pyrolytic Graphite up to 2750°C*

H. E. Martens and L. D. Jaffe
Jet Propulsion Laboratory, California Institute of Technology, Pasadena, California
(Received March 7, 1960)

THE ultimate tensile strength of a pyrolytic graphite has been measured from room temperature to 2750°C.

According to the manufacturer,[1] the polycrystalline material tested[2] was deposited against a synthetic graphite substrate by decomposition of a methane-hydrogen mixture at 2100°C; its specific gravity prior to tensile testing was 2.20. Specimens were 2 in. long×approximately 0.1 in. thick (5.1 cm long×0.25 cm thick); deposition took place in the thickness direction. Specimen width was 0.75 in. (1.9 cm) at the ends, reduced to 0.06 in. (0.15 cm) at the center by side radii of 0.75 in. (1.9 cm).

The methods of test have been described previously.[3,4] Stress was applied parallel to the plane of deposition. This is parallel to the (00.1) basal planes of the hexagonal lattice; the crystallite orientation about the [00.1] normal to this plane was random. The cross-head speed during testing was 1.5×10^{-4} in./sec (4×10^{-4} cm/sec). Tests were made in helium.

Results obtained are shown in Fig. 1. Each point on the figure represents a single test. At 2750°C, only minimum values for the strength were obtained, as the holders broke before the specimens. Though the geometry of the specimens did not permit quantitative measurements of ductility, the cross-head motion during testing indicated that appreciable plastic deformation occurred at 1650°C and above. Visual observation of specimens before and after testing at 2500–2750°C suggested that deformations were larger than those found at the same temperatures in commercial synthetic graphites, made from petroleum coke and coal tar pitch.

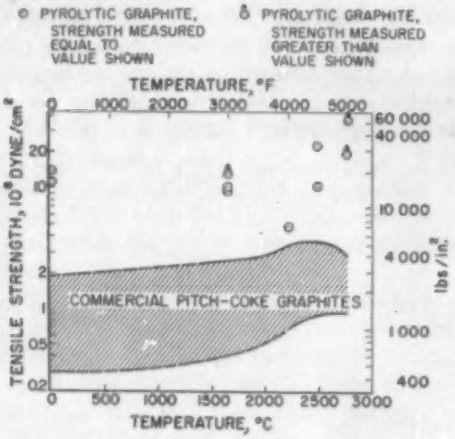

FIG. 1. Tensile strength of pyrolytic graphite.

For comparison, strengths of commercial synthetic graphites (specific gravity 1.5 to 1.8) are also shown in Fig. 1. The strength of the pyrolytic material is greater by about one order of magnitude. Also, there is no indication in the data for pyrolytic graphite of a maximum in the strength vs temperature curve, which graphites usually show near 2500°C. Instead, the pyrolytic graphite seems to increase in strength as the temperature is increased to 2750°C, or higher.

Because of the limited number of tests and the experimental difficulties encountered, the data are considered preliminary. Work is countinuing.

* Sponsored by the National Aeronautics and Space Administration under contract.
[1] Raytheon Manufacturing Company.
[2] Supplied by Special Projects Branch, Bureau of Naval Weapons, U. S. Navy.
[3] H. E. Martens, L. D. Jaffe, and J. O. Jepson, "High temperature tensile properties of graphites" in *Proceedings of the Third Conference on Carbon* (Pergamon Press, London, 1959), p. 529. Also, Mem. Scientifiques Rev. Met. 56, 721 (1959).
[4] H. E. Martens, D. D. Button, D. B. Fischbach, and L. D. Jaffe, "Tensile and creep behavior of graphites above 3000°F" in *Proceedings of the Fourth Conference on Carbon* [Pergamon Press, London (to be published)

Discussion of Criteria for the *In Situ* Combustion of Crude Oil

S. E. Szasz
Sinclair Research Laboratories, Inc., Tulsa, Oklahoma
(Received November 2, 1959)

STARTING from the assumption that an underground combustion-supported linear heat wave reaches steady state, P. Cooperman has in a recent paper[1] derived three criteria for the possibility of such a process. These conditions state that the oil saturation (Eqs. 37 and 38, see work cited in footnote 1), the carbon-hydrogen ratio of the fuel (Eq. 51, see work cited in footnote 1) and the rate of gas injection (Eq. 60, see work cited in footnote 1) must exceed certain minimum values. It is the purpose of this letter to show that these criteria and the assumptions on which they are based do not apply to a real, physical system; indeed, that the assumption of steady state cannot be justified.

1. In deriving the first criterion from Eq. (36) (see work cited in footnote 1), Cooperman seems to assume that k_0 and k_w are always finite; this is true for k_w, but not necessarily for k_0, which is actually a function of S_0 and can reach zero for a finite value of S_0. In other words, the inequality (36) of footnote reference 1 can be satisfied not only if S_0 is large enough, but also if k_0 is small enough, e.g., zero; and this being true for all oil saturations less than the irreducible minimum, inequality (36) (footnote reference 1) cannot be used to define a finite minimum value for S_0. This is not to say that a finite minimum oil saturation would not be required by some other condition not discussed by Cooperman; e.g., production of some liquid oil, or generation of a minimum amount of heat, or maintenance of a given minimum peak temperature.

2. From the chemical equation (50) (footnote reference 1) the difference between the heat capacities of the reactants and that of the reaction products is

$$\Delta=2(12n+2m)c_0+32(2n+m)c_g-88nc_g-36mc_w, \qquad (1)$$

or, with the same numerical values for the specific heats as in footnote reference 1,

$$\Delta=8.4m(n/m-3.05). \qquad (2)$$

Thus, Cooperman's second criterion merely states that the heat capacity of the reactants must be greater than that of the reaction products. For the assumptions on which this is based, see below. Note that Benham and Poettmann[2] show that in the experiments of Martin, Alexander, and Dew,[3] n/m was between 1.25 and 2.0; thus, condition (51), footnote reference 1, was not fulfilled.

3. On dividing both sides of Eq. (1) by the weight of oxygen in the reaction, and noting that the coefficients of c_0, c_w, and c_g are R_0, $-R_w$, and (R_w-R_0), respectively, in the notation of footnote reference 1, we obtain for the difference in heat capacities between reactants and reaction products, per pound of oxygen utilized, the expression

$$\Delta'=R_0(c_0-c_g)-R_w(c_w-c_g). \qquad (3)$$

If, now, the gas injection velocity is v_{g1} and the front moves at a velocity v_f leaving behind, per unit time, a volume φS_f to be

filled by injected gas which does not cross the boundary, the rate at which gas does cross the boundary representing the heat front is given by $v_{g1}-\varphi v_f$. Assume the same temperature T_0 at both inlet and outlet ends of the system, and $\Delta'>0$ to satisfy Cooperman's second criterion; with ρ_g and y having the same meaning as in footnote reference 1, the expression

$$H=(v_{g1}-\varphi v_f)y\rho_g T_0\Delta' \qquad (4)$$

represents the excess heat per unit time carried into the system by the reactants over and above the heat carried away by the reaction products, because of the difference in heat capacities. The change in heat capacity being caused by the chemical reaction, it occurs at the zone boundary. But Eq. (4) is equivalent to Eq. (60), footnote reference 1, in the adiabatic case; thus, Cooperman's work must assume implicitly that the change in heat capacity at the boundary is the only mechanism of heat release, and that the heat generated by the combustion reaction itself is zero or negligible. This is also apparent from the fact that Eq. (57), footnote reference 1, which Cooperman claims to connect the heat generated with the flux of air, contains only specific heats and inlet and outlet temperatures, but not the heat of combustion either for fuel or for oxygen. Note also that according to Cooperman, if his second condition is not satisfied and $n/m=3.05$, there would be no heat flux and no release of heat although the reaction Eq. (50), footnote reference 1, would still be going on. The magnitude of the error involved is readily seen from a numerical example: with $n/m=6$, $y=0.21$ (injection of air, complete oxygen utilization), $T_0=600°\text{R}=140°\text{F}$. and the same specific heats as in the foregoing, Eq. (4) yields only 0.6 Btu/std cu ft of air passing through the "combustion" zone, while the heat of combustion for air, with petroleum fuels, is on the order of 100 Btu/std cu ft.

4. Consider a segment extending, both upstream and downstream of the front, far enough so that the temperature is substantially equal to T_0 and the temperature gradient is negligible. This segment has, in steady state, a constant heat content and any heat generated must be removed by the sensible heat of the flowing fluids. This is possible in Cooperman's theory because he assumes a rate of heat generation based on the heat carrying capacity of the flowing fluids; but if we are to take into account the much larger amounts of heat generated by the combustion reaction in a real system, the heat capacities of the flowing fluids become grossly inadequate to remove all the heat generated at any reasonable temperature level. Hence, the assumption of steady state in a linear system with real combustion cannot be justified.

[1] P. Cooperman, J. Appl. Phys. 30, 1376 (1959).
[2] A. L. Benham and F. H. Poettmann, Trans. A.I.M.E. 213, 406 (1958).
[3] W. L. Martin, J. D. Alexander, and J. N. Dew, Trans. A.I.M.E. 213, 28 (1958).

Remarks on "Some Criteria for the *In Situ* Combustion of Crude Oil"

H. R. Bailey and B. K. Larkin
The Ohio Oil Research Center, Littleton, Colorado
(Received October 12, 1959; revised manuscript received February 1, 1960)

In a recent paper[1] by P. Cooperman, the following three criteria for *in situ* combustion of crude oil are obtained: (i) A hydrodynamic condition—that the oil saturation S_0 must be greater than a certain constant times the water saturation (Inequality 38, footnote reference 1); (ii) A condition based on thermal and chemical considerations—that the carbon-hydrogen mole ratio of the burning hydrocarbon must exceed 3.05 (Inequality 51; footnote reference 1); and (iii) A thermal condition—that the gas velocity behind the moving combustion front must exceed a certain minimum (Inequality 60, footnote reference 1.)

As pointed out in footnote reference 1, the *in situ* combustion process consists of a combination of thermal, hydrodynamic, and chemical processes. Any model of these processes must include many simplifications in order that the resulting equations be amenable to solution.

Criteria (ii) and (iii) are not in agreement with experimental results and it is the purpose of this letter to show where the model considered in footnote reference 1 is not realistic and to indicate criteria which can be obtained from a more realistic model.

In particular, the steady-state temperature behind the moving combustion front is of the form

$$T_1=A_1e^{-\beta_1\xi}+B_1,$$

and from Eqs. (18) and (22) of footnote reference 1 we have

$$\beta_1=(1-\phi)\rho_r c_r v_f+\phi v_f\rho_{g1}c_{g1}-v_{g1}\rho_{g1}c_{g1}.$$

The notation used in this letter is the same as footnote reference 1 and, where needed, the units are lb, ft, hr, btu, and °F. It can be shown[2,3] that for typical combustion conditions

$$v_{g1}\rho_{g1}\cong 14.7wv_f.$$

This result is based on material balance considerations and is in good agreement with laboratory results. W is the amount of fuel on a unit volume of rock (fuel density). Typical values for the foregoing parameters are $(1-\phi)\rho_r c_r=28$, $W\gtrsim 3$, $\phi=0.25$ and $c_{g1}=0.25$. By using these values in the two foregoing relations it is seen that β_1, must be positive.

Since $\beta_1>0$, it is clear that $A_1=0$ since otherwise T_1 would be unbounded as $\xi\to-\infty$. Thus the solution behind the front is of the form $T_1=B_1$, a constant. If vertical losses are considered then the temperature does fall behind the combustion front; however, the adiabatic case is a good first approximation.

Both criteria (ii) and (iii) of footnote reference 1 are based on the premise that $A_1\neq 0$. This is explicitly stated in the derivation of criterion (ii) and it is implicitly used in deriving criterion (iii) by assuming that the constant B_1 is determined by the boundary temperature at $\xi\to-\infty$. Since $A_1=0$, the constant B_1 is determined by the heat flux supplied at the source. This problem is considered by Jakob[4] for the case of heat flow by conduction from a moving source.

The conclusion that B_1 is determined by a boundary condition results in a formula, criteria (iii) (Inequality 60, footnote reference 1), for minimum gas velocity which becomes infinite for the case of zero-boundary conditions and this result does not seem reasonable.

Criterion (ii)—that the carbon-hydrogen mole ratio n/m must exceed 3.05—is violated by all published experimental results which we have seen. Some known results[5-7] are given below in Table I.

Table I. Experimental values for fuel composition.

Type of experiment	n/m	Reference number
Laboratory	1.4–2.0	5
Field	1.2	6
Laboratory & field	0.69–1.1	7

Transient solutions including vertical losses have been obtained[8,9] for a conduction model of heat flow. A model including convection effects has also been considered[3] and the steady-state adiabatic (no vertical losses) temperature is given by

$$T-T_i/T_m-T_i=v_f/v_f-\theta, \quad \xi\lesssim 0$$
$$T-T_i/T_m-T_i=v_f/v_f-\theta\exp[-(v_f-\theta)\xi\alpha^{-1}], \quad \xi\gtrsim 0,$$

where

$$\theta=v_{g1}\rho_{g1}c_{g1}/\rho_m c_m, \quad \alpha=k/\rho_m c_m,$$

$\rho_m c_m=\rho_r c_r(1-\phi)+\rho_{g1}c_{g1}\phi$, $T_i=$ ambient temperature, $T_m=\Delta HW/\rho_m c_m$, $\Delta H=$ heat of combustion of the fuel in btu/lb and W—the fuel density in lb/cu ft. The assumption that W is a constant in a particular *in situ* combustion process is basic in our model. W is the fuel density of a coke that is deposited ahead of the combustion front, and it has been shown[5] in tube-run experiments that W is practically a constant for any given experiment.

A criterion for the minimum air injection rate required to sustain combustion is given in footnote 2 and 9. These results are based on a transient solution of a radial heat flow model, assuming that a minimum ignition temperature for the fuel is known. Copies of various reports and papers describing this work can be obtained by writing the authors.

[1] P. Cooperman, J. Appl. Phys. 30, 1376 (1959).
[2] H. R. Bailey and B. K. Larkin, "Conduction-convection in underground combustion." Presented to an A.I.Ch.E.-S.P.E. Symposium on *in situ* Combustion, San Francisco, December, 1959.
[3] A. L. Benham and F. H. Poetmann, Trans. AIME 213, 46 (1958).
[4] M. Jacob, *Heat Transfer* (John Wiley & Sons, Inc., New York, 1949), Vol. 1.
[5] W. L. Martin, J. D. Alexander, and J. N. Dew, Trans. AIME 213, 28 (1958).
[6] C. F. Gates and H. J. Ramey, J. Petrol. Technol. 10, 236–244 (1958).
[7] J. T. Moss, P. D. White, and J. S. McNiel, J. Petrol. Technol. 11, 55–64 (1959).
[8] H. J. Ramey, Trans. AIME 216 (1959); AIME paper 1133-G (1958).
[9] H. R. Bailey and B. K. Larkin, Trans. AIME 216 (1959); AIME paper 1134-G (1958).

Reply to the Letters of Szasz, and Bailey and Larkin

PHILIP COOPERMAN
University of Pittsburgh, Pittsburgh, Pennsylvania
(Received January 12, 1960; revised manuscript received March 7, 1960)

BECAUSE of a lack of reliable evidence on the nature of many of the processes of *in situ* combustion, theoretical developments must be limited to qualitative rather than quantitative results. The two-zone version of my theory had only this restricted goal, as was clearly indicated at the beginning and end of my paper. It would, therefore, be no surprise to learn that some of the criteria (e.g., carbon-hydrogen mole ratio for combusion) had to be modified. However, the point of the paper was not that the C/H ratio had to exceed 3.05, but that it had to exceed *some* minimum value. Similar statements could be made for the other criteria.

There is no point, however, in changing or discarding these criteria unless a sufficient reason is given. In my opinion, no such reason has been presented in the above letters. For example, Szasz's first criticism of the theory is that the criterion specifying a minimum oil saturation for nonzero oil mobility is also satisfied for saturations for which the oil mobility vanishes. Subsequently, he remarks that if oil is to be produced from the reservoir, the mobility must be different from zero, and that this requirement would forestall his criticism. Since the production of oil is the point of *in situ* combustion, Szasz has answered himself.

Secondly, Szasz claims that the experiments of Martin *et al.*, as interpreted by Benham and Poettmann, indicate that the C/H ratio can be smaller than 3.05. This would be no surprise even if the data from these experiments could be accepted, but when the experimental conditions are considered, it is clear that the data must be viewed with great suspicion. The apparatus used consisted of materials of extremely low thermal conductivities (sand, oil) encased in a tube of high-conductivity material (steel). Elementary calculations show that, under these circumstances, the larger part of the heat flux bypasses the sand-oil mixture and travels through the steel tube. Because of this, the temperature profile and thermal history of the oil differs from what it would otherwise be, and the deviations are in such a direction as to make it appear that successful combustion can be attained at a lower C/H ratio. It should be emphasized that the magnitude of the deviations from ideal is not reasonably small; under ideal conditions, none of the heat would travel through the tube, but in practice, 60–80% of the total does.

The third question raised by Szasz is based on a misinterpretation of Eq. (4) of his letter. Szasz understands this equation as the *definition* of a heat flux density H, which is the difference in the convected upstream and downstream heat flux densities. However, this is not the case. H is defined in my paper as the heat flux density resulting from the combustion itself. By virtue of the first law of thermodynamics, H is the difference (or vector sum) of the total flux densities conveyed by conduction and convection. At the ends of an infinitely long tube, the temperature gradient vanishes, and hence, there is no conducted heat there. Thus the heat of combustion H must be equal to the convected heat at the tube ends. This is the significance of Eq. (4), and in objecting to it, Szasz is opposing the first law. His numerical example stems from the same misconception in that H is given as the heat of combustion, and cannot be calculated by Eq. (4). What is to be calculated is the requisite air flux and the contradiction means that Szasz has not used correct values in the right-hand side of Eq. (4). Since his last point also is connected with his misinterpretation, there is no need to discuss it separately.

The remarks of Bailey and Larkin are mostly concerned with the discrepancy between the theoretical criteria for combustion and experimental data obtained in tube experiments. In particular, they question the validity of the criterion for the C/H ratio, and cite field and laboratory data in support of their argument. It has already been shown that laboratory data are insufficient for this purpose; field data are even more unsatisfactory because of the many disturbing factors (e.g., inhomogeneities and gravity segregation of fluids), and because of poor instrumentation caused by limited access to the reservoir. Hence, these data do not force any modification of the criteria in question.

These writers also make use of the equation

$$\rho_{g1}v_{g1}\cong 14.7Wv_f$$

to show that the quantity β_1 must be positive, whereas the C/H criterion depends on it's being negative. However, W, which is the weight of coke per unit volume of rock has been determined by steel tube experiments. Since the formation of coke is obviously dependent on the thermal history of oil, the values of W used by Bailey and Larkin have not been established, and their argument concerning the other constants of the theory is left resting on an infirm foundation.

The temperature equations advanced by Bailey and Larkin offer a clue to the reason for their rejection of the C/H criterion. Their equation for the temperature upstream from the combustion front states that it is constant. This is impossible unless there is a source of heat at the upstream end. In tube experiments, there is usually a heater placed at this end for the purpose of initiating the combustion, but I have seen no paper in which it has been specifically stated that these end heaters are turned off after the initial period. The temperature equation for the region $\xi\leq 0$ given by Bailey and Larkin is consistent with the experimental condition in which end heaters are permitted to operate after ignition. Under these circumstances, the combustion is *not* self-sustaining and, as shown in my paper [under Eq. (43)], the C/H criterion need not be obeyed. From a practical viewpoint, in situ combustion may become commercially practicable only if a supplemental source of heat is used since most crude oils do not have a sufficiently high C/H ratio.

The downstream temperature of Bailey and Larkin is identical with the one appearing in the original paper for the upstream temperature. It is clearly invalid if $\beta_1<0$ since it would lead to a rising temperature downstream. Furthermore, it predicts the temperature downstream on the basis of a knowledge of the entering gas upstream, but contains no reference to oil, water, or gas downstream from the combustion front. Such a result seems highly implausible.

To summarize, my position is as follows:

(1) The criteria developed in the original paper are to be regarded as qualitatively rather than quantitatively valid;

(2) However, the experimental data available at present does not provide a basis for modifying or abandoning them;

(3) The steady-state theory advanced by Bailey and Larkin leads to implausible temperature formulas.

Dielectric Behavior of Single Crystals of Tri-Glycine Sulfate (TGS) from 1 kc to 2500 Mc

A. Lurio and E. Stern
IBM Watson Research Laboratory, New York, New York
(Received March 2, 1960)

THE dielectric properties of single crystals of TGS were measured in the ferroelectric direction as a function of temperature and frequency. At each frequency, the relative dielectric constant ϵ', was measured as a function of temperature, giving rise to a family of curves with shapes characteristic of a second order transition.[1] These measurements were made over a frequency range of 1 kc to 2000 Mc.

The dielectrometer line consisted of a 46.3Ω ¼ in. od coaxial line in which the sample was mounted between the end of the center conductor and a spring loaded movable short-circuit. The dimensions of the sample were 1×1×0.3 mm with evaporated silver electrodes on the 1×0.3 mm faces. The line was contained in a cylindrical oven in which provisions were made for controlling and monitoring the temperature of the specimen. Measurements were made as the temperature drifted through the region of interest, namely 40–60°C, at a rate of 20°/hr.

At 1 kc, the dielectrometer cell was attached to the output of a Beco Impedance bridge from which the capacitance and tanδ of the sample could be read directly as a function of temperature. Above that frequency and up to 100 Mc, a Boonton 190-AQ meter was used in the same fashion. However, above 50 Mc, corrections for the length of the line l between the Q meter and the sample had to be made, to obtain the actual values of C and Q. Thus, if the capacitance and Q read off the Q-meter dials were C_{in} and Q_{in}, the resulting input admittance would be

$$Y_{in}=G_{in}+jB_{in}=\omega C_0[(1/Q_{in})-(1/Q_0)]+j\omega C_{in}, \quad (1)$$

where C_0=the capacitance read at resonance with the Q-meter terminals open, and an indicated Q of magnitude Q_0. To find the admittance Y_L of the sample itself requires transforming Y_{in} to the end of the line by the relationship

$$Y_L=Y_0\frac{Y_{in}-jY_0\tan\beta l}{Y_0-jY_{in}\tan\beta l}, \quad (2)$$

where Y_0=characteristic admittance of the line=2.16×10^{-2} mhos and

$$\beta=2\pi/\lambda. \quad (3)$$

Since

$$Y_L=G_L+jB_L \quad (4)$$

$$\tan\delta=G_L/B_L, \quad C_L=B_L/\omega, \quad (5)$$

which give the actual capacitance and loss factor of the sample.

The next frequency range investigated was between 500 and 2000 Mc. In this region the dielectrometer cell was attached to a HP 805-B slotted-line; rf was supplied by G-R Unit Oscillators. The detected power was observed on a HP 425-A microvoltammeter with a sensitivity of the order of 1 μv. In this technique, the position "d" of the VSW minimum with respect to a fixed reference plane d_0 and the VSWR ν itself, are measured as a function of temperature. The impedance of the load Z_L of a transmission line, in terms of the input impedance Z_{in}, is given by

$$Z_L=Z_0\frac{Z_{in}-jZ_0\tan(d-d_0)}{Z_0-jZ_{in}\tan(d-d_0)}. \quad (6)$$

If we substitute in Eq. (6) the fact that

$$\sigma=Z_0/Z_{in}, \quad (7)$$

we obtain the more useful relation

$$Z_L=Z_0\frac{\sigma(1+T^2)}{\sigma^2+T^2}-j\frac{T(\sigma^2-1)}{\sigma^2+T^2}=R+jX. \quad (8)$$

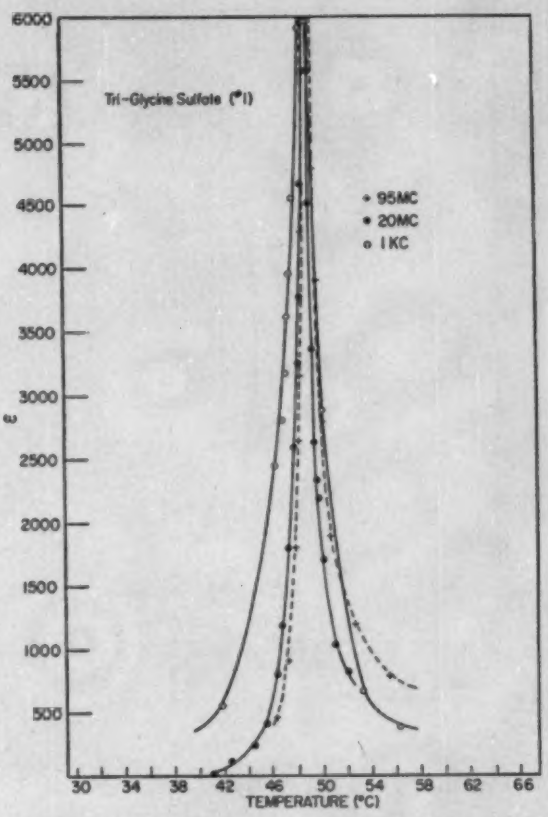

FIG. 1. Dielectric constant vs temperature plotted for 1 kc, 20 95 Mc.

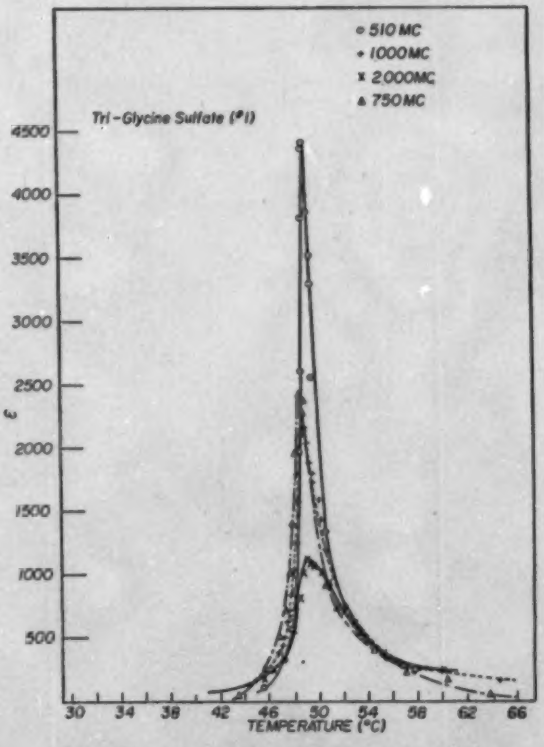

FIG. 2. Dielectric constant vs temperature plotted for 510, 750, 1000, and 2000 Mc.

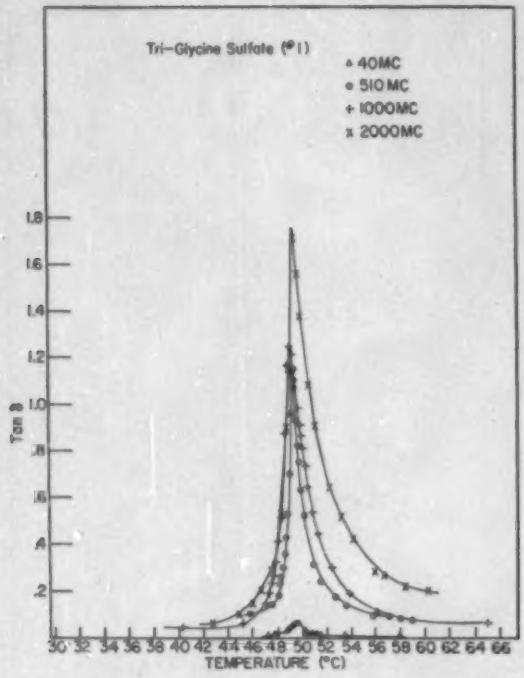

FIG. 3. Tan δ vs temperature plotted for a number of increasing frequencies.

Thus Z_L is given solely in terms of the experimental variables σ and T. The values of C and $\tan\delta$ follow from

$$\tan\delta = R/X = \frac{1+T^2}{\sigma T} \quad \text{for large } \epsilon' \tag{9}$$

and

$$C = \frac{1}{Z_0 \omega X} = \frac{1}{Z_0 \omega T}\frac{\sigma^2+T^2}{\sigma^2}. \tag{10}$$

If we represent the sample by a parallel plate capacitor, then the dielectric constant

$$\epsilon' = \frac{l}{A\epsilon_0}C, \tag{11}$$

where l = length of sample in meters; A = area of electroded surface in (meters)^2; $\epsilon_0 = 8.854\times10^{-12}$ fd/m. Figures 1 and 2 show the dielectric constant as a function of temperature for a number of frequencies; Fig. 3 shows similar curves for $\tan\delta$. In the paraelectric region ($T > T_0$), where the spontaneous polarization is zero[2]

$$4\pi/\epsilon' = 2A(T-T_0). \tag{12}$$

By plotting $1/\epsilon'$ against temperature, it is seen that the dielectric constant follows a Curie-Weiss law. From the slope of this line, the A constants were computed at the various frequencies. Table I summarizes some of the results.

TABLE I.[a]

Frequency	Peak ϵ' measured	Peak $\tan\delta$ measured	T_0 (°C)	A (°C^{-1})
1 kc	~6000	0.10	49.1	2.26×10^{-3}
20 Mc	~6000	0.10	48.8	2.8×10^{-3}
95 Mc	~6000	0.18	48.4	1.4×10^{-3}
510 Mc	4500	1.15	49.1	2.73×10^{-3}
750 Mc	2500	1.20	48.0	2.48×10^{-3}
1000 Mc	2200	1.30	48.4	2.14×10^{-3}
2000 Mc	1200	1.75	47.8	2.00×10^{-3}

[a] It is quite evident that a rapid relaxation of ϵ' starts somewhere between 100 and 500 Mc; the relaxation spectrum is shown in Fig. 4.

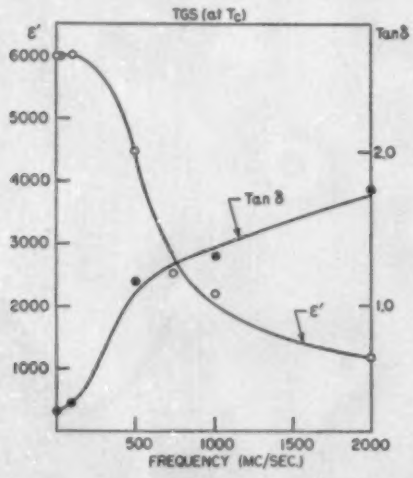

FIG. 4. Relaxation spectrum of TGS showing dielectric constant vs frequency at the Curie point.

[1] S. Triebwasser, IBM J. Research 2, 212 (1958).
[2] A. F. Devonshire, Phil. Mag. Suppl. 3, 85 (1954).

Hooke's Law in Shear and Polymer Melt Fracture

E. B. BAGLEY
Canadian Industries Limited, Central Research Laboratory, McMasterville, Quebec, Canada
(Received March 4, 1960)

IT is the purpose of this paper to show that the assumption of Hook's law in shear, coupled with the results of recent work by Philippoff and Gaskins,[1] leads to a linear relationship between capillary end corrections and shear stress. The slope of this plot is related in a simple fashion to the shear modulus of the liquid, from which, for linear polymer molecules, a molecular weight in good agreement with experiment can be computed. In the case of these polymer molecules, the analysis cannot be applied strictly at shear stresses greater than τ_d, the critical shear stress above which extruded polymer filaments become distorted[2,3] and above which polymer melt fracture is believed to be occurring.[4] The experimental results, however, can be interpreted to show that melt fracture occurs after the recoverable shear reaches a certain critical value.

Let τ be the shear stress, μ the shear modulus, and S_r the recoverable shear strain. Hooke's law in shear can be written

$$\tau = \mu S_r. \tag{1}$$

The recoverable shear is given by the following expression[1]:

$$S_r = 2(e-n), \tag{2}$$

where e is the total capillary end correction and n is the viscous part of the total end correction, called the Couette term. Substitution of Eq. (2) in Eq. (1) gives

$$e = (1/2\mu)\tau + n. \tag{3}$$

Equation (3) predicts a linear relationship between the total end correction e and the shear stress, provided that the Couette term n is constant. To check the validity of Eq. (3), total end corrections have been determined on a number of polyethylene samples as described previously[5] and it was found that e is linear with τ up to the critical shear stress τ_d at, and above, which melt

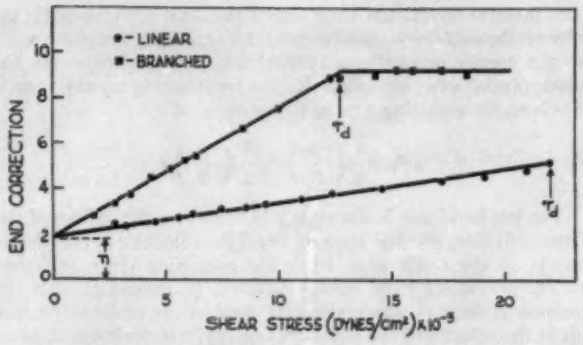

FIG. 1. Total capillary end corrections plotted against true shear stress for a linear and a branched polyethylene. The plots are straight lines as required by Eq. (3), up to the critical shearing stress τ_d at which filament distortion begins.

fracture occurs. (The shear stress τ is the true shear stress at the wall of the capillary.[5]) This is illustrated in Fig. 1 for a linear and a branched polyethylene of melt indices[6] 0.9 and 2.0, respectively. Above τ_d the flow curve of the linear polyethylene is discontinuous[5] and values of e are thus not obtainable for the linear material immediately above τ_d. For the particular branched polymer in Fig. 1, however, e becomes essentially constant above τ_d, although in general, e is found to increase slowly with τ above τ_d.

For both the polymers of Fig. 1 the ordinate intercept gives a value for the Couette correction of about two. From the slopes of the plots of Fig. 1 the shear modulus can be calculated and values of 3.4×10^5 and 8.3×10^5 d/cm² are obtained for the linear and branched material, respectively.

Now Wall was led by theoretical reasoning to conclude that rubber should obey Hooke's law in shear even though it does not obey Hooke's law for extension.[7,8] Wall's value for the shear modulus is

$$\mu = RT\rho/M, \tag{4}$$

where M is the polymer molecular weight, R is the gas constant, T is the absolute temperature, and ρ is the polymer melt density. On assuming Eq. (4) and using the value $\mu=3.4\times10^5$ d/cm² obtained from the slope of the end correction vs shear stress curve for the linear polyethylene, a molecular weight of 85 000 is calculated. This is in reasonable agreement with the value of 90 000 for the weight average molecular weight found for this polymer from intrinsic viscosity measurements in tetralin at 120°C.[9]

The importance of elasticity in the phenomenon of extrudate distortion was clearly recognized by Spencer and Dillon.[2] They suggested that the onset of distortion was at an "isoelongated" state, and that at this critical distortion point the product of shear stress and molecular weight should be constant. They confirmed this prediction experimentally for polystyrene.[2] The substitution of Eq. (4) in Eq. (1) gives, at the critical shear stress τ_d,

$$\tau_d M = (RT\rho)S_{rd}. \tag{5}$$

The constancy of the product $\tau_d M$, found experimentally for polystyrene, shows that the amount of recoverable shear which a polymer can undergo before melt fracture occurs is independent of molecular weight, R and T being constant and ρ, independent of molecular weight.

[1] W. Philippoff and F. H. Gaskins, *Transactions of the Society of Rheology* (Interscience Publishers, Inc., New York, 1958), Vol. II, p. 263.
[2] R. S. Spencer and R. E. Dillon, J. Colloid. Sci. **4**, 251 (1949).
[3] E. B. Bagley, I. M. Cabott, and D. C. West, J. Appl. Phys. **29**, 109 (1958).
[4] J. P. Tordella, J. Appl. Phys. **27**, 454 (1956).
[5] E. B. Bagley, J. Appl. Phys. **28**, 624 (1957). Note that in this reference n refers to the total end correction and not to the Couette portion alone as in the present paper.
[6] Am. Soc. Testing Materials, D-1238-57T.
[7] F. T. Wall, J. Chem. Phys. **10**, 485 (1942).
[8] L. R. G. Treloar, Trans. Faraday Soc. **39**, 36 (1943).
[9] E. Duch and L. Kuchler, Z. Elektrochem. **60**, 218 (1956).

Surface Deformation of Aluminum in Fatigue*

J. C. GROSSKREUTZ AND C. M. GOSSELIN
Midwest Research Institute, Kansas City, Missouri
(Received February 15, 1960)

THE surface contour of slip striations produced by fatigue stressing of metals has been reported recently by Wood and Segall,[1,2] Hirsch, Partridge and Segall,[3] and Backofen.[4]

All have made use of a taper-sectioning technique[3] which magnifies the surface contour (in the direction of cut) by the cosecant of the angle of section (Fig. 1). In order to protect the slipped surface during sectioning and polishing, Wood and Backofen have electroplated the sample. While this procedure provides good contrast between the sectioned and unsectioned surfaces when viewed microscopically, it does obscure the pattern of surface slip, whose contour is being viewed at the interface. Hirsch *et al.*, using transmission electron microscopy, observed the sample edge which had been tapered during the chemical thinning process. Although this technique provides magnification of the order of 500 000, there is some question regarding artifacts introduced by preferential electropolishing at the slip planes.

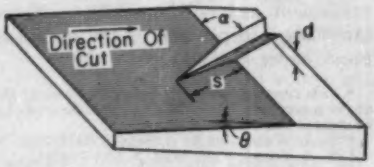

FIG. 1. Schematic representation of taper-sectioning method. The groove corresponds to a slip band on the surface of the sample. The true depth d is given by $d=(s\sin\alpha)\theta/M$, where θ is the taper angle ($\theta<<1$) and M is the optical magnification.

Both of the objections listed have been overcome by taper sectioning fatigued specimens "as received" in a Porter-Blum microtome using a diamond knife. No intervening treatment of the specimen is necessary, except for casting in a 25% methyl methacrylate-75% butyl methacrylate mixture to facilitate sectioning. The angle of the taper section is set roughly (to an angle less than 5°) by means of the movable microtome chuck. The exact angle is measured later by viewing the sample edge-on.

Figure 2 is a photomicrograph of an aluminum specimen 0.004 in. thick run to failure in pulsating tension between 0 and 20 000 psi for 8×10^6 cycles. The area chosen was about 0.030 in. from the failure crack. The direction of the cut can be seen easily from the marks left by the diamond knife. The taper angle is 1°. The star patterns in the lower half of the picture were formed in the

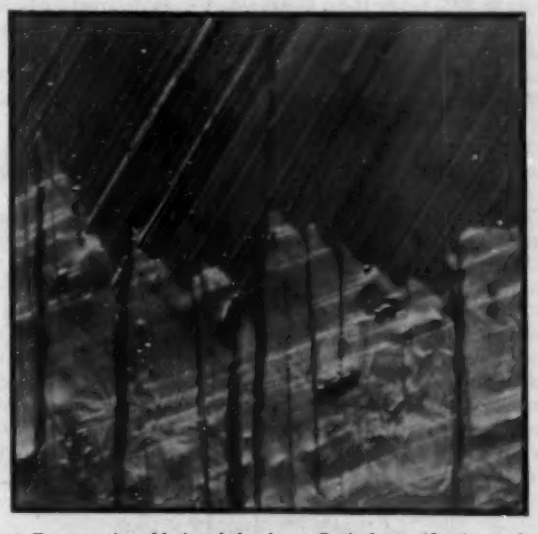

FIG. 2. Taper section of fatigued aluminum. Optical magnification as shown; taper magnification (along cut) 19× ($\theta=1°$).

plastic by the stresses induced during sectioning. The surface contour is clearly seen in juxtaposition with the surface slip markings. Uncut material extending into the sectioned surface corresponds to depressions in the surface. Caution should be exercised to distinguish between actual slip contours and artifacts introduced by irregularities in the cutting edge of the knife. At least one slip band can be seen extending a considerable distance into the sectioned surface, corresponding to a depth of 0.17μ. The average pitch of the "stairstep" contour is $\sim 0.02\mu$.

Experiment has shown that fatigue cracks always originate in the deeper, "persistent" slip bands,[5] which may be considered as notches created by the cyclic slip characteristic of fatigue. A convenient and rapid method of viewing these notches simultaneously in depth and on the surface is afforded by the microtomed-taper sections reported here.

* This research was supported in whole or in part by the U. S. Air Force under a contract monitored by the Materials Laboratory, WADD, Wright-Patterson Air Force Base, Ohio.

[1] W. A. Wood and R. L. Segall, Bull. Inst. Metals 3, 160 (1957).
[2] W. A. Wood, Phil. Mag. 3, 692 (1958).
[3] P. B. Hirsch, P. G. Partridge, and R. L. Segall, Phil. Mag. 4, 721 (1959).
[4] W. A. Backofen (private communication).
[5] N. Thompson, N. J. Wadsworth, and N. Louat, Phil. Mag. 1, 113 (1956).

Comments on a Ruptured Soap Film

F. E. C. Culick
Massachusetts Institute of Technology, Naval Supersonic Laboratory, Cambridge, Massachusetts

(Received January 5, 1960)

SUBSEQUENT to puncturing at a point, a horizontal soap film develops a hole whose edge, owing to surface tension, propagates outward from the point of puncture at apparently constant velocity. Measurements by Ranz[1] yielded results roughly 10% lower than those calculated on the basis of a simple energy conservation suggested by Rayleigh.[2] The discrepancy was attributed to an additional retarding viscous stress not included in the analysis. It appears, however, that the energy balance quoted[1] neglects an important contribution, indeed related to the viscous effect noted by Ranz, but which reduces the calculated values to 20% below those measured. A more detailed analysis of the motion of the edge gives this result; the neglected contribution arises from inelastic acceleration of the undisturbed fluid up to the velocity of the edge. The concomitant loss in mechanical energy may be identified with viscous dissipation which is estimated to be confined to a relatively thin region. Lack of agreement between calculated and measured values of the edge velocity seems to be caused by a second-order effect in the method used[1] to determine the thickness of the film.

The film is assumed to have uniform thickness h and uniform properties (in particular constant surface tension σ everywhere), so the flow is ideally symmetric about an axis through A, the point of puncturing. While the fluid from the destroyed portion of the film collects around the edge, the film outside the edge is, according to observation, undisturbed. Consider a sector in the plane of the film of small included angle α and vertex at A; the fraction of rolled edge within this sector and located at distance r from A may treated as a system of variable mass m as it progresses outward at velocity $v=dr/dt$. Then relative to the point A, one may write for the sum of forces acting on the rolling edge, ignoring the effects of gravity and aerodynamic drag

$$F=\frac{d}{dt}(mv)=\frac{d}{dr}\left(\frac{mv^2}{2}\right)+\frac{v^2}{2}\frac{dm}{dr}$$

$$Fdr=d\left(\frac{mv^2}{2}\right)+\frac{v^2}{2}dm.$$

By conservation of mass, $m=\frac{1}{2}\rho r^2 h\alpha$ and integrating over r,

$$\int_0^r Fdr=\frac{1}{4}\rho r^2 h v^2\alpha+\frac{\rho h\alpha}{2}\int_0^r v^2 r dr.$$

The integral on the left-hand side is the total work done by the film on the edge in the motion from A to r, and is, therefore, equal to the energy originally associated with the surface which has dissappeared $\sigma r^2\alpha$; alternatively, the force acting on the edge is $F=2\sigma r\alpha$. On assuming v to be independent of r,

$$\sigma r^2\alpha=\frac{1}{2}\rho\left(\frac{r^2 h\alpha}{2}\right)v^2+\frac{1}{2}\rho\left(\frac{r^2 h\alpha}{2}\right)v^2.$$

The left-hand side is the energy liberated by the surface of the destroyed film; the first term on the right-hand side is the kinetic energy of the rolled edge, while the remaining term, neglected in the previously cited energy balance, is associated with the inelastic process of accelerating the fluid in the undisturbed film up to the velocity of the edge. This energy, which always appears in a problem involving "plastic pick-up" of mass, is evidently lost as regards the mechanical energy of the system; it is dissipated by internal fluid friction. The expression for the velocity of the edge is now

$$v=\left(\frac{2\sigma}{h\rho}\right)^{\frac{1}{2}},$$

which is $1/\sqrt{2}$ smaller than that computed by Rayleigh and is equal to the propagation speed of elastic waves in the sheet.

That the calculated values of velocity differ so greatly from Ranz' measurements is probably more correctly ascribed to errors in the values of the ratio σ/h. σ has been assumed known (with questionable accuracy) and σ/h was measured in a manner which might lead to quite large errors. For example, as the film sags, since it does not rupture, ensuing gradients in concentration lead to increasing values of σ away from the lowest point. Assume variations in h to be moderate, but approximate σ by $\sigma\approx\sigma_0+\sigma' x$ in the coordinate system adopted by Ranz (Fig. 4)[1]; the force balance for a small circular section of film centered at the lowest point is

$$\rho g\pi x^2 h\approx 4\pi x(\sigma_0+\sigma' x)dy/dx,$$

which can be integrated to

$$y=\frac{\rho g h}{4\sigma_0}\left[\frac{x}{\sigma_1}-\frac{1}{\sigma_1^2}\log(1+\sigma_1 x)\right];\quad \sigma_1=\frac{\sigma'}{\sigma_0}.$$

For small $\sigma_1 x$,

$$y\approx\frac{\rho g h}{4\sigma_0}\left[\frac{x^2}{2}-\frac{\sigma_1 x^3}{3}-\cdots\right].$$

The second term in brackets constitutes a correction to Ranz' Eq. (5), which assumed $\sigma'=0$. The sign of this correction implies that the shape of the film is something between a paraboloid and a plane; that is, for a given h/σ_0 the focal length f is larger,

$$f=\frac{x^2}{4y}=\frac{2\sigma_0}{\rho g h};\quad \sigma \text{ const}$$

$$f\approx\frac{x^2}{4y}\approx\frac{2\sigma_0}{\rho g h}[1+\tfrac{2}{3}\sigma_1 x+\cdots];\quad \sigma=\sigma_0+\sigma' x.$$

Conversely, a given measured f implies a smaller actual h/σ_0 than that deduced from Ranz' equation. Consequently, the calculated values of v should be higher, reducing the difference between the experimental results and those computed from the expression derived in the foregoing.

Since the measured focal length is proportional to the radius of curvature of the film, it is likely to be quite sensitive to small variations in the film shape. On the other hand, the expression for v probably predicts the edge velocity quite accurately providing local values of h/σ are used.

Finally, it is a simple matter to estimate the extent of the region in which the acceleration of the fluid, and hence the dissipation of energy, occur. Suppose the acceleration of the undisturbed fluid to take place in a distance δ at the outer boundary of the rolled edge where the thickness is still approximately h. The

volume in which dissipation occurs is then approximately $\alpha r h \delta$; the rate at which energy is dissipated is

$$\mu \int \left(\frac{dv}{dr}\right)^2 d\tau,$$

the integral being over volume. Since $dv/dr \sim v/\delta$, mechanical energy is lost to the system at the rate

$$\mu \frac{v^2}{\delta^2}(\alpha r \delta h).$$

From the foregoing results, this must equal half the rate at which surface energy in the film is released,

$$\mu \frac{v^2}{\delta}(\alpha r h) = \frac{1}{2}\frac{d}{dt}(\alpha r^2 \sigma),$$

$$\frac{\delta}{h} \sim \frac{\mu v}{\sigma}.$$

With $v \approx 500$ cm/sec, $\mu \approx 10^{-2}$ poises and $\sigma \approx 26$ d/cm, $\delta/h \sim 0.2$, indicating that the viewpoint adopted here seems to be consistent. The temperature rise of the rolled edge can easily be computed to be negligibly small, of the order of 0.006°C, assuming all the heat to be retained in the edge.

Associated with the surface of the rolling edge itself is an amount of surface energy, which is contantly increasing as the edge collects fluid. This energy need not be included in previous considerations since it does not derive from the destroyed film but rather from the work done by the pressure difference across the surface of the edge. For, consider a unit length of edge, very nearly a cylinder, of radius a. The surface energy is then $2\pi a\sigma$ (neglecting the small area intersected by the undisturbed film); the pressure difference across the surface is $\Delta p = \sigma/a$ and the net normal force on the surface is $\Delta p \cdot 2\pi a$. Hence, in a small radial expansion δa, the work done by the normal force is $2\pi\sigma\delta a$, which exactly equals the change in surface energy $\delta(2\pi\sigma a) = 2\pi\sigma\delta a$. This work done by the fluid internal to the edge of course results in a slight lowering of the temperature which, however, is much less than the increase computed in the previous paragraph.

It is rather an amusing result that the viscous stresses can have such a significant influence on the energy distribution. Another example of this is Rayleigh's problem[3] of the infinite plate bounded on one side by an incompressible fluid and started impulsively in motion with constant velocity at $t=0$. One can easily compute that at any later time, of the work done in overcoming surface friction, the $\sqrt{2}/2$ part has been dissipated by internal friction, the remainder appearing as kinetic energy.

[1] W. E. Ranz, J. Appl. Phys. 30, 1950 (1959).
[2] Lord Rayleigh, Sci. Papers 3, 441 (1902).
[3] Lord Rayleigh, Sci. Papers 1, 474 (1899).

More Experiments on Liquid Films

R. M. Koros, J. Deckers, and M. Boudart*
Chemical Engineering Laboratory, Princeton University, Princeton, New Jersey
(Received March 14, 1960)

When two opposed vertical jets collide, a stable liquid horizontal sheet of radius r_0 is formed. Some experiments on such liquid films were reported recently by Ranz[1] and Taylor.[2] The former rediscovered a simple relation between r_0 and the surface tension of the liquid. This relation first derived and checked experimentally with water, mercury, and aqueous solutions of soaps and alcohols by Bond and Puls[3–5] is based on a straight momentum balance, assuming no losses either in the region of impact or in the film itself.

More experiments on liquid films are summarized here to show that the second assumption is correct but that the first one applies only to liquids of low viscosity. The electrical conductivity of the films was measured in the apparatus shown in Fig. 1. Clearly, as the distance r between the probe and the external metal ring is increased, the measured voltage drop should increase linearly if the cross-sectional area A of the film perpendicular to the direction of current and fluid flow stays constant. This is indeed the case as shown by the data of Fig. 2. But if A does not change with r, no detectable momentum loss takes place in the film itself.

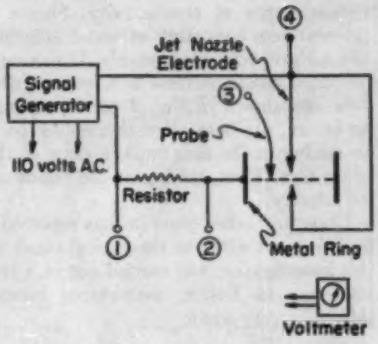

Fig. 1. Schematic diagram of experimental apparatus. Voltmeter was connected to points 1 and 2 to measure reference voltage in the voltage divider circuit. Potential drop at various radial positions in the liquid film was measured across points 3 and 4. The voltmeter was a high internal impedance vacuum tube voltmeter.

On the other hand, comparison between the slopes of the straight lines for water (viscosity: 1 cps) and a glycerol water solution (viscosity: 91 cps) reveals that, in the latter case, the calculated area A is now larger. This implies a loss of momentum in the region of impact for the more viscous fluid.

A similar situation obtains for mixing between the liquid jets. While some mixing occurs at the region of impact, no detectable mixing takes place in the sheet itself. This again was shown by

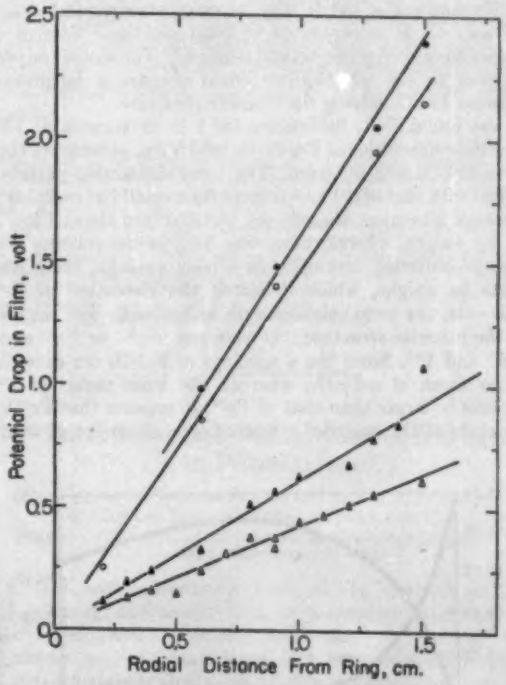

Fig. 2. Potential drop in film (volt) vs radial distance from ring (cm). Upper nozzle diameter: 0.191 cm; lower jet diameter: 0.193 cm. ▲ Upper jet: dilute water solution of NaCl, viscosity 1 cps, velocity at the nozzle: 392 cm/sec; lower jet: same liquid, velocity at the nozzle: 384 cm/sec. △ Upper jet: a mixture of water, glycerol, and NaCl, viscosity 91 cps, velocity at the nozzle; 236 cm/sec: lower jet: same liquid, velocity at the nozzle: 231 cm/sec. ● Upper jet: dilute water solution of $Ba(OH)_2$, velocity at the nozzle: 381 cm/sec; lower jet: dilute water solution of H_2SO_4, velocity at the nozzle: 392 cm/sec. ○ Upper jet: dilute water solution of $Ba(OH)_2$, velocity at the nozzle: 213 cm/sec; lower jet: dilute water solution of H_2SO_4, velocity at the nozzle: 228 cm/sec.

measurements of conductivity. Sheets were formed from two different jets consisting of water solutions of barium hydroxide and sulfuric acid, respectively. If mixing occurs, the resistance of the sheet should increase as a result of neutralization. Two sets of data are shown in Fig. 2 corresponding to different velocities. As before, the data align themselves on straight lines indicating no mixing in the film but the slope of the line is steeper for the faster film. Thus, mixing at the region of impact increases with jet velocity.

These and other observations reported in detail elsewhere,[6] are in agreement with the theoretical views of Taylor.[2] In particular, this investigation was carried out in a region of velocities where, according to Taylor, momentum losses due to air resistance should be very small.

[*] This work was supported in part by the Office of Scientific Research, United States Air Force, under a contract.

[1] W. E. Ranz, J. Appl. Phys. **30**, 1950 (1960).
[2] G. I. Taylor, Proc. Roy. Soc. (London) **A253**, 289 (1959).
[3] W. N. Bond, Proc. Phys. Soc. **47**, 549 (1935).
[4] H. O. Puls, Phil. Mag. **22**, 970 (1936).
[5] W. N. Bond, Phil. Mag. **24**, 864 (1937).
[6] R. M. Koros, M.Sc. Thesis, Princeton University (1950) and Air Force Technical Note.

Antiferromagnetic $FeVO_3$

CHESTER R. BERRY AND CHARLES M. COMBS
Research Laboratories, Eastman Kodak Company, Rochester, New York
(Received February 16, 1960)

COMPOUNDS having the rhombohedral structure of ilmenite $FeTiO_3$ have interesting magnetic properties. Recently, $CoMnO_3$ and $NiMnO_3$ have been made and are ferromagnetic.[1,2] Hematite,[3,4] α-Fe_2O_3, and Cr_2O_3[5,6] are antiferromagnetic. $FeTiO_3$ is antiferromagnetic but it may be made strongly ferromagnetic when α-Fe_2O_3 is incorporated in solid solution.[7] Several other titanates have been prepared and studied.[8,9] The aim of the present work was to see whether we could prepare a ferromagnetic compound $FeVO_3$ having the ilmenite structure.

It was found that, by heating for 1 hr in vacuum at 1200°C appropriate quantities of Fe, Fe_2O_3, and V_2O_3, a complete conversion to $FeVO_3$ was obtained. The x-ray diffraction pattern was identical with that of α-Fe_2O_3, except for a small but real change in d spacings. Chemical analysis for metallic iron showed less than 0.5% by weight, whereas there was 24% in the starting charge. When the sintering was done in a poor vacuum, there was an increase in weight, which indicated the formation of $FeVO_4$. In this case, the ionic valences were undoubtedly Fe^{3+} and V^{3+}.

In the ilmenite structure, the valences might be Fe^{2+} and V^{3+} or Fe^{3+} and V^{4+}. Since the d spacings of $FeVO_3$ are exceedingly close to those of α-Fe_2O_3, whereas the ionic radius of V^{3+} is substantially larger than that of Fe^{3+}, it appears that $Fe^{2+}V^{4+}O_3$ is the state of the material produced. For either set of valences, the spin-only magnetism per molecule would be the same and rather large, 3 Bohr magnetons, provided the Fe and V ions occur in separate layers along the hexagonal axis (the ordered structure) and the adjacent cationic layers are antiferromagnetically coupled. No measurements of the magnetic susceptibility are available, but traces of the B—H curve of dispersions of the $FeVO_3$ failed to show any ferromagnetism at room temperature.

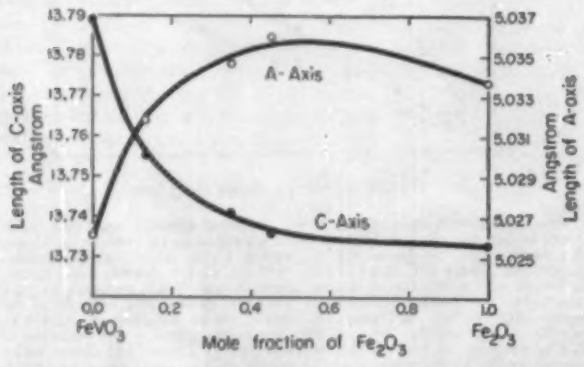

FIG. 1. Lattice dimensions of solid solution of Fe_2O_3 in $FeVO_3$.

Because of the success of Ishikawa and Akimoto[7] in producing ordered structure and ferromagnetism in $FeTiO_3$ by cooling slowly solid solutions of α-Fe_2O_3 in $FeTiO_3$, this scheme was investigated for $FeVO_3$. With additions of 20, 40, and 50 mole % of Fe_2O_3 to $FeVO_3$, solid solution was demonstrated from x-ray diffraction measurements. Changes in lattice dimensions are shown in Fig. 1. Measurements of the unit-cell dimensions were made using $CuK\alpha_1$ reflections from the two back-reflection lines, (2,3,10) and (4,2,4). In addition to the solid solution, there was, in the diffraction patterns, evidence of somewhat less than 10% of a spinel component, apparently Fe_3O_4. In plotting the values of composition in Fig. 1, account was taken of the loss of the iron to the spinel phase. Changes of lattice dimension and unit-cell volume are very small in this system. For this reason, it seems likely that solid solution occurs over the entire range of compositions.

There was no indication of the superlattice lines (003) or (011) in $FeVO_3$ or in the solid solutions. There was no indication of ferromagnetism other than the small amount associated with the spinal component of the mixtures. The lack of ferromagnetism and of superstructure lines indicates that these preparations of $FeVO_3$ and its solid solutions have the disordered ilmenite structure.

We wish to thank Dr. M. L. Huggins for suggesting the investigation of this material.

[1] T. J. Swoboda, R. C. Toole, and J. D. Vaughan, J. Phys. Chem. Solids **5**, 293 (1958).
[2] R. M. Bozorth and D. E. Walsh, J. Phys. Chem. Solids **5**, 299 (1958).
[3] L. Néel, Ann. phys. **4**, 249 (1949).
[4] C. G. Shull, W. A. Strauser, and E. O. Wollan, Phys. Rev. **83**, 333 (1951).
[5] J. Foex and M. Graf, Compt. rend. **209**, 160 (1939).
[6] B. N. Brockhouse, J. Chem. Phys. **21**, 961 (1953).
[7] Y. Ishikawa and S. Akimoto, J. Phys. Soc. Japan **12**, 834, 1083 (1957).
[8] Y. Ishikawa and S. Akimoto, J. Phys. Soc. Japan **13**, 1110, 1298 (1958).
[9] G. Shirane, S. J. Pickart, and Y. Ishikawa, J. Phys. Soc. Japan **14**, 1352 (1959).

Comments on "Determination of Atomic Scattering Factors"

D. R. CHIPMAN AND ARTHUR PASKIN
Materials Research Laboratory, Ordnance Materials Research Office, Watertown, Massachusetts
(Received October 19, 1959; revised manuscript received January 22, 1960)

ROOF[1] has recently published x-ray measurements of the atomic scattering factor of Al as obtained from absolute measurements on powders. We believe that both the procedure and the measurements are in error. Roof has used the wrong equation for relating powder intensities to the scattering factors and further has used incorrect values for some of the parameters. The correct equation is

$$\frac{\Sigma\omega'}{I_0}=|F_0|^2\frac{lw}{R^2}\left(\frac{e^2}{mc^2}\right)^2\frac{\lambda^3}{64\pi}\left(\frac{1+\cos^2 2\theta}{\sin^2\theta\cos\theta}\right)\frac{nN^2}{\mu},$$

where ω' is the angular velocity of the counter, w is the width of the receiving slit, and all other quantities are as defined by Roof. If we compare this equation with Roof's, we find that his measured form factors $|F_0|^2_R$ should differ from the correct values $|F_0|^2$ by the factor $(R/w)\ (\omega'/\omega)=(5.73/0.020)(2/1)=573$. The fact that this is not the case means compensating errors must have been made. There is not sufficient detail in the article to pinpoint the compensating errors, but the following is a possible explanation. To begin with, comparing the value of ω used by Roof with

those commonly available in the GE diffraction unit, we deduce that ω is probably in deg/sec, rather than the required rad/sec. Further, Roof has incorrectly used 2.46, the density of the powder slab rather than 2.69, the required density of the bulk aluminum in calculating μ. These two errors compensate for most of the factor 573. We believe that the remaining factor of about 10 probably arises from measuring too small a value of I_0. This might have occurred, for example, if I_0 had been measured through the small receiving slit used in recording the diffraction peaks. We find (by duplicating Roof's experimental arrangement) that I_0 so measured is about a factor of 13 smaller than the required total power in the primary beam. Regardless of the details of the compensating errors, however, it is apparent that the erroneous absolute standardization makes comparisons between measurements made at different wavelengths questionable, although the relative form factors at a given wavelength may still be meaningful. Arbitrarily normalizing the three sets of form factors so that they are equal at a given Bragg peak, we find that all the data are in agreement.

[1] R. B. Roof, Jr., J. Appl. Phys. 30, 1599 (1959).

Reply to Comments on "Determination of Atomic Scattering Factors"

R. B. Roof, Jr.
Los Alamos Scientific Laboratory, Los Alamos, New Mexico
(Received February 22, 1960)

In the preceding note Chipman and Paskin[1] have reinterpreted some experimental data obtained by the author. A point of contention is the author's use of the experimental density instead of the theoretical density to calculate the linear absorption coefficient of the sample. Upon reexamination of this problem the author concludes that Chipman and Paskin are correct in this point, i.e., the theoretical density should be used to calculate the linear absorption coefficient of the sample. An incorrect treatment of this problem is given in Peiser, Rooksby, and Wilson,[2] whereas a correct solution is given by Zachariasen.[3]

Unfortunately, the techniques proposed by the author in the original paper[4] *do not* lead to an absolute determination of an atomic scattering factor as was hoped. Review of criticisms of some of the techniques, coupled with the clarity of hindsight, lead the author to the conclusion that a calibration procedure must be employed. Under the ground rules and definitions of the original experiment an observed experimental scattering curve is obtained which, when compared with a theoretical scattering curve, allows the instrument and slit systems to be calibrated. This is accomplished as follows. Let ω be redefined as the angular velocity of the detector, let the correct density be used, and let all other terms remain defined as before. Then an experimental scattering curve is obtained which may be compared with a theoretical curve (assumed to be correct) according to the following equation:

$$f_{\text{theoret}} = k f_{\text{obs}},$$

where k is defined as an instrument calibration function. The variation of k as a function of $\sin\theta/\lambda$ is shown in Fig. 1. Curve A is obtained from the author's data after correcting for the original error in the density. Curve B is obtained from Chipman and Paskin's handling of the author's data. Surface roughness (which Chipman and Paskin ignore) has very little effect and the main difference between the two curves is due to Chipman and Paskin using absorption coefficients that are ultimately derived from Jonsson[5] while the author uses those obtained from Grodstein.[6] The author favors the use of the Grodstein coefficients as Jonsson's method of representation is in error for elements of both low atomic number (Woernle[7]) and high atomic number (Roof[8]).

The author feels that such calibration procedure is valid, since its employment on data obtained from powder samples other than aluminum yields scattering curves which, when compared with theoretical curves result in correct signs for the real and imaginary part of the anomalous dispersion corrections. (Data to be published at a later date.) Failure to use the calibration procedure results in a reversal of sign for the real part of the anomalous dispersion correction and the sign of the imaginary part of the anomalous dispersion correction is faced with the bleak prospect of being imaginary. Such results are in violent disagreement with any reasonable theory that can be proposed for the effects of anomalous dispersion. In summary the author wishes to reiterate the following points: 1. The techniques described in the original paper *do not* lead to an absolute measurement of an atomic scattering factor. 2. The techniques described in the original paper, however, do lead to an observed scattering factor, which may be compared to a theoretically correct scattering factor according to $f_{\text{theoret}} = k f_{\text{obs}}$, where k is defined as an instrument calibration function.

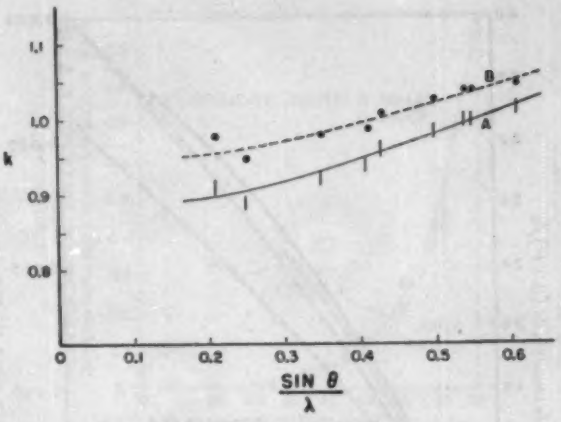

FIG. 1. The variation of an instrument calibration function k with $\sin\theta/\lambda$. Curve A based on author's data, curve B based on Chipman and Paskin handling of author's data. Main difference caused by use of different absorption coefficients by the author and Chipman and Paskin.

[1] D. R. Chipman and A. Paskin, J. Appl. Phys. 31, 1130 (1960).
[2] H. S. Peiser, H. P. Rooksby, and A. J. C. Wilson, *X-ray Diffraction by Polycrystalline Materials* (The Institute of Physics, London, 1955), p. 402.
[3] W. H. Zachariasen, *Theory of X-ray Diffraction in Crystals* (John Wiley & Sons, Inc., New York, 1945), p. 175.
[4] R. F. Roof, Jr., J. Appl. Phys. 30, 1599 (1959).
[5] E. Jonsson, thesis, Upsala, 1928 (unpublished).
[6] G. W. Grodstein, *X-Ray Attenuation Coefficients from 10 kev to 100 Mev*, National Bureau of Standards Circular No. 583 (U. S. Government Printing Office, Washington, D. C., 1957).
[7] B. Woernle, Am. Physik 5, 475 (1930).
[8] R. B. Roof, Jr., Phys. Rev. 113, 820 (1959).

Solubilities and Diffusivities of Nitrogen in Polyethylene*

J. L. Lundberg, M. B. Wilk, and M. J. Huyett
Bell Telephone Laboratories, Inc., Murray Hill, New Jersey
(Received January 7, 1960; revised manuscript received February 8, 1960)

This note summarizes some of the methods and results, kinetic and equilibrium, of a sorption study of nitrogen into polyethylene at elevated pressures.

Molten polymer constrained in a cylindrical shape in a tube of sintered glass or steel is placed in a thermostatted high-pressure system of known volume. The sintered cylinder is impermeable to the viscous liquid polymer and is assumed to offer no barrier to gas. Gas is admitted, and the system is closed quickly. Pressure measurements are made with a Bourdon tube at 15-sec intervals at the outset of the experiment and at progressively longer intervals (to 10 min after 10 hr) as the sorption in the closed system progresses. Sorption is complete within Bourdon

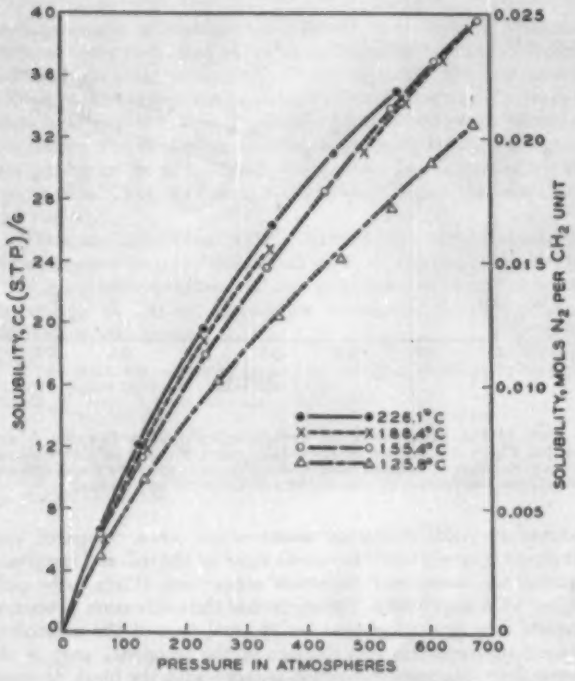

FIG. 1. Plot of the solutility of nitrogen in liquid polyethylene vs equilibrium pressure.

tube sensitivity in about 12 hr for nitrogen diffusing into a 1.9-cm diam cylinder of molten polyethylene. Gas is added to the system in a series of cumulative increments of 70 to 110-atm pressure change each day over eight successive days to a final pressure of 650 to 680 atm.

Pressure readings are converted to numbers of free moles of gas external to the polymer by a virial expansion of the gas law using the known temperatures and volume of the gas phase of the system. An interpolated compressibility factor, calculated from a virial equation of state determined by least-squares fit of selected published P-V-T data for nitrogen, is used.

On assuming an infinite cylinder and a diffusion coefficient invariant with concentration and time, the Fourier differential

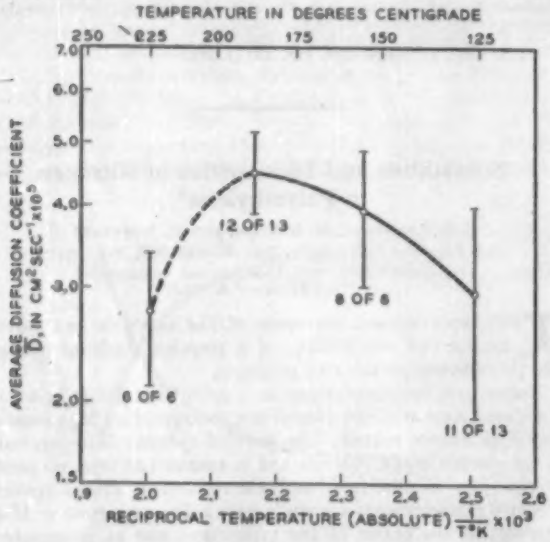

FIG. 2. Plot of the logarithm of the diffusion coefficient vs the reciprocal of absolute temperature for nitrogen diffusing in liquid polyethylene. (Approximate 95% confidence intervals are shown by end points.)

equation[1] for radial diffusion from a closed, "well-stirred" solution may be solved explicitly as an infinite series involving successive roots of a nonlinear equation involving Bessel functions.[2] This diffusion equation is approximated for numerical convenience by two equations.[3]

The unknown parameters of the diffusion equation or its approximation are the diffusion coefficient, the initial number of free moles, and the final number of free moles. The last of these is known quite accurately from pressure measurements after long periods of time. The other two unknown parameters are estimated from the mole-time data by fitting the approximations to the diffusion equation to the data using the criterion of least squares. The solubility estimate is then easily deduced from the estimated initial number of free moles, the final number of free moles, and the known weight of polymer. Stable graphical or analytical extrapolation to zero time is difficult in systems of high diffusivity even over periods as short as 15 sec because of the interdependence of the estimates of the initial number of free moles and the diffusion coefficient. Graphical extrapolation to zero time tends to lead to underestimates of the solubility. Admitting gas in too large increments at the start of a single sorption run leads to similar errors. (For example, see the 188.4°C solubility isotherm of Fig. 1.)

The dependencies on pressure and temperature of estimated solubilities of nitrogen in liquid polyethylene are shown in Fig. 1. These solubilities are high for gases in polymers,[4] increasing with pressure (but less rapidly than linearly as predicted by Henry's law) up to 2.5 mole % nitrogen based on methylene ($-CH_2-$) content of the polyethylene at 680-atm pressure. Solubilities increase with increasing temperature.

The diffusion coefficients for nitrogen in polyethylene are high (from 2.8×10^{-5} to 4.5×10^{-5} cm^2 sec^{-1}) and appear to first increase and then decrease with increasing temperature. (See Fig. 2.) The observed maximum in the diffusion coefficient with temperature probably errs in being too pronounced and may even be an artifact of the experimental technique because gas charges were not preheated. This would tend to make estimated diffusion constants too small especially at the higher temperatures. Activation energies of diffusion of nitrogen into polyethylene are small, less than 4 kcal/mole at 125.8°C, and apparently decreasing at higher temperatures.

A partial indication of the reliability of the experimental results is given by approximate 95% confidence interval allowances. These are ±24% of the diffusion coefficient estimates and ±1% of the solubility estimates. These allowances apply to the solubility and diffusion coefficient estimates separately, but do not indicate the very considerable statistical interdependence of the estimates. This interdependence of estimates, as well as the concentration, pressure, and time dependence of the diffusion coefficient, has been investigated on this and other systems and will be reported in detail elsewhere.

[a] Presented in part before the Division of High Polymer Physics, Cambridge, Massachusetts, April 2, 1959.

[1] Joseph Fourier, "Theory analytique de la chaleur" (1822).

[2] H. S. Carslaw and J. C. Jaeger, *Conduction of Heat in Solids* (Oxford University Press, New York, 1947).

[3] J. Crank, *The Mathematics of Diffusion* (Oxford University Press, New York, 1956); P. C. Carman and R. A. W. Haul, Proc. Roy. Soc. (London) **A222**, 109 (1954).

[4] G. J. van Amerongen, J. Polymer Sci. **5**, 307 (1950).

Distribution of Spray From Impinging Liquid Jets

K. DEXTER MILLER, JR.
The M. W. Kellogg Company, Jersey City, New Jersey
(Received March 2, 1960)

THE impingement of two equal liquid jets produces a flat sheet of spray in a plane perpendicular to the plane containing the jet counterlines. As in many spray-forming devices, the droplets in this case originate in a thin film of liquid surrounding

the point of impingement. If the jets impinge head-on, the flow in the film and the resulting spray are equally distributed in all directions. As the angle between the jets is reduced, the flow rapidly shifts to the forward direction.

In his article W. E. Ranz[1] obtains analytical results which differ significantly from those obtained by the author. At total included angles of 120° or less, Ranz predicts no backward flow. The author's prediction and experiments agree that small but measurable amounts of backward flow exist at a 90° impingement angle. Analytically, the amount of backward flow reaches zero only when the included angle disappears.

In the free-space impingement of two jets, the eventual course of the spray is affected not only by the hydrodynamic flow conditions in the liquid film, but by surface tension, viscosity, and gravitational factors. In some cases, the entrainment of air by the jets may also cause changes in this pattern. In many cases of practical interest, fluid flowing backward in the film is brought around toward the front in two side streams.[2]

The author's work has been, however, directed principally toward the hydrodynamically analogous situation in which a single jet is directed against an inclined baffle plate. In this circumstance, the initial distribution of the liquid film can be of primary importance.

Analytical considerations. The basic flow equations and assumptions used by the author and by Ranz are identical, and may be summarized as follows, adopting Ranz' notation. Two equal circular jets of diameter d_0 are considered, impinging on each other at a total angle 2θ. A film of liquid spreads between the jets, making an angle θ with each. The fluid velocity in this film is considered constant, equal to the jet velocity, and radial to the center of impact. The component of the momentum of the jets lying in the film plane is considered conserved. Gravity, viscosity, and surface tension effects are ignored.

If r is the radial distance of a point in the film from the impact center, and ϕ its angular position from the forward direction of the jets, and if h is the film thickness at this point, the continuity condition may be expressed as

$$2(\pi d_0^2/4)v_0\rho = \int_0^{2\pi} \rho v_0 h r d\phi. \tag{1}$$

The momentum balance condition leads to

$$2(\pi d_0^2/4)\rho v_0^2 \cos\theta = \int_0^{2\pi} \rho v_0^2 h r \cos\phi d\phi. \tag{2}$$

Equations (1) and (2) are identical to Eqs. (13) and (14) in footnote reference 1.

Since the flow must be symmetrical about the intersection of the two planes,

$$\int_0^{2\pi} h \sin\phi d\phi = 0. \tag{3}$$

It is desired to find a function $h=h(r,\phi,\theta)$ which will satisfy Eqs. (1) through (3), and which will meet the further restriction that $h \geq 0$ for all values of the variables in the range of interest.

Ranz proposes [Eq. (15) of footnote reference 1], the following relationship:

$$h = (d_0^2/4r)(1+2\cos\theta\cos\phi). \tag{4}$$

This is a solution of the three integral equations, but indicates negative film thicknesses for values of θ less than 60°. The use of this expression is, therefore, limited to larger values of θ.

An alternative solution, which avoids this difficulty is

$$h = (d_0^2/4r)\left(\frac{1-\cos^2\theta}{1+\cos^2\theta}\right)\left(\frac{1}{1-\dfrac{2\cos\theta\cos\phi}{1+\cos^2\theta}}\right). \tag{5}$$

This expression is a solution of Eqs. (1) to (3), and for all values of θ and ϕ it predicts positive film thickness. At large θ, such that $\cos^2\theta$ terms may be neglected, Eqs. (4) and (5) converge and predict identical flow conditions. As θ is decreased, the difference between the expressions increases.

Experimental results. In a series of experiments, the author directed a jet of water with a diameter of 0.1 in. against a 0.5-in.-diam horizontal baffle plate at a velocity of approximately 50 ft/sec. Water spraying from this plate was collected in 1.6 segmental collection chambers equally spaced about the periphery of the plate. The jet was carefully aligned to strike the center of the baffle plate. Tests were conducted at various values of θ between 45° and 90°, and the flow distribution recorded. Repeated runs were made to assure satisfactory reproducibility.

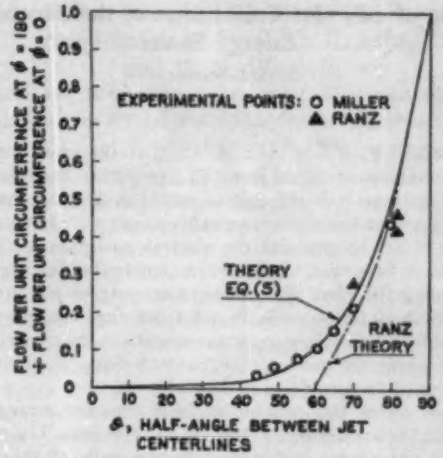

FIG. 1. Variation in the ratio of backward to forward film flow in the impingent spray of circular jets as the impingement angle is varied.

The flow distribution measured in these tests conformed well with that predicted by Eq. (5) as is shown in Figs. 1 and 2. Figure 1 shows the ratio between the backward and forward film flow as predicted by Eq. (5) and by Ranz in Eq. (4). Also shown are experimental points by the author and by Ranz (as scaled from footnote reference 1). In the range of θ between 70° and 90°, where Ranz' experiments were conducted, both analyses predict similar results and the experimental data agree. Below 70°, the author's analysis and experiments show more backward flow.

Figure 2 shows the angular distribution of film thickness as predicted by Ranz and by the author, with the author's experimental points. It may be seen that the Ranz relationship underestimates the forward and backward flow, while overestimating the lateral flow.

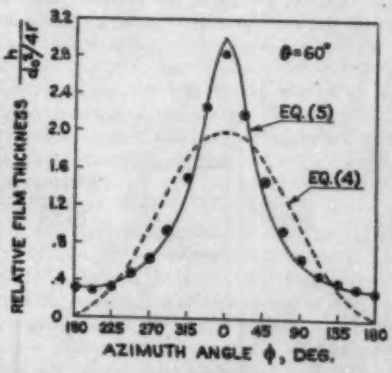

FIG. 2. Circumferential distribution of flow in the spray formed by two impinging circular jets at a half-angle of 60°.

From these data, it appears that Eq. (5) predicts the distribution of film flow more accurately than does that proposed by Ranz. Although the general conclusions drawn by Ranz are fully applicable, there are circumstances where a more accurate determination of flow distribution is desirable.

This work was carried out at the M. W. Kellogg Company under a contract with the U. S. Department of the Air Force.

[1] W. E. Ranz, J. Appl. Phys. 30, 1950 (1959).
[2] Heidmann, Priem, and Humphrey, Nat'l. Advisory Comm. Aeronaut. Tech. Note 3835 (March, 1957).

Use of SF_6^- for Calibration of the Electron Energy Scale

G. J. SCHULZ
Westinghouse Research Laboratories, Pittsburgh 35, Pennsylvania
(Received February 7, 1960)

RECENTLY, it has been shown that the cross section for production of SF_6^- from SF_6 peaks at essentially zero energy.[1] Because it is difficult to establish an accurate energy scale for negative ion studies, some investigators[2-5] have used this property of SF_6 to establish the electron energy scale. All these investigators have used the retarding potential difference method for obtaining the effect of a nearly monoenergetic electron beam. The purpose of this note is to point out that the energy scale thus established may, under certain conditions, be erroneous. The potential along the path of the electron beam in the collision chamber must be considered in detail.

Figure 1 shows two possible collision chamber arrangements, differing in the extraction method for negative ions. The potential along the electron path (referred to the walls of the collision chamber) is positive in arrangement A and negative in arrangement B. As we reduce the accelerating voltage in arrangement A, the electron beam is cut off at $V_A=\varphi$ where φ is the contact potential between the retarding electrode and the entrance to the collision chamber. (In the subsequent discussion we assume $\varphi=0$.) At this accelerating voltage the energy of the electron beam in the collision chamber has a value equal to W. (See Fig. 1) Because electrons can never enter the collision chamber with an energy less than W, the SF_6^- current will have an apparent peak at $V_A=0$, i.e., when the electron energy is W. It should be noted that in this mode of operation the SF_6^- ions are formed mostly near the edges of the collision chamber, where the electron energy is close to zero. The measured magnitude of the effective cross section would be small compared to the true cross section. Thus we have to add to our energy scale the quantity W, which is usually not known. In this arrangement an electron retarding experiment in front of the collision chamber[6] and the SF_6^- peak agree, but neither experiment defines the zero of the energy scale properly. It should be noted that at the low currents usually used for mass spectrometer experiments ($10^{-7}-10^{-6}$ amp), the potential in the collision chamber determines the potential in the beam.[7]

As we reduce the accelerating voltage V_A in arrangement B (see Fig. 1), the electrons will be cut off at an accelerating voltage, $+W$ (provided that $\varphi<W$). At this accelerating voltage ($V_A=W$), the electron energy in the collision chamber is zero and the SF_6 peak, therefore, occurs at an accelerating potential $V_A=W$. Thus, there is agreement between the energy scale established by retarding the electron beam in front of the collision chamber, so that both calibration by SF_6^- and electron retarding yields the proper zero of the energy scale.

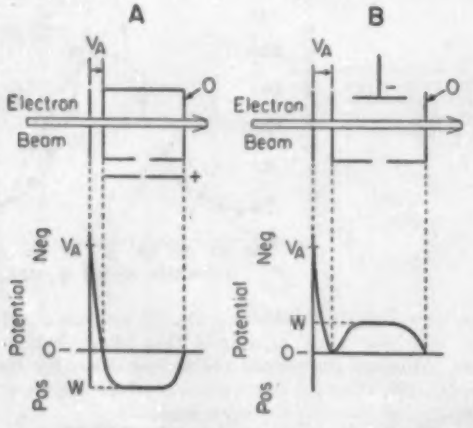

[1] FIG. 1. Schematic diagram of two possible collision chamber arrangements for negative ion studies in a mass spectrometer and potential distribution along the path of the electron beam for the two arrangements. The potential of the collision chamber electrode is taken as zero. V_A is the electron accelerating voltage, W is the potential at the center of the electron beam path. The contact potential is assumed to be zero.

In a Lozier-type apparatus used for negative ion studies where the electron beam is surrounded by a grid and a cylindrical negative ion collector, the potential along the path of the electron beam is always positive with respect to the collision chamber electrodes (because the ions must be drawn to the collector). Therefore, a reliable energy scale calibration using SF_6^- can be obtained only when the penetrating potential W is small.

We conclude that establishing an electron energy scale using SF_6^- is in most cases equivalent to establishing the energy scale by electron retarding in front of the collision chamber. Serious errors in energy scale calibration can ensue if the potential along the path of the electron beam is positive with respect to the potential along the path of the electron beam is positive with respect to the potential of the entrance hole of the collision chamber.

The author wishes to thank T. Kjeldaas, Jr., A. V. Phelps, and R. E. Fox for many discussions of the problem.

[1] W. M. Hickam and R. E. Fox, J. Chem. Phys. **25**, 1956. In this experiment a pulsed "pusher field" assures that the potential along the beam path is equal to the potential of the collision chamber electrodes when the electron beam traverses the chamber.
[2] D. C. Frost and C. A. McDowell, *Joint Conference on Mass Spectrometry* (Pergamon Press, New York, 1958).
[3] P. L. Randolph and R. Geballe, Paper presented at the 11th Gaseous Electronics Conference, New York, 1958. See also Technical Rept. No. 6 Department of Physics, University of Washington. The drawout potential in this mass spectrometer is applied in such a way that the axis of the collision chamber is at the potential of the collision chamber electrodes (the entrance and exit plates). Thus, if the electron beam truly traverses the axis of the collision chamber, both electron retarding and the SF_6^- should yield a proper calibration. The symmetrical application of the drawout potential could also be used for the calibration of the energy scale for negative ions from the positive ion onset.
[4] N. S. Buchel'nikova, J. Exptl. Theoret. Phys. (U.S.S.R.) **34**, 519 (1958); Translation Soviet Physics, J. Exptl. Theoret. Phys. **34**, 358 (1958). In a Lozier-type tube such as used in this experiment, the penetrating potential can be minimized by using a tight grid surrounding the electron beam.
[5] G. C. Cloutier and H. I. Schiff, J. Chem. Phys. **31**, 793 (1959). The mass spectrometer used in this experiment employs a "drawout electrode" for extracting the ions. (Type B, Fig. 1).
[6] When retarding in front of the collision chamber, the electron current is collected at the electron collector behind the collision chamber. The electron collector is kept at a positive potential of several volts with respect to the collision chamber.
[7] G. J. Schulz, Phys. Rev. **116**, 1141 (1959).

Diode Capacitors for Parametric Amplification

R. C. KNECHTLI AND R. D. WEGLEIN
Research Laboratories, Hughes Aircraft Company, Culver City, California
(Received December 16, 1959)

IN his recent paper,[1] K. E. Mortenson defines the quantity $F_D=1/R_BC_{min}(C_{max}/C_{min})$ as the over-all figure of merit of a variable-capacitance semiconductor diode for parametric amplification. He shows that this figure of merit, as he defines it, can be increased by reducing the doping level. The purpose of this communication is to point out a more appropriate definition for a figure of merit, i.e., one based on experimentally verified theoretical considerations. The new definition of the figure of merit[2] indicates that there exists an optimum doping level (near 10^{17} donors/cm^3 for G_e) for the best design of a parametric amplifier diode. This conclusion is at variance with K. E. Mortenson's results.

The figure of merit proposed in this letter is defined by

$$F_D'=\frac{1}{R_BC_0}\frac{\Delta C}{\bar{C}}=2\pi f_c\frac{\Delta C}{\bar{C}}, \tag{1}$$

where f_c=cutoff frequency at zero bias; C_0=capacitance at zero bias; $\Delta C=C_{max}-C_{min}$; and $\bar{C}=\frac{1}{2}[C_{max}+C_{min}]$. It can indeed be shown[3] that when the diode losses predominate over circuit losses (this normally occurs at microwave frequencies in properly designed amplifiers) the minimum amplifier noise temperature

attainable is determined by F_D' as given in (1) rather than by F_D as defined by Mortenson. This distinction is important for optimization, and it is particularly important in regard to the voltage-dependent part of capacitance. In order to maximize F_D (Mortenson's definition), one may be inclined to make C_{min} as small as possible by increasing the diode breakdown voltage at the expense of deteriorating the effective Q of the diode. It is futile to pursue this course since one wishes to bias the diode in a region of reasonable nonlinearity, usually within 1 or 2 v of zero bias, and further, because the package and circuit capacitances determine the final value C_{min}. Alternately, to optimize F_D' (authors' definition), there is little incentive in minimizing C_{min} to less than, say, 0.25 C_{max} because, in this case, $\Delta C/C$ tends asymptotically toward unity; whereas, C_{max}/C_{min} tends toward infinity as C_{min} approaches zero.

On the basis of these comments, as well as published data on the donor concentration for maximum cutoff frequency,[3] it is suggested that the behavior of the figure of merit defined by (1) is shown in Fig. 1 together with the previously defined cutoff frequency.[4]

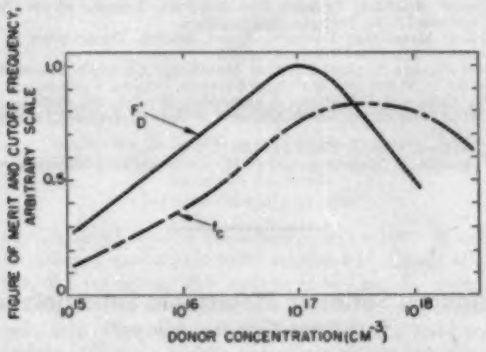

FIG. 1. Variation of figure of merit cutoff frequency of abrupt-junction germanium diode with impurity concentration.

It is evident that both the F_D' figure of merit and the cutoff frequency can be optimized when the donor concentration is somewhat in excess of 10^{17}/cc. The validity of this optimization in terms of the above-defined quantities is borne out in practice. It is to be noted that this conclusion differs from Mortenson's findings which lead to rather opposite criteria.

Finally, attention is drawn to the fact that this discussion has centered on the figure of merit of the germanium abrupt-junction diode, for which Fig. 1 holds. Sufficient information is now available, largely in the published literature, for deriving similar figures of merit for other geometries and materials, all of which should have a similarly well-defined optimum impurity concentration.[3,5-7] The choice of the type of junction which is most suitable for low-noise parametric amplification is often made on technological grounds rather than on the basis of idealized material behavior, while the choice of material may be governed by practical considerations such as how much, if any, reduction in excess noise can be achieved by refrigeration.

[1] K. E. Mortenson, J. Appl. Phys. 30, 1543 (1959).
[2] R. C. Knechtli and R. D. Weglein, Proc. IRE 47, 584 (1959). The derivation of the figure of merit μ_0 is contained in a subsequent paper submitted to Proc. IRE.
[3] G. C. Messenger and C. T. McCoy, Proc. IRE 45, 1269–1283 (1957); see particularly 1277–1278.
[4] In computing these curves, use was made of the following relations data:

$$F_D' = \frac{1}{R_D C_0}\frac{\Delta C}{\bar{C}} = (2\pi f_0)\left(\frac{\eta(Nd)-1}{\eta(Nd)+1}\right),$$

where

$$f_0 = \text{const} \times \mu_n N_d^{\frac{1}{2}} \text{ (data from work cited in footnote 3)}$$

$$\eta(Nd) = \frac{C_{max}}{C_{min}} = \left(1+\frac{V_{BD}(Nd)}{\phi}\right)^{\frac{1}{2}}$$

$V_{BD}(Nd)$ data from footnote (5); $\phi_{Ge} \cong 0.4$.

[5] S. L. Miller, Phys. Rev. 99, 1234 (1955).
[6] M. B. Prince, Phys. Rev. 93, 914 (1954).
[7] J. Maserjian, J. Appl. Phys. 30, 1613 (1959).

Comments on "Diode Capacitors for Parametric Amplification" by R. C. Knechtli and R. D. Weglein

K. E. MORTENSON
General Electric Research Laboratory, Schenectady, New York
(Received February 8, 1960)

IN their letter, Knechtli and Weglein propose a new figure of merit for diode capacitors which they feel to be more appropriate than that proposed earlier by this author.[1] Further, from this proposed figure of merit they conclude that a *specific* optimum diode base doping exists.

First, let it be said that the original figure of merit put forth by this author was a first attempt to incorporate a gain parameter, capacitance swing (defined as C_{max}/C_{min}), together with the "cutoff" frequency (Uhlir's definition[2]) to establish an over-all device figure of merit. In comparing this figure of merit F_D with that proposed by Knechtli and Weglein F_D', it can be seen that the factors included (some "cutoff" frequency and a measure of time-dependent capacitance) are the same, the expressions differing largely in the definition of these quantities. Considering first the quantity proportional to some "cutoff" frequency, the difference is concerned with the bias point at which the capacitance is to be determined. This author originally specified the capacitance at breakdown (consistent with Uhlir's definition of "cutoff" frequency), while Knechtli and Weglein have chosen zero bias. From a study of a more precise derivation of amplifier noise figure and diode figure of merit (submitted for publication in this journal), it has been concluded that the capacitance (or "cutoff" frequency) should be specified at the *operating* bias point. The operating bias for minimum noise figure should be chosen to be approximately half the breakdown voltage (assuming full, sinusoidal pump voltage). Considering next the quantity proportional to the time-dependent capacitance, both C_{max}/C_{min} and $\Delta C/\bar{C}$ are representative, aside from a scale factor, with $\Delta C/\bar{C}$ being the better of the two. However, the most precise way to represent the time-dependent capacitance is to specify the appropriate normalized Fourier capacitance coefficient a_n for the pumped diode. These coefficients are dependent only upon the *relative* pump swing and the particular $C-V$ law. Finally, considering both of these factors related to a diode figure of merit, the following, improved expression has been arrived at which is directly usable by the circuit as well as the device designer. (Details are given in the submitted paper.)

$$F_D = a_n/4\pi a_0^2 C_0 R_D,$$

where a_n is the normalized Fourier capacitance coefficient, C_0 is the capacitance at the *operating* bias point, and R_D is the equivalent diode series resistance at the operating bias point.

With regard to the evaluation of the figures of merit for the germanium abrupt-junction diodes, particularly with respect to base doping, it can be stated that the conclusion that F_D increases with decreasing doping arrived at previously by this author remains essentially unchanged, even in the light of the more precise figure of merit, although the increase is significantly less than that originally indicated. This result stems principally from the fact that the diode Q for any bias (greater than zero) as specified at a fraction of the breakdown voltage is nearly *independent* of base doping over the range $10^{15}-10^{18}$ atoms/cc. Further, with greater breakdown voltage units, a greater *relative* pump swing is possible (without conduction) such that a_n/a_0^2 can be increased. Certainly, under these conditions, if some arbitrary absolute voltage swing is specified for use, an "optimum" doping can be determined. However, as a number of different constraints or limitations may be specified depending upon the particular application circumstances or price to be paid for the lowest possible noise figure, it can be concluded that there is no one "optimum" choice of base doping.

The author wishes to thank Knechtli and Weglein for their keen interest and obvious effort in this timely topic.

[1] K. E. Mortenson, J. Appl. Phys. 30, 1542 (1959).
[2] A. Uhlir, Jr., Proc. I.R.E. 46, 1099 (1958).

Preparation of Tin Single Crystals for Transmission Electron Microscopy*

J. T. Fourie†, F. Weinberg‡ and F. W. C. Boswell§
Canada Department of Mines and Technical Surveys Mines Branch, Physical Metallurgy Division, Ottawa, Ontario
(Received February 26, 1960)

THE investigation of metals by transmission electron microscopy has become almost general in its application. Accordingly, methods of preparing thin foils have been developed for a large number of metals and alloys.[1,2] However, a preparation method for tin has not been reported and this paper will describe an electropolishing technique used for thinning down single crystals of tin.

The crystals, which had been grown by a controlled orientation technique (Chalmers[3]), originally had dimensions 1×20×40 mm. The orientations of the large faces were generally either (001) or (110).

The thinning by electropolishing was carried out in two stages. The first stage brought about rapid dissolution of the specimen down to a thickness of about 0.2 mm without producing a bright polish. In the second stage, which required a much lower current density, a mirror like polish was obtained. The details of the two stages are as follows:

(i) Rapid dissolution of bulk specimen. First, the edges of the specimen were insulated. For this purpose a lacquer known as "Miccrostop" (manufactured by Michigan Chrome and Chemical Company of Detroit) was found to be excellent.

The specimen was then mounted symmetrically between two stainless steel cathodes, each about four times the area of the specimen. The specimen was parallel to the cathodes and spaced about 2 cm from them.

The polishing bath consisted of 20% perchloric acid (62%), 10% ethylene glycol monobutyl ether (butyl cellosolve) and 70% ethyl alcohol. About 12 v was applied to the cell which was kept at a temperature of 15–20°C. The rate of stirring was moderate. It is important to ensure that the stirrer does not cause a turbulence at the specimen surface, since this produces a rippled surface. After the specimen had reached a thickness of about 0.2 mm, this stage of the polishing was discontinued.

(ii) Final stage. One side of the specimen was blanked off completely with lacquer, while the other was masked along the edges leaving exposed a slightly smaller area than before.

The electrolyte consisted of 5% perchloric acid (62%), 10% butyl cellosolve, and 85% ethyl alcohol. A potential of about 30 v was applied to the electrode arrangement, which was similar in principle to that described by Boswell and Smith.[2] The main differences were that only *one* pointed cathode was used and the specimen was mounted at 60° to the vertical, tilted toward the cathode. The separation between the cathode point and the specimen was about 5 mm.

The reason for the slantwise arrangement of the specimen was to slow down the flow of the viscous layer of reaction products, since this produced a better polish. For the same reason the stirring was so arranged that the flow of the electrolyte over the specimen surface would retard the flow of the viscous layer. It is again important that no turbulence should be produced at the surface, and the viscous layer should flow at a slow but uniform rate.

FIG. 1. Dislocations and a twin in a deformed single crystal foil of tin. ×60 000.

The bath temperature was kept at 10°C.

The first side was polished until a mirror like finish was obtained, after which the sample was washed in a stream of water and then placed in acetone to dissolve the lacquer. The *polished* side was then blanked off completely with lacquer and the same polishing procedure carried out on the other side. On this occasion, however, polishing was continued until holes appeared in the center of the specimen, after which it was washed in water and ethyl alcohol and dried. The material near the edges of the holes was generally sufficiently thin for electron transmission.

It should be noted that during the final stage of polishing, the specimen was at all times backed with a thick layer of lacquer, which prevented any deformation from being introduced during polishing. Thus it was possible to preserve the single crystal nature of the foils, which were later examined[4] with special reference to the formation and growth of twins. An example of twins and dislocations as they appeared in a deformed single crystal foil of tin, is shown in Fig. 1.

* Published by permission of the Director, Mines Branch, Department of Mines and Technical Surveys, Ottawa, Canada.
† National Research Council Postdoctorate Fellow, Mines Branch; present address CSIR, Pretoria, South Africa.
‡ Physical Metallurgy Division, Mines Branch, Department of Mines and Technical Surveys, Ottawa, Canada.
§ Metal Physics Section, Physical Metallurgy Division, Mines Branch, Department of Mines and Technical Surveys, Ottawa, Canada.
[1] P. M. Kelly and J. Nutting, J. Inst. Met. 87 (12), 385 (1959).
[2] F. W. C. Boswell and E. Smith, ASTM Special Technical Publication 245, 31 (1959).
[3] B. Chalmers, Can. J. Phys. 31, 136 (1953).
[4] J. T. Fourie, F. Weinberg, and F. W. C. Boswell (to be published).

Continuous Series of Metastable Solid Solutions in Silver-Copper Alloys*

Pol Duwez, R. H. Willens, and W. Klement Jr
Division of Engineering, California Institute of Technology, Pasadena, California
(Received January 12, 1960)

A TECHNIQUE has been devised by which small amounts of liquid alloys can be cooled at rates high enough to prevent the normal process of nucleation and growth of equilibrium phases. The classical method for achieving high rates of cooling consists of injecting a small droplet of molten alloy into a liquid quenching bath. Olsen and Hultgren used such a technique in a study of the effect of the rate of cooling on the homogeneity of solid solutions.[1]

The rate of heat transfer between a metallic liquid droplet and the quenching liquid is limited by the formation of a gaseous layer due to the evaporation of the quenching liquid. This limitation can be removed by replacing convective heat transfer through the vapor layer by conductive heat transfer between the liquid alloy and a solid wall made of a good heat conductor. In this case two conditions must be satisfied. First, the liquid alloy must strike the cold surface at high speed in order to spread the liquid into a thin layer. Secondly, a good contact must be assured between the liquid alloy and the target material during the process of solidification. The first condition has been satisfied by propelling a small liquid droplet (about 25 mg) by means of a shock wave against a solid copper target. In regard to the second condition, a high speed rotating cylinder was used as the target; the liquid was ejected against the inside surface of the cylinder at a suitable angle. The centrifugal force acting on the molten material insured a good thermal contact with the target. The relative motion of the target and the droplet also helped in spreading the liquid over a larger area. This spreading lead to a thinner layer of solidified material, and hence a large over-all heat transfer rate.

Experiments were made with copper-silver alloys. In this system a eutectic exists at 60.1 at. % Ag, 39.9 at. % Cu, and there is a limited solid solubility range at both ends of the phase diagram.

The copper-silver system was chosen as a crucial test of the method because the existence of a eutectic is not in agreement with the Hume-Rothery rules, which would predict complete miscibility of the two metals. Four alloys containing 23.0, 39.9 (eutectic composition), 62.9, and 88.5 at. % copper were quenched from melt. The x-ray diffraction patterns of these alloys showed a single phase. On a plot of unit cell size vs concentration, the lattice parameters obtained with the four metastable alloys fell on a smooth curve connecting the two previously known segments of curves within the solubility limits at both ends of the phase diagram (14.1 and 95.1 at. % Cu). The maximum deviation from linearity (Vegard's law) was less than 1% at 50% Cu. Such a deviation is not unusual in solid solution binary alloys. These results establish without doubt that, during solidification, the two stable phases, copper rich and silver rich, did not have time to nucleate and grow, and metastable solid solutions were obtained.

[*] This work was jointly sponsored by the Atomic Energy Commission and the Office of Naval Research.
[1] W. T. Olsen, Jr. and Ralph Hultgren, Trans. AIME, 188, 1223 (1950).

Metastable Electron Compound in Ag-Ge Alloys

POL DUWEZ, R. H. WILLENS, AND W. KLEMENT, JR.
Division of Engineering, California Institute of Technology, Pasadena, California
(Received February 19, 1960)

IN the previous Letter to the Editor,[1] the existence of a continuous series of metastable solid solutions in Cu-Ag alloys was reported. By quenching the molten alloys rapidly enough, the normal processes of nucleation and growth were prevented and solid solutions were obtained. These metastable solid solutions were predictable since copper and silver satisfy the criteria for complete solid solubility proposed by Hume-Rothery.

In Ag-Ge alloys complete solid solubility is precluded because of dissimilar crystal structures. The Ag-Ge equilibrium phase diagram[2] is of the eutectic type with a maximum solubility of germanium in silver of 9.6 at.% and negligible solubility of silver in germanium. The eutectic composition is at 25.9 at.% Ge. It was expected that the solubility limits on both ends of the phase diagram would be extended by rapid quenching. An alloy containing 25.7 at.% Ge was quenched from the melt. This alloy had a crystal structure that was neither face-centered cubic nor diamond cubic, but rather hexagonal close-packed with $a=2.987\pm0.003$, $c=4.716\pm0.002$, and $c/a=1.628\pm0.003$. The presence of a small amount of a diamond cubic germanium phase was indicated by a few weak diffraction peaks on the x-ray pattern. The new metastable hexagonal phase is considered to be an electron compound with an electron concentration of 7/4 electrons/atom.

In 1940, Hume-Rothery *et al.*[3] suspected the existence of a $\frac{3}{2}$ electron compound in Ag-Ge alloys, but failed to detect it under equilibrium conditions. In order to determine if such a compound could be synthesized by rapid quenching, an alloy containing 16.4 at.% Ge was investigated. No body-centered cubic phase was found, but again a hexagonal close-packed structure occurred with $a=2.891\pm0.002$, $c=4.718\pm0.006$, and $c/a=1.632\pm0.003$. The existence of the hexagonal structure instead of the body-centered cubic structure at the electron concentration of $\frac{3}{2}$ has been noted in other alloy systems. Satisfactory explanations for the occurrence of a hexagonal close-packed structure in the region of a $\frac{3}{2}$ electron concentration have not been advanced. It might be noted, however, that when a $\frac{3}{2}$ electron compound (β-phase) does exist, it is usually more stable at high temperatures. It is probable that the electronic configurational energy is not the main factor in creating a $\frac{3}{2}$ electron compound (β-phase). It is suggested that the high-lattice entropy contribution, characteristic of a body-centered cubic structure, has a prominent role in lowering the free energy of this phase at high temperatures.

The interpretation of the structure of alloys containing less than 16.4 at.% Ge has not been completed. It appears, however, that the solubility of germanium in face-centered cubic silver is extended beyond 9.6 at.% Ge. In the alloys containing more than 25.7 at.% Ge, both the hexagonal compound and diamond cubic germanium were found. No measurable change in the lattice parameter of the diamond cubic germanium could be observed. Because of the nearly equal size of silver and germanium (as deduced from the change in lattice parameter at the silver-rich end of the phase diagram),[4] and the openness of the diamond cubic lattice, silver could probably be retained in the germanium structure without any appreciable change in the cell size. Therefore, measurements other than the lattice parameter will be necessary to establish whether there is any significant solubility of silver in germanium.

[1] P. Duwez, R. H. Willens, and W. Klement, Jr., J. Appl. Phys. 31, 1136 (1960).
[2] M. Hansen, *Constitution of Binary Alloys* (McGraw-Hill Book Company, Inc., New York, 1958).
[3] W. Hume-Rothery, G. V. Raynor, P. W. Reynolds, and H. K. Packer, J. Inst. Metals 66, 209 (1940).
[4] E. A. Owen and V. W. Rowlands, J. Inst. Metals 66, 361 (1940).

Erratum: Motion of High-Speed Arc Spots in Magnetic Fields

D. ZEI AND J. G. WINANS
University of Wisconsin, Madison, Wisconsin
[J. Appl. Phys. 30, 1813 (1959).]

IN Fig. 5, the A at the left of the figure should be replaced by (b) and the B at the left side of the figure should be replaced by (a).

Books Reviewed

Prompt, noncritical reviews appear in this column. Critical reviews of many of the books described here will appear in Physics Today, The Review of Scientific Instruments, *or* American Journal of Physics.

Exploding Wires. W. G. CHACE AND H. K. MOORE, EDITORS. Plenum Press, Inc., New York, 1959. Price $9.50.

The collection of papers which were presented at the conference on the exploding wire phenomenon (April, 1959) comprises the first book published on this topic. These have been arranged into three broad groups: theoretical and experimental, shock wave, and applications and techniques. For those who are not acquainted with this field, the editor, W. G. Chace, has written an introduction which is compact and informative. In the papers which follow, many aspects dealing with the electrical, optical, spectroscopic, and radiometric observations are covered. The variety of uses of exploding wires listed and the collection of specialized techniques which have been developed, as described in this volume, will make a useful addition to the store of "knowhow" for operations in this range of very rapid discharges from high-capacity condensers, of the production of intense light sources, and of very high temperatures.

Physical Metallurgy of Stress Corrosion Fracture. T. N. RHODIN, EDITOR. Pp. 394. Interscience Publishers, New York, 1959. Price $13.00.

This book covers recent advances in research on the phenomena of stress corrosion cracking presented at a technical conference April 2–3, 1959, on the subject sponsored by the Metallurgical Society of the American Institute of Mining, Metallurgical, and Petroleum Engineers. The first half of the book is concerned mainly with general principles relating the influence of structure and stress on chemical reactivity and fracture in metals. The second half is directed towards interpretation of mechanisms of stress corrosion cracking in terms of specific alloys and chemical environments. The publication provides a broad perspective on the present state of knowledge on the subject of fracture mechanisms associated with corrosion in many important metals and alloys. The photomicrographs are well reproduced and the discussion sections especially contain comprehensive references both to research in progress and to the published literature. A condensed source of information is provided by this volume for research workers interested in an up-to-date review of the stress corrosion fracture phenomenon.

Recent Research in Molecular Beams. A Collection of Papers Dedicated to Otto Stern on the Occasion of his Seventieth Birthday. IMMANUEL ESTERMANN, EDITOR. Academic Press, Inc., New York, 1959. Price $6.50.

This publication is an interesting collection of papers, which spans a large range of activity in the field of molecular-beam research. Some of the papers deal with current work on specific problems; some are review papers covering broad areas, and some describe the early history of molecular-beam research. The introductory historical chapter by I. Estermann on the period 1922–33 describing work done in the Hamburg Laboratory proved most interesting. The breadth of the scope of the program as visualized by Professor Stern is indicated by a series of over thirty publications. The difficult technique, which at first appeared to provide only crude results, was recognized on its inception by its originator as having tremendous potential. The program of exploration he outlined was justified by the events which followed, and these are chronicled by the papers in this compilation.

Landolt-Börnstein, Zahlenwerte und Funktionen. Vol. II. Part 6. **Electric Properties I.** 6th ed. K. H. HELLWEGE AND A. M. HELLWEGE, EDITORS. Pp. 1018. Springer-Verlag, Berlin, 1959.

This book is part 6 of Vol. II, which deals with "Properties of matter in its states of aggregation." It gives by means of numerical tables and graphical representations, a comprehensive survey of experimental data covering the following fields as indicated by the chapter headings: "Electric conductivity of metals and solid ionic conductors," "Semiconductors," "Electric, piezoelectric, and dielectric constants of piezoelectric crystals," "Dielectric properties," "Thermogalvanic effects and emission effects." The single chapers are mostly headed by a brief explanation of the physical background. The sources of all represented data are quoted for further reference.

Nuclear Fuel Elements. H. H. HAUSNER AND E. SCHUMAR, EDITORS. Pp. 409. Reinhold Publishing Corporation, New York, 1959. Price $12.50.

Contains papers presented at the First International Symposium on Nuclear Fuel Elements held at Columbia University in January, 1959. Twenty papers by workers in Europe, Canada, and the USA give information on design, fabrication, and behavior of fuel elements for research and power-producing reactors. An appendix contains specifications for army power package reactor and control rod components. Another appendix is a bibliography on solid fuel elements containing 494 references.

Instationare Warmespannungen. HEINZ PARKUS. Pp. 165. Springer-Verlag, Berlin, 1959.

The timely occurrence of the book under review is most welcome by all people who are interested in thermal stresses. In less than 200 pages, the author presents a systematic and comprehensive treatment with numerous examples gathered from about 280 references dated up to 1958. As the sequel to the previous volume, "Warmespannungen infolge Stationarer Temperaturfelder" Professor Parkus extends the discussion to the thermal stresses, which are caused by nonsteady temperature distribution. The treatment is further extended from elastic medium to viscoelastic and elastoplastic media. It is devoted mainly to a theoretical exposition of the basic principles and methods used to obtain the solutions of a set of coupled equations of elasticity and heat conduction. The reader is expected to have some familarity with the theory of elasticity, the theory of heat conductions, and the method of Laplace transform. Occasionally, references are made to the previous booklet. Although the author has tried to make this volume self-contained, a knowledge of the earlier book will benefit the reader considerably. The book is divided into seven chapters. The general theories of thermoelasticity are gathered in the first chapter. Chapter 2 discusses the sudden heating and cooling of elastic bodies with various configurations and different kinds of heat sources. Chapter 3 and Chapter 4 treat the periodically time-varying and constantly moving heat sources, respectively. The dynamical influence on thermal stresses is discussed in Chapter 5.

Handbuch der Kaltetechnik. Vol. 3. R. PLANK, EDITOR. Pp. 511. Springer-Verlag, Berlin, 1959. Price DM 84 (approx. $21.00).

This book, which is written primarily for cryogenic and refrigeration engineers, discusses methods of refrigeration and problems of heat transfer. The first part of the book (100 pages) treats the various methods of achieving low temperatures including detailed studies of electric (thermoelectric) refrigeration and magnetic refrigeration (adiabatic demagnetization to reach temperatures near absolute zero). A brief discussion of cyclic and noncyclic refrigeration involving fluids is also included. The second and major portion of the book (400 pages) gives a detailed account of the methods of heat transfer (conduction, convection, and radiation of heat) with emphasis on problems of interest to the engineer.

Handbuch der Kaltetechnik. Vol. 7. R. PLANK, EDITOR. W. NIEBERGALL. Pp. 540. Springer-Verlag, Berlin, 1959. Price DM 96 (approx. $24.00).

This book deals with the theoretical foundation, methods of calculation, and in particular, the practical application of sorption refrigeration (absorption and adsorption with continuous or periodic operation as well as diffusion refrigerators). It is written primarily for refrigeration engineers. In the first part, the thermodynamics of sorption refrigeration is discussed. In parts two and three an account is given of the practical applications with separate treatments of devices with large and small cooling capacities including detailed directions for installation, operation, and maintenance.

The Johnson Recording Oscillometer. CARL A. JOHNSON. Pp. 112+vii. Pergamon Press, New York, 1959. Price $5.00.

The Johnson Recording Oscillometer, Its Use in the Study of Arterial Circulation, describes a new calibrated pneumatic recording instrument of high sensitivity and accuracy, which is particularly adapted for the study of small volumetric changes such as the blood pulse in any portion of the body. The oscillometer has demonstrated its value in experimental and clinical medicine, and is potentially valuable in many engineering and industrial applications.

Vector Analysis. M. SCHWARTZ, S. GREEN, AND W. A. RUTLEDGE. Pp. 550. Harper & Brothers, New York, 1960. Price $7.50.

This new text has been written primarily to facilitate the grasp of both the fundamental concepts and the techniques of vector analysis by the beginning student. However, the numerous examples and exercises, the many applications of the theory to geometry and physics, and the inclusion of problems that deal with the more difficult aspects of the subject all make VECTOR ANALYSIS suitable for use as a reference for advanced students, especially in the engineering and physical science fields. Since the authors view vector anaylsis as both a mathematical discipline and as a language of physics, throughout the text chapters on applications are interspersed with the mathematical theory and development. There is a wide range of applications: statics, kinetics, dynamics, potential theory, electricity, and magnetism; some elasticity, hydrostatics, and hydrodynamics; and techniques in analytic and differential geometry.

Theory of Elasticity. L. D. LANDAU AND E. M. LIFSHITZ. Pp. 131. Addison-Wesley Publishing Company, Inc., Reading, Massachusetts, 1959. Price $6.50.

Since this volume is written primarily for physicists, it includes not only the ordinary theory of the deformation of solids, but also some topics not usually found in textbooks on the subject, such as thermal conduction and viscosity in solids, and various problems in the theory of elastic vibrations and waves. On the other hand, the authors have discussed only very briefly certain topics in which they are not specialists, such as complex mathematical methods in the theory of elasticity and the theory of shells.

Advances in Space Science. FREDERICK I. ORDWAY, III. Pp. 382+xiv. Academic Press, Inc., New York, 1959. Price $12.00.

The Advances in Space Science series was conceived for scientists and engineers working in the many related fields of astronautics. It is designed to permit them to keep abreast of research and developments in their own specialties and in other branches of endeavor, insofar as they contribute to progress in the astronautical sciences. The series records advances in those selected areas of space science that merit reviewing and assessing. Among the topics examined in Vol. I are interplanetary rocket trajectories, interplanetary communications, power supplies, manned spaced cabin systems, radiation, and nutrition in space flight.

Beam and Wave Electronics in Microwave Tubes. RUDOLF G. E. HUTTER. Pp. 367. D. Van Nostrand Company, Inc., Princeton, New Jersey, 1960. Price $9.75.

This new work analyzes the basic physical principles of microwave devices, from klystrons and magnetrons to the most recent traveling-wave tubes. The mathematical treatment is kept simple; it brings out the relations between electron streams and the circuit elements characteristic of microwave tubes. After discussing the limitations of conventional tubes, the author schematically describes certain classes of microwave tubes. He then develops microwave circuitry, beams in gaps and beams in drift regions, the principles of beam and wave electronics in longitudinal dc magnetic fields and in crossed fields, conversion of dc energy to rf energy, effect of the coupling of beam modes and circuit modes, and the subject of noise.

Electromagnetic Fields, Energy, and Forces. R. M. FANO, L. J. CHU, AND R. B. ADLER. Pp. 452+lx. John Wiley & Sons, Inc., New York, 1960. Price $12.00.

This book develops a consistent macroscopic theory of electromagnetism and discusses the relation between circuit theory and field theory. The theory is developed in successive steps from the Lorentz force, the integral form of Maxwell's equations in free space, and suitable macroscopic models of polarized and magnetized matter. The text covers the electromagnetism of moving bodies and the process of electromechanical energy conversion, introduces a power-series technique for analyzing quasi-static fields and quasi-stationary systems, and emphasizes the synthesis of fields as opposed to the analysis of fields.

Theory of Mechanical Vibration. KIN N. TONG. Pp. 341. John Wiley & Sons, Inc., New York, 1960. Price $9.75.

The book is aimed at demonstrating the unity and coherence of the theory and its connection with other engineering sciences. Topics receiving special consideration are principle of superposition, eigenvalue problem in matrix, differential and integral equations, and energy methods.

Fracture. B. L. AVERBACH, D. K. FELBECK, G. T. HAHN, AND D. A. THOMAS. Pp. 640. The Technology Press of Massachusetts Institute of Technology and John Wiley & Sons, Inc., New York, 1959. Price $17.50.

This book is concerned with the question of what actually occurs on an atomic scale when materials fracture. It is based on the proceedings of a conference sponsored by the National Science Foundation, Office of Naval Research, Air Force Office of Scientific Research, Ship Structure Committee. It was organized and directed by the Conference on Fracture of the National Academy of Sciences—National Research Council.

Radioisotope Techniques. RALPH T. OVERMAN AND HERBERT M. CLARK. Pp. 441+xxi. McGraw-Hill Book Company, Inc., New York, 1960. Price $10.00.

Radioisotope Techniques may be used both as a text, in formal courses dealing with radioactivity techniques, and also as a reference and source book for these laboratory procedures and manipulations. A major purpose is to present the theory and principles underlying the techniques, along with the discussion of laboratory procedures. Discussions and techniques are included relative to the detection of radiation, errors in radioactivity measurements, the preparation of radioactive sources, the laboratory characterizations of radiation, the standardization of radioactive sources and the calibration of radiation detectors, the rates of radioactive processes, radiochemical separation methods, and applications of radioisotopes. Approximately 45 experiments are included. Emphasis throughout the book is on radiological safety, and a separate chapter is devoted to a discussion of these problems. A set of typical problems is included as a teaching aid.

Books Received

Electronic Circuits, Signals and Systems. SAMUEL J. MASON AND HENRY J. ZIMMERMAN. Pp. 611. John Wiley & Sons, Inc., New York, 1960. Price $12.50.

Flat Rolled Products: Rolling and Treatment. (Metallurgical Society Conference, Chicago—January 21, 1959). T. E. DANCY AND E. L. ROBINSON, Editors. Pp. 128. Interscience Publishers, Inc., New York, 1959.

Fundamentals of Electronics. E. NORMAN LURCH. Pp. 611+ii. John Wiley & Sons, New York, 1960. Price $8.25.

Guide to the Space Age. C. W. BESSERER AND HAZEL C. BESSERER. Pp. 315+v. Prentice-Hall, Inc., Englewood Cliff, New Jersey, 1959. Price $7.95.

Cemented Carbides. PAUL SCHWARZKOPF AND RICHARD KIEFFER. Pp. 336. The Macmillan Company, New York,1960. Price $15.00.

Industrial Electronics and Control. 2nd ed. ROYCE GERALD KLOEFFLER. Pp. 533. John Wiley & Sons, Inc., New York, 1960. Price $10.00.

Announcements

Techniques in High-Speed Photography

The scientific and engineering uses of high-speed photographic measurement techniques will be the subject of a one-week seminar at the Massachusetts Institute of Technology, starting Monday, August 15. The meetings will center at the Stroboscopic Light Laboratory, where the theory and application of numerous methods will be discussed and studied. For further information, inquire from the Office of the Summer Session, Room 7-103, M.I.T., Cambridge 39, Massachusetts.

Symposium on Engineering Aspects of Solidification of Metals

Among the topics to be covered will be mechanism of solidification heat transfer in metal and refractory molds, segregation and microporosity in ferrous and nonferrous metals, vacuum melting, thermodynamics of metals, techniques for producing premium quality aluminum, magnesium, and steel castings, etc.

For further information write to: Office of the Summer Session, Massachusetts Institute of Technology, Cambridge 39, Massachusetts.

Structural imperfections, represented by this dislocation network in thin tantalum foil, determine the properties of a superconductor (electron transmission; 64,000x).

Superconductivity in Metals and Alloys

Superconductivity—the absence of electrical resistance at very low temperatures—is one of the most challenging of physical phenomena. Its appeal is almost universal; its application seems almost unlimited.

It has been suggested for use in frictionless bearings, motors, amplifiers, electromagnets, gyroscopes and electron-beam apparatus. IBM is concerned with still another possibility: the application of superconductivity to computer devices.

Scientists at IBM Research have demonstrated, with a thin-film superconducting device capable of switching in a few millimicroseconds, that computers of the future may be limited in their operating speeds only by the speed of light. Whether or not a metal is a superconductor depends on many things: its structure, its valence, and the presence and position of alien atoms, missing atoms or electrons. The operation of superconducting devices depends upon the fact that a magnetic field will drive a superconductor into the normal (resistive) state.

A superconductor placed in a magnetic field develops a surface current which shields out any external magnetic field to a characteristic penetration depth. Since this penetration depth is comparable to the film thickness used in making superconducting devices, the penetration depth is an important property.

Superconducting alloys, with their inherent normal-state resistivity, offer promise for superior devices. Alloying can change the penetration depth, the electron density, and the ease by which a superconductor can be switched from one state to another.

Work is under way to outline the part played by impurities and structural defects in determining superconductivity. This work has already shown that microscopic homogeneity is a prerequisite of well-defined superconductive behavior. From such work may come devices that will make it possible to operate miniature computers at extremely high speeds.

IBM.RESEARCH

Investigate the many career opportunities available in exciting new fields at IBM
International Business Machines Corporation, Dept. 579R, 590 Madison Avenue, New York 22, New York

NOW— 15,000°F. PLASMA FLAME SPRAY IN YOUR OWN PLANT

Apply coatings of high melting point materials such as tungsten, tungsten carbide, molybdenum, chromium carbide, titanium oxides, calcium zirconate, rare earth oxides. Operates at 10,000°-15,000°F.

Plasma flame spraying hi-temperature crucible

Now any material that can be melted without decomposing can be sprayed. Despite high melting temperature, object sprayed stays cool.

High fluidity of particles and high velocity of impingement bond the particles together to produce high density coatings semi-fused to work. Absence of air eliminates oxidation.

The METCO Plasma Flame Spray Gun is a valuable new tool for the metalworking research department or production line. Operates on inexpensive inert gases with high electrical power conversion efficiency, long component life. Continuous gas streams, as high as 30,000°F., with accurate control of temperature, generated at costs of ⅓ to ½ those of oxygen-fuel gas equipment for equivalent heat output. No combustion—uses inert gases. No flashback or explosion hazards—push-button operation.

Write today for free bulletin describing the METCO Plasma Flame Gun.

Metallizing Engineering Co., Inc.
Flame Spray Equipment and Supplies
1143 Prospect Avenue, Westbury, Long Island, N. Y.
In Great Britain METALLIZING EQUIPMENT CO., Ltd.
Chobham-near-Woking, England

Please send me free bulletin on the Metco Plasma Flame Spray Gun.

Name _____ Title _____

Company _____

Address _____

City _____ Zone _____ State _____

Nuclear Scientists,
Engineers & Mathematicians:

"A man's mind stretched by a new idea can never go back to its original dimensions."

...OLIVER WENDELL HOLMES

The collective "mind" of The Knolls Atomic Power Laboratory has been stretched to new dimensions frequently by such milestone achievements in reactor technology as the *Triton* twin-reactor propulsion system, the sodium-cooled reactor system for *Seawolf* and the development of a number of unique critical assemblies for applied research and experimental programs.

Exploratory work, now underway, again calls for reactor engineers and scientists to reach beyond the conventional bounds of nuclear technology — to apply their broadest knowledge to the problems of achieving major breakthroughs in reactor simplification.

That imaginative thinking may be unobstructed by material barriers, KAPL maintains a full complement of experimental and test facilities, many of them unique, ranking with the finest in the free world.

A limited number of vacancies are available to physicists, nuclear engineers and mathematicians of demonstrated calibre. *U. S. citizenship and appropriate engineering or scientific degree required.* Address inquiries in confidence to Mr. A. J. Scipione, Dept. 37-MF.

Knolls Atomic Power Laboratory
OPERATED FOR A.E.C. BY
GENERAL ELECTRIC
Schenectady, New York

"KAPL Review," a publication describing the Laboratory's current activities, facilities, and recent achievements is available on request to interested engineers and scientists.

INDEX TO ADVERTISERS

Name	*Page*
A.C.F. INDUSTRIES, INC.	xxv
BECKMAN & WHITLEY, INC. — Manufacturers of high-speed research cameras—both framing and sweeping-image type; specialized meteorological instruments; heat-flow transducers; and explosive-actuated mechanisms.	Cover 2
BELL TELEPHONE LABORATORIES	v
C.B.S. ELECTRONICS	x
CENTRAL SCIENTIFIC CO. — Manufacturers of Cenco physical apparatus and instruments to meet all requirements of University, College and High School Physics Laboratories. Specializing in high vacuum pumps and development of instruments and apparatus for various sciences.	xxii, xxiii
COLLINS RADIO CO.	xix
CONSOLIDATED MINING & SMELTING CO.	xxiv
CONSULTANTS BUREAU	xiv
CORNELL-DUBILIER ELECTRIC CORP. — Primarily interested in the design and manufacture of special type capacitors for thermonuclear work along the lines of the enclosed illustrations. These special fast discharge low inductance capacitors, operating in voltages up to 160 KV, have extensive use in the advanced study of high temperature and high current fields.	xxxii
D. A. M., LYON	xvii
EMERSON ELECTRIC MFG. CO.	xxiv
GAERTNER SCIENTIFIC CORP. — Spectroscopes, spectrometers, spectrographs, spectrophotometers, heliostats, measuring microscopes, comparators, cathetometers, reading telescopes, interferometers, chronographs, dividing machines, etc.	xxii
GENERAL ELECTRIC Knolls Atomic Power Lab.	xxvi
GENERAL MOTORS Delco Radio Div.	vi
GENERAL RADIO CO. — Manufacturers of electronic measuring instruments; vacuum-tube voltmeters, amplifiers, and oscillators; wave analyzers, noise meters and analyzers, stroboscopes, laboratory standards of capacitance; inductance and frequency; impedance bridges, decade resistors and condensers, air condensers and variable inductors; rheostats, variacs, transformers; other laboratory accessories.	Cover 3
HUGHES AIRCRAFT CO.	iv
I.B.M. CORPORATION	iii, xxi, xxix
KEITHLEY INSTRUMENTS, INC. — Vacuum tube electrometers, microammeters, kilovoltmeters, static detectors, megmegohm-meters, high gain dc amplifiers, dc vacuum tube voltmeters, high input impedance ac isolation amplifiers.	ix
LEVINTHAL ELECTRONIC PRODUCTS	xxxi
LOCKHEED MISSILES & SPACE DIV.	xiii
LOS ALAMOS SCIENTIFIC LAB.	vii
McGRAW-HILL BOOK CO., INC.	xii
MELPAR, INC.	xxvii
METALLIZING ENGINEERING CO., INC.	xxvi

INDEX—*Continued*

Name — *Page*

NRC EQUIPMENT CORP. xxv
Manufacturers of standard and special high vacuum components, equipment, and systems including mechanical booster, and diffusion pumps; gauges; valves; seals; connectors; melting and heat-treating furnaces; coaters; impregnators; gas in metal analyzers; driers and freeze driers; altitude chambers; and leak detectors.

NEWPORT INSTRUMENTS LTD. .. xxiii

PACIFIC SEMICONDUCTORS, INC. . xv

PITNEY-BOWES, INC. xxiv

PRECISION INSTRUMENT CO. viii

RAMO-WOOLDRIDGE LABS. .... Cover 4
Research, development, and manufacture in the field of electronic systems for commercial and military applications, and in the field of guided missiles.

REPUBLIC AVIATION xxxii

STANFORD UNIVERSITY PRESS . xxii

STOKES CORP., F. J. xxxi
Mechanical and oil vapor pumps; vacuum valves, gauges and other components; vacuum furnaces, metalizers, processing systems and other special high vacuum equipment.

SYLVANIA ELECTRIC PRODUCTS, INC. xi

TIFFEN OPTICAL CO. xxiii

VEECO VACUUM CORP. xxv

WELCH SCIENTIFIC CO., W. M. ... xx
Manufacturers of high-vacuum pumps, both mechanical and diffusion; vacuum gauges; electrical measuring instruments; physics equipment; and other items for the physical and chemical laboratories.

WILLIAMS & CO., C. K. xxvii

American Institute of Physics

A Federation of Professional Societies in Physics

The American Institute of Physics was founded to assist in "the advancement and diffusion of knowledge of the science of physics and its application to human welfare." All of the societies listed below are members, associate members, or affiliates of the Institute. Eight journals are published by the Institute for the Member Societies. These, together with fourteen journals owned by the Institute, constitute a coordinated publishing program of high standards, efficiency and economy.

The Institute also carries on other activities designed to advance physics and to serve the public interest through physics. Its education program is concerned with strengthening education in physics at all levels, and its public relations program is directed toward promoting a wider public understanding of physics. The Institute works with the Societies in seeking cooperation with other fields of science, with departments of the Federal Government, with educational institutions, and with industrial organizations. In addition, the Institute maintains a free Placement Service for the use of employers and of physicists seeking jobs.

Corporate Associates: A special class of membership is available to corporations, institutions and laboratories who pay annual dues in accordance with a graduated scale ranging from $350 to $3500. Through their membership the Corporate Associates contribute to the support of the work of the Institute. With membership they may receive certain journals, programs of meetings of societies, and other privileges.

Student Sections: College physics students may form local organizations which may, upon application and approval, become Student Sections of the Institute. The Student Sections provide an opportunity for students to obtain official status in the Institute and thus establish their members as part of the physics profession.

Information: Address Wallace Waterfall, Secretary, 335 East 45 Street, New York 17, N. Y. for information about the Institute and its activities. For information about any member society, address its Secretary.

Member Societies:

AMERICAN PHYSICAL SOCIETY

The Society has as its object the advancement and diffusion of the knowledge of physics. All branches of fundamental and applied physics are generally included in its scope. Both experimental and theoretical researches are reported in its journals and meetings.

Dues: Members, $15; Fellows, $25.

Address: Karl K. Darrow, Secretary, Columbia University, New York 27, New York.

OPTICAL SOCIETY OF AMERICA

The Society devotes itself to the advancement of optics, pure and applied, in all its branches. Its scope includes research in fundamental optics as well as problems concerned with design and production of optical instruments.

Dues: Associate Members, $13.00; Regular Members and Fellows, $17.00; Student Members, $2.00; Corporation Members, $125.00 minimum; Patrons, $1000.

Address: Mary E. Warga, Executive Secretary, 1155 16th Street, N.W., Washington 6, D. C.

ACOUSTICAL SOCIETY OF AMERICA

The Society's purpose is to increase and diffuse the knowledge of acoustics and promote its practical applications. The scope includes fundamental researches on the intensity, transmission, and absorption of sound; also on noise, reverberation in rooms, the processes of speech and hearing, the performance and reproduction of music, etc.

Dues: Associate Members, $10; Members and Fellows, $15; Sustaining Members $200.00.

Address: Wallace Waterfall, Secretary, 335 East 45 Street, New York 17, New York.

AMERICAN ASSOCIATION OF PHYSICS TEACHERS

Whereas the other Societies are mainly concerned with research, this Association has provided a much needed forum for the discussion of the problems of teaching. In cooperation with the other groups, the Association promotes the advancement of physics and emphasizes its place in the general culture.

Dues: Members, $7.50; Junior Members, $4.00; Sustaining Members, $200.00.

Address: Frank Verbrugge, Secretary, Univ. of Minnesota, Minneapolis 14, Minnesota.

SOCIETY OF RHEOLOGY

This small but active society is composed of physicists, chemists, and engineers interested in "rheology," which is defined as the science of deformation and flow of matter.

Dues: Members, $6.00; Sustaining Members, $25.00.

Address: W. R. Willets, Secretary-Treasurer, Titanium Pigment Corp., 99 Hudson Street, New York 13, N. Y.

Associate Member Societies:

American Crystallographic Association

Address: Leroy E. Alexander, Secretary, Mellon Institute, 4400 Fifth Avenue, Pittsburgh 13, Pennsylvania.

American Astronomical Society

Address: J. Allen Hynek, Secretary, Smithsonian Astrophysical Observatory, 60 Garden Street, Cambridge 38, Massachusetts.

Affiliated Societies:

American Society for Metals • Cleveland Physics Society • Electron Microscope Society of America • Foundation for Instrumentation Education and Research, Inc. • Philosophical Society of Washington • Physical Society of Pittsburgh • Physics Club of Chicago • Physics Club of Lehigh Valley • Physics Club of Philadelphia • Sigma Pi Sigma

Inquiries regarding membership in the Affiliated Societies may be sent to the American Institute of Physics, 335 East 45 Street, New York 17, New York. Such inquiries will be forwarded to the respective secretaries.

WANTED!

BRAIN

to direct these hands

CRYSTAL GROWING: physicist or physical chemist for senior position in currently growing research and development activity in solid-state materials with present emphasis on scintillation crystals. Require experience in crystal-growing techniques and materials-purification and some knowledge of scintillation spectroscopy. Desire leadership, initiative, and imagination in generating and carrying out new programs to expand present activities.

Combined with the opportunity to assume high-level responsibilities are the advantages of a full program of health benefits, life insurance, and participation in a profit-sharing plan.

Plant is located in Stanford Industrial Park, Palo Alto, in an outstanding center of science and technology. The climate is one of the most favorable in the world. The area offers the best in housing, recreation, and technical stimulation.

For more information, telephone DAvenport 6-1640 or write today, including your resume, to Dr. Elliott C. Levinthal at:

LEVINTHAL ELECTRONIC PRODUCTS

STANFORD INDUSTRIAL PARK · PALO ALTO 3, CALIFORNIA

SUBSIDIARY OF

RADIATION INCORPORATED

a vacuum pump as compact as a . . .

Yes, designed for compactness . . . and with no costly extras to buy. Saves up to 50% of your valuable floor space. But these are just a few of the revolutionary features of the new Stokes Series H Microvac pump.

Find out why Stokes offers you *more pumping performance per dollar*. Just write: Vacuum Equipment Division, F. J. STOKES CORPORATION, 5500 TABOR RD., PHILA. 20, PA.

STOKES

SEND TODAY
for your free
Vacuum Slide Calculator!

A *Versatile* PULSE SOURCE FOR TRANSISTOR TESTING . . .

Turn-On Time, Rise Time, Fall Time . . . three of the more important transistor characteristics measured at Philco's Lansdale Division with the aid of a General Radio 1391-B Pulse, Sweep, and Time-Delay Generator — a *complete* pulse system. To make repetitive measurements of the various transistor types faster and with minimum resetting of their test console, Lansdale's engineers have designed a circuit jig (shown on the work table) for each transistor type. Type 1219-A Pulse Amplifier (shown under Type 1391-B) provides additional pulse amplification.

Features of the Pulse Generator that are particularly useful in Lansdale's quality control program include: excellent rise and decay time characteristics (0.015 μsec); the extremely wide range of pulse durations; lack of duty ratio restrictions; variable output impedance; the ability to put the pulse's zero reference level above ground level; and in general, the wide variety of useful waveforms that the generator can produce.

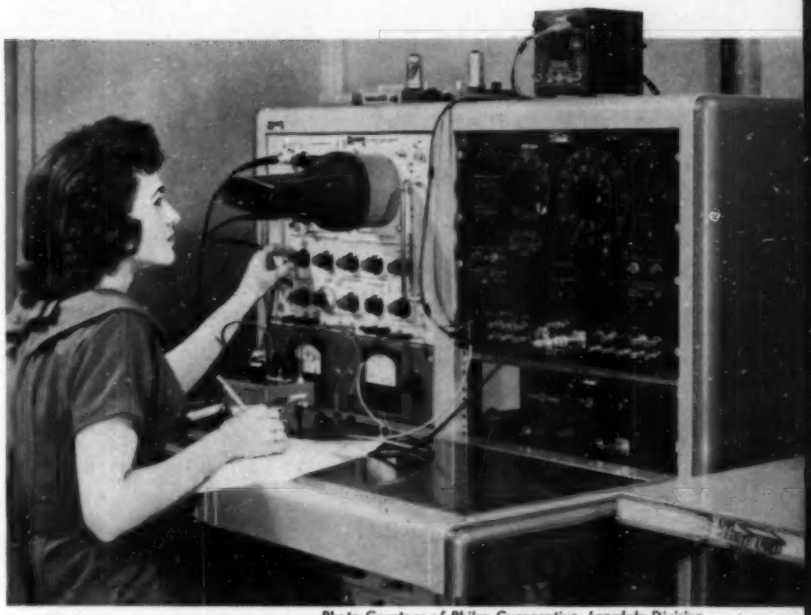

Photo Courtesy of Philco Corporation, Lansdale Division

. . . A *Versatile* PULSE SOURCE FOR MANY OTHER MEASUREMENTS

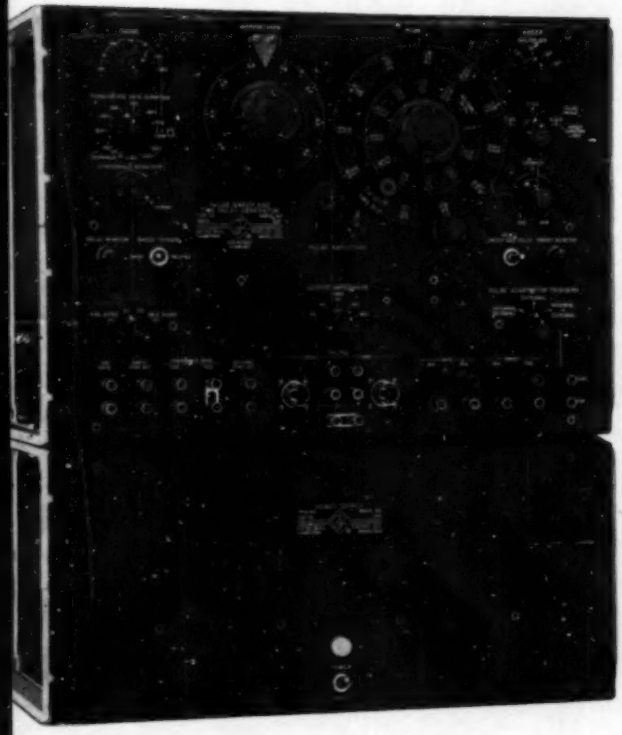

Echo Ranging, Telemetering, Computer Research, Television, Radio Navigation

- ★ Rise and Decay Times Better Than 0.015 μsec
- ★ Pulse Durations From 0.025 μsec to 1.1 sec
- ★ Time Delays From 1 μsec to 1.1 sec

Type 1391-B Pulse, Sweep, and Time-Delay Generator . . . $2025

Direct synchronizing pulse timed by the input signal.

Delayed synchronizing pulse accurately adjustable in time by delay generator. Built-in coincidence circuit for timing the delayed synchronizing pulse by externally generated pulses fed into the instrument.

Push-pull sawtooth voltage of sufficient amplitude to be applied to the deflection plates of oscilloscope for examining the generator's output pulses, or for use in driving auxiliary equipment.

Push-pull gating pulses with same duration as the sweep.

Positive or negative pulses with excellent shape characteristics, continuously adjustable in duration, amplitude, impedance level, and delay with respect to (a) the direct sync pulse and (b) the sweep.

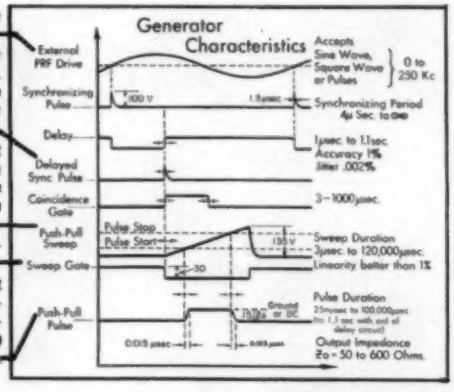

Write For Complete Information

GENERAL RADIO COMPANY

WEST CONCORD, MASSACHUSETTS

our 45th year in Electronics

NEW YORK, WOrth 4-2722 District Office in Ridgefield, N. J. WHitney 3-3140	CHICAGO Oak Park Village 8-9400	PHILADELPHIA Abington HAncock 4-7419	WASHINGTON, D.C. Silver Spring JUniper 5-1088	SAN FRANCISCO Los Altos WHitecliff 8-8233	LOS ANGELES Los Angeles HOllywood 9-6201	IN CANADA Toronto CHerry 6-2171

At The Ramo-Wooldridge Laboratories... integrated programs of research & development of electronic systems and components.

The new Ramo-Wooldridge Laboratories in Canoga Park provide an environment for creative work in an academic setting. Here, scientists and engineers seek solutions to the technological problems of today. The Ramo-Wooldridge research and development philosophy places major emphasis on the imaginative contributions of the members of the technical staff. ■ There are outstanding opportunities for scientists and engineers. *Write* Dr. Richard C. Potter, Head, Technical Staff Development, Department 16-D.

THE RAMO-WOOLDRIDGE LABORATORIES

A DIVISION OF THOMPSON RAMO WOOLDRIDGE INC.

8433 FALLBROOK AVENUE, CANOGA PARK, CALIFORNIA

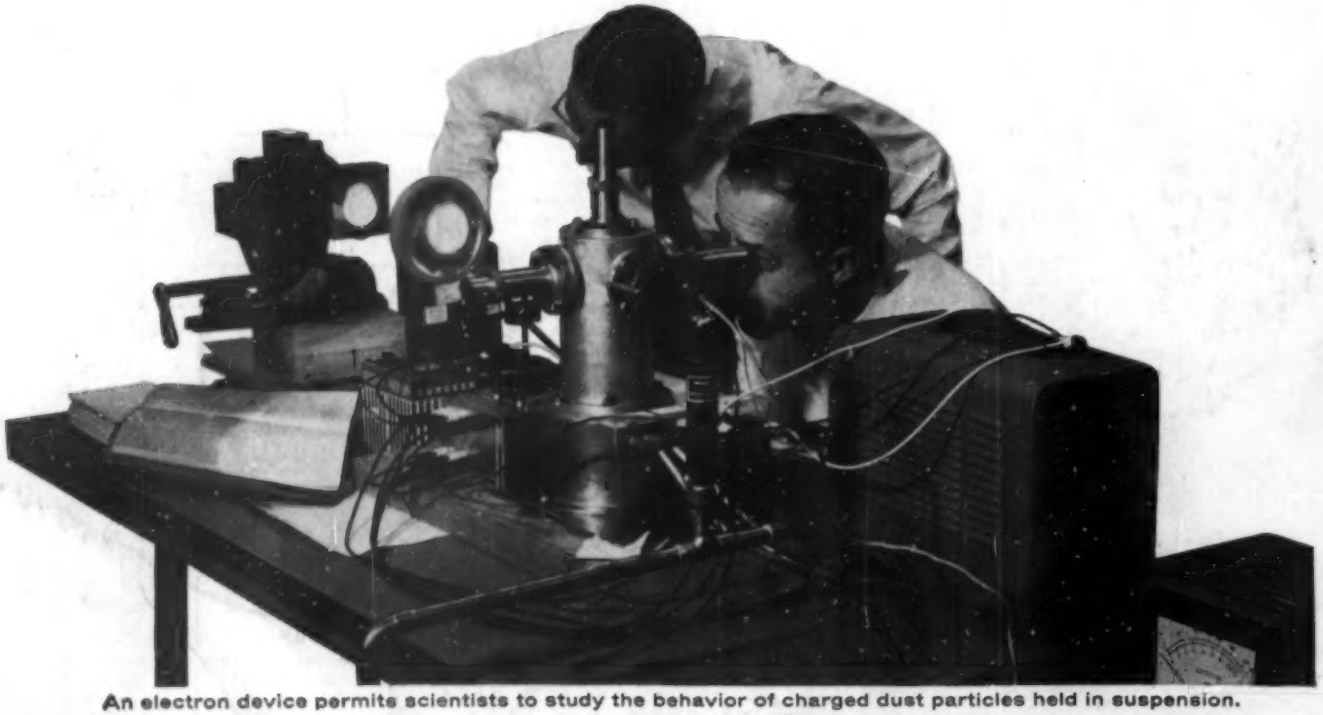

An electron device permits scientists to study the behavior of charged dust particles held in suspension.